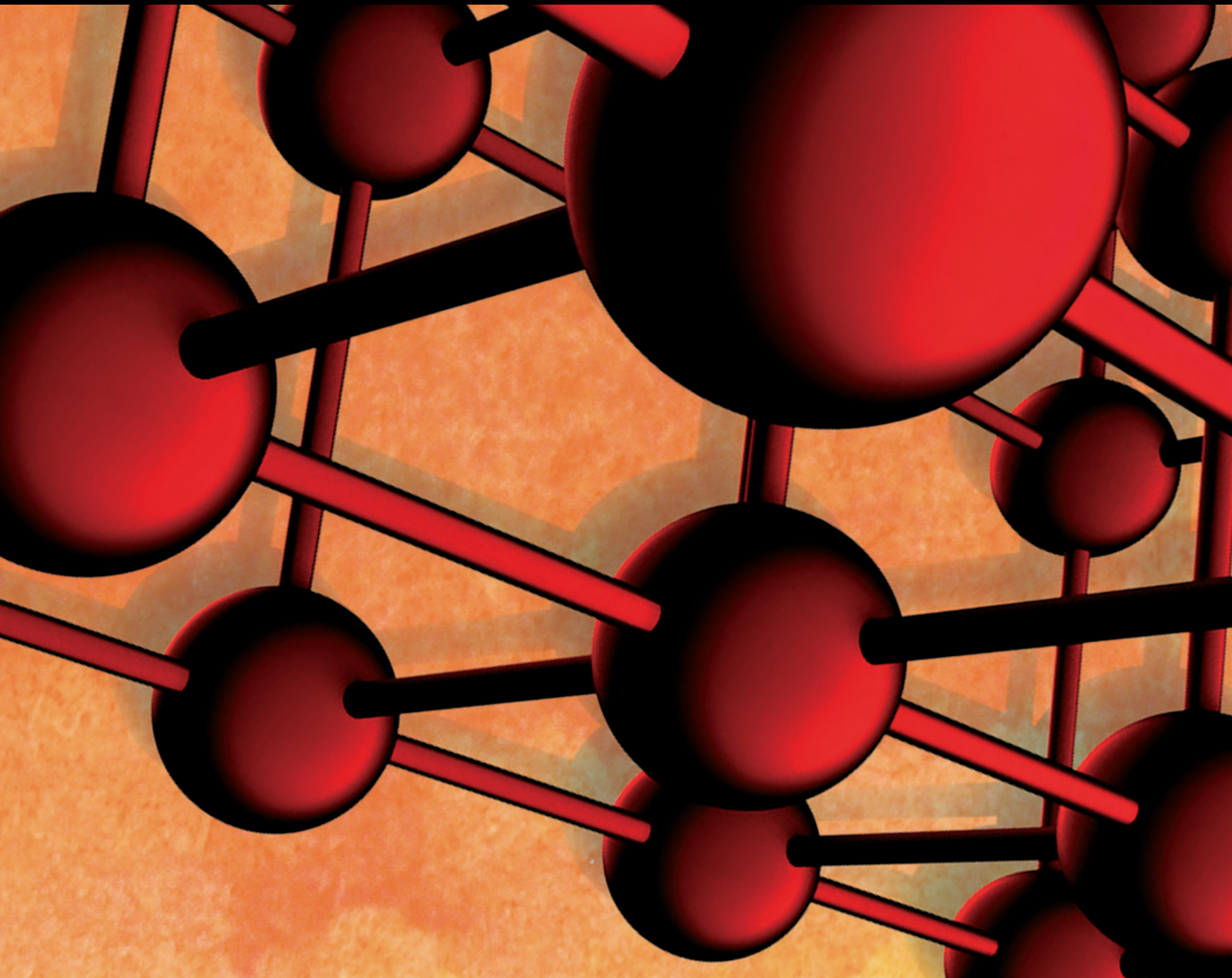


# Innovation, Sustainability and Resilience of Asphalt Pavement Materials

Lead Guest Editor: Meng Guo

Guest Editors: Zhen Leng and Dawei Wang





---

# **Innovation, Sustainability and Resilience of Asphalt Pavement Materials**

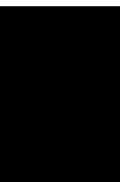
Advances in Materials Science and Engineering

---

**Innovation, Sustainability and  
Resilience of Asphalt Pavement  
Materials**

Lead Guest Editor: Meng Guo

Guest Editors: Zhen Leng and Dawei Wang




---

Copyright © 2021 Hindawi Limited. All rights reserved.

This is a special issue published in "Advances in Materials Science and Engineering." All articles are open access articles distributed under the Creative Commons Attribution License, which permits unrestricted use, distribution, and reproduction in any medium, provided the original work is properly cited.

# Chief Editor



















Amit Bandyopadhyay , USA

## Associate Editors

Vamsi Balla , India  
Mitun Das , USA  
Sandip Harimkar, USA  
Ravi Kumar , India  
Peter Majewski , Australia  
Enzo Martinelli , Italy  
Luigi Nicolais , Italy  
Carlos R. Rambo , Brazil  
Michael J. Schütze , Germany  
Kohji Tashiro , Japan  
Zhonghua Yao , China  
Dongdong Yuan , China  
Wei Zhou , China

## Academic Editors

Antonio Abate , Germany  
Hany Abdo , Saudi Arabia  
H.P.S. Abdul Khalil , Malaysia  
Ismael Alejandro Aguayo Villarreal , Mexico  
Sheraz Ahmad , Pakistan  
Michael Aizenshtein, Israel  
Jarir Aktaa, Germany  
Bandar AlMangour, Saudi Arabia  
Huaming An, China  
Alicia Esther Ares , Argentina  
Siva Avudaiappan , Chile  
Habib Awais , Pakistan  
NEERAJ KUMAR BHOI, India  
Enrico Babilio , Italy  
Renal Backov, France  
M Bahubalendruni , India  
Sudharsan Balasubramanian , India  
Markus Bambach, Germany  
Irene Bavasso , Italy  
Stefano Bellucci , Italy  
Brahim Benmokrane, Canada  
Jean-Michel Bergheau , France  
Guillaume Bernard-Granger, France  
Giovanni Berselli, Italy  
Patrice Berthod , France  
Michele Bianchi , Italy  
Hugo C. Biscaia , Portugal

Antonio Boccaccio, Italy  
Mohamed Bououdina , Saudi Arabia  
Gianlorenzo Bussetti , Italy  
Antonio Caggiano , Germany  
Marco Cannas , Italy  
Qi Cao, China  
Gianfranco Carotenuto , Italy  
Paolo Andrea Carraro , Italy  
Jose Cesar de Sa , Portugal  
Wen-Shao Chang , United Kingdom  
Qian Chen , China  
Francisco Chinesta , France  
Er-Yuan Chuang , Taiwan  
Francesco Colangelo, Italy  
María Criado , Spain  
Enrique Cuan-Urquizo , Mexico  
Lucas Da Silva , Portugal  
Angela De Bonis , Italy  
Abílio De Jesus , Portugal  
José António Fonseca De Oliveira  
Correia , Portugal  
Ismail Demir , Turkey  
Luigi Di Benedetto , Italy  
Maria Laura Di Lorenzo, Italy  
Marisa Di Sabatino, Norway  
Luigi Di Sarno, Italy  
Ana María Díez-Pascual , Spain  
Guru P. Dinda , USA  
Hongbiao Dong, China  
Mingdong Dong , Denmark  
Frederic Dumur , France  
Stanislaw Dymek, Poland  
Kaveh Edalati , Japan  
Philip Eisenlohr , USA  
Luis Evangelista , Norway  
Michele Fedel , Italy  
Francisco Javier Fernández Fernández , Spain  
Spain  
Isabel J. Ferrer , Spain  
Massimo Fresta, Italy  
Samia Gad , Egypt  
Pasquale Gallo , Finland  
Sharanabasava Ganachari, India  
Santiago Garcia-Granda , Spain  
Carlos Garcia-Mateo , Spain

Achraf Ghorbal , Tunisia  
Georgios I. Giannopoulos , Greece  
Ivan Giorgio , Italy  
Andrea Grilli , Italy  
Vincenzo Guarino , Italy  
Daniel Guay, Canada  
Jenő Gubicza , Hungary  
Xuchun Gui , China  
Benoit Guiffard , France  
Zhixing Guo, China  
Ivan Gutierrez-Urrutia , Japan  
Weiwei Han , Republic of Korea  
Simo-Pekka Hannula, Finland  
A. M. Hassan , Egypt  
Akbar Heidarzadeh, Iran  
Yi Huang , United Kingdom  
Joshua Ighalo, Nigeria  
Saliha Ilican , Turkey  
Md Mainul Islam , Australia  
Ilia Ivanov , USA  
Jijo James , India  
Hafsa Jamshaid , Pakistan  
Hom Kandel , USA  
Kenji Kaneko, Japan  
Rajesh Kannan A , Democratic People's  
Republic of Korea  
Mehran Khan , Hong Kong  
Akihiko Kimura, Japan  
Ling B. Kong , Singapore  
Pramod Koshy, Australia  
Hongchao Kou , China  
Alexander Kromka, Czech Republic  
Abhinay Kumar, India  
Avvaru Praveen Kumar , Ethiopia  
Sachin Kumar, India  
Paweł Kłosowski , Poland  
Wing-Fu Lai , Hong Kong  
Luciano Lamberti, Italy  
Fulvio Lavecchia , Italy  
Laurent Lebrun , France  
Joon-Hyung Lee , Republic of Korea  
Cristina Leonelli, Italy  
Chenggao Li , China  
Rongrong Li , China  
Yuanshi Li, Canada

Guang-xing Liang , China  
Barbara Liguori , Italy  
Jun Liu , China  
Yunqi Liu, China  
Rong Lu, China  
Zhiping Luo , USA  
Fernando Lusquiños , Spain  
Himadri Majumder , India  
Dimitrios E. Manolakos , Greece  
Necmettin Maraşlı , Turkey  
Alessandro Martucci , Italy  
Roshan Mayadunne , Australia  
Mamoun Medraj , Canada  
Shazim A. Memon , Kazakhstan  
Pratima Meshram , India  
Mohsen Mhadhbi , Tunisia  
Philippe Miele, France  
Andrey E. Miroshnichenko, Australia  
Ajay Kumar Mishra , South Africa  
Hossein Moayedi , Vietnam  
Dhanesh G. Mohan , United Kingdom  
Sakar Mohan , India  
Namdev More, USA  
Tahir Muhmood , China  
Faisal Mukhtar , Pakistan  
Dr. Tauseef Munawar , Pakistan  
Roger Narayan , USA  
Saleem Nasir , Pakistan  
Elango Natarajan, Malaysia  
Rufino M. Navarro, Spain  
Miguel Navarro-Cia , United Kingdom  
Behzad Nematollahi , Australia  
Peter Niemz, Switzerland  
Hiroschi Noguchi, Japan  
Dariusz Oleszak , Poland  
Laurent Orgéas , France  
Togay Ozbakkaloglu, United Kingdom  
Marián Palcut , Slovakia  
Davide Palumbo , Italy  
Gianfranco Palumbo , Italy  
Murlidhar Patel, India  
Zbyšek Pavlík , Czech Republic  
Alessandro Pegoretti , Italy  
Gianluca Percoco , Italy  
Andrea Petrella, Italy

Claudio Pettinari , Italy  
Giorgio Pia , Italy  
Candido Fabrizio Pirri, Italy  
Marinos Pitsikalis , Greece  
Alain Portavoce , France  
Simon C. Potter, Canada  
Ulrich Prah, Germany  
Veena Ragupathi , India  
Kawaljit Singh Randhawa , India  
Baskaran Rangasamy , Zambia  
Paulo Reis , Portugal  
Hilda E. Reynel-Avila , Mexico  
Yuri Ribakov , Israel  
Aniello Riccio , Italy  
Anna Richelli , Italy  
Antonio Riveiro , Spain  
Marco Rossi , Italy  
Fernando Rubio-Marcos , Spain  
Francesco Ruffino , Italy  
Giuseppe Ruta , Italy  
Sachin Salunkhe , India  
P Sangeetha , India  
Carlo Santulli, Italy  
Fabrizio Sarasini , Italy  
Senthil Kumaran Selvaraj , India  
Raffaele Sepe , Italy  
Aabid H Shalla, India  
Poorva Sharma , China  
Mercedes Solla, Spain  
Tushar Sonar , Russia  
Donato Sorgente , Italy  
Charles C. Sorrell , Australia  
Damien Soulat , France  
Adolfo Speghini , Italy  
Antonino Squillace , Italy  
Koichi Sugimoto, Japan  
Jirapornchai Suksaeree , Thailand  
Baozhong Sun, China  
Sam-Shajing Sun , USA  
Xiaolong Sun, China  
Yongding Tian , China  
Hao Tong, China  
Achim Trampert, Germany  
Tomasz Trzepieciński , Poland  
Kavimani V , India

Matjaz Valant , Slovenia  
Mostafa Vamegh, Iran  
Lijing Wang , Australia  
Jörg M. K. Wiezorek , USA  
Guosong Wu, China  
Junhui Xiao , China  
Guoqiang Xie , China  
YASHPAL YASHPAL, India  
Anil Singh Yadav , India  
Yee-wen Yen, Taiwan  
Hao Yi , China  
Wenbin Yi, China  
Tetsu Yonezawa, Japan  
Hiroshi Yoshihara , Japan  
Bin Yu , China  
Rahadian Zainul , Indonesia  
Lenka Zaji#c#kova# , Czech Republic  
Zhigang Zang , China  
Michele Zappalorto , Italy  
Gang Zhang, Singapore  
Jinghuai Zhang, China  
Zengping Zhang, China  
You Zhou , Japan  
Robert Černý , Czech Republic

# Contents

## **Evaluation of the Physical and Adhesive Properties of Natural Weathering Asphalt**

Yanzhu Wang , Xudong Wang , Xingye Zhou, Guang Yang, and Lei Zhang





Research Article (10 pages), Article ID 5783256, Volume 2021 (2021)

## **Investigation on Properties of Cement Bitumen Emulsion Mortars (CBEM) in Consideration of Emulsifier Types**

Zhuoran Liu, Jinyang Huo, and Zhenjun Wang 

Research Article (10 pages), Article ID 4820938, Volume 2020 (2020)

## **High-Temperature Performance of Asphalt Mixtures: Preliminary Analysis for the Standard Technical Index Based on Gray Relational Analysis Method**

Jian Xu , Yan Gong , Li-Biao Chen, Tao Ma, Jun-Cheng Zeng , Er-Hu Yan , and Guang-Shu Xiao


Research Article (13 pages), Article ID 5818036, Volume 2020 (2020)

## **Study on the Construction Performance of Zeolite Asphalt Mixture Based on Macro-Micro Scale**

Zhuolin Li , Junda Ren , Jianping Zhu , Wei Li , Xingsheng Fu , and Liying Yang 


Research Article (21 pages), Article ID 4137321, Volume 2020 (2020)

## **Development and Evaluation of Solvent-Based Cold Patching Asphalt Mixture Based on Multiscale**

Shuolei Huang , Junda Ren, Mingguang Li, Zhuolin Li, and Shuiwen Zhou

Research Article (16 pages), Article ID 1984972, Volume 2020 (2020)

## **Investigating Automobile Passengers' Comfort and Safety on Scenic Road Using Sideway Force Coefficient**

Ronghua Wang, Xingliang Liu , and Feijie Han

Research Article (13 pages), Article ID 8327645, Volume 2020 (2020)

## **Research on Design Indicators for Graded Crushed Stone Mixture Based on Vibration Molding Method**

Li-biao Chen, Er-hu Yan , Jian Xu, Tao Ma, Jun-cheng Zeng, and Yan Gong



Research Article (9 pages), Article ID 5179563, Volume 2020 (2020)

## **Hybrid Modification of Stone Mastic Asphalt with Cellulose and Basalt Fiber**

You Huang , Zhaohui Liu, Li Liu , Yunbao Zhang, and Qingxiang Xu





Research Article (11 pages), Article ID 5671256, Volume 2020 (2020)

## **Evaluating the Physical and Rheological Properties of Rejuvenated Styrene-Butadiene-Styrene-Modified Asphalt Binders**

Xiaobing Chen , Juntian Wang, Xiaorui Zhang , Han Liu, Jinhu Tong, and Ronglong Zhao

Research Article (14 pages), Article ID 4513824, Volume 2020 (2020)

## **Electrolytic Manganese Residue-Modified Asphalt Performance Test and Micromechanism Analysis**

Tao Fu , Bin Pang, Haoxu Li , Junlin Liang , and Huiming Bao 




Research Article (12 pages), Article ID 9014649, Volume 2020 (2020)





**Investigating the Fatigue Characteristics of Large Stone Asphalt Mixtures Based on the Disturbed State Concept**

Jianhui Wei , Tao Fu, Yongjun Meng , and Chengming Xiao  
Research Article (10 pages), Article ID 3873174, Volume 2020 (2020)





**Modeling of Surface Drainage during the Service Life of Asphalt Pavements Showing Long-Term Rutting: A Modular Hydromechanical Approach**

Stefan Alber , Barbara Schuck, Wolfram Ressel, Ronny Behnke , Gustavo Canon Falla, Michael Kaliske , Sabine Leischner, and Frohmut Wellner  
Research Article (15 pages), Article ID 8793652, Volume 2020 (2020)


**Research on Rheological Properties of High-Percentage Artificial RAP Binder with WMA Additives**

Weiyang Wang , Songchang Huang, Yongchun Qin, Yiren Sun, Rui Dong, and Jingyun Chen   
Research Article (24 pages), Article ID 1238378, Volume 2020 (2020)

**Effect of Used Motor Oil and Bitumen as Additive on the Permeability and Mechanical Properties of Low Plastic Soil**

Kamran Iqbal , Chengshun Xu, Hassan Nasir , Muhammad Alam , Asim Farooq , and Edward J. Williams  
Research Article (10 pages), Article ID 1360197, Volume 2020 (2020)

**Research of Deicing and Melting Snow on Airport Asphalt Pavement by Carbon Fiber Heating Wire**

Xin Su, Yong Lai , Yan Liu, Daoxun Ma, and Peng Wang  
Research Article (6 pages), Article ID 5209350, Volume 2020 (2020)

**Crude Oil Source Identification of Asphalt via ATR-FTIR Approach Combined with Multivariate Statistical Analysis**

Ruibo Ren, Wenmiao Fan, Pinhui Zhao , Hao Zhou, Weikun Meng, and Ping Ji  
Research Article (13 pages), Article ID 2025072, Volume 2020 (2020)




**Micromechanical Prediction Model of Viscoelastic Properties for Asphalt Mastic Based on Morphologically Representative Pattern Approach**

Zhichen Wang, Naisheng Guo , Xu Yang , and Shuang Wang  
Research Article (12 pages), Article ID 7915140, Volume 2020 (2020)

**Influence of Antistripping Additives and Rejuvenators on Healing Performance of Moisture-Damaged HMA**

Dae-Wook Park , Tam Minh Phan , and Yeong-Min Kim   
Research Article (12 pages), Article ID 9260978, Volume 2020 (2020)



**Effects of Surfactant Warm-Mix Additives on the Rheological Properties of High-Viscosity Asphalt**

Jingtao Shi , Weiyu Fan , Yi Lin , Pinhui Zhao , and Jian Ouyang   
Research Article (11 pages), Article ID 6506938, Volume 2020 (2020)

## Contents

---

### **Mechanism and Rheological Properties of High-Modulus Asphalt**

Xinquan Xu , Guilin Lu, Jun Yang , and Xinhai Liu

Research Article (13 pages), Article ID 8795429, Volume 2020 (2020)

## Research Article

# Evaluation of the Physical and Adhesive Properties of Natural Weathering Asphalt

Yanzhu Wang <sup>1</sup>, Xudong Wang <sup>1,2</sup>, Xingye Zhou,<sup>2</sup> Guang Yang,<sup>1</sup> and Lei Zhang<sup>2</sup>

<sup>1</sup>School of Transportation Science and Engineering, Harbin Institute of Technology, Harbin 150090, China

<sup>2</sup>Research Institute of Highway, Ministry of Transport, Beijing 100088, China

Correspondence should be addressed to Xudong Wang; [xd.wang@rioh.cn](mailto:xd.wang@rioh.cn)

Received 23 July 2020; Revised 5 November 2020; Accepted 16 December 2020; Published 2 January 2021

Academic Editor: Meng Guo

Copyright © 2021 Yanzhu Wang et al. This is an open access article distributed under the Creative Commons Attribution License, which permits unrestricted use, distribution, and reproduction in any medium, provided the original work is properly cited.

Asphalt suffers from a series of aging processes in the natural environment. This is a significant factor in asphalt pavement diseases. Research of the properties of the decay processes in the natural weathering of asphalt will be helpful in distinguishing the characteristics of the various types of asphalt and in the selection of pavement materials. Neat asphalt A70, a styrene-butadiene-styrene- (SBS-) modified asphalt, and crumb-rubber-modified asphalt AR are exposed to outdoor conditions to weather naturally. This process is traced by testing the basic physical properties and the surface free energy of asphalts, using the sessile drop method. Results illustrate that the basic physical properties of asphalt change significantly during the natural weathering process and that the rubber asphalt has the superior aging resistance, while the neat asphalt A70 has a high aging susceptibility. Furthermore, the presence of the SBS and rubber-powder modifiers transforms the change trend of the surface free energy of neat asphalt. The adhesion work between aggregate and asphalt can be used to quantitatively evaluate the adhesive properties between them. Meanwhile, the presence of moisture between the asphalt and aggregate changes cohesive failure into adhesive failure.

## 1. Introduction

In the natural environment, asphalt will undergo complex physical and chemical reactions under the influence of sunlight, oxygen, and heat and lead to the deterioration of asphalt performance [1–3]. The adhesion failure of asphalt that manifests as the peeling off from the aggregate surface (caused by the presence of moisture) is another important factor that affects the durability of the asphalt pavement [4–6]. Thus, understanding the physical and adhesive properties of the naturally weathering asphalt is crucial.

Currently, research on the simulation of the aging of asphalt is widespread. Most of this research is carried out in laboratories. Aging methods include the thin-film oven test (TFOT), the rolling TFOT, and the pressurized aging vessel [7]. These standard laboratory-aging methods are the short-term and long-term aging simulations of asphalt [8–11]. To simulate natural weathering conditions optimally, researchers evaluate the performance of asphalt after accelerated weather aging. An asphalt sample with a certain

thickness is irradiated for a period of time at a designated temperature and with an irradiance of ultraviolet radiation intensity [12–14]. However, the methods of the laboratory simulation of the asphalt sample still cannot reflect the natural environment fully. Thus, to study the real situation of asphalt aging in the natural environment, some researchers are exposing modified asphalts to outdoor conditions to subject them to natural weathering for one year at most [2, 15, 16]. This is insufficient time for achieving a simulation of the entire service life of asphalt exposed to outdoor conditions.

Asphalt-aging research aims mainly to establish performance indicators to quantify the aging-degree of asphalt in order to improve predictions of the properties of asphalt. At present, the traditional evaluation indexes of asphalt-aging performance include basic physical properties (e.g., penetration, softening point, and ductility) and rheological indicators (e.g., viscosity, complex modulus ( $G^*$ ), and phase angle ( $\delta$ )) [7]. Many modern test methods, such as the atom force microscope (AFM), have been applied. AFM has

the potential to measure adhesion differences among micron-sized domains in asphalt binders [17]. Yu et al. evaluated the adhesive property of aging asphalt binders quantitatively by using the AFM method [18]. Research shows that asphalt pavement performance is related to the cohesive and adhesive bonding within the asphalt-aggregate system, and the cohesive-adhesive bonding is related to the surface free energy characteristics of the system [19]. However, studies of the changes of cohesive and adhesive properties of asphalt after natural weathering (based on surface free energy theory) are few.

Generally, traditional and advanced performance indicators can realize the evaluation and prediction of asphalt-aging performance by standard laboratory aging methods and by self-designed aging methods. However, research on the natural weathering of asphalt in regard to aging methods is still insufficient, and the allowed natural-aging times are not long enough. However, studies of the cohesive and adhesive properties of asphalt after natural weathering (based on surface free energy theory) are significant.

To evaluate the physical and adhesive properties of naturally weathered asphalt, three kinds of asphalt are exposed to natural weathering. Every year, samples are retrieved for performance evaluation. At this point, they have been aging for 4 years. The performance indicators include penetration, softening point, ductility, and viscosity. The surface free energy of the asphalt samples is investigated at various aging times.

## 2. Materials and Experiment Design

**2.1. Materials.** Neat asphalt A70 with penetration grade 70 and SBS-modified asphalt (SBSMA) were used in this study. Three kinds of rubber asphalt were made, using the “wet process.” The performance indexes of rubber asphalt are shown in Table 1. According to the “Specification for Asphalt Rubber Pavement and Construction” provisions in China, the elastic recovery rate shall not be less than 70% when the softening point is greater than 60°C. Finally, rubber asphalt with 22 wt. % crumb-rubber-powder content was used. The PG grades of A70, SBSMA, and AR-22% were PG64-22, PG82-22, and PG82-28, respectively. The aggregates used were limestone, basalt, and granite.

**2.2. Aging Procedure.** A certain amount of asphalt was weighed and poured on folded and fixed-size silver paper. Then, the silver paper with its asphalt load was placed on a glass plate and then into the oven. The glass plate was adjusted with a level ruler to be horizontal. The oven temperature was controlled at 100°C and 135°C, so that the base and modified asphalts distribute evenly, such that the thickness of the asphalt film is 2 mm. Finally, all the samples were exposed to outdoor conditions—in this case, to the weather in Beijing City, a temperate-zone monsoon climate area—to age in the natural environment (see Figure 1). The weather-aging was carried out over 4 years, from January 2016 to January 2020. The asphalts were retrieved for testing at yearly intervals.

### 2.3. Characterization Methods

**2.3.1. Basic Performance Test.** Penetration, softening point, and ductility were measured according to ASTM D5, ASTM D36, and ASTM D113, respectively. Viscosity was obtained by using a Brookfield viscometer. Approximately 8.5 g of sample was placed into a Brookfield viscometer test tube and tested with a spindle rotating at 20 rpm, for neat asphalt and SBSMA (ASTM D4402) [7]. The torque was controlled at 50% in the viscosity test for AR, and the stretching speed in the ductility test for AR asphalt was 1 cm/min, in accordance with the provisions of the “Guidelines for Design and Construction of Asphalt Rubber and Mixture in Beijing” (2006).

**2.3.2. Contact Angle Test.** To calculate the surface energy of asphalt, the contact angle of the standard liquid with known surface-energy parameters on the asphalt surface must be measured. In this research, the contact angle was measured by the sessile drop method on a drop-shape analysis instrument made in Germany. The sessile drop method schematic is shown in Figure 2.

According to the theory of van Oss et al., the total surface free energy can be divided into two components, namely, the nonpolar Lifshitz–van der Waals (LW) component and the polar Lewis acid-base (AB) component [20].

$$\gamma = \gamma^d + \gamma^p, \quad (1)$$

where  $\gamma$  is the surface free energy of the solid material,  $\gamma^d$  is the dispersive component of surface free energy, and  $\gamma^p$  is the polarity component of the surface free energy.

The contact angle ( $\theta$ ) can be measured when a liquid ( $L$ ) is wetted on a solid ( $S$ ) surface, and the interaction energy between  $L$  and  $S$  can be described by Young’s equation as follows [21, 22]:

$$\gamma_L \cos \theta = \gamma_S - \gamma_{SL}, \quad (2)$$

where  $\gamma_L$  is the surface energy (or surface tension) of the liquid,  $\gamma_S$  is the surface energy of the solid, and  $\gamma_{SL}$  is the interfacial tension between  $L$  and  $S$ .

According to the theory of interfacial tension, the L-S interface free energy can be expressed as follows [23, 24]:

$$\gamma_{SL} = \gamma_S + \gamma_L - 2\sqrt{\gamma_S^d \gamma_L^d} - 2\sqrt{\gamma_S^p \gamma_L^p}, \quad (3)$$

where  $\gamma_S^d$  is the dispersive component of  $S$  surface free energy,  $\gamma_S^p$  is the polarity component of  $S$  surface free energy,  $\gamma_L^d$  is the dispersive component of  $L$  surface free energy, and  $\gamma_L^p$  is the polarity component of  $L$  surface free energy.

Equation (4) can be obtained by combining equations (2) and (3) as follows:

$$\gamma_L (1 + \cos \theta) = 2\sqrt{\gamma_S^d \gamma_L^d} + 2\sqrt{\gamma_S^p \gamma_L^p}. \quad (4)$$

The transposed form equation (4) is shown as follows:

TABLE 1: Performance indexes of AR at three contents.

Crumb-rubber content (%)	Penetration 0.1 mm (25°C)	Softening point °C	Elastic recovery rate %
22	55.1	64.7	74.0
20	55.8	62.1	68.9
18	56.5	60.2	65.2

TABLE 2: Surface free energy components of reagents [25].

Liquids	Surface free energy components (mJ·m <sup>-2</sup> )		
	$\gamma$	$\gamma^d$	$\gamma^p$
Distilled water	72.30	18.70	53.60
Formamide	59.00	39.40	19.60
Glycerol	65.20	28.30	36.90
Ethylene glycol	48.20	29.29	18.91



FIGURE 1: Aging environment conditions of natural weathering.

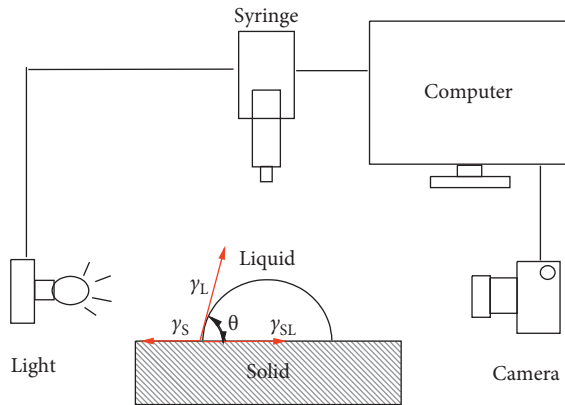


FIGURE 2: Schematic of contact angle measurement.

$$\frac{(1 + \cos \theta)\gamma_L}{2\sqrt{\gamma_L^d}} = \sqrt{\gamma_S^p} \sqrt{\frac{\gamma_L^p}{\gamma_L^d}} + \sqrt{\gamma_S^d} \quad (5)$$

According to equation (5), the surface energy parameters of S can be obtained by linear analysis when the surface energy parameters of more than two standard reagents are known, and the contact angle on the S surface is measured. In this study, the reagents used to test the surface free energy include distilled water, formamide, glycerol, and ethylene glycol. The surface free energy and components of the reagents are shown in Table 2.

### 3. Results and Discussion

**3.1. Basic Physical Properties.** The penetration index is used to evaluate the consistency of asphalt. The result can be

considered a property of the material, and its softness is described. Figure 3 shows the penetration of asphalts of different natural weathering times. The penetration index of asphalt decreases greatly after one year of natural weathering, and the attenuation rate slows down in the three following years. Table 3 presents the residual penetration ratio (penetration ratio after aging and before aging) of asphalt. Among the three kinds of asphalt, the penetration of A70 asphalt decreases the fastest. Its residual penetration ratio is only 39.4% and 18.5% after 1 year and after 4 years of natural weathering, respectively. The penetration of AR asphalt decreases the slowest, and its residual penetration ratio is 59.4% and 37.0% after 1 year and after 4 years of natural weathering, respectively. The penetration change rate of modified asphalt SBSMA falls between the two. The pavement will be prone to cracking when the penetration value of asphalt at 25°C drops below 20 (0.1 mm). The penetration value of A70 and SBSMA dropped below 20 in the second and third year, respectively. However, the value of AR is still higher than 20 after four years of natural weathering. This finding indicates that rubber asphalt AR is still soft and difficult to crack after weathering.

The softening point can be used to evaluate the asphalt's susceptibility to heat. Figure 4 presents the softening point of the asphalts with different natural weathering times. Comparison shows that, after the first year of aging, the softening point of asphalt increases the most and rises steadily in the subsequent aging process. The effect of natural weathering on the softening point of neat asphalt A70 is the most significant, but the effect on the modified asphalt is relatively small, and the change rate of the softening point of the two modified asphalts is close. After four years of natural weathering, the softening point change rates of A70, SBSMA, and AR are 48.8%, 22.3%, and 26.2% respectively, as Table 4 shows.

The rheological properties of asphalt are evaluated by viscosity indicator, and its viscosity at 160°C is studied. Figure 5 presents the viscosity of the asphalts with different natural weathering times. The viscosity (160°C) of asphalt increases gradually with the progress of aging. The viscosity change rate of rubber asphalt AR is smaller when compared to the other two kinds of asphalt, and the increase in viscosity after four years of aging is only 45.7%, whereas the viscosity increases of neat asphalt and SBS-modified asphalt reach as high as 432.4% and 372.9%, respectively, as shown in Table 5. This also shows that viscosity is the most sensitive property index of aging asphalt and that the rubber asphalt has superior aging resistance.

Asphalt ductility is an important performance indicator in evaluating crack resistance. Table 6 presents the ductility dates

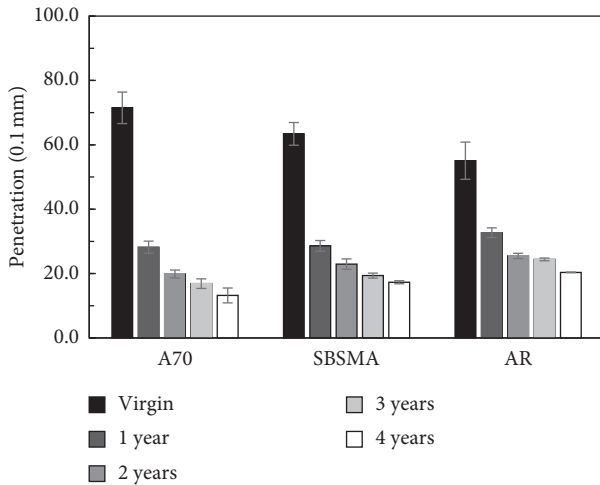


FIGURE 3: Penetration of asphalt with different weathering time.

TABLE 3: Residual penetration ratio of asphalt.

Asphalt	Residual penetration ratio (%)			
	1 year	2 years	3 years	4 years
A70	39.4	27.8	23.6	18.5
SBSMA	45.1	36.2	30.5	27.3
AR	59.4	46.2	44.3	37.0

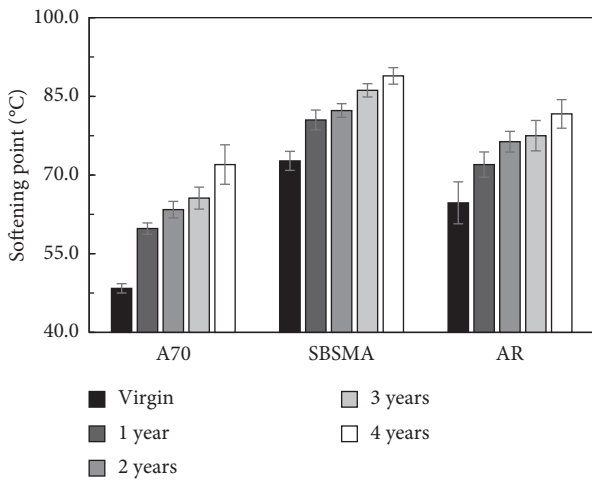


FIGURE 4: Softening point comparison of asphalts with different weathering times.

of the asphalt at various weathering times. The data in Table 5 show that brittle fracturing occurs in neat asphalt A70 and that in the modified asphalt SBSMA, the ductility test after natural-weather aging for 1 year. Ductility data are at value 0. The ductility dates of SBS-modified asphalt are 11.6 (10°C) and 0 (5°C) after weathering for 1 year. In subsequent experiments, when the test temperature is increased to 10°C, brittle fracture still occurs in asphalt A70 and SBSMA, while the ductility value of rubber asphalt continues to be measurable. This finding indicates that rubber asphalt has good ductility under natural weathering conditions.

TABLE 4: Change rate of softening point.

Asphalt	Change rate of softening point (%)			
	1 year	2 years	3 years	4 years
A70	23.6	31.0	35.5	48.8
SBSMA	10.7	13.2	18.5	22.3
AR	11.3	18.0	19.8	26.2

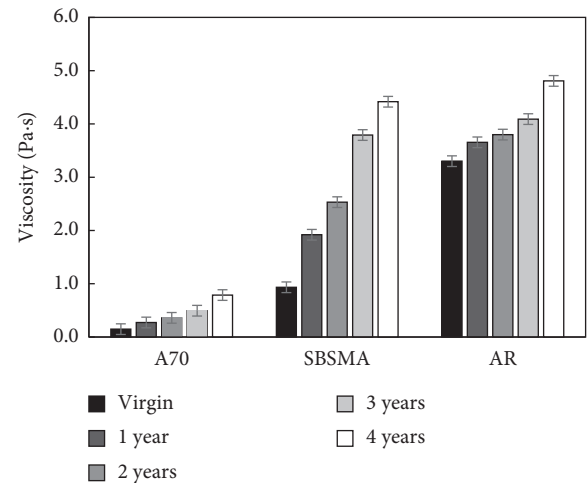


FIGURE 5: Viscosity of asphalt with different weathering time.

TABLE 5: Viscosity change rate of asphalt.

Asphalt	Viscosity increase rate (%)			
	1 year	2 years	3 years	4 years
A70	84.5	143.2	233.8	432.4
SBSMA	105.6	171.1	306.0	372.9
AR	10.7	15.1	23.9	45.7

The above analysis suggests that natural weathering has a significant impact on the basic physical properties of asphalt. After 4 years of aging, the penetration, softening point, viscosity, and ductility of asphalt exhibited different degrees of attenuation; the aging in the first year has the most significant effect. The performance of rubber asphalt is relatively stable, and base asphalt A70 has a high aging susceptibility.

Asphalt will suffer from a series of complex physicochemical reactions in the natural environment, such as volatilization, oxidation, and condensation. These reactions will happen in asphalt, and they make it even harder and more brittle. Oxidation plays an important role in asphalt performance. According to the research of Zhao et al. [16], when the asphalt is exposed to the natural environment, oxidation will occur and lead to an increase in its carbonyl and sulfoxide content. The change of the carbonyl index (CI) agrees with the obvious change in rheological properties. Meanwhile, the increase of carbonyl content is less in SBSMA, compared with that of neat asphalt. This indicates that SBSMA is, in terms of oxidation, the superior of neat asphalt in regard to the resistance to the aging process. The

TABLE 6: Ductility dates of asphalt.

Asphalt	Ductility (cm)						
	Virgin		1 year		2 years		4 years
	10°C	5°C	10°C	5°C	10°C	10°C	10°C
A70	37.3	—	0	—	0	0	0
SBSMA	48.7	28.5	11.6	0	0	0	0
AR	—	15.0	—	5.1	6.3	5.5	3.3

higher viscosity of SBSMA results in the slower flow of the asphalt, which reduces the chance of oxidation. This leads to a change in the physical properties of base asphalt, more so than in that of SBS-modified asphalt. The carbonyl content increase is lesser in crumb-rubber-modified asphalt than in SBSMA [2]. This indicates that the aging resistance of AR is superior to that of SBSMA. The change rates of carbonyl content are also in agreement with the change ratio of rheological properties. This is consistent with the research findings outlined in this paper. That is, rubber asphalt has superior aging resistance, and base asphalt A70 has high aging susceptibility.

**3.2. Cohesive and Adhesive Performance.** The contact angle values of asphalt with distilled water, formamide, glycerol, and ethylene glycol reagents are measured by sessile drop testing. The surface energy components of asphalt can be obtained by equation (5), a calculation of the relationship between contact angle and surface free energy. Table 7 lists the surface free energy components of the asphalt with various natural weathering times.

The comparative analysis of the data in Table 7 indicates that the surface free energy of base asphalt A70 increases with aging time, and the change rate reaches 16.9% after 4 years of aging. However, the surface free energy of SBSMA and AR first increases, reaches the maximum value after the second year of aging, and then decreases gradually in the next 2 years. Asphalt is composed mainly of nonpolar hydrocarbons that cause the dispersive component of asphalt to become far greater than the polarity component. However, the existence of polar chemical groups in asphalt, such as in some functional groups that include carbonyl (C=O) and sulfoxide (S=O), has an important role in asphalt performance. After natural weathering, the change characteristics of the polar component of surface energy are also significant. The polarity component of A70 asphalt decreases with aging time, whereas the polar component of the two other kinds of modified asphalt reaches the lowest value after 3 years of aging and increases in the 4th year. The influence of aging on asphalt composition and the relationship between asphalt chemical composition and surface free energy need further study.

TABLE 7: Surface free energy components of asphalt.

Asphalt	Aging time (year)	$\gamma$ (mJ·m <sup>-2</sup> )	$\gamma^d$ (mJ·m <sup>-2</sup> )	$\gamma^p$ (mJ·m <sup>-2</sup> )
A70	0	14.49	11.95	2.55
	1	16.17	14.69	1.48
	2	16.20	14.72	1.48
	3	16.52	15.35	1.17
	4	16.94	15.86	1.08
SBSMA	0	14.48	11.52	2.97
	1	15.68	13.80	1.87
	2	17.16	15.82	1.34
	3	17.00	15.88	1.12
	4	16.92	15.78	1.15
AR	0	15.63	13.60	2.03
	1	17.24	15.72	1.52
	2	17.44	16.17	1.27
	3	17.15	15.90	1.25
	4	16.77	15.16	1.61

The work of cohesion is defined as the energy consumed when a homogeneous material is divided into two new surfaces. Value can be calculated from the surface free energy on the following equation:

$$W_{\text{cohesion}} = 2\gamma_{\text{asphalt}} = 2\left(\gamma_{\text{asphalt}}^d + \gamma_{\text{asphalt}}^p\right), \quad (6)$$

where  $W_{\text{cohesion}}$  is the work of cohesion,  $\gamma_{\text{asphalt}}$  is the surface free energy of asphalt,  $\gamma_{\text{asphalt}}^d$  is the dispersive component, and  $\gamma_{\text{asphalt}}^p$  is the polarity component.

Figure 6 presents the work of asphalt cohesion with different natural weathering times. The work of cohesion has the same change trend as the surface free energy of asphalt. The cohesive work of base asphalt increases gradually with aging time, and the cohesive work of modified asphalt rises initially, reaches the maximum value after the second year of aging, and then decreases gradually in the next two years. The results show that the presence of SBS and rubber powder transforms the change trend of the cohesive work of the matrix asphalt. This phenomenon causes the modified asphalt to become more prone to cohesive failure after long-term natural weathering.

The work of adhesion can be observed in the decrease in free energy when a two-phase material is separated. In dry conditions, the value can be calculated from the surface free energy according to the following equation [25]:

$$\begin{aligned} W_{\text{adhesion,dry}} &= \gamma_{\text{asphalt}} + \gamma_{\text{aggregate}} - \gamma_{\text{asphalt-aggregate}} \\ &= 2\sqrt{\gamma_{\text{asphalt}}^d \gamma_{\text{aggregate}}^d} + 2\sqrt{\gamma_{\text{asphalt}}^p \gamma_{\text{aggregate}}^p}. \end{aligned} \quad (7)$$

Under water conditions, the work of adhesion between asphalt and aggregate can be formulated as follows [25]:

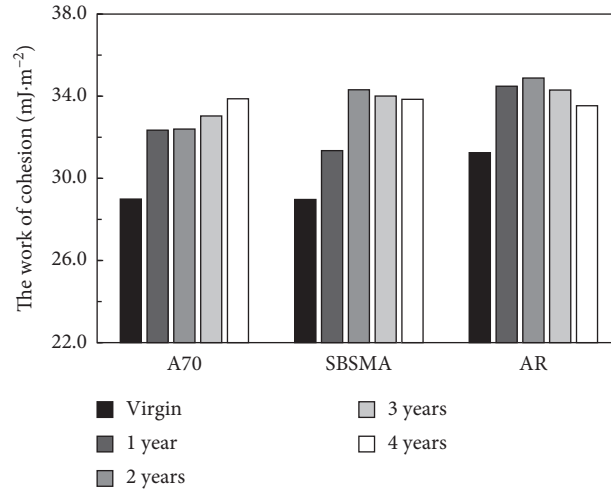


FIGURE 6: Work of cohesion of asphalt.

TABLE 8: Surface free energy components of aggregates.

Aggregates	$\gamma$ (mJ·m <sup>-2</sup> )	$\gamma^d$ (mJ·m <sup>-2</sup> )	$\gamma^p$ (mJ·m <sup>-2</sup> )
Limestone	47.1	24.3	22.8
Basalt	58.5	30.1	28.4
Granite	57.3	16.9	40.4

$$\begin{aligned}
 W_{\text{adhesion,wet}} &= \gamma_{\text{asphalt-water}} + \gamma_{\text{aggregate-water}} - \gamma_{\text{asphalt-aggregate}} \\
 &= 2 \left( \gamma_{\text{water}} + \sqrt{\gamma_{\text{aggregate}}^d \cdot \gamma_{\text{asphalt}}^d} + \sqrt{\gamma_{\text{aggregate}}^p \cdot \gamma_{\text{asphalt}}^p} \right. \\
 &\quad \left. - \sqrt{\gamma_{\text{asphalt}}^d \cdot \gamma_{\text{water}}^d} - \sqrt{\gamma_{\text{asphalt}}^p \cdot \gamma_{\text{water}}^p} - \sqrt{\gamma_{\text{aggregate}}^d \cdot \gamma_{\text{water}}^d} - \sqrt{\gamma_{\text{aggregate}}^p \cdot \gamma_{\text{water}}^p} \right), \quad (8)
 \end{aligned}$$

where  $W_{\text{adhesion,dry}}$  is the work of adhesion under dry conditions,  $W_{\text{adhesion,wet}}$  is the work of adhesion under water condition,  $\gamma_{\text{aggregate}}$  is the surface free energy of the aggregate,  $\gamma_{\text{aggregate}}^d$ ,  $\gamma_{\text{aggregate}}^p$  are the dispersive and polarity components of aggregate surface free energy,  $\gamma_{\text{asphalt-water}}$  is the interface of the free energy between asphalt and water,  $\gamma_{\text{aggregate-water}}$  is the interface of free energy between aggregate and water, and  $\gamma_{\text{asphalt-aggregate}}$  is the interface free energy between aggregate and asphalt.

The surface free energy components of aggregates are listed in Table 8. The surface free energy of limestone is lower than those of basalt and granite. The dispersion components of limestone and basalt are slightly larger than that of the polar component, whereas the dispersion component of granite is much smaller than that of the polar component. According to equations (7) and (8), the adhesion work of asphalt and aggregate under dry and water conditions can be obtained.

The work of adhesion between asphalt and aggregate under dry conditions is shown in Figure 7. The results in this study show that the surface energy of the aggregate is the main factor that affects adhesive performance. Under dry conditions, the work of adhesion between asphalt and basalt is maximal and that of granite is minimal. This result indicates that the adhesive property and antispalling ability of

asphalt and basalt are better than that of granite. Compared with the cohesion work of asphalt, as shown in Figure 6, the adhesion work of asphalt and the three kinds of aggregate is greater than that of asphalt cohesion work under dry conditions. This indicates that the cohesive failure of the asphalt mixture will occur preferentially when subjected to external forces under dry conditions.

However, with the deepening of the natural weathering of asphalt, the work of adhesion between asphalt and aggregate under dry conditions shows a decreasing trend, and the numerical value changes slightly. Nevertheless, its influence on the adhesion of granite is relatively significant. Natural weathering reduces the adhesive properties of asphalt.

The presence of moisture is an important factor in the acceleration of the water damage of the asphalt mixture. The work of adhesion between asphalt and aggregate under water conditions is shown in Figure 8. The adhesion work of asphalt and aggregate in a water environment is significantly reduced and is less than the cohesion work of asphalt in dry conditions. The presence of water leads to the poor adhesive strength of asphalt and aggregate. When moisture damage occurs, asphalt will tend to peel off from the surface of the aggregate, rather than fail cohesively. Comparing the three aggregates, the order of adhesion work, from the greatest to



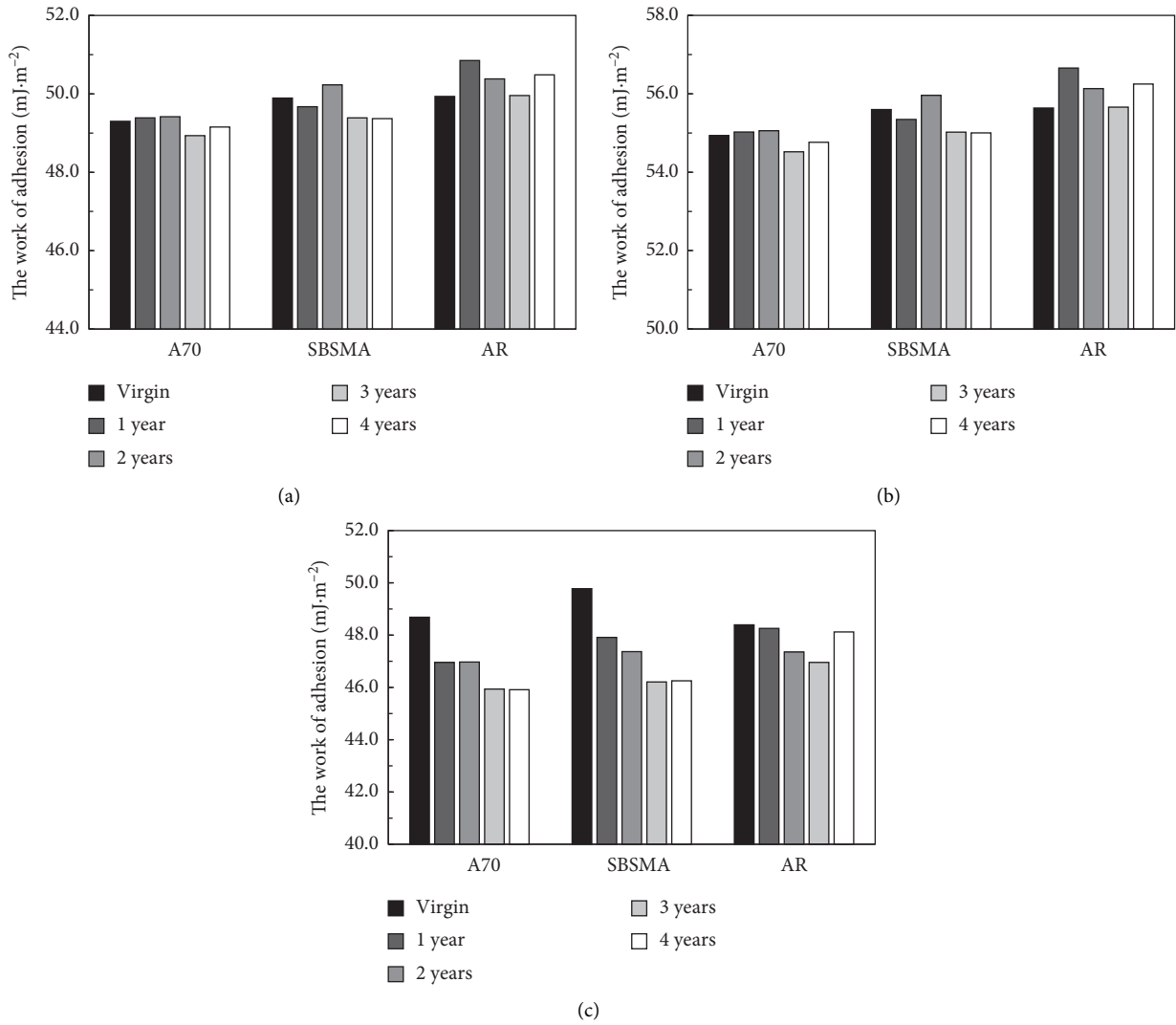


FIGURE 7: Work of adhesion between asphalt and (a) limestone, (b) basalt, and (c) granite under dry conditions.

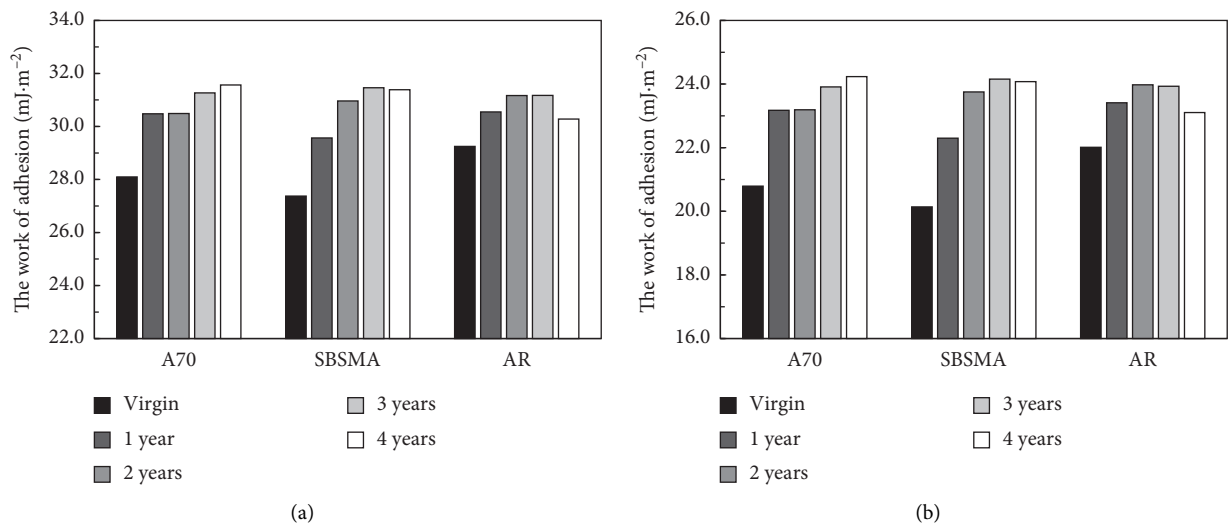


FIGURE 8: Continued.

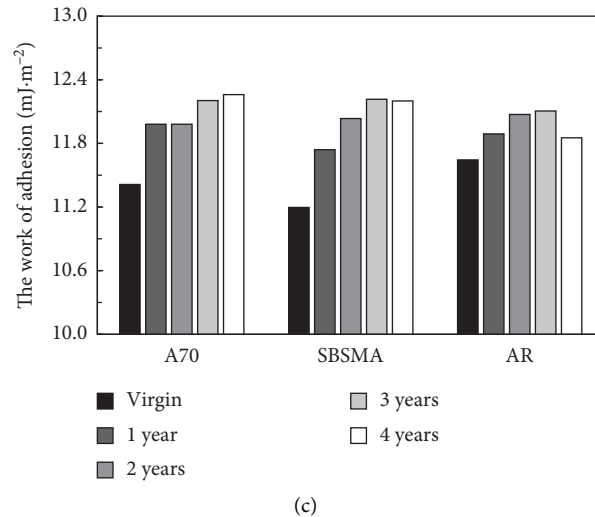


FIGURE 8: Work of adhesion with asphalt and (a) limestone, (b) basalt, and (c) granite under water condition.

the least, is limestone, basalt, and granite. Asphalt is a kind of weak acid material that easily adheres to alkaline aggregates. However, granite is an acid stone, and the adhesion work of granite and asphalt is less than those of the two other aggregates, regardless of whether water is present. Therefore, from the point of view of adhesion work theory, granite and asphalt have a poor adhesive performance.

Furthermore, under water conditions, the work of adhesion with neat asphalt A70 increases gradually with aging time and that of modified asphalt increases initially and then decreases after 4 years of natural aging. This observation is consistent with the change trend of the surface free energy of asphalt but different from that under dry conditions.

Asphalt will suffer from a series of complex physical and chemical reactions in the natural environment because of sunlight, heat, oxygen, and moisture. When the asphalt is exposed to the natural environment, some light components will volatilize. The components of asphalt will also change in sequence. That is, the aromatics will be converted into the resin, the resin will be transformed into asphaltene, and the asphaltene can be transformed also into a toluene insoluble substance, because of molecular association and condensation. Carbonyl sulfoxide and other compound groups will be produced because of the reaction of the functional groups to oxygen.

Overall, the molecular weight of asphalt increases. However, the aging process of modified asphalt is more complex. The interaction between SBS copolymer, which has a higher molecular weight, and neat asphalt causes the modified asphalt to have better oxidation resistance. The deepening of the aging of SBS will degrade into small molecular substances [16]. Similarly, in rubber asphalt, the rubber powder will pyrolyze, and the pyrolysis products will oxidize and condense, thereby making the aging mechanism of rubber asphalt more complex. This phenomenon may be the reason for the change trend of surface energy. Alternately, the adhesion work of modified asphalt differs from that of neat asphalt.

The above analysis of the adhesion of asphalt and the aggregates shows that the property of each aggregate is the main factor in adhesion, whereas the influences of asphalt properties and natural weathering are relatively mild. For granite, whether water is present or absent, adhesion to asphalt is less likely than it is for the two other aggregates. Compared with limestone, basalt has better adhesion under dry conditions, whereas limestone has better adhesion when water is present. The presence of moisture changes cohesive failure into adhesion failure between asphalt and aggregate. The adhesive performance indicator is relatively independent of basic physical properties and needs further research.

#### 4. Conclusions

The neat asphalt A70, SBS-modified asphalt SBSMA, and crumb-rubber-modified asphalt AR were exposed to outdoor conditions for four years, for natural weathering. The physical properties, surface free energy, and adhesive properties of asphalt were evaluated. The following conclusions can be drawn:

- (1) Natural weathering causes asphalt to harden and become brittle, thereby reducing penetrability and increasing softening points and viscosity. After four years of aging, the residual penetration ratio of asphalt is only 18.5%~37.0%, and the increased rates of the softening point reach 22.3%~48.8%. Meanwhile, aging in the first year has the most significant effect.
- (2) The rubber asphalt AR has superior aging resistance, and base asphalt A70 has a high aging susceptibility. The viscosity change rate of rubber asphalt AR is only 45.7% after four years of aging, whereas viscosity increases for neat asphalt and SBS-modified asphalt reaches as high as 432.4% and 372.9%. After four years of aging, the ductility value of rubber asphalt is still greater than 3 cm, while the other two kinds of asphalt have deteriorated to a state of brittle fracture.

- (3) The surface free energy of neat asphalt gradually increases with aging time, while that of modified asphalt increases initially, reaches the maximum value after the second year of aging, and then decreases gradually in the next two years. The presence of SBS and rubber powder transform the change trend of the surface free energy of neat asphalt.
- (4) The work of adhesion can evaluate adhesive properties effectively, and the surface free energy of aggregate and moisture are the main factors that affect adhesive performance. Under dry conditions, the adhesion work is about  $50 \text{ mJ}\cdot\text{m}^{-2}$ , but when moisture is present, the adhesion work of limestone, basalt, and granite decrease to about  $30 \text{ mJ}\cdot\text{m}^{-2}$ ,  $23 \text{ mJ}\cdot\text{m}^{-2}$ , and  $12 \text{ mJ}\cdot\text{m}^{-2}$ , respectively. These are less than the cohesion work of asphalt, which is about  $33 \text{ mJ}\cdot\text{m}^{-2}$ . This means that the presence of moisture changes cohesive failure into adhesive failure.

Asphalt will suffer from a series of complex physical and chemical reactions in the natural environment because of sunlight, heat, oxygen, and moisture. The change in asphalt chemical components should be studied further to discover the natural weathering law that should guide the production and application of asphalt.

## Data Availability

The data used to support the findings of this study are available from the corresponding author upon request.

## Conflicts of Interest

The authors declare that they have no conflicts of interest.

## Acknowledgments

This research was supported by the Special Fund of Chinese Central Government for Basic Scientific Research Operations in Commonweal Research Institutes (no.2018–9016).

## References

- [1] S. Xu, A. García, J. Su et al., “Self-healing asphalt review: from idea to practice,” *Advanced Materials Interfaces*, vol. 17, no. 17, 2018.
- [2] Q. Wang, S. Li, X. Wu, S. Wang, and C. Ouyang, “Weather aging resistance of different rubber modified asphalts,” *Construction and Building Materials*, vol. 106, no. 106, pp. 443–448, 2016.
- [3] W. D. Fernández-Gómez, H. A. Rondón Quintana, C. E. Daza, and F. A. Reyes Lizcano, “The effects of environmental aging on Colombian asphalts,” *Fuel*, vol. 115, no. 115, pp. 321–328, 2014.
- [4] R. Moraes, R. Velasquez, and H. Bahia, “Using bond strength and surface energy to estimate moisture resistance of asphalt-aggregate systems,” *Construction and Building Materials*, vol. 130, no. 130, pp. 156–170, 2017.
- [5] M. Koc and R. Bulut, “Assessment of a sessile drop device and a new testing approach measuring contact angles on aggregates and asphalt binders,” *Journal of Materials in Civil Engineering*, vol. 26, no. 3, pp. 391–398, 2014.
- [6] A. W. Hefer, A. Bhasin, and D. N. Little, “Bitumen surface energy characterization using a contact angle Approach,” *Journal of Materials in Civil Engineering*, vol. 18, no. 6, pp. 759–767, 2006.
- [7] F. Wang, Y. Xiao, P. Cui et al., “Correlation of asphalt performance indicators and aging Degrees: a review,” *Construction and Building Materials*, vol. 250, no. 250, Article ID 118824, 2020.
- [8] J. Lin, J. Hong, J. Liu, and S. Wu, “Investigation on physical and chemical parameters to predict long-term aging of asphalt binder,” *Construction and Building Materials*, vol. 122, no. 122, pp. 753–759, 2016.
- [9] D. Zhang, H. Zhang, and C. Shi, “Investigation of aging performance of SBS modified asphalt with various aging methods,” *Construction and Building Materials*, vol. 145, no. 145, pp. 445–451, 2017.
- [10] S.-J. Lee, S. N. Amirkhani, K. Shatanawi, and K. W. Kim, “Short-term aging characterization of asphalt binders using gel permeation chromatography and selected Superpave binder tests,” *Construction and Building Materials*, vol. 22, no. 11, pp. 2220–2227, 2008.
- [11] P. Li, Z. Ding, Z. Zhang, and D. Zhang, “Comparative evaluation of laboratory and field ageing of asphalt binder using a non-linear differential model,” *Road Materials and Pavement Design*, vol. 17, no. 2, pp. 434–445, 2016.
- [12] V. Mouillet, F. Farcas, E. Chailleux et al., “Evolution of bituminous mix behaviour submitted to UV rays in laboratory compared to field exposure,” *Materials and Structures*, vol. 47, no. 8, pp. 1287–1299, 2014.
- [13] J. Tu, J. Yuan, C. O. Bao et al., “Study on ultraviolet radiation aging of road asphalt and SBS modified asphalt,” *Petroleum Asphalt*, vol. 22, no. 6, pp. 43–47, 2008.
- [14] P. Xiao, M. P. Wu, and D. A. Jiang, “Study on properties of ultraviolet aged rubber asphalt,” *Journal of Nanjing University of Aeronautics & Astronautics*, vol. 45, no. 1, pp. 152–156, 2013.
- [15] C. Z. Zhu, H. L. Zhang, D. M. Zhang et al., “Influence of base asphalt and SBS modifier on the weathering aging behaviors of SBS modified asphalt,” *Journal of Materials In Civil Engineering*, vol. 30, no. 3, Article ID 04017306, 2018.
- [16] X. Zhao, S. Wang, Q. Wang, and H. Yao, “Rheological and structural evolution of SBS modified asphalts under natural weathering,” *Fuel*, vol. 184, no. 184, pp. 242–247, 2016.
- [17] X. Yu, N. A. Burnham, R. B. Mallick, and M. Tao, “A systematic AFM-based method to measure adhesion differences between micron-sized domains in asphalt binders,” *Fuel*, vol. 113, pp. 443–447, 2013.
- [18] J. Yu, Z. Dai, J. Shen, H. Zhu, and P. Shi, “Aging of asphalt binders from weathered asphalt mixtures compared with a SHRP process,” *Construction and Building Materials*, vol. 160, no. 160, pp. 475–486, 2018.
- [19] S.-H. Kim, J.-H. Jeong, and N. Kim, “Use of surface free energy properties to predict moisture damage potential of Asphalt concrete mixture in cyclic loading condition,” *KSCE Journal of Civil Engineering*, vol. 7, no. 4, pp. 381–387, 2003.
- [20] C. J. van Oss, M. K. Chaudhury, and R. J. Good, “Monopolar surfaces,” *Advances in Colloid and Interface Science*, vol. 28, no. 1, pp. 35–64, 1987.
- [21] D. Y. Kwok and A. W. Neumann, “Contact angle measurement and contact angle interpretation,” *Advances in Colloid and Interface Science*, vol. 81, no. 3, pp. 167–249, 1999.

- [22] C. J. Van, "Use of the combined Lifshitz-van der Waals and Lewis acid-base approaches in determining the apolar and polar contributions to surface and interfacial tensions and free energies," *Journal of Adhesion Science and Technology*, vol. 16, no. 6, pp. 669–677, 2002.
- [23] D. K. Owens and R. C. Wendt, "Estimation of the surface free energy of polymers," *Journal of Applied Polymer Science*, vol. 13, no. 13, pp. 1741–1747, 1969.
- [24] F. M. Fowkes, "Additivity of intermolecular forces at interfaces. I. determination of the contribution to surface and interfacial tensions of dispersion forces in various liquids<sup>1</sup>," *The Journal of Physical Chemistry*, vol. 67, no. 12, pp. 2538–2541, 1963.
- [25] Y. Tan and M. Guo, "Using surface free energy method to study the cohesion and adhesion of asphalt mastic," *Construction and Building Materials*, vol. 47, no. 47, pp. 254–260, 2013.

## Research Article

# Investigation on Properties of Cement Bitumen Emulsion Mortars (CBEM) in Consideration of Emulsifier Types

Zhuoran Liu,<sup>1</sup> Jinyang Huo,<sup>1</sup> and Zhenjun Wang<sup>1,2</sup> 

<sup>1</sup>School of Materials Science and Engineering, Chang'an University, Xi'an 710061, China

<sup>2</sup>Engineering Research Center of Pavement Materials, Ministry of Education of China, Chang'an University, Xi'an 710061, China

Correspondence should be addressed to Zhenjun Wang; zjwang@chd.edu.cn

Received 24 July 2020; Revised 28 October 2020; Accepted 16 November 2020; Published 23 November 2020

Academic Editor: Meng Guo

Copyright © 2020 Zhuoran Liu et al. This is an open access article distributed under the Creative Commons Attribution License, which permits unrestricted use, distribution, and reproduction in any medium, provided the original work is properly cited.

In order to investigate the influences of emulsifier types on properties of cement bitumen emulsion mortars (CBEM), anionic and cationic emulsifiers were used to prepare CBEM in this work. Influences of anionic and cationic bitumen emulsions on workability, mechanical properties, and viscoelastic property of CBEM were studied. The workability of CBEM was evaluated by fluidity and extensibility tests. The mechanical properties were assessed by compressive strength and flexural strength tests. XRD was used to analyze the phase before and after bitumen emulsion was added. The viscoelastic property was studied by a dynamic mechanical analyzer (DMA). The results show that CBEM prepared by cationic bitumen emulsion (CBE) has better workability. The mechanical properties of CBEM are negatively affected by bitumen emulsion. The impact on the compressive strength of CBEM prepared by CBE is higher. Bitumen emulsion can significantly improve the viscoelastic property of CBEM. With the increase of bitumen emulsion dosage, the loss factor of CBEM increases. The viscoelastic property at low frequency is better than that at high frequency. In contrast to CBEM prepared by CBE, CBEM prepared with anionic bitumen emulsion (ABE) possesses better viscoelastic property.

## 1. Introduction

Cement bitumen emulsion mortars (CBEM) are prepared by cement, bitumen emulsion, water, fine aggregate, and admixtures. The elasticity of bitumen materials and high strength of cement materials are combined in CBEM, which have been widely used in high-speed railway construction. Nowadays, more and more attentions are paid to CBEM [1–4]. Pure bitumen and bitumen emulsion have different influences on the property of CBEM [5]. Studies have shown that anionic bitumen emulsion (ABE) has retarding effect on hydration of cement in CBEM [6]. As the ratio of bitumen to cement increases, the setting time of the new bitumen emulsion cement paste increases [7]. Generally speaking, the cement hydration is insufficient when the content of the emulsifier is low, but the cement hydration is more complete when the content of the emulsifier is high. It is mainly due to the demulsification process of bitumen emulsion in CBEM [8]. Another study shows that the presence of the emulsifier

can accelerate the hydration of cement [9]. The demulsification process of bitumen emulsion can be studied and evaluated by ultraviolet spectroscopy [10].

Because of the influence of bitumen emulsion on the mechanical properties of CBEM, the mechanical properties of CBEM have been widely concerned by researchers [11, 12]. The mechanical behavior of cement bitumen blends is affected by the bitumen/cement (B/C) ratio [13]. In addition, environmental factors also have a great influence on the mechanical properties of CBEM [14]. Microwave heating environment has an effect on the early strength of CBEM [15]. High-temperature environment has a certain negative impact on the compressive strength and elastic modulus of CBEM [16]. CBEM in acidic environment for a long time can also affect its mechanical properties. The compressive strength of CBEM soaked in ammonium nitrate solution has a certain decrease [17]. Moreover, the deterioration of its external surface seriously affects the railway traffic safety [18]. In addition, the higher

B/C ratio can promote the bond strength between CBEM and concrete slab [19]. Bitumen emulsion has a certain effect on the properties of CBEM. Some studies have shown that CBEM with a high B/C ratio has better workability [20, 21]. In addition, the sand-to-cement ratio of CBEM has a certain influence on its flow property [22]. The workability of CBEM can be evaluated by orthogonal test, and CBEM with excellent workability can be prepared [23].

As a viscoelastic material, the viscoelastic property of CBEM should be paid more attention to. The results show that the viscoelastic property of CBEM is the main reason for decreasing the track slab degumming phenomenon [24]. The addition of superplasticizers can stabilize the viscosity of CBEM [25]. However, the superplasticizers have a negative effect on the plastic viscosity of bitumen emulsion [26]. Dynamic mechanical analysis (DMA) is widely used as a method to evaluate the viscoelastic property of asphaltic materials [27–29]. The stress relaxation stage of CBEM can be explored by a dynamic mechanical thermal spectrometer [30]. In addition, the B/C ratio has an effect on the viscoelastic property of CBEM [31], and the viscosity of bitumen emulsion increases sharply with the addition of cement [32]. The type of emulsifier also has a certain influence on the viscoelastic property of CBEM [33]. In addition, cement can improve the microstructure of CBEM, so as to improve the adhesion between bitumen and aggregate [34].

In this paper, the influences of emulsifier types on the workability, mechanical properties, and viscoelastic property of CBEM were studied. The workability of CBEM was evaluated by fluidity and extensibility tests. The CBE and ABE were used to improve the workability of CBEM. The mechanical properties of CBEM were evaluated by compressive strength and flexural strength tests. The influences of CBE and ABE on the mechanical properties of CBEM are discussed. Dynamic mechanical analysis (DMA) was used to study the influence of different bitumen emulsion content, loading frequency, and bitumen emulsion types on the viscoelastic properties of CBEM. The CBE and ABE were used to improve the viscoelastic properties of CBEM. The CBEM samples with bitumen emulsions prepared by two different emulsifiers are treated with XRD because the mechanism of the anion-cation bitumen emulsion in the demulsification process is different.

## 2. Raw Materials and Test Methods

**2.1. Raw Materials.** Composite Portland cement was used and its properties are shown in Table 1. Properties of bitumen are shown in Table 2. The properties of fine aggregate are shown in Table 3. Cationic emulsifier and anionic emulsifier were used as emulsifiers, and the properties of the emulsifiers are shown in Table 4. The organosilicon defoaming agent was used as a defoaming agent and its properties are shown in Table 5.

**2.2. Preparation of CBEM.** Firstly, cationic and anionic emulsifiers were used to prepare bitumen emulsion with solid content of 60%. The emulsion soap liquid was set up by

TABLE 1: Properties of composite Portland cement.

Properties	Test results	
Density ( $\text{g}/\text{cm}^3$ )	2.923	
Average pore size ( $\mu\text{m}$ )	20.689	
Compressive strength (MPa)	3 d	18.9
	28 d	32.2
Flexural strength (MPa)	3 d	2.5
	28 d	5.7
Setting time (MPa)	Initial setting	123
	Final setting	169

TABLE 2: Properties of original bitumen.

Properties	Specification	Test values
Needle penetration (25°C, 100 g, 5 s) (0.1 mm)	60–80	78
Ductility (5°C, 5 cm/min) (cm)	$\geq 40$	47
Softening point (°C)	$\geq 50$	53.4
Density (15°C, $\text{g}/\text{cm}^3$ )	—	1.036
Wax content (%)	—	1.4

TABLE 3: Properties of fine aggregate.

Properties	Test results	
Apparent density ( $\text{g}/\text{cm}^3$ )	2.605	
Sediment percentage (%)	0.5	
Fineness modulus	2.44	
Bulk density ( $\text{g}/\text{cm}^3$ )	1.465	
Water absorption (%)	1.5	

TABLE 4: Properties of emulsifiers.

Types	Component	Density (25°C, $\text{g}/\text{cm}^3$ )	Viscosity (25°C, Pa·s)
CBE	Quaternary ammonium salt	1.180	9.13
ABE	Sodium hexadecyl acetate	1.210	8.75

TABLE 5: Properties of defoaming agent.

Project	Results
Appearance	White liquid at normal temperature
Solid content (%)	60%
pH value	6–8
Stability	No stratification and no precipitation

400 g water (60°C), 20–24 g emulsifier (cationic/anionic), and 15 g  $\text{CaCl}_2$ . The pH value of the cationic emulsifier was adjusted to 2–3 by HCl, and the anionic emulsifier was adjusted to 9–10 by NaOH. After melting bitumen to the temperature of 180°C, the emulsifier was first poured into the colloid mill, and the melted bitumen with a mass of 600 g was poured into the running colloid mill and emulsified to prepare cationic bitumen emulsion (CBE) and anionic bitumen emulsion (ABE). The water-cement ratio (w/c) was 0.4 (including the water content in bitumen emulsion), the sand-cement ratio (s/c) was 1.2, and the amount of

defoaming agent was 2% of the water weight. The different bitumen emulsion content was allocated according to the cement quality of 0–50% with 5% interval. Firstly, the dry materials (cement and sand), water, and bitumen emulsion were mixed into an agitator. Then, the defoaming agent of 2.0% water quality was added to the agitator. The mixing process is slowly stirred by 20 r/min–30 r/min for 5 minutes to avoid more bubbles. The mortars were put into steel modules at room temperature for maintenance. After 24 hours, the samples were cured for 3 d, 7 d, or 28 d at the temperature of 20°C and relative humidity of 90%. The flowchart of CBEM preparation is shown in Figure 1.

### 2.3. Experiments

**2.3.1. Workability Tests.** Fluidity and extensibility were tested to evaluate CBEM workability. The fluidity was tested by a fluidity tester. The funnel was wetted and placed on the funnel rack. The axis of the hopper was vertical to the ground, and the container bucket was placed below the funnel. The funnel hole was blocked by fingers and 1L CBEM was poured into the funnel slowly and evenly. Release the fingers and start the stopwatch at the same time and then measure the time required for the completion of CBEM in the funnel. The extensibility was tested by the relevant national standard method. The surface of the glass plate and the extension cylinder were wetted and the cylinder was vertical in the middle of the glass plate. The mixed CBEM was filled into the cylinder till the upper edge of the cylinder. The cylinder was raised by  $15 \pm 2$  cm vertically and the height was kept for 10 s. Meanwhile, the time of extensibility of CBEM reaching 280 mm was recorded by stopwatch. After CBEM stopped flowing, the extension diameter of two perpendicular directions was measured.

**2.3.2. Mechanical Properties Tests.** Compressive strength and flexural strength of the CBEM with 3 d, 7 d, and 28 d curing ages were tested according to the instructions for Type II cement bitumen emulsion mortar [35]. The sizes of specimens were 40 mm × 40 mm × 160 mm. The loading rate is 500 N/s and the test temperature is 20°C. Three samples with different bitumen emulsion content were selected for each group and the average of the three specimens was adopted as the strength value of each group.

**2.3.3. Viscoelastic Property Tests.** The viscoelastic property of the CBEM was tested by the DMA-Q800 dynamic mechanical analyzer. The 35 mm × 15 mm × 5 mm specimens with 28-day curing ages were used according to the size of the double cantilever mold. The test amplitude was set to 15 μm and the test temperature was 25°C. The viscoelastic property of CBEM at 24 frequency points from 0.0 Hz to 12.0 Hz was tested.

The DMA method is always used to test the viscoelastic property of materials. When the material has viscoelastic property, the deformation lags behind the applied load and

there is a phase difference between the load and the deformation. Generally, the complex constant modulus is defined as

$$E^* = \frac{\sigma}{\varepsilon} = \frac{\sigma_0}{\varepsilon_0} (\cos \varphi + i \sin \varphi) = E (\cos \varphi + i \sin \varphi), \quad (1)$$

where  $E^*$  represents the complex modulus of the material;  $\sigma$  represents the stress of the material;  $\varepsilon$  represents the strain generated after the material is stressed; and  $\varphi$  represents the phase angle.

Compared with the general elastic complex modulus definition

$$E^* = E' + iE'' = E' (1 + i\eta), \quad (2)$$

it can get that as equations (3), (4), and (5):

$$E' = E \cos \varphi, \quad (3)$$

$$E'' = E \sin \varphi, \quad (4)$$

$$\eta = \tan \varphi = \frac{E \sin \varphi}{E \cos \varphi} = \frac{E''}{E'}. \quad (5)$$

The loss factor  $\eta$ , which represents the viscoelastic property of the material, is an important parameter that represents the material's ability to dissipate.

**2.3.4. XRD Analyses.** CBEM with 50% bitumen emulsion and cement mortars without bitumen emulsion were used for the XRD test. The specimens were selected for the curing of 28 days. After the sample was crushed, an appropriate amount of small particles was used and fully ground into powder (up to 0.063 mm). The ground powder was used in the XRD test. The test temperature is 20°C, the test angle is 0–90°, the voltage is 40 kV, and the current is 30 mA.

## 3. Results

**3.1. Influences of Bitumen Emulsion on CBEM Workability.** As shown in Figure 2, the average fluidity of CBEM without bitumen emulsion is 209 s, and the fluidity of CBEM mixed with 50% bitumen emulsion increases to 102 s (ABE) and 99 s (CBE), respectively, which is 52% higher than that of the control group. With the increase of bitumen emulsion content, the growth rate of fluidity decreased. The results showed that the fluidity of CBEM increased with the increase of bitumen emulsion content. Compared with CBEM prepared by ABE, the fluidity of CBEM prepared by CBE is better. Figure 3 shows the influences of bitumen emulsion content on CBEM extensibility. It can be seen from Figure 3 that the extensibility of CBEM can be improved by adding bitumen emulsion. It increases to 308 mm (CBE) and 316 mm (ABE) from 240 mm, and bitumen emulsion content has no significant influence on the extensibility of the CBEM. The addition of bitumen emulsion can effectively improve the extensibility of the CBEM and the influence of the emulsifier types is not significant. The extensibility of CBEM was more than 280 mm.

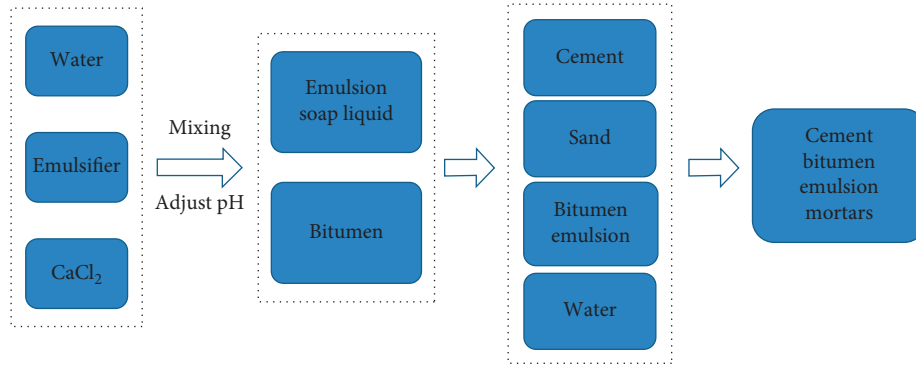


FIGURE 1: Flowchart of CBEM preparation.

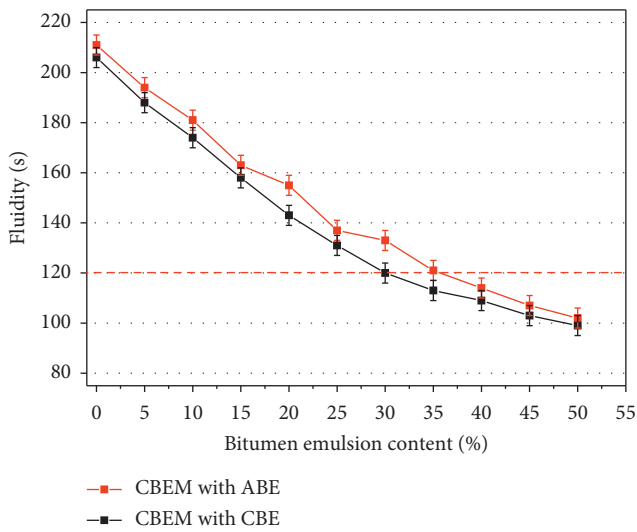


FIGURE 2: Influences of bitumen emulsion content on CBEM fluidity.

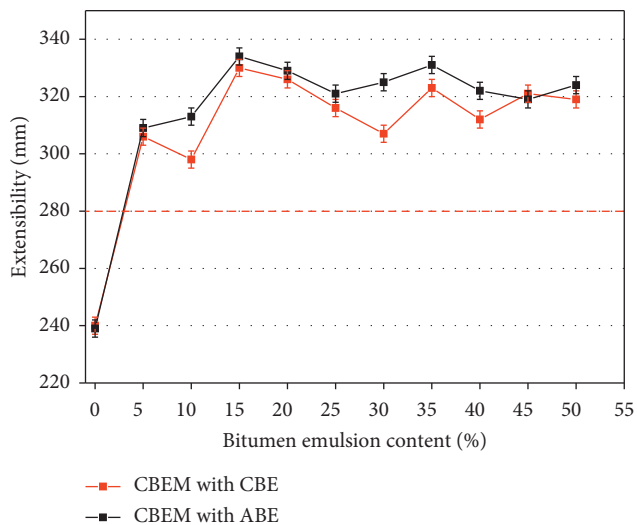


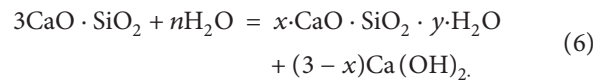
FIGURE 3: Influences of bitumen emulsion content on CBEM extensibility.

### 3.2. Influences of Bitumen Emulsion on CBEM Mechanical Properties.

As shown in Figures 4 and 5, it can be seen that adding bitumen emulsion can significantly reduce the compressive and flexural strength of CBEM in the early 3 and 7 days. It also can reduce the compressive and flexural strength of CBEM at 28-day curing age. The higher the content of the bitumen emulsion is, the greater the strength loss of CBEM can be. With the increase of cationic bitumen emulsion content, the compressive strength of CBEM is decreased by 63.9%, 43.7%, and 44.1% in 3 d, 7 d, and 28 d, respectively. With the increase of ABE content, the compressive strength of CBEM is decreased by 51.8%, 33.3%, and 39.0% in 3 d, 7 d, and 28 d, respectively.

With the increase of cationic bitumen emulsion content, the flexural strength of CBEM is decreased by 60.9%, 55.3%, and 40.6% in 3 d, 7 d, and 28 d, respectively. With the increase of ABE content, the flexural strength of CBEM is decreased by 63.4%, 57.4%, and 44.0% at 3 d, 7 d, and 28 d, respectively. The strength loss of CBEM prepared by CBE is lower than that of CBEM prepared by ABE.

Hydration of tricalcium silicate produces hydrated calcium silicate and calcium hydroxide. The chemistry reaction equation is shown in



As shown in Figure 6, the XRD result shows that the tricalcium silicate phase, limestone phase, and hydrated lime phase appeared in the CBEM materials after bitumen emulsion demulsification and cement hydration. It shows that there is no chemical reaction between bitumen and cement as an inert admixture and no new mineral phase is formed. Compared with the cement mortars without bitumen emulsion, the addition of bitumen emulsion cannot change the type of cement hydration products.

### 3.3. Viscoelastic Property of CBEM

**3.3.1. Influences of Bitumen Emulsion Types.** In this work, two groups of different types of emulsifier with bitumen emulsion content of 50% were selected for the DMA test. As



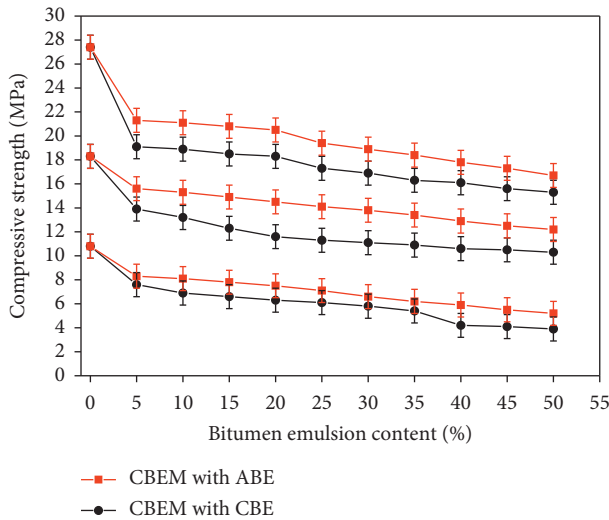


FIGURE 4: Influences of bitumen emulsion content on the compressive strength.

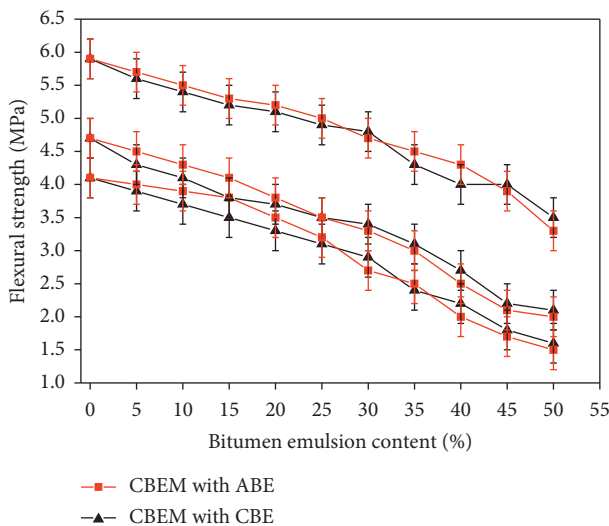


FIGURE 5: Influences of bitumen emulsion content on the flexural strength.

shown in Figure 7, with the increase of frequency, the loss factor  $\eta$  of CBEM decreases. The loss factor of the CBEM prepared with CBE and the 50% bitumen emulsion dosage group is 0.120, which is 3 times higher than that of the control group. Under the same amount of bitumen emulsion, the loss factor  $\eta$  at 12.0 Hz is 0.094, which is 21% lower than that at 0.5 Hz. The loss factor of the CBEM prepared with ABE and the 50% bitumen emulsion dosage group is 0.129, which is 3.5 times higher than that of the control group. Under the same amount of bitumen emulsion, the loss factor  $\eta$  at 12.0 Hz is 0.117, which is 9% lower than that at 0.5 Hz.

The complex modulus  $E^*$  can be used to characterize the viscoelastic property of materials. Among them, the real part of the complex modulus represents the strain energy of the material, which is the storage modulus  $E'$ . The imaginary

part of the complex modulus represents the thermal energy of the material, namely, the loss modulus  $E''$ . Therefore, the viscoelastic property of the material is positively related to the loss factor. With the increase of the loss factor, the dissipation capacity of the material increases, and the viscoelastic property of the material is better. Therefore, it can be seen from Figure 7 that the viscoelastic property of CBEM prepared by ABE is better than that of CBEM prepared by CBE.

### 3.3.2. Influences of Bitumen Emulsion Dosage and Frequency.

As shown in Figures 8 and 9, in contrast to the control group, the loss factor of CBEM can be significantly improved by adding a different amount of bitumen emulsion. The loss factor  $\eta$  of CBEM prepared with CBE increased from 0.039 to 0.059, 0.063, 0.058, 0.064, 0.070, 0.083, 0.088, 0.092, 0.097, and 0.107. When the bitumen emulsion content was 0.107, the maximum increase of loss factor  $\eta$  was 64%. The loss factor  $\eta$  of CBEM prepared with ABE increased from 0.039 to 0.066, 0.069, 0.072, 0.077, 0.084, 0.093, 0.101, 0.109, 0.114, and 0.118. When the bitumen emulsion content was 0.118, the maximum increase of loss factor  $\eta$  was 67%. At the same frequency, the loss factor  $\eta$  of CBEM increases with the increase of bitumen emulsion content, and the energy dissipation capacity of the material increases.

The results are influenced by the frequency and the loss factor  $\eta$  values of each group decrease by 18% and 12%. High frequency causes CBEM to deform more and the CBEM needs to convert this part of the deformation into heat energy through its own energy consumption to dissipate the energy. With the increase of vibration frequency, the energy consumption increases, and the energy consumption capacity of materials decreases. Therefore, under high frequency, the viscoelastic property of the material is not as good as that of the low frequency.

## 4. Discussion

**4.1. Reason Analyses for Bitumen Emulsion on CBEM Workability.** CBEM can be regarded as the coexistence system of bitumen emulsion and cement mortars. Because of the particle size of cement and sand and the double action of interfacial film and interfacial charge layer, the CBEM system has good stability. When the dry materials and bitumen emulsion just contacted, the system is still in a relatively stable state. Figure 10 shows the influence of bitumen emulsion on CBEM workability. Figure 10(a) shows dispersion distribution of cement, sand, bitumen particles, and emulsifier molecules. When the dry materials contacted with bitumen emulsion, the hydration reaction of cement with water can produce a large number of  $\text{Ca}^{2+}$ ,  $\text{K}^+$ ,  $\text{Na}^+$ ,  $\text{OH}^-$ ,  $\text{SO}_4^{2-}$ , and  $\text{HSO}_3^-$  plasma, attracting the surrounding free emulsifier molecules (Figure 10(b)).

From 3.1 test conclusions, it is known that the fluidity and extensibility of CBEM can be improved by bitumen emulsion and the fluidity of CBEM is influenced by the bitumen emulsion dosage. The main reason is that when the molecular content of free emulsifier is low, the cement

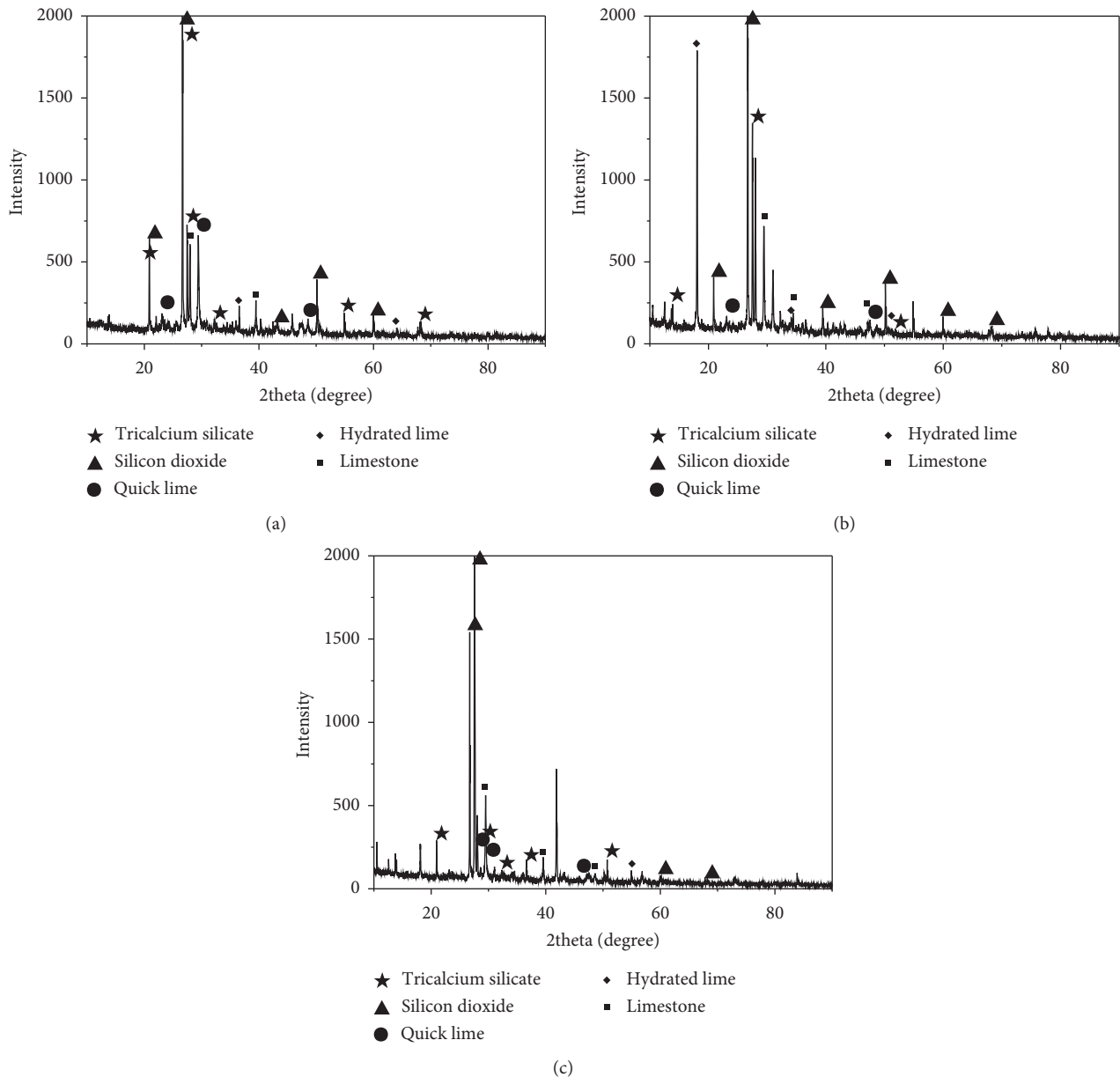


FIGURE 6: XRD pattern of CBEM: (a) without bitumen emulsion; (b) with ABE; (c) with CBE.

particles begin to absorb bitumen emulsion around the cement particles (Figure 10(c)). Due to the reduction of free water in the system caused by cement hydration reaction and the adsorption of cement particles on bitumen emulsion, the mortars can gradually lose stability and demulsification and condensation occurred on the surface of cement particles. The hydration of cement particles and water is prevented and the volume fraction of the continuous phase is not decreased. Thus, the increase of internal friction between dispersed phases in CBEM is prevented and the fluidity of CBEM is improved (Figure 10(d)).

**4.2. Reason Analyses for Emulsifier Types on CBEM Workability.** The cationic emulsifiers are the main derivatives of an organic amine. The molecular structure of the

cationic bitumen emulsifier used in this work is shown in Figure 11. When the dry materials are mixed with CBE, the nitrogen atom in the cationic emulsifier has strong adsorption and affinity with the acid alkali aggregate, which can pull the bitumen emulsion bead particles to the surface of the dry materials. As the cement hydration, the pressure between the emulsifier molecules and the dry materials can squeeze the water from the two and this process can make the bitumen form a film between the cement hydration product and the gravel. At the same time, due to the positive charge of the cationic emulsifier and the negative charge of the particles after the cement hydration, the bitumen particles are easily adsorbed on the surface of the cement particles. CBE is faster in demulsification, condensation, and molding, so the water consumption of CBEM prepared by

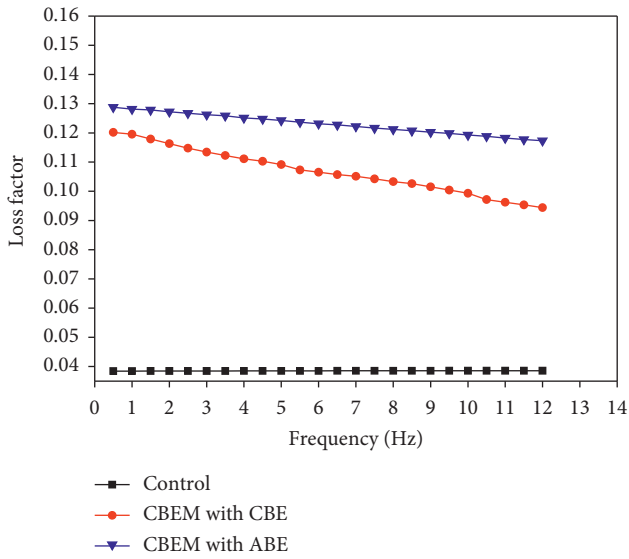


FIGURE 7: Influences of bitumen emulsion on CBEM viscoelastic property.

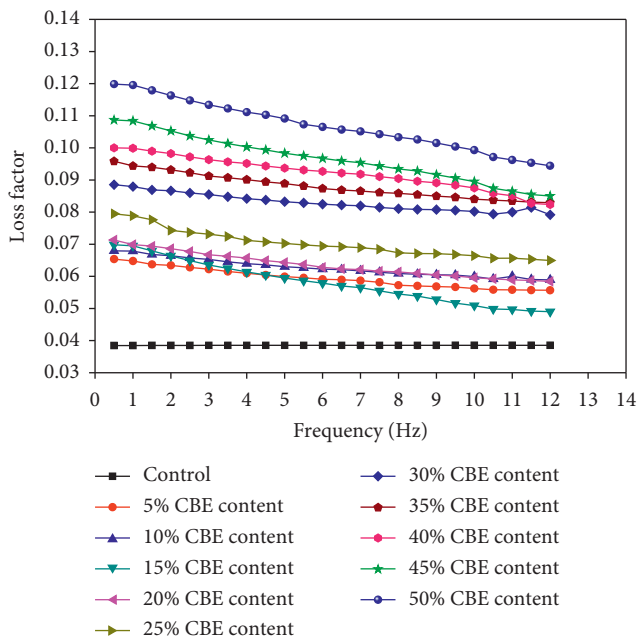


FIGURE 8: Influences of CBE content on the viscoelastic property.

CBE is less. The improvement of the fluidity of CBEM prepared by CBE is better than that of CBEM prepared by ABE. The experimental conclusions of 3.1 are verified.

The lipophilic group of the anionic emulsifier molecular is the same as the cationic emulsifier, but the hydrophobic group contains many oxygen atoms except the sulfur atom and the carbon atom. The molecular structure of the anionic bitumen emulsifier used in this work is shown in Figure 12. When the dry materials are mixed with ABE, the affinity and adsorption of the oxygen, sulfur, and carbon atoms of the hydrophilic group of the anionic emulsifier with the dry materials are worse compared with the

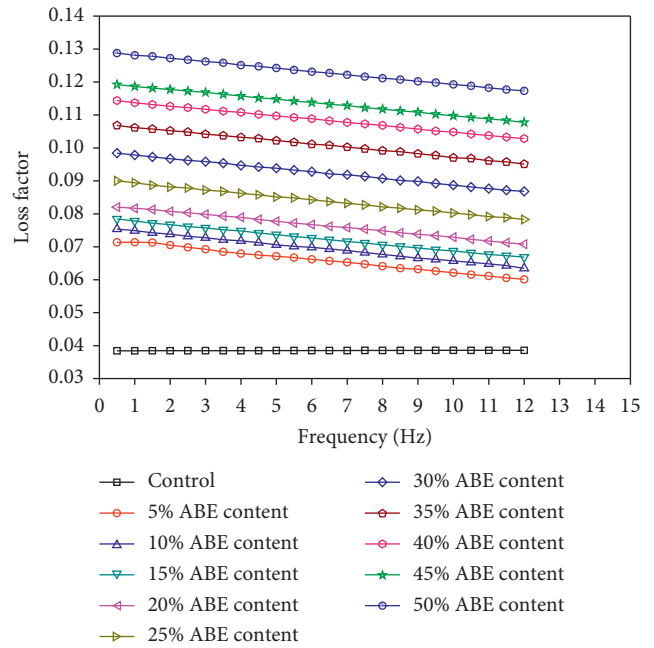


FIGURE 9: Influences of ABE content on the viscoelastic property.

nitrogen atoms in the hydrophilic group of the cationic emulsifier molecule. At the same time, the oxygen atoms in the hydrophilic group adsorb the hydrogen atoms in the water molecules and form a large number of hydrogen bonds in the bitumen emulsion. The combination of hydrogen bonds and water molecules occupies a large space, which makes it difficult for emulsifier molecules to contact the surface of dry materials directly. The aqueous phase between the bitumen emulsion and the cement hydration products cannot be easily squeezed out.

At the same time, because the particles after hydration of anionic emulsifier and cement had a large number of negative charges, bitumen and aggregate repelled each other, which makes it difficult to get close to bitumen and aggregate and hinder the demulsification of bitumen. The hydrogen bonding water of the hydrophilic group of the anionic emulsifier molecules is relatively strong and the water volatilizes at a slow speed, which results in the fact that the bitumen film cannot wrap up the dry materials in a short time. Therefore, in contrast to cationic emulsifier, the improvement of CBEM fluidity by anionic emulsifier is not as good as that by cationic emulsifier.

4.3. Reason Analyses for Mechanical Property Changes. Due to the addition of bitumen emulsion, the hydration of some cement particles is hindered. The water after demulsification of bitumen emulsion contacts with cement particles, which makes the hydration reaction continue. When the demulsification process of bitumen emulsion reaches a certain process, the bitumen emulsion penetrates between the cement particles and the hydration products, and the cement hydration process is hindered. This is why the compressive strength of CBEM at different ages after the addition of bitumen emulsion in Figure 4 is significantly

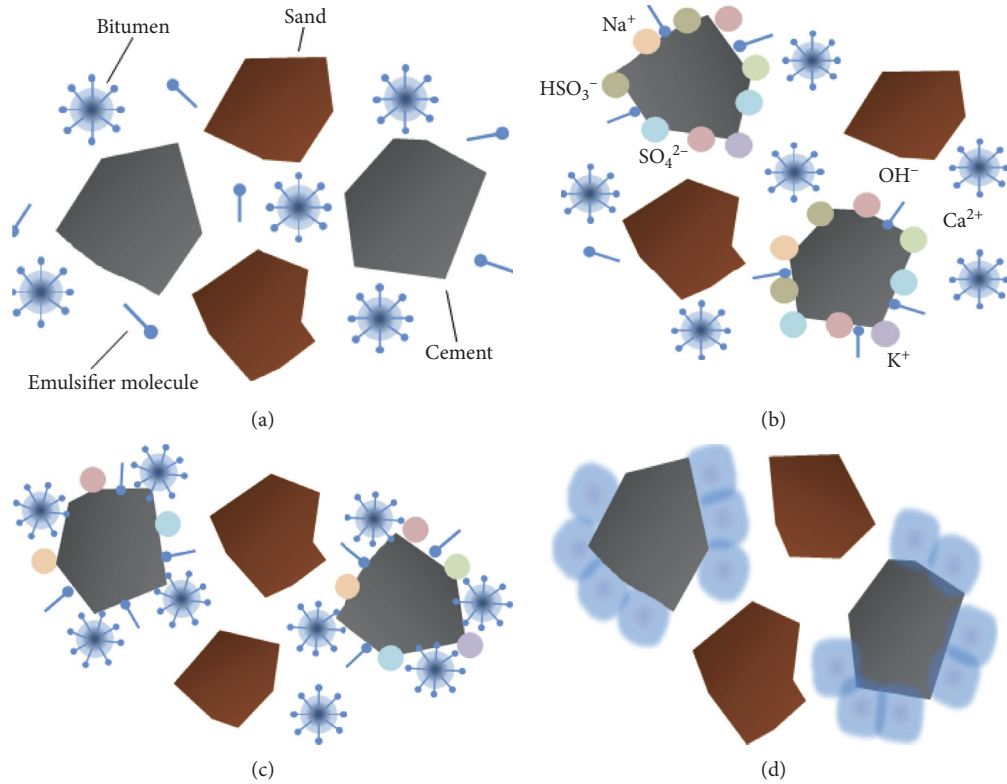


FIGURE 10: Influences of bitumen emulsion on CBEM workability: (a) contact stage; (b) prereaction stage; (c) late stage of reaction; (d) demulsification and coagulation stage.

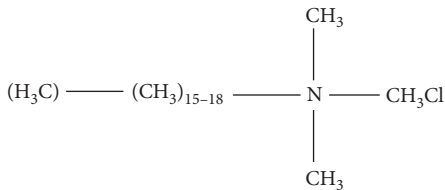


FIGURE 11: Quaternary ammonium salt.

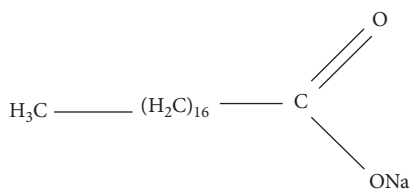


FIGURE 12: Sodium hexadecyl acetate.

reduced. The interaction of the entire cement hydration-bitumen demulsification causes the mechanical strength of the CBEM to be reduced, and the compressive and flexural strength is decreased correspondingly.

4.4. Reason Analyses for Viscoelastic Property Changes. Because the CBEM with anion has a poor affinity to the aggregate surface and has no influence on activating aggregate, the adhesion between ABE and dry materials

depends on the adhesion between bitumen itself and dry materials. The addition of cement in CBEM improves the alkaline component of the mortars and makes the aggregate alkaline [36]. As shown in Figure 13, because the bitumen contains acid active groups, such as carboxyl, anhydrides, and phenols, it can react with  $\text{Ca}^{2+}$  and  $\text{Mg}^{2+}$  on the surface of aggregate to form water-insoluble organic acid salts. Through the organic acid salt, the cement hydrate surface is formed as a chemical adsorption layer, which can tightly absorb the cement hydration product and bitumen together, greatly enhancing the adhesion between them [37]. When CBEM with anion is completely demulsified, the bitumen emulsion fills the pores of CBEM. The bitumen emulsion is interwoven with hydration products to form a network structure after demulsification. The deformation ability of CBEM is improved, so the viscoelastic property of CBEM is improved.

For CBEM prepared by CBE, there is no evident chemical reaction between CBE and dry materials, so there is no chemical adsorption between bitumen emulsion and cement hydration products. After demulsification, most of the hydration reaction of cement has been completed, and the ion concentration is greatly reduced. Therefore, the adsorption between bitumen and cement hydration products is only physical adsorption or molecular directed adsorption. Because the influence of chemical adsorption is better than that of physical adsorption and molecular directed adsorption, the viscoelastic property of CBEM prepared by ABE is better than that of CBEM prepared by CBE.

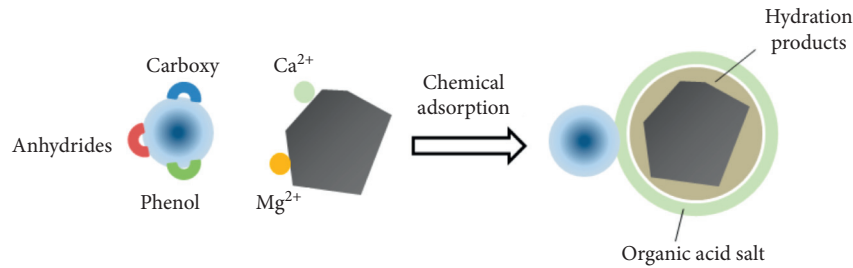


FIGURE 13: Chemical adsorption of CBEM by ABE.

## 5. Conclusions

In this work, the influences of emulsifier types on the workability, mechanical properties, and viscoelastic property of CBEM were systematically investigated. The workability of CBEM was evaluated by fluidity and extensibility, the mechanical properties of CBEM were evaluated by compressive strength and flexural strength tests, and the viscoelastic property of CBEM was evaluated by DMA test. In addition, the phase of CBEM was analyzed by XRD. The following conclusions could be drawn:

- (1) The addition of anionic and cationic bitumen emulsion can significantly improve the workability of CBEM. The CBEM prepared by CBE has high fluidity. When the content of bitumen emulsion is between 35% and 50%, the CBEM possesses high workability.
- (2) The addition of anionic and cationic bitumen emulsion can reduce the compressive strength and flexural strength of CBEM and adversely affect the mechanical properties. CBE has a more negative influence on the compressive strength of CBEM than ABE.
- (3) The loss factor  $\eta$  can reflect the viscoelastic property of CBEM. After adding the bitumen emulsion, the dissipative capacity of the CBEM was improved. The loss factor  $\eta$  of two different CBEM increased by 67% (ABE) and 64% (CBE) compared with cement mortars without bitumen emulsion. The viscoelastic property of CBEM has been obviously improved.
- (4) Frequency is the main factor affecting the viscoelastic property of CBEM. The loss factor  $\eta$  of two different CBEM is decreased by 18% (ABE) and 12% (CBE), respectively, under when the high frequency (12.0 Hz) compared with the low frequency (0.5 Hz). In high frequency, the loss factor  $\eta$  loss rate is reduced by 9%, while the influence of frequency on the loss factor is low. The viscoelastic property of CBEM is improved obviously.
- (5) The viscoelastic property and mechanical properties of CBEM should be considered according to different needs in practical engineering. CBEM prepared by CBE has better workability, while CBEM prepared by ABE has better mechanical properties and viscoelastic properties.

## Data Availability

The data used to support the findings of this study are included within the article.

## Conflicts of Interest

The authors declare that they have no conflicts of interest.

## Acknowledgments

This work was supported by National Natural Science Foundation of China (no. 51978067), Science and Technology Development Project of Xinjiang Production and Construction Corps (no. 2019AB013), and Henan Transportation Science and Technology Plan Project (no. 2019J1).

## References

- [1] R. Li, F. Xiao, and P. Zhu, "Research progress of special emulsified asphalt for cement emulsified asphalt mortar on high-speed railway," *Chemical Journal*, vol. 52, no. 2, pp. 123–126, 2011.
- [2] Z. Wang, N. Dai, X. Wang, G. Li, and H. Guo, "Early-stage road property improvements of cold recycled asphalt emulsion mixture with microwave technology," *Journal of Cleaner Production*, vol. 263, Article ID 121451, 2020.
- [3] C. Chen and B. Zhan, "Study on crack resistance of CA mortar based on low temperature bending test," *Journal of Hefei University of Technology (Natural Science Edition)*, vol. 43, no. 4, pp. 530–535, 2020.
- [4] Z. Wang, X. Shu, T. Rutherford, B. Huang, and D. Clarke, "Effects of asphalt emulsion on properties of fresh cement emulsified asphalt mortar," *Construction and Building Materials*, vol. 75, pp. 25–30, 2015.
- [5] H. Zhang, L. Meng, and G. Zhang, "Comparative study on mechanical performance of asphalt-cement mortar and emulsified asphalt-cement mortar," *Road Materials and Pavement Design*, vol. 18, no. 5, pp. 1239–1250, 2017.
- [6] W. Li, J. Hong, X. Zhu et al., "Retardation mechanism of anionic asphalt emulsion on the hydration of Portland cement," *Construction and Building Materials*, vol. 163, pp. 714–723, 2018.
- [7] E. Garilli, F. Autelitano, C. Godenzoni, A. Graziani, and F. Giuliani, "Early age evolution of rheological properties of over-stabilized bitumen emulsion-cement pastes," *Construction and Building Materials*, vol. 125, pp. 352–360, 2016.
- [8] Z. Song, P. Xu, and J. Tao, "Study on demulsification mechanism of emulsified asphalt," *Petroleum Asphalt*, vol. 3, pp. 23–29, 1995.

- [9] M. Miljković, M. Radenberg, X. Fang, and P. Lura, "Influence of emulsifier content on cement hydration and mechanical performance of bitumen emulsion mortar," *Materials and Structures*, vol. 50, no. 3, p. 185, 2017.
- [10] L. Kong, F. Tang, Y. Xu, P. Zhao, and Y. Zhang, "Evaluation of emulsified asphalt demulsification process by ultraviolet spectroscopy," *Journal of Chang'an University: Natural Science Edition*, vol. 37, no. 6, pp. 17–23, 2017.
- [11] Q. Fu, Y. Xie, K. Zheng, H. Song, and X. Zhou, "Influence of asphalt on mechanical property of cement asphalt mortar," *Acta Silicate Sinica*, vol. 42, no. 5, pp. 642–647, 2014.
- [12] X. Fang, A. Garcia, F. Winnefeld, N. Partl, and P. Lura, "Impact of rapid-hardening cements on mechanical property of cement asphalt emulsion asphalt," *Materials and Structures*, vol. 49, no. 1-2, pp. 487–498, 2016.
- [13] M. Miljkovic, L. Poulikakos, F. Piemontese, M. Shakoorioskooie, and P. Lura, "Mechanical behaviour of bitumen emulsion-cement composites across the structural transition of the co-binder system," *Construction and Building Materials*, vol. 215, pp. 217–232, 2019.
- [14] Q. Wang, J. Feng, and P. Yan, "Strength loss of cement asphalt mortar under outdoor natural conditions," *Journal of Tsinghua University (Nature Science Edition)*, vol. 53, no. 1, pp. 1–5, 2013.
- [15] Z. Wang, N. Dai, X. Wang, J. Zhang, and H. Guo, "Laboratory investigation on effects of microwave heating on early strength of cement bitumen emulsion mixture," *Construction and Building Materials*, vol. 236, 2020.
- [16] J. Wang, W. Wang, and X. Wu, "Mechanical property of cement asphalt mortar under low temperature condition," *Journal of Testing and Evaluation*, vol. 47, no. 3, pp. 1995–2009, 2019.
- [17] H. Peng, Y. Zhang, J. Wang, Y. Liu, and L. Gao, "Interfacial bonding strength between cement asphalt mortar and concrete in slab track," *Journal of Materials in Civil Engineering*, vol. 31, no. 7, Article ID 04019107, 2019.
- [18] Y. Wang, Q. Yuan, and D. Deng, "Degradation of mechanical properties of CA mortar caused by calcium leaching," *Construction and Building Materials*, vol. 208, pp. 613–621, 2019.
- [19] X. Zeng, Y. Li, Y. Ran, K. Yang, F. Qu, and P. Wang, "Deterioration mechanism of CA mortar due to simulated acid rain," *Construction and Building Materials*, vol. 168, pp. 1008–1015, 2018.
- [20] B. Liu and D. Liang, "Effect of mass ratio of asphalt to cement on the properties of cement modified asphalt emulsion mortar," *Construction and Building Materials*, vol. 134, pp. 39–43, 2017.
- [21] X. She, R. Li, H. Zhang, X. Chen, and H. Deng, "Preparation and property of anionic CA mortar," *Chemical Journal*, vol. 53, no. 1, pp. 1–4, 2012.
- [22] Q. Wang and P. Yan, "Effect of sand-ash ratio and sand-level matching on the compressive strength and fluidity of CA mortar," *Journal of Railway Science and Engineering*, vol. 5, no. 6, pp. 1–5, 2008.
- [23] D. Li, K. Wu, G. Yang, and X. Bao, "Evaluation and analysis of factors affecting performance of cement emulsified asphalt mortar," *Highway*, vol. 8, pp. 212–215, 2012.
- [24] J. Ren, H. Li, X. Cai, S. Deng, J. Wang, and W. Du, "Viscoelastic deformation behavior of cement and emulsified asphalt mortar in China railway track system I prefabricated slab track," *Journal of Zhejiang University-Science A: Applied Physics and Engineering*, vol. 21, no. 10, pp. 304–316, 2020.
- [25] J. Ouyang, Y. Tan, Y. Li, and J. Zhao, "Demulsification process of asphalt emulsion in fresh cement-asphalt emulsion paste," *Materials and Structures*, vol. 48, no. 12, pp. 3875–3883, 2015.
- [26] J. Ouyang and Y. Tan, "Rheology of fresh cement asphalt emulsion pastes," *Construction and Building Materials*, vol. 80, pp. 236–243, 2015.
- [27] Q. Fu, Y. Xie, G. Long, D. Niu, and H. Song, "Dynamic mechanical thermo-analysis of cement and asphalt mortar," *Powder Technology*, vol. 313, pp. 36–43, 2017.
- [28] Z. Wang, X. Xu, X. Wang, J. Huo, H. Guo, and B. Yang, "Performance of modified asphalt of rubber powder through tetraethyl orthosilicate (TEOS)," *Construction and Building Materials*, 2020.
- [29] J. Wang, J. Ouyang, J. Zhao, Y. Tan, and Y. Li, "Viscoelastic property of CRTS II type CA mortar," *Journal of China University of Petroleum: Natural Science*, vol. 37, no. 4, pp. 165–168, 2013.
- [30] Q. Fu, Y.-J. Xie, G.-C. Long, F. Meng, and H. Song, "Temperature sensitivity and model of stress relaxation properties of cement and asphalt mortar," *Construction and Building Materials*, vol. 84, pp. 1–11, 2015.
- [31] X.-T. Qin, S.-Y. Zhu, S.-F. Chen, X. Li, and H.-B. Dou, "Comparative study on the deformation behaviors of cement emulsified asphalt mortars," *Materials and Structures*, vol. 48, no. 10, pp. 3241–3247, 2015.
- [32] X. Fang, A. Garcia-Hernandez, F. Winnefeld, and P. Lura, "Influence of cement on rheology and stability of rosin emulsified anionic bitumen emulsion," *Journal of Materials in Civil Engineering*, vol. 28, no. 5, Article ID 04015199, 2016.
- [33] J. Ouyang, H. Li, and B. Han, "The rheological properties and mechanisms of cement asphalt emulsion paste with different charge types of emulsion," *Construction and Building Materials*, vol. 147, pp. 566–575, 2017.
- [34] Z. Wang and A. Sha, "Microstructure characteristics of cement emulsified asphalt composite mastic," *Journal of Chang'an University: Natural Science Edition*, vol. 29, no. 5, pp. 11–14, 2009.
- [35] Ministry of Railways of the People's Republic of China, *Instructions for Type II Cement Emulsified Asphalt Mortar*, Ministry of Railways of the People's Republic of China, Beijing, China, 2008.
- [36] T. Oey, E. C. La Plante, G. Falzone et al., "Calcium nitrate: a chemical admixture to inhibit aggregate dissolution and mitigate expansion caused by alkali-silica reaction," *Cement and Concrete Composites*, vol. 110, Article ID 103592, 2020.
- [37] Z. Wang, P. Wang, H. Guo, X. Wang, and G. Li, "Adhesion improvement between RAP and emulsified asphalt by modifying the surface characteristics of RAP," *Advances in Materials Science and Engineering*, vol. 2020, Article ID 4545971, 2020.

## Research Article

# High-Temperature Performance of Asphalt Mixtures: Preliminary Analysis for the Standard Technical Index Based on Gray Relational Analysis Method

Jian Xu <sup>1</sup>, Yan Gong <sup>1</sup>, Li-Biao Chen,<sup>2</sup> Tao Ma,<sup>3</sup> Jun-Cheng Zeng <sup>2</sup>, Er-Hu Yan <sup>1</sup>,  
and Guang-Shu Xiao<sup>4</sup>

<sup>1</sup>Research Institute of Highway, Ministry of Transport, Beijing 100088, China

<sup>2</sup>Fujian Expressway Construction Directorate, Fuzhou, Fujian 350001, China

<sup>3</sup>Transportation College, Southeast University, Nanjing, Jiangsu 210096, China

<sup>4</sup>Fujian Road and Bridge Construction Co., Ltd., Fuzhou, Fujian 350002, China

Correspondence should be addressed to Yan Gong; gy.1991@163.com

Received 13 July 2020; Revised 28 September 2020; Accepted 20 October 2020; Published 11 November 2020

Academic Editor: Meng Guo

Copyright © 2020 Jian Xu et al. This is an open access article distributed under the Creative Commons Attribution License, which permits unrestricted use, distribution, and reproduction in any medium, provided the original work is properly cited.

Aiming to evaluate the high-temperature performance of asphalt binders and asphalt mixtures and to investigate the reliability of the standard technical indexes to evaluate the performance of the asphalt, six typically used asphalt types were employed in this study. The standard high-temperature rheological test, the multiple stress creep recovery (MSCR) test, and the zero-shear viscosity (ZSV) test were employed to characterize the high-temperature performance and non-Newtonian fluid properties of the asphalt. Meanwhile, the high-temperature performance of the asphalt mixture was evaluated through the rutting tests based on the mixture design of AC-13. In general, the modified asphalt performed better than the unmodified asphalt according to the high-temperature rheological properties tests. The ranking of the six kinds of asphalt was confirmed to be different in various laboratory tests. The test results of the asphalt binders showed that the Tack Super- (TPS-) modified asphalt performed best in the MSCR and ZSV tests, while the low-grade asphalt PEN20 had the best technical indexes in the dynamic shear rheometer (DSR) test. Besides, the relation between the asphalt and the asphalt mixture was analyzed by gray relational analysis (GRA) method. The present rutting indicator ( $G^*/\sin \delta$  and  $G^*/(1 - (\sin \delta \cdot \tan \delta)^{-1})$ ) for evaluating the asphalt mixtures' high-temperature performance might no longer be suitable. The Cross/Williamson model was the most suitable for calculating and fitting the ZSV, which could be used as the key indicator of the high-temperature performance evaluation of the asphalt. This work lays a foundation for the further study of the high-temperature performance evaluation of asphalt binders.

## 1. Introduction

At present, the Superpave asphalt performance evaluation system is widely used, which is a main outcome of the Strategic Highway Research Program (SHRP). In the Superpave specification, the shear complex modulus ( $G^*$ ), the phase angle ( $\delta$ ), and the rutting factor ( $G^*/\sin \delta$ ) from dynamic shear rheometer (DSR) test are used to evaluate the high-temperature mechanical performance of asphalt binders based on the law of energy dissipation and the rutting resistance [1–4]. For the base asphalt, some

researches indicated that the rutting factor ( $G^*/\sin \delta$ ) had a good relation with the rutting resistance of the asphalt mixtures. However, for the modified asphalt, the applicability of traditional rutting factor ( $G^*/\sin \delta$ ) in the evaluation of high-temperature performance has been discussed over the years [5, 6]. It was because, under the uninterrupted sinusoidal alternating loading in DSR test, the influence of the delayed elasticity was neglected, which played an important role in the deformation response of the modified asphalt [7]. In the research of National Cooperative Highway Research Program (NCHRP), the relational coefficient

between the rutting factor and the permanent deformation rate of the mixture, measured by the repeated shear test (constant height) (RSCH), was only 0.23.

Recently, some new test methods and evaluation indexes have been proposed [8–11]. Considering the viscoelastic properties of asphalt, the elastic and viscous terms of shear complex modulus were defined, respectively. In the United States, Shenoy et al. [12, 13] put forward modified rutting factors ( $G^*/1 - (\sin \delta \cdot \tan \delta)^{-1}$ ) and ( $G^*/(\sin \delta)^9$ ) on the basis of the traditional rutting factor, which were proved to be more accurate in judging the rutting resistance of the modified asphalt. At the same time, the repeated creep-recovery test (RCRT) was suggested [14]. Based on RCRT, two new evaluation indexes in the multistress creep recovery (MSCR) test, percent deformation recovery ( $R$ ) and non-recoverable deformation compliance ( $J_{nr}$ ), were also proposed to solve the nonlinearity associated with the modified asphalt [15, 16]. According to the AASHTO TP70 test method [17], two stress levels (0.1 and 3.2 kPa) were adopted as the test loads. The stress sensitivity indexes ( $R_{diff}$ ,  $J_{nr,diff}$ ) were also calculated from the difference in  $R$  and  $J_{nr}$  between two stress levels to evaluate the high-temperature performance of asphalt. Since the loading method in MSCR test takes into account the delayed elasticity of asphalt, this test method is applicable for predicting the high-temperature stability of both unmodified asphalt and polymer-modified asphalt [18–21], especially adopting higher stress load to simulate the actual situation [22, 23]. Besides, the zero-shear viscosity (ZSV) test has attracted much attention in Europe. The polymer-modified asphalt is a typical non-Newtonian fluid at high temperatures, and the viscosity decreases with the increasing shear rate. Some researches found that the viscosity of the asphalt tended to have a stable value when the shear rate was very small or extremely large. Thus, in order to exclude the effect of shear rate on the test results, the zero-shear viscosity (ZSV) was proposed as an evaluation index to characterize rutting resistance of the asphalt, especially the polymer-modified asphalt [2, 24–26]. Therefore, in this study, the ZSV and MSCR tests, as well as their technical indexes, were used for the high-temperature performance evaluations on both the base asphalt and modified asphalt.

Gray relation analysis (GRA) method has been applied in many fields to explain the problems of the uncertain systems with the multiple input, incomplete information and discrete data. In road engineering fields, it is indicated that GRA is applicable to research the performance of asphalt and its mixture [27]. Based on gray system approach, the relationship between composition of the asphalt and the service performance was analyzed to study the asphalt aging mechanism [28]. Wu et al. [29] predict normal incidence sound absorption coefficient and tire/road noise on asphalt pavements using the gray system model with Fourier residual correction. Zhang et al. [30] evaluated the effects of the regenerant's viscosity and acid value on the basic, rheological, and chemical properties of a typical rejuvenated asphalt by using GRA method. In Gao's work [31], the highest gray entropy relation between the dynamic viscosity of bioasphalt and the dynamic stability of the mixture

provided a key index of bioasphalt's high-temperature performance evaluation. These results showed that GRA method could be considered as an alternative to the asphalt performance evaluation and mixture design analysis, of which the analysis results were accurate and reliable.

Although a lot of effort has been made to investigate high-temperature performance of various types of asphalt including the base asphalt binders and modifiers in recent years, the existing relationship models between the asphalt and its mixture still have application limitations and accuracy problems. Most of the existing literatures focus on the materials and properties evolution, instead of the development of technical indexes for characterizing the high-temperature performance of both the unmodified and modified asphalt mixtures. Therefore, aiming to evaluate the high-temperature performance of the asphalt binders and their mixtures and to investigate the relation between the performance indexes of the asphalt binders and their mixture, six typically used asphalt types (including three types belonging to base asphalt and three types belonging to polymer-modified asphalt) were employed in this study. The standard high-temperature rheological test, the MSCR test, and the ZSV test were employed to characterize the high-temperature performance. Meanwhile, the high-temperature performance of the asphalt mixture was evaluated through Marshall stability and rutting tests based on the mixture design of AC-13. Furthermore, the relation was determined by the gray relational analysis method. This study will provide a more systematic perspective for the further study of the high-temperature performance evaluation of asphalt binders.

## 2. Materials

**2.1. Asphalt Binders.** Because the applicability of the relationship between different kind of asphalt and asphalt mixture is controversial, the study is to investigate the reliability of the standard technical indexes to evaluate the performance of both the base asphalt and modified asphalt. Thus, in this study, three penetration grades of asphalt (PEN20, PEN50, and PEN90) and three types of polymer-modified asphalt, which are two kinds of SBS- (styrene-butadiene-styrene-) modified asphalt named SBS I-C and SBS I-D (from Jiangsu Sinopec) and TPS- (Tafpack Super-) modified asphalt (from Gansu), were selected to investigate the high-temperature performance. The basic physical properties of six asphalt binders are shown in Table 1. Note that since the TPS is a kind of new modifier, one of the objectives of the study is to compare the high-temperature performance of SBS-modified asphalt and that of TPS-modified asphalt.

**2.2. Asphalt Mixture Design.** In this study, the fine-grained continuous gradation asphalt concrete (AC-13) mixtures with the six kinds of asphalt binder were adopted for the high-temperature performance evaluations, according to the Chinese standard of JTJ F40-2004 [32]. Table 2 shows the detailed gradation of AC-13.



TABLE 1: The basic physical properties of six asphalt binders.

Asphalt binders		Penetration (25°C, 100 g, 5 g), 0.1 mm	Penetration index $n/a$	Softening point, °C	Ductility (5/15°C), cm	Viscosity (60°C), Pa·s
Unmodified	PEN20	23	0.81	64.2	10/62	3315.2
	PEN50	54	0.29	52.4	1/87	393.8
	PEN90	91	-0.94	47.7	0.5/100	198
Modified	SBS I-C	74	0.03	66.0	56/100	27360
	SBS I-D	57	-0.05	66.9	26/100	49755
	TPS	69	0.89	80.7	38/100	82459

Note that the date of ductility before “/” was tested at 5°C, and date of ductility after “/” was tested at 15°C.

TABLE 2: Gradation of aggregate for AC-13.

Sieve size, mm	13.2	9.5	4.75	2.36	1.18	0.6	0.3	0.15	0.075
Selected (%)	97	82	47	31	21.5	15	11	8	6
Upper (%)	100	85	68	50	38	28	20	15	8
Lower (%)	90	68	38	24	15	10	7	5	4
Intermediate (%)	95	76.5	53	37	26.5	19	13.5	10	6

Based on the gradation of aggregate for AC-13 mixtures, different asphalt contents were selected for applying in the Marshall test to determine the optimum asphalt content (OAC) of the six kinds of asphalt binder. According to the Chinese standard of JTG F40-2004 [32], the testing data of the asphalt mixture Marshall specimen are shown in Table 3, including the asphalt-aggregate ratio, the apparent density, the theoretical maximum density, the air void (VV), the voids in mineral aggregate (VMA), and the voids filled with asphalt (VFA). The Marshall tests mentioned earlier were based on the SBS-modified asphalt binder. The air void (VV) of the Marshall specimen could be calculated through measuring the apparent density and the theoretical maximum density. In order to ensure that the air void of the Marshall specimen was around 4%, the different asphalt binders had various OACs. The final determined OAC of AC-13 mixtures in the study was 4.6 wt% for PEN50 and PEN90 asphalt binder, 4.8 wt% for PEN20 asphalt binder, 4.9 wt% for SBS-modified asphalt binder, and 5.1 wt% for TPS-modified asphalt binder, respectively.

### 3. Testing Methods and Analysis Models

**3.1. DSR Test.** DSR tests were performed in accordance with the method specified in AASHTO T315 [33]. The complex modulus  $G^*$ , the phase angle  $\delta$ , and the rutting indicator ( $G^*/\sin \delta$ ) were obtained on the virgin asphalt binder samples (except for the correlation analysis in Section 4.3) via Kinexus Ultra+ (Malvern Panalytical) DSR at 64°C, 70°C, 76°C, 82°C, and 88°C, with the sample diameter of 25 mm and the thickness of 1 mm. The loading frequency in the DSR tests was 10 rad/s. For the correlation analysis, the DSR tests were conducted on both the unaged asphalt and the aged asphalt (rolling thin film oven test (RTFOT)). Three repeated tests were employed to ensure the reliability of the results.

**3.2. MSCR Test.** MSCR tests were performed on Kinexus Ultra+ (Malvern Panalytical) DSR at 64°C, 70°C, 76°C, 82°C,

and 88°C. The sample was the rolling thin film oven test (RTFOT) residue of asphalt binder, which is applied to simulate the short-term aging condition of asphalt. The percent recovery and nonrecoverable creep compliance were obtained by applying a continuous cyclic load to the samples, with the sample diameter of 25 mm and the thickness of 1 mm. Each creep recovery cycle consisted of a stress loading period (1 s) and then a zero-stress recovery period (9 s). The test process was under two stress levels (0.1 and 3.2 kPa). The first 20 cycles of creep recovery were conducted under the shear load stress of 0.1 kPa, followed by additional 10 cycles under 3.2 kPa. Besides, the RTFOT were conducted at 163°C for 85 min [34]. It is worth noting that three repeated tests were carried out on each type of asphalt binder to ensure the reliability of the results.

**3.3. ZSV Test.** ZSV tests were performed on Kinexus Ultra+ (Malvern Panalytical) DSR at the test temperature of 60°C. The sample was the rolling thin film oven test (RTFOT) residue of asphalt binder, with the same diameter and thickness as those of the samples in MSCR tests (25 mm and 1 mm). The steady-state flow test was used to determine the viscosity at different shear frequencies, which ranged from 10 to 0.01 rad/s. Then the zero-shear viscosity (ZSV) was calculated by the shear rheological fitting curve. For each type of asphalt binder, at least ten repeated tests were conducted within each order of magnitude to ensure the reliability. At present, the commonly used fitting models, which were used to calculate the value of ZSV, include the Cross/Sybilski model, Cross/Williamson model, and Carreau model. The Cross/Sybilski model, Cross/Williamson model, and Carreau model were expressed as follows:

$$\frac{\eta}{\eta_0} = \frac{1}{1 + (K\omega)^m}, \quad (1)$$

$$\frac{\eta - \eta_\infty}{\eta_0 - \eta_\infty} = \frac{1}{1 + (K\omega)^m}, \quad (2)$$

TABLE 3: Testing data of the asphalt mixture Marshall specimen.

Asphalt binders		Asphalt-aggregate ratio %	Apparent density g/cm <sup>3</sup>	Theoretical maximum density g/cm <sup>3</sup>	VV %	VMA %	VFA %
Unmodified	PEN20	4.8	2.431	2.542	4.35	14.28	69.5
	PEN50	4.6	2.433	2.547	4.42	14.21	68.7
	PEN90	4.6	2.437	2.553	4.55	14.11	67.8
Modified	SBS I-C	4.9	2.414	2.522	4.30	14.83	71
	SBS I-D	4.9	2.419	2.528	4.33	14.66	70.5
	TPS	5.1	2.409	2.516	4.25	14.97	71.6

$$\frac{\eta - \eta_{\infty}}{\eta_0 - \eta_{\infty}} = \frac{1}{[1 + (K\omega)^2]^{(m/2)}}. \quad (3)$$

Equation (1) was for the Cross/Sybilski model, equation (2) was for the Cross/Williamson model, and equation (3) was for the Carreau model.  $\eta$  was the complex viscosity of the asphalt sample,  $\eta_0$  was the ZSV of the asphalt sample, and  $\eta_{\infty}$  was the complex viscosity when the shear frequency is infinite. Note that the value of  $\eta_{\infty}$  cannot be directly obtained from the tests and was replaced with the complex viscosity at 10 rad/s.  $K$  and  $m$  are the property coefficients of the asphalt sample.

The accelerated loading facility test in the United States showed that the Carreau model was more suitable than the Cross/Williamson model for calculating the value of ZSV. In this paper, the three models were all adopted and compared to characterize rutting resistance of the asphalt sample better.

**3.4. Rutting Test.** In order to evaluate the high-temperature performance of the asphalt mixtures, the rutting test adopted in this paper was carried out in accordance with the method specified in the Chinese standard of JTG E20-2011 [35]. The test pieces of asphalt mixture should have the size of  $300 \times 300 \times 50 (L \times b \times h) \text{mm}^3$ . The rutting formed on the test piece surface under the repeated passing action of the wheel along the same trajectory at a frequency of  $42 \pm 1$  cycles/min. The dynamic stability (DS) of the test piece was calculated, as shown in the following equation:

$$DS = \frac{(t_2 - t_1) \times N}{d_2 - d_1}, \quad (4)$$

where  $d_1$  and  $d_2$  were the rutting depths at  $t_1$  (45 min) and  $t_2$  (60 min), respectively.  $N$  was the frequency of the wheel passing through the test pieces. The antirutting property of asphalt mixture was evaluated by the dynamic stability. It is worth noting that three repeated tests were carried out on each type of asphalt binder to ensure the reliability of the results.

**3.5. GRA Method.** Gray relational analysis (GRA) method is a mathematical analysis method to measure the relationship

between the factors and the system behaviors based on the finite and irregular data [36, 37]. In the principle of GRA, the relation among the data array curves is usually judged based on the similarity among geometric shapes. The gray relational coefficient can be calculated quantitatively by the normalization and comparison of the data arrays. The gray relational degree is subsequently calculated by taking the arithmetic average of the gray relational coefficients at different time point. A larger relational degree means a higher similarity among the data.

The detailed calculating methods of the gray relational coefficient and gray relational degree are as follows.

Suppose that there was a matrix, composed of a series of data arrays:

$$\begin{aligned} &\{X_0^{(0)}(r)\}, \quad r = 1, 2, 3, \dots, n, \\ &\{X_1^{(0)}(r)\}, \quad r = 1, 2, 3, \dots, n, \\ &\{X_2^{(0)}(r)\}, \quad r = 1, 2, 3, \dots, n, \\ &\dots \\ &\{X_k^{(0)}(r)\}, \quad r = 1, 2, 3, \dots, n. \end{aligned} \quad (5)$$

$X$  was the gray relational factor set, and the  $k$  arrays were  $k$  factors.  $n$  was the dimension of different  $k$  factors, which was the same value in this paper.  $X_0^{(0)}$  was the main array (or the reference array) and  $X_m^{(0)} (m = 1, 2, 3, \dots, k)$  were the subarrays (or the comparison arrays).

As different values in the matrix have a great difference, the normalization of the arrays is necessary for comparing different factors directly and eliminating the dimension divergence. In this paper, the equalization method was utilized for normalizing treatment. The main array and the subarrays were processed as follows:

$$\{X_m^{(1)}(r)\} = \frac{\{X_m^{(0)}(r)\}}{\overline{X_m}}, \quad (6)$$

$$\overline{X_m} = \frac{1}{N_m} \left\{ \sum_{r=1}^{N_m} X_m^{(0)}(r) \right\}. \quad (7)$$

$\frac{X_m^{(1)}}{\overline{X_m}} (m = 0, 1, 2, 3, \dots, k)$  were the normalized arrays and  $\frac{X_m^{(1)}}{\overline{X_m}}$  was the arithmetic average value of the original arrays.

The gray relational coefficient ( $\gamma_m(r)$ ) between  $X_0^{(0)}$  and  $X_m^{(0)}$  was expressed as follows:

$$\gamma_m(r) = \frac{\min_{(m)} \min_{(r)} |X_0^{(1)}(r) - X_m^{(1)}(r)| + \xi \max_{(m)} \max_{(r)} |X_0^{(1)}(r) - X_m^{(1)}(r)|}{|X_0^{(1)}(r) - X_m^{(1)}(r)| + \xi \max_{(m)} \max_{(r)} |X_0^{(1)}(r) - X_m^{(1)}(r)|} \quad (8)$$

The gray relational degree ( $\Gamma_m$ ) indicated the relational degree between the main array and the subarrays, which was calculated as follows:

$$\Gamma_m = \sum_{r=1}^n \beta_r \gamma_m(r), \quad (9)$$

and  $\xi$  was the distinguishing coefficient, which was 0.2 in this paper [31], according to the previous research.  $\beta_r$  was the weighting of gray relational coefficient.

Gray relational entropy is a kind of gray entropy to characterize the distances between the points and each reference point. The density value of distribution of the subarrays ( $P_m$ ) was calculated as follows:

$$R_m = \{\gamma_m(r)\}, \quad r = 1, 2, 3, \dots, n; \quad m = 0, 1, 2, 3, \dots, k, \quad (10)$$

$$P_m \triangleq \frac{\gamma_m(r)}{\sum_{r=1}^n \gamma_m(r)}, \quad m = 0, 1, 2, 3, \dots, k, \quad (11)$$

$$H(R_m) \triangleq \sum_{r=1}^n P_m \ln P_m, \quad m = 0, 1, 2, 3, \dots, k. \quad (12)$$

$R_m$  is a matrix composed of the gray relational coefficient ( $\gamma_m(r)$ ). The gray relational entropy of the sequence  $X_m$  was introduced as follows:

The entropy relational degree  $E(X_m)$  of the sequence  $X_m$  was calculated as follows:

$$E(X_m) \triangleq \frac{H(R_m)}{H_m}, \quad (13)$$

where  $H_m$  was the maximum value of the gray relational entropy.

The entropy relational degree was used to characterize the correlation between the subarrays and the main arrays. The larger the gray relational degree of the sequence  $X_m$  was, the closer the geometry of the sequence  $X_m$  to that of the reference sequence would be. Therefore, using the GRA model, the degree of correlation between the high-temperature performance of asphalt binders and the dynamic stability of the mixtures was determined.

When studying the relationship between the asphalt and mixture, the steps used to calculate the gray correlation degree and the entropy relational degree are listed as follows. Firstly, the test results of asphalt binders, including the penetration, softening point, viscosity, rutting factor, modified rutting factor, percent recovery, nonrecoverable

creep compliance, and zero-shear viscosity, were the subarrays. The DS of asphalt mixtures was the main array. Then, the main array and subarrays were both normalized. Finally, the gray relational coefficients and gray relational degree could be calculated according to equations (8)~(13).

## 4. Results and Discussion

### 4.1. High-Temperature Rheological Properties of Asphalt

**4.1.1. DSR Test Results.** The high-temperature rheological properties of six asphalt binders including the complex modulus  $G^*$ , the phase angle  $\delta$ , and the rutting indicator ( $G^*/\sin \delta$ ) are shown in Figure 1, respectively. The high-temperature grades of the polymer-modified asphalt were 82, 70, 64, 76, 82, and 82°C for PEN20, PEN50, PEN90, SBS I-C, SBS I-C, and TPS-modified asphalt. It was found that the phase angle curves had different forms in Figure 1(b), which was related to whether the modifiers were added and the properties of various modifiers. For the unmodified asphalt, the phase angle curves both rose with the increasing of the temperature. Meanwhile, for the modified asphalt, the trend of rising had slowed down, and there was a certain degree of decline in the temperature range of 76–88°C. The phase angle was an important feature to characterize the viscosity change of asphalt under the external shear force, which reflected that the addition of SBS and TPS was beneficial for the asphalt to maintain a relatively good shear strain recovery ability at higher temperatures. Among them, TPS-modified asphalt was the preferred except in the temperature range of 82–88°C, at which SBS I-D-modified asphalt had the smaller phase angle.

Besides, as shown in Figures 1(a) and 1(c), the complex modulus  $G^*$  and the rutting indicator ( $G^*/\sin \delta$ ) value of low-grade asphalt PEN20 were significantly larger than the other five kinds of asphalt in the interval of 64–82°C. When the temperature was higher than 82°C, the rutting indicator ( $G^*/\sin \delta$ ) of TPS-modified asphalt was the best, while the high-temperature performances of PEN90 and PEN50 asphalt were always weak. The rheological properties of the six kinds of asphalt at the PG grade temperatures were summarized in Figure 1(d). It can be observed that the SBS I-D presented the lowest complex modulus  $G^*$  and rutting indicator ( $G^*/\sin \delta$ ), and PEN20 had the largest phase angle  $\delta$ . Since the difference between the SBS I-D and TPS-modified asphalt was less than 20%, TPS had similar high-temperature responses to SBS, and it could be considered for replacing the traditional SBS with proper regard to the high-temperature performances.

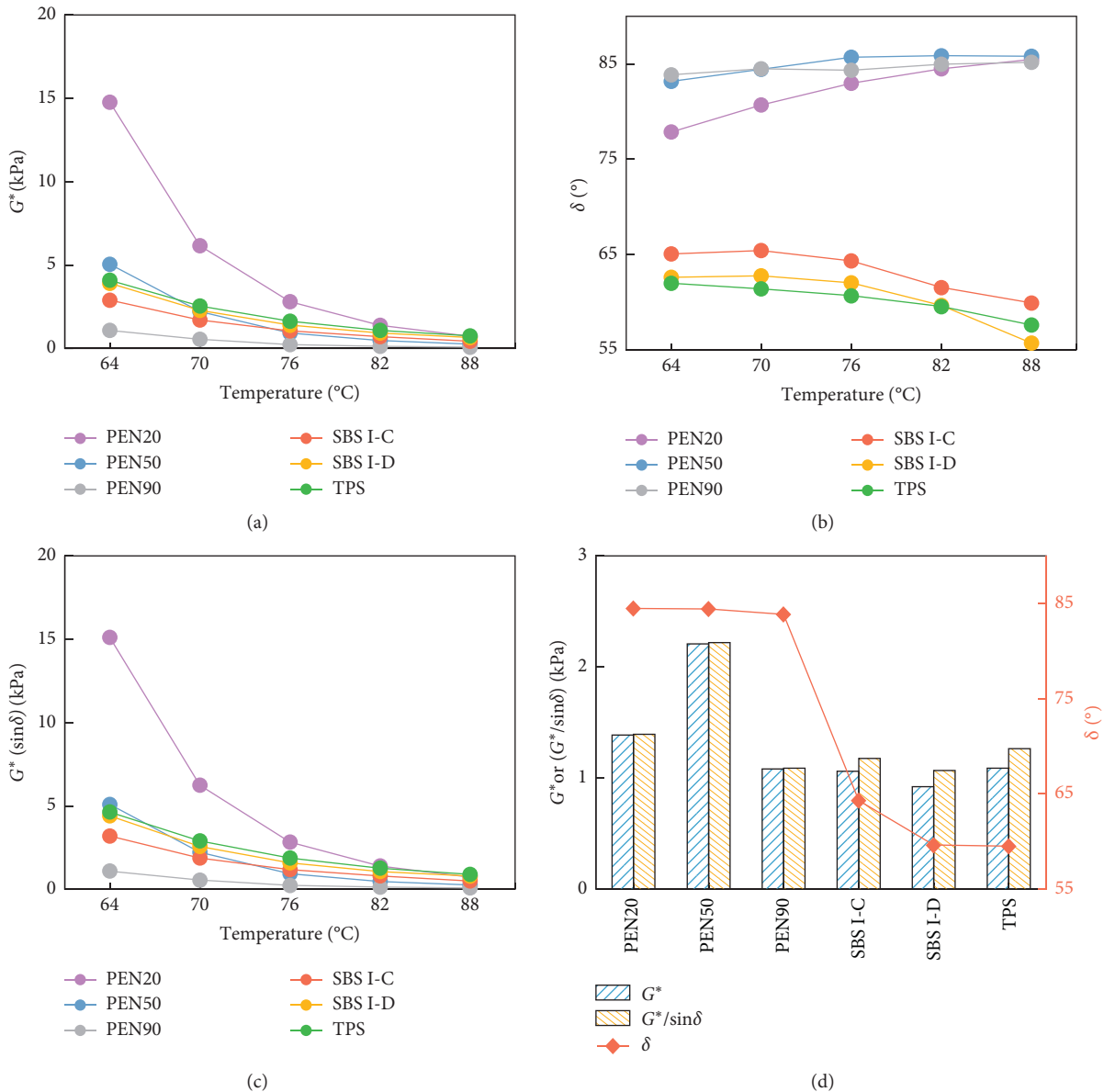


FIGURE 1: High-temperature rheological properties of six asphalt binders: (a) complex modulus, (b) phase angles, (c) rutting indicator, and (d) rheological parameters at the PG grade temperatures.

**4.1.2. MSCR Test Results.** The MSCR test results of the six asphalt binders at different temperature are shown in Figure 2. These results indicated the significant viscoelastic-plastic properties of the asphalt. Figure 2(a) illustrates the nonrecoverable deformation compliance  $J_{nr}$  of the six asphalt binders at 3.2 kPa. It could be found that the nonrecoverable deformation compliance  $J_{nr}$  values all had an exponential relationship with the temperature, indicating that the high-temperature stability of asphalt would be significantly weakened as the temperature increased. The difference in  $J_{nr}$  between two stress levels (0.1 kPa and 3.2 kPa) was an important indicator to evaluate the high-temperature performance related to the external stress response. The larger  $J_{nr \text{ diff}}$  value indicated the greater stress sensitivity of the resistance to cumulative deformation. As

shown in Figure 2(b), TPS-modified asphalt showed the greatest stress sensitivity, followed by SBS I-D-modified asphalt. It was concluded that the modified asphalt had greater stress sensitivity of the resistance to cumulative deformation than the base asphalt.

Figure 2(c) shows the creep and recovery rate of the asphalt at 3.2 kPa. The curves had different forms, which were automatically divided into two shapes according to whether the modifiers were added. Under the creep load condition, the PEN90 asphalt had a significant degree of deformation and a low deformation recovery rate, which indicated that the PEN90 asphalt performed soft viscosities compared with the other types of asphalt. Note that the  $R_{3,2}$  value of the PEN90 asphalt was lower than zero, indicating that the destruction of the structure made the asphalt

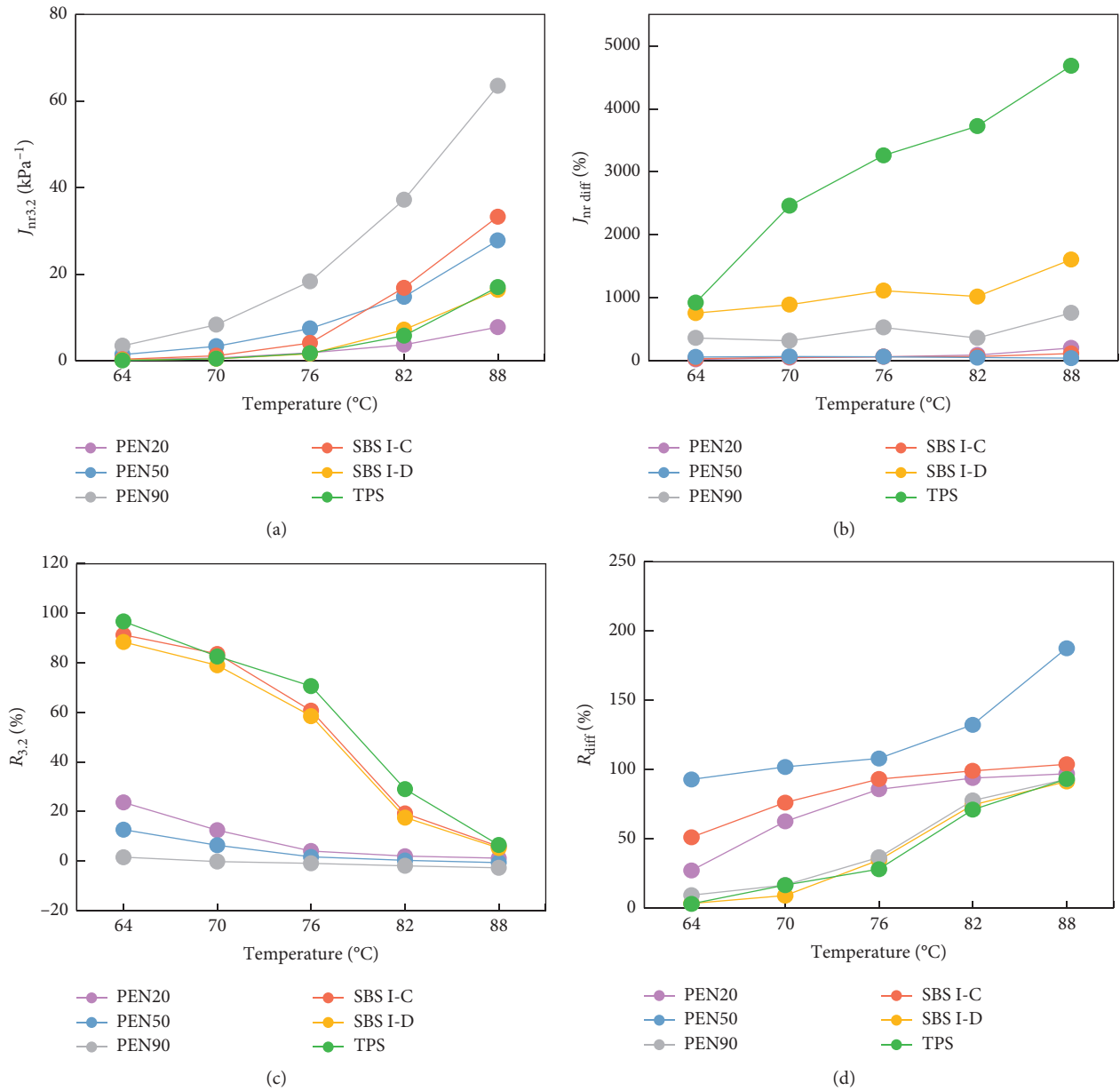


FIGURE 2: Multiple stress creep recovery (MSCR) test results of six asphalt binders.

completely lose its elasticity and become a fluid. Figure 2(d) shows the change in the stress sensitivity index  $R_{diff}$  of the asphalt with temperature. The large  $R_{diff}$  value indicated the recovery capability of asphalt was sensitive to the applied stress. It was reconfirmed that the six asphalt binders all exhibited greater sensitivity to the stress at the high temperature, as shown in Figure 2(b). Generally speaking, the TPS-modified asphalt performed best in the MSCR test, followed by the SBS I-D-modified asphalt, because they had the least deformation and the most substantial deformation recovery ability. It is worth noting that the low-grade PEN20 asphalt also had the low deformation, while its deformation recovery ability was poor.

**4.1.3. ZSV Test Results.** The ZSV test results of the six asphalt binders at 60 °C are shown in Figure 3 as well as the complex viscosity  $\eta$ -frequency  $\omega$  curves, the fitted  $K$ ,  $m$ , and ZSV values using the Cross/Sybilski model, Cross/Williamson model, and Carreau model.

As shown in Figure 3, there were substantial differences in  $K$ ,  $m$ , and ZSV values between different kinds of asphalt using three different models, especially the base asphalt and modified asphalt. In order to present the data more clearly and in detail, the standard deviation  $\sigma$  for data is shown in Table 4.

It has been proved that the parameter  $m$  mainly reflected the sensitivity of the asphalt to shear stress, and the closer the

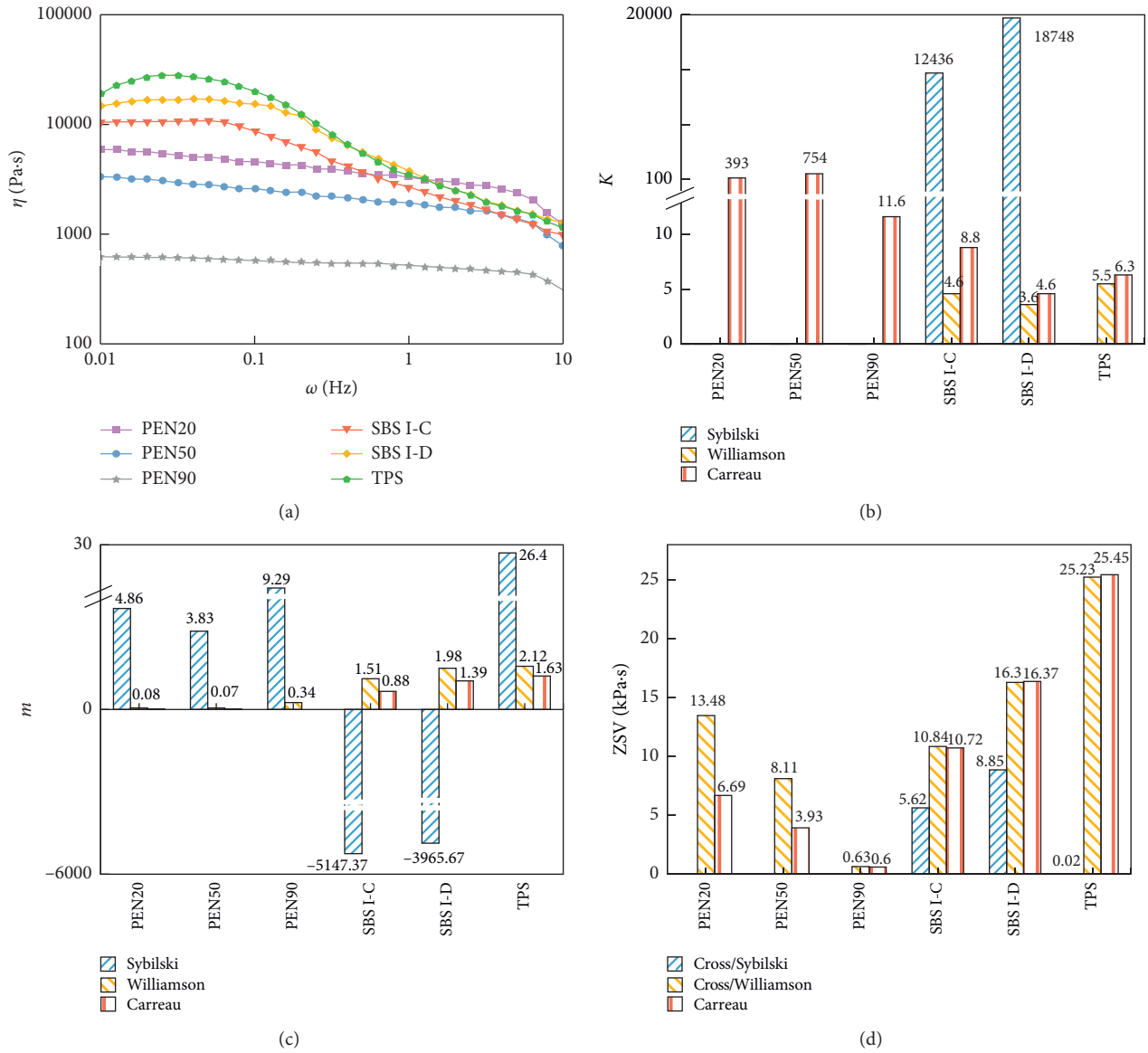


FIGURE 3: Zero-shear viscosity (ZSV) test results of six asphalt binders.

$K$  and  $m$  values were to zero, the closer the property of the material was to Newtonian fluid based on the Cross/Sybilski model [38]. Thus, the large  $m$  value indicated that the asphalt was sensitive to the shear frequency. As shown in Figure 3(b), the  $K$  value of SBS I-D-modified asphalt was the highest, which reflected that the SBS I-D-modified asphalt was more similar to the non-Newtonian fluid. Thus, it was necessary to adopt ZSV value to analyze the high-temperature performance.

Based on the fitted  $m$  value from Cross/Williamson model in Figure 3(c), the viscosity values of the modified asphalt were more sensitive to the shearing frequency than those of the base asphalt. The TPS-modified asphalt had the most considerable  $m$  value, indicating that the viscosity test result was most affected by the shear frequency. In the results of the SBS-modified asphalt, it was found that the fitted  $m$

from the Cross/Sybilski model were negative values, which may be caused by the small range of the selected shear frequency in this study. As shown in in Figure 3(d), the ZSV value obtained by the Cross/Sybilski model fluctuated greatly between different types of asphalt; in particular, the standard errors of ZSV of the base asphalt binders were large. In order to distinguish the high-temperature performance of different asphalt by using ZSV test, it is necessary to perform relational analysis with the calculation results through three different calculation models.

In addition, it could be concluded that the SBS I-D-modified asphalt performed best to resist high-temperature deformations, followed by the SBS I-C-modified asphalt, due to the large and harmonious ZSV value in three different models. The ZSV of the PEN90 asphalt was significantly less than the other five types of asphalt, which

TABLE 4: Fitting  $K$ ,  $m$ , and ZSV values in three ZSV models.

Asphalt binders		$K$	$\sigma_K$	$m$	$\sigma_m$	ZSV (kPa·s)	$\sigma_{ZSV}$ (kPa·s)
PEN20	Sybilski	$5.06 \times 10^{-4}$	$2.33 \times 10^{-12}$	4.86	4.54	1.71	80.4
	Williamson	$2.21 \times 10^{-6}$	$7.97 \times 10^{-10}$	0.08	0.06	13483.06	4521.4
	Carreau	392.95	297.34	$6.04 \times 10^{-4}$	$2.07 \times 10^{-3}$	6694.85	424.38
PEN50	Sybilski	$1.56 \times 10^{-3}$	4.67	3.83	1.11	1.56	46.74
	Williamson	$1.45 \times 10^{-6}$	$5.35 \times 10^{-9}$	0.07	0.06	8106.44	3400.58
	Carreau	753.61	195.47	$7.83 \times 10^{-4}$	$2 \times 10^{-3}$	3926.12	812.54
PEN90	Sybilski	$3.3 \times 10^{-3}$	$3.89 \times 10^{-2}$	9.29	2.93	2.08	10.24
	Williamson	$8.62 \times 10^{-9}$	$1.41 \times 10^{-11}$	0.34	0.25	630.81	36.71
	Carreau	11.63	8.16	$1.44 \times 10^{-4}$	$8.29 \times 10^{-3}$	599.17	8.32
SBS I-C	Sybilski	12435.68	0	-5147.37	0	5622.27	704.7
	Williamson	4.64	0.25	1.51	0.12	10841.59	183.54
	Carreau	8.78	0.91	0.88	0.05	10718.52	108.85
SBS I-D	Sybilski	18747.94	0	-3965.67	0	8845.34	1155.74
	Williamson	3.59	0.18	1.98	0.18	16295.35	253.91
	Carreau	4.62	0.73	1.39	0.14	16365.79	220.56
TPS	Sybilski	0.02	0	26.44	0	17.46	2.92
	Williamson	5.45	0.43	2.12	0.31	25233.52	729.53
	Carreau	6.28	1.71	1.63	0.28	25453.75	670.56

was similar to the MSCR and DSR test results. Thus, the PEN90 asphalt performance was significantly soft-viscoelastic.

In summary, for the SBS-modified asphalt with high viscosity, the high-temperature performance could be well characterized by using three ZSV models, of which the results coincided with each other. Meanwhile, for the asphalt with low viscosity but large complex modulus  $G^*$  (such as the low-grade PEN20 asphalt) and the asphalt with especially high viscosity (such as TPS-modified asphalt), the ZSV value by one ZSV model did not reflect their low stress sensitivity and good rutting resistance. This result was consistent with the results of previous studies [16].

**4.2. High-Temperature Properties of Asphalt Mixtures.** As shown in Table 5, the dynamic stability (DS) of the TPS-modified asphalt mixture was 9965 times/mm, while the DS of SBS I-D, PEN20, SBS I-C, PEN50, and PEN90 asphalt mixture were 8150, 5415, 4603, 1986, and 580 times/mm, respectively. The DS results concluded that the TPS-modified asphalt mixture performed best for resisting the rutting deformations.

**4.3. GRA for the Technical Indexes.** In order to comprehensively analyze the high-temperature performance of the asphalt and its mixtures, the high-temperature performance technical indexes were normalized based on the maximum test values of the different series, as shown in equation (14). It is worth noting that the DSR and MSCR data were all at the temperature of 64°C. Aiming to ensure the reliability of the conclusions, DSR data were also obtained from the RTFOT residue of asphalt binders to study the correlation between rutting factor and dynamic stability under different experimental conditions.

TABLE 5: Rutting testing data of six asphalt mixtures.

Parameters	Unmodified			Modified		
	PEN20	PEN50	PEN90	SBS I-C	SBS I-D	TPS
DS, times/mm	5415	1986	580	4603	8150	9965
$\sigma$ , times/mm	601.1	186.7	45.8	580	1352.9	1135.3

$\sigma$  denotes the standard deviation.

$$\text{Normalized } x_i(k) = \frac{x_i(k)}{x_{\max}(k)}, \quad (14)$$

where  $x$  was the technical index, such as softening point, viscosity, rutting indicator,  $R$ , and ZSV.  $k$  was the type of the asphalt binders, which includes the unmodified asphalt and modified asphalt.

As shown in Figure 4, the normalized high-temperature performance technical indexes of the asphalt were drawn in hexagonal envelope diagram. The asphalt with the largest hexagonal envelope area should have the best high-temperature overall performance. Thus, the high-temperature performance ranking of the asphalt was TPS-modified asphalt, followed by SBS I-D, SBS I-C, PEN20, PEN50, and PEN90. The presented analysis results had a good match with the viscosity at 60°C and the Carreau modeled ZSV test, while they were different from the traditional DSR and MSCR results. In general, the modified asphalt performed better than the unmodified asphalt according to the high-temperature rheological properties tests. Despite the excellent performance in some test results, such as the low deformation in MSCR, the hexagonal envelope area analysis showed that the PEN20 asphalt presented the unbalanced high-temperature performance.

Besides, in the previous research, dynamic stability (DS) was a useful indicator to characterize the high-temperature

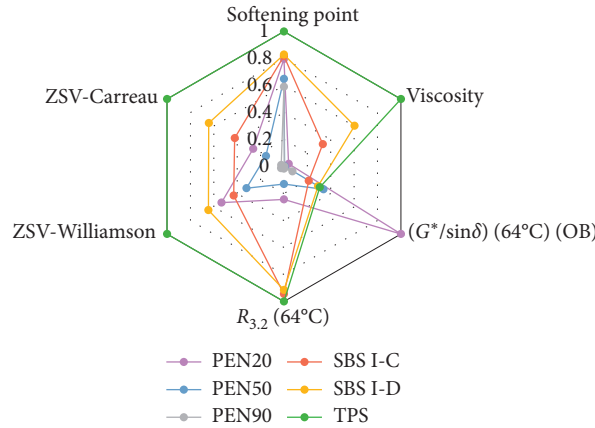


FIGURE 4: High-temperature performance distributions of six asphalt binders in hexagonal envelope diagram.

TABLE 6: Data preprocessing for GRA.

Parameters	$X_m$	Unmodified				Modified	
		PEN20	PEN50	PEN90	SBS I-C	SBS I-D	TPS
Original sequence							
DS (times/mm)	$X_0^{(0)}$	5415	1986	580	4603	8150	9965
Penetration (25°C) (0.1 mm)	$X_1^{(0)}$	23	54	91	74	57	69
Softening point (°C)	$X_2^{(0)}$	64.2	52.4	47.7	66	66.9	80.7
Viscosity (60°C) (Pa·s)	$X_3^{(0)}$	3315	394	198	27360	49755	82459
$(G^*/\sin \delta)$ (64°C) (OB)	$X_4^{(0)}$	15.11	5.09	1.09	3.20	4.40	4.63
$(G^*/1 - (\sin \delta \cdot \tan \delta)^{-1})$ (64°C) (OB)	$X_5^{(0)}$	18.94	5.75	1.21	5.95	9.4	10.30
$J_{nr3.2}$ (kPa <sup>-1</sup> ) (64°C)	$X_6^{(0)}$	0.2391	1.3976	3.43	0.3328	0.1369	0.0473
$J_{nr0.1}$ (kPa <sup>-1</sup> ) (64°C)	$X_7^{(0)}$	0.2009	1.0635	2.175	0.0389	0.0297	0.0046
$R_{3,2}$ (%) (64°C)	$X_8^{(0)}$	23.6	12.6	1.5	91.3	88.4	96.7
$R_{0,1}$ (%) (64°C)	$X_9^{(0)}$	32.3	25.7	20.8	94.3	97.3	99.6
ZSV-Sybilski (Pa·s)	$X_{10}^{(0)}$	1.71	1.56	2.08	5622.27	8845.34	17.46
ZSV-Williamson (Pa·s)	$X_{11}^{(0)}$	13483.1	8106.44	630.81	10841.6	16295.4	25233.5
ZSV-Carreau (Pa·s)	$X_{12}^{(0)}$	6694.85	3926.12	599.17	10718.5	16365.8	25453.8
$(G^*/\sin \delta)$ (64°C) (RTFOT)	$X_{13}^{(0)}$	27.59	8.81	1.98	5.20	6.85	5.87
Normalized sequence							
DS (times/mm)	$X_0^{(1)}$	1.06	0.39	0.11	0.90	1.59	1.95
Penetration (25°C) (0.1 mm)	$X_1^{(1)}$	0.38	0.88	1.48	1.21	0.93	1.13
Softening point (°C)	$X_2^{(1)}$	1.02	0.83	0.76	1.05	1.06	1.28
Viscosity (60°C) (Pa·s)	$X_3^{(1)}$	0.12	0.01	0.01	1.00	1.83	3.03
$(G^*/\sin \delta)$ (64°C)	$X_4^{(1)}$	2.71	0.91	0.20	0.57	0.79	0.83
$(G^*/1 - (\sin \delta \cdot \tan \delta)^{-1})$ (64°C)	$X_5^{(1)}$	2.20	0.67	0.14	0.69	1.10	1.20
$J_{nr3.2}$ (kPa <sup>-1</sup> ) (64°C)	$X_6^{(1)}$	0.26	1.50	3.69	0.36	0.15	0.05
$J_{nr0.1}$ (kPa <sup>-1</sup> ) (64°C)	$X_7^{(1)}$	0.34	1.82	3.72	0.07	0.05	0.01
$R_{3,2}$ (%) (64°C)	$X_8^{(1)}$	0.45	0.24	0.03	1.74	1.69	1.85
$R_{0,1}$ (%) (64°C)	$X_9^{(1)}$	0.52	0.42	0.34	1.53	1.58	1.62
ZSV-Sybilski (Pa·s)	$X_{10}^{(1)}$	0.00	0.00	0.00	2.33	3.66	0.01
ZSV-Williamson (Pa·s)	$X_{11}^{(1)}$	1.08	0.65	0.05	0.87	1.31	2.03
ZSV-Carreau (Pa·s)	$X_{12}^{(1)}$	0.63	0.37	0.06	1.01	1.54	2.40
$(G^*/\sin \delta)$ (64°C) (RTFOT)	$X_{13}^{(1)}$	2.94	0.94	0.21	0.55	0.73	0.63



TABLE 7: Gray relational coefficients between asphalt indexes and dynamic stability.

Parameters	Unmodified			Modified			Gray relational degree
	PEN20	PEN50	PEN90	SBS I-C	SBS I-D	TPS	
$\gamma_1$	0.52	0.61	0.35	0.72	0.53	0.48	0.53
$\gamma_2$	0.97	0.63	0.54	0.85	0.59	0.53	0.68
$\gamma_3$	0.44	0.67	0.89	0.89	0.77	0.41	0.68
$\gamma_4$	0.31	0.59	0.92	0.70	0.48	0.40	0.57
$\gamma_5$	0.39	0.73	0.98	0.79	0.60	0.50	0.67
$\gamma_6$	0.48	0.40	0.17	0.58	0.34	0.28	0.38
$\gamma_7$	0.51	0.34	0.17	0.47	0.33	0.28	0.35
$\gamma_8$	0.55	0.85	0.91	0.47	0.90	0.90	0.76
$\gamma_9$	0.59	0.98	0.78	0.54	1.00	0.70	0.77
$\gamma_{10}$	0.41	0.66	0.88	0.34	0.26	0.28	0.47
$\gamma_{11}$	0.99	0.75	0.94	0.98	0.73	0.92	0.88
$\gamma_{12}$	0.64	1.00	0.95	0.89	0.95	0.63	0.84
$\gamma_{13}$	0.28	0.58	0.90	0.69	0.46	0.36	0.55

performance of asphalt mixtures [39–41]. The DS ranking of the asphalt mixtures was TPS-modified asphalt, followed by SBS I-D, PEN20, SBS I-C, PEN50, and PEN90, which was also different from the result by the envelope area analysis.

In order to create the relationship between the performance evaluation indexes of the asphalt and the performance of the asphalt mixture, GRA was adopted and the results of different asphalt binders and asphalt mixtures were defined as  $X_m^{(0)}$  (where  $m = 0, 1, 2, \dots, 13$ ) and listed in Table 6. The DS of the asphalt mixture were selected for the main arrays, while the high-temperature performance indexes of asphalt were taken as the subarrays. In this section, the normalized results were calculated based on equations (6) and (7), as shown in Table 6.

In order to further analyze whether the rutting indicator ( $G^*/\sin \delta$ ) was the suitable candidate for the high-temperature performance evaluation of the asphalt, both the unaged samples (marked as OB) and RTFOT aged samples (marked as RTFOT) were analyzed in this part. In addition, the modified rutting indicator ( $G^*/1 - (\sin \delta \cdot \tan \delta)^{-1}$ ) was also introduced. The absolute difference between the two sequences was calculated, and then the gray relational coefficients and gray relational degree were calculated, based on equations (8) and (9). The detailed results are shown in Table 7.

The gray entropy relational degree was calculated by using equations (10)~(13). Figure 5 shows the gray relational degree and entropy relational degree between asphalt binder indexes and dynamic stability of the corresponding asphalt mixtures. The gray relational degree was to take the arithmetic average of the gray relational coefficients of each type of asphalt, which would cause the loss of the tendency information of each local point. But the entropy relational degree could effectively evaluate the correlation on the entire sequence correlation degree rather than the influence of the single-point correlation coefficient. According to the entropy relational criterion, the larger the gray relational degree and entropy relational degree values of the high-temperature performance indexes were, the stronger the correlation between the high-temperature performance of the asphalt binder and the dynamic stability of asphalt

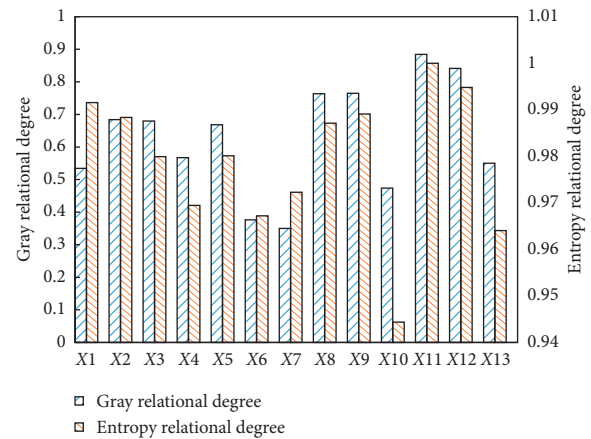


FIGURE 5: Gray relational degree and entropy relational degree between asphalt indexes and DS.

mixtures would be. For the gray relational degree,  $\Gamma_{11} > \Gamma_{12} > \Gamma_9 > \Gamma_8 > \Gamma_2 > \Gamma_3 > \Gamma_5 > \Gamma_4 > \Gamma_{13} > \Gamma_1 > \Gamma_{10} > \Gamma_6 > \Gamma_7$ , while, for the entropy relational degree,  $E(X_{11}) > E(X_{12}) > E(X_1) > E(X_9) > E(X_2) > E(X_8) > E(X_5) > E(X_3) > E(X_7) > E(X_4) > E(X_6) > E(X_{13}) > E(X_{10})$ . Although the two indicators were arranged in different rank order, the  $X_{11}$  sequence, representing the Cross/Williamson modeled ZSV value, was the most relevant to the main array. Since the DS value would well reflect the high-temperature performance of the asphalt mixture, the ZSV test results fitted by the Cross/Williamson model had the highest correlation with the DS and would best characterize the high-temperature performance. The Cross/Williamson model was the most suitable for calculating and fitting the ZSV. Besides, it was found that the rutting indicator ( $G^*/\sin \delta$ ) of the unaged asphalt (named  $X_4$ ) and the RTFOT asphalt (named  $X_{13}$ ) had a similar trend, since the values of the gray relational degree were close. The results indicated that the correlation between the rutting indicator ( $G^*/\sin \delta$ ) in the asphalt's DSR tests and the DS value of asphalt mixture was very poor. The present rutting indicator for evaluating the asphalt mixtures' high-temperature performance might no longer be suitable. Although the

correlation between the modified rutting factor (named  $X_5$ ) and the DS value had improved, the accuracy of its evaluation was still lower than the MSCR and ZSV test results. However, the conclusion should be further proved based on more laboratory tests for the asphalt binder and its mixture.

## 5. Conclusion

Aiming to evaluate the relation between the high-temperature performance of the asphalt binders and their mixture, six typically used asphalt types were employed in this study. The DSR, MSCR, and ZSV tests were conducted on the asphalt binders, and the rutting tests were conducted on the asphalt mixture. Besides, to analyze the gray relational degree and entropy relational degree of the technical index, the correlation between the asphalt binder and the dynamic stability of the mixture was studied through the GRA method. Results in this paper provided a more systematic perspective for the further study of the high-temperature performance evaluation of asphalt binders.

Conclusions are listed as follows:

- (1) In general, the modified asphalt performed better than the unmodified asphalt according to the high-temperature rheological properties tests. Despite the excellent performance in some test results, such as the lowest deformation in MSCR test, the hexagonal envelope area analysis showed that the PEN20 asphalt presented the unbalanced high-temperature performance.
- (2) The ranking of the six kinds of asphalt binders from various tests was different. The TPS-modified asphalt performed best in the MSCR and ZSV tests, while the low-grade asphalt PEN20 had the best technical indexes in the DSR test.
- (3) The Cross/Williamson model fitted zero-shear viscosity of the asphalt and the dynamic stability of the asphalt mixture had the highest gray relational degree and entropy relational degree, which indicated that the Cross/Williamson modeled ZSV value had the highest correlation with the DS value. Thus, the Cross/Williamson model was the most suitable for calculating and fitting the ZSV, which could be used as the key indicator of the high-temperature performance evaluation of the asphalt.
- (4) Furthermore, according to the preliminary results on the six kinds of asphalt and its mixtures, the correlation between the rutting indicator in the asphalt's DSR tests and the DS value of asphalt mixture was very poor. The present rutting indicator ( $G^*/\sin \delta$  and  $G^*/(1 - (\sin \delta \cdot \tan \delta)^{-1})$ ) for evaluating the asphalt mixtures' high-temperature performance might no longer be suitable. However, the conclusion should be further proved based on more laboratory tests for the asphalt binder and its mixture.

## Data Availability

The data used to support the findings of this study are available from the corresponding author upon request.

## Conflicts of Interest

The authors declare that there are no conflicts of interest regarding the publication of this paper.

## Acknowledgments

The authors acknowledge the research funding by the Basic Scientific Research Foundation of Research Institute of Highway (no. 2020-9050), the National Natural Science Foundation of China (NSFC, no. 51908261), and the China Postdoctoral Science Foundation (no. 2020M670252).

## References

- [1] D. A. Anderson and T. W. Kennedy, "Development of SHRP binder specification," *Journal of the Association of Asphalt Paving Technologists*, vol. 62, pp. 481–507, 1993.
- [2] M. Rahi, E. Fini, P. Hajikarimi, and F. M. Nejad, "Rutting characteristics of styrene-ethylene/propylene-styrene polymer modified asphalt," *Journal of Materials in Civil Engineering*, vol. 27, no. 4, Article ID 04014154, 2015.
- [3] K. Yan, H. Xu, and L. You, "Rheological properties of asphalts modified by waste tire rubber and reclaimed low density polyethylene," *Construction and Building Materials*, vol. 83, pp. 143–149, 2015.
- [4] L. You, Z. You, Q. Dai, and L. Zhang, "Assessment of nanoparticles dispersion in asphalt during bubble escaping and bursting: nano hydrated lime modified foamed asphalt," *Construction and Building Materials*, vol. 184, pp. 391–399, 2018.
- [5] G. Zou, X. Zhang, and Z. Li, "Discussions on high temperature grading of Superpave PG system for asphalt binders," *Central South Highway Engineering*, vol. 29, no. 1, pp. 42–44, 2004.
- [6] K. Yan, L. You, and D. Wang, "High-temperature performance of polymer-modified asphalt mixes: preliminary evaluation of the usefulness of standard technical index in polymer-modified asphalt," *Polymers*, vol. 11, no. 9, p. 1404, 2019.
- [7] K. D. Stuart and W. S. Mogawer, "Validation of asphalt binder and mixture test that predict rutting susceptibility using FWHA ALF (with discussion)," *Journal of the Association of Asphalt Paving Technologists*, vol. 66, pp. 109–152, 1997.
- [8] Z. Hu, H. Zhang, S. Wang, and T. Xu, "Thermal-oxidative aging mechanism of asphalt binder based on isothermal thermal analysis at the SARA level," *Construction and Building Materials*, vol. 255, Article ID 119349, 2020.
- [9] X. Sheng, T. Xu, and M. Wang, "Preparation, shape memory performance and microstructures of emulsified asphalt modified by multi-walled carbon nanotubes," *Construction and Building Materials*, vol. 230, Article ID 116954, 2020.
- [10] M. Guo and Y. Tan, "Interaction between asphalt and mineral fillers and its correlation to mastics' viscoelasticity," *International Journal of Pavement Engineering*, pp. 1–10, 2019.
- [11] M. Guo, H. Liu, Y. Jiao et al., "Effect of WMA-RAP technology on pavement performance of asphalt mixture: a state-of-the-

- art review,” *Journal of Cleaner Production*, vol. 266, Article ID 121704, 2020.
- [12] A. Mo, “Refinement of the superpave specification parameter for performance grading of asphalt,” *Journal of Transportation Engineering*, vol. 127, no. 5, pp. 357–362, 2001.
- [13] A. Shenoy, “High temperature performance grading of asphalts through a specification criterion that could capture field performance,” *Journal of Transportation Engineering*, vol. 130, no. 1, pp. 132–137, 2004.
- [14] H. U. Bahia, D. I. Hanson, M. Zeng et al., *Characterization of Modified Asphalt Binders in Superpave Mix Design. NCHRP Rep. No. 459*, National Academy Press, Washington, DC, USA, 2001.
- [15] J. D’Angelo, R. Kluttz, R. N. Dongre et al., “Revision of the superpave high temperature binder specification: the multiple stress creep recovery test,” *Journal of the Association of Asphalt Paving Technologists*, vol. 76, pp. 123–162, 2007.
- [16] J. D’Angelo, “The relationship of the MSCR test to rutting,” *Road Materials and Pavement Design*, vol. 10, no. sup1, pp. 61–80, 2009.
- [17] AASHTO, *Standard Method of Test for Multiple Stress Creep Recovery (MSCR) Test of Asphalt Binder Using a Dynamic Shear Rheometer (DSR)*, American Association of State Highway and Transportation Officials, Washington, DC, USA, 2009.
- [18] S. E. Zoorob, J. P. Castro-Gomes, L. A. Pereira Oliveira, and J. O’Connell, “Investigating the multiple stress creep recovery bitumen characterisation test,” *Construction and Building Materials*, vol. 30, pp. 734–745, 2012.
- [19] B. Singh, N. Saboo, and P. Kumar, “Effect of short-term aging on creep and recovery response of asphalt binders,” *Journal of Transportation Engineering, Part B: Pavements*, vol. 143, no. 4, Article ID 04017017, 2017.
- [20] E. DuBois, D. Y. Mehta, and A. Nolan, “Correlation between multiple stress creep recovery (MSCR) results and polymer modification of binder,” *Construction and Building Materials*, vol. 65, pp. 184–190, 2014.
- [21] N. Saboo, R. Kumar, P. Kumar, and A. Gupta, “Ranking the rheological response of SBS-and EVA-modified bitumen using MSCR and LAS tests,” *Journal of Materials in Civil Engineering*, vol. 30, no. 8, Article ID 04018165, 2018.
- [22] A. Gopalipour, H. U. Bahia, and H. A. Tabatabaee, “Critical considerations toward better implementation of the multiple stress creep and recovery test,” *Journal of Materials in Civil Engineering*, vol. 29, no. 5, Article ID 04016295, 2017.
- [23] A. V. Kataware and D. Singh, “A study on rutting susceptibility of asphalt binders at high stresses using MSCR test,” *Innovative Infrastructure Solutions*, vol. 2, no. 1, p. 4, 2017.
- [24] D. Sybilski, “Zero-shear viscosity of bituminous binder and its relation to bituminous mixture’s rutting resistance,” *Transportation Research Record: Journal of the Transportation Research Board*, vol. 1535, no. 1, pp. 15–21, 1996.
- [25] M. A. Notani and M. Mokhtarnejad, “Investigating the rheological and self-healing capability of toner-modified asphalt binder,” *Proceedings of the Institution of Civil Engineers-Construction Materials*, vol. 173, no. 3, pp. 123–131, 2020.
- [26] N. Saboo and P. Kumar, “Analysis of different test methods for quantifying rutting susceptibility of asphalt binders,” *Journal of Materials in Civil Engineering*, vol. 28, no. 7, Article ID 04016024, 2016.
- [27] R. Romera, A. Santamaría, J. J. Peña et al., “Rheological aspects of the rejuvenation of aged bitumen,” *Rheologica Acta*, vol. 45, no. 4, pp. 474–478, 2006.
- [28] P. Muñoz, Z. Liu, F. Yan, and K. Liao, “Application of grey system theory in studying asphalt aging,” *Petroleum Science and Technology*, vol. 20, no. 9–10, pp. 939–949, 2002.
- [29] C.-M. Wu, C.-C. Lee, J.-C. Du, and D.-H. Shen, “Development of acoustical prediction model for asphalt pavements using grey system approach,” *Road Materials and Pavement Design*, vol. 11, no. 4, pp. 783–805, 2010.
- [30] D. Zhang, M. Chen, S. Wu, J. Liu, and S. Amirhanian, “Analysis of the relationships between waste cooking oil qualities and rejuvenated asphalt properties,” *Materials*, vol. 10, no. 5, p. 508, 2017.
- [31] J. Gao, H. Wang, Z. You, and X. Yang, “Gray relational entropy analysis of high temperature performance of bio-asphalt binder and its mixture,” *International Journal of Pavement Research and Technology*, vol. 11, pp. 698–708, 2018.
- [32] China M, *Technical Specification for Construction of Highway Asphalt Pavements, JTG F40-2004*, China Communications Press, Beijing, China, 2004.
- [33] AASHTO, *Determining the Rheological Properties of Asphalt Binder Using a Dynamic Shear Rheometer (DSR)*, American Association of State Highway and Transportation Officials, Washington, DC, USA, 2010.
- [34] AASHTO, *Standard Method of Test for Effect of Heat and Air on a Moving Film of Asphalt Binder (Rolling Thin-Film Oven Test)*, American Association of State Highway and Transportation Officials, Washington, DC, USA, 2009.
- [35] China M, *Standard Test Methods of Bitumen and Bituminous Mixtures for Highway Engineering, JTG E20-2011*, China Communications Press, Beijing, China, 2011.
- [36] J. L. Deng, “Control problems of grey systems,” *Systems & Control Letters*, vol. 1, pp. 288–294, 1982.
- [37] J. L. Deng, “Introduction to grey system theory,” *Journal of Grey System*, vol. 1, pp. 1–24, 1989.
- [38] D. Sybilski, “Non-Newtonian viscosity of polymer-modified bitumens,” *Materials and Structures*, vol. 26, no. 1, pp. 15–23, 1993.
- [39] H. Wang, Y. Bu, Y. Wang, X. Yang, and Z. You, “The effect of morphological characteristic of coarse aggregates measured with fractal dimension on asphalt mixture’s high-temperature performance,” *Advances in Materials Science and Engineering*, vol. 2016, Article ID 6264317, 2016.
- [40] R. Zhang, H. Wang, J. Gao, Z. You, and X. Yang, “High temperature performance of SBS modified bio-asphalt,” *Construction and Building Materials*, vol. 144, pp. 99–105, 2017.
- [41] J. You, J. Wang, F. Xiao, S. Amirhanian, J. Wang, and Z. Xu, “Impacts of multiple-polymer components on high temperature performance characteristics of airfield modified binders,” *Construction and Building Materials*, vol. 134, pp. 694–702, 2017.

## Research Article

# Study on the Construction Performance of Zeolite Asphalt Mixture Based on Macro-Micro Scale

Zhuolin Li <sup>1</sup>, Junda Ren <sup>1</sup>, Jianping Zhu <sup>1</sup>, Wei Li <sup>1</sup>, Xingsheng Fu <sup>1</sup>,  
and Liying Yang <sup>2</sup>

<sup>1</sup>Liaoning Transportation Research Institute Co., Ltd.,

Key Laboratory of Transport Industry of Expressway Maintenance Technology, Shenyang 110000, China

<sup>2</sup>Beijing Municipal Road & Bridge Building Material Group Co., Ltd., Beijing 100000, China

Correspondence should be addressed to Zhuolin Li; 15771955902@163.com

Received 28 June 2020; Revised 23 August 2020; Accepted 21 October 2020; Published 4 November 2020

Academic Editor: Meng Guo

Copyright © 2020 Zhuolin Li et al. This is an open access article distributed under the Creative Commons Attribution License, which permits unrestricted use, distribution, and reproduction in any medium, provided the original work is properly cited.

In order to explore the construction performance of zeolite asphalt mixture, the microproperties of zeolite and the macroproperties of zeolite asphalt mixture were studied. The structure composition, surface properties, and pore characteristics of zeolite were analyzed by infrared spectroscopy and pressure pump method. The structure, composition, and thermal stability of zeolite were analyzed by differential scanning calorimetry and thermogravimetry, the mechanism of moisture absorption and loss of water was explored, and the properties of moisture absorption and loss of water were studied. The effect of the type and amount of zeolite on the viscosity of asphalt was studied by the viscosity test. According to the mixing current and the compaction void ratio, the influence of zeolite on the construction performance of zeolite asphalt mixture was studied. The results show that zeolite contains special zeolite water and the pore content of zeolite is much higher than that of mineral powder. Zeolite loses water at 90°C~120°C, which is the necessary condition for zeolite to be used in warm mix asphalt mixture. The water absorption and loss capacity of zeolite mainly depend on pore volume. The larger the pore volume is, the stronger the water holding capacity of zeolite is. Meanwhile, the water holding capacity and loss capacity of zeolite are related to pore size distribution. According to the viscosity temperature equation, the mixing and compaction temperature of the asphalt mixture are determined. The mixing and initial pressure temperature of the zeolite asphalt mixture are lower than those of the hot asphalt mixture. Based on the principle of mixing current equivalence, the mixing temperature of zeolite asphalt mixture can be reduced by 20°C compared with that of hot asphalt mixture. The better the water loss performance of zeolite is, the easier the mixture is to be compacted. For the base asphalt mixture, the compaction temperature of the mixture is 120–130°C, and, for the modified asphalt mixture, the compaction temperature is 130–140°C.

## 1. Introduction

Under the premise of ensuring the mechanical performance and durability, warm mix asphalt mixture can effectively reduce the construction temperature and mixing temperature, reduce the emission of harmful gases in the construction process, the energy consumption in the construction, and reduce the aging of asphalt. Therefore, warm mix asphalt mixture conforms to the green traffic concept and is widely used in road construction [1–3]. In the aspect of construction characteristics of warm mix asphalt mixture, Ulmgren et al. [4] suggest that the method of evaluating the working performance of cold mix asphalt

mixture and the method of rotating compaction of mixture should be used to evaluate the working performance of zeolite asphalt mortar under certain temperature conditions. These two methods are helpful to analyze the mixing characteristics of warm mix asphalt mixture to some extent, so as to distinguish the performance of mixture. Vaiana et al. [5] evaluated the volume and mechanical properties of warm mix asphalt mixture and discussed the influence of foaming time (between mixing and compaction) on mixture workability. Sengoz et al. [6] found that the penetration of zeolite asphalt decreased, but the softening point increased. Kutay and Ozturk [7] studied the dissipation process of bubble water in zeolite asphalt system by X-ray

microchromatography. It was found that the dissipation speed of bubble water in hard asphalt was slower than that in soft asphalt and the volume of bubble in different asphalt was different. Wozzuk et al. [8, 9] investigated the foam effect through the dynamic viscosity of synthetic zeolite and clinoptilolite and further analyzed the relationship between the foam effect and the physical and chemical properties of the two kinds of zeolite. It was found that the foam effect had a very important relationship with the water content in the zeolite, the release mode of water with time, and the type of exchangeable cation. Sengoz et al. [10] compared the asphalt with natural zeolite and different types of warm mix agent and determined the basic properties and rheological properties of different types of warm additive asphalt samples by conventional asphalt test method and dynamic shear rheometer (DSR). Dubravský and Mandula [11] studied the mixing ability of natural zeolite in the subbase asphalt layer and studied the performance of asphalt mixture before and after adding natural zeolite. Wozzuk et al. [12] analyzed the influence of zeolite and other fillers on the performance of asphalt mastic and found that clinoptilolite can partially replace the traditional lime fillers, without negative impact on the performance of asphalt mastic. Vaiana et al. [13] studied the volumetric and mechanical properties of zeolite mixtures under laboratory conditions and also studied the effect of foaming time (mixing and compaction) on the workability of the mixture. Leo et al. [14] concluded that the asphalt mixture with synthetic zeolite can be prepared at a temperature lower than 30°C of the mixing and compaction temperature of the hot mixture, and, through Marshall test, when the zeolite content is 0.3% of the total weight of the mixture, the characteristic value of the asphalt mixture still meets the requirements of the use specification. Wozzuk et al. [15] studied the performance of the water filled zeolite foam asphalt added with waste oil. It was found that the addition of waste oil reduced the viscosity and softening point of asphalt and increased penetration. Handayani et al. [16] studied the performance of asphalt mixture with natural zeolite. Through the Marshall test, it was found that when the content of natural zeolite was 1%, the mixing temperature and compaction temperature of polymer modified asphalt mixture could be reduced by 30°C, which was lower than the mixing temperature of zeolite-free polymer modified asphalt mixture. Wozzuk and Franus [17] reviewed the research results of zeolite asphalt mixture technology at home and abroad, including the influence of zeolite on asphalt performance and mixture asphalt performance, as well as the related environmental, economic, and technical benefits. Sanchez-Alonso et al. [18] evaluated the feasibility of preparing warm mix asphalt mixture by adding rap based on natural zeolite through SEM, fluorescence, and Marshall parameters. Sol-Sánchez [19] prepared two kinds of warm mix asphalt with two different types of zeolite waste as additives and compared with the mechanical properties of conventional warm mix asphalt and hot mix asphalt; it was found that the zeolite waste with lower particle size has higher water absorption capacity and 0.3% of the content allows the production of warm mix asphalt at 145°C and has the same workability as traditional

HMA at 165°C and compactness, without reducing its bearing capacity, fatigue life, and water damage resistance. de Castro Amoni et al. [20] synthesized NaA zeolite with fly ash as the main raw material and fly ash from different sources. Through dynamic shear rheometer (DSR), the mechanical tests of tensile strength (TS), resilient modulus (RM), dynamic creep (DC), and tensile strength (POTS) of modified asphalt mixture showed slight positive difference. It can be seen from the above research that zeolite, as a kind of warm mixture, plays a significant role in reducing the construction temperature. At present, the research on the performance of zeolite asphalt mixture at home and abroad mainly focuses on the construction performance verification and road performance analysis of zeolite asphalt mixture, while the research on the microcosmic of zeolite and zeolite asphalt mixture is less.

Therefore, this paper starts from the microperformance of zeolite, analyzes the structure and performance differences between zeolite and mineral powder, and then analyzes the construction performance differences between zeolite asphalt, zeolite asphalt mixture, and hot mix asphalt mixture.

## 2. Materials and Methods

*2.1. Selection of Zeolite and Mineral Powder Materials.* Zeolite is a general term for a group of rack like hydrous aluminosilicate minerals, including natural zeolite generated in nature, as well as synthetic crystals. The properties of zeolite and mineral powder used in this paper are shown in Table 1.

*2.2. Selection of Asphalt Materials.* The asphalt and modified asphalt used in this study are 70# road petroleum asphalt and SBS modified asphalt, and their performance indexes are shown in Tables 2 and 3, respectively.

## 3. Results and Discussion

### 3.1. Microproperties of Zeolite

*3.1.1. Infrared Spectrum of Zeolite.* Infrared spectrum analysis uses the structure analysis of the selective absorption of infrared electromagnetic radiation by objects. Due to the different infrared spectra of different substances, different substances have their own infrared spectrum, and different molecular groups and chemical bonds also have their own vibration frequency, peak shape, and peak strength. Therefore, the identification and analysis of material composition can be carried out by infrared spectrogram [21].

The infrared spectrum data of three kinds of zeolites were analyzed by using the infrared spectrum analysis software OMNIC. The infrared spectrum of three kinds of zeolites is shown in Figure 1.

The absorption band of zeolite infrared spectrum is mainly composed of four parts [22, 23]:

TABLE 1: Apparent density of zeolites and mineral filler.

Sample	Apparent density (g/cm <sup>3</sup> )
1# natural zeolite	2.145
2# natural zeolite	2.623
3# synthetic zeolite	2.297
4# limestone powder	2.811

- (1) 3700–1600 cm<sup>-1</sup> is the absorption band of combined water in zeolite
- (2) 1200–400 cm<sup>-1</sup> is the framework vibration absorption band of zeolite
- (3) 700–500 cm<sup>-1</sup> is the vibration absorption band of zeolite structure unit
- (4) 500–400 cm<sup>-1</sup> is the bending vibration band of Si-O or Al-O

Taking 1# zeolite as an example, the hydroxyl band and lattice water absorption peak appeared near 1636.50 cm<sup>-1</sup> and 3455.08 cm<sup>-1</sup>, indicating the existence of water molecules with different orientations and forces. The 1066.29 cm<sup>-1</sup> strong absorption band is the skeleton vibration of Si-O-Si, 793.52 cm<sup>-1</sup> has the external expansion vibration peak of tetrahedron, the absorption at 606.04 cm<sup>-1</sup> is caused by the expansion vibration of tetrahedron internal structure, and the absorption at 469.58 cm<sup>-1</sup> is caused by the bending vibration of Si-O or Al-O [24, 25].

Compared with them, the absorption peaks at 530.54 cm<sup>-1</sup> and 647.96 cm<sup>-1</sup> are quite different in the 2# zeolite spectrum, which are mainly caused by the stretching vibration of tetrahedron structure, and the absorption peaks at 758.44 cm<sup>-1</sup> are Si-O-Si or Al-O-Si.

There are some differences between 3# zeolite and natural zeolite. The main reason is that there is a small peak at 1383 cm<sup>-1</sup> of synthetic zeolite. The peak of 1383 cm<sup>-1</sup> may be from the original materials of synthetic zeolite, or the peak of some materials adsorbed on the surface of zeolite, but no chemical bond is formed.

Through the analysis of the infrared spectrum of the above-mentioned zeolite, it can be seen that the three kinds of zeolite have wide and strong absorption band of binding water in the approximate vibration range of 3400<sup>-1</sup>~3600 cm<sup>-1</sup> and there are wave peaks near 1600 cm<sup>-1</sup>. These two wave peaks indicate that there are water molecules with different forces and orientations in the zeolite, which is unique to the zeolite.

**3.2. Pore Structure Characteristics.** There are a lot of pores in zeolite, which is one of the most typical and basic physical properties of zeolite.

In this paper, the micropore iv9500 mercury porosimeter of micromeritics company in the United States is used to determine the pore content and pore distribution of zeolite by continuous pressure boosting. The maximum pressure of the mercury porosimeter is 228 MPa, the radius of the measurable hole is 3 nm~360 μm, the surface tension of mercury is 0.485 n/m, the angle of immersion is 130°, and the density is 13.5325 g/ml.

After drying and pretreatment of zeolite samples at 105°C, mercury injection test is carried out. The mercury injection curve of each zeolite is shown in Figure 2.

Figure 2 is the pore size distribution curve of zeolite. The peak value of the curve represents the maximum volume pore in zeolite and its corresponding pore size. The width of the curve represents the range of pore size distribution, that is, the dispersion degree and dispersion degree of different pore sizes of zeolite [26–28]. The pore size distribution curves of three kinds of zeolites are different; among them, the pore size distribution area of 3# synthetic zeolites is the smallest, and its pore size distribution is more uniform.

The pore characteristic parameters of zeolite are analyzed. Figure 3 shows the distribution proportion of various pores in zeolite, and Figure 4 shows the comparison of pore parameters of zeolite.

It can be seen from Figures 3 and 4 that different zeolites have different pore distribution. According to the pore volume, the order is 3# > 1# > 2# > mineral powder; according to the internal specific area, the order is 1# > 2# > 3# > mineral powder.

In general, the pore content of zeolite is much higher than that of mineral powder. Among the three kinds of zeolite, 3# synthetic zeolite has the largest pore volume and the smallest internal specific surface area, which indicates that the pores in synthetic zeolite are mainly macropores. In natural zeolite, 1# in pore size distribution, pore size distribution is more uniform.

### 3.3. Moisture Absorption and Water Loss Characteristics of Zeolite

**3.3.1. Thermal Analysis of Zeolite.** The physical and chemical properties of zeolite are heat-related. According to the infrared spectrum analysis of zeolite, it is found that there is crystal water in the zeolite. Therefore, the thermal analysis of zeolite is carried out in this section.

**(1) DSC Analysis.** DSC analysis is differential scanning calorimetry. By measuring the heat difference between the sample and the reference at the same temperature at the same heating or cooling rate, the DSC curve with the temperature as the abscissa and the heat difference as the ordinate is obtained. The heat flow difference can reflect the enthalpy change of the sample with the temperature change [29, 30].

Mettler Toledo heat flow DSC analyzer was used to analyze zeolite, and the heat curve of zeolite was shown in Figure 5.

In DSC diagram, the melting of crystalline components and the change of phase state of amorphous components will produce endothermic peak. The size and position of the peak can reflect the phase state change of different components. The area surrounded by endothermic peak is large, which shows that there are many components changed and the stability is poor in macroscopic observation. From the DSC curve of Figure 5 zeolite, the curve is relatively flat, indicating that the overall thermal stability of zeolite is good. However,

TABLE 2: Properties of AH-70 asphalt.

Project	Unit	Technical requirements	Test results	Test method
Penetration (25°C)	0.1 mm	60~80	71.9	T0604
Ductility (10°C)	cm	≥20	23.4	T0605
Softening point (R&B)	°C	≥46	47.0	T0606

TABLE 3: Properties of modified asphalt.

Project	Unit	Technical requirements	Test results	Test method
Penetration (25°C)	0.1 mm	60~80	63.6	T0604
Ductility (10°C)	cm	≥30	37.7	T0605
Softening point (R&B)	°C	≥70	72.2	T0606

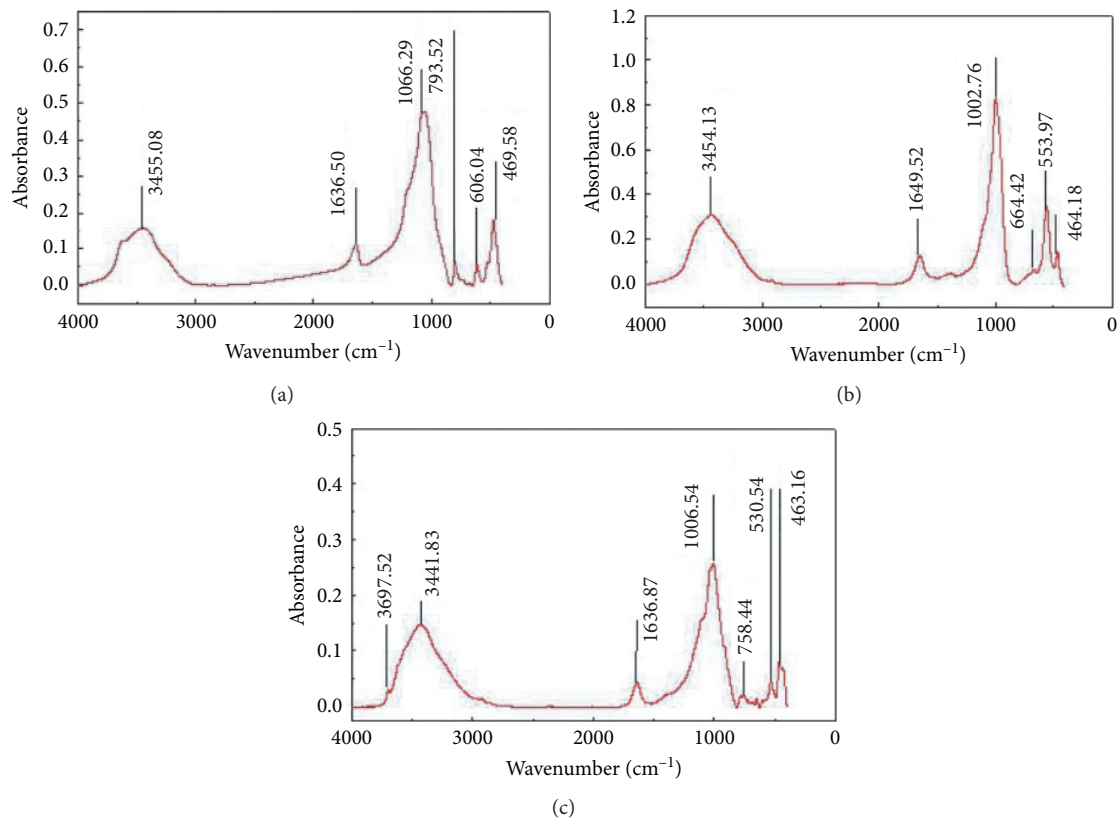


FIGURE 1: Spectra of zeolites. (a) 1# zeolite. (b) 2# zeolite. (c) 3# zeolite.

with the increase of temperature, there is an endothermic peak on the DSC curve of zeolite, which indicates that the phase state changes. The positions of the endothermic peaks of the three kinds of zeolites are different, and the temperatures of phase transformation are different. The DSC data are summarized in Table 4.

In Table 4, the water loss starting point of 2# zeolite is higher; the zeolite loses water at a higher temperature (120°C) or above, while the other two kinds of zeolite basically begin to lose water at 90°C. This is because the density of zeolites 1# and 3# is close to and less than that of zeolite 2#; this shows that the volume number of 1# and 3# is more than that of 2# under the same conditions, and, according to the analysis of pore characteristics of zeolites, the median pore

sizes are 3# > 1# > 2#. The results show that, under the same conditions, the number of mesoporous pores of zeolite 2# is less than that of zeolites 1# and 3#. The more the pores are, the more favourable the phase change of zeolite water is. Therefore, the phase change temperature of zeolite 2# is required to be higher than that of zeolites 1# and 3#, and the phase change temperature of 1# and 3# is close since the density of 1# and 3# is almost equal.

(2) *Thermogravimetric Analysis*. Thermogravimetric analysis (TGA) is to analyze the thermal stability of materials by measuring the change of the mass of objects with the temperature. Its basic principle is that the mass changes when the objects vaporize, decompose, or lose the crystal

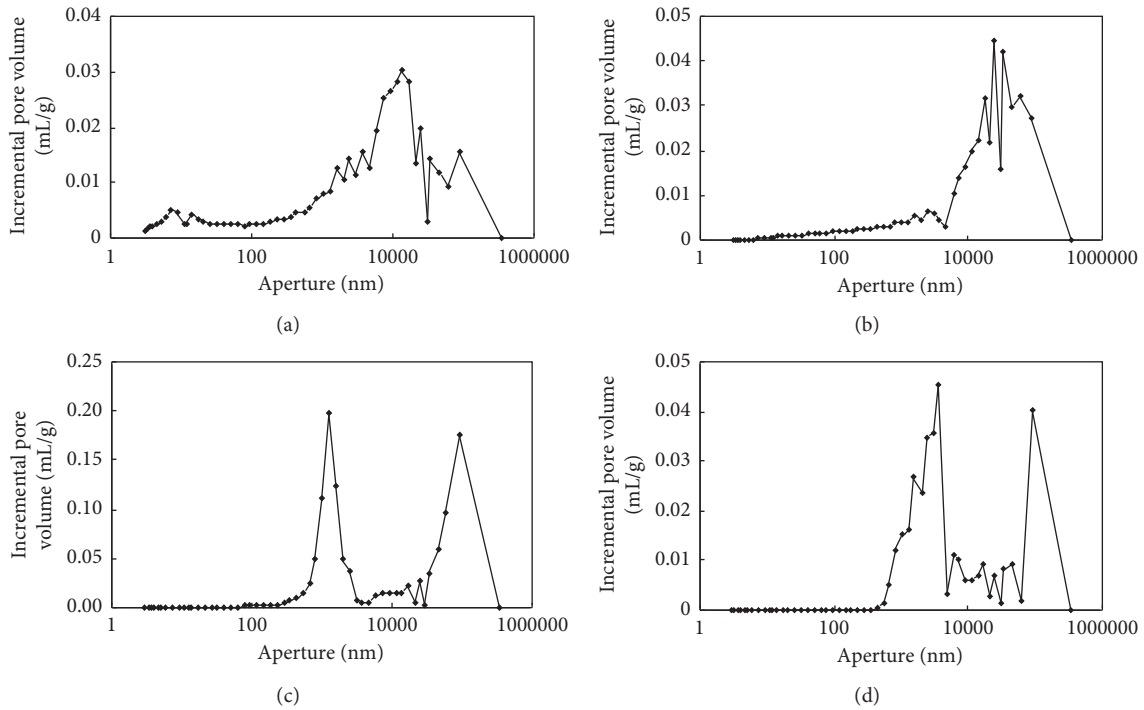


FIGURE 2: Pore distribution of zeolites and mineral filler. (a) 1# zeolite. (b) 2# zeolite. (c) 3# zeolite. (d) 4# mineral filler.

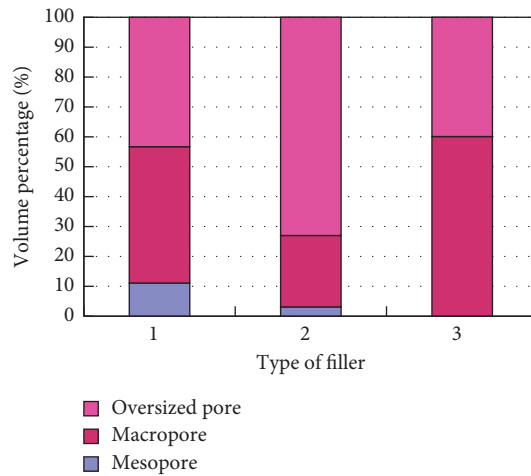


FIGURE 3: Pore distribution of zeolites.

water. Through the mass temperature curve (TGA curve), quantitative information such as the composition and thermal stability of materials can be analyzed [31, 32].

The thermogravimetric analysis of zeolite was carried out on the star system thermogravimetric analyzer. The test temperature range is 30–800°C, and the thermogravimetric curve of zeolite is shown in Figure 6.

Zeolite is used in asphalt mixture, and its working temperature is lower than 200°C. Therefore, when analyzing its heat and weight loss, it focuses on analyzing the quality change within the temperature range of 30–200°C, as shown in Table 5.

From the TGA curves of the three types of zeolites in Figure 6, it can be seen that the decomposition temperature

and the heat weight loss of zeolites are different. The heat weight loss curves of 1# and 3# zeolites are steeper, while the curves of 2# zeolites are relatively flat, indicating that the water loss rate of zeolites is different. 2# zeolite loses water at 70°C and 120–160°C; the rate of water loss is slow, while the decomposition temperature of 3# zeolite and 1# zeolite is low, which is basically consistent with DSC test results. In terms of heat and weight loss, the mass loss of 3# zeolite is the most, and that of 2# zeolite is the least; that is to say, the water loss of 3# zeolite is the most, while that of 2# zeolite is the least.

Through the above analysis, it is found that the zeolite will show endothermic peak with the rise of temperature, which indicates that there is a phase transformation process



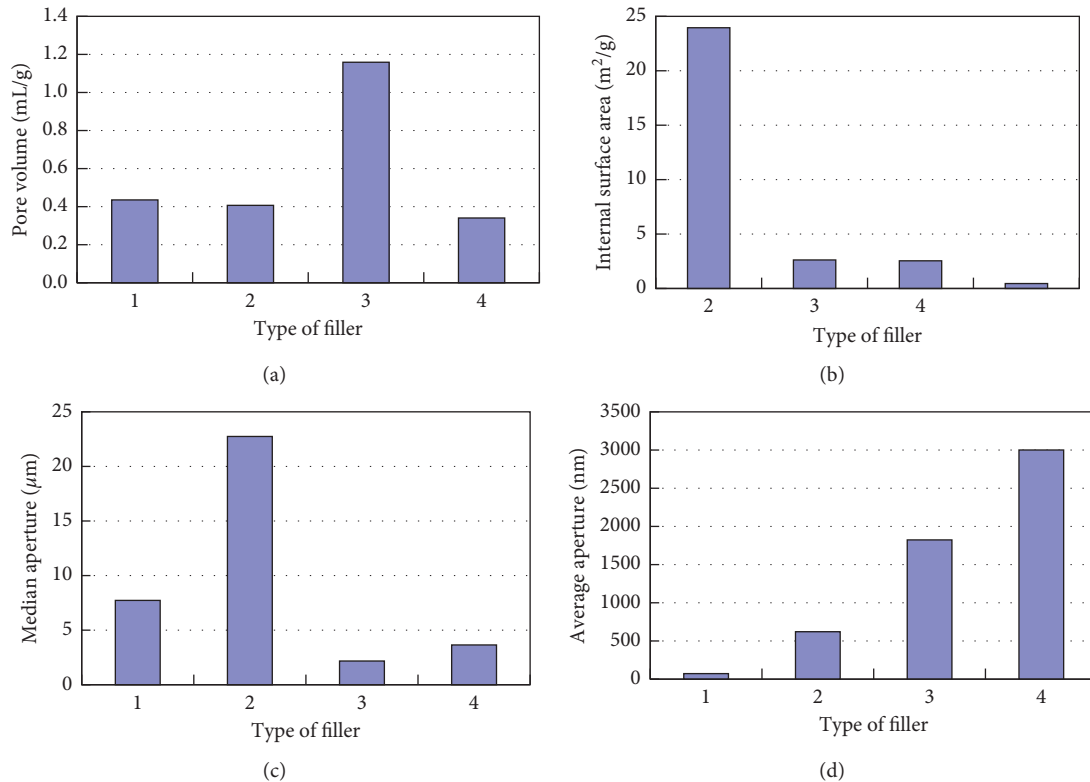


FIGURE 4: Pore parameters of zeolites and mineral filler. (a) Pore volume. (b) Internal surface area. (c) Median pore diameter. (d) Average pore diameter.

of water in the zeolite and the thermal stability of different zeolites is different. As temperature mixing additives, these kinds of zeolites can start to absorb heat and lose water in the temperature range of 90–120°C. The gasification of zeolite water in this temperature range is consistent with the working temperature range of asphalt in the construction process, which can affect the flow characteristics of asphalt and meet the requirements of asphalt mixture for temperature mixing additives.

**3.3.2. Water Absorption of Zeolite.** In the framework structure of zeolite, there are two forms of water, adsorbed water and free water, which are called zeolite crystal water or zeolite water. Under the condition of natural storage, the natural water content of different zeolites is different, and the zeolites water in the pores of zeolites skeleton is in a relatively stable state. This relative balance will change due to the change of temperature and humidity conditions. In order to understand the water content and the amount of water loss during heating of zeolite under natural storage conditions, this paper analyzes the water loss rate of different zeolites under different heating temperatures.

When determining the heating temperature, the production and construction of asphalt mixture are mainly considered. The different temperatures are encountered by zeolite in different processes, such as those under 105°C; the free water in zeolite is separated out, which is also the commonly used temperature for measuring the moisture

content of mineral materials. 120–140°C is the heating temperature of asphalt, 120–160°C is the mixing temperature of asphalt mixture, and the mixing temperature of modified SMA asphalt mixture can reach 180°C. In the above temperature range, the water of different properties in zeolite overlaps and loses, which continuously makes the asphalt mixture microfoaming in the process of heating, mixing, storage, and construction. In this way, the mixture has good workability in the above construction processes. Figure 7 shows the comparison of water loss rate between zeolite and mineral powder.

It can be seen from Figure 7 that the water loss rate of zeolite at different temperatures is much higher than that of limestone powder, indicating that the water content of zeolite is much higher than that of limestone powder. The water loss rate of different zeolites is very different, the highest is 3# synthetic zeolites, and the lowest is 2# synthetic zeolites. The water content of zeolites mainly depends on the composition of zeolites, diagenesis process, and storage conditions.

Under heating conditions, zeolite water with different properties escapes from different heating temperatures. Free water and capillary water are mainly lost at 105°C, capillary water and adsorbed water are mainly lost between 100–200°C, and adsorbed water is lost at 300–400°C [33]. In asphalt mixture, the state change of zeolite water under 200°C is studied. For mineral materials, the water loss rate under certain conditions can reflect their water content and properties, and the water loss rate of zeolite under specific

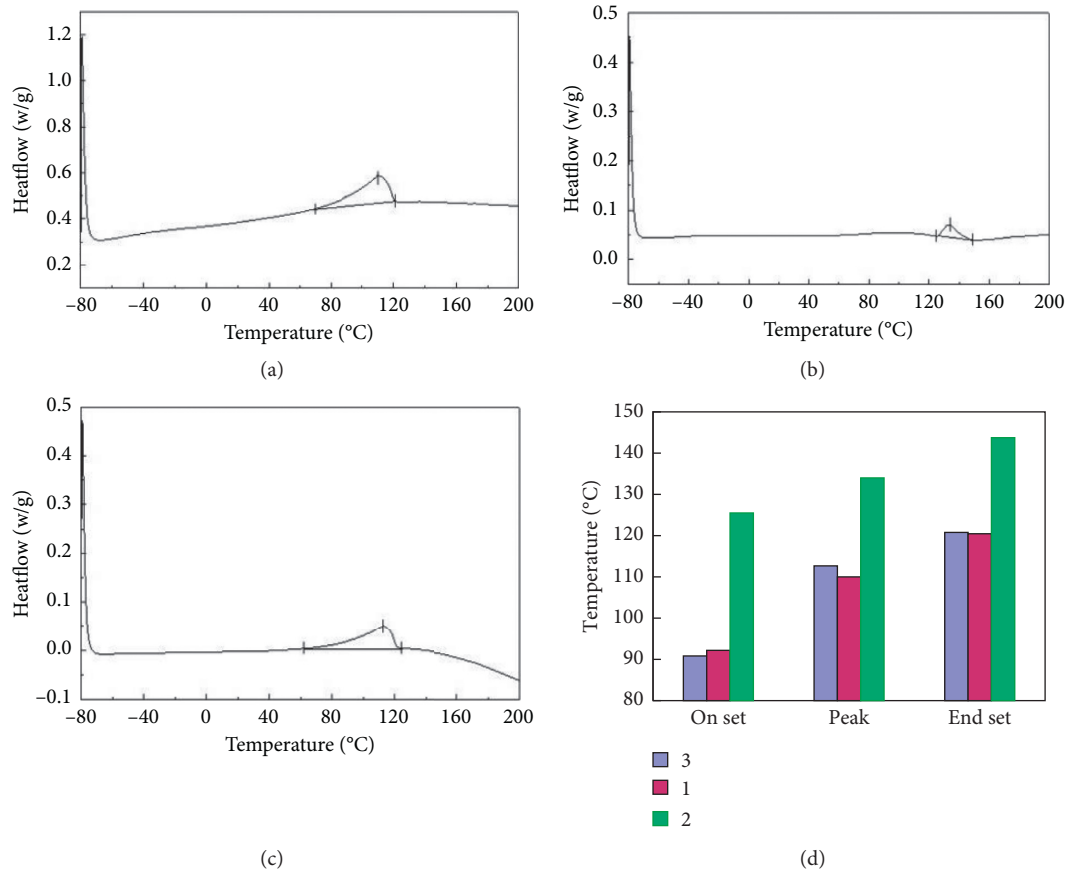


FIGURE 5: DSC curve of zeolites. (a) 1# zeolite. (b) 2# zeolite. (c) 3# zeolite. (d) Temperature comparison of zeolites.

TABLE 4: Summary of DSC data.

Zeolite	Starting temperature (°C)	Peak temperature (°C)	End temperature (°C)
1#	92.19	110.00	120.46
2#	125.50	134.00	143.75
3#	90.83	112.67	120.78

temperature can reflect their water holding capacity. It can be found that, with the increase of temperature, the water loss rate of zeolite gradually increases, but the growth range is different. The water loss rate of limestone powder is basically kept at 105°C, which indicates that the water in limestone powder is completely separated out at 105°C and the water is mainly free water. The water loss rate of 2# zeolite did not increase obviously with the increase of temperature. However, for 1# and 3# zeolites, they show different water loss properties. With the increase of temperature, the water loss rate increases to a certain extent, and the water loss rate continues to increase with the increase of temperature, which can better realize the continuous water loss and foaming in the hot asphalt.

Through the analysis of the water loss rate of zeolite, the water loss track of zeolite can be described, thus reflecting the water holding capacity of zeolite and the nature of zeolite water. The water holding capacity of three kinds of zeolites is in the order of 3# > 1# >> 2# > mineral powder. The comparison shows that 3# zeolite has the largest water holding

capacity and its water loss process is more balanced. With the increase of temperature, the water in it gradually volatilizes.

Zeolite water exists in the pores of zeolite, and the pore structure has a certain impact on the water release of zeolite. Figure 8 shows the relationship between the water loss rate of zeolite and pore volume. From the change trend of the water loss rate of zeolite with the pore volume, the larger the pore volume is, the greater the water loss rate of zeolite is.

**3.3.3. Moisture Absorption Capacity and Water Loss Mechanism.** The existence of a large number of pores in porous materials makes them have the characteristics of water absorption. The pore structure and the distribution and diffusion of water molecules in the pores determine their water absorption and loss behavior. For zeolite, the zeolite water in the pores can be adsorbed and discharged freely without affecting the mineral skeleton, which is a major feature of zeolite. This water absorption and loss feature is

TABLE 5: Summary of TG data.

Zeolite	Decomposition temperature (°C)	Decomposition temperature (°C)	Thermal weight (%)
1#	80	—	94.3
2#	70	120-160	95.2
3#	80	100	91.8

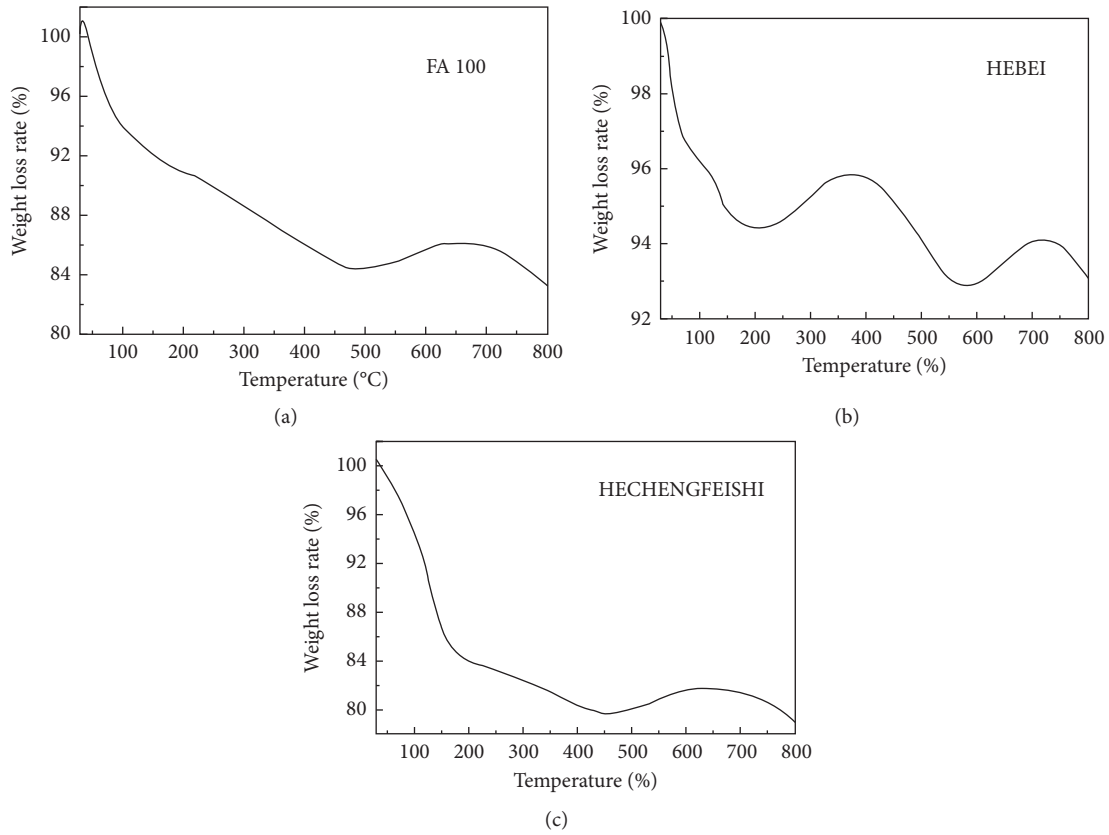


FIGURE 6: TGA curve of zeolites. (a) No. 1 zeolite. (b) No. 2 zeolite. (c) No. 3 zeolite.

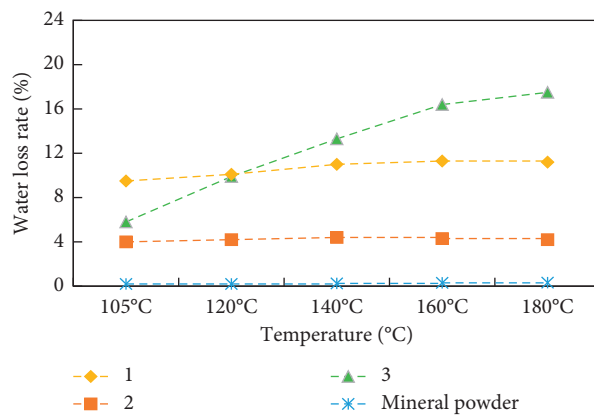


FIGURE 7: Comparison of water loss of zeolites and mineral filler.

mainly due to the skeleton pore structure of zeolite. Porous zeolites have affinity for water molecules with strong polarity, which makes zeolites have certain water absorption.

The mechanism of water absorption can be analyzed by capillary condensation principle and solid surface adsorption.

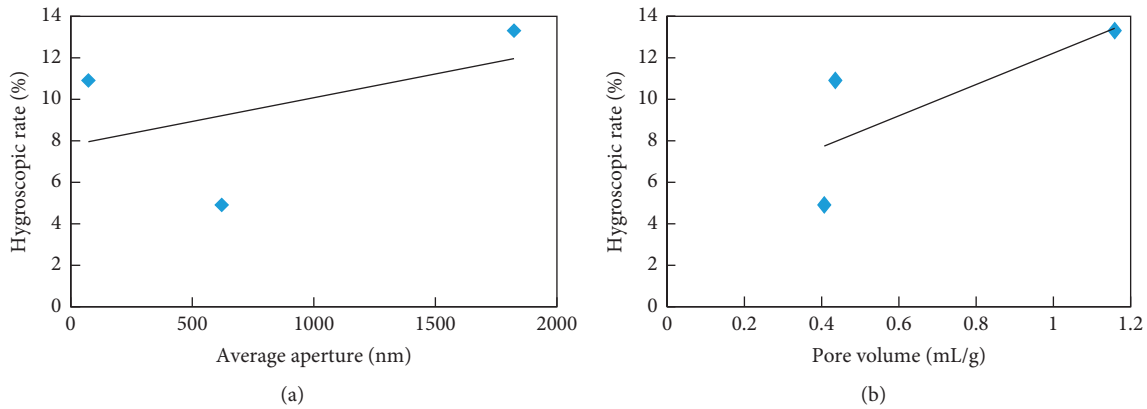


FIGURE 8: Relationship between water loss and porosity. (a) 120°C water loss. (b) 140°C water loss.

(1) *Moisture Absorption Capacity.* For zeolite minerals, the rich internal channels make the capillary phenomenon have an important impact on the moisture absorption capacity of zeolite. For the analysis of the moisture absorption capacity of the internal channels of zeolite based on the capillary condensation principle, Kelvin formula [34, 35] is used to calculate the critical pore size of zeolite under different temperature and humidity conditions, as shown in Table 6.

It can be seen from Table 6 that the critical pore size of zeolite varies a little under different temperatures. However, with the increase of humidity, the critical pore size increases significantly. Therefore, the critical pore size of zeolite is mainly related to the ambient temperature and humidity.

According to the distribution characteristics of zeolite pores, it can be analyzed that there are three situations of water in zeolite, as shown in Figures 8(a) and 8(b), respectively. When the pore size is less than or equal to the critical pore size, the water absorption is as shown in Figure 8(a); mainly, due to the capillary action, the adsorbed water molecules condense in the pore wall to form zeolite water. When the pore size is larger than the critical pore size, the pore water absorption is as shown at C in Figure 9, and the surface water absorption of zeolite is as shown at B.

Only micropores can adsorb pore water through capillary action. Comparing the critical pore size distribution of Table 6 with that of Figure 3, it is found that the proportion of micropores (3–50 nm) in zeolite is below 11% and the number and volume of pores smaller than the critical pore size are less. It can be inferred that there is relatively less capillary water in zeolite. When the pore size of zeolite is larger than the critical pore size, zeolite can form pore water or surface water through physical adsorption, so there are relatively less capillary water, more pore water, and surface water in zeolite, and the escape temperature of this water is lower. It is because of the above pore characteristics and the characteristics of adsorbed water that the evaporation and migration of zeolite water are different from those of general adsorbed water. The properties of zeolite water are between adsorbed water and crystal water, which also explains the reason why zeolite begins to lose water at low temperature.

(2) *Water Loss Performance.* Hydrous zeolite is a composite medium composed of solid skeleton and fluid. Under

the high temperature conditions of asphalt mixture production and construction, the water in hydrous zeolite volatilizes to the outside of zeolite skeleton through the interference of external thermal energy. In this rapid heating process, zeolite water undergoes a complex heat transfer process. Free water is discharged in the form of liquid water diffusion or seepage, and combined water is discharged in the form of evaporation [36].

In the process of heating, the evaporation of zeolite water is first carried out on the surface of zeolite, which is similar to the evaporation process of pure water. Due to the different adsorption degree of zeolite water and particles, the difficulty and ease of desorption are also different. With the increase of temperature, the water in the capillary moves. The smaller the capillary radius  $R$  is, the slower the water evaporation rate is, and the more difficult it is for zeolite to lose water [37–39].

Structure of zeolite is loose and the channels and cavities are well developed, which provides a place for the existence of zeolite water. The existing state of zeolite water and the characteristics of its loss in the heating process are the material basis for the use of zeolite in warm mix asphalt mixture. As the water carrying medium of warm mix asphalt mixture, the characteristics of water holding and loss of zeolite are particularly important. Only with proper water holding performance and continuous water loss in mixing, compaction, and other construction processes, zeolite can play a real role as a warm mix additive. Next, the moisture absorption and water loss properties of zeolite are analyzed through experiments.

### 3.3.4. Moisture Absorption and Water Loss Performance of Zeolite

(1) *Hygroscopic Properties of Zeolite.* The zeolite sample is dried at 105°C and placed in a humidity regulating box. The temperature in the box is set at 20°C, and the relative humidity is 60%, 70%, 80%, and 90%, respectively. The isothermal moisture absorption capacity of the zeolite is tested under different humidity conditions until the mass of the sample no longer increases. At this time, the sample is

TABLE 6: Critical aperture at different temperature and humidity (nm).

Humidity (%)	0°C	20°C	30°C	40°C
20	0.74	0.67	0.64	0.62
30	1.00	0.89	0.86	0.82
40	1.31	1.17	1.13	1.08
50	1.72	1.55	1.49	1.43
60	2.36	2.11	2.03	1.94
70	3.36	3.01	2.91	2.78
80	5.37	4.82	4.65	4.44
90	11.37	10.2	9.84	9.40
95	23.36	20.9	20.22	19.30

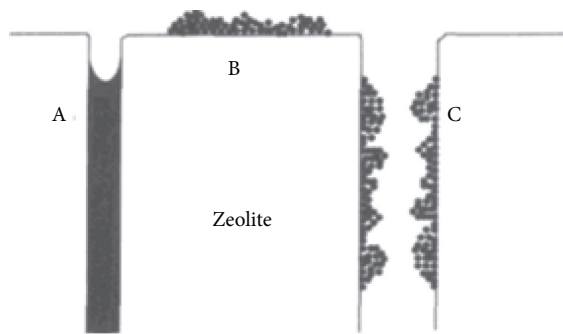


FIGURE 9: Water absorption of zeolite.

considered to reach the equilibrium state under the corresponding humidity [40–43]. Figure 10 shows the change of moisture absorption rate of zeolite with time, and Figure 11 shows the comparison of moisture absorption rate of zeolite under different humidity.

According to the change curve of zeolite moisture absorption performance in Figure 10, the moisture absorption capacity of zeolite increases gradually with the extension of time and increases greatly before 10h. Then, the moisture absorption rate increases slowly and basically reaches the relative moisture balance. In Figure 11, the hygroscopic rate of zeolite is related to the environmental humidity. The higher the environmental humidity is, the higher the hygroscopic rate of zeolite will be, which also verifies the mechanism of zeolite water absorption. When the relative saturation state is reached, the hygroscopic rate of different zeolites is very different; the largest the 3# synthetic zeolites are, the smallest the 2# zeolites become.

The relationship between the hygroscopic capacity and pore structure of zeolite is analyzed, as shown in Figure 12.

Figure 12 shows the relationship between the hygroscopic rate of zeolite and pore structure characteristics. It can be found that the hygroscopic rate of zeolite increases with the increase of pore volume. There are enough pores in zeolite to provide space for zeolite water. The larger the pore volume is, the stronger the moisture absorption capacity of zeolite is. 3# zeolite has the largest pore volume and the largest moisture absorption rate; 2# zeolite has the smallest pore volume and its moisture absorption rate is also small. Therefore, from the perspective of water absorption, the pore

volume is large; that is, the pore is more conducive to zeolite water absorption.

It is related to pore structure characteristics, as shown in Figure 12(b); with the increase of average pore size, the water absorption of zeolite shows an increasing trend. The water absorption performance of different zeolites is also related to the pore distribution. For natural zeolites, the larger the pore size is, the larger the water absorption is, but the larger the proportion of super pores is, the smaller the water absorption is, as shown in Figure 12(c). Therefore, the pores of zeolite are mainly macropores with the strongest water absorption capacity. For synthetic zeolites, the pores of 3# zeolites are mainly macropores with the largest water absorption. Therefore, the water absorption capacity of zeolite is related to the pore distribution, and the super pore is not conducive to water absorption, while the middle pore and the large pore are easier to absorb water.

(2) *Water Loss Performance of Zeolite.* The mixing and rolling of asphalt mixture are carried out under certain high temperature conditions. In order to study the water loss performance of zeolite, it is necessary to simulate the water loss track of zeolite under high temperature conditions. In this paper, the water loss of absorbent zeolite in the temperature range of 50°C~180°C is tested to simulate the water loss of asphalt mixture in the process of mixing and rolling, as shown in Figures 13 and 14.

In the water loss curve of Figure 13, with the increase of temperature, zeolite shows the characteristics of gradual water loss. At lower temperature (lower than 70°C), the water absorption of zeolite has little difference, and the water loss curve is relatively flat. With the increase of temperature, the water loss rate of zeolite increases gradually, and the difference of water loss rate of different zeolites becomes larger. The change range of water loss rate of different zeolites is different. Except for 3# zeolites, the water loss rate is basically stable at 125°C~135°C.

In Figure 14, of the three kinds of zeolites, the most water loss rate is 3# zeolite, and the least is 2# zeolite. From the above analysis of zeolite water loss rate, it can be seen that the volatilization of zeolite water is a continuous process, which is related to temperature and duration. With the increase of temperature, zeolite water is gradually discharged, which makes its foaming effect in asphalt last for a certain period of time, thus ensuring the workability of asphalt mixture in a certain period of time.

See Figure 15 for comparison with water absorption. It can be seen that zeolite has the characteristics of “energy absorption and energy loss,” with high water absorption and water loss. 3# zeolite has the largest water loss rate, while 2# zeolite has the smallest water loss rate. Comparing the water loss rate of zeolite with the pore distribution characteristics of zeolite, as shown in Figure 16(b), the water loss rate of zeolite is related to the pore volume. The larger the pore volume is, the more easily the zeolite loses water. Taking 3# synthetic zeolite as an example, it has the largest pore volume and relatively concentrated pore size distribution, and it has the largest water loss rate. 2# zeolites have the smallest pore volume and a wide range of particle size distribution.

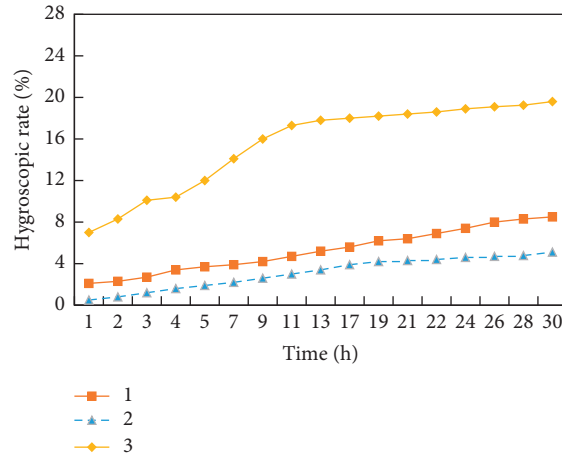


FIGURE 10: Moisture absorption of zeolites at 90% humidity.

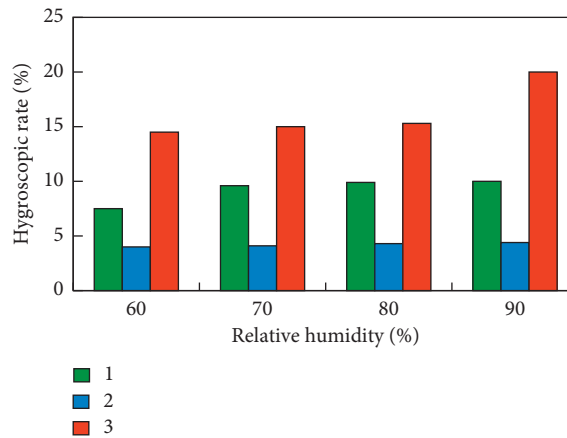


FIGURE 11: Comparison of moisture absorption of zeolite.

Therefore, the water loss rate of zeolite mainly depends on water content and pore volume.

#### 4. Effect of Zeolite on Viscosity of Asphalt

4.1. *Viscosity Temperature Relationship.* As a viscoelastic material, temperature is the most important factor affecting the viscosity of asphalt. The viscosity temperature relationship of asphalt reflects the degree of change of asphalt viscosity with temperature, which is an important factor affecting the performance and service quality of asphalt. Under the construction temperature, asphalt should have a smaller viscosity to facilitate the mixing and compaction of asphalt mixture, while, under the used temperature, asphalt should have a higher viscosity to prevent the pavement from flowing deformation and improve its durability. For zeolite asphalt mixture, the following focuses on the viscosity characteristics of asphalt in the process of high temperature construction. See Figure 16 for the influence of zeolite on the apparent viscosity of matrix asphalt.

The effect of zeolite on the viscosity of asphalt is mainly at a lower temperature. From Figure 16, it can be seen that, at 100°C, the viscosity of different zeolites varies greatly, while,

at 140°C, the viscosity of zeolites asphalt varies a little. In other words, the effect of zeolite on the viscosity of asphalt is significant at lower temperature. Zeolite has a great influence on the low temperature viscosity of asphalt. This result is because zeolite contains zeolite water which can move freely or enter and exit the pore channel under specific temperature conditions. According to the thermal analysis of zeolite, zeolite begins to absorb heat and lose water in a lower temperature range. Within this temperature range, the zeolite water will generate gas and then influence the viscosity of asphalt. In order to further describe the viscosity temperature relationship of zeolite asphalt, the viscosity temperature equation of zeolite asphalt is established according to Saal formula:

$$\log(\eta \times 10^3) = a - b \log(T + 273.13), \quad (1)$$

where  $a$  and  $b$  are regression coefficients;  $\eta$  is viscosity of asphalt (Pa · s);  $T$  is temperature (°C).

The regression coefficient of viscosity temperature equation of asphalt zeolite is determined through regression analysis, and the mixing and compaction temperature of each zeolite asphalt mixture are determined, as shown in Table 7.

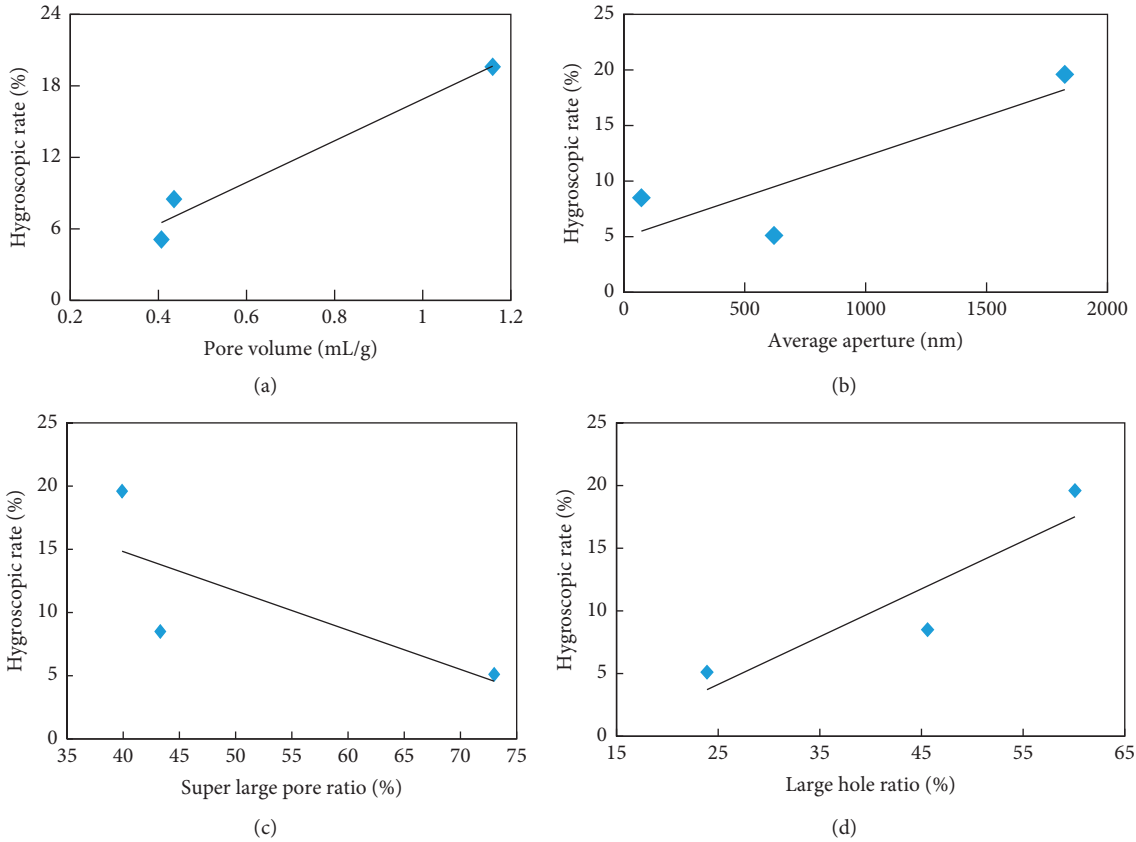


FIGURE 12: Influence of pore structure on moisture absorption. (a) Porosity. (b) Average pore diameter. (c) Proportion of super pore. (d) Proportion of big pore.

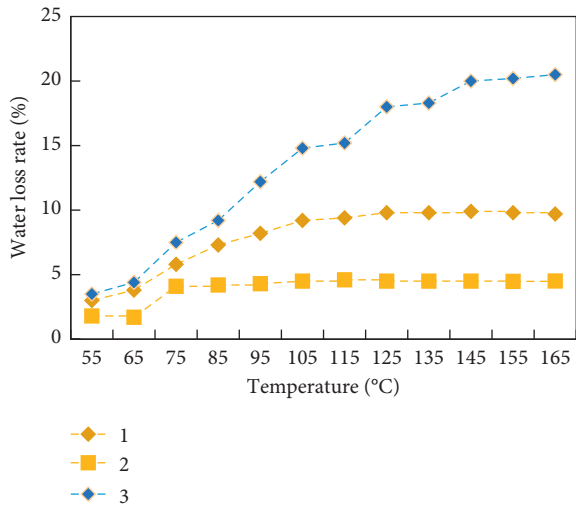


FIGURE 13: Water loss of zeolites.

From the coefficient of viscosity temperature equation in Table 7, the influence trend and degree of zeolite on the viscosity change of asphalt can be analyzed. Compared with matrix asphalt, the addition of zeolite makes the  $b$  value increase; that is, the sensitivity of asphalt viscosity to temperature increases. According to the viscosity temperature equation, the mixing and compaction temperature of the

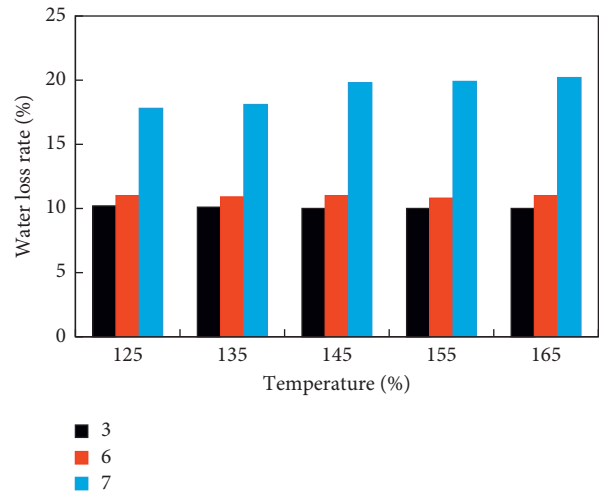


FIGURE 14: Comparison of water losses at different temperatures.

asphalt mixture are determined. The mixing and initial pressure temperature of the zeolite asphalt mixture are lower than those of the hot asphalt mixture.

4.2. Viscosity Time Relationship. In order to analyze the influence of zeolite hydration on the viscosity of asphalt, three kinds of zeolites were added to the asphalt and placed

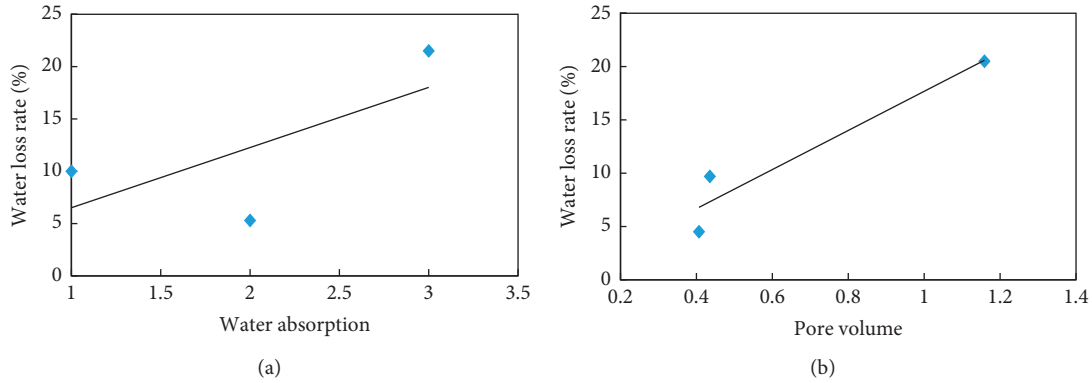


FIGURE 15: Relationship of water losses with absorption and porosity. (a) Water absorption. (b) Porosity.

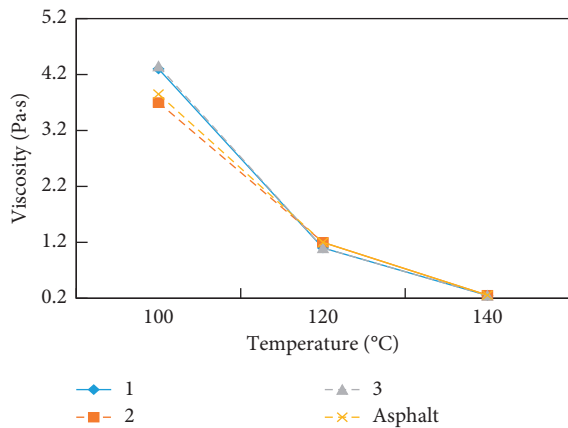


FIGURE 16: Viscosity change of asphalt at different temperatures.

in a 120°C incubator for curing. After curing for different times (1 h–4 h), the viscosity of asphalt at 120°C was measured, respectively. The curve of the viscosity of each zeolite with time was fitted by quadratic polynomial, as shown in Figure 17.

From the viscosity time curve of zeolite in Figure 17, it can be seen that, in asphalt zeolite, the viscosity of asphalt changes with time, which is different from the viscosity change characteristics of matrix asphalt. The viscosity of base asphalt is basically horizontal with the extension of curing time; that is to say, the viscosity of asphalt is basically constant at a certain temperature and shear rate. The addition of zeolite changes the viscosity of asphalt. From the viscosity change of each zeolite asphalt, it can be seen that the viscosity of asphalt is higher at the initial stage of adding zeolite into asphalt. With a long period of time, the viscosity began to decline. When the minimum value was relatively stable, the viscosity of asphalt increased and finally tended to be stable. According to the change characteristics of viscosity, the change of viscosity of zeolite asphalt can be divided into three stages: decline stage, stability stage, and growth stage. In these three different stages, the viscosity shows different change properties. The different change characteristics of viscosity in these three stages reflect the change process of zeolite water: volatilization stage, stability stage, and decay stage. Therefore, the change of asphalt

viscosity with time can reflect the volatilization process of zeolite water on the other hand. At the initial stage of adding zeolite into asphalt, the viscosity of asphalt is relatively large because the zeolite water has not yet fully escaped. With the volatilization and foaming of water, the concentration of bubbles in asphalt increases, and the viscosity of asphalt decreases. When zeolite water foams at a relatively uniform rate, the viscosity of asphalt remains stable. With the continuous precipitation of zeolite water, the bubble concentration in asphalt began to decrease, and the viscosity of asphalt began to increase. Finally, when the water in the zeolite is separated out and the pores in the zeolite absorb a certain amount of asphalt, the viscosity of the asphalt reaches a stable state.

In Figure 17, 2# zeolite viscosity has the smallest change with time. The analysis of viscosity curve with time can reflect the change track of zeolite water and provide basis for determining mixing temperature and time. In order to evaluate the effect of zeolite on the viscosity of asphalt, considering the different materials and compositions of zeolite, the relative index is adopted, and the viscosity change rate when the viscosity of asphalt is the lowest and reaches the final stable state is taken as the index to investigate the effect of zeolite on the viscosity, which is defined as the viscosity change rate. When the viscosity of asphalt reaches the final stable state, the evaporation of water in zeolite is completed, and the viscosity is the viscosity of zeolite particles and asphalt. Using this index to compare the influence of zeolite on asphalt viscosity, we can eliminate the influence of the density, particle size, and pore of zeolite itself and only consider the influence of zeolite water escaping and bubbling process:

$$\eta' = \frac{\eta_0 - \eta_{\min}}{\eta_0} \times 100\%, \quad (2)$$

where  $\eta'$  is the viscosity change rate (%);  $\eta_0$  is the viscosity of zeolite asphalt without bubbles (Pa·s);  $\eta_{\min}$  is the minimum viscosity of zeolite asphalt (Pa·s).

After three kinds of zeolites are added into asphalt, the relationship between the water loss rate of zeolites and the viscosity change rate of asphalt is analyzed, as shown in Figure 18.



TABLE 7: Coefficient of viscosity temperature equation.

Sample	$a$	$b$	Mixing temperature (°C)	Compaction temperature (°C)
Base asphalt	8.889	3.240	156.3~162.4	144.6~149.6
1	9.541	3.492	153.2~158.9	142.5~147.1
2	9.297	3.400	152.6~158.5	141.6~146.3
3	9.527	3.487	152.9~158.5	142.1~146.7

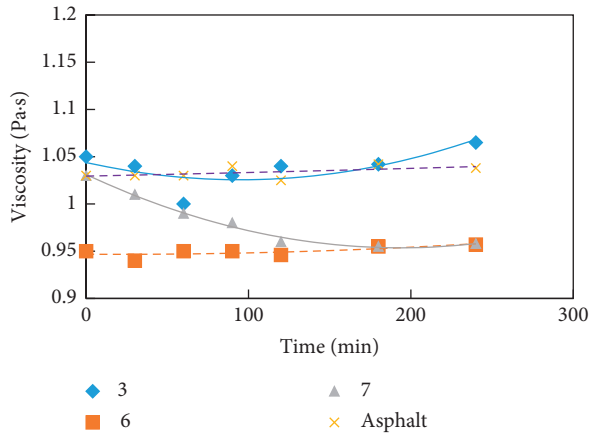


FIGURE 17: Viscosity development of asphalt with different zeolites.

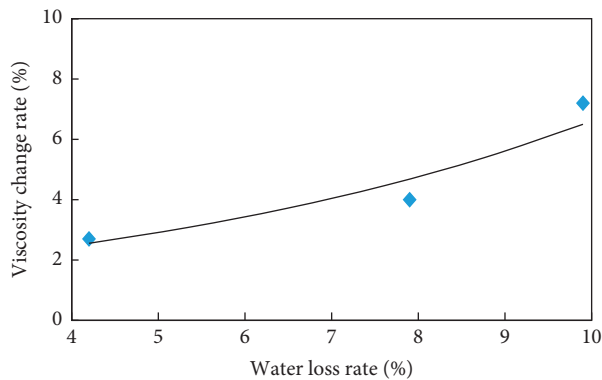


FIGURE 18: Relationship of viscosity change rate with water loss.

In Figure 18, the correlation between the viscosity change rate of asphalt and the water loss rate of zeolite is analyzed by quadratic polynomial regression, and the correlation coefficient  $R^2 = 0.9103$ , which shows that the viscosity change rate has a good correlation with the water loss rate of zeolite at this temperature.

The time when the viscosity of asphalt reaches the lowest value after adding zeolite is taken as the effective time to characterize the effect of zeolite on the viscosity of asphalt:

$$T = t_0 - t_{\min}, \quad (3)$$

where  $T$  is effective time of zeolite viscosity (min);  $t_0$  is initial time (min);  $t_{\min}$  is minimum viscosity time (min).

Therefore, the influence degree of zeolite on asphalt viscosity is reflected by viscosity change rate index, and the influence time is reflected by effective action time of zeolite.

These two indexes can reflect the degree and time range of asphalt viscosity change. At the same time, according to the requirements of asphalt mixture on viscosity, the applicability of zeolite as temperature mixing additive of asphalt mixture can be analyzed.

**4.3. Influence of Zeolite Varieties.** Different kinds of zeolites have different structure and material composition, and their water content and pore characteristics are also very different. These differences will have a certain impact on the viscosity of asphalt. Add three kinds of zeolites into asphalt, respectively, and test the viscosity of asphalt at different temperatures (100°C, 120°C, and 140°C), as shown in Figure 19.

In Figure 19, the influence of zeolite varieties on asphalt viscosity shows different regularity at different temperatures. At the temperature of 100°C, except that the viscosity of asphalt decreased with the addition of 2# zeolite, the viscosity of asphalt increased with the addition of other zeolites; that is to say, zeolite did not play a role in reducing the viscosity of asphalt. At 140°C, the addition of zeolite makes the viscosity of asphalt decrease in varying degrees. This phenomenon can be explained as follows: zeolite water precipitates in hot asphalt to produce microbubbles, which makes the viscosity of asphalt decrease; on the other hand, zeolite particles also play a role of volume enhancement, resulting in the increase of asphalt viscosity. The mutual counteraction of the two effects of viscosity reduction and stiffening is the change of asphalt viscosity. Due to the difference of density and moisture content of different zeolites, the effect of zeolites on the strength and viscosity reduction of asphalt is different. At 140°C, a large number of zeolite particles precipitate, so it has a strong drag reduction effect, the viscosity reduction effect is greater than that of zeolite particles, which shows that the viscosity of asphalt decreases. Taking 2# zeolite as an example, the density of the two kinds of zeolites is the largest. Under the same dosage, the volume of the two zeolites in asphalt is smaller, the viscosity increasing effect is weaker, and the viscosity of asphalt is reduced.

**4.4. Effect of Zeolite Dosage.** The effect of zeolite dosage on viscosity is shown in Figure 20. At 140°C, the viscosity of three kinds of zeolites in asphalt is lower than that of base asphalt. With the increase of zeolites content from 4% to 8%, the viscosity of asphalt increases in varying degrees. At 120°C, the viscosity of asphalt increases with the increase of zeolite content from 4% to 8%. The variation of asphalt viscosity with the amount of zeolite is not significant, which is related to the factors such as water volatilization rate,

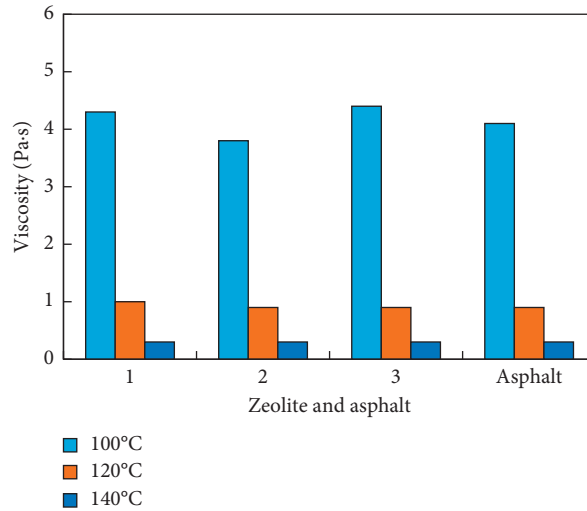


FIGURE 19: Viscosity of asphalt with different zeolites.

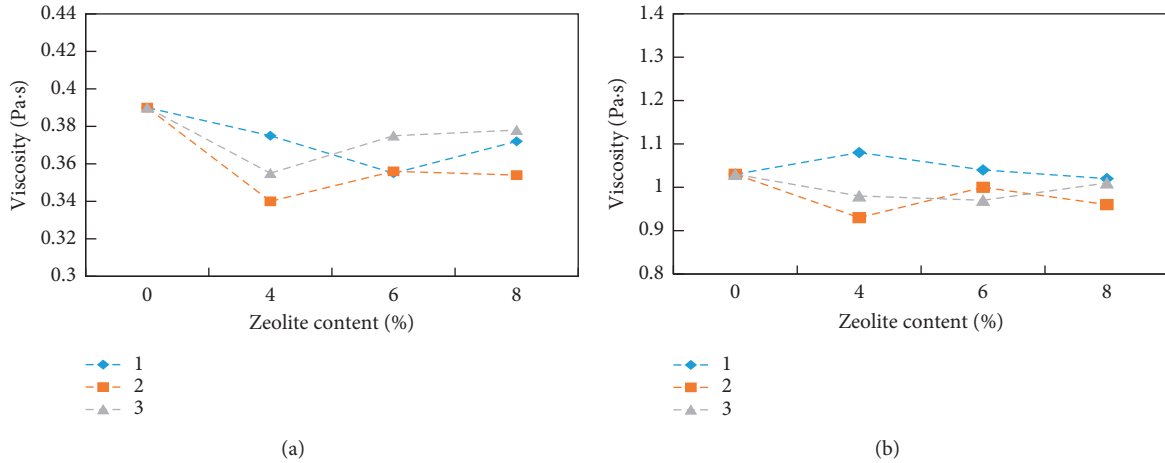


FIGURE 20: Influence of zeolite content on viscosity. (a) 140°C viscosity. (b) 120°C viscosity.

zeolite density, and testing time. The interaction of these factors makes the variation of asphalt viscosity less regular.

### 5. Effect of Zeolite Water on Construction Performance of Asphalt Mixture

In this paper, the construction performance of the commonly used AC-20 mineral aggregate grade matching zeolite asphalt mixture is analyzed, and the grading of the used AC-20 mineral aggregate is shown in Table 8.

The best ratio of oil to stone is 4.4%, the corresponding void ratio and mineral aggregate void ratio are 4.4% and 14.0%, the corresponding powder to binder ratio is 1.3, and the effective thickness of asphalt membrane is 9.0  $\mu\text{m}$ . For the convenience of comparison, zeolite asphalt mixture

adopts the same gradation and oil stone ratio as hot mix asphalt mixture.

*5.1. Mixing Performance.* As a warm mix asphalt mixture, it should be able to mix at a lower temperature, which requires the workability and workability of the mixture. On the premise that the voltage remains unchanged, the electric power consumed is directly proportional to the current in the circuit; the power consumption of mixing paddle of asphalt mixing pot in laboratory test is closely related to the resistance; then, the resistance of the mixing paddle can be characterized by electric current to evaluate the workability of asphalt mixture. Obviously, the greater the internal friction and the cohesion of the mixture are, the greater the resistance of mixing is, and the more the energy support is

TABLE 8: Gradation of AC-20.

Sieve hole (mm)	26.5	19	16	13.2	9.5	4.75	2.36	1.18	0.60	0.30	0.15	0.075
Design grading (%)	100	95.0	83.0	72.0	57.0	38.0	26.0	18.0	13.0	9.0	6.5	5.0
Grading range (%)	100	90–100	76–90	64–80	50–64	33–43	21–31	13–23	9–17	6–12	4–9	3–7

needed in the mixing process. Therefore, the mixing power can be used to evaluate the difficulty of mixing asphalt mixture. When the voltage is fixed, comparing the difference of electric power with the index of mixing current can indirectly reflect the workability of warm mix asphalt mixture.

Use clamp ammeter to measure the current of zeolite asphalt mixture in the mixing process and compare it with hot asphalt mixture, as shown in Figures 21 and 22.

Figure 21 shows the mixing current of base asphalt mixture and Figure 22 shows the mixing current of modified asphalt mixture. It can be seen that, for the same asphalt mixture, the mixing current decreases with the increase of temperature, which indicates that the mixing temperature increases and the mixing resistance decreases, which is related to the decrease of asphalt viscosity and the increase of asphalt mortar fluidity under high temperature.

Compared with hot mix asphalt mixture, the mixing current of zeolite asphalt mixture is less than that of hot mix asphalt mixture at the same temperature, which shows that zeolite can improve the workability of mixture when used in asphalt mixture. Taking the mixing current as the index, for the base asphalt mixture, the mixing current at 130°C is slightly lower than that at 150°C, so it can be inferred that the mixing resistance of zeolite asphalt mixture at 130°C is equivalent to that at 150°C; that is to say, under the same mixing effect, the mixing temperature of zeolite asphalt mixture can be reduced by 20°C. For the modified asphalt mixture, the mixing temperature of zeolite asphalt mixture can be reduced to 20°C. Different types of zeolite have certain influence on the mixing current of the mixture.

**5.2. Compaction Performance.** Due to the different flow characteristics of asphalt at different temperatures, the compaction energy required to overcome the cohesion of asphalt is temperature dependent [40, 41]. In order to understand the response of zeolite asphalt mixture under different compaction methods, this paper uses SGC, which is more close to the compaction situation of the open project, to make an experimental analysis of the compaction effect of zeolite asphalt mixture. Using the rotary compactor, rotate at the rate of 1.25° and 30 R/min under the vertical pressure of 60 kPa and evaluate the volume index of the zeolite asphalt mixture after compaction. Figure 23 shows the compaction curve of the matrix asphalt mixture, and Figure 24 shows the compaction curve of the modified asphalt mixture.

As shown in Figures 23 and 24, the compaction curve of zeolite asphalt mixture is under the hot mix asphalt mixture, which indicates that zeolite asphalt mixture is easier to be compacted under the same compaction temperature and compaction work.

From the point of view of similar void ratio, the void ratio of zeolite asphalt mixture at 120°C can reach the void

ratio level of 140°C of hot mix asphalt mixture, so the compaction temperature of zeolite asphalt mixture can be reduced to 120°C.

For modified asphalt mixture, the porosity of zeolite asphalt mixture decreases with the increase of temperature by rotary compaction. Taking the void ratio as the evaluation index, the hot mix asphalt mixture can meet the design requirements at 160°C, and the zeolite asphalt mixture can basically reach the same level at 140°C, but the void ratio of 2# zeolite is high.

According to the above compaction curve of asphalt mixture, the compactness of asphalt mixture is less than 4% when the compaction temperature of matrix asphalt mixture is 140°C and modified asphalt mixture is 160°C. Therefore, in order to ensure that the mixture has a reasonable void ratio, in addition to the lower limit of compaction temperature, the upper limit of compaction temperature should be controlled to avoid excessive compaction of the mixture resulting in low void ratio.

### 5.3. Compaction Curve and Compaction Energy Index

**5.3.1. Compaction Curve of Asphalt Mixture.** In the process of rotary compaction, the height change of asphalt mixture can be collected in real time, so as to describe the change track of compactness in the process of mixture compaction, which provides the possibility to study the compaction characteristics of asphalt mixture. From the analysis of the physical meaning of the compaction curve, the slope of the compaction curve can relatively evaluate the compaction rate of the mixture. The larger the slope is, the greater the compaction rate of the mixture is, and the easier the mixture is to be compacted [44–46].

In the semilogarithmic coordinate system, a straight line is used to fit the change of compaction density of the mixture, as shown in Figure 25. The fitted compaction equation is

$$K = a \ln N + b, \quad (4)$$

where  $K$  is density of mixture (%);  $N$  is times of rotary compaction (times); and  $a$  and  $b$  are coefficients.

For various zeolite asphalt mixtures and hot mix asphalt mixtures, the change of  $a$  and  $b$  coefficients is shown in Figure 26.

In Figure 26, the coefficients  $a$  and  $b$  represent different physical meanings,  $a$  reflects the compaction speed of asphalt mixture, and  $b$  reflects the initial compaction degree of mixture. According to the compaction fitting equation of each asphalt mixture, the compaction speed of zeolite asphalt mixture is higher than that of hot asphalt mixture at lower temperature (100°C). However, with the increase of

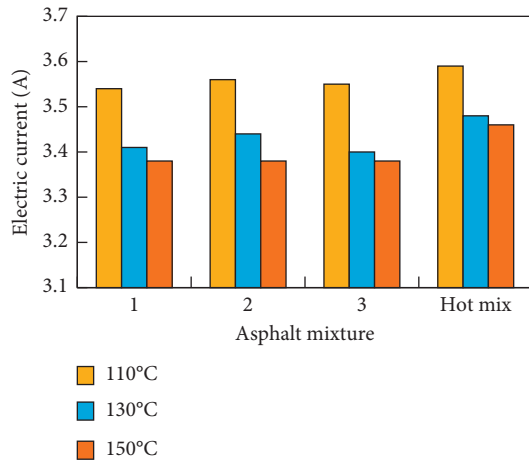


FIGURE 21: Electric current of mixture.

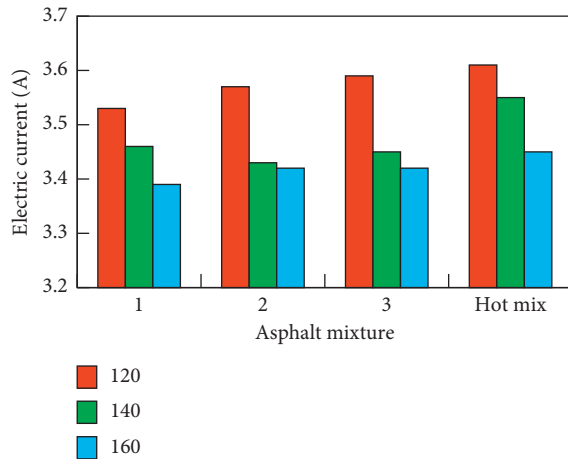


FIGURE 22: Electric current of modified mixture.

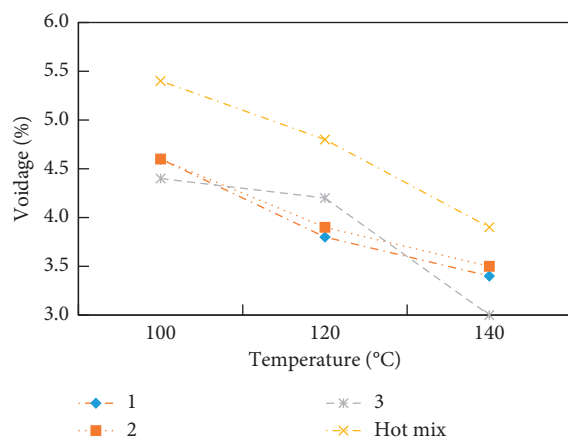


FIGURE 23: Air void of gyratory compacted asphalt mixtures.

temperature, the compaction speed of the two has little difference.

The difference of  $b$  value in the mixture compaction equation is not big, which shows that the zeolite type has little influence on the initial compactness of the mixture. For

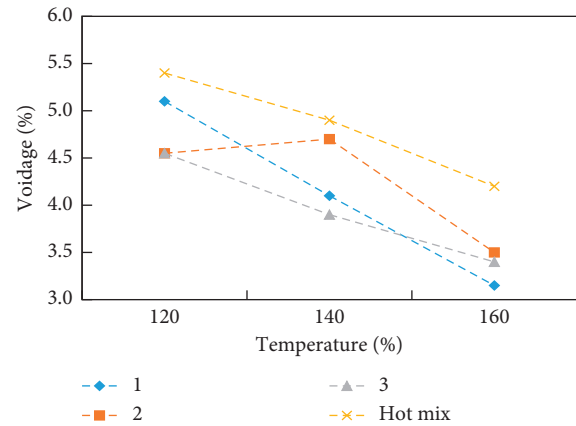


FIGURE 24: Air void of gyratory compacted modified asphalt mixtures.

hot mix asphalt mixture and zeolite asphalt mixture, the initial compactness fluctuates with the increase of temperature to a certain extent.

**5.3.2. Compaction Energy Index.** The coefficients  $a$  and  $b$  of the above fitting compaction curve can relatively evaluate the compaction speed and initial compaction degree of asphalt mixture but cannot accurately evaluate the compaction energy and compaction work of the mixture. In order to evaluate the compaction and workability of asphalt mixture, it is necessary to study the energy demand in the process of mixture compaction. Because of the difficulty of energy testing, the concept of compaction energy index in Superpave design method is used for [47, 48].

In this study, when calculating the compaction energy index, the initial state of asphalt mixture adopts the compactness of the mixture after 8 times of rotation, because the 8% void ratio is the lowest standard of the mixture compaction.

The compaction curve of asphalt mixture is as shown in Figure 26(b). The power function is used to fit the compaction curve of asphalt mixture. Assuming that the function is continuous, the envelope area of the curve between any two points of the compaction curve can be obtained by integrating the equation. As the compaction energy index (CEI) of asphalt mixture, it indicates the difficulty of compaction of mixture.

(1) *Base Asphalt Mixture.* The compaction energy index of various asphalt mixtures is shown in Figure 27.

It can be seen from Figure 27 that the asphalt mixture at different temperatures has different rotary compaction energy index. Compared with the hot mix asphalt mixture, the energy index of zeolite asphalt mixture is lower, indicating that it has good workability and is easy to compact. At 100°C, 3# zeolite has the minimum energy index, and the zeolite asphalt mixture is easy to compact at this temperature. At this temperature, the order of compaction of three kinds of zeolite asphalt mixture is 3# > 1# > 2# > hot mix.

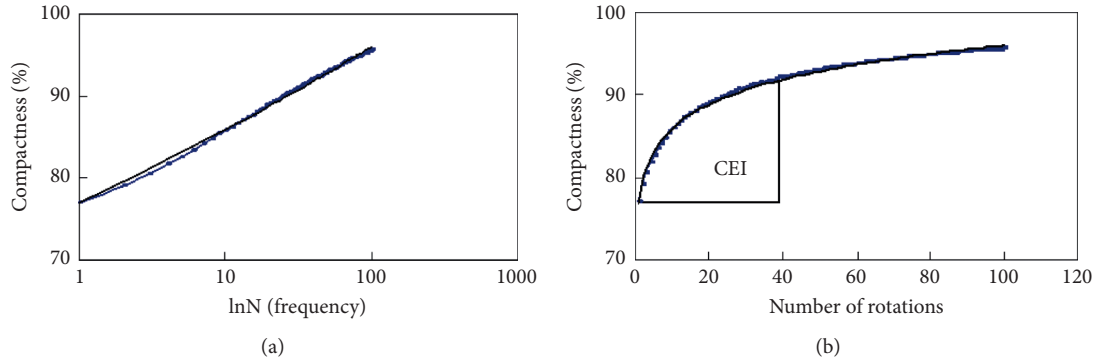


FIGURE 25: Gyratory compacting curve of asphalt mixture. (a) Semilogarithmic coordinate. (b) Rectangular coordinate.

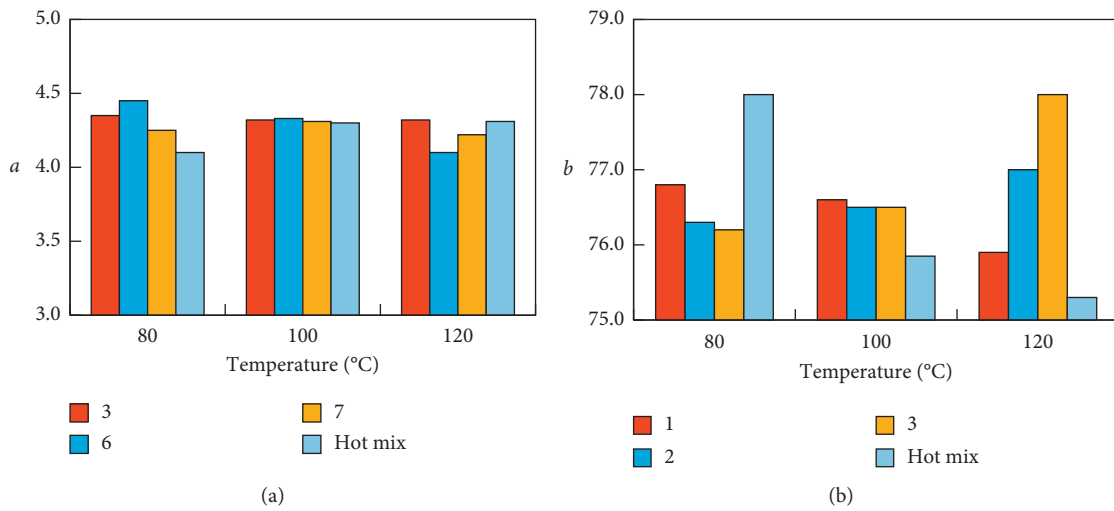


FIGURE 26: Coefficients of gyratory compaction. (a) Coefficient *a*. (b) Coefficient *b*.



FIGURE 27: Compact energy index of asphalt mixtures.

It can be seen from the energy index comparison between zeolite and hot mix asphalt that the energy index of hot mix asphalt at 120°C is higher than that of zeolite asphalt

at 100°C, indicating that the workability of hot mix asphalt at 120°C is lower than that of zeolite asphalt at 100°C. At 140°C, the energy index of hot mix asphalt is slightly higher than that of zeolite asphalt at 120°C, which also proves that zeolite asphalt has good workability.

(2) *Modified Asphalt Mixture.* The compaction energy index of the mixture with modified asphalt is analyzed, as shown in Figure 28.

Similarly, for the modified asphalt mixture, the compaction energy index of the asphalt mixture is temperature dependent. In addition to 2#, the energy index of zeolite asphalt mixture at 140°C is lower than that of hot asphalt mixture at 160°C, which indicates that zeolite asphalt mixture has good compactability.

(3) *Influence of Zeolite Characteristics on Compaction Energy Index.* As mentioned before, zeolite has a certain impact on compaction energy index. The relationship between water loss performance of zeolite and compaction energy index is analyzed. Figure 29 shows the relationship between compaction energy index of matrix asphalt mixture and modified asphalt mixture and water loss rate of zeolite.

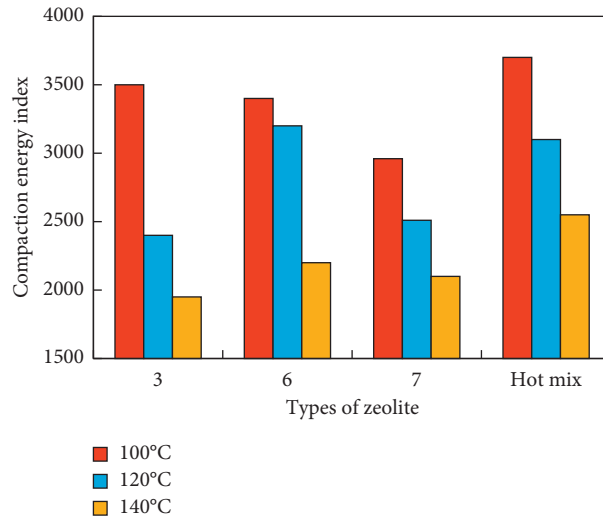


FIGURE 28: Compact energy index of modified asphalt mixtures.

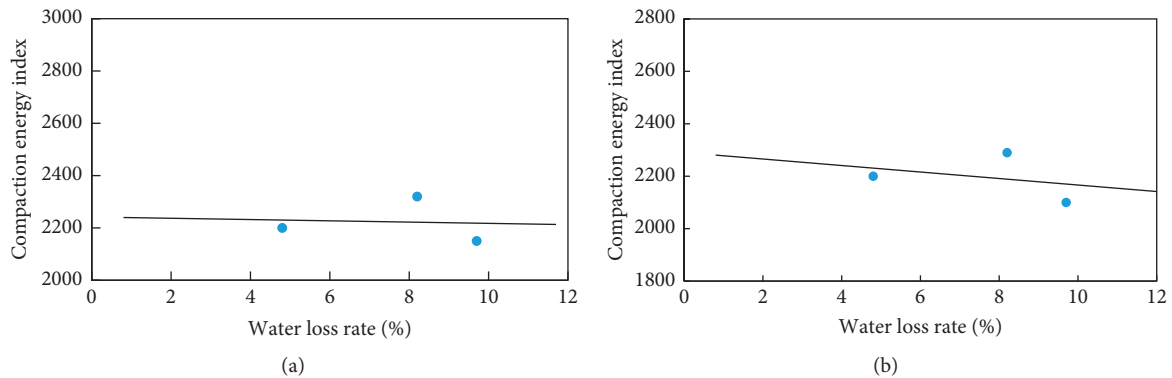


FIGURE 29: Influence of water loss on compact energy index.

It can be seen from Figure 28 that the compaction energy index of asphalt mixture decreases with the increase of zeolite water loss rate, indicating that the water loss performance of zeolite directly affects the compaction energy index of asphalt mixture. The more the water loss of zeolite, the more the bubbles formed, the greater the reduction of compaction friction, and the easier the compaction of mixture.

## 6. Conclusions

- (1) The results show that there are water molecules with different forces and orientations in the zeolite, which is unique to zeolite.
- (2) Through SEM observation and pore structure analysis, it is found that natural zeolite particles have different shapes and uneven size distribution and the pore content of zeolite is far greater than that of mineral powder.
- (3) TGA and DSC were used to analyze the zeolite. Under certain conditions, the water loss of zeolite was different. The three types of zeolite had the
- (4) The water absorption and loss performance of zeolite mainly depend on pore volume. The larger the pore volume is, the stronger the water holding capacity of zeolite is. At the same time, the water holding capacity and water loss capacity of zeolite are related to the pore size distribution, and the appropriate pore size is conducive to the volatilization of water.
- (5) The effect of zeolite on the viscosity of asphalt is time-dependent. As time extends, the viscosity of zeolite asphalt changes dynamically, which can be characterized by viscosity change rate and effective action time. The former reflects the degree of influence of zeolite on the viscosity of asphalt, and the latter reflects the time range of change.
- (6) The mixing resistance is characterized by the mixing current. The comparison between zeolite asphalt mixture and hot asphalt mixture shows that, under the same temperature, the mixing current of zeolite asphalt mixture is less than that of hot asphalt

mixture, which shows that zeolite can improve the workability of asphalt mixture.

- (7) This paper studies the compaction behavior of zeolite asphalt mixture, analyzes the influence of temperature and zeolite on the compaction performance of asphalt mixture, and indicates that zeolite asphalt mixture has good compaction performance. There is a flat area on Marshall compaction curve, in which the mixture is easy to compact. The compaction temperature of zeolite asphalt mixture can be reduced by 20~30°C.
- (8) Comprehensive analysis of the influence of zeolite on the voidage of asphalt mixture shows that the better the water loss performance of zeolite is, the easier the mixture is to be compacted. For the base asphalt mixture, the compaction temperature of the mixture is 120–130°C, and, for the modified asphalt mixture, the compaction temperature is 130–140°C.

### Data Availability

The data in this paper are given in the tables and figures within the manuscript.

### Conflicts of Interest

The authors declare no conflicts of interest.

### Authors' Contributions

Zhuolin Li and Junda Ren conceived and designed the experiments; Wei Li performed the experiments; Xingsheng Fu and Liying Yang analyzed the data; Zhuolin Li and Junda Ren wrote the paper.

### References

- [1] N. M. Wasiuddin, S. Selvamohan, M. M. Zaman, and M. L. T. A. Guegan, "Comparative laboratory study of sasobit and aspha-min additives in warm-mix asphalt," *Transportation Research Record: Journal of the Transportation Research Board*, vol. 1998, no. 1, pp. 82–88, 2007.
- [2] G. Valdes-Vidal, A. Calabi-Floody, and E. Sanchez-Alonso, "Performance evaluation of warm mix asphalt involving natural zeolite and reclaimed asphalt pavement (RAP) for sustainable pavement construction," *Construction and Building Materials*, vol. 174, pp. 576–585, 2018.
- [3] A. Sharma and B.-K. Lee, "Energy savings and reduction of CO<sub>2</sub> emission using Ca(OH)<sub>2</sub> incorporated zeolite as an additive for warm and hot mix asphalt production," *Energy*, vol. 136, 2016.
- [4] Ulmgren, Lundberg, and Lundqvist, "Low temperature asphalt (WMA) in Sweden," in *Proceedings of the 2nd International Warm-Mix Conference*, pp. 12–15, St. Louis, MO, USA, October 2011.
- [5] R. Vaiana, T. Iuele, and V. Gallelli, "Warm mix asphalt with synthetic zeolite: a laboratory study on mixes workability," *International Journal of Pavement Research and Technology*, vol. 6, no. 5, 2013.
- [6] B. Sengoz, T. Ali, and C. Gorkem, "Evaluation of natural zeolite as warm mix asphalt additive and its comparison with other warm mix additives," *Construction and Building Materials*, vol. 43, 2013.
- [7] M. E. Kutay and H. I. Ozturk, "Investigation of moisture dissipation in foam-based warm mix asphalt using synchrotron-based X-ray microtomography," *Journal of Materials in Civil Engineering*, vol. 24, no. 6, pp. 674–683, 2012.
- [8] A. Wozzuk, A. Zofka, L. Bandura, and W. Franus, "Effect of zeolite properties on asphalt foaming," *Construction and Building Materials*, vol. 139, pp. 247–255, 2017.
- [9] A. Wozzuk and W. Franus, "Properties of the Warm Mix Asphalt involving clinoptilolite and Na-P1 zeolite additives," *Construction and Building Materials*, vol. 114, pp. 556–563, 2016.
- [10] B. Sengoz, A. Topal, and C. Gorkem, "Evaluation of natural zeolite as warm mix asphalt additive and its comparison with other warm mix additives," *Construction and Building Materials*, vol. 43, pp. 242–252, 2013.
- [11] M. Dubravský and J. Mandula, "Modified asphalt binder with natural zeolite for warm mix asphalt," *Selected Scientific Papers-Journal of Civil Engineering*, vol. 10, no. 2, pp. 61–68, 2015.
- [12] A. Wozzuk, M. Wróbel, and W. Franus, "Application of zeolite tuffs as mineral filler in warm mix asphalt," *Materials*, vol. 13, no. 1, 2019.
- [13] R. Vaiana, T. Iuele, and V. Gallelli, "Warm mix asphalt with synthetic zeolite: a laboratory study on mixes workability," *Chinese Society of Pavement Engineering*, vol. 6, no. 5, pp. 562–569, 2013.
- [14] S. Leo, S. Subagio Bambang, H. Rahman et al., "Warm mix asphalt mixture using modified asbuton semi extraction modify and synthetic zeolite additive," in *Proceedings of the International Conference on Advances in Civil and Environmental Engineering (ICAnCEE 2018)*, vol. 276, Bali, Indonesia, October 2018.
- [15] A. Wozzuk, M. Wróbel, and W. Franus, "Influence of waste engine oil addition on the properties of zeolite-foamed asphalt," *Materials (Basel, Switzerland)*, vol. 12, no. 14, 2019.
- [16] A. T. Handayani, B. Hario Setiaji, and S. Prabandiyani, "The use of natural zeolite as an additive in warm mix asphalt with polymer modified," *Asphalt Binder*, vol. 4056, pp. 35–46, 2015.
- [17] A. Wozzuk and W. Franus, "A review of the application of zeolite materials in warm mix asphalt technologies," *Applied Sciences*, vol. 7, no. 3, p. 293, 2017.
- [18] E. Sanchez-Alonso, G. Valdes-Vidal, and A. Calabi-Floody, "Experimental study to design warm mix asphalts and recycled warm mix asphalts using natural zeolite as additive for sustainable pavements," *Sustainability*, vol. 12, no. 3, 2020.
- [19] M. Sol-Sánchez, F. Moreno-Navarro, M. C. Rubio-Gómez et al., "Reuse of zeolite by-products derived from petroleum refining for sustainable roads," *Advances in Materials Science and Engineering*, vol. 2019, Article ID 4256989, 10 pages, 2019.
- [20] B. de Castro Amoni, A. D. L. de Freitas, A. R. Loiola, J. B. Soares, and S. de Aguiar Soares, "A method for NaA zeolite synthesis from coal fly ash and its application in warm mix asphalt," *Road Materials and Pavement Design*, vol. 20, no. 2, pp. S558–S567, 2019.
- [21] C. John, *Interpretation of Infrared Spectra, A Practical Approach*, John Wiley & Sons Ltd, Hoboken, NJ, USA, 2000.
- [22] G.-Y. Yang, L. Zhu, and Y.-H. Li, "Analysis of FT-IR, XRD and SEM about natural zeolite," *Journal of Anyang Normal University*, vol. 2, pp. 77–79, 2006.
- [23] W. Mozgawa, "The influence of some heavy metals cations on the FTIR spectra of zeolites," *Journal of Molecular Structure*, vol. 555, no. 1–3, pp. 299–304, 2000.

- [24] X. Ren, P. Qin, Y. Hong, H. Sheng, and C. Sheng, *Chemistry of Molecular Sieves and Porous Materials*, Science Press, Beijing, China, 2004.
- [25] S.-R. Sun, H.-Y. Li, and J.-L. Xu, "The clino ptilolite of altered volcanic rocks in Gansu Province," *Journal of Lanzhou University*, vol. 30, no. 4, pp. 111–115, 1994.
- [26] Y.-X. Liu, "Measurement and characterization of pore structure of granular materials," *China Powder Science and Technology*, vol. 6, no. 4, pp. 21–22, 2008.
- [27] Y.-Z. Tian and K.-F. Chen, "Determination of pore size distribution and surface area of several materials using mercury porosimetry and gas adsorption," *China Paper-making*, vol. 23, no. 4, pp. 21–23, 2004.
- [28] D.-W. Chang, "The method and analysis of reducing the error in measuring the pore with mercury injection method," *Experimental Technology and Management*, vol. 20, no. 5, pp. 76–79, 2003.
- [29] H. Zhou, Y.-G. Fang, and C. Zeng, "Application of mercury injection method in the study of pore distribution of saturated soft soil," *Yellow River*, vol. 32, no. 5, pp. 101–105, 2010.
- [30] N.-X. Liang and X.-D. Liang, "Study of polymer modified bitumen by DSC," *Journal of Xi'an Highway University*, vol. 20, no. 3, pp. 29–30, 2007.
- [31] Hu Guo-ling, Zhu Zhi-ling, and Guo Xiao-ling, "Differential Scanning Calorimetry (DSC) and its Application in Asphalt research," *Shanxi Architecture*, vol. 31, no. 8, pp. 113–114, 2005.
- [32] H.-F. Xie, J. Dai, and C.-G. Liu, "Thermal analysis of epoxy asphalts," *Polymer Materials Science and Engineering*, vol. 25, no. 11, pp. 115–117, 2009.
- [33] X. Li, "NMR analysis of water in chabazite from Xuyun, Zhejiang," *Acta Mineralogica Sinica*, vol. 6, no. 2, pp. 174–178, 1986.
- [34] L.K. Daniels, ZAHNG. Qi-yuan, and GAO. Jing-zong, "Rapid in-office and in-vivo desensitization of an injection phobia utilizing hypnosis," *The American Journal of Clinical Hypnosis*, vol. 18, no. 3, 1976.
- [35] Catutiaf and M. Molina-sabio, "Adsorption desorption of water vapor by natural and heat-treated sepiolite in ambient air," *Applied Clay Science*, vol. 15, pp. 367–380, 1999.
- [36] W. Liu, A.-W. Fan, and X.-M. Huang, *Theory and Application of Heat and Mass Transfer in Porous Media*, Science Press, Beijing, China, 2006.
- [37] Y. Zheng, C.-H. Liao, and Z. Huang, "Drying characteristics of porous media containing moisture," *Mechanical and Electrical Information*, vol. 4, pp. 30–32, 2006.
- [38] Y. Zheng, C.-H. Liao, and Z. Huang, "Moisture migration in porous media based on Capillary Theory," *Drying Technology and Equipment*, vol. 3, pp. 130–132, 2005.
- [39] L. Yang and B.-B. Tao, "Heat and mass transfer for drying process of porous media," *Transactions of the Chinese Society of Agricultural Engineering*, vol. 21, no. 1, pp. 27–31, 2005.
- [40] M.-Y. Ran, "Review of research and application of air humidity controlling materials in Japan," *Materials Review*, vol. 16, no. 11, pp. 42–44, 2002.
- [41] N.-Q. Feng, G.-Z. Li, and F. Xing, "Research on humidity control materials," *New Building Material*, vol. 6, pp. 16–19, 1994.
- [42] Z.-W. Jiang, "Research progress of humidity-controlling materials," *Materials Review*, vol. 20, no. 10, pp. 8–11, 2006.
- [43] N.-Q. Feng, Y.-X. Shi, and Q.-L. Niu, "Characteristics and engineering application of zeolite water reducing and plasticizer," *China Concrete and Cement Products*, vol. 2, pp. 1–4, 2009.
- [44] P. Li, B.-G. Wang, and Z.-Q. Wang, "Research on simplified prediction method of rutting performance of asphalt mixture," *Journal of Highway and Transportation Research and Development*, vol. 28, no. 3, pp. 30–34, 2011.
- [45] Q. Yang, X. Li, L. Zhang et al., "Performance evaluation of bitumen with a homogeneous dispersion of carbon nanotubes," *Carbon*, vol. 158, pp. 465–471, 2020.
- [46] M. Guo and Y. Tan, "Interaction between asphalt and mineral fillers and its correlation to mastics' viscoelasticity," *International Journal of Pavement Engineering*, vol. 1, 2019.
- [47] M. Guo, H. Liu, Y. Jiao et al., "Effect of WMA-RAP technology on pavement performance of asphalt mixture: a state-of-the-art review," *Journal of Cleaner Production*, vol. 266, Article ID 121704, 2020.
- [48] Y. Tan and M. Guo, "Using surface free energy method to study the cohesion and adhesion of asphalt mastic," *Construction and Building Materials*, vol. 47, pp. 254–260, 2013.



## Research Article

# Development and Evaluation of Solvent-Based Cold Patching Asphalt Mixture Based on Multiscale

Shuolei Huang <sup>1</sup>, Junda Ren,<sup>1</sup> Mingguang Li,<sup>1</sup> Zhuolin Li,<sup>1</sup> and Shuiwen Zhou<sup>2</sup>

<sup>1</sup>Liaoning Transportation Research Institute Co., Ltd.,

Key Laboratory of Transport Industry of Expressway Maintenance Technology, Shenyang 110000, China

<sup>2</sup>Sichuan Provincial Transport Department Highway Planning, Survey, Design and Research Institute, Chengdu 611141, China

Correspondence should be addressed to Shuolei Huang; [h\\_shuolei@163.com](mailto:h_shuolei@163.com)

Received 18 June 2020; Revised 15 September 2020; Accepted 14 October 2020; Published 28 October 2020

Academic Editor: Meng Guo

Copyright © 2020 Shuolei Huang et al. This is an open access article distributed under the Creative Commons Attribution License, which permits unrestricted use, distribution, and reproduction in any medium, provided the original work is properly cited.

In order to prepare a kind of high-performance asphalt pavement pit repair material and extend the service life of the road, this paper starts from the microscopic view of the raw materials, uses infrared spectrum, four component analysis method, lying drop method, column wick technology principle, etc. to select the raw materials and determine the initial amount of the cold patching asphalt mixture, and optimizes the formula through the orthogonal test design and adhesion, cohesion, initial stage strength, later strength, residual stability, and other performance indexes, and determines the final formula of cold patching asphalt mixture as follows: the design porosity is  $15 \pm 0.5\%$ , compatibilizer is 2.5%, linear SBS modifier is 5%, tackifier is 4%, antistripping agent is 3.5%, and the dosage of diluent D should be determined according to the ambient temperature. The results show that the performance of the self-made cold patching asphalt mixture is good verified by adhesion grade, strength, high temperature stability, water stability, and other road performance.

## 1. Introduction

The existence of pavement potholes has a serious impact on driving safety and comfort [1]. Therefore, asphalt pavement pothole repair materials and technologies have gradually become the direction and focus of road materials research. For pavement repair with scattered locations and small quantities, hot mix asphalt mixture is used for pavement pit repair, which is not only difficult to produce due to the small quantity but also inconvenient for the construction unit to heat preservation and repair operation of hot mix asphalt, especially in rainy season and winter [2, 3]. Therefore, the solvent pit cold patching material is widely used and the temperature range is large and mature in technology and has gradually become the research focus of road engineering personnel. It has the advantages of low temperature mixing, simple construction equipment, small environmental pollution, and good social and economic benefits.

Khan et al. [4] determined through precise specific surface areas of four aggregates and seven minerals using

BET (Brunauer, Emmett, and Teller) theory, by measuring the physical adsorption of selected gas vapors on their surfaces and calculating amounts of adsorbed vapors corresponding to monolayer occupancy on the surfaces. Interfacial bond strengths between bitumen and aggregates were also calculated, based on measured surface-free energy components of minerals/aggregates and binders, in both dry and wet conditions. Ferrotti et al. [5] focuses on the experimental characterization of a high-performance cold mix asphalt mixture reinforced with three types of fibers (cellulose, glass-cellulose, and nylon-polyester-cellulose) dosed at two different contents (0.15% and 0.30% by the aggregate weight). The results show that the cellulose-fiber-reinforced material and the standard one showed enhanced performance, allowing the conclusion that they can be more successfully used in maintenance activities. Dash and Panda [6] added some virgin aggregate and rice husk ash as filler material and cement into the mixture. The results show that the increased strength at early aged, at tropical room temperature, was found more dominant due to the water

evaporation than cement content cold. Geng et al. [7] used cold patching asphalt (CPA) to repair pavement potholes, prepared from a simple mixture of CWO and diesel as the diluent, and the performance of this CPA is evaluated in the laboratory; the results show that CPA has good adhesion to aggregates (>95%) at CWO contents from 15 wt% to 35 wt% in the diluent. In addition, the introduction of CWO in CPAM has no discernible effect on its strength. Wang [8] investigated the effect of reducing moisture susceptibility of cutback asphalt mixture by adding Portland cement and bentonite. Test results showed that adding cement and nanoclay significantly improved the initial strength and cracking resistance and reduced moisture susceptibility. Cheng [9] used the improved boiling method and digital imaging technology to evaluate the cold patching asphalt mixture after boiling. At the same time, "coating ratio" was proposed as the index to evaluate the coating quality. The results show that the improved boiling test results have a good correlation with the results of BBS test and TSR test, indicating that the improved boiling test can be used to evaluate the water damage of CMA effectively. Lv [10] pointed out that the adhesive strength of cold patched asphalt mixture mainly comes from asphalt molecules, and the density of asphalt molecules in cold patched asphalt determines the adhesive strength of asphalt. Bi et al. [11] improved the performance of cold patch by adding water-based epoxy resin and put forward the evaluation method of initial strength and forming strength of water-based epoxy emulsified asphalt mixture (weeam).

At present, the research on cold patching asphalt mixture at home and abroad is mainly divided into three categories: solvent cold patching asphalt mixture, emulsion cold patching asphalt mixture, and reaction cold patching asphalt mixture [12, 13]. In emulsified cold patching asphalt mixture, how to control the demulsification time of emulsified asphalt is difficult, and the stability of emulsified asphalt is not very ideal. Therefore, there are big problems in the forming time and storage performance of this type of cold patching asphalt mixture. Reactive cold patching asphalt mixture needs complex reaction of many components and has a certain reaction time. Therefore, this kind of cold patching asphalt mixture generally needs to be mixed on-site and repaired on-site. Although reactive cold patching asphalt mixture has good road performance, the cost of preparing this type of cold patching asphalt mixture is high, and it has not been large-scale application. At the same time, in the existing research of cold patching asphalt mixture, most of the diluents and additives are different, and the micromodification mechanism of the additives is not analyzed, and the aggregates selected are not tested and analyzed from the microlevel to determine which is more suitable for the preparation of cold patching asphalt mixture, resulting in the road performance instability of cold patching asphalt mixture. Therefore, based on the micromechanism of the raw materials, this paper selects and optimizes the raw materials of the cold patching asphalt mixture by the lying

drop method and columnar wick technology principle to prepare a high-performance cold patching asphalt mixture.

## 2. Materials and Methods

### 2.1. Raw Materials

*2.1.1. The Base Asphalt.* The selection of base asphalt for cold patching asphalt mixture shall comply with [14]. In this study, heavy traffic 90# base asphalt is selected as the basic material, and the main performance indexes are shown in Table 1.

*2.1.2. Coarse Aggregate, Fine Aggregate, and Mineral Powder.* The coarse aggregate and fine aggregate used in this study are one of the granite, basalt, and limestone aggregate determined by subsequent tests. The performance indexes of the coarse aggregate, fine aggregate, and mineral powder meet the requirements of [14].

*2.1.3. Diluent.* According to the special road use requirements of cold patching asphalt mixture, it should have certain looseness under low-temperature environment, which requires that a certain amount of diluent must be added to the base asphalt to reduce its viscosity so that the mixture after mixing does not condense at low temperature. In this study, four diluents A, B, C, and D are selected for research. The performance indexes are shown in Table 2.

*2.1.4. Additives.* The main function of cold patching additive is to make up and improve some properties of cold patching asphalt lost due to the addition of diluent so that the cold patching asphalt mixture can not only meet the workability under low temperature conditions but also have good road performance after being used in pavement repair. In this study, compatibilizer, tackifier, and antistripping agent (E, F, G, and H) were selected to be added into asphalt for test. Specific performance indexes are shown in Tables 3–5.

*2.1.5. Modifier.* Due to the addition of organic solvent to the cold patching asphalt mixture to dilute the base asphalt, its initial strength, water damage resistance, and high temperature stability are reduced. It is necessary to add modifiers to improve the elasticity, temperature sensitivity, and low temperature ductility of asphalt and improve the adhesion between cold patching asphalt and aggregate, so as to improve the road performance of cold patching asphalt mixture. In this paper, SBS1301 with linear structure is selected as the modifier, and the performance indexes are shown in Table 6.

*2.2. Analysis of Microstructure and Properties of Materials.* In order to study the modification mechanism of self-made cold patching asphalt mixture and its compatibility with

matrix asphalt, this paper analyzes the microstructure of tackifier and antistripping agent, further clarifies the modification mechanism of cold patching asphalt, and provides the basis for optimizing material selection.

**2.2.1. FTIR Test Results of Tackifier.** The infrared spectrum test results of the tackifier used in this paper are shown in Figure 1. The peaks at 3030 cm<sup>-1</sup> belong to the C-H stretching vibration and the methylene stretching vibration of the aromatic ring of the tackifier; the peak at 1605 cm<sup>-1</sup> and the absorption peak at 800–690 cm<sup>-1</sup> belong to the out of plane bending vibration of aromatic unsaturated C-H, all of which indicate that there are aromatic rings in the tackifier. In addition, the peak of 2928 cm<sup>-1</sup> is saturated C-H stretching vibration, the peak of 1448 cm<sup>-1</sup> and 1374 cm<sup>-1</sup> is saturated C-H bending vibration, and the peak of 1737 cm<sup>-1</sup> is carbonyl stretching vibration.

In order to discuss the mechanism of tackifier-modified asphalt, the four components of matrix asphalt, SBS tackifier-modified asphalt, and tackifier-modified asphalt are analyzed, as shown in Table 7.

It can be seen from the above test analysis that the addition of tackifier increases the aromatic content of matrix asphalt, while the mass content of saturated content and asphaltene decreases. This may be due to the addition of aromatic ring in the tackifier, which makes the components of matrix asphalt redistributed. According to the principle of similar compatibility, the tackifier has good compatibility with asphalt. The addition of SBS redistributes the four components of tackifier-modified asphalt, which may be due to SBS. By absorbing the aromatic and saturated components of the modified asphalt, the mass fraction of the aromatic component and the resin is reduced, but the mass fraction of the aromatic component is still greater than the mass fraction of the matrix asphaltene, which indicates that the increase of the mass fraction of the aromatic ring in the tackifier can improve the compatibility of the modified asphalt.

In the system of tackifier, SBS, and asphalt, the addition of tackifier will increase the aromatic content of the system and improve the solubility of asphalt. In addition, SBS absorbs light components to reduce the distance between asphaltenes, thus changing the viscosity of asphalt. As the mass fraction of SBS increases, the number of active nodes of SBS increases and the viscosity enhancer molecules can better adsorb on SBS, which enhances SBS. The binding force between polymer network structures improves the restriction of SBS on asphalt, forming a new and stable network structure. The strong interaction between grids in this “network” structure restrains the displacement between asphalt particles, limits the fluidity of asphalt colloid system, and increases its ability to resist certain external forces, thus improving the modification to a certain extent high temperature performance of asphalt.

**2.2.2. FTIR Test Results of Antistripping Agent.** In order to clarify the modification mechanism of the adhesion effect of antistripping agent on cold patching asphalt, this paper uses

FTIR to test the antistripping agent, and the test results are shown in Figure 2.

As shown in the figure, the peaks at 1550 cm<sup>-1</sup> and 1641 cm<sup>-1</sup> belong to the vibration absorption of amide, the peaks at 3305 are the characteristic peaks of amino group, and the peaks at 3007 cm<sup>-1</sup>, 2953 cm<sup>-1</sup>, and 2852 cm<sup>-1</sup> are the expansion vibration of methylene group, so the sample composition contains polyamide. Compared with the strength of methylene absorption peak, the absorption peaks of amide and amino group are weaker and less, indicating that the alkyl chain of polyamide in the sample is very long.

There is hydrogen bond between the molecules of polyamide, and the polarity of polyamide is very strong, which can produce a strong intermolecular force, has excellent bonding performance, and can form a high-strength bond, which can improve the adhesion performance of cold patching asphalt and stone.

### 3. Study on Preparation of Cold Patching Asphalt Liquid and Composition Design of Its Mixture

#### 3.1. Preparation of Cold Make-Up Solution

**3.1.1. Preparation Process of Cold Patching Asphalt.** The preparation process of cold patching asphalt is basically the same as that of modified asphalt, and the preparation steps are as follows:

- (1) Preheat and melt the 90<sup>#</sup> base asphalt sample (at 150°C), and place it in a shear vessel
- (2) Add compatibilizer to the base asphalt, mix evenly, and then add SBS modifier, mix evenly, keep the temperature constant at 160°C, keep the asphalt, SBS modifier, and shear head together for heat preservation and swelling, and the heat preservation and swelling time is 30 min
- (3) The asphalt is heated to 175°C, the shear is turned on, and the asphalt is sheared at low speed for 30 min and then at high speed for 1 h
- (4) The shear rate was 5500 R/min, and the shear time was 10 min
- (5) Lower the temperature of the modified asphalt to 170°C and keep it warm for 2 h so that the modified asphalt can be fully developed
- (6) Add antistripping agent and stir for 10 min
- (7) When the temperature is reduced to 110°C, the above modified asphalt is added with the diluent in proportion and sheared at a shear rate of 2000 R/min for 5 min, and the preparation is completed.

**3.1.2. Determination of Diluent and Antistripping Agent Type and Dosage Based on Surface-Free Energy Change.** In this paper, a four factor four level orthogonal test is designed to measure the contact angle between the test liquid and the asphalt by the drop method [15–19] and calculate the change value of the surface energy between the low temperature

TABLE 1: The main performance indexes of 90# base asphalt.

Indexes	Experimental data	Specification requirements
Penetration (25°C, 5s, 100 g)	88.3	80 ~ 100
Penetration index PI	0.47	-1.5 ~ +1.0
Softening point (ring and ball method)/°C	52.4	≥44
Ductility (15°C, 5 cm/min)	>150	≥100
Dynamic viscosity of 60°C (Pa·s)	≥140	149
Solubility (%)	≥99.5	99.5
Residue after heating test in RTFO		
Mass loss (%)	0.002	±0.8
Penetration ratio 25°C (%)	62	≥57
Ductility 10°C (cm)	22	≥8
Adhesion grade to coarse aggregate	5	≥4

TABLE 2: Properties of diluent.

Number	Open flash point (°C )	Boiling point (°C )	Toxicity	Smell	Volatilization rate
A	>55	180~304	Low toxicity	Slightly smelly	Moderate
B	-50 ~ -20°C	30~205	Low toxicity	Slightly smelly	Fast
C	61	170~222	Low toxicity	Slightly smelly	Faster
D	58	161~200	Low toxicity	No peculiar smell	Fast

TABLE 3: Basic properties of tackifier.

Project	Appearance	Softening point (global method)/°C	Acid value (mg·KOH/g)	Ash content (%)	Iodine value (g/100 g)
Detection result	Light yellow or dark brown solid	80~140	≤1.0	≤0.1	40~100

TABLE 4: Basic properties of antistripping agent.

Number	Density (g/cm3)	Flash point (open)	Physical form
E	1	>300	Brown viscous liquid
F	0.89	>200	Brown liquid
G	0.95	>300	Dark brown viscous liquid
H	1.02	>300	Brown viscous liquid

TABLE 5: Performance index of compatibilizer.

Test items	Unit	Detection index	Test standard
Kinematic viscosity	(100°C) mm <sup>2</sup> /s	25	GB/T265
Open flash point	°C	≥200	GB/T3536
Ash content	%	0.3	GB/T508
Water content	%	0.01	GB/T260-1977
Heating reduction	(120°C × 15')	≤0.7	GB/T11409-2008
Aromatics content	%	≥90	—
Appearance		Coffee color	Visual inspection

TABLE 6: Properties of SBS modifier.

Number	Ratio of S/B	Oil filling rate (%)	Volatile matter (≤%)	Ash content (≤%)	300% extension stress (≥MPa)	Tensile strength (≥MPa)	Elongation at break (≥%)	Permanent set (≤%)	Shore hardness (A)	Melt flow rate (g/10 min)
SBS1301 (YH-791)	30/70	0	0.7	0.20	2.0	15.0	700	40	≥68	0.10-5.00

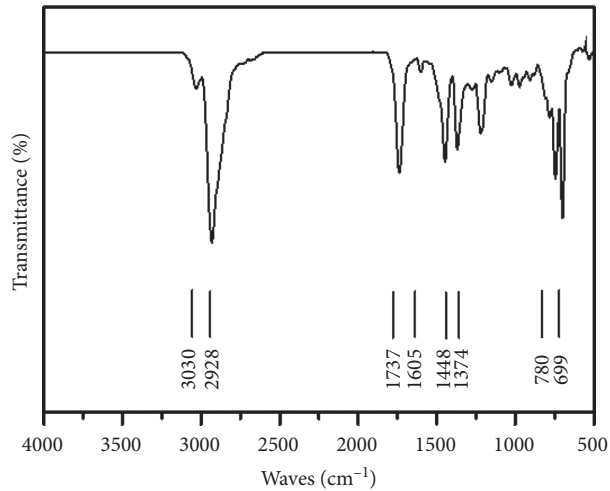


FIGURE 1: Infrared spectrum test results of tackifier.

TABLE 7: Analysis results of four components of base asphalt and tackifier-modified asphalt.

Test sample	$\omega\%$ (saturation fraction)	$\omega\%$ (aromatics)	$\omega\%$ (colloid)	$\omega\%$ (asphaltene)
Base asphalt	23.06	31.48	40.53	4.93
Tackifier-modified asphalt	6.43	49.63	41.51	2.43
Tackifier-SBS-modified asphalt	18.22	40.46	35.47	5.85

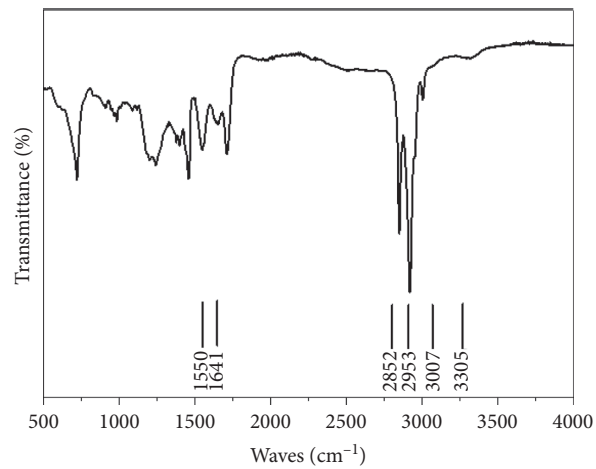


FIGURE 2: Infrared spectrum test results of antistripping agent.

TABLE 8: Change of surface-free energy of asphalt in orthogonal test (mJ/m<sup>2</sup>).

Test number	Variation value	Test number	Variation value	Test number	Variation value	Test number	Variation value
1	2.51	5	14.05	9	5.08	13	6.78
2	6.00	6	18.32	10	8.37	14	3.12
3	3.30	7	10.17	11	6.21	15	8.52
4	8.79	8	8.08	12	3.54	16	9.86

asphalt and the 90<sup>#</sup> base asphalt. The results are shown in Table 8.

(1) Range analysis: the results are shown in Table 9.

It can be seen from Table 9 that the influence of various factors on the surface-free energy is in the order of diluent type > additive amount > diluent amount > additive type. Therefore, when determining the type and amount of raw

TABLE 9: Range analysis of surface-free energy change.

Factor	Diluent type	Type of antistripping agent	Diluent content	Dosage of antistripping agent
K1	5.149	7.106	9.223	4.832
K2	12.655	8.951	8.028	6.770
K3	5.799	7.049	4.894	8.893
K4	7.070	7.565	8.527	10.178
R	7.506	1.902	4.339	5.346

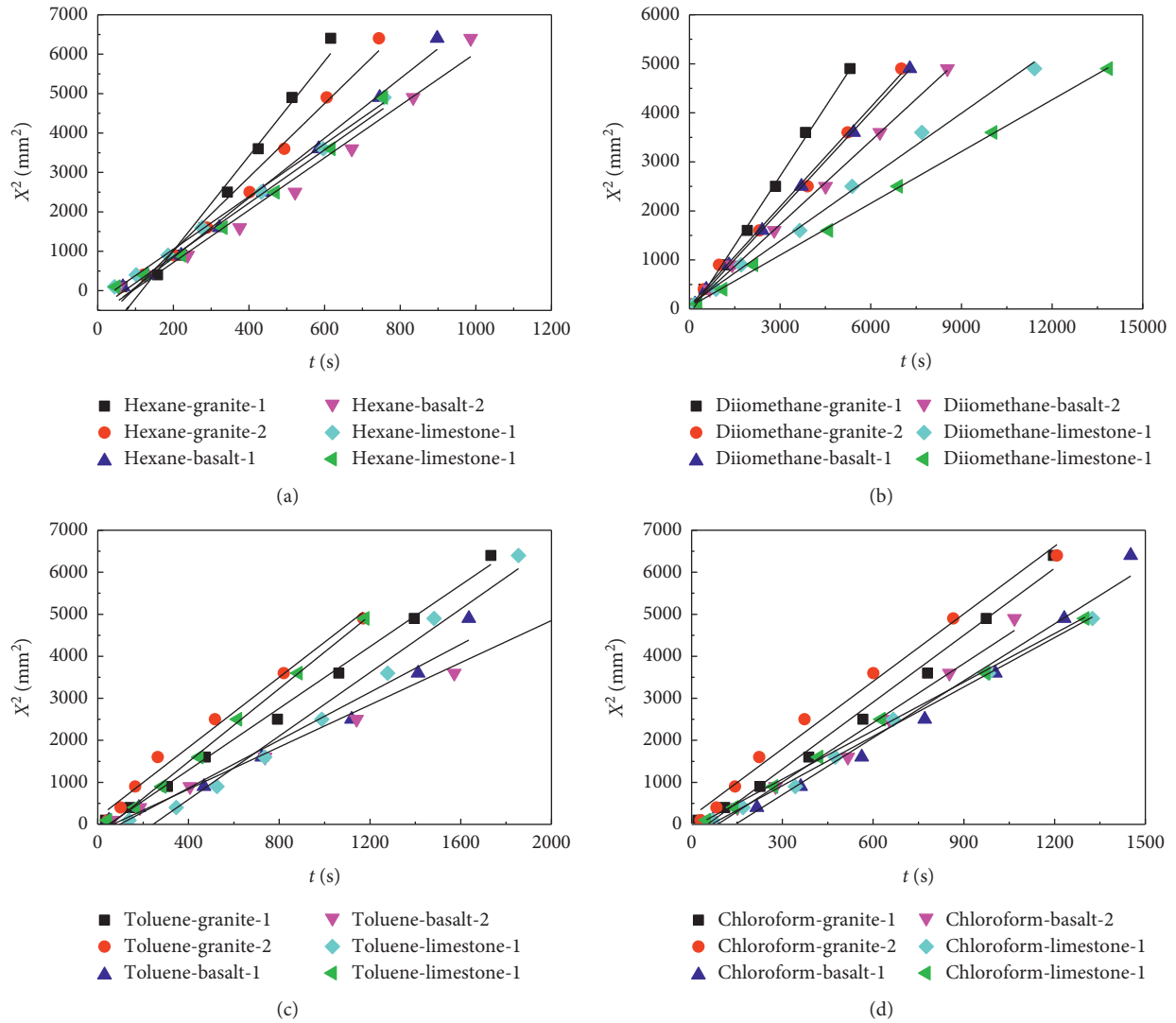


FIGURE 3: Relation between impregnation time  $t$  of liquid impregnated aggregate powder and square  $x^2$  of impregnation distance: (a) hexane, (b) diomethane, (c) toluene, and (d) chloroform.

TABLE 10: Variance analysis of surface-free energy change.

Index	Factor	SS	df	MS	P	Critical value	Significance
Surface free energy	Diluent type	140.256	3	46.752	0.007	$\alpha = 0.10$ $\alpha = 0.01$ $\alpha = 0.025$ $\alpha = 0.05$	Very significant
	Type of antistripping agent	9.424	3	3.141	0.222		
	Diluent content	43.916	3	14.639	0.034		Significant
	Dosage of antistripping agent	66.605	3	22.203	0.019		Significant
	e	3.548	3	1.183	0.007		
	The sum	263.749	15				

materials, consider in the order of diluent type, additive amount, diluent amount, and additive type.

(2) Analysis of variance: the results are shown in Table 10.

Table 10 shows that  $P$  (diluent type) = 0.007 <  $\alpha$  = 0.01, indicating that the diluent type has a very significant impact on the surface-free energy,  $P$  (diluent content) = 0.034 <  $\alpha$  = 0.05, and  $P$  (additive content) = 0.019 <  $\alpha$  = 0.025, indicating that the diluent content and additive content have a significant impact on the surface-free energy of asphalt.

At the same time, according to the experimental data of the change of the surface-free energy of asphalt, when diluent B is used, the change of the surface-free energy is the largest, and with the increase of the diluent content, the change of the surface-free energy of asphalt increases first and then decreases, when the content is 10%, the change is the largest. When F antistripping agent is used, the change of surface-free energy is the largest, and with the increase of antistripping agent content, the change of surface-free energy of asphalt increases. When the content of antistripping agent is 4%, the change is the largest.

Therefore, the best ratio of low-temperature asphalt is as follows: diluent B content is 10%, base asphalt is 80%, and antistripping agent F content is 4% (admixture). Considering the safety risks of diluent B, diluent D is selected for subsequent test.

**3.1.3. Measurement and Analysis of Aggregate Surface-Free Energy.** According to the technical principle of columnar wick [20–22], the samples of granite, basalt, and limestone are, respectively, impregnated with hexane, and the relation diagram is made, as shown in Figure 3(a). According to the relevant parameters of slope and hexane, the effective radius of capillary is calculated as  $R_{\text{Granite}} = 3.3 \pm 0.30 \mu\text{m}$ ,  $R_{\text{Basalt}} = 2.4 \pm 0.20 \mu\text{m}$ , and  $R_{\text{limestone}} = 2.2 \pm 0.10$ , respectively.

Then, diiomethane, toluene, and chloroform are, respectively, impregnated with granite, basalt, and limestone aggregate powder, and the relation diagram is made, as shown in Figure 4(b–d). The surface energy and its components of various aggregates are calculated, as shown in Table 11.

It can be seen from Table 11 that the surface energy of different aggregates is quite different and the van der Waals force is relatively small, which is mainly caused by different Lewis acid-base forces. The surface energy and its components of limestone aggregate powder are the largest among the three kinds of aggregate, the surface energy of granite is the lowest, and Lewis acid-base force and van der Waals force are the lowest. It shows that the compatibility of limestone aggregate and aggregate will be better, and limestone aggregate is selected for subsequent test.

### 3.2. Research on Material Composition Design of Cold Patching Asphalt Mixture

**3.2.1. Material Selection and Mineral Aggregate Grading Design of Cold Patching Asphalt Mixture.** The main

components of cold patching asphalt mixture are as follows: 90# base asphalt, modifier, tackifier, compatibilizer, antistripping agent, diluent, and limestone aggregate.

Combined with the research experience of cold patching gradation at home and abroad, according to the environmental characteristics of northern China, the LB-10-1 gradation shown in Table 12 is determined for the preparation of subsequent cold patching asphalt mixture. In order to improve the antistripping performance of cold patching material, 1.5% cement is added [23].

**3.2.2. Prediction and Determination of the Best Cold Patching Asphalt Content.** In this paper, the empirical formula method is used to design the optimal asphalt content of cold patching asphalt mixture, and the paper trail test is used to adjust the optimal asphalt content.

Based on the California experience formula, the oil stone ratio of cold patching asphalt mixture is calculated by determining the mineral aggregate gradation and the thickness of oil film on the surface of mineral aggregate. Formula (1) is as follows:

$$h = P \times (2 + 0.02a + 0.046b + 0.08c + 0.14d + 0.3e + 0.6f + 1.6g), \quad (1)$$

where  $a$ ,  $b$ ,  $c$ ,  $d$ ,  $e$ ,  $f$ , and  $g$  are the percentages of passing through the 5 mm, 2.5 mm, 1.2 mm, 0.6 mm, 0.3 mm, 0.15 mm, and 0.074 mm sieve holes, respectively ( $\mu\text{m}$ ),  $h$  is the thickness of asphalt oil film (mm), and  $P$  is the ratio of asphalt to stone (%).

In order to determine the oil stone ratio more accurately, it is necessary to carry out paper trace test and auxiliary judgment. Typical paper trace test results are shown in Figure 4–6.

According to the calculation of empirical formula and the analysis of paper trace test, the optimal initial amount of cold make-up liquid is 4.5%.

**3.2.3. Determination of Design Parameters and Material Proportion.** In order to determine the design parameters of cold patching asphalt mixture and the proportion of the materials used, the orthogonal test was designed to determine the design void ratio, the amount of diluent, and the amount of various admixtures.

Firstly, four design indexes, i.e., design void ratio, tackifier content, diluent content, and antistripping agent, are selected for sensitivity analysis of cold patching performance. The design orthogonal test level is shown in Table 13.

Using the gradation of cold patching asphalt mixture and the optimal asphalt content of 4.5% provided above, the preparation of cold patching asphalt mixture with various factors combination is completed, and the performance test of each formula of cold patching asphalt mixture in Table 13 is carried out, the results are as follows.

**Adhesion test.** The experimental results of 9 formulations are all adhesive grade 5, no significant difference. It is proved

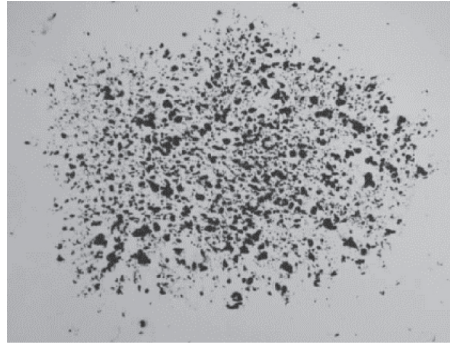


FIGURE 4: Too little oil.

TABLE 11: Aggregate surface energy and its components (mJ/m<sup>2</sup>).

Stone	Surface energy ( $\gamma_s$ )	van der Waals force ( $\gamma_{sLW}$ )	Lewis acid-alkali force ( $\gamma_{sAB}$ )	Lewis acid-alkali force ( $\gamma_{s+}$ )	Lewis acid-alkali force ( $\gamma_{s-}$ )
Granite	19.10	18.20	0.90	0.05	4.29
Basalt	23.81	21.71	2.10	0.93	1.19
Limestone	28.94	21.91	7.03	1.99	6.21

TABLE 12: Screening test results of ore and filler.

Composite grading	Percentage passing the following sieve (mm) (%)											
	26.5	19	16	13.2	9.5	4.75	2.36	1.18	0.6	0.3	0.15	0.075
Upper limit	100	100	100	100	100	50	25	20	15	10	8	5
Lower limit	100	100	100	100	80	30	10	8	6	4	3	2
Median	100	100	100	100	90	40	17.5	14	10.5	7	5.5	3.5
Composite grading	100.0	100.0	100.0	100.0	96.5	31.1	15.2	9.0	6.8	5.0	3.9	3.1

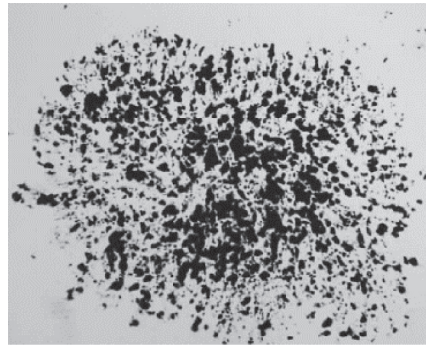


FIGURE 5: Moderate oil.

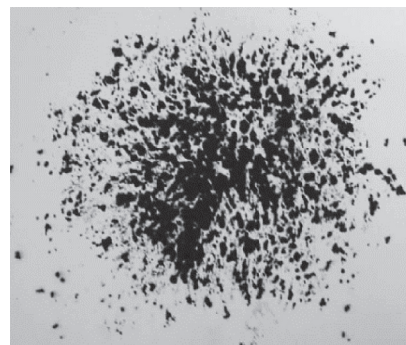


FIGURE 6: Too much oil.



TABLE 13:  $L_9$  ( $4^3$ ) orthogonal test table.

Test number	Factor			
	Factor A Design voidage (%)	Factor B Tackifier content (%)	Factor C Diluent content (%)	Factor D Dosage of antistripping agent (%)
1	10 ± 0.5	2	30	2.5
2	10 ± 0.5	3	32	3.0
3	10 ± 0.5	4	34	3.5
4	15 ± 0.5	2	32	3.5
5	15 ± 0.5	3	34	2.5
6	15 ± 0.5	4	30	3.0
7	20 ± 0.5	2	34	3.0
8	20 ± 0.5	3	30	3.5
9	20 ± 0.5	4	32	2.5

that the addition of tackifier and modifier in 9 formulations changes the four component ratio of matrix asphalt, and the network structure formed can produce better adhesive performance with aggregate.

*Cohesion test.* The cohesion study was carried out by the method provided in «The code for construction of highway asphalt pavement» (JTG F40-2004), and the results are shown in Table 14.

The damage rate of each cold patching asphalt mixture is very low and its cohesion is good. It shows that the 9 kinds of cold patching asphalt mixture are easy to form a whole with the original pavement structure, combined with compactness.

*Initial strength test.* In this paper, the Marshall specimens, which were compacted 50 times on both sides, were placed in a constant temperature box and kept at 15°C to constant temperature. The test results are shown in Figure 7–10.

From Figure 7–10, it can be seen that the smaller the diluent dosage, the higher the tackifier dosage, and the smaller the void ratio, the better the initial strength of the cold patch. Considering the best combination scheme of initial strength, the maximum amount of tackifier should be taken, and the minimum void ratio should be taken, and the sensitivity of void ratio to initial strength is in the middle, but for later strength, the influence of void ratio is far greater than that of other indexes. Therefore, while improving the design void ratio to ensure a rapid strength growth rate and initial strength of cold patch, the void ratio should not be too large to prevent the defect of low initial strength of cold patch, so the median value should be selected.

*Later strength and residual stability test.* The results of later strength test are shown in Figures 11–18, and the results of residual stability are shown in Tables 15–17.

It can be seen from Figures 11–18 that, for the later strength performance, the influence of the void ratio is far greater than that of diluent and tackifier, and the later strength is a performance index greatly affected by the void ratio. The porosity of 15 ± 0.5% is slightly better than 20 ± 0.5%, the difference is not significant. When the void ratio is 10 ± 0.5%, the later strength indexes are obviously lower. Therefore, it is suggested that the void ratio of cold

patching asphalt mixture should be controlled between 15% and 18%, which can not only meet the requirements of initial strength but also make the later strength of the mixture higher.

From Tables 15 to 17, it can be seen that the sensitivity factors of residual stability are mainly tackifier and antistripping agent, which show that with the increase of the content of tackifier and antistripping agent, the adhesion force of cold patching asphalt mixture is higher and higher. This is because the performance of the original modified asphalt is destroyed after adding diluent. The addition of additives improves the performance of cold make-up fluid and makes the cold patching asphalt mixture have better adhesion. Moreover, the influence of tackifier on the residual stability of cold patching asphalt mixture is far greater than that of other materials. When the content of tackifier is 3.5% and the content of antistripping agent is 3.5%, the residual stability of cold patching asphalt mixture is the highest.

*Comparison and selection of optimum design of cold patching asphalt mixture.* Through the analysis of the key factors affecting the performance of cold patching asphalt mixture, the voidage, additives, diluents, etc. were screened, and the proportion of cold patching asphalt mixture was gradually optimized. Finally, the design void ratio is 15 ± 0.5%, compatibilizer 2.5%, linear SBS modifier 5%, tackifier 4%, antistripping agent 3.5%, and diluent D content should be determined according to the use environment temperature.

#### 4. Performance Evaluation of Cold Patching Asphalt Mixture

On the basis of the composition, gradation type and optimum asphalt consumption of the cold patching asphalt mixture determined above, according to the provisions of «Finished asphalt pavement pit cold patching material» (JT/T972-2015), «Technical code for construction of highway asphalt pavement» (JTG F40-2004), and referring to the test methods and standards of some hot mix asphalt mixtures, the strength, high temperature performance and water damage resistance of cold patching asphalt mixtures are evaluated.

TABLE 14: Data sheet of cohesion test.

Test number	1	2	3	4	5	6	7	8	9
Residue rate (%)	99.7	99.8	99.6	99.7	100.1	99.9	99.9	100.0	100.0
Breakage rate (%)	0.3	0.2	0.4	0.3	-0.1	0.1	0.1	0	0

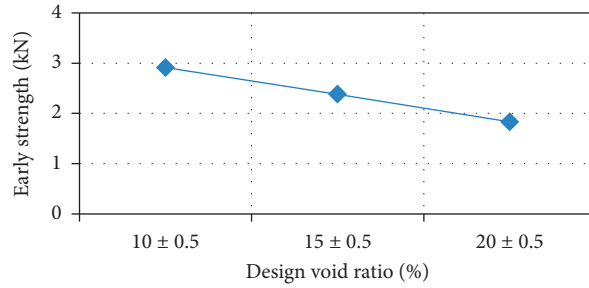


FIGURE 7: Relationship between early strength and design void ratio.

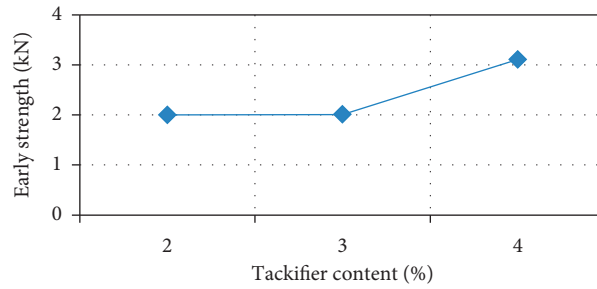


FIGURE 8: Relationship between early strength and amount of tackifier.

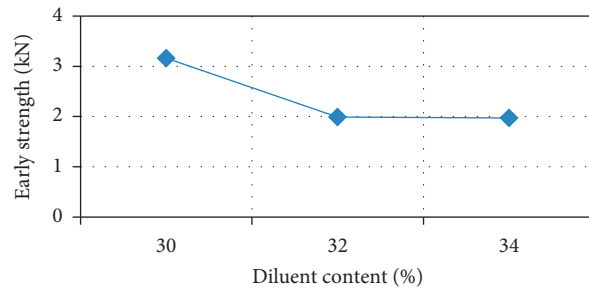


FIGURE 9: Relationship between early strength and diluent dosage.

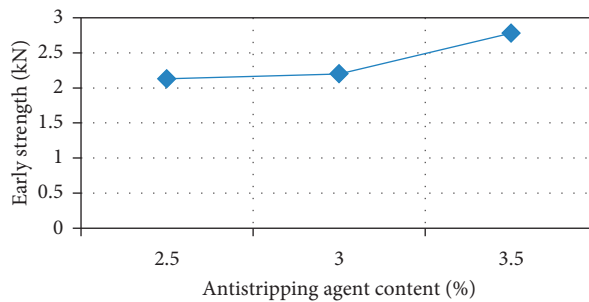


FIGURE 10: Relationship between early strength and antistripping agent dosage.

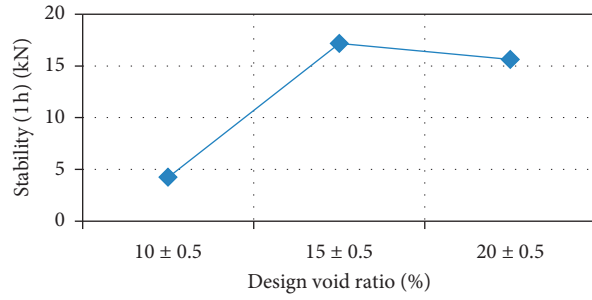


FIGURE 11: Relationship between late strength (60 min) and design porosity.

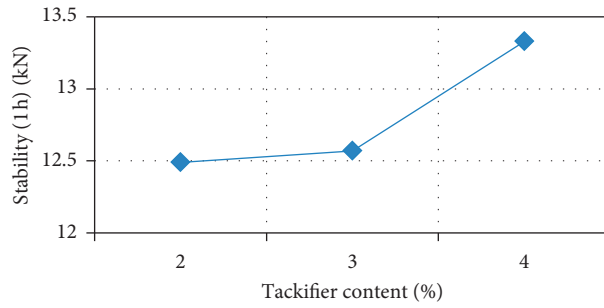


FIGURE 12: Relationship between late strength (60 min) and tackifier content.

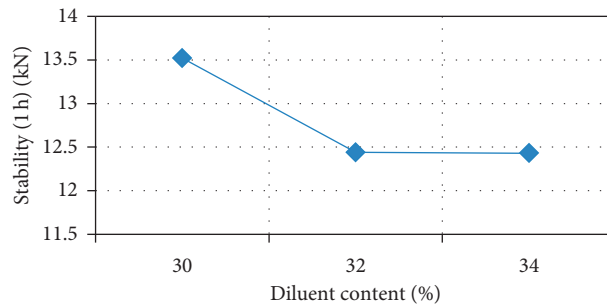


FIGURE 13: Relationship between late strength (60 min) and diluent dosage.

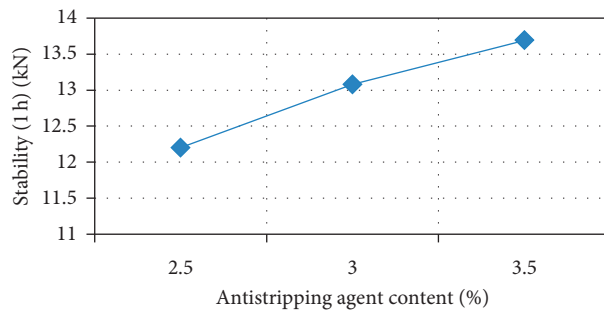


FIGURE 14: Relationship between late strength (60 min) and antistripping agent dosage.

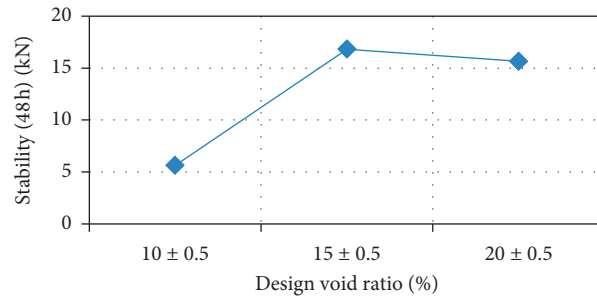


FIGURE 15: Relationship between late strength (48 h) and design porosity.

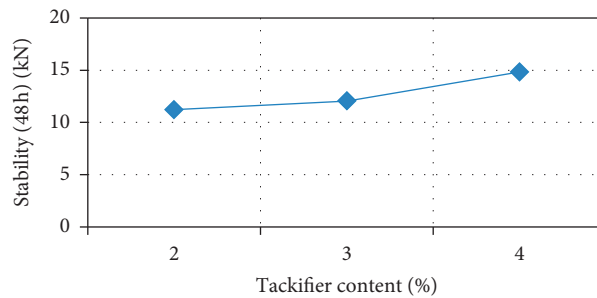


FIGURE 16: Relationship between late strength (48 h) and tackifier content.

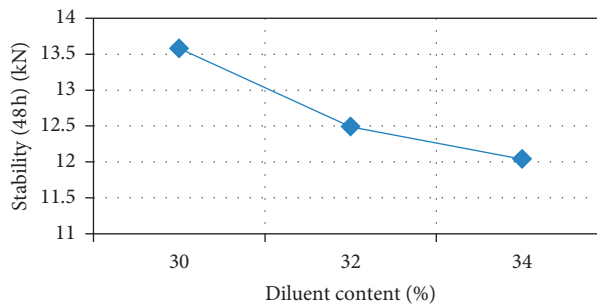


FIGURE 17: Relationship between late strength (48 h) and diluent dosage.

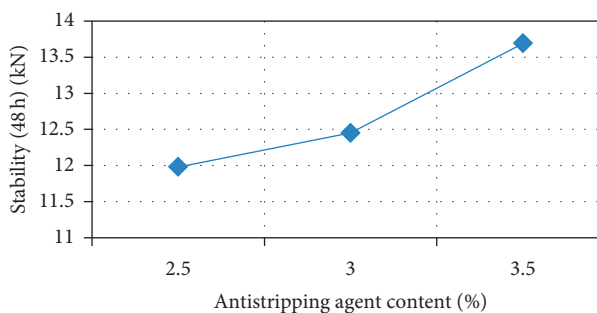


FIGURE 18: Relationship between late strength (48 h) and antistripping agent dosage.

**4.1. Adhesion Grade.** The adhesive grade of the cold patching asphalt mixture prepared after the optimized ratio is grade 5, and the product conforms to «The technical requirements of finished cold patching material for asphalt pavement pit and groove» (JT/T 972–2015).

**4.2. Strength Test.** The strength of cold patching asphalt mixture was tested by the methods of stability and residual stability in «Finished cold patching material for asphalt pavement pit and groove» JT/T 972–2015. Data result is shown in Table 18.

TABLE 15: Sensitivity analysis of cold patching asphalt mixture residual stability test.

Test number	Factor			
	Factor A Design void ratio	Factor B Tackifier content	Factor C Diluent content	Factor D Dosage of antistripping agent
K1	99.163	87.470	95.610	94.260
K2	97.620	93.380	97.220	92.270
K3	100.160	116.093	104.113	110.413
Range	2.540	28.623	8.503	18.143

TABLE 16: Variance analysis results of cold patching asphalt mixture residual stability test.

Factor	Sum of squares of deviations	Freedom	F Ratio
Design void ratio	9.827	2	0.019
Tackifier content	1370.119	2	2.614
Diluent content	122.417	2	0.234
Antistripping agent content	594.071	2	1.133
Error	2096.43	8	

TABLE 17: Optimal parameter combination scheme and sensitivity sequence of strength stability in later stage of cold feed.

Performance index	Design parameters				Parameter sensitivity ranking
	Design void ratio	Tackifier content	Diluent content	Antistripping agent content	
Initial strength	2	3	1	3	Diluent > void ratio > tackifier > antistripping agent
Late stability (1 h)	2	3	1	3	Void ratio >> diluent > antistripping agent > tackifier
Late stability (48 h)	2	3	1	3	Void ratio >> tackifier > antistripping agent ≥ diluent
Residual stability	3	3	3	3	Tackifier > antistripping agent > diluent > void ratio

TABLE 18: Strength test results.

Test number	1	2	3	4	5	6	Average value	Residual stability (%)
Stability (1 h, kN)	17.83	16.92	17.55	18.04	17.38	17.2	17.5	101.7
Stability (48 h, kN)	17.26	17.82	17.69	17.72	18.03	18.45	17.8	

According to «The finished cold patching material for asphalt pavement pit and groove»JT/T972-2015, the stability shall be greater than 3 kN and the residual stability shall be greater than 85%. The test results show that the stability of the self-made cold patching asphalt mixture is more than 3 kN, the strength meets the requirements, and the residual stability is also high. It is preliminarily verified that the cold patching asphalt mixture has good water damage resistance. In the future, the freeze-thaw split test and mist dynamic water erosion test will be used for further test.

**4.3. High Temperature Stability.** Because there are still some diluents in the cold patching asphalt mixture rut after forming, the dynamic stability value is too low when the rut test method suitable for hot patching asphalt mixture is used to test its high-temperature stability. Therefore, in this paper, the test method is improved to place the rutting test piece after cold patch rolling in the oven for curing and conduct

the rutting test after the diluent volatilizes. The test results are shown in Table 19.

According to the test results in Table 19, the self-made cold patching asphalt mixture has good high-temperature performance, which is equivalent to the performance of ordinary hot patching asphalt mixture and meets the road performance requirements of cold patching asphalt mixture.

#### 4.4. Water Stability

**4.4.1. Freeze-Thaw Split Test.** Because the 40°C water bath temperature can reflect the actual environment temperature when the cold patching asphalt mixture produces water damage, at the same time, it can solve the problem of loose collapse of the cold patching asphalt mixture due to the existence of diluent when the water bath temperature is too high, so as to ensure the smooth progress of the test. In this paper, the water bath temperature of freeze-thaw splitting test in «Test code for asphalt and asphalt mixture of

TABLE 19: High-temperature stability test results.

Test number	Dynamic stability (second/mm)	45 minrut depth (mm)	60 minrut depth (mm)
1	6750	0.790	0.794
2	6366	0.805	0.807
3	5857	0.852	0.852
4	6095	0.826	0.827
5	5353	0.865	0.865
6	5687	0.857	0.859

TABLE 20: Freeze-thaw split test results.

Test number	Splitting tensile strength (MPa)			Average splitting tensile strength (MPa)	TSR%
	1	2	3		
Without freeze-thaw cycle (kN)	0.2725	0.2418	0.2067	0.24	95.0%
After freeze-thaw cycle (kN)	0.2568	0.2254	0.2025	0.23	

Highway Engineering》(JTG E20-2011) is modified to 40°C. The test results are shown in Table 20.

The test results in Table 20 show that the freeze-thaw splitting strength ratio of the self-made cold patching asphalt mixture in this paper is 95%, which meets the requirement that the freeze-thaw splitting strength ratio of the common hot mix asphalt mixture should not be less than 70%, indicating that its water damage resistance is good.

**4.4.2. MIST Hydrodynamic Scour Test.** Mist water sensitivity tester (Figure 19) can simulate the scour effect of wheel on wet road and the high temperature and periodic pressure environment and detect the water stability in about 3 hours. The pressure is cycled from 0 to 40 PSI, and the pores in the sample are continuously pressurized and depressurized. The high-temperature water in and out of the pores not only produces the scour effect similar to that of the actual tire rolling over the road but also accelerates the damage rate of the integrity of the sample and the adhesion between the aggregate and the adhesive caused by this effect. Under high pressure, water acts between the aggregate and binder in this way, which accelerates the peeling rate. The most obvious change is the relative density of wool volume. The test pieces of MIST are generally prepared by the rotary compactor, in order to keep the consistency with the data of freeze-thaw splitting test, and the Marshall specimen is used instead. The test results are shown in Table 21.

The test standard is that the void ratio of cold patching asphalt mixture before and after treatment by mist is not more than 1.5%; no obvious peeling and damage on the appearance; the splitting strength shall not be less than 80%. If two of the above conditions meet the requirements, it can be judged as qualified and insensitive to moisture. The ratio of freeze-thaw splitting strength of self-made cold patching asphalt mixture and commercial cold patching asphalt mixture is 93.7% and 82.7%, respectively, which meets the requirements of detection standard no less than 80%. The percentage (%) of voidage (before and after) difference is 0.8 and 1.0, respectively, which is no more than 1.5% meeting the requirements of the test standard. There is no obvious

peeling and damage in appearance, but the self-made cold patching asphalt mixture is better. 93.7% of freeze-thaw splitting strength ratio of the self-made sample MIST test is close to that of the freeze -thaw splitting test, so the water stability of the cold patched asphalt mixture is good.

## 5. Results and Discussion

- (1) The infrared spectrum analysis of the tackifier was supplemented by the four components analysis of base asphalt, SBS tackifier-modified asphalt, and tackifier-modified asphalt. The results showed that the addition of tackifier increased the aromatic content of the base asphalt, so the tackifier had good compatibility with asphalt; SBS absorbs the aromatics and saturates of the asphalt modified by tackifier. The increase of the mass fraction of aromatic ring in the tackifier can improve the compatibility of the modified asphalt.
- (2) The results of IR spectrum analysis of antistripping agent show that the alkyl chain of polyamide in the sample is very long, and there is hydrogen bond between the molecules of polyamide, and the polarity of polyamide is very strong, which can produce very strong intermolecular force, has excellent bonding performance, and can form a high-strength bond, which can improve the adhesion performance of cold patching asphalt and stone.
- (3) Based on the principle of lying drop test and the orthogonal test design method, the free energy of asphalt surface is measured, so as to determine the material selection and preliminary mixing proportion of diluent and antistripping agent. Based on the principle of columnar wick technology, the free energy of aggregate surface is measured, and it is determined that limestone aggregate is most suitable for the preparation of cold patching asphalt mixture.
- (4) The orthogonal test is used to optimize the material composition design of cold patch asphalt mixture. The performance test results show that, in order to



FIGURE 19: MIST water sensitivity tester.

TABLE 21: Test results of dynamic water erosion of MIST.

Number index	Self-made sample	Commercial samples
Splitting strength ratio of freeze-thaw %	93.7	82.7
Percentage of voidage difference (before and after) (%)	0.8	1.0
Visual inspection	No abnormality	No abnormality

ensure the strength requirements of cold patch asphalt mixture, the void ratio should be between 15% and 18%, and the content of antistripping agent has great influence on the water stability, and its content should be controlled between 3% and 5%.

- (5) The design parameters and material proportion of cold patching asphalt mixture are optimized by orthogonal test. The results show that the design void ratio is  $15 \pm 0.5\%$ , compatibilizer is 2.5%, linear SBS modifier is 5%, tackifier is 4%, antistripping agent is 3.5%, and diluent D should be determined according to the use environment temperature. The properties of the cold patching asphalt mixture meet the requirements of the hot mix asphalt mixture.

### Data Availability

The data used to support the findings of this study are included within the article.

### Conflicts of Interest

The authors declare no conflicts of interest.

### Authors' Contributions

Shuolei Huang and Junda Ren conceived and designed the experiments; Mingguang Li performed the experiments; Shuiwen Zhou and Zhuolin Li analyzed the data; and Shuolei Huang and Junda Ren wrote the paper.

### Acknowledgments

The research was funded by Research on Pit Repair Material of High-Performance Asphalt Pavement approved by Liaoning Provincial Department of Communications.

### References

- [1] Q. Dai, "Discussion on the repair measures of the potholes and cracks in the highway pavement," *Sichuan Cement*, vol. 1, p. 351, 2020.
- [2] J. Wang, *Study on Design and Durability of Cold Patching Asphalt Mixture*, Harbin University of Technology, Harbin, China, 2016.
- [3] X. Xing, *Study on the Preparation and Properties of Cold Patching Asphalt Mixture*, Southeast University, Nanjing, China, 2016.
- [4] A. Khan, P. Redelius, and N. Kringos, "Evaluation of adhesive properties of mineral-bitumen interfaces in cold asphalt

- mixtures," *Construction and Building Materials*, vol. 125, pp. 1005–1021, 2016.
- [5] G. Ferrotti, E. Pasquini, and F. Canestrari, "Experimental characterization of high-performance fiber-reinforced cold mix asphalt mixtures," *Construction and Building Materials*, vol. 57, pp. 117–125, 2014.
  - [6] S. S. Dash and M. Panda, "Influence of mix parameters on design of cold bituminous mix," *Construction and Building Materials*, vol. 191, pp. 376–385, 2018.
  - [7] L. Geng, Q. Xu, X. Yu, C. Jiang, Z. Zhang, and C. Li, "Laboratory performance evaluation of a cold patching asphalt material containing cooking waste oil," *Construction and Building Materials*, vol. 246, p. 117637, 2020.
  - [8] Z. Wang, "Early-stage road property improvements of cold recycled asphalt emulsion mixture with microwave technology," *Cleaner Production*, vol. 263, 2020.
  - [9] L. Cheng, "Measuring moisture susceptibility of Cold Mix Asphalt with a modified boiling test based on digital imaging," *Construction and Building Materials*, vol. 105, pp. 391–399, 2016.
  - [10] W. Lv, *Characteristics and Preparation Technology of Cold Laid Asphalt Material*, Huadong Gonglu, Kaohsiung, Taiwan, 2002.
  - [11] Y. Bi, R. Li, S. Han, J. Pei, and J. Zhang, "Development and performance evaluation of cold-patching materials using waterborne epoxy-emulsified asphalt mixtures," *Materials*, vol. 13, no. 5, p. 1224, 2020.
  - [12] L. Cui, *Study on Cold Patching Asphalt Mixture*, Chang'an University, Xi'an, China, 2006.
  - [13] F. Li, "Research on composition design of cold patching asphalt mixture," *Journal of Wuhan University of Technology*, vol. 32, no. 14, pp. 79–82, 2010.
  - [14] People's Communications Press, *Industrial Standard of the People's Republic of China. JTG F40-2004 Technical Code for Construction of Highway Asphalt Pavement*, People's Communications Press, Beijing, China, 2004.
  - [15] F. M. Fowkes, "Attractive forces at interfaces," *Industrial & Engineering Chemistry*, vol. 56, no. 12, pp. 40–52, 1964.
  - [16] R. J. Good, "Contact angle, wetting, and adhesion: a critical review," *Journal of Adhesion Science and Technology*, vol. 6, no. 12, pp. 1269–1302, 1992.
  - [17] C. J. Van Oss, R. J. Good, and M. K. Chaudhury, "Additive and nonadditive surface tension components and the interpretation of contact angles," *Langmuir*, vol. 4, no. 4, pp. 884–891, 1988.
  - [18] C. J. Van Oss, M. K. Chaudhury, and R. J. Good, "Interfacial Lifshitz-van der Waals and polar interactions in macroscopic systems," *Chemical Reviews*, vol. 88, no. 6, pp. 927–941, 1988.
  - [19] Y. Tan and M. Guo, "Using surface free energy method to study the cohesion and adhesion of asphalt mastic," *Construction and Building Materials*, vol. 47, pp. 254–260, 2013.
  - [20] E. W. Washburn, "The dynamics of capillary flow," *Physical Review*, vol. 17, no. 3, p. 273, 1921.
  - [21] E. Chibowski, "Solid surface free energy components determination by the thin-layer wicking technique," *Journal of Adhesion Science and Technology*, vol. 6, no. 9, pp. 1069–1090, 1992.
  - [22] C. J. Van Oss, *Interfacial Forces in Aqueous Media*, CRC Press, Boca Raton, FL, USA, 2006.
  - [23] M. Guo and Y. Tan, "Interaction between asphalt and mineral fillers and its correlation to mastics' viscoelasticity," *International Journal of Pavement Engineering*, p. 1575379, 2019.



## Research Article

# Investigating Automobile Passengers' Comfort and Safety on Scenic Road Using Sideway Force Coefficient

Ronghua Wang,<sup>1</sup> Xingliang Liu ,<sup>2</sup> and Feijie Han<sup>3</sup>

<sup>1</sup>College of Architecture and Civil Engineering, Beijing University of Technology, Beijing 100124, China

<sup>2</sup>College of Traffic & Transportation, Chongqing Jiaotong University, Chongqing 400074, China

<sup>3</sup>CCCC FIRST Highway Consultants Co.,LTD, Xi'an 710064, China

Correspondence should be addressed to Xingliang Liu; xingliang1125@outlook.com

Received 18 July 2020; Revised 1 September 2020; Accepted 5 October 2020; Published 21 October 2020

Academic Editor: Zhen Leng

Copyright © 2020 Ronghua Wang et al. This is an open access article distributed under the Creative Commons Attribution License, which permits unrestricted use, distribution, and reproduction in any medium, provided the original work is properly cited.

To satisfy passengers' experiential demand in scenic roads, a study on passengers' comfort in the aspect of horizontal curve design is stated in this study. A new indicator sideway force coefficient (*SFC*) describing passengers' comfort is introduced, which differs from lateral acceleration. The mechanism of *SFC* is provided depending on the dynamic balance condition of the vehicle on horizontal curve and  $SFC_c$  representing passengers' comfort tolerance limitation is investigated. A large scale naturalistic driving experiments along a park road are conducted, and the  $SFC_c$  value from naturalistic driving experiments is verified through numerical simulation of 15 horizontal curves from 5 scenic roads from the perspectives of both passengers' comfort and driving safety. The statistical analysis on data collected in field tests indicates that age and gender have no effect on  $SFC_c$ , and the value of  $SFC_c$  is determined as 0.291. The corresponding minimum radius limits under 20–60 km/h and superelevation 6%, 8%, and 10% are proposed. The numerical simulation denotes, when satisfying the comfort demand of passengers (*SFC* less than 0.291), the lateral distance path is in a safe range, which could also satisfy the safe driving requirements. Thus,  $SFC_c$  and minimum radius limits proposed in this study are proved to be credible and appropriate for the curve design of horizontal alignment in scenic roads.

## 1. Introduction

Scenic roads refer to the roads inside scenic tourist areas, nature reserves, and parks, only providing services to travelers. In 1968, the “Park Road Standards” [1] was provided to USA Interior Ministry by National Park Service (NPS). This report indicated that scenic road should be distinguished from ordinary state highway for the first time. Moreover, the scenic road design method considering passengers' comfort and experience was also put forward. Usually, the design indicators of scenic road were directly adopted from the criterion for ordinary highway “A Policy on Geometric Design of Highway and Streets” [2]. Although this criterion considered passengers' comfort and experience by introducing traffic quality, a more comprehensive way of promoting passengers'

comfort in scenic road, and, to be more specific, an indicator representing passengers' comfort in scenic road is still not put into practice.

The concept of passengers' comfort, or ride comfort, is understood as one aspect of transportation service quality [3]. The essence of passengers' comfort measurement is human perception, defined as “subjective state of well-being or absence of mechanical disturbance in relation to the induced environment” in ISO 5805 [4, 5]. This is one of the most challenge topics. Firstly, it is affected by several factors, including age, gender (human factors), temperature, noise, pressure (environmental factors), seat, and workspace (spatial factor) [6]. Secondly, comfort measurement is based on statistic data from large scale personal interviews, which could be a relatively expensive task in terms of human resources [7, 8]. Thirdly, it was stated in related works that the

object of evaluating passengers' comfort should be carefully implemented because it might vary among individuals [5].

Previous studies focused on two main aspects related to evaluating passengers' comfort: vehicle dynamics and road geometrics. In aspect of vehicle dynamics, studies related to suspension system which could improve passengers' comfort took the major part, including passive suspension cases with fixed characteristics [9–11] and active suspension cases involving applications of control laws [12–14]. Besides, some researches paid their attention on other aspects in vehicle riding smoothness, for instance, the comfort of passenger seat [15, 16], the mechanism of vehicle vibration generation and spreading path [17, 18], tolerance limitation of passengers [19], temperature, and noise within the vehicle [20, 21].

Another aspect is road geometrics related ones, and also the research topic in this study, interpreted as the geometric design related methods. Among these researches, lateral and longitudinal acceleration were used as indicators to represent the overload on passengers in acceleration/deceleration or turning process. In study by Cafiso and La Cava [22], acceleration was used as the indicator to evaluate the consistency of highway alignment. The safety level of curves and comfort level of various road types in two-lane rural highways were estimated by Lee et al. [23]. Moreover, various acceleration models were developed in road related passengers' comfort studies, including a lateral acceleration model for curved-and-sloped sections [24], a lateral acceleration model for passenger cars considering curve radius as independent variable [25], a longitudinal acceleration model for horizontal curves [26], and a lateral acceleration model for different types of highway and different vehicle [27]. The abovementioned studies basically depended on real road collected data. However, as depicted previously, personal interview is a relatively expensive method. The data collected sometimes seems insufficient to complete all the analysis. Therefore, to compensate this shortage, simulation or calculation data was also used. For instance, simulation speed and acceleration data could be used in analyzing the effects of curve radius, diurnal variation, season on driving comfort [28], passengers' comfort for buses [29], passengers' comfort in mountainous highway [30], and so on.

To sum up, previous studies analyzing passengers' comfort using road geometric indicators mainly choose acceleration to evaluate passengers' comfort, based on both real road data and simulation data. However, it should be noticed that studies listed above rarely focus on scenic road. That is to say, a comprehensive way of promoting passengers' comfort in scenic road is needed. According to related studies [31], the passengers usually feel uncomfortable in curves, owing to the centrifugal force loaded on them. Therefore, lateral acceleration should be considered in evaluating passengers' comfort. However, lateral acceleration does not stand for horizontal overload on passengers [31]. It is not parallel to actual road surface, which means the superelevation is neglected, and lateral acceleration could not fully represent the passengers' overload because human body is vertical to road surface. To solve this critical problem,

the indicator sideway force coefficient (SFC) which stands for real overload in a curve is adopted in this study.

As SFC is the key indicator in this study, its derivation process based on dynamic response is firstly provided, and this content also explains why SFC stands for real overload in a curve. To depict passengers' comfort in scenic road using SFC, field tests on over 1000 participants are carried out in 5 different scenic road curves, to determine the value of SFC when passengers feel uncomfortable. Moreover, numerical simulations of 15 horizontal curves from 5 scenic roads are also provided to verify if the SFC representing passengers' comfort would also satisfy the safety demand. In that, a comprehensive way of promoting passengers' comfort in scenic road is developed in this study.

This study is organized as follows. Section 2 depicts the mechanism of SFC by dynamic response. Section 3 states the field test research of passenger comfort and data simulation derived from actual scenic roads. Section 4 provides the determination of maximum value of tolerable SFC and the verification of real scenic road considering passenger comfort and safety.

## 2. Dynamic Response-Based SFC

When driving on scenic road curve, SFC represents driver and passengers' sideway burden, which is the comfort mentioned in Section 1. In aspect of classical dynamic response, SFC is defined as the sideway load on unit vehicle weight. In vehicle's turning process mechanical analysis, the vehicle could be seen as a particle, which is subjected a centrifugal force  $F$  on centroid, pointing the direction deviating from the center of this circle, see equation (1). The centrifugal force  $F$  will affect the vehicle's operation stability on the curve, which leads to sideway slip and rollover in extreme situation. Therefore, the horizontal superelevation  $i_h$  is designed in road curve to prevent this situation. The dynamic mechanical balance of the vehicle is shown in Figure 1.

$$F = \frac{Gv^2}{gR}. \quad (1)$$

In Figure 1 and (1),  $G$  represents the gravitational force (N),  $v$  represents the velocity (m/s),  $R$  represents the radius of this curve, and  $g$  represents gravity acceleration ( $m/s^2$ ). When operating on actual scenic road curve, the horizontal part of gravitational force will offset the centrifugal force to some degree, and the rest will be balanced with the friction between tire and road surface, as shown in (2). In the figure depicted above,  $\sin \alpha \approx \tan \alpha = i_h$ . Then, (3) could be obtained.

$$\begin{cases} X = F \cos \alpha - G \sin \alpha, \\ Y = F \sin \alpha + G \cos \alpha, \end{cases} \quad (2)$$

$$X = F - Gi_h = G \left( \frac{v^2}{gR} - i_h \right). \quad (3)$$

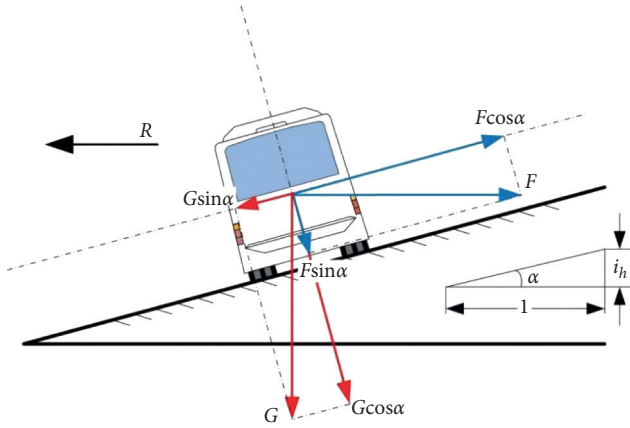


FIGURE 1: The dynamic mechanical balance of the vehicle on the curve.

In (2) and (3), vertical force  $Y$  ( $N$ ) is the stable element in vehicle operation, and sideway force  $X$  ( $N$ ) is the unstable element. However, the value of sideway force could not represent the stability of vehicles with different weight. For example, a sideway force of 5000  $N$  on passenger car might lead to rollover accident, but this might not happen on a heavy vehicle. Thus, SFC represents the sideway load on unit vehicle weight is defined in the following.

$$SFC = \frac{x}{G} = \frac{v^2}{gR} - i_h. \quad (4)$$

The relationship among velocity, radius of the curve, horizontal superelevation, and SFC is obtained in (4) based on the method of dynamic response. According to (4), if velocity was controlled the same, SFC will be inversely proportional to  $R$ , as shown in Figure 2. In actual scenic road design, there exists a  $R_0$  where SFC equals 0. It means that when the radius of a curve could be larger than  $R_0$ , it is unnecessary to set a superelevation  $i_h$ , and  $R_0$  could be seen as the upper boundary of curve design in some degree. Relatively, there exists a lower radius boundary  $R_u$  which is related to velocity and terrain. However, as mentioned in Section 1, SFC could represent the driver and passengers' comfort, and human physiological tolerance is limited, which could be interpreted as  $SFC_c$  in this situation. The element of tourist experience is not taken into consideration in scenic road design, and if the situation  $SFC_c > SFC_u$  depicted in Figure 2 exists, the scenic road will not satisfy the passengers' demand.

Therefore, the SFC considering the passengers' comfort will be studied in the next part. To further check if a current used scenic road curve radius satisfied the passengers' comfort demand, (5) could be used:

$$SFC_c = \frac{v^2}{127R_u} - i_h. \quad (5)$$

### 3. Field Tests and Data Simulation

In Section 2, the relationship between SFC and curve radius has been found based on dynamic response analysis. Besides, according to the description upon SFC and the passengers'

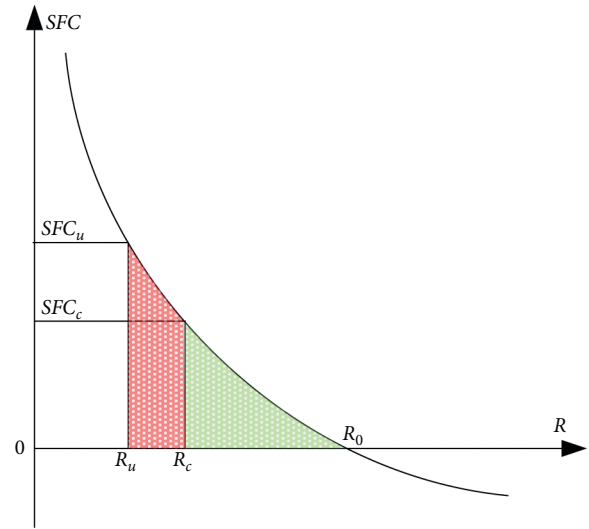


FIGURE 2: The relationship between SFC and  $R$  in scenic road curve design.

comfort in Section 1, it is reasonable to assume that there would be a limited value  $SFC_c$ , which represents the physiological tolerance of the passengers while operating on a scenic road curve. In that, to find the accurate value of  $SFC_c$ , field tests should be carried out, owing to that human feeling is very complex and inaccurate to be theoretically modeled. Once  $SFC_c$  is found, superelevation values and corresponding minimum radius limits  $R_c$  considering passengers' comfort, under different design speeds, could be obtained using (4). Besides, the objective of studying  $SFC_c$  based on passengers' comfort is to develop scenic road design methods. Therefore, a data simulation is adopted to check if the radius  $R_c$  corresponding to  $SFC_c$  would satisfy the safety principle.

**3.1.  $SFC_c$  Field Tests.** According to the statement in related reference [32], human has the full ability to identify the boundary of comfortable feeling and uncomfortable feeling. But there is no evidence which shows the boundary will vary among different individuals. Besides, it is known from (4) that SFC is proportional to the vehicle's operation velocity when driving on a specific scenic road curve. Therefore, driving velocity could be used as a tool to find  $SFC_c$ . In current scenic road design criterion, the speed limit is 60 km/h, and the curve radius limitation is 150 m. Based on the contents mentioned above, the field tests should follow the principles given below:

- (i) The group of participants should cover people with different gender and age. The amount of men and women should be roughly equal, and the amount of the elder should process the minority, considering the actual passengers situation in scenic spot.
- (ii) Different bending speed should be adopted to find  $SFC_c$  in specific curves, and curves with different radius should be also studied.

- (iii) During the field test, the driving velocity and radius adopted should be less than the limitations in current scenic road design criterion.

Before planning detailed field test scheme, five scenic road curves were chosen in Nanhu Park, Xi'an, China, where horizontal alignment of scenic road is complex, containing several ideal test curves, while the vertical alignment is simple, without many slopes, which decreases the difficulty of carrying out this field test. Furthermore, the pavement material in this scenic road is consistent, and there are also no obstacles such as deceleration zone in this road. Positions of road curves are shown in Figure 3; radius and other information of these curves are provided in Table 1.

In each curve, participants were randomly chosen, following the principle mentioned above. In one single test group, the participant was blindfolded, because passengers under this condition have more sensitive perception on centripetal force [21]. The test vehicle (Volkswagen Bora 2008, 110 kW/250 N·m) traveled through the curve with stable velocity varied from 10 km/h–60 km/h, with the step of 5 km/h. A self-designed instrument was used to measure the real-time *SFC*. This instrument contains a MPU6050 three-axis gyroscope to percept the lateral acceleration, an AT89S52 control unit embedded the program calculating *SFC* using method provided in Section 2 and a LCD screen to display the value of *SFC*. There is also a specific button to start the program. Whenever participants felt unable to tolerate sideway load, they would press the button on this instrument for once to record the value of *SFC* in this single test as  $SFC_c$ . Instrument used in this study and record of field experiment is shown in Figure 4.

Field tests were carried out for 1056 groups in 85 days, which means 1056 participants were investigated. Among them, 487 were males, 569 were females, and 447 were 18–40 years old (interpreted as the youth), 575 were 41–65 (the middle-aged), and 34 were above 66 (the elder) [33–35]. It should be noticed that not all the test results were available. Though the participants were blindfolded to strengthen their perception, not all the influencing factors could be excluded. Therefore, the participants were asked to answer two questions after the tests. (1) Did they clearly percept the uncomfortable feeling brought by centripetal force? (2) Did they press the button at the best opportunity? Only answers of these two questions were both “yes”; the participant could be regarded as valid. Detailed information could be seen in Table 2.

**3.2. Data Simulation.** As depicted in the first paragraph in this section, the objective of this paper is to improve the design method of scenic road curve based on the passengers' comfort demand. Therefore, the current used scenic road should be verified in both comfort and safety principle. According to road design criterion, the current used scenic road curve radius varied from 10 m to 110 m, and the speed limit varied from 20 km/h to 60 km/h. In common situation, a specific scenic spot will adopt a consistent speed limit which largely depends on the terrain and will also affect the chosen curve radius. Thus, it is difficult to launch a complete

field experiment in one single scenic spot because it does not contain enough curve samples.

To make up the shortage mentioned above, data simulations were adopted based on CarSim platform, which provides sufficient vehicle models, driver models, road models and parameters related to driving environment, vehicle control, and so on. The first step is to build road simulation model. Five real scenic road sections were chosen to form the background of simulation models. The basic information on these road sections are shown in Table 3.

Based on the investigation of the five background scenic spots, it could be concluded that two typical vehicle types are commonly used, large gasoline consuming passenger vehicle, and small electric power passenger vehicle. The operation velocity of large passenger vehicle varies from 30 km/h–60 km/h, which could be found in section  $C_2$ ,  $C_3$ ,  $C_4$ , and  $C_5$ . The operation velocity of small passenger vehicle varies from 20 km/h to 30 km/h, which could be found in sections  $C_1$  and  $C_2$ . With the detailed information collected, the models of two typical vehicle types were built up, shown in Tables 4 and 5.

To complete the data simulation model, the driver's microscopic control model should be built. According to theory of driver's path preview, the total preview length of 100 m was adopted, and the preview interval was set to 4 m. Parameters of longitudinal maximum acceleration (LMA), longitudinal maximum deceleration (LMD), and horizontal maximum acceleration (HMA) were defined in Figure 5 based on driver's path preview theory.

## 4. Results

In this part, data from field test were analyzed using statistical methods and hypothetical test. The limited value  $SFC_c$ , which represents the physiological tolerance of the passengers while operating on a scenic road section, was found. Besides, in data simulation, 15 scenic road sections were verified based on safety and comfort principle.

**4.1. Determination of  $SFC_c$ .** As depicted in previous work [36], people have full ability to identify the boundary between comfortable feeling and uncomfortable feeling. However, it is still unknown if the boundary ( $SFC_c$ ) would vary among different individuals. In field tests, 1056 subjects were investigated in 5 curves to observe the values of their  $SFC_c$ . In the test group, age and gender could be directly used as two independent variables to study  $SFC_c$ . Therefore, the participants in each curve could be divided into younger group (age 18–40) and elder group (age 41–65), and it could also be divided into male group and female group.

In curve 1 (radius = 130 m, length = 246 m, gradient = 0%), 152 subjects were tested, and only 22 subjects recorded their  $SFC_c$ . The rest subjects did not have any uncomfortable feeling during the test process. However, according to the road design criterion, the speed limit in scenic spots is 60 km/h. Therefore, the results in curve 1 were excluded.

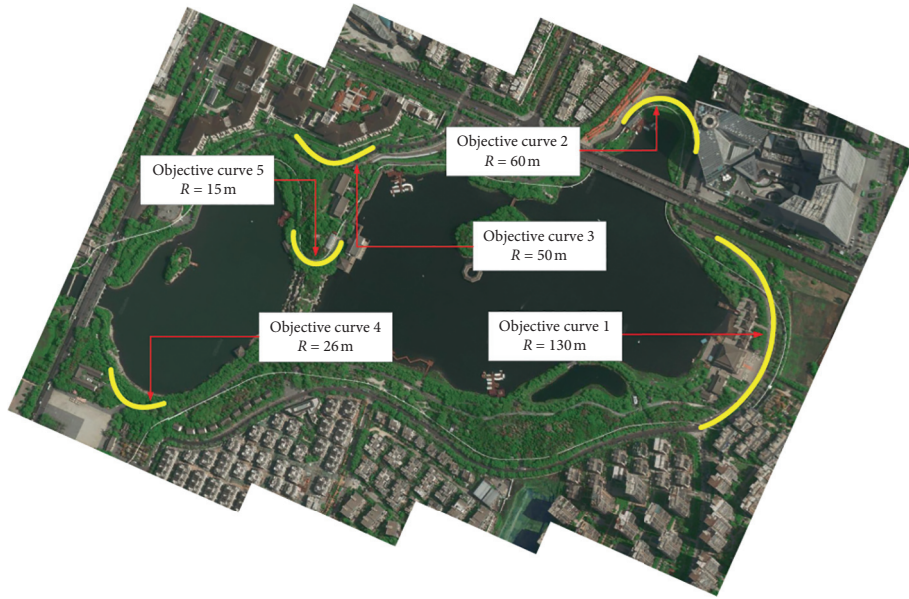


FIGURE 3: Field tests positions in Nanhu Park, Xi'an, China.

TABLE 1: Radius and related information of horizontal curves.

Number	Radius (m)	Length (m)	Gradient (%)
1	130	246	0
2	60	182	1
3	50	134	1.5
4	26	52	0.5
5	15	22	0

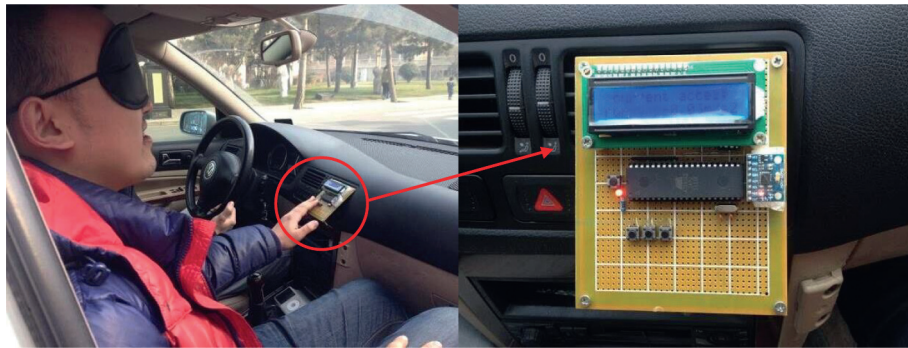


FIGURE 4: Instrument used in this study and record of field experiment.

TABLE 2: Statistical description information.

Group division	Test curve 1		Test curve 2		Test curve 3		Test curve 4		Test curve 5	
	Total	Excluded	Total	Excluded	Total	Excluded	Total	Excluded	Total	Excluded
<i>Gender</i>										
Male	82	7	114	6	109	5	108	6	74	11
Female	70	4	140	4	139	7	141	8	79	4
<i>Age</i>										
18-40	65	5	101	3	96	1	98	2	87	5
41-65	80	3	147	1	144	3	143	4	61	5
Above 66	7	2	6	1	8	1	8	2	5	0

TABLE 3: Basic information of background road sections.

Number	Background scenic spot	Section number	Curve radius (m)	Road section length (m)	Speed limit (km/h)	Superelevation (%)
1			8			10
2	Cuihua mountain area, China	C <sub>1</sub>	17	323.9	20	10
3			20			10
4			20			8
5	Taibai mountain area, China	C <sub>2</sub>	32	570.5	30	8
6			50			4
7			35			10
8	Taibai mountain area, China	C <sub>3</sub>	55	764.4	40	6
9			75			6
10			55			8
11	Nalati prairie, China	C <sub>4</sub>	55	798.4	50	8
12			75			4
13			75			10
14	Nalati prairie, China	C <sub>5</sub>	90	1049.2	60	10
15			110			10

TABLE 4: Model of large gasoline consuming passenger vehicle.



Sprung mass	Dually pickup truck sprung mass	
Aerodynamics	Cab-forward truck, 5 m Ref.	
Animator shape	2A tour bus	
Tires	2000 kg steer, 2000 kg drive (425 mm)	
Steer torque	1/25	
Maximum power	132 kw	
Axle 1	Susp. Kin. Comp. Brakes Steering	
Axle 2	Susp. Kin. Comp. Brakes Steering	Dually pickup rear, dual wheels-kin. 5.5 t Leaf: +150 mm, -60 mm travel 6 kN-m capacity, hydraulic No steering

TABLE 5: Model of small electric power passenger vehicle.

Sprung mass	C-class, hatchback sprung mass	
Aerodynamics	C-class, hatchback aero	
Animator shape	Large European van	
Rear drive torque	3800	
Maximum power	28.5 kw	
Brake system	4-wheel, w/o ABS	
Steering system	4-wheel, power, R&P	
Front	Front kinematics Front compliance Right-front tire Left-front tire	C-class, hatchback-front suspension C-class, hatchback-front comp 205/55 R16 205/55 R16
Rear	Rear kinematics Rear compliance Right-rear tire Left-rear tire	C-class, hatchback, rear suspension C-class, hatchback, rear comp 205/55 R16 205/55 R16

The results of younger group and elder group in curves 2-5 are shown in Figure 6. In figures given below, the horizontal axis represents the serial number of participants, and the vertical axis represents the  $SFC_c$  observed in field

test. The blue polyline shows the results of younger group, and the red polyline shows the results of elder group. Besides, the average value of  $SFC_c$  in each group was also provided.

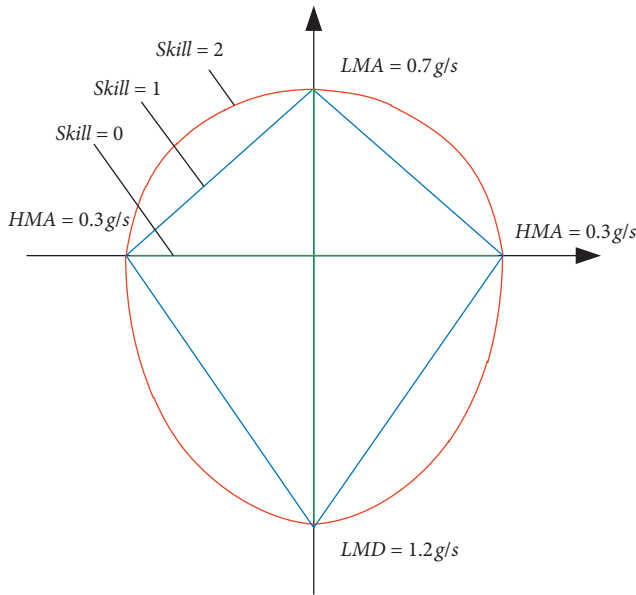


FIGURE 5: The driver's microscopic control model.

In Figure 6, it is not complex to find out that observed  $SFC_c$  in each group of section 2–5 were scattered around a certain value, which is the average value of this group. It means that the boundary between comfortable feeling and uncomfortable feeling of different individual varies in a relatively small range, and the distribution is also random. In Figure 6, the average  $SFC_c$  values of younger groups in curve 2–5 are 0.2903, 0.2910, 0.2905, and 0.2866, and the average  $SFC_c$  values of elder groups in curve 2–5 are 0.2910, 0.2910, 0.2886, and 0.2954. Depending on the values given above, it is reasonable to account that  $SFC_c$  of the younger and the elder are the same. To further prove this point, the method of hypothetical test is used. In field test, each subject is relatively independent, and the sample obeys normal distribution. Using Levene's test to check if the sample variance is homogeneous, the significance equals to 0.208 which larger than 0.05, which shows that the sample variance is homogeneous. Further, using  $T$ -test to check if there was significant difference between  $SFC_c$  of the younger and the elder, the significance equals 0.628 which is larger than 0.05, which proved the point given above.

The results of male group and female group in curve 2–5 are shown in Figure 7. The information expressed by Figure 7 is the same of Figure 6.

Figure 7 shows mainly the same characters of Figure 6. Overall speaking,  $SFC_c$  in each group of curve 2–5 was scattered around the average value of this group. It also proved that the boundary between comfortable feeling and uncomfortable feeling of different individual remains the same. In Figure 7, the average  $SFC_c$  values of male groups in curve 2–5 are 0.2907, 0.2941, 0.2910, and 0.2919, and the average  $SFC_c$  values of female groups in curve 2–5 are 0.2945, 0.2917, 0.2868, and 0.2919. Also, the method of hypothetical test is used. In field test, each subject is relatively independent, and the sample obeys normal distribution. Using Levene's test to check if the sample variance is homogeneous, the significance equals 0.792 which is larger

than 0.05, which shows that the sample variance is homogeneous. Further, using  $T$ -test to check if there was significant difference between  $SFC_c$  of the male and the female, the significance equals 0.210 which is larger than 0.05, proving the point given above.

Based on the analysis given above, it could be concluded that the boundary between comfortable feeling and uncomfortable feeling of different individual remains the same, which could be represented by a certain value  $SFC_c$ , equals 0.291. Restricted by terrain condition, ecological and environment protection and larger superelevation values were considered and the corresponding minimum radii limits under different design speeds were given using (4) as shown in Table 6.

#### 4.2. Comfort and Driving Safety Verification of Scenic Road Curve Design.

The objective of this paper is to promote the design method of scenic road curve based on the passengers' comfort demand. To meet this objective, 5 simulation models were built based on real background scenic road sections, including 15 road curves, depicted in Table 3. In Section 4.1, the value of  $SFC_c$  was determined, which equals 0.291. This provides a basis to check if current scenic road curves satisfied the passengers' comfort demand. Besides, it is also important to examine if the curve radius satisfied the requirement of safe driving. Based on the Vehicle Maneuverability Objective Evaluation System (VMOES) developed by Guo [32], it is known that the parameter Lateral Distance to Path (LDP) should be less than 0.3 m, while the vehicle is operating on a certain curve.

The simulation model of Section 1 consists of three small reverse curves, whose radiuses are 8 m, 17 m, and 20 m, and detailed information could be found in Table 3. The simulation results of Section 1 are provided in Figure 8.

In Figure 8(a), supervised LDP in each small curve falls in  $[-0.3 \text{ m}, 0.3 \text{ m}]$ , which means the requirement of safe driving is satisfied. In Figure 8(b), supervised SFC in small curve 2 and 3 falls in  $[-0.291, 0.291]$ ; however, SFC in small curve 1 whose radius equals 8 m is  $-0.310$ , which exceeds the bottom boundary. This means small curve 1 did not satisfy the passengers' comfort demand.

The simulation model of Section 2 also consists of three small reverse curves, whose radiuses are 20 m, 32 m, and 50 m. In Section 2, large gasoline consuming passenger vehicle and small electric power passenger vehicle could both be found. The simulation results of Section 2 are provided in Figure 9 shown below.

In Figure 9(a), supervised LDP in each small curve of both vehicle types falls in  $[-0.3 \text{ m}, 0.3 \text{ m}]$ , which means the requirement of safe driving is satisfied. In Figure 9(b), supervised SFC of both vehicle types in small curve 2 and 3 falls in  $[-0.291, 0.291]$ ; however, SFC of both vehicle types in small curve 1 whose radius equal to 20 m is  $-0.312$  and  $-0.314$ , which exceed the bottom boundary. This means small curve 1 did not satisfy the passengers' comfort demand.

The simulation model of Section 3 consists of three small reverse curves, whose radiuses are 35 m, 55 m, and 75 m. In Section 3, only large gasoline consuming passenger vehicle

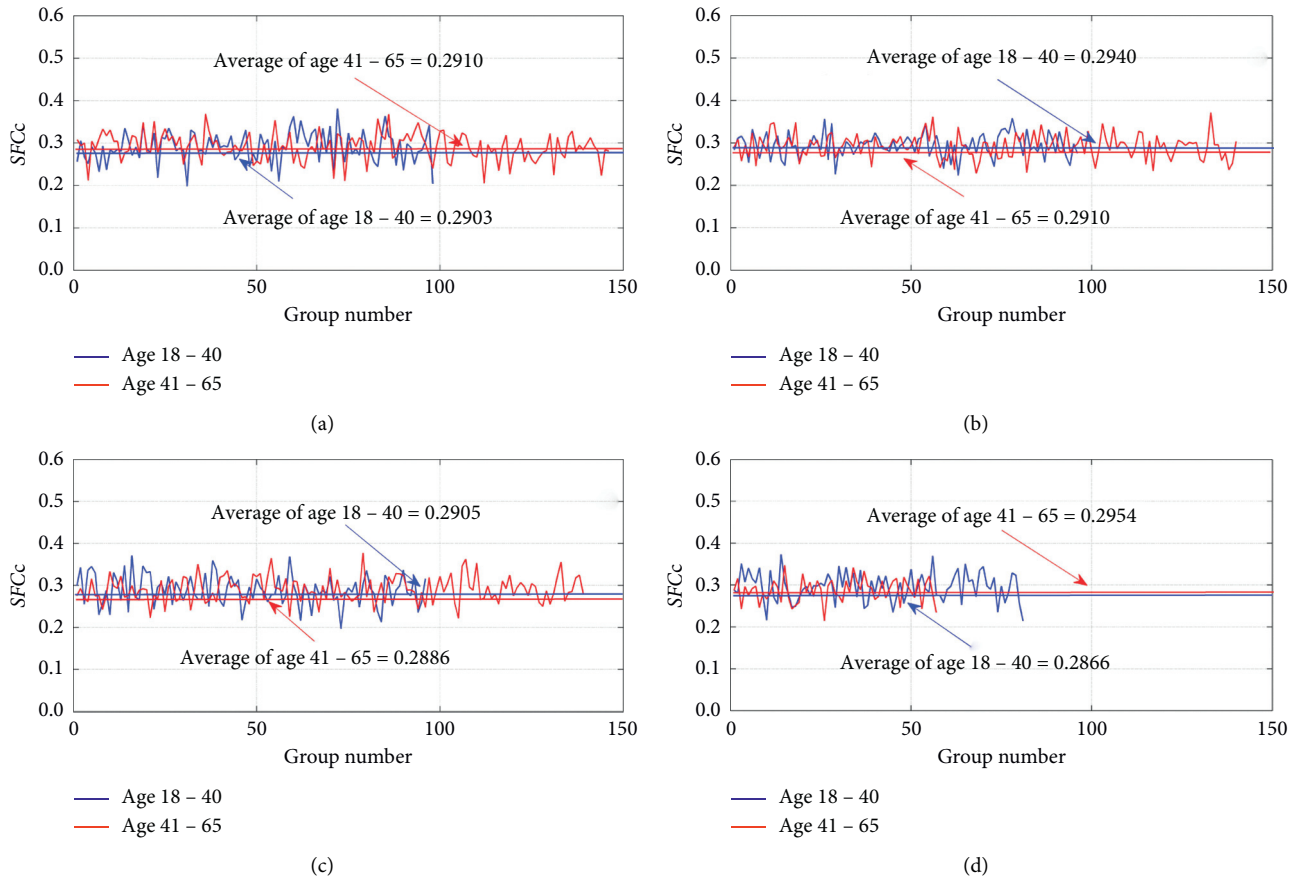


FIGURE 6: The  $SFC_c$  of different age group. (a) Section 2. (b) Section 3. (c) Section 4. (d) Section 5.

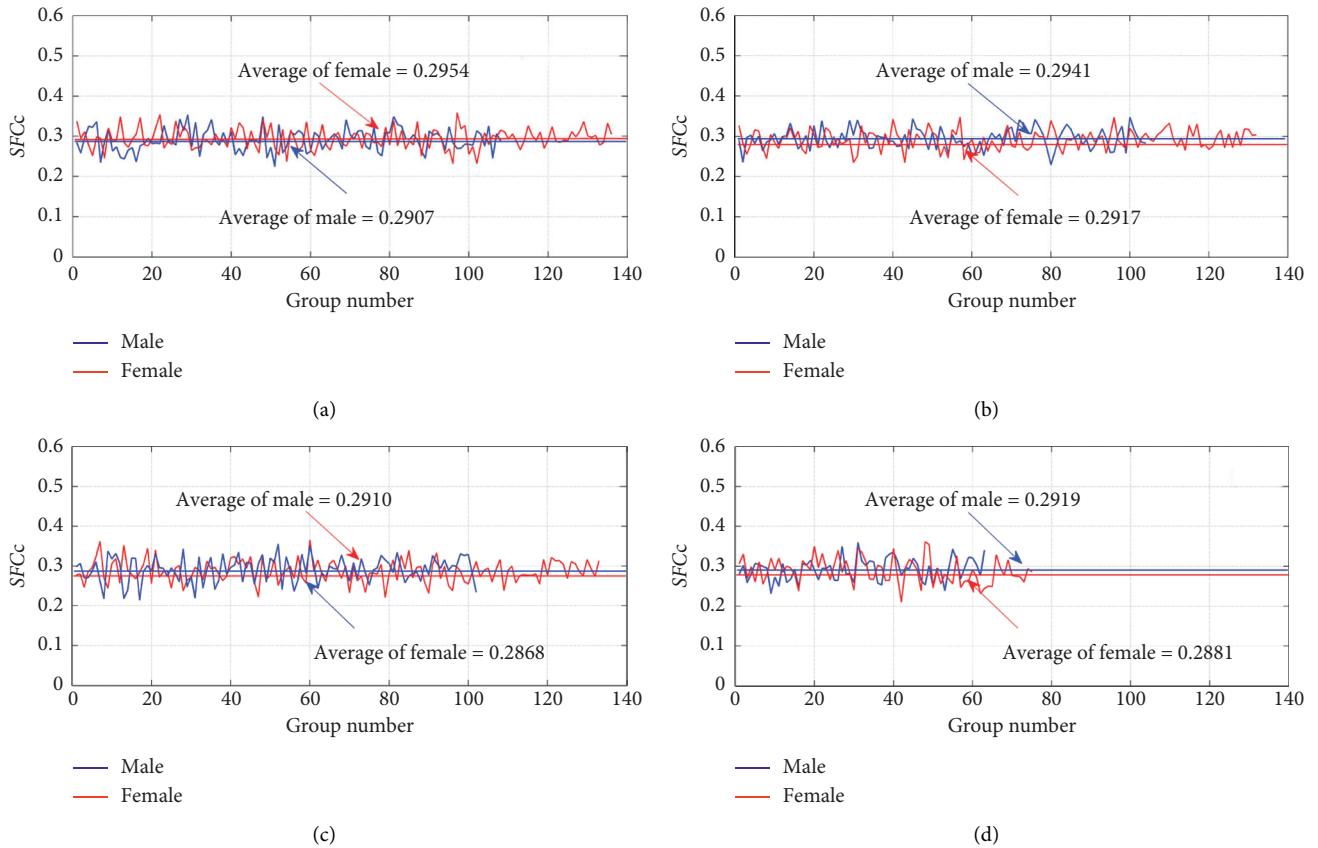


FIGURE 7: The  $SFC_c$  of different gender group. (a) Section 2. (b) Section 3. (c) Section 4. (d) Section 5.



TABLE 6: Minimum radii limit for design superelevation and design speeds.

Design speed (km/h)		60	50	40	30	20
Minimum radii limit (m)	$i_h = 10\%$	75	55	35	20	10
	$i_h = 8\%$	80	55	35	20	10
	$i_h = 6\%$	85	60	40	20	10

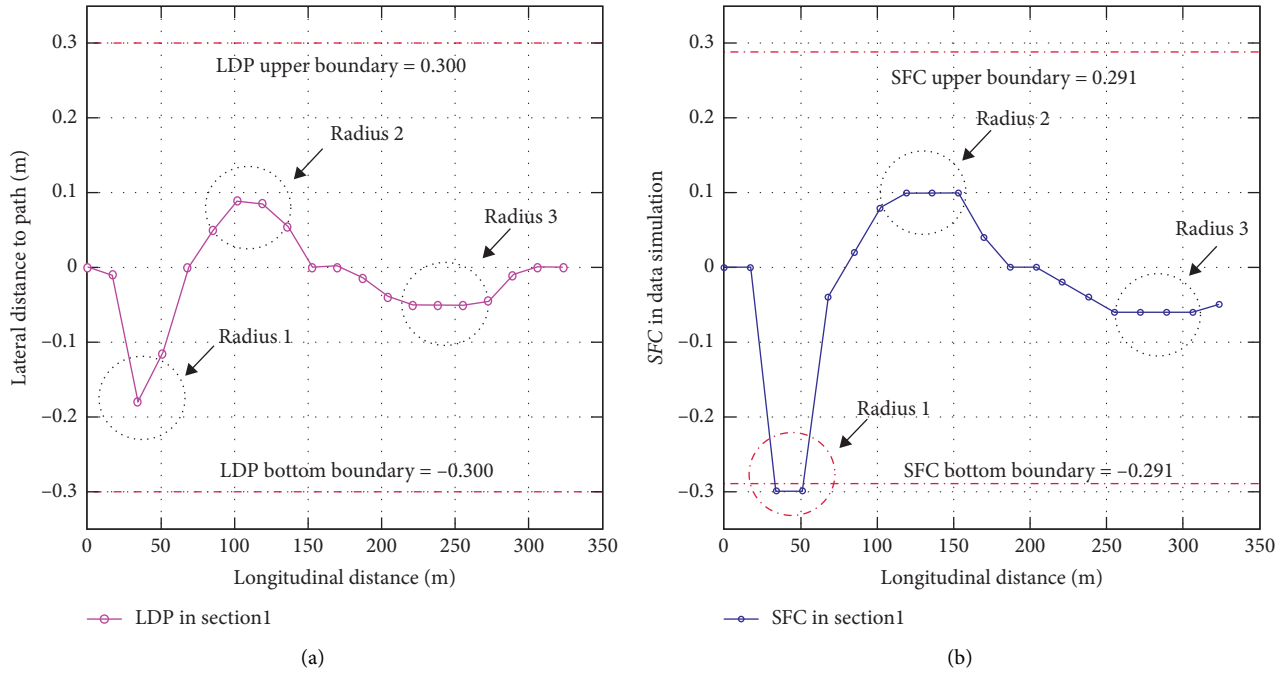


FIGURE 8: The simulation results of Section 1. (a) Lateral Distance Path Change Trend. (b) SFC Change Trend.

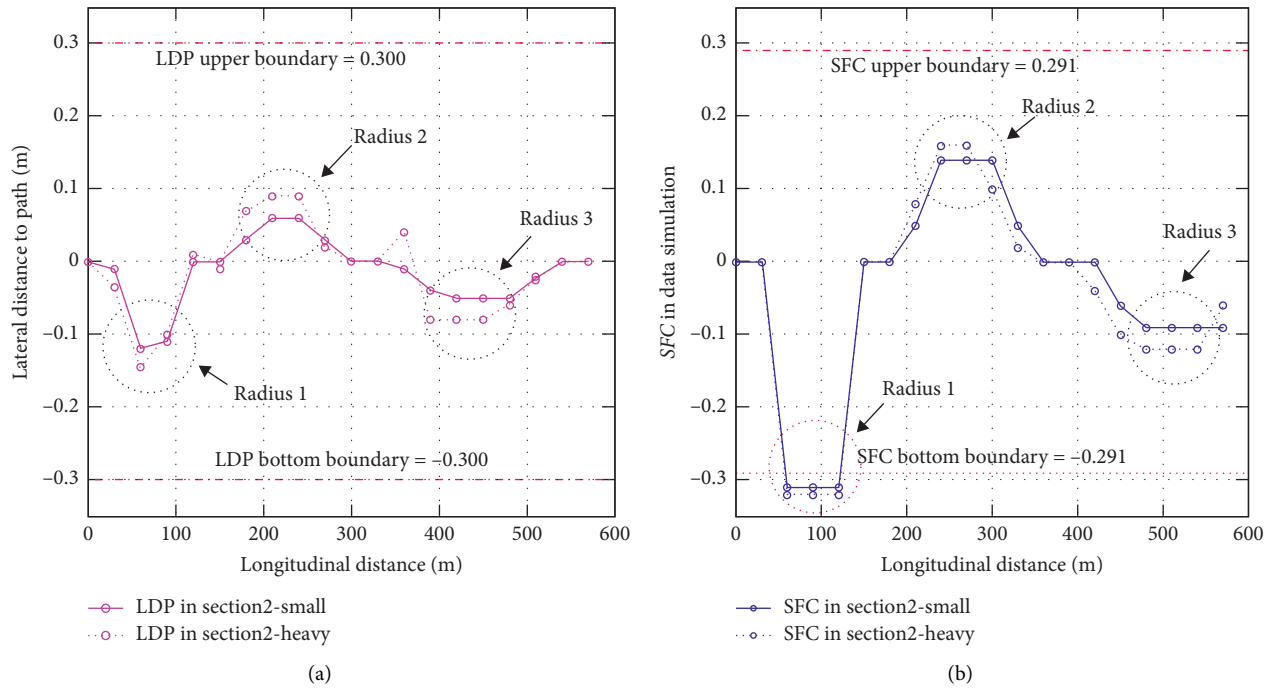


FIGURE 9: The simulation results of Section 2. (a) Lateral Distance Path Change Trend. (b) SFC Change Trend.

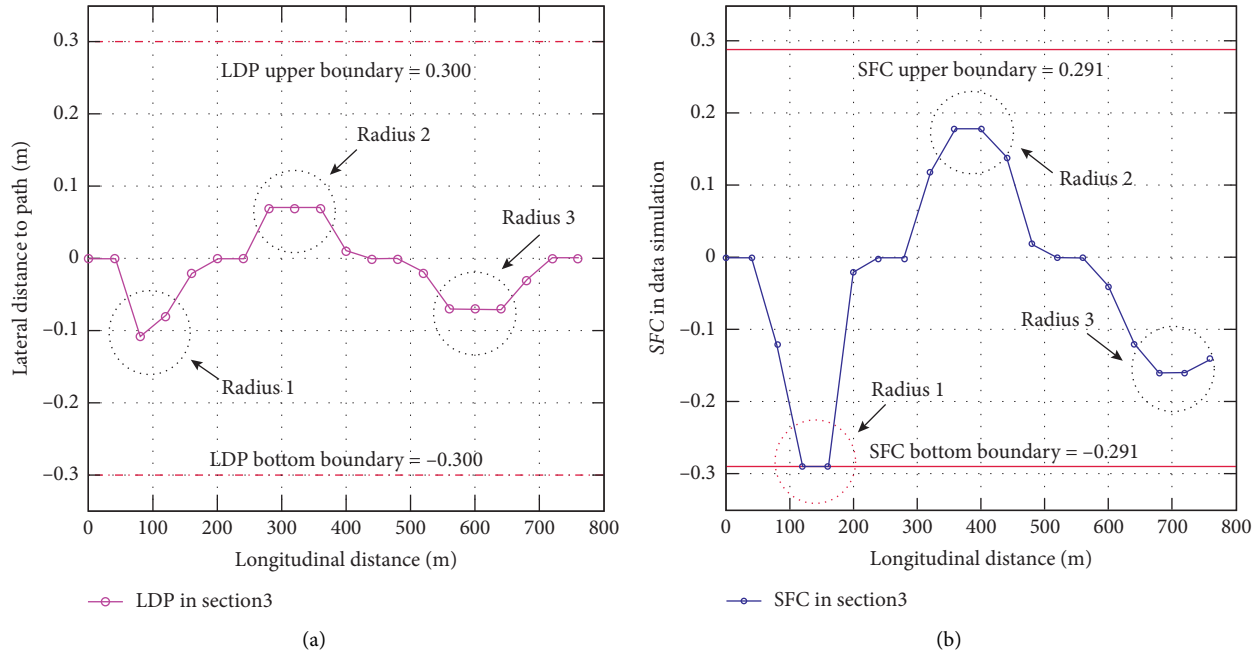


FIGURE 10: The simulation results of section 3. (a) Lateral Distance Path Change Trend. (b) SFC Change Trend.

could be found. The simulation results of Section 3 are provided in Figure 10.

In Figure 10(a), supervised LDP in each small curve falls in  $[-0.3 \text{ m}, 0.3 \text{ m}]$ , which means the requirement of safe driving is satisfied. In Figure 10(b), supervised SFC in small curve 2 and 3 falls in  $[-0.291, 0.291]$ ; however, SFC in small curve 1 whose radius equals 35 m is  $-0.291$ , which equals the bottom boundary. This means small curve 1 did not satisfy the passengers' comfort demand.

The simulation model of Section 4 consists of three small reverse curves, whose radiuses are 55 m, 55 m, and 75 m. In Section 4, only large gasoline consuming passenger vehicle could be found. The simulation results of section 4 are provided in Figure 11 shown below.

In Figure 11(a), supervised LDP in each small curve falls in  $[-0.3 \text{ m}, 0.3 \text{ m}]$ , which means the requirement of safe driving is satisfied. In Figure 11(b), supervised SFC in small curve 3 falls in  $[-0.291, 0.291]$ ; however, SFC in small curve 1 and 2 whose radius equal to 55 m and 75 m is  $-0.305$  and  $0.300$ , which exceed the bottom boundary and upper boundary, respectively. This means small curve 1 and 2 did not satisfy the passengers' comfort demand.

The simulation model of Section 5 consists of three small reverse curves, whose radiuses are 75 m, 90 m, and 110 m. The simulation results of Section 5 are provided in Figure 12.

In Figure 12(a), supervised LDP in each small curve falls in  $[-0.3 \text{ m}, 0.3 \text{ m}]$ , which means the requirement of safe driving is satisfied. In Figure 12(b), supervised SFC in small curve 2 and 3 falls in  $[-0.291, 0.291]$ ; however, SFC in small curve 1 whose radius equals 75 m is  $-0.300$ , which exceeds the bottom boundary. This means small curve 1 did not satisfy the passengers' comfort demand.

To further study the contents given above, some detailed information could be discovered. Considering the

supervised LFD as a whole, it is easy to find that LFD is a loose criterion. In curves with small radius, the volatilities of LFDs are obvious; however, they basically fall in  $[-0.15 \text{ m}, 0.15 \text{ m}]$ , far less than the limitation. Besides, comparing the supervised SFC in each curve, when the operation velocity is stationary, the situation of dissatisfying the passengers' comfort demand only exists in curve with relatively small radius. Therefore, in the process of scenic road curve design, when the operation velocity is settled, minimum radius should be determined considering  $SFC_c$ .

## 5. Discussion

As depicted in Section 1, factors of age, gender, temperature, noise, pressure, seat, and workspace have influence on passengers' comfort [6]. In this paper, interior environment was controlled by using the same test vehicle. Thus, factors of age and gender became the major consideration. From the results in Section 4.1,  $SFC_c$  of younger group varies in  $[0.2866, 0.2910]$ , and  $SFC_c$  of elder group varies in  $[0.2886, 0.2954]$ .  $SFC_c$  of male group varies in  $[0.2907, 0.2941]$ , and  $SFC_c$  of female group varies in  $[0.2868, 0.2945]$ . Overall, younger group distribution interval is about 1.1% less than elder group, and male group distribution interval is about 0.7% larger than female group. Directly from the data, there is little difference in age groups and gender groups, also proved in Section 4.1 using  $T$ -test. This indicates that factors of age and gender basically have no influence on passengers' comfort, which is different from traditional result [6]. Considering the large-scale real road samples obtained in this study, the result is credible.

Further, Section 1 states that SFC is different from lateral acceleration. From mechanism of SFC in Figure 1, the gap between SFC and lateral acceleration will not be

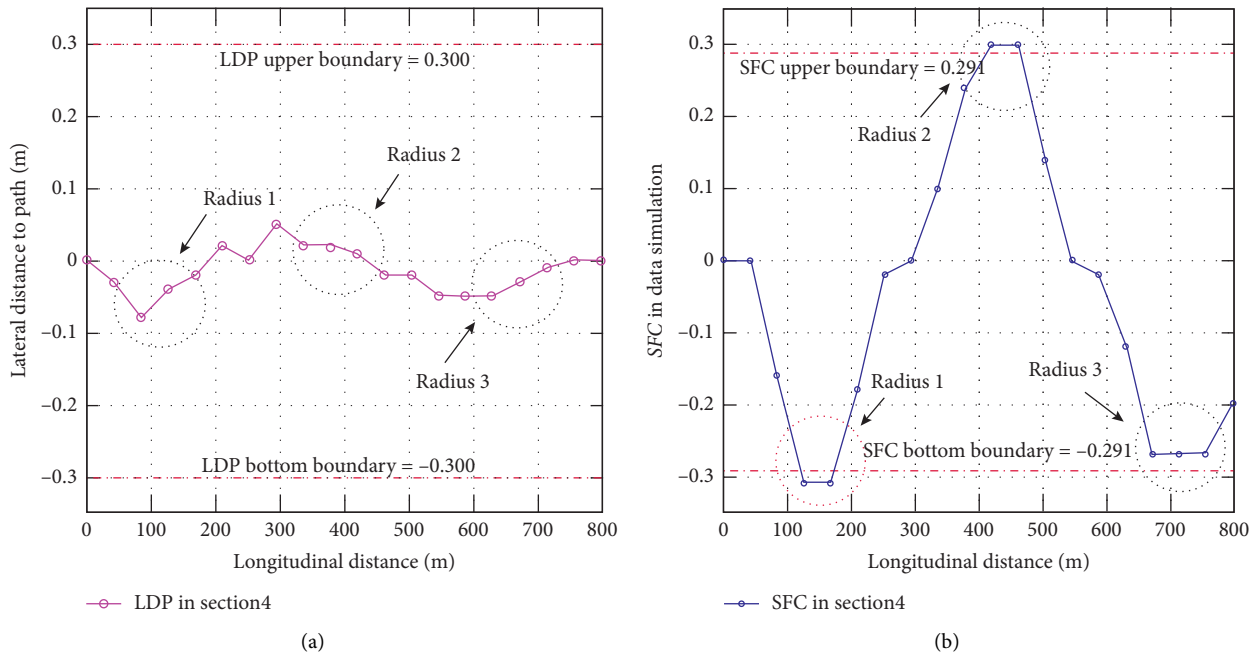


FIGURE 11: The simulation results of Section 4. (a) Lateral Distance Path Change Trend. (b) SFC Change Trend.

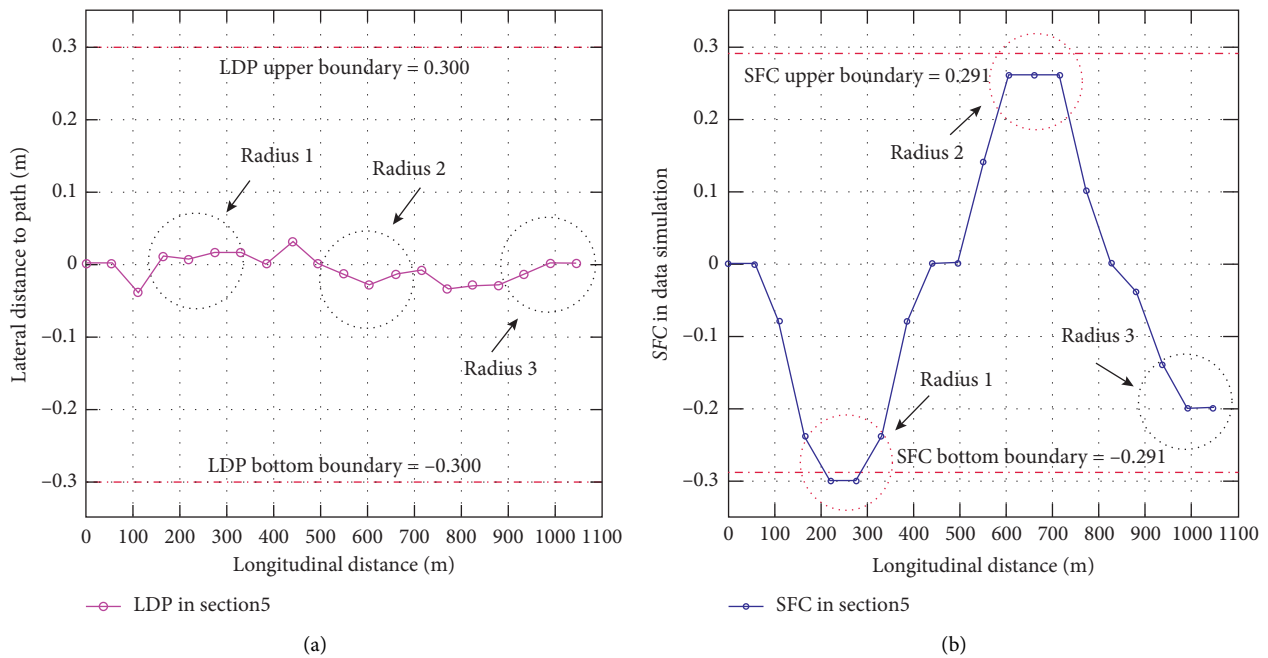


FIGURE 12: The simulation results of Section 5. (a) Lateral Distance Path Change Trend. (b) SFC Change Trend.

too large, owing to small value of superelevation angle. In current ISO standard [36], passengers' comfort was defined as index shown in Table 7. Moreover, the passengers' comfort was also specifically defined in China [27], also provided in Table 7. It could be directly concluded that Chinese passengers have significant stronger endurance. In related references, passengers' comfort was divided into several levels varying from not uncomfortable to extremely uncomfortable.  $SFC_c$  obtained in this

paper lies in the third level of China range, interpreted as fairly uncomfortable or a little uncomfortable. In ISO range,  $SFC_c$  is more than extremely uncomfortable, which is inappropriate in China. The boundary of comfortable and uncomfortable in China range is 0.184, which is less than  $SFC_c$ . This is because the samples used in this study were adopted in scenic roads. Considering the special environment and stronger data set,  $SFC_c$  has more practicality in scenic road design.

TABLE 7: Passengers' comfort index.

ISO range	China range	Event description
Greater than 0.229	Greater than 0.510	Extremely uncomfortable
0.145–0.229		Very uncomfortable
0.092–0.145	0.367–0.510	Uncomfortable
0.057–0.092	0.184–0.367	Fairly uncomfortable
0.032–0.057		A little uncomfortable
Less than 0.032	Less than 0.184	Not uncomfortable

In Section 4.2, 15 curves from 5 scenic roads were verified using passengers' comfort and safety criterion. As depicted in Section 4.2, safety condition could be easily satisfied, but passengers' comfort could not be satisfied in curves with small radius. The scenic roads in this study were chosen from nature reserves with superior scenic road systems, which mean limit radius is rarely found. In scenic roads with worse terrain conditions, the situation mentioned above will be more rigorous. It is known that passengers' comfort is related to operation velocity, curve radius, and superelevation. Therefore, to meet passengers' demand, scenic road design should take these three indicators as a whole based on  $SFC_c$ .

## 6. Conclusions

In this study, a new indicator SFC means passengers' comfort was introduced, which is different from lateral acceleration used in current criterions and related studies. Lateral acceleration could not fully represent the passengers' overload because human body is vertical to road surface. Thus, considering the superelevation, SFC could stand for real overload in a curve. Based on dynamic balance condition of the vehicle on horizontal curve, the derivation process of SFC was provided. Field tests on over 1000 participants were carried out in 5 different scenic road curves to investigate  $SFC_c$  representing passengers' comfort tolerance limitation. To verify  $SFC_c$  from the perspectives of both passengers' comfort and driving safety, numerical simulations of 15 horizontal curves from 5 scenic roads were also conducted. The value of  $SFC_c$  was determined as 0.291 based on the statistical analysis on data obtained in field tests. The results also showed that age and gender have no effect on  $SFC_c$ . Moreover, the corresponding minimum radius limits under 20–60 km/h and superelevation 6%, 8%, and 10% were proposed. The results of numerical simulations denoted two points. First, in current in-service scenic roads, there are curves that could not satisfy the passengers' comfort demand, which showed that finding an appropriate way promoting passengers' comfort in scenic road is promising. Second, when passengers' comfort demand  $SFC_c$  is satisfied, the safe driving requirements could also be satisfied. Therefore,  $SFC_c$  and minimum radius limits proposed in this study were proved to be credible and appropriate for the curve design of horizontal alignment in scenic roads.

This study also has a shortage. Field tests were carried out in Xi'an, whose terrain is relatively flat. That means citizens in this city might have higher comfort demand in daily commute and recreation travel, compared to citizens living in mountainous and hilly areas. Therefore, values of  $SFC_c$  determined in different areas may vary. The following researches will focus on this issue, providing more practical values of  $SFC_c$  in different areas by enlarging the investigation scope.

## Data Availability

The data used to support the findings of this study are available from the corresponding author upon request.

## Conflicts of Interest

The authors declare that there are no conflicts of interest regarding the publication of this paper.

## Acknowledgments

This research was funded by National Key R&D Program of China (Grants nos. 2018YFB1600302 and 2018YFB1600300) and supported by Science Foundation project of Chongqing Jiaotong University (Grant no. 20JDKJC-B001).

## References

- [1] National Park Service, *Park Road Standards*, National Park Service, Washington, DC, USA, 1968.
- [2] American Association of State Highway and Transportation Officials, *A Policy on Geometric Design of Highway and Streets*, AASHTO, Washington, DC, USA, 1984.
- [3] Transportation Research Board, *Highway Capacity Manual*, TRB, Washington, DC, USA, 5th edition, 2010.
- [4] International Organization for Standardization, *Mechanical Vibration and Shock-Human Exposure-Vocabulary*, ISO, Geneva, Switzerland, 1997.
- [5] K. Strandemar, *On Objective Measures for Ride Comfort Evaluation*, Royal Institute of Technology (KTH), Stockholm, Sweden, 2005.
- [6] J. Forstberg, *Ride Comfort and Motion Sickness in Tilting Trains*, Royal Institute of Technology (KTH), Stockholm, Sweden, 2000.
- [7] M. O. Rodrigues, *An Evaluation of the Level of Service in the Public Transportation System of the City of Sao Carlos*, Masters dissertation. University of Sao Paulo, Sao Carlos, Brazil, 2006.
- [8] C. Y. Lin, L. J. Chen, Y. Y. Chen, and W. C. Lee, "A comfort measuring system for public transportation systems using participatory phone sensing," in *Proceedings of Phone Sense 2010*, Zurich, Switzerland, 2010.
- [9] R. Alkhatib, G. Nakhaie Jazarb, and M. F. Golnaraghi, "Optimal design of passive linear suspension using genetic algorithm," *Journal of Sound and Vibration*, vol. 275, no. 3–5, pp. 665–691, 2004.
- [10] D. V. Koulocheris, V. K. Dertimanis, and K. N. Spentzas, "Analysis and optimization of a fixed-tank vehicle," *Forschung im Ingenieurwesen*, vol. 70, no. 3, pp. 171–178, 2006.
- [11] D. V. Koulocheris, V. K. Dertimanis, V. Spitas, and C. Spitas, "Heavy vehicle roll plane modeling and optimization of transmissibility ratios," in *Proceedings of the 5th IC-SCCE*, Athens, Greece, 2012.

- [12] D. V. Koulocheris, H. Vrazopoulos, and V. K. Dertimanis, "Optimization methodology for tuning fuzzy logic controllers," in *Proceedings of the 15th IFAC Triennial World Congress*, IFAC, Barcelona, Spain, 2002.
- [13] W. Belgacem, A. Berry, and P. Masson, "Active vibration control on a quarter-car for cancellation of road noise disturbance," *Journal of Sound and Vibration*, vol. 331, no. 14, pp. 3240–3254, 2012.
- [14] J. Meng, Q. Chen, and R. He, "Research on optimal control for the vehicle suspension based on the simulated annealing algorithm," *Journal of Applied Mathematics*, vol. 2014, pp. 1–5, Article ID 420719, 2014.
- [15] M. Brogioli, M. Gobbi, G. Mastinu, and M. Pennati, "Parameter sensitivity analysis of a passenger/seat model for ride comfort assessment," *Experimental Mechanics*, vol. 51, no. 8, pp. 1237–1249, 2011.
- [16] F. A. Joseph, J. C. Issac, and T. J. Paulson, "Low frequency vibration analysis on passenger car seats," *International Journal of Scientific & Engineering*, vol. 4, no. 8, pp. 1–5, 2013.
- [17] M. Demicid, J. Lukicd, and Z. Milicd, "Some aspects of the investigation of random vibration influence on ride comfort," *Journal of Sound and Vibration*, vol. 253, no. 1, pp. 109–128, 2002.
- [18] S. Lerspalungsanti, A. Albers, S. Ott, and T. Düser, "Human ride comfort prediction of drive train using modeling method based on artificial neural networks," *International Journal of Automotive Technology*, vol. 16, no. 1, pp. 153–166, 2015.
- [19] N. J. Mansfield and M. J. Griffin, "Deference thresholds for automobile seat vibration," *Applied Ergonomics*, vol. 31, no. 1, pp. 255–261, 2000.
- [20] M. Kilic and S. M. Akyol, "Experimental investigation of thermal comfort and air quality in an automobile cabin during the cooling period," *Heat and Mass Transfer*, vol. 48, no. 8, pp. 1375–1384, 2012.
- [21] M. J. M. Nor, M. Hosseini Fouladi, H. Nahvi, and A. Kamal Ariffin, "Index for vehicle acoustical comfort inside a passenger car," *Applied Acoustics*, vol. 69, no. 4, pp. 343–353, 2008.
- [22] S. Cafiso and G. La Cava, "Driving performance, alignment consistency, and road safety," *Transportation Research Record: Journal of the Transportation Research Board*, vol. 2102, no. 1, pp. 1–8, 2009.
- [23] J.-H. Lee, J.-J. Park, S. H. Park, and C. Baek, "Development of evaluation criteria for curve-section safety level with visual distortions on two-lane rural highways," *KSCE Journal of Civil Engineering*, vol. 20, no. 2, pp. 873–880, 2016.
- [24] X. Wang, T. Wang, A. Tarko, and P. J. Tremont, "The influence of combined alignments on lateral acceleration on mountainous freeways: A driving simulator study," *Accident Analysis & Prevention*, vol. 76, no. 3, pp. 110–117, 2015.
- [25] M. Nicke and W. Hugemann, "Longitudinal and lateral accelerations in normal day driving," in *Proceedings of the ITAI Conference, the Institute of Traffic Accident Investigators*, Croydon, England, 2003.
- [26] A. Altamira, Y. Garcia, T. Echaveguren, and J. Marcet, "Acceleration and deceleration patterns on horizontal curves and their tangents on two-lane rural roads," in *Proceedings of the TRB 93rd Annual Meeting*, Washington DC, USA, 2014.
- [27] J. Xu, K. Yang, Y. M. Shao, and G. Y. Lu, "An experimental study on lateral acceleration of cars in different environments in Sichuan, southwest China," *Discrete Dynamics in Nature and Society*, vol. 2015, Article ID 494130, 16 pages, 2015.
- [28] R. A. Tokunaga, M. Asano, K. Munehiro, and T. Hagiwara, "Effects of curve designs and road conditions on driver's curve sharpness judgment and driving behavior," *Journal of the Eastern Asia Society for Transportation Studies*, vol. 6, pp. 3536–3550, 2005.
- [29] J. C. Castellanos and F. Fruett, "Embedded system to evaluate the passenger comfort in public transportation based on dynamical vehicle behavior with user's feedback," *Measurement*, vol. 47, no. 1, pp. 442–451, 2014.
- [30] F. Yakar and F. Celik, "A highway alignment determination model incorporating GIS and multi-criteria decision making," *KSCE Journal of Civil Engineering*, vol. 18, no. 6, pp. 1847–1857, 2014.
- [31] P. Jia, L. J. Chu, and T. F. Fwa, "Determination of safe vehicle speeds on wet horizontal pavement curves," *Road Materials and Pavement Design*, vol. 21, no. 7, 2020.
- [32] C. Zong and K. Guo, "Objective evaluation index for handling and stability of vehicle," *Natural Science Journal of Jilin University of Technology*, vol. 30, no. 1, pp. 1–6, 2000.
- [33] Y. Guo, J. Wang, S. Peeta, and P. Anastasopoulos, "Personal and societal impacts of motorcycle ban policy on motorcyclists' home-to-work morning commute in China," *Travel Behaviour and Society*, vol. 19, pp. 137–150, 2020.
- [34] Y. T. Guo and S. Peeta, "Impacts of personalized accessibility information on residential location choice and travel behavior," *Travel Behaviour and Society*, vol. 19, pp. 99–111, 2019.
- [35] Y. Guo, J. Wang, S. Peeta, and P. Anastasopoulos, "Impacts of internal migration, household registration system, and family planning policy on travel mode choice in China," *Travel Behaviour and Society*, vol. 13, pp. 128–143, 2018.
- [36] International Organization for Standardization, *Mechanical Vibration and Shock-Evaluation of Human Exposure to Whole-Body Vibration-Part 1: General Requirements*, ISO, Geneva, Switzerland, 1997.

## Research Article

# Research on Design Indicators for Graded Crushed Stone Mixture Based on Vibration Molding Method

Li-biao Chen,<sup>1</sup> Er-hu Yan ,<sup>2</sup> Jian Xu,<sup>2</sup> Tao Ma,<sup>3</sup> Jun-cheng Zeng,<sup>1</sup> and Yan Gong<sup>2</sup>

<sup>1</sup>Fujian Expressway Construction Directorate, Fuzhou, Fujian 350001, China

<sup>2</sup>Research Institute of Expressway, Ministry of Transport, Beijing 100088, China

<sup>3</sup>Transportation College, Southeast University, Nanjing 210096, Jiangsu, China

Correspondence should be addressed to Er-hu Yan; eh.yan@rioh.cn

Received 22 July 2020; Revised 1 September 2020; Accepted 22 September 2020; Published 10 October 2020

Academic Editor: Meng Guo

Copyright © 2020 Li-biao Chen et al. This is an open access article distributed under the Creative Commons Attribution License, which permits unrestricted use, distribution, and reproduction in any medium, provided the original work is properly cited.

The asphalt pavement easily shows the diseases like cracking, rutting, and structural water damage during the early service life in Fujian province for the complex effects of very high temperature, easily rainy climatic condition, and high-frequency heavy loading. However, the corresponding studies and strategies are still rare. Herein, in order to study the relationship of compaction methods on the stress-strain characteristics and shear strength of graded crushed stone mixtures, 11 kinds of typical graded crushed stone mixtures, which were taken from the five different expressways under construction in Fujian Province, were molded by both the modified vibration compaction and modified Proctor compaction. The results indicate that the modified vibration molding method matches much better with the compaction of practical projects and can be used to evaluate the performance of graded crushed stone mixtures. Further, the performance indexes got by the modified vibration compaction and the modified Proctor compaction have strong correlations. Therefore, based on the modified vibration compaction, the guidelines for standardized mix design of graded crushed stone mixture in Fujian province are proposed: the resilient modulus of 300 MPa and the deformation rate of  $10^{-8}$  in the dynamic triaxial test are used as the performance indicators of the bearing capacity and the antideformation ability; the shear strength of 400 kPa in the static triaxial test is used as the performance indicators of the shear failure resistance. Besides, most limestone mixtures perform well and have the advantages of good resistance to permanent deformation and shear resistance.

## 1. Introduction

The different climatic environments and load conditions have a great influence on the early damage and durability of asphalt pavement [1, 2]. Choosing the appropriate pavement structure depending on the traffic, climate, and load conditions in different regions is the focus of research in the field of road engineering. Since the climate of Fujian province is characterized as mountainous, rainy, and long duration of high temperature, the early damage phenomena, including cracking, rutting, and structural water damage, widely appeared on the asphalt pavement with traditional semirigid base. According to the current situation, different pavement structures have been tried in Fujian Province, including the improved semirigid base, the thickened asphalt surface layer,

the pavement structure with the inverted thin asphalt layer, and the fully flexible asphalt pavement. However, the poor durability of asphalt pavement under high temperature and rainy environment still cannot be effectively solved. Therefore, in order to adapt to the climatic environment and load conditions of Fujian province and to enhance the service life, the asphalt pavement with composite bases is proposed and applied, which overlay a graded crushed stone layer with a thickness of 15–18 cm between the asphalt surface layer and the semirigid base layer [3]. It shows that the water permeability coefficient of the graded crushed stone layer is  $5 \times 10^{-3} - 1 \times 10^{-4}$  m/s, so the asphalt pavement with the graded crushed stone layer has good drainage performance. In addition, the graded crushed stone layer plays a significant role in restraining the reflection cracking

of asphalt surface course caused by shrinkage cracks in semirigid base [4]. Thus, the durability of the combined base asphalt pavement would be effectively improved due to the strong drainage ability and the decrease of reflection cracks in semirigid materials. According to relevant literature, for the raw materials and energy consumption during construction, it is about 840 MJ/t, 460 MJ/t, and 180 MJ/t for the asphalt concrete, the semirigid materials, and the graded crushed stone, respectively. So, the appropriate usage of the graded crushed stone base could effectively reduce energy consumption and emission.

For the asphalt pavement with composite bases, the mechanical characters of the graded crushed stone mixtures are critical to pavement performance. The pavement rutting and further structural failure may be caused by the low strength, low rigidity, and large plastic deformation in the traditional graded crushed stone layer [5–7], so the application of the composite bases asphalt pavement in the high-grade expressways is limited. How to accurately predict and improve the antipermanent deformation and antirutting abilities of graded crushed stone has attracted the road researchers' interest [8–12]. In earlier studies, the shear characteristics of graded crushed stone must be better characterized, because rutting in this type of pavement is primarily caused by the permanent deformations of base materials [13, 14]. The degree of compaction has been regarded as significantly important for the long-term behavior of graded crushed stone [15–18]. It is proved that compaction of the graded crushed stone layer is important to enhance the deformation resistance of asphalt pavement [16–18]. So, the reasonable gradation is essential to improve the strength and stability of graded crushed stone. Based on the material optimization design method, it is an effective way to improve the road performance by proposing new indexes and standardization for mix design of the graded crushed stone. This will lay the foundation for taking advantage of graded crushed stone and expanding the application in high-grade expressways.

At present, researchers have conducted a lot of research on the effects of different molding methods on the performance of the graded crushed stone [19–22], the indexes' development for the graded crushed stone [23], and different material designs [24, 25]. Meanwhile, the performance characterization and the evolution under various conditions (such as the layer thickness, the degree of compaction, and so on) are analyzed [5, 26, 27] to improve the performance of the graded crushed stone mixture. Although a lot of effort has been made to investigate the performance improvement and evaluation indicators of the graded crushed stone mixtures, the effects of high temperature and rainy factors and the systematically analyzation of the relationship between various performance parameters still have limitations and accuracy problems. At present, the mix design specifications of the graded crushed stone are mainly based on the modified Proctor compaction method. However, practical engineering shows that the modified Proctor compaction standard is seriously lower than the degree of the on-site compaction. Therefore, the solid volume ratio, CBR, dynamic triaxial, and static triaxial tests are used in this study

to explore the effects and the relationship of two laboratory compaction methods on the stress-strain characteristics and shear strength of graded crushed stone mixtures. This work will not only better simulate the physical and mechanical performance of the mixture on the practical project, but also improve the quality of the graded crushed stone mixture.

## 2. Graded Crushed Stone Mixtures

11 kinds of the typical graded crushed stone mixtures in Fujian province are selected in this study, and the gradations are shown in Table 1. The mixtures are taken from the five different expressways under construction in Fujian Province, and the gradations are determined according to the engineering mix design. The raw materials, such as limestone, sandstone, tuff, and granite, are widely used on Fujian expressways. The technical indexes of the 11 kinds of the typical graded crushed stone mixtures, such as the particle breakage and the Los Angeles abrasion, accord with the requirements for graded macadam mixture in the guidelines of Fujian Province [28].

## 3. Test Methods

*3.1. Comparison and Selection of Molding Methods.* At present, the compaction method is used for determining the optimal moisture content and maximum dry density of graded crushed stone mixture in China. The modified Proctor compaction method is currently used to simulate the static rolling effect of 12–15t. The vibration compaction method used in this study is modified by using the synchronous motor pneumatic loading, which is different from the traditional single-motor weight loading. The work parameters of the three used compaction instruments are shown in Table 2. The compaction degree of the laboratory vibration compaction molding instrument is more representative and has a better correlation with the working of on-site roller. Therefore, the vibration compaction molding method is increasingly used in expressway engineering.

The modified vibration and traditional vibration molding test equipment are shown in Figure 1. The single-motor counterweight loading is commonly used in the vibration compaction testing equipment. In order to reach the requirements for the graded crushed stone mixture, the parameters of the single-motor counterweight loading vary through adding or subtracting the number of the counterweights. So, the standardization of the device of the centrifugal force is low. Besides, the effects of vibration compaction depend on the different parameters and quality of the devices. The synchronous motor pressure loading vibration is adopted in the modified vibration molding test equipment, rather than the traditional single-motor counterweight loading. At the same time, it is conducive to the standardization of vibration compaction parameters. The equipment structure has the advantages of simple operation, low noise, and good stability.

The maximum dry density test results of graded crushed stone mixtures with different molding methods are shown in Table 3. For different mixtures with various raw materials,

TABLE 1: The gradations of the mixtures of graded crushed stone used in the test.

No.	31.5	26.5	19	16	13.2	9.5	4.75	2.36	1.18	0.6	0.3	0.15	0.075	Raw material
1#	100	99.9	83.6	74.0	63.9	53.5	35.1	24.1	18.5	13.6	8.7	6.3	3.8	Limestone
2#	100	99.0	85.5	71.7	61.2	55.2	39.2	28.9	23.2	18.5	13.1	9.4	4.6	Limestone
3#	100	99.8	85.7	75.0	67.0	60.2	40.6	29.9	22.3	16.8	11.0	7.8	4.9	Limestone
4#	100	96.9	85.7	74.2	65.4	60.6	40.9	25.5	17.4	11.7	6.9	4.4	2.6	Sandstone
5#	100	98.6	79.8	70.5	63.4	56.0	41.9	26.3	18.0	12.1	7.5	5.4	3.7	Sandstone
6#	100	100	84.2	74.6	66.3	56.0	39.8	22.9	15.7	10.8	7.4	5.7	4.0	Tuff
7#	100	99.9	89.4	81.4	74.4	64.3	42.8	27.1	20.0	14.5	10.0	7.7	5.0	Limestone
8#	100	97.4	84.2	73.9	66.6	58.0	40.5	31.7	22.5	14.2	8.9	6.9	4.7	Limestone
9#	100	96.8	80.6	69.7	62.1	53.2	34.9	27.0	19.2	12.2	7.7	6.0	4.1	Limestone
10#	100	96.1	80	68.9	59.8	47.5	34.8	24.3	18.4	13.0	9.1	6.2	4.3	Sandstone
11#	100	98.6	86.1	76.9	70.6	53.8	36.7	26.5	20.7	14.7	10.2	7.8	5.0	Granite

TABLE 2: Parameters of three compaction instruments.

Modified Proctor compaction	Hammer mass 4.5 kg	Hammer diameter 5.0 cm	Height 45 cm	Compact layer 3	Compact times 98	Compaction work 2.677 J
Traditional vibration compaction	Frequency 5-50 Hz	Counterweight (up/down) 5.5/4.5 kg	Amplitude Various	Centrifugal force Various	Vibratory time 2 min	Compaction work Various
Modified vibration compaction	Frequency 28-30 Hz	Amplitude 0.5-2.5 mm	Centrifugal force 6000-8000 N	Intensity of pressure 140 ± 10 kPa	Vibratory time 2 min	Compaction work 5.881 J

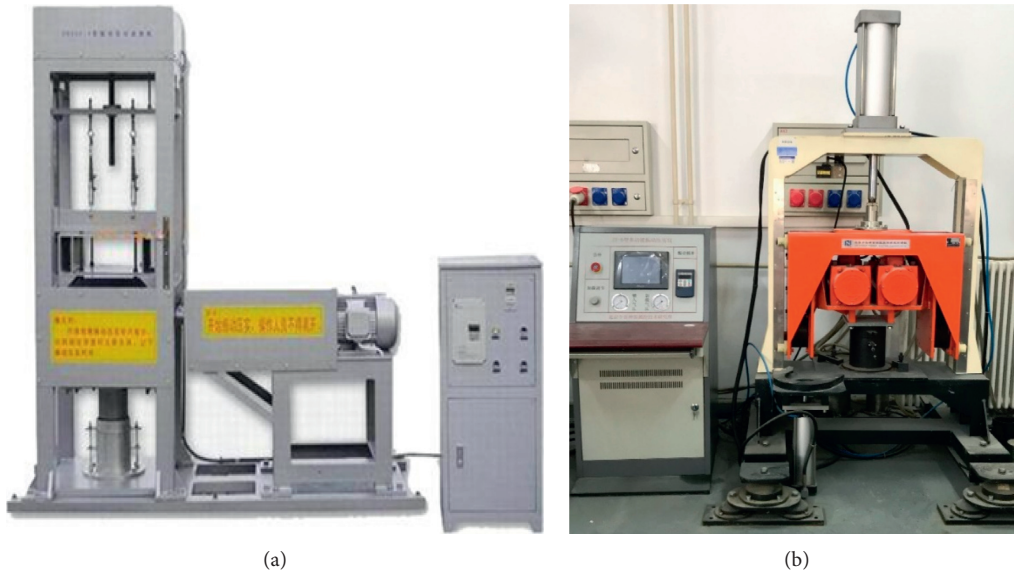


FIGURE 1: Vibration molding test equipment. (a) Traditional single-motor weight loading. (b) Modified synchronous motor pneumatic loading.

the molding methods have the same effect on the density; that is, the ranking of the maximum dry density determined by different molding methods is the traditional vibration compaction > the modified vibration compaction > the practical construction site > the modified Proctor compaction. On the one hand, this is related to the compaction work. On the other hand, the materials fully move in the state of dynamic friction during the compaction process because of the centrifugal force applied by the vibration molding method, which make the structure of the mixture specimen denser. Therefore, the maximum dry density of graded crushed stone mixture is greatly increased based on

the vibration compaction method. As for the two kinds of the vibration compaction methods, the difference of maximum dry density with traditional vibration compaction method is larger than that with the modified vibration compaction method, which confirmed that it is difficult for the traditional single-motor counterweight-loading vibration compaction to ensure the consistency of the compaction degree. Besides, comparing to the gradation and material types of mixtures, the molding method has more significant effect on the maximum dry density. Among the three kinds of laboratory compaction methods, the value of maximum dry density with the modified vibration compaction method



TABLE 3: Maximum dry density of graded crushed stone mixtures with different molding methods.

No.	Modified Proctor compaction		Traditional vibration compaction			Modified vibration compaction		Practical construction
	Maximum dry density (g/cm <sup>3</sup> )	Difference of maximum dry density (g/cm <sup>3</sup> )	Maximum dry density (g/cm <sup>3</sup> )	Difference of maximum dry density (g/cm <sup>3</sup> )	Average jump time (s)	Maximum dry density (g/cm <sup>3</sup> )	Difference of maximum dry density (g/cm <sup>3</sup> )	Maximum dry density (g/cm <sup>3</sup> )
1#	2.317	0.014	2.462	0.032	137	2.357	0.013	2.366
2#	2.297	0.011	2.433	0.038	121	2.331	0.027	2.332
3#	2.320	0.021	2.419	0.033	129	2.360	0.014	2.367
4#	2.259	0.025	2.375	0.022	136	2.307	0.016	2.307
5#	2.201	0.019	2.257	0.027	89	2.219	0.009	2.241
6#	2.165	0.014	2.288	0.022	114	2.206	0.014	2.223
7#	2.306	0.016	2.452	0.029	137	2.359	0.018	2.358
8#	2.274	0.022	2.327	0.054	65	2.324	0.019	2.335
9#	2.314	0.028	2.419	0.022	93	2.359	0.015	2.374
10#	2.218	0.024	2.358	0.041	118	2.252	0.024	2.274
11#	2.223	0.017	2.350	0.034	102	2.272	0.023	2.289

is closest to that of the practical construction site. Generally, the vibration molding method matches much better with the working of on-site roller and can be used to evaluate the performance of graded crushed stone mixtures.

3.2. *Solid Volume Ratio Test* [29]. Under the optimal water content condition, the test specimen was molded by the modified vibration compaction method and the modified Proctor compaction method. The dry density and the bulk density of each graded material were both measured. The solid volume ratio is calculated as follows:

$$V_G = \frac{\rho_{\mp}}{\rho_{sb}}, \quad (1)$$

$V_G$  is the solid volume ratio,  $\rho_{\mp}$  is the dry density of compact specimen, and  $\rho_{sb}$  is the comprehensive bulk density. According to the standard in Fujian province [30], the solid volume ratio of graded macadam should be larger than 85%.

3.3. *California Bearing Ratio (CBR) Test* [31]. The modified vibration compaction method and the modified Proctor compaction method were used to mold the test specimen, and the CBR was calculated after the specimen being saturated with water as required [31]. According to the standard in Fujian province [30], the CBR value of graded macadam should be larger than 100%.

3.4. *Dynamic Triaxial Test*. The dynamic triaxial test was basically carried out in accordance with the test method for the resilient modulus of unbound granular materials [32], where the adjustments were as follows:

- (1) The specimens were molded by the vibration with the diameter of 150 mm and height of 300 mm and then cured at room temperature for 24h to balance the water content.

- (2) The vertical partial stress was 460 kPa and the confining pressure was 196 kPa.
- (3) The specimens were under the 50,000 times repeat loading.

After the dynamic triaxial test was completed, the resilient modulus under the 20,000 times loading was calculated as the value of the modulus of the mixture. The permanent deformation rate was calculated as the evaluation index of the resistance to deformation according to the difference of the permanent deformation rate of 20,000 to 50,000 times.

3.5. *Static Triaxial Test*. The specimens were molded according to the method of the dynamic triaxial test. The shear test was carried out under the confining pressure of 60 kPa, 90 kPa, and 120 kPa. The friction angle and cohesion could be calculated using the Coulomb model, as shown in equation (2). Further, the shear strength was calculated based on the axial stress of 400 kPa.

$$\tau = \sigma_1 \tan \phi + c, \quad (2)$$

$\tau$  is the shear strength,  $\sigma_1$  is the axial stress,  $\phi$  is the internal friction angle, and  $c$  is the cohesive force.

## 4. Comparative Analysis of Mechanical Properties

4.1. *Solid Volume Ratio Test Results*. The test specimen was molded by the modified vibration compaction method and the modified Proctor compaction method, respectively. The solid volume ratio was calculated, and the relationship of the solid volume ratio with two molding method is shown in Figure 2. It was found that the solid volume rate value obtained by the modified vibration compaction method was larger than that of the modified Proctor compaction method, with the ratio of 1.02. The correlation coefficient of two test results was 0.9. In addition, the 3# limestone mixture has the

best performance in the solid volume ratio test, following by the 2# limestone mixture and the 9# limestone mixture.

**4.2. CBR Test Results.** The value of CBR was calculated and the relationship of the CBR with the two molding methods is shown in Figure 3. It was found that the CBR value obtained by the modified vibration compaction method was larger than that of the modified Proctor compaction method, with the ratio of 1.17. The correlation coefficient of the two test results was 0.87. In addition, the 3# limestone mixture has the best performance in the CBR test, following by the 7# limestone mixture and the 9# limestone mixture.

**4.3. Dynamic Triaxial Test Results.** The mechanical characters of graded crushed stone mixture depended on the applying stress. So, the dynamic triaxial tests were both carried out under the same stress condition, with the vertical partial stress of 460 kPa and the confining pressure of 196 kPa. The permanent deformation rate and resilient modulus of different mixtures are shown in Table 4.

The permanent deformation curves of different mixtures in dynamic triaxial tests are shown in Figure 4. The curve color depended on the raw materials. Among these, the blue, yellow, green, and red one were the limestone, sandstone, tuff, and granite mixture, respectively.

As shown in Figure 4 and Table 4, the permanent deformation of different mixture is quite different. 6# tuff mixture (the green one) had the largest deformation and the corresponding deformation rate was the largest. It indicated that the tuff had poor resistance to permanent deformation. This was mainly due to the porous structure of tuff, which had the characteristics of large pores, low density, and large water absorption. Besides, 5# sandstone mixture, 8# limestone mixture, and 7# limestone mixture had the relatively large permanent deformation rate. 2# limestone mixture performed best and had good resistance to permanent deformation. For the resilient modulus, the performance of 3# limestone mixture was the best, followed by 11# granite mixture and 8# limestone mixture.

The permanent deformation curves of different mixtures basically conformed to the following models:

$$\delta_{\alpha}N = k_1 e^{-k_2 N^{-a}}, \quad (3)$$

where  $\delta_{\alpha}$  is the permanent deformation, and  $N$  is the times of the repeated loading.  $k_1$ ,  $k_2$  and  $a$  both are the parameters related to the intrinsic characters of the materials.

The material parameters of permanent deformation curves of different graded crushed stone mixtures are shown in Table 5. The fluctuation of the value of the simulated material parameter  $a$  was relatively small, which was within 10%, indicating that the material parameter  $a$  was not sensitive to the type of material. The material parameters  $k_1$  and  $k_2$  showed significant changes with the different mixtures, which might be related to the physical and chemical properties of the raw material. It was found that the material parameter  $k_1$  had a good relationship with the permanent deformation, with the correlation coefficient of 0.93, as

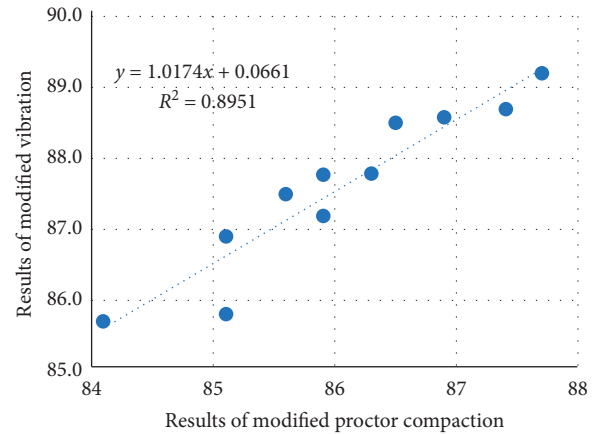


FIGURE 2: The relationship of the solid volume ratio with two molding methods.

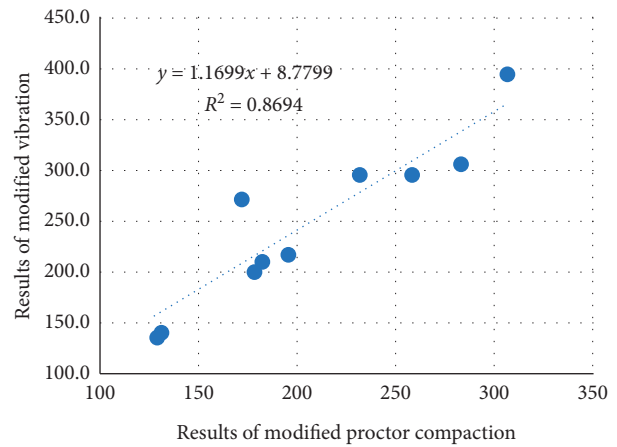


FIGURE 3: The relationship of CBR with two molding methods.

shown in Figure 5. The larger the material parameter  $k_1$  was, the greater the permanent deformation rate and the poorer permanent deformation resistance of the corresponding mixture were, such as 6# tuff mixture. In sense, the material parameter  $k_1$  could be used to evaluate the permanent deformation resistance of the graded crushed stone mixture. Besides, it can be found that both material parameters  $a$  and  $k_2$  show weak correlation with the permanent deformation at 50,000 times of loading.

**4.4. Static Triaxial Test Results.** According to the Mohr–Coulomb model, the shear strength could be calculated under the stress condition of 400 kPa, as shown in Table 6.

Theoretically, the graded crushed stone material is a kind of unbound granular materials with negligible cohesive force. However, the limestone mixtures had large cohesive forces, because the fine aggregate contained some viscous material, while the cohesive force of granite mixture was quite small.

The shear strength was related to the internal friction angle, cohesive force, and stress level. As shown in Table 6,

TABLE 4: Test results of repeated load triaxial test.

No.	Permanent deformation rate ( $10^{-8}$ )	Resilient modulus (MPa)	Raw material
1#	0.150	342	Limestone
2#	0.219	383	Limestone
3#	0.166	399	Limestone
4#	0.163	344	Sandstone
5#	0.894	341	Sandstone
6#	1.712	311	Tuff
7#	0.277	329	Limestone
8#	0.486	387	Limestone
9#	0.231	356	Limestone
10#	0.118	318	Sandstone
11#	0.402	396	Granite

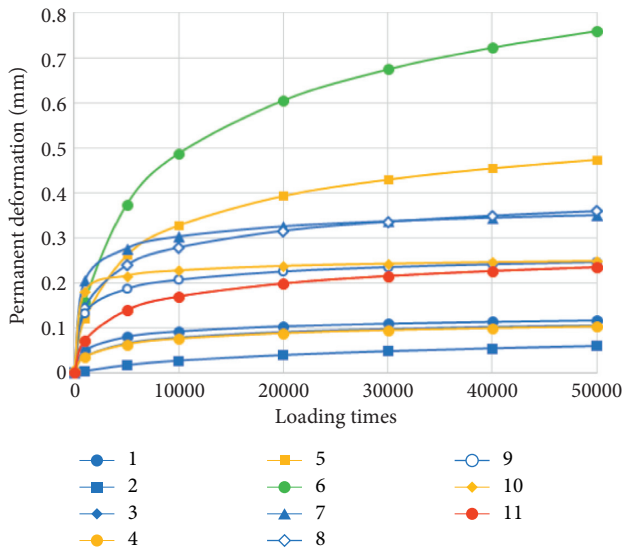


FIGURE 4: Permanent deformation curves in dynamic triaxial tests.

the shear strength of each graded crushed stone mixture varied greatly, due to the large difference of the internal friction angle. It proved that increasing the internal friction angle was beneficial to the shear strength due to the stress sensitivity of graded crushed stone materials.

In general, for most limestone mixtures, the permanent deformation and deformation rate were small, while the resilient modulus and shear strength were large. Most limestone mixtures performed well and had the advantages of good resistance to permanent deformation and shear resistance.

### 5. Standard for Design of Graded Crushed Stone Based on Vibration Molding Method

The reasonable mechanical indicators are extremely important for the quality control of the graded crushed stone mixture. It will be of benefit to guide the design and construction performance of graded crushed stone mixture and ensure the quality of the practical project. However, when the standard is too low, the performance of asphalt pavement with the graded crushed stone layer cannot meet the actual mechanical requirements, which will cause pavement

TABLE 5: Material parameters of permanent deformation curves of graded crushed stone mixtures.

No.	$k_1$	$k_2$	$a$	Raw material	Correlation coefficient
1#	0.173	9.71	0.297	Limestone	0.989
2#	0.217	32.90	0.298	Limestone	0.997
3#	0.169	12.97	0.307	Limestone	0.995
4#	0.172	11.34	0.284	Sandstone	0.994
5#	0.812	17.93	0.324	Sandstone	0.997
6#	1.595	17.29	0.291	Tuff	0.996
7#	0.437	6.49	0.311	Limestone	0.988
8#	0.546	10.14	0.294	Limestone	0.993
9#	0.327	6.85	0.293	Limestone	0.989
10#	0.283	3.75	0.307	Sandstone	0.995
11#	0.392	13.92	0.305	Granite	0.997

damage. Similarly, when the standard is too high, it is difficult to meet the requirements and practically apply in the practical project. Therefore, the reasonable theory and the simple experiment is the basis for ensuring the road performance of the asphalt pavement with the graded crushed stone layer.

5.1. *Solid Volume Ratio.* The solid volume ratio is an important design index of the graded crushed stone, which is generally considered to be related to the permanent deformation and resilient modulus. In the technical guidance in Fujian Province [30], the solid volume ratio should be larger than 85% based on the modified Proctor compaction method. According to the linear regression equation of the measured solid volume ratio values of the two methods, it was recommended that the solid volume ratio be not less than 86.5%.

5.2. *CBR.* For the modified Proctor compaction molding method, it is generally required that the CBR of the graded crushed stone for the base layer be not less than 80% in the world, while in the Chinese construction technical specification, the standard of the CBR index is determined according to the traffic load. For the medium traffic, the CBR value is not less than 160%. But for heavy and extremely heavy traffic, the index changes to be 180% and 200%, respectively. Therefore, the CBR value based on the modified

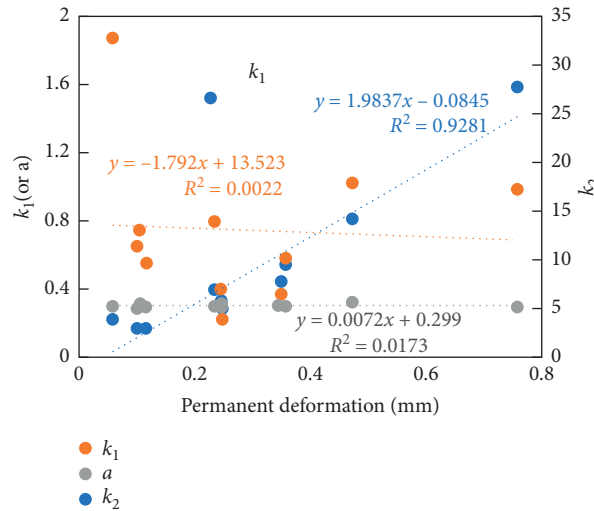


FIGURE 5: Relationship between the material parameters and the permanent deformation at 50,000 times of loading.

TABLE 6: Test results in the static triaxial test.

No.	Internal friction angle (°)	Cohesive force (kPa)	Shear strength (kPa)	Raw material
1#	48.7	40.1	495	Limestone
2#	49.5	51.9	520	Limestone
3#	51.1	39.2	534	Limestone
4#	45.6	20.3	428	Sandstone
5#	44.9	13.7	412	Sandstone
6#	44.8	6.9	404	Tuff
7#	48.4	49.3	499	Limestone
8#	49.1	37.8	499	Limestone
9#	48.9	46.1	504	Limestone
10#	47.2	8.4	440	Sandstone
11#	51.2	9.5	507	Granite

Proctor compaction molding method should be larger than 180%. Among the 11 kinds of mixtures in this study, 5 mixtures did not meet the requirements, which mainly were granite, tuff, and sandstone mixtures. Most of the limestone mixtures met the requirements. So, the current technical standard of CBR was too high.

The higher CBR value does not mean the better performance of the graded crushed stone mixture. According to the correlation analysis, the CBR value, which was an empirical indicator, was poorly correlated with the shear strength, dynamic modulus, and permanent deformation of the graded crushed stone mixture. The previous engineering practice showed that it was difficult to obtain the suitable engineering materials if the CBR value was too high. This was because the CBR value was mainly determined by the material type, rather than the gradation of mixtures. So its requirement should not be too high. According to the engineering practices, the CBR value of the graded crushed stone mixture based on the modified Proctor compaction molding method should be 120%. It was deduced that the CBR value based on the modified vibration compaction molding method was not less than 150% from the CBR correlation of the two molding methods.

5.3. *Permanent Deformation.* The permanent deformation of the graded crushed stone is very critical to control the rut depth in asphalt pavement structure. According to the standard load [30], for typical structures in Fujian province, the deformation rate of the graded crushed stone mixture should not be greater than  $10^{-8}$ . As shown in Table 4, it was found that 90% of the mixture met the performance index requirements based on the vibration molding method. So, it was reasonable that the deformation rate of  $10^{-8}$  in the dynamic triaxial test could be used as the performance indicators of the antideformation ability based on the vibration molding method.

5.4. *Resilient Modulus.* According to JTG D50-2017 [32], the range of the resilient modulus of the graded crushed stone is 200–400 MPa. Generally, the value is 300 MPa in engineering. According to the test results in the dynamic triaxial tests, the values were both greater than 300 MPa, so the resilient modulus of 300 MPa under the vertical partial stress of 460 kPa and the confining pressure of 196 kPa could be used as the performance indicators of the bearing capacity ability.

5.5. *Shear Strength.* According to the literature [30], the maximum shear strength of the grade crushed stone in Fujian typical structure was calculated to be 332.8 kPa. Considering the reliability factor of 1.2, 395 kPa was taken as the shear strength standard of the grade crushed stone mixture based on the modified Proctor compaction molding method. In this study, the shear strength of 400 kPa in the static triaxial test could be used as the performance indicators of the shear failure resistance, which was convenient for engineering applications.

## 6. Conclusion

Aiming to solve the problems, such as cracking, rutting, and structural water damage, appeared on the asphalt pavement under the combined effect of the high-temperature and rainy climatic condition and heavy loading in Fujian province, 11 kinds of graded crushed stone mixtures were selected in this study to compare the two experience indexes (solid volume ratio, CBR) and three performance indicators (resilient modulus, permanent deformation, and shear strength) of the specimens. Two laboratory compaction methods, namely, vibration compaction and modified Proctor compaction, were adopted to study the effects and the relationship of compaction methods on the stress-strain characteristics and shear strength of graded crushed stone mixtures. Results lay an experimental foundation for the mix design and engineering application of graded crushed stone mixture in Fujian province. Conclusions are listed as follows:

- (1) It was confirmed that the vibration molding method could be used to evaluate the performance of graded crushed stone mixtures. In addition, the standardization for mix design based on vibration compaction was proposed to guide the mix design of graded crushed stone mixture in Fujian province. The results indicated that the vibration molding method matched much better with the working of on-site roller. Comparing with the modified Proctor compaction, the maximum dry density designed by the vibration molding method was improved remarkably. Further, the mechanical indexes of graded crushed stone got by the synchronous motor pneumatic loading vibration molding, including CBR, the antideformation ability, and the shear failure resistance, were much better. At the same time, the results obtained by the synchronous motor pneumatic loading vibration molding method were more stable, which was an advantage over the traditional vibration molding method.
- (2) The performance indexes of vibration molding method, such as the solid volume ratio and CBR, had strong correlations with the corresponding parameters of the modified Proctor compaction. It was recommended that the solid volume ratio be not less than 86.5% and CBR be not less than 150%.
- (3) Based on the vibration molding method, the resilient modulus of 300 MPa and the deformation rate of  $10^{-8}$  in the dynamic triaxial test could be used as the

performance indicators of the bearing capacity and the antideformation ability; the shear strength of 400 kPa in the static triaxial test could be used as the performance indicators of the shear failure resistance. These performance indexes need further verification in road engineering.

- (4) Besides, for most limestone mixtures, the permanent deformation and deformation rate were small, while the resilient modulus and shear strength were large. Most limestone mixtures performed well and had the advantages of good resistance to permanent deformation and shear resistance.

## Data Availability

Data used in this paper are available from the corresponding author upon request.

## Conflicts of Interest

The authors declare that there are no conflicts of interest regarding the publication of this paper.

## Acknowledgments

The authors would like to appreciate the research funding provided by the Fujian Expressway Technology Project (no. 201809).

## References

- [1] R. L. Lytton, Y. Zhang, F. Gu, and X. Luo, "Characteristics of damaged asphalt mixtures in tension and compression," *International Journal of Pavement Engineering*, vol. 19, no. 3, pp. 292–306, 2018.
- [2] M. Sol-Sánchez, F. Moreno-Navarro, G. García-Travé, and M. C. Rubio-Gámez, "Laboratory study of the long-term climatic deterioration of asphalt mixtures," *Construction and Building Materials*, vol. 88, pp. 32–40, 2015.
- [3] Y. J. Xiao, E. Tutumluer, and J. Siekmeier, "Resilient modulus behavior estimated from aggregate source properties," in *Geofrontiers 2011: Advances in Geotechnical Engineering*, American Society of Civil Engineers (ASCE), pp. 4843–4852, Reston, VA, USA, 2011.
- [4] S. J. Ma, X. Y. Wang, and Z. W. Hu, "The analysis of the thickness of the layers influence on graded broken stone stress state," *Applied Mechanics and Materials*, vol. 587–589, pp. 952–955, 2014.
- [5] G. Cerni, F. Cardone, A. Virgili, and S. Camilli, "Characterisation of permanent deformation behaviour of unbound granular materials under repeated triaxial loading," *Construction and Building Materials*, vol. 28, no. 1, pp. 79–87, 2012.
- [6] E. Pan, E. Chen, and W. Alkasawneh, "Layered flexible pavement studies: challenges in forward and inverse problems," *International Journal of Pavement Research Technology*, vol. 1, no. 1, pp. 12–16, 2008.
- [7] J. Uzan, "Permanent deformation in flexible pavements," *Journal of Transportation Engineering*, vol. 130, no. 1, pp. 6–13, 2004.
- [8] G. Xu, Z. Chen, X. Li et al., "Simple prediction model for plastic deformation of graded crushed stone base for flexible

- pavement,” *Materials and Structures*, vol. 53, no. 2, pp. 1–16, 2020.
- [9] C. Lima and L. Motta, “Study of permanent deformation and granulometric distribution of graded crushed stone pavement material,” *Procedia Engineering*, vol. 143, pp. 854–861, 2016.
- [10] M. S. Rahman and S. Erlingsson, “A model for predicting permanent deformation of unbound granular materials,” *Road Materials and Pavement Design*, vol. 16, no. 3, pp. 653–673, 2015.
- [11] H. Wang, “Research on surface and reflective crack propagation and fatigue life of graded crushed stone base asphalt pavement,” in *Proceedings of the 11th International Conference of Chinese Transportation Professionals 2011, Towards Sustainable Transportation Systems*, pp. 3103–3114, Nanjing, China, August 2011.
- [12] F. Gu, Y. Zhang, X. Luo, H. Sahin, and R. L. Lytton, “Characterization and prediction of permanent deformation properties of unbound granular materials for pavement ME design,” *Construction and Building Materials*, vol. 155, pp. 584–592, 2017.
- [13] A. R. Dawson, N. H. Thom, and J. L. Paute, *Mechanical Characteristics of Unbound Granular Materials as a Function of Condition*, Flexible Pavements: Proceedings of the European Symposium of Euroflex, Rotterdam, Netherlands, 1996.
- [14] F. Lekarp and A. Dawson, “Modelling permanent deformation behaviour of unbound granular materials,” *Construction and Building Materials*, vol. 12, no. 1, pp. 9–18, 1998.
- [15] M. S. Rahman, *Characterising the deformation behavior of unbound granular materials in pavement structures*, Ph.D. thesis, KTH Royal Institute of Technology, Stockholm, Sweden, 2015.
- [16] R. D. Barksdale, “Laboratory evaluation of rutting in base coarse materials,” in *Proceedings of the 3rd International Conference on Structural Design of Asphalt Pavements*, pp. 161–174, 1972, [https://en.wikipedia.org/wiki/Washtenaw\\_County,\\_Michigan](https://en.wikipedia.org/wiki/Washtenaw_County,_Michigan).
- [17] J. Allen, *The effect of non-constant lateral pressures of the resilient response of granular materials*, Ph.D. thesis, University of Illinois at Urbana-Champaign, Urbana, IL, USA, 1973.
- [18] I. Holubec, “Cyclic creep of granular materials,” vol. 147, Department of Expressways, Ontario, Canada, 1969, Report RR.
- [19] A. Alnedawi, K. P. Nepal, and R. Al-Ameri, “Permanent deformation prediction model of unbound granular materials for flexible pavement design,” *Transportation Infrastructure Geotechnology*, vol. 6, no. 1, pp. 39–55, 2019.
- [20] L. Wang, X. Xie, and H. Luan, “Influence of laboratory compaction methods on shear performance of graded crushed stone,” *Journal of Materials in Civil Engineering*, vol. 23, no. 10, pp. 1483–1487, 2011.
- [21] I. Pe’rez, L. Medina, and M. G. Romana, “Permanent deformation models for a granular material used in road pavements,” *Construction and Building Materials*, vol. 20, no. 9, pp. 790–800, 2006.
- [22] C. Chen, L. Ge, and J. Zhang, “Modeling permanent deformation of unbound granular materials under repeated loads,” *International Journal of Geomechanics*, vol. 10, no. 6, pp. 236–241, 2010.
- [23] M. Tu Mu-xi, E. Yan, L. Chen et al., “Performance-based design indicator for grade macadam mixture,” *Journal of Expressway and Transportation Research and Development*, vol. 36, no. 9, pp. 28–33, 2019, in Chinese.
- [24] S. Mo and W. Binggang, “The reasonable scope of the key sieve of the grade macadam for the shear performance,” *The Transportation Engineering Transaction Journal*, vol. 5, no. 4, pp. 27–31, 2005.
- [25] S. M. H. Amlashi, M. Vaillancourt, A. Carter et al., “Resilient modulus of pavement unbound granular materials containing recycled glass aggregate,” *Materials and Structures*, vol. 51, no. 4, p. 89, 2018.
- [26] A. A. Araya, *Characterization of Unbound Granular Materials for Pavements*, Delft University of Technology, Netherlands, Europe, 2011.
- [27] T. C. Hopkins, T. L. Beckham, and C. Sun, *Resilient Modulus of Compacted Crushed Stone Aggregate Bases*, University of Kentucky, Lexington, KY, USA, 2007.
- [28] Fujian Provincial Expressway Construction Headquarters, *Guidelines for Standardized Management of Expressway Construction in Fujian Province (Roadbed and Pavement)*, China Communications Press, Beijing, China, 2010, in Chinese.
- [29] Ministry of Transport of China, *Test Methods of Unbound Mixtures for Highway Engineering, JTG 3431-2020*, China Communications Press, Beijing, China, 2020, in Chinese.
- [30] Fujian Provincial Expressway Construction Headquarters, *Fujian Provincial Expressway Construction Standardization Management Guide, Volume III: Road Engineering and Traffic Safety Facilities Engineering*, China Communications Press, Beijing, China, 2013, in Chinese.
- [31] American Society for Testing and Materials, *Standard Test Method for CBR (California Bearing Ratio) of Laboratory Compacted Soils*, American Society for Testing Materials, West Conshohocken, PA, USA, 1978.
- [32] China Communications Press, *Specification for Design of Expressway Asphalt Pavement, JTG D50-2017*, China Communications Press, Beijing, China, 2017, in Chinese.

## Research Article

# Hybrid Modification of Stone Mastic Asphalt with Cellulose and Basalt Fiber

You Huang <sup>1</sup>, Zhaohui Liu,<sup>1</sup> Li Liu <sup>1</sup>, Yunbao Zhang,<sup>1,2</sup> and Qingxiang Xu<sup>1</sup>

<sup>1</sup>School of Traffic and Transportation Engineering, Changsha University of Science and Technology, Changsha 410114, China

<sup>2</sup>Department of Transportation of Hunan Province, Changsha 410116, China

Correspondence should be addressed to Li Liu; 805296712@qq.com

Received 2 June 2020; Revised 23 August 2020; Accepted 15 September 2020; Published 22 September 2020

Academic Editor: Meng Guo

Copyright © 2020 You Huang et al. This is an open access article distributed under the Creative Commons Attribution License, which permits unrestricted use, distribution, and reproduction in any medium, provided the original work is properly cited.

In this study, cellulose and basalt fiber were introduced simultaneously to stone mastic asphalt (SMA) to investigate the effects of hybrid modification on performance improvement of asphalt mixture. The study consists of three parts. The first part investigated material properties of cellulose and basalt fiber, including microscope electrical scanning. The second part conducted a series of tests to evaluate the effects of different combinations of cellulose and basalt fiber on performance. With a total addition of fiber 0.4% by the weight of mixture, five different cellulose-basalt fiber ratios, 0:4, 1:3, 2:2, 3:1, and 4:0, were introduced to the asphalt mixtures. A series of tests including draindown, permanent deformation, low temperature bending, beam fatigue, and moisture damage resistance were conducted. In the final part, a benefit-cost ratio was designed to help determine the optimum cellulose-basalt fiber combination in the economic aspect. Results show that material properties of the two fibers are very different, including thermostability, modulus, surface, and microstructure, especially oil absorption. In general, all samples with fibers outperformed the control group in all the performance tests. Specifically, cellulose fiber improved draindown, ductility, and fatigue more significantly, whilst basalt fiber has more influence on improving permanent deformation, deflection strength, and stress sensitivity. Equal portion of cellulose and basalt fiber has the best moisture damage resistance. The mechanisms of the two fibers are different, resulting in different performance improvements on asphalt mixtures. Overall, an appropriate combination of the two fibers would produce paving materials with more balanced performance in an economical way.

## 1. Introduction

Asphalt mixture is made of bitumen, aggregates, and filler, of which the properties are very sensitive to many factors including temperature, load-time, moisture, and stress level. Researchers and engineers are constantly trying to improve the performance of asphalt mixture. Fibers have been used to improve paving materials for decades in many parts of the world and are gaining more attention due to their effects. Researches have stated that fibers can significantly improve asphalt mixture performances in one way or another [1]. The finely divided fiber provides a high surface area per unit weight so that mixtures with fiber showed an increase in the optimum binder content [2]. Another function that fiber plays is to reinforce the asphalt mixture, which carries more tensile load and prevent propagation of cracks [3]. In all,

fiber changes the viscoelasticity of modified asphalt mixture, improves the dynamic modulus, moisture susceptibility, creep compliance, fatigue life, and rutting resistance, and reduces reflective cracking of asphalt pavement [4–11].

Although fibers have many aforementioned advantages in asphalt concrete, economy should be taken into consideration. Studies showed that the cost of the fiber mixture was about 11% higher than the cost of control mixture, and this increased cost could be justified by an increase in the service life of 0.9~1.1 years [12]. However, they may not be cost-effective if the improvement is not substantial. Currently, fibers have shown obvious performance promotion in gap graded asphalt mixtures, like SMA (stone matrix asphalt). SMA is a type of hot mix asphalt consisting of a coarse aggregate skeleton and a high binder content mortar. As the stone-on-stone structure improves rutting resistance, the

high asphalt content brings in problems like draindown or bleeding during the processes of production, storage, transportation, and paving [13, 14]. By far, the most common practice is to introduce fiber into the asphalt mixture to prevent draindown or bleeding.

Cellulose fiber is plant-based fiber most commonly from woody plants or recycled papers. This kind of fiber has a rough texture, porous surface, and diameter varied along the length [15, 16]. As a result, it has fairly high absorption of asphalt. It is this nature that helps holding higher binder contents in mixtures. Cellulose fibers in asphalt mixtures allow asphalt content to be increased while drastically decreasing draindown/bleeding of asphalt binder [17–19]. Cellulose fibers are widely available and inexpensive and may be provided either in loose form or in pellets.

Basalt fiber is a mineral fiber manufactured by melting crushed basalt, a hard, dense and stable igneous rock, then physically forming fibers by spinning or extruding at about 1500°C. Basalt fiber has high elastic modulus and tensile strength and has no toxic reaction with air or water. When in contact with chemicals, they produce no chemical reactions that may damage health or environment [20]. As it is strong and stable, it makes a perfect reinforcement material for infrastructure. But due to the relative smooth surface, it is not as absorptive as cellulose. High price is another disadvantage that may hinder its application in engineering projects. Some scholars also pointed out the damage basalt fiber may have on vehicle tires [21].

Most studies focusing on fiber-reinforced paving materials generally investigate the effect of fiber separately. This paper introduced an idea of hybrid modification of asphalt mixture by introducing cellulose and basalt fiber simultaneously into SMA so as to take advantages of both fibers to produce more balanced designed paving material. Properties of the two fibers were investigated first. Then, draindown test, wheel tracking test at high temperature, low-temperature bending, beam fatigue test, and moisture damage test were conducted to evaluate the performance of SMA with different fiber combinations. Finally, an economic solution is provided to get optimum benefit-cost efficiency taking consideration of economy.

## 2. Material Property Test

The basic mechanical properties of the basalt fiber are listed in Table 1. The cellulose fiber used in this study is 6 mm long, with ash content about 17.6%. Other properties including oil absorption, water absorption, and pH will be tested and shown in Section 2.1. Three replicates were used for each test, and results were averaged for analysis.

*2.1. Thermostability Test.* Technically, there are two approaches of introducing fiber: wet process and dry process. In the wet approach, fibers are blended with asphalt binder first and then blended into mixture, while in the dry approach, fiber is mixed with the aggregate before adding asphalt binder. Generally, the dry process is preferred as it is easy to perform and fiber can be distributed evenly in the

mixture [24]. During the production of SMA, the temperature of aggregates can easily reach 170~180°C. If styrene-butadiene-styrene- (SBS-) modified asphalt is used, which is the normal case in SMA production, the blending temperature could be even higher. As a result, stability of fiber at a high temperature is a property worth looking into. In thermostability tests, randomly weighted samples of the two fibers were first kept in 50°C for 4h to dry up. Then, they were heated to 165°C/200°C and kept for 2 h/5 h. The mass loss was recorded as an indication of thermostability as is listed in Table 2.

The results show that mass loss of cellulose is much higher than that of basalt fiber, indicating that basalt fiber is much more durable than cellulose. Mass loss of basalt fiber was very small, generally less than 1%. Cellulose was not as stable as basalt fiber in high temperature, and the mass loss was much higher, about 5% at 165°C for 2 h. The mass loss increased as temperature and duration increased, up to nearly 12% at 200°C for 5 h. In Figure 1, it is also seen that the appearance of basalt fiber does not change with heating time, while the color of cellulose under 200°C/5 h becomes darker and more curled than that under 200°C/2 h. In general, the mass loss of cellulose is 20 times that of basalt fiber. The relative high mass loss in cellulose raises the consciousness of strict temperature control during the production of asphalt mixtures with fiber. It is also implied that adding basalt fiber to replace some cellulose can decrease fiber loss in mixture production.

*2.2. Compatibility Test.* Compatibility with asphalt cement is a key factor of fiber to enhance the asphalt mixture performance. Evaluation of compatibility includes pH, oil absorption, and stripping test. The pH test is an indication of chemical bond of asphalt with fiber, while oil absorption is an indication of physical bond. The stripping test is a performance-related evaluation of bond between asphalt and fiber.

The pH test is typically done by soaking fiber in distilled water and measuring the pH of the water with pH meter. 5 g dry cellulose and basalt fiber were put into 100 ml distilled water, respectively, and stirred for a while to disperse the fiber for full contact with water. After a rest of 30 minutes, fibers were taken out and pH of the water was measured. Test results showed that pH of water with cellulose was 7.24, and pH of water with basalt fiber was 7.92. Both fiber are weak alkaline, but the pH of basalt fiber is a little higher because the basalt fiber is mainly composed of SiO<sub>2</sub>, Al<sub>2</sub>O<sub>3</sub>, and FeO<sub>x</sub>, which produce alkaline chemical reaction. According to the bond theory of asphalt with aggregates, it is the acidic components of asphalt that reacts with alkali components of aggregates to form water insoluble salts which become a very strong bond. Hicks stated that chemical reaction between most asphalts and acidic aggregates is weaker compared with alkali aggregates [25]. As such, both fibers have a good potential of chemical bond with asphalt.

Oil absorption is an important index to test the fiber's ability of holding asphalt due to the surface texture (e.g., smoothness and porosity) of fibers. 5 g dry cellulose and



TABLE 1: Basic properties of basalt fiber.

Item	Value	Standards
Density (g/cm <sup>3</sup> )	2.56~3.05	ASTM D3800-16 [22]
Diameter ( $\mu$ m)	13	ASTM D3800-16 [22]
Length (mm)	6	
Tensile strength (MPa)	4100~4830	
Elastic modulus (GPa)	90~110	ASTM D5034-17 [23]
Elongation rate (%)	3.0~3.3	
pH	9.72	

TABLE 2: Mass loss of cellulose and basal fiber.

Fiber	Test procedure	Mass before heat (g)	Mass after heat (g)	Mass loss (%)	Visual change of fiber
Basalt fiber	165°C, 2 h	1.0180	1.0155	0.246	No change.
	165°C, 5 h	1.0442	1.0416	0.249	
	200°C, 2 h	1.0334	1.0269	0.629	
	200°C, 5 h	1.0118	1.0053	0.642	
Cellulose fiber	165°C, 2 h	1.0120	0.9624	4.901	Fiber curl, and color of surface becomes darker.
	165°C, 5 h	1.0563	0.9829	6.949	
	200°C, 2 h	1.0248	0.9278	9.465	
	200°C, 5 h	1.0007	0.8809	11.972	

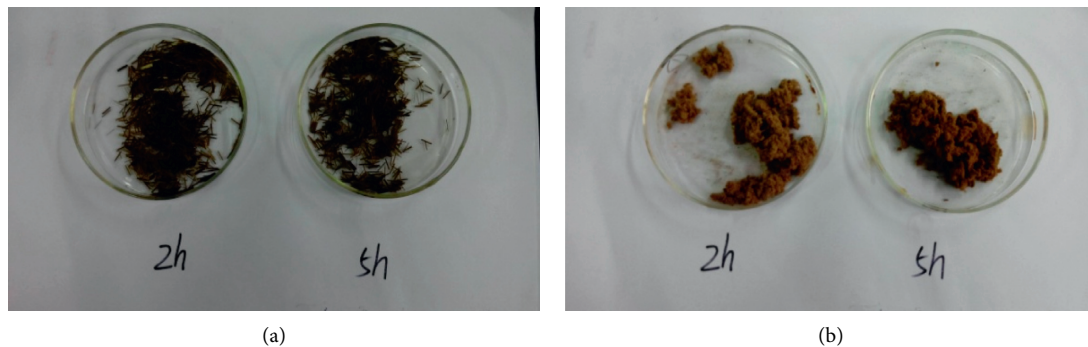


FIGURE 1: Visual change of fibers after the thermostability test. (a) Basalt fiber (200°C). (b) Cellulose (200°C).

basalt fiber were put in 100 ml mineral spirit (kerosene), respectively, and stirred for a while for full contact. After 30 minutes' rest, the fibers were taken out and put into a 0.25 mm sieve and shaken gently for 10 mins to get rid of excessive mineral spirit and then weighed. The mass change in terms of how many times the mass of fiber was used to evaluate absorption. The test results of cellulose and basalt fiber were 683.4% and 145%, respectively. It was clearly shown that oil absorption of cellulose is much higher, nearly 5 times that of basalt fiber. High absorption of cellulose is a very good complement for basalt fiber to help hold asphalt and solves problems like draindown and bleeding in SMA. Similar tests were done with distilled water, and the absorption was 510% and 96% for cellulose and basalt fiber, respectively. Although the absorptions of oil were fairly larger than water for both fibers, higher oil absorption of cellulose indicates possible higher vulnerability of water deterioration of asphalt pavement with cellulose. In this sense, replacing some cellulose with basalt fiber could reduce

the risk of moisture damage and increase the service life of asphalt pavement.

The stripping test of bond between asphalt and fiber was designed similarly to the "boiling water test" for bond between asphalt and aggregate. 4 g cellulose or basalt fiber was put in 100 g asphalt separately and stirred for a while for full contact. Another sample with 2 g cellulose and 2 g basalt fiber was also prepared. The fibers covered with asphalt were then put onto a 0.25 mm sieve and kept at 165°C for 1 h to let excessive asphalt draindown. After that, samples were cooled down to room temperature. Randomly selected fibers covered with asphalt were put into boiling water for 3 minutes. At last, pick the fiber out, observe the surface, and estimate the stripped area of asphalt. No strip was observed in the 4 g cellulose, 2 g cellulose, and 2 g basalt fiber; but about 6%~10% area was stripped in the 4 g basalt fiber. Results indicated that the bond of cellulose with asphalt was stronger than that of basalt fiber. Combination of cellulose and basalt fiber demonstrated similarly excellent bond as cellulose.

**2.3. Microscope Detection.** As mentioned before, the surface of cellulose and basalt fiber is very different, which may influence the interface between asphalt and fiber. The absorption test and bond test above verified that cellulose has a better absorption and better bond with asphalt than basalt fiber. To get a more direct comparison of asphalt absorption of the two fibers, an environmental scanning electron microscope (ESEM) was employed to detect the microscale state of cellulose and basalt fiber mixed with asphalt, as is shown in Figure 2.

In Figure 2(a), basically, the surface of basalt fiber is smooth with a thin and evenly distributed asphalt film covering the basalt fiber along the length. On contrast, Figure 1(b) shows that there was a lot more asphalt adhered to the cellulose. As the asphalt molecules align near to the internal and external surfaces of cellulose filament, they increase the thickness of asphalt membrane and effectively increase the bond between asphalt and cellulose. Furthermore, there is a “root structure” that forms at the root of cellulose, which is believed to enhance the bond between asphalt and the fiber greatly. It is visually clearly shown in the pictures that cellulose absorbs much more asphalt than the basalt fiber does and forms stronger bond with asphalt.

The properties above indicate that cellulose and basalt fiber have different material properties. Comparatively, cellulose has better absorption of and stronger bond with asphalt material, while basalt fiber demonstrates better thermal stability and mechanical behavior (higher elastic modulus and higher tensile strength). It is preliminarily hypothesized that the introduction of both fibers will complement each other and leads to more balanced performances of asphalt mixture than only one fiber.

### 3. Performance Test

**3.1. Mixture Design and Specimen Preparation.** Performance tests were designed to test the hypothesis that hybrid introduction of both cellulose and basalt fiber would result in asphalt mixture with more balanced performance. SMA-13 (stone mastic asphalt with nominal maximum aggregate size 13 mm) specimens were prepared as per the Marshall mixture design method [26]. The Marshall mixture design method is a classical method of designing asphalt mixture mainly based on volumetric properties together with mechanical properties. First, asphalt mixtures with different asphalt contents (usually 5 asphalt contents) were prepared, and then, a series of tests are conducted to inquire volumetric parameters: volumetric voids (VVs), voids of mineral aggregates (VMAs), and voids of mineral aggregates that are filled with asphalt (VFA), as well as mechanical properties: Marshall stability and flow number and dynamic stability of the prepared asphalt mixtures. Change of volumetric properties and mechanical properties against asphalt content is plotted and fitted by second-order polynomial, and the optimum asphalt content (OAC) is determined as the

asphalt content that gives the best volumetric and mechanical properties based on a comprehensive evaluation. The gradation of basalt aggregates is shown in Figure 3. Properties of styrene-butadiene-styrene- (SBS-) modified asphalt are listed in Table 3.

The cellulose and basalt fiber were both 6 mm long. The total introduction of fiber was 0.4% of the mixture by weight as most literatures and practices recommended [1, 6, 27]. Five combinations of cellulose and basalt fiber were designed with the portions of cellulose to basalt fiber, 0 : 4, 1 : 3, 2 : 2, 3 : 1, and 4 : 0, by weight. A control group without any fiber was marked as 0 : 0. As fiber portion changes, the OAC was anticipated to change too. Marshall tests were conducted to determine OAC for each fiber combination. OAC and volumetric properties are listed in Table 4.

Generally, OAC increases with cellulose. This is because cellulose has strong asphalt absorption. At the same time, the volumetric properties also changed. For example, the VV and VMA increased first and then began to decrease; on contrary, VFA declined a little but went up afterwards. All these changes are mainly due to the asphalt content change caused by different combinations of fibers. Another contribution is the volumetric difference of different fiber combinations. The addition of fiber is controlled by weight, but cellulose and basalt fiber have different densities, meaning volume of fibers are different, which could in turn affect the volumetric properties of SMA specimen.

**3.2. Draindown Test.** A draindown test was carried out as per ASTM D6390 [28]. A certain amount (about 1 kg) of loose SMA was put in a glass beaker after mixing with fiber. The covered beaker was held in an oven at  $185^{\circ}\text{C} \pm 1^{\circ}\text{C}$  for about  $60 \text{ min} \pm 1 \text{ min}$ . Then the beaker was turned over, allowing the mix to fall into a tared bowl. The difference of mass, expressed in the percentage of the original mass, was the draindown loss. The upper-limit of draindown loss is 0.3%. Four replicates were tested, and results were averaged for analysis. Test results are shown in Figure 4.

The results were pretty straight forward, draindown loss decreased with higher portion of cellulose, and this is a direct sign that cellulose can hold asphalt better than basalt fiber. More cellulose would improve the asphalt draindown in SMA. SMA without fiber showed much higher draindown loss, about 0.35%, which failed the criterion of 0.3%. A one-tail  $t$  test was carried out to check the difference between different fiber combinations. The null hypothesis was that the draindown of different fiber combinations was the same. The  $P$  value was calculated and compared with the critical value of 0.05 to reject or accept the null hypothesis. In this study,  $P \leq 0.05$  means the results of different fiber combinations are statistically different. As listed in Table 5, most of the test results are significantly different from each other. Especially, the control group (0 : 0) is significantly different from all other samples with fibers, meaning that fibers,

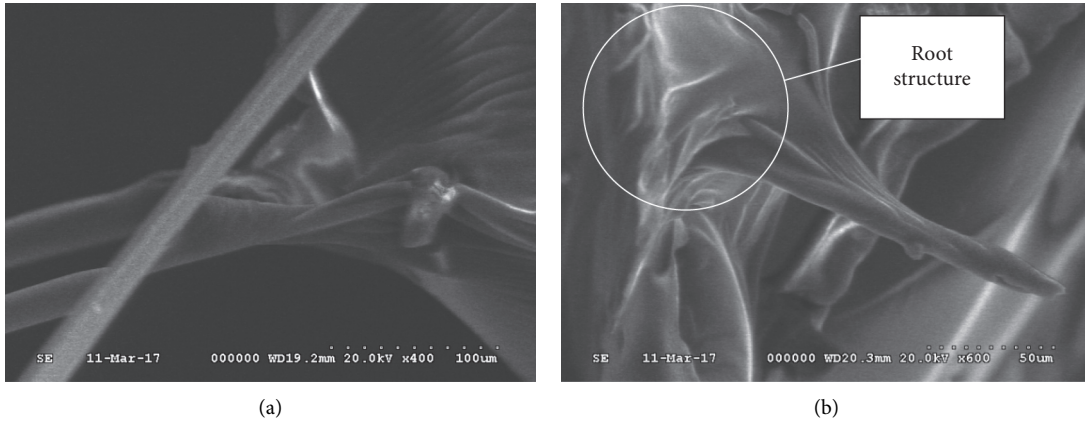


FIGURE 2: Image of ESEM (magnified by 500 times). (a) Basalt fiber. (b) Cellulose.

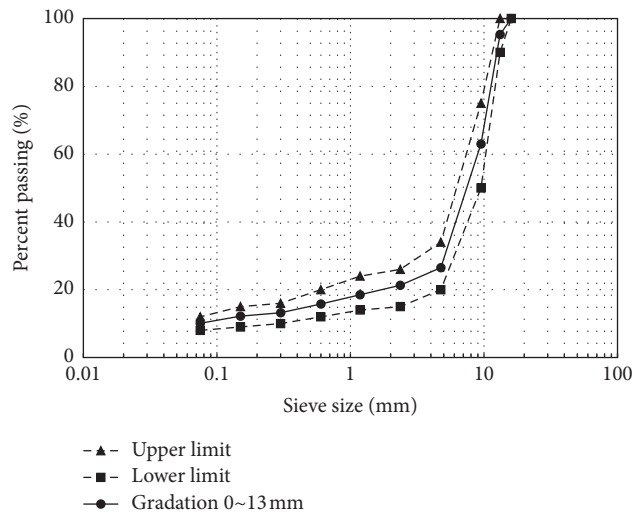


FIGURE 3: Gradation of SMA.

TABLE 3: Physical properties of base asphalt.

Properties	Values	Standards
Specific gravity at 25°C (g/cm <sup>3</sup> )	1.03	ASTM D70
Penetration at 25°C (1/10 mm)	55	ASTM D5M
Softening point (°C)	50.1	ASTM D36 M
Flash point (°C)	298	ASTM D92
Ductility at 25°C (cm)	>100	ASTM D113
Viscosity at 60°C (Pa·s)	876	ASTM D4402
Loss on heating (%)	0.042	ASTM D6M

TABLE 4: OAC and volumetric properties of SMA with different fiber combinations.

Cellulose : basalt	OAC (%) (asphalt-aggregate ratio)	VV (%)	VMA (%)	VFA (%)
0 : 4	5.9	3.6	16.5	79.4
1 : 3	6.0	3.8	16.6	77.1
2 : 2	6.1	3.9	17.0	77.6
3 : 1	6.1	3.2	16.7	80.8
4 : 0	6.2	3.4	17.2	79.0
0 : 0	5.4	4.2	16.0	75.3

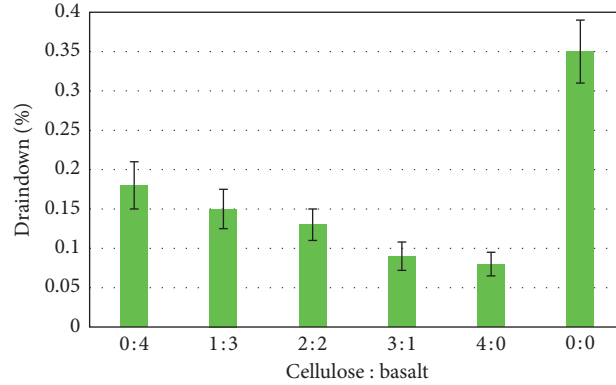


FIGURE 4: Draindown test of SMA with different fiber combinations.

TABLE 5:  $P$  values of draindown of different fiber combinations.

Cellulose : basalt	0 : 4	1 : 3	2 : 2	3 : 1	4 : 0	0 : 0
0 : 4	—	0.173	0.067	<b>0.019</b>	<b>0.013</b>	<b>0.009</b>
1 : 3	—	—	0.193	<b>0.019</b>	<b>0.017</b>	<b>0.005</b>
2 : 2	—	—	—	0.06	<b>0.042</b>	<b>0.004</b>
3 : 1	—	—	—	—	0.336	<b>0.002</b>
4 : 0	—	—	—	—	—	<b>0.007</b>
0 : 0	—	—	—	—	—	—

whether cellulose or basalt fiber or the combination of both, has significant improvement on the draindown of asphalt mixture.

**3.3. Permanent Deformation Test.** The main advantage of SMA lies in its excellent rutting resistance. The wheel tracking test was carried out to compare the permanent deformation of SMA with different fiber combinations at high temperature. Wheel tracking test simulates traffic moving on pavement to test the permanent deformation resistance of asphalt mixture at high temperature as per JTG E20-2011[29]. The test temperature was set at  $60^{\circ}\text{C} \pm 1^{\circ}\text{C}$  and contact pressure  $0.7\text{ MPa} \pm 0.05\text{ MPa}$ . During test, the wheel runs to and fro at frequency of 42 passes/min  $\pm 1$  pass/min. Dynamic stability (DS) indicating the passes to achieve every 1 mm of deformation was used to evaluate the rutting resistance of asphalt mixture, as shown in equation (1). Specimens of 300 mm length and 300 mm width by 50 mm thick were prepared for the test. At least four replicates were tested for each fiber combination:

$$DS = \frac{(t_2 - t_1) \times N}{d_2 - d_1} \times C_1 \times C_2, \quad (1)$$

where  $d_1$  and  $d_2$  correspond to the deformation at time  $t_1$  and  $t_2$ , respectively;  $C_1$  and  $C_2$  are test parameters based on equipment model and sample dimension, as standard test equipment and samples are used in this study,  $C_1 = 1.0$ ,  $C_2 = 1.0$ ; and  $N$  is the passes per min.

Figure 5 displays the change of DS with fiber combinations. First of all, specimens with fibers outperform the control group in general. Secondly, mixtures with higher

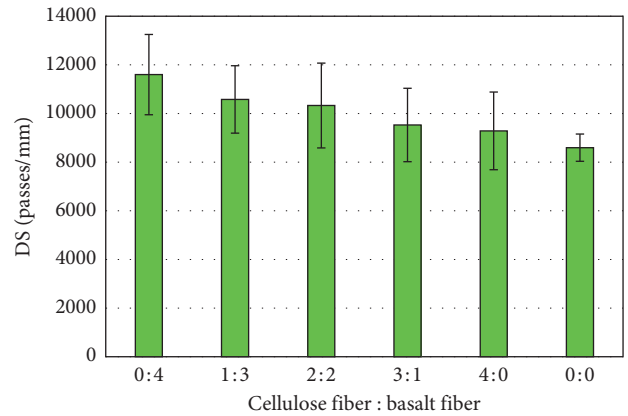


FIGURE 5: DS of SMA with different fiber combinations.

basalt fiber portions had higher DS values, indicating that basalt fiber improves the rutting resistance more significantly. As the permanent deformation performance of different fiber combinations looks close to each other, a one-tail  $t$  test was carried out to check the difference between different fiber combinations. The null hypothesis was that the DS of different fiber combinations were the same. The  $P$  value was calculated and compared with the critical value of 0.05 to reject or accept the null hypothesis. In this study,  $P \leq 0.05$  means the results of different fiber combinations are statistically different. Table 6 shows that only one case (cellulose : basalt = 0 : 4 against cellulose : basalt = 0 : 0) shows significance ( $P = 0.048$ ), meaning that when only basalt fiber is added, the difference of DS are significantly different from the control group. Basalt fiber has very high modulus and tensile strength. When blended in SMA, it forms a strong fiber network and restricted the movement of mastic and thus improves the antideformation ability of asphalt mixture. Another reason for the nonsignificant improvement of DS by the other fiber combinations is that when cellulose is added, asphalt content is increased at the same time, which has the potential of increasing permanent deformation at high temperatures. In general, the addition of fibers can improve permanent deformation resistance of asphalt mixture, but the effects are not significant.

TABLE 6:  $P$  values of draindown of different fiber combinations.

Cellulose : basalt	0 : 4	1 : 3	2 : 2	3 : 1	4 : 0	0 : 0
0 : 4	—	0.229	0.205	0.092	0.078	<b>0.048</b>
1 : 3	—	—	0.427	0.212	0.175	0.053
2 : 2	—	—	—	0.290	0.244	0.121
3 : 1	—	—	—	—	0.429	0.195
4 : 0	—	—	—	—	—	0.277
0 : 0	—	—	—	—	—	—

**3.4. Low-Temperature Performance Test.** As environmental temperature drops, the body of pavement would contract and internal stress builds up. If this contraction occurs fast enough, tensile stress accumulates in asphalt mixture and may cause cracking. Three-point beam test was carried out at  $-10^{\circ}\text{C} \pm 0.5^{\circ}\text{C}$  to check bending resistance at low temperature as per JTG E20-2011(29). A loading is exerted at the mid-point of the beam at a speed of 50 mm/min. The specimen is 250 mm long  $\times$  30 mm wide  $\times$  35 mm high, with a supporting span of 200 mm. The deflection strength  $R_B$ , maximum tensile strain  $\varepsilon_B$  at the bottom of beam, and stiffness modulus  $S_B$  are calculated as follows:

$$R_B = \frac{3LP_B}{2bh^2},$$

$$\varepsilon_B = \frac{6hd}{L^2}, \quad (2)$$

$$S_B = \frac{R_B}{\varepsilon_B},$$

where  $L$  is the supporting span,  $P_B$  is the maximum load (N),  $b$  is the width of the beam,  $h$  is the height of the beam, and  $d$  is the maximum deflection (at the loading point).  $R_B$ ,  $\varepsilon_B$ , and  $S_B$  of different fiber combinations are listed in Table 7.

It is found that, with the increase of basalt fiber,  $R_B$  and  $S_B$  increase, while  $\varepsilon_B$  decreases. On the contrary, as more cellulose is added,  $R_B$  and  $S_B$  decrease, while  $\varepsilon_B$  increases. This is due to the different mechanisms of the two fibers. Basalt fiber is a strong material with very high modulus, the fibers form interconnected three-dimensional network and helps transfer the internal stresses, thus increasing the stiffness of SMA, acting like the reinforcing bar. The main effect of cellulose is increasing the asphalt content, which is believed to increase the ductility of samples. To avoid low-temperature cracking, the asphalt mixture is required to either relax fast to release the stress or be strong enough to resist the stress. The introduction of both cellulose and basalt fiber at the same time seems to increase the deflection strength and ductility at the same time, resulting in a more balanced asphalt mixture. For example, in the case of cellulose: basalt = 3 : 1, when compared with the control group (cellulose: basalt = 0 : 0), it increases the  $\varepsilon_B$  by about 5.3% from 3397 to 3575 as well as increases  $R_B$  by about 7.1% from 11.31 to 12.11.

**3.5. Beam Fatigue Test.** Intermediate temperature fatigue cracking by repeated loading is the one of the major

distresses of asphalt pavement. Many test methods such as beam fatigue, semicircle beam (SCB), indirect tension (IDT) strength, Texas overlay tester (OT), and asphalt mixture performance tester (AMPT) have been used to characterize the resistance of asphalt mixtures to cracking.

One of the most widely accepted methods is the repeated loading beam fatigue test. Beam specimens with dimension of 380 mm long  $\times$  63 mm wide  $\times$  50 mm thick were subjected to four-point bending by IPC<sup>®</sup> fatigue test apparatus, as per ASTM D7460 [30]. Test temperature was set at  $15^{\circ}\text{C} \pm 0.5^{\circ}\text{C}$ . Haversine loading with controlled stress was conducted at a frequency of  $10 \text{ Hz} \pm 0.1 \text{ Hz}$ . Stress levels to flexural strength was set in four levels: 0.2, 0.3, 0.4, and 0.5. Before the fatigue test, flexural strength of beam was determined and correspondingly the stress levels. At least four replicates were tested for each stress level. Typical fatigue relation is stated as follows:

$$\lg(N_f) = a - b \lg(\sigma), \quad (3)$$

where  $N_f$  is the fatigue repetition;  $\sigma$  is stress level; and  $a$  and  $b$  are regression parameters.

Fatigue curves on log-log scale are shown in Figure 6. The strength test results and fatigue equations are listed in Table 8.

The fatigue models in this study have not been calibrated with field data, so they cannot be used to predict fatigue life. But, they are able to provide a comparison between specimens to evaluate the effects of different fiber combinations on fatigue. It is clearly shown that, as the stress level increased, the fatigue life declined. Overall, specimens with fiber had better fatigue than the control group. With the increase in the cellulose portion, the specimen demonstrated higher flexural strength and better fatigue property. This is mainly because of the increase of asphalt content. The slope of the fatigue line is an indication of sensitivity to stress level. Smaller slope means less sensitive to stress level. As indicated by parameter  $b$  in fatigue equations in Table 8, the slope decreased with the increase of basalt fiber. This makes sense as the basalt fiber forms a strong fiber network that helps mitigate the propagation of cracks to make asphalt mixtures more stable. As a result, a combination of cellulose and basalt fiber would lead to higher bending strength and better fatigue compared with sole basalt fiber and less stress sensitivity compared with sole cellulose.

**3.6. Moisture Damage Test.** The resistance of asphalt pavement to moisture damage is critical to its long-term performance and sustainability. A moisture test was conducted to evaluate moisture resistance of asphalt mixture with different fiber combinations as per ASTM D4867M [31]. 8 samples were prepared for each fiber combination and evenly divided into two groups: wet subset and dry subset. A freeze-thaw conditioning was employed for the wet subset samples: the specimens were first saturated in a vacuum chamber to reach a partial saturation of 55%~80% and then wrapped in leak-proof bag with about 3 ml distilled water and placed in an air bath freezer at  $-18^{\circ}\text{C} \pm 2.0^{\circ}\text{C}$  for at least 15 h; after that, the specimens were immersed in a water bath

TABLE 7: Three-point beam tests at low temperature.

Cellulose: basalt	OAC (%)	$P_B$ (N)	$d$ (mm)	$R_B$ (MPa)	$\epsilon_B$ ( $\mu\epsilon$ )	$S_B$ (MPa)	Critical $\epsilon_B$ ( $\mu\epsilon$ )
0:4	6.0	1531	0.626	12.97	3287	3947	>2800
1:3	6.0	1505	0.631	12.53	3313	3783	
1:1	6.1	1454	0.661	12.28	3470	3538	
3:1	6.1	1404	0.681	12.11	3575	3388	
4:0	6.2	1352	0.693	11.85	3638	3258	
0:0	5.4	1385	0.647	11.31	3397	3329	

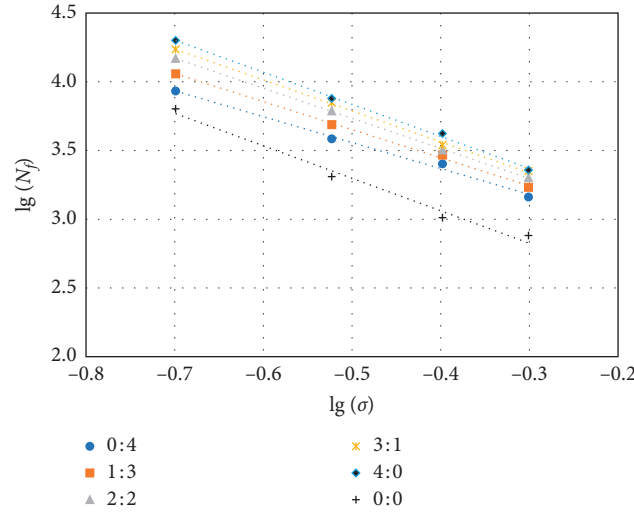


FIGURE 6: Fatigue curves of SMA with different fiber combinations.

TABLE 8: The strength and fatigue equations of SMA with different fiber combinations.

Cellulose : Basalt	Flexural strength (MPa)	Fatigue equations	$R^2$
0:4	4.88	$\lg(N_f) = 2.6147 - 1.8858 \lg(\sigma)$	0.9914
1:3	5.35	$\lg(N_f) = 2.6308 - 2.0416 \lg(\sigma)$	0.9953
2:2	5.47	$\lg(N_f) = 2.6388 - 2.1904 \lg(\sigma)$	0.9980
3:1	6.90	$\lg(N_f) = 2.6615 - 2.2533 \lg(\sigma)$	0.9950
4:0	7.09	$\lg(N_f) = 2.6690 - 2.3346 \lg(\sigma)$	0.9930
0:0	4.17	$\lg(N_f) = 2.1162 - 2.3634 \lg(\sigma)$	0.9843

at  $60^\circ\text{C} \pm 1.0^\circ\text{C}$ ; at last, both the dry subset specimens and wet subset specimens were tested in the indirect tensile test. Moisture damage is indicated by the tensile strength ratio (TSR) of the wet subset ( $S_{tm}$ ) to that of the dry subset ( $S_{td}$ ), calculated from equations (4) and (5). The higher the residual strength is, the better the moisture stability is. Test results are listed in Table 9.

$$S_t = \frac{2P}{\pi t D}, \quad (4)$$

$$\text{TSR} = \frac{S_{tm}}{S_{td}}, \quad (5)$$

where  $S_t$  is the tensile strength (kPa),  $P$  is the maximum load (N),  $t$  is the specimen height immediately before test (mm),  $D$  is specimen diameter (mm).  $S_{tm}$  is the average strength of moisture conditioned subset (kPa), and  $S_{td}$  is the average strength of dry subset (kPa).

Asphalt mixtures with different cellulose-basalt fiber ratios showed different moisture resistances. With the increase in a portion of cellulose, the residual strength increased first and then began to decline. When cellulose-basalt fiber ratio reached 2:2, the moisture stability was the best. This is because of the composite effect of the asphalt absorption by cellulose and the strength enforcement by basalt fiber, which together improve the resistance to moisture. All cases with fiber have better moisture damage resistance than the control group.

**3.7. Economy Analysis.** The aforementioned technical analysis has demonstrated that cellulose and basalt fiber enhance SMA properties and performances in different ways and work as good complements for each other. Nevertheless, when applied in real projects, economy is a must consideration. In fact, one of the purposes of hybrid enforcement is to replace a portion of expensive basalt fiber with cheap

TABLE 9: Moisture test of SMA with different fiber combinations.

Cellulose : basalt	Air voids (%)	Degree of saturation (%)	Average $S_{um}$ (kPa)	Average $S_{td}$ (kPa)	TSR (%)
0 : 4	6.9	64	498	548	90.8
1 : 3	6.6	60	497	537	92.4
2 : 2	7.2	71	597	640	93.2
3 : 1	6.3	78	646	704	91.7
4 : 0	7.7	73	602	677	89.0
0 : 0	7.5	68	347	416	83.4

cellulose to bring down the cost. The costs of different fiber combinations and asphalt mixtures were calculated and are listed in Table 10. This case was based on average market price of China in 2018: 4000 yuan/ton for cellulose, 10000 yuan/ton for basalt fiber, and 6000 yuan/ton for SBS modified asphalt. The unit price of fiber combination was calculated by multiplying the unit price of each fiber and its portion, as displayed in column 2. The total amount of fiber was set at 0.4% of asphalt mixture by weight, and the cost of hybrid fibers was displayed in column 3. The total cost (hybrid fiber + asphalt) was displayed in the last column, regardless of aggregates.

As the table shows, with the increase in cellulose, the cost of fiber decreases as less basalt fiber was used. Correspondingly, the cost of asphalt goes up a little as a result of higher asphalt content. The net effect is that the total cost declines with more cellulose. As a result, the hybrid fiber has a price advantage over sole basalt fiber.

To get an optimum fiber combination, the benefit-cost ratio  $B$  is termed as the ratio of “percent performance change” to “percent cost change.” Obviously, the bigger the  $B$  is, the more the cost-effective it is:

$$B = \frac{P}{C}, \quad (6)$$

where  $P$  is the percent performance change and  $C$  is the percent cost change.

The  $B$  values of different fiber combinations for different characteristics based on the results of this study are listed in Table 11. As is shown in the table, the  $B$  value of different performances shows different trends. For draindown and fatigue,  $B$  value increases as cellulose increases; but for permanent deformation,  $B$  value decreases as cellulose increase. For moisture damage,  $B$  value increases first and then declines. This would bring in conflicts when performances with opposite  $B$  trends are needed at the same time, e.g., a fiber combination that achieves higher  $B$  value in permanent deformation would result in a lower  $B$  value in fatigue. Asphalt pavement in service is subjected to traffic and environmental change, and an optimum fiber combination is to produce SMA with balanced characteristics to improve all required performances. One simple and effective solution is to assign different weight coefficients to different performances to get a comprehensive  $B$  value,  $B_{total}$ :

$$B_{total} = \sum w_i B_i. \quad (7)$$

where  $w_i$  is the weight coefficient,  $\sum w_i = 1$ ;  $w_i$  is determined based on traffic, environmental condition, pavement structure, etc; and  $B_i$  is the  $B$  value for the  $i$ th characteristic.

In general, replacing some basalt fiber with cellulose would bring down the price and improve the fatigue and draindown at the same time. In this study, the moisture damage indicates that the best moisture resistance is achieved when the portion of cellulose and basalt fiber is equal. For specific projects, designers can determine the weight coefficient and calculate an economic combination of fibers in accordance with equation (7).

#### 4. Discussions

Cellulose and basalt fiber are widely used additives to improve the asphalt mixture performance, especially SMA. This study showed that, when used in good proportion, the combination of cellulose and basalt fiber can lead to a more balanced performance.

This study has three main parts. The first part was material tests, which revealed basic properties including advantages and disadvantages of the two fibers. Basalt fiber had much better high temperature stability than cellulose. The mass loss of cellulose was nearly 20 times that of basalt fiber. At the same time, thanks to its porous and ribbon type surface, the absorption of cellulose was more than 5 times that of basalt fiber. Results from the pH test showed that both fibers were weak alkaline. Stripping test and microscope electric scanning demonstrated that bond between cellulose and asphalt cement was better than that of basalt fiber. From these material properties, it is hypothesized that the two fibers can serve as a complement to each other to balance the performance of asphalt mixtures.

A series of performance tests were conducted in the second part to validate the hypothesis. Combinations of different cellulose-basalt fiber portions were introduced into SMA13. The total amount of fiber addition is set at 0.4% of asphalt mixture by weight, in accordance with relevant literature. Five portions 0 : 4, 1 : 3, 2 : 2, 3 : 1, and 4 : 0 as well as a control group (0 : 0) without any fiber were designed, and OAC was determined for each combination. With the increase in the cellulose, the OAC increased mainly because of the high absorption of cellulose. Volumetric properties changed as a result of the different asphalt content and fiber volumetric properties. The draindown tests showed that cellulose has a more significant influence on draindown. Performance tests including permanent deformation, low temperature bending, fatigue, and moisture damage were evaluated and compared. The mechanisms of the two fibers were also analyzed. The addition of cellulose fiber mainly increases asphalt content, increasing the fatigue performance and ductility at low temperature, whilst basalt fiber

TABLE 10: Costs of hybrid fibers and asphalt for 1 ton SMA with different fiber combinations.

Cellulose : basalt	Unit price of hybrid fiber (yuan/ton)	Cost of hybrid fiber (yuan/ton)	OAC (%)	Unit price of asphalt (yuan/ton)	Cost of asphalt (yuan/ton)	Total cost (yuan/ton)
0 : 4	10000	40	5.98	6000	338.4	378.4
1 : 3	8500	34	6.02	6000	340.8	374.8
2 : 2	7000	28	6.06	6000	342.6	370.6
3 : 1	5500	22	6.12	6000	346.2	368.2
4 : 0	4000	16	6.17	6000	348.6	364.6
0 : 0	0	0	5.41	6000	307.8	307.8

TABLE 11: Benefit-cost ratio of different fiber combinations for different characteristics.

Cellulose : basalt fiber	Draindown	Permanent deformation	Low-temperature strain	Fatigue	Moisture damage
0 : 4	2.118	1.524	-0.142	3.845	0.387
1 : 3	2.625	1.060	-0.114	6.377	0.496
2 : 2	3.081	0.988	0.106	9.827	0.576
3 : 1	3.786	0.553	0.268	12.492	0.507
4 : 0	4.180	0.435	0.385	14.659	0.364

works like reinforcement bars in the asphalt mixture due to its high strength and modulus. As a result, it improves the permanent deformation significantly and increases the deflection strength at low temperature but does not increase the fatigue much. However, due to its enforcement, the addition of basalt fiber improved the stress sensitivity of fatigue. As for moisture damage resistance, the combination of the two fibers with equal proportion showed the best performance. Although differences exist among different fiber combinations, SMA with fiber overall outperformed the control group in all tests. As the mechanisms of the two fibers are different, they have effects on different aspects of performance of asphalt mixture. Hybrid modification with cellulose and basalt fiber in asphalt mixture can produce more balanced asphalt mixture performances than adding only one fiber. A good example is shown in the low-temperature test that the addition of cellulose and basalt fiber increases the ductility and deflection strength at the same time. Another good demonstration is the fatigue test, in which the addition of cellulose increases fatigue resistance and the basalt fiber decreases stress sensitivity.

In the third part, economy was taken into consideration, as normally, the price of basalt fiber is over twice as much as cellulose. The increase of cellulose would increase the cost of asphalt, but the total cost is still much lower compared with that of basalt fiber. To help identify the optimum fiber combination, the benefit-cost ratio  $B$  was introduced to take into account the performance improvement with regard to cost. Altogether, compared with solely basalt fiber modification, hybrid modification with both cellulose fiber and basalt fiber can reduce the cost and improve the performance at the same time.

## 5. Conclusions

Cellulose and basalt fibers were introduced to SMA simultaneously to investigate the performance improvement through a series of laboratory tests. Main conclusions are as follows:

- (1) Cellulose fiber and basalt fiber have different material properties, and the basalt fiber has better high temperature stability while cellulose fiber has better absorption and bond with asphalt due to its porous surface.
- (2) The two fibers improve different aspects of SMA performance. Cellulose fiber improves drain down, ductility, and fatigue significantly; at the same time, basalt fiber contributes mainly on the improvement of permanent deformation, deflection strength, and stress sensitivity of fatigue. The existence of both basalt fiber and cellulose fiber improve the moisture damage resistance.
- (3) The mechanism of the two fibers is different. Addition of cellulose increases the asphalt content as well as its bond of the asphalt mixture. Basalt fiber, due to its good mechanical property of high strength and modulus, acts like reinforcement in the asphalt mixture.
- (4) The hybrid modification of SMA using cellulose fiber and basalt fiber can achieve a more balanced performance at an economical cost.

## Data Availability

The data used to support the study are available upon request from the corresponding author through e-mail (805296712@qq.com).

## Conflicts of Interest

The authors declare that there are no conflicts of interest regarding the publication of this paper.

## Acknowledgments

This study was funded by the National Key R&D Program Projects of China (2018YFB1600200); National Natural



Science Foundation of China (51678078); Natural Science Foundation of Hunan Province (2020JJ5578), and China Scholarship Council (201608430123).

## References

- [1] R. S. McDaniel, *NCHRP Synthesis 475: Fiber Additives in Asphalt Mixtures: A Synthesis of Highway Practice*, Transportation Research Board, Washington, DC, USA, 2015.
- [2] P. Peltonen, "Wear and deformation of characteristics of fiber reinforced asphalt pavements," *Construction and Building Materials*, vol. 5, no. 1, pp. 18–22, 1991.
- [3] A. Mahrez, M. Karim, and H. Katman, "Prospect of using glass fiber reinforced bituminous mixes," *Journal of the Eastern Asia Society for Transportation Studies*, vol. 5, pp. 794–807, 2003.
- [4] R. L. Fitzgerald, "Novel applications of carbon fiber for hot mix asphalt reinforcement and carbon-carbon pre-forms," MSc Thesis, Department of Chemical Engineering, Michigan Technological University, Houghton, MI, USA, 2000.
- [5] M. Guo and Y. Tan, "Interaction between asphalt and mineral fillers and its correlation to mastics' viscoelasticity," *International Journal of Pavement Engineering*, pp. 1–10, 2019.
- [6] S. Wu, Q. Ye, N. Li, and H. Yue, "Effects of fibers on the dynamic properties of asphalt mixtures," *Journal of Wuhan University of Technology -Material (Science Edition)*, vol. 22, no. 4, pp. 733–736, 2007.
- [7] M. Guo, H. Liu, Y. Jiao et al., "Effect of WMA-RAP technology on pavement performance of asphalt mixture: a state-of-the-art review," *Journal of Cleaner Production*, vol. 266, Article ID 121704, 2020.
- [8] Y. Tan and M. Guo, "Using surface free energy method to study the cohesion and adhesion of asphalt mastic," *Construction and Building Materials*, vol. 47, pp. 254–260, 2013.
- [9] Y. Zheng, Y. Cai, G. Zhang, and H. Fang, "Fatigue property of basalt fiber-modified asphalt mixture under complicated environment," *Journal of Wuhan University of Technology—Material (Science Edition)*, vol. 29, no. 5, pp. 996–1004, 2014.
- [10] S. Tapkin, "The effect of polypropylene fibers on asphalt performance," *Building and Environment*, vol. 43, no. 6, pp. 1065–1071, 2008.
- [11] H. Taherkhani, "Investigating the effects of nanoclay and nylon fibers on the mechanical properties of asphalt concrete," *Civil Engineering Infrastructure Journal*, vol. 49, no. 2, pp. 235–249, 2016.
- [12] J. J. Stempihar, M. I. Souliman, and K. E. Kaloush, "Fiber-reinforced asphalt concrete as sustainable paving material for airfields," *Transportation Research Record: Journal of the Transportation Research Board*, vol. 2266, no. 1, pp. 60–68, 2012.
- [13] E. R. Brown, R. B. Mallick, J. E. Haddock, and J. Bukowski, "Performance of stone matrix asphalt (SMA) mixtures in the United States," NCAT Report No.97-1, National Center for Asphalt Technology, Auburn, AL, USA, 1997.
- [14] E. R. Brown, J. E. Haddock, R. B. Mallick, and T. Lynn, "Development of A Mixture design procedure for stone matrix asphalt (SMA)," NCAT Report No.97-3, National Center for Asphalt Technology, Auburn, AL, USA, 1997.
- [15] H. Chen and Q. Xu, "Experimental study of fibers in stabilizing and reinforcing asphalt binder," *Fuel*, vol. 89, no. 7, pp. 1616–1622, 2010.
- [16] Q. Ye and S. Wu, "Rheological properties and fiber reinforced asphalt binders," *Indian Journal of Engineering and Materials Sciences*, vol. 16, no. 2, pp. 93–99, 2009.
- [17] Y. Decoene, "Contribution of cellulose fibers to the performance of porous asphalts," *Transportation Research Record: Journal of the Transportation Research Board*, vol. 1265, pp. 82–86, 1990.
- [18] L. A. Cooley Jr., E. R. Brown, and D. E. Watson, "Evaluation of open-graded friction course mixtures containing cellulose fibers," *Transportation Research Record: Journal of the Transportation Research Board*, vol. 1723, pp. 19–25, 2000.
- [19] K. D. Stuart and P. Malmquist, "Evaluation of using different stabilizers in US route 15 (Maryland) stone matrix asphalt," *Transportation Research Record: Journal of the Transportation Research Board*, vol. 1454, pp. 48–57, 1994.
- [20] K. Singha, "A short review on basalt fiber," *International Journal of Textile Science*, vol. 1, no. 4, pp. 19–28, 2012.
- [21] N. Morova, "Investigation of usability of basalt fibers in hot mix asphalt concrete," *Construction and Building Materials*, vol. 47, pp. 175–180, 2013.
- [22] ASTM D3800-16, *Standard Test Method for Density of High-Modulus Fibers*, ASTM International, West Conshohocken, PA, USA, 2016.
- [23] ASTM D5034-17, *Standard Test Method for Breaking Strength and Elongation of Textile Fabrics (Grab Test)*, ASTM International, West Conshohocken, PA, USA, 2017.
- [24] S. M. Abtahi, M. Sheikhzadeh, and S. M. Hejazi, "Fiber-reinforced asphalt-concrete - a review," *Construction and Building Materials*, vol. 24, no. 6, pp. 871–877, 2010.
- [25] G. R. Hicks, *Moisture Damage in Asphalt Concrete*, Transportation Research Board, National Research Council, Washington, DC, USA, 1991.
- [26] JTG F40-2017, *Technical Specification For Construction Of Highway Asphalt Pavements*, China Communications Press, Beijing, China, 2017.
- [27] JT/T 533-2004, *Plant Fibers Used in Asphalt Pavements*, China Communications Press, Beijing, China, 2004.
- [28] ASTM (D6390-11), *Standard Test Method for Determination of Draindown Characteristics in Uncompacted Asphalt Mixtures*, ASTM, West Conshohocken, USA, 2017.
- [29] JTE E20-2011, *Standard Test Methods of Binder and Bituminous Mixtures for Highway Engineering*, China Communications Press, Beijing, China, 2011.
- [30] ASTM (D7460-10), *Standard Test Method for Determining Fatigue Failure of Compacted Asphalt Concrete Subjected to Repeated Flexure Bending*, ASTM, West Conshohocken, USA, 2010.
- [31] ASTM (D4867M-09), *Standard Test Method for Effect of Moisture on Asphalt Concrete Paving Mixtures*, ASTM, West Conshohocken, USA, 2014.

## Research Article

# Evaluating the Physical and Rheological Properties of Rejuvenated Styrene-Butadiene-Styrene-Modified Asphalt Binders

Xiaobing Chen <sup>1</sup>, Juntian Wang,<sup>1</sup> Xiaorui Zhang <sup>1</sup>, Han Liu,<sup>2</sup> Jinhu Tong,<sup>1</sup>  
and Ronglong Zhao<sup>1</sup>

<sup>1</sup>School of Transportation, Southeast University, Nanjing 211189, China

<sup>2</sup>Municipal Transportation Design Branch, The Architectural Design and Research Institute of Zhejiang University, Hangzhou 310028, China

Correspondence should be addressed to Xiaobing Chen; [xbchen@seu.edu.cn](mailto:xbchen@seu.edu.cn) and Xiaorui Zhang; [zxr@seu.edu.cn](mailto:zxr@seu.edu.cn)

Received 30 May 2020; Revised 19 July 2020; Accepted 1 August 2020; Published 28 August 2020

Guest Editor: Zhen Leng

Copyright © 2020 Xiaobing Chen et al. This is an open access article distributed under the Creative Commons Attribution License, which permits unrestricted use, distribution, and reproduction in any medium, provided the original work is properly cited.

To evaluate the physical and rheological properties of rejuvenated styrene-butadiene-styrene-modified asphalt (SBSMA) binders designed for rapid in-place pavement recycling, an aged SBSMA binder was rejuvenated with three rejuvenators (i.e., Types I, II, and III) in different dosages. The physical properties of rejuvenated SBSMA were obtained to determine the optimal type and dosage of rejuvenators for the first and second rejuvenation. Performance grade (PG) tests, multiple stress creep recovery (MSCR) tests, and linear amplitude sweep (LAS) tests were conducted to measure the rheological properties using the dynamic shear rheometer (DSR) and bending beam rheometer (BBR). The results exhibited that the rejuvenators could soften the multiple aged binder and enhance its high- and low-temperature performance. The rejuvenation effect of rejuvenator Type I with the optimal dosage of 6~8% was the most appropriate for the first rejuvenation. The optimal dosage of the second rejuvenation was 10~12%. The addition of rejuvenators decreased the rutting factor ( $G^*/\sin \delta$ ), creep stiffness ( $S$ ), delta  $T_c$  ( $\Delta T_c$ ) parameter, recovery response ( $R$ ), and yield stress of rejuvenated SBSMA. On the other hand, an increase in the rate of relaxation ( $m$ -value), nonrecoverable creep compliance ( $J_{nr}$ ), and yield strain of rejuvenated SBSMA was recorded. Overall, the study findings indicated an improvement in the elastic properties of rejuvenated SBSMA, which contributes to improving the rutting, thermal, and fatigue cracking resistance of asphalt binder and ultimately the response of asphalt pavements.

## 1. Introduction

Asphalt binder, which is a by-product of petroleum, is an essential material used in the construction of flexible pavements [1]. Styrene-butadiene-styrene (SBS) polymer, which is an elastomer thermoplastic polymer, is widely used as an asphalt binder modifier to enhance the high- and low-temperature performance of asphalt mixtures [2]. However, aging and degradation of the SBS-modified asphalt (SBSMA) binders under the actions of oxygen, sunlight, rainfall, and vehicle loading can detrimentally deteriorate the performance of asphalt mixtures and eventually lead to pavement failures [3, 4]. The aging phenomenon usually encompasses some internal changes in the chemical composition of the asphalt binder that ultimately leads to changes in the overall

structural integrity of the asphalt mixture. For instance, because of the oxidation of the naphthalene aromatics and the polar aromatics, the ratio of asphaltene to maltene of aged SBSMA tends to increase [5]. The aged asphalt binder usually turns into a gel-type asphalt binder that exhibits low ductility, high stiffness, and high thixotropy [6]. The aging of SBS-modified asphalt binder is a combination of asphalt phase oxidation and polymer phase degradation [7]. The chain scission reaction at polybutadiene (PB) segments plays a primary role in the thermooxidative degradation of SBS polymer [8]. The PB segments containing the unsaturated double carbon bonds (C=C) are easy targets to oxygen and degrade rapidly into smaller polymer chains under the effect of heat and ultraviolet light (UV) [9, 10]. Because of increased modulus due to oxidation and low SBS modification,

asphalt mixtures also tend to be brittle with a high propensity to thermal and fatigue cracking [11, 12].

Asphalt mixtures are self-healing materials. In other words, under certain energy conditions, the microcracks can be self-repaired [13]. To enhance (and expedite) this self-repairing process, rejuvenators are often added to aged asphalt binders to soften them and make the rejuvenated asphalt binders more fluid so as to be able to infiltrate into and fill up the cracks [14]. Rapid in-place pavement recycling is a preventive maintenance technology based on spraying the rejuvenator onto the aged pavement surface to seal off the cracks and soften the asphalt binder. Compared with other asphalt pavement recycling technologies, Liu [15] asserts that rapid in-place pavement recycling technology is quick, time-efficient, and the most economical and effective solution for asphalt pavement preservation.

As reported in the literature, rejuvenators have the potential to recover and enhance the material properties and mechanical performances of aged SBSMA [16]. However, having and/or injecting an optimum amount of rejuvenator is one of the key aspects of achieving the desired material properties and enhanced performance characteristics [17]. Balanced rejuvenating design based on multicriteria evaluation has been used by many researchers to optimize the rutting, cracking, and fatigue performances of asphalt binders [18, 19]. Koudelka et al. [20] used two rheological parameters: the Glover-Rowe (G-R) parameter obtained from the dynamic shear rheometer (DSR) tests and the delta  $T_c$  ( $\Delta T_c$ ) obtained from the bending beam rheometer (BBR) tests to determine the optimum dosages of recycling agents. Elkashef et al. [21] found that the extent of rejuvenation/regeneration of the soybean-derived rejuvenator was more pronounced for the stiffer binders. Shen et al. [22] investigated the changes in molecular weights of crumb rubber-modified asphalt binders both after aging and after rejuvenation. The addition of rejuvenator was found to have reduced the macromolecular substances and increased the micromolecular substances of aged asphalt binders. Zau-manis et al. [23] proved that the recycled asphalt mixtures with six rejuvenators could ensure excellent rutting and cracking resistances while providing longer fatigue life. Cui et al. [24] found that the rejuvenator can alleviate the self-aggregation of asphaltenes but cannot completely restore the colloidal structure of the aged asphalt binders by the means of molecular dynamics (MD) simulations. The rejuvenator/recycling agent could deagglomerate the oxidized asphaltenes, which led to a concurrent increase in the crossover modulus and crossover frequency of aged binder [25]. Xu et al. [26] studied the rejuvenator diffusion behavior and thermodynamic properties of asphalt binder using all-atom MD simulations.

Traditional grading parameters of asphalt binders such as penetration, softening point, and viscosity cannot fully reflect the viscoelasticity of asphalt binders. In particular, these parameters have been considered to be insufficient in characterizing the performances of asphalt binders at high temperatures [27]. Furthermore, the Superpave rutting parameter  $G^*/\sin \delta$  has been reported to exhibit poor correlation with the rutting resistance of polymer-modified

asphalt mixtures measured in the laboratory [28]. Multiple stress creep recovery (MSCR) test, developed by D'Angelo et al. [29], can more fundamentally represent the nonlinear viscoelastic behavior of asphalt binders over a range of high temperatures [30, 31].

Similarly, the Superpave fatigue parameter,  $G^*/\sin \delta$ , could not accurately estimate the maximum fatigue life of asphalt mixtures under nonlinear viscoelastic loading [32]. The viscoelastic continuum damage (VECD) theory is a novel approach used to characterize the fatigue behavior of viscoelastic materials. Linear amplitude sweep (LAS) test has been developed based on VECD theory and provides more reliable parameters to estimate and quantify the fatigue life of asphalt binders at varying stress levels [33, 34].

The primary aim of this study was to investigate the effects of rejuvenators on the physical and rheological performances of the aged and rejuvenated SBSMA. The optimal types and dosages of rejuvenators were determined based on multicriteria evaluation to provide a laboratory assessment framework for rapid in-place pavement recycling. Because the performance evaluation of rejuvenated asphalt binders is often limited to traditional grading parameters such as viscosity, penetration, and softening point, another aim of this study was to evaluate the rutting and fatigue characteristics of rejuvenated SBSMA through measurement and quantification of their rheological properties using the MSCR and LAS tests.

## 2. Materials and Test Methods

**2.1. Asphalt Binders and Rejuvenators.** The basic properties of the Shell SBS-modified asphalt binders are listed in Table 1. The amount of SBS polymer incorporated in asphalt binder was 4.5%. The rejuvenator was prepared with a heavy naphthenic base oil and the polymer-modified asphalt. The principal properties of three rejuvenators used, designated as Types I, II, and III, respectively, are similarly listed in Table 2. The samples of three rejuvenators are shown in Figure 1.

**2.2. Laboratory Experimentation.** Agings of the SBSMA were accomplished using the rolling thin-film oven test (RTFOT, aging at 163°C for 5 h) and pressurized aging vessel test (PAV, aging at 100°C for 20 h under 2.1 MPa of air pressure) according to ASTM D2872 and ASTM D6521, respectively. RTFOT was used to simulate the short-term aging of the SBSMA at the construction stage such as production, mixing, transporting, and paving processes. PAV was employed to simulate the long-term field aging of the SBSMA at the service stage.

The virgin SBSMA was aged by RTFOT and PAV to obtain the first aged SBSMA. Then the first aged SBSMA was blended with the three rejuvenators at a mixing temperature 140~160°C for 30 min to prepare the first rejuvenated SBSMA. The rejuvenator at dosages/contents was 2%, 4%, 6%, 8%, and 10%, respectively, by weight of aged asphalt binders.

Because there is no heating applied on the aged asphalt mixtures through the rapid in-place pavement recycling, the

TABLE 1: The basic properties of SBS-modified asphalt binders.

Properties	Methods	Limits	Values
<i>Virgin asphalt binders</i>			
Penetration at 25°C (0.1 mm)	ASTM D5	40~60	51
Softening point (°C)	ASTM D36	≥60	79
Ductility at 5°C (cm)	ASTM D113	≥20	26
Elastic recovery at 25°C (%)	ASTM D6084	≥70	88
Storage stability, ΔSoft. Points, 48 h (°C)	ASTM D5976	≤2.5	1.5
Solubility in trichloroethane (%)	ASTM D2042	≥99	99.5
Flash point COC (°C)	ASTM D92	≥230	280
Viscosity at 135°C (Pa·s)	ASTM D4402	≤3	1.5
<i>RTFOT residues</i>			
Mass loss (%)	ASTM D2872	≤0.6	0.2
Penetration ratio at 25°C (%)	ASTM D5	≥65	69
Ductility at 5°C (cm)	ASTM D113	≥15	17

second aging of SBSMA is a long-term aging. The first rejuvenated SBSMA with optimal types and dosages of rejuvenators (I + 6%, I + 8%, II + 6%, and II + 8%) was aged by PAV and then rejuvenated with rejuvenators Type I and Type II to obtain the second rejuvenated SBSMA. The rejuvenators at dosage increments were 0%, 2%, 4%, and 6%. Thereafter, the aged and rejuvenated SBSMA were tested to evaluate and quantify their physical and rheological properties (Figure 2).

**2.3. Physical Property Tests.** Physical properties of the aged and rejuvenated SBSMA, including penetration (25°C), softening point, and ductility (5°C), were tested as per ASTM D5, ASTM D36, and ASTM D113, respectively.

**2.4. Rheological Property Tests.** Dynamic rheological properties of the virgin, aged, and rejuvenated SBSMA were performed using the DSR (Discovery HR-1, TA Instruments, USA) and the BBR (TE-BBR, Cannon, USA).

**2.4.1. Dynamic Shear Rheometer Test.** Temperature sweep tests were carried out using DSR at the strain-controlled mode. The temperature range was 64~82°C with increment of 6°C. The asphalt binder specimens were molded to a diameter of 25 mm by 1 mm thick. High-temperature PG was determined based on the established rutting factor criteria ( $G^*/\sin \delta = 2.2$  kPa) as per ASTM D6373.

**2.4.2. Bending Beam Rheometer Test.** The low-temperature PG was estimated using the BBR at two test temperatures (-12°C and -18°C). Low-temperature PG was determined based on the thermal cracking criteria ( $S(t) = 300$  MPa,  $m$ -value = 0.3) in accordance with ASTM D6373. The  $S(t)$  and  $m$ -value were estimated using equations (1) and (2) as per ASTM D6648. The  $\Delta T_c$  parameter was developed by Anderson et al. [35] to evaluate age-related cracking

potential. Delta  $T_c$  ( $\Delta T_c$ ) parameter, described as in equation (5), is defined as the numerical difference between two low continuous grading temperatures obtained from the BBR stiffness and  $m$ -value criteria [36]:

$$S(t) = \frac{PL^3}{4bh^3\delta(t)}, \quad (1)$$

$$m(t) = \left| \frac{\text{dlog } S(t)}{\text{dlog } (t)} \right|, \quad (2)$$

$$T_{c,S} = T_1 + \left( \frac{(T_1 - T_2) \times (\log 300 - \log S_1)}{\log S_1 - \log S_2} \right) - 10, \quad (3)$$

$$T_{c,m} = T_1 + \left( \frac{(T_1 - T_2) \times (0.3 - m_1)}{m_1 - m_2} \right) - 10, \quad (4)$$

$$\Delta T_c = T_{c,S} - T_{c,m}, \quad (5)$$

where  $S(t)$  is the creep stiffness at loading time  $t$  (MPa);  $m(t)$  is the rate of relaxation,  $m$ -value, at loading time  $t$ ;  $P$  is the applied load (N);  $L$  is the span length (mm);  $b$  is the width of the asphalt binder beam (mm);  $h$  is the depth of the asphalt binder beam (mm);  $\delta(t)$  is the deflection of the asphalt binder beam at time  $t$  (mm);  $S_i$  is the creep stiffness at temperature  $T_i$  (MPa);  $m_i$  is the rate of relaxation at temperature  $T_i$ ;  $T_{c,S}$  is the critical temperature where  $S = 300$  MPa (°C);  $T_{c,m}$  is the critical temperature where  $m = 0.3$  (°C); and  $\Delta T_c$  is the numerical difference between  $T_{c,S}$  and  $T_{c,m}$  (°C).

**2.4.3. Multiple Stress Creep Recovery (MSCR) Test.** The MSCR tests were performed at 70°C in accordance with the ASTM D7405 test procedure. Two loading stress levels of 0.1 kPa and 3.2 kPa were used. Each stress level had 10 repeated cycles with creep stage of 1 s-loading and recovery stage of 9 s-unloading. The total test time for one specimen was 200 s. In this study, the MSCR test was used to characterize the high-temperature rheological behavior and stress-related rutting resistance of rejuvenated SBSMA. Percent recovery ( $R$ ) parameter and nonrecoverable creep compliance ( $J_{nr}$ ) were used to characterize the recovery properties and high-temperature performance of asphalt binders. The stress sensitivity index ( $J_{nr-diff}$ ), defined as the percentage difference of the  $J_{nr}$  at two stress levels, was used to evaluate the stress sensitivity of the rejuvenated SBSMA to traffic loading.

**2.4.4. Linear Amplitude Sweep (LAS) Test.** The LAS test was used to evaluate the fatigue behavior of the rejuvenated SBSMA. The asphalt binder specimens were molded to a diameter of 8 mm by 2 mm thick. In this study, the LAS test was conducted at 25°C in accordance with the AASHTO TP101 test procedure. The procedure of the LAS test was comprised of two steps. First, the frequency sweep test with a frequency range of 0.1~30 Hz was performed at a low strain level of 0.1% to obtain the undamaged property of specimen ( $\alpha$ ) and fatigue parameter  $A$ . Then, the amplitude sweep test in strain-controlled mode was conducted at 10 Hz for 300 s.

TABLE 2: The principal properties of rejuvenators Types I, II, and III.

Properties	Methods	Rejuvenators		
		Type I	Type II	Type III
<i>Test on emulsions</i>				
Viscosity at 25°C (SFS)	ASTM D7496	25~150	20~60	25~150
Residue (%)	ASTM D6934	>64	60~65	>64
Miscibility test	ASTM D6999	Nonseparation	Nonseparation	Nonseparation
Sieve test (%)	ASTM D6933	<0.1	<0.1	<0.1
Particle charge test	ASTM D7402	Positive	Positive	Positive
Cement mixing test (%)	ASTM D6935	<2	<2	<2
Pumping stability <sup>1</sup>		Pass	Pass	Pass
<i>Tests on residue from distillation test</i>				
Viscosity at 60°C (cSt)	ASTM D2170	1000~4000	200~500	1000~4000
Asphaltenes (%)	ASTM D2007	<11.2	2~4	<11
Maltene distribution ratio (PC + A <sub>1</sub> )/(S + A <sub>2</sub> ) <sup>2</sup>	ASTM D2007	0.8~1.5	0.5~0.9	0.7~1.1
PC/S ratio <sup>2</sup>	ASTM D2007	>1.2	>1.2	>0.5

Note: 1: pumping stability is tested by pumping 475 mL of rejuvenators, diluted one part concentrate to one part water, at 25°C, through a 6 mm gear pump operating 1750 rpm for 10 minutes with no significant separation or coagulation. 2: PC is a polar compound; A<sub>1</sub> is the first acidaffins; A<sub>2</sub> is the second acidaffins; S is the saturated hydrocarbons.

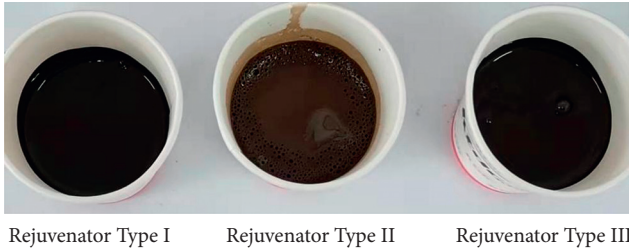


FIGURE 1: Samples of rejuvenators Types I, II, and III.

The amplitude of sine wave load form increased linearly from 0.1% to 30%. The LAS test data was processed and analyzed using a VECD model approach to determine the fatigue parameters  $A$  and  $B$ . Given the fundamental nature of these fatigue parameters, the fatigue life of the asphalt binder can be estimated through the fatigue model given in

$$N_f = A(\gamma_{\max})^{-B}, \quad (6)$$

$$A = \frac{f(D_f)^{(1+(1-C_2)\alpha)}}{(1+(1-C_2)\alpha) \times (\pi C_1 C_2)^\alpha}, \quad (7)$$

$$B = -2\alpha, \quad (8)$$

where  $N_f$  is the fatigue life;  $\gamma_{\max}$  is the estimated maximum strain (%);  $A$  and  $B$  are the fatigue parameters;  $f$  is the loading frequency (Hz);  $D_f$  is the failure point at a 35% reduction in the initial specimen modulus;  $\alpha$  is the undamaged property of the specimen; and  $C_1$  and  $C_2$  are the fitting factors of the power-law model.

### 3. Test Results, Analysis, and Discussions

**3.1. Physical Properties of Rejuvenated SBSMA.** Figure 3 shows the physical properties of the first and second rejuvenated SBSMA with different types and dosages of rejuvenators.

**3.1.1. The First Rejuvenated SBSMA.** With the increase of the rejuvenator dosage, the penetration and ductility of rejuvenated SBSMA increased, while the softening point decreased (Figures 3(a), 3(c), and 3(e)). When the rejuvenator dosage was 0~4%, the penetration improvement of aged SBSMA was Type III > Type I > Type II. When the rejuvenator dosage was 4~10%, the efficiency of Type III on penetration improvement was weaker than that of Type I and Type II (Figure 3(a)). A small amount of rejuvenator could obviously reduce the softening point of aged SBSMA, but the further addition of rejuvenator had not a significant effect as before. Compared with Type I and Type III, Type II had a weaker effect on reducing the softening point (Figure 3(c)). For each 1% rejuvenator added to the aged SBSMA, the ductility of the rejuvenated SBSMA could be increased by about 1 cm. The ductility improvement of aged SBSMA was Type I  $\approx$  Type II > Type III (Figure 3(e)). Therefore, the asphalt blends with rejuvenators Type I and Type II exhibited improved low-temperature crack resistance. The rejuvenators containing the maltenes could effectively reduce the consistency and restore the temperature sensitivity of aged SBSMA. The physical properties of the first rejuvenated SBSMA with 6~8% rejuvenators were closest to those of RTFOT residues. The rejuvenation effect of Type I and Type II with the optimal dosage of 6~8% was superior to that of Type III for the first rejuvenation.

**3.1.2. The Second Rejuvenated SBSMA.** After the second aging of SBSMA, the addition of rejuvenators could still rejuvenate the second aged SBSMA and improve the physical properties of the second rejuvenated SBSMA (Figures 3(b), 3(d), and 3(f)). The physical properties of the second rejuvenated SBSMA were linearly related to the increments of rejuvenator dosages. However, the second rejuvenation was more difficult than the first rejuvenation. In order to recover the performance loss of the second aging, the second rejuvenation of SBSMA needed to increase the dosage of rejuvenator. When the rejuvenator dosage was increased by 4%,

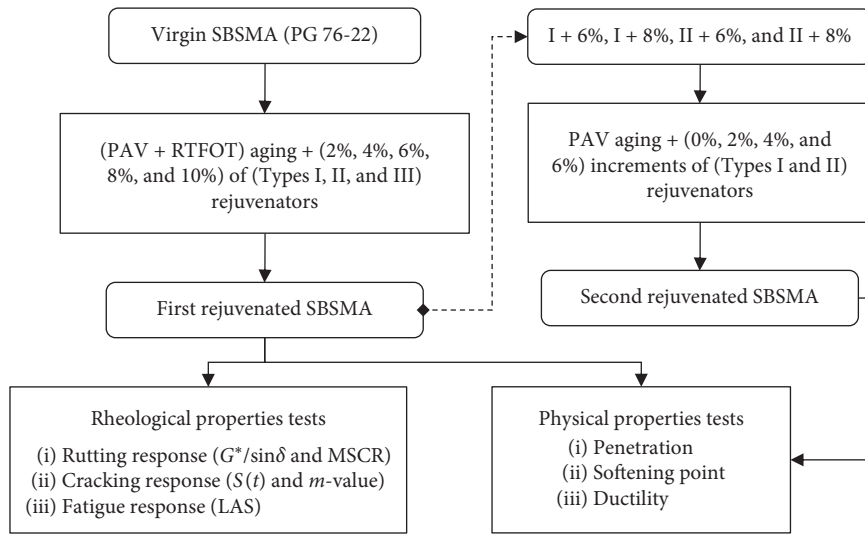


FIGURE 2: Flowchart of experimental plan.

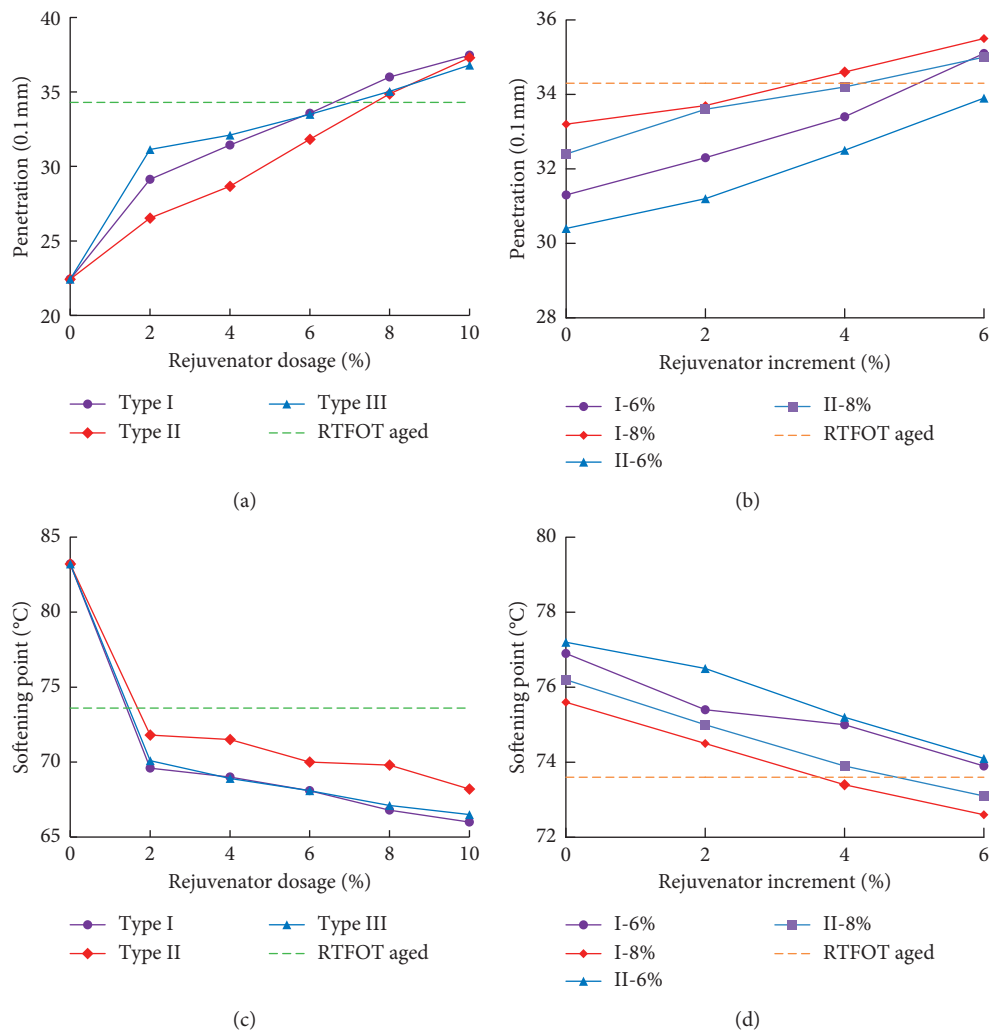


FIGURE 3: Continued.

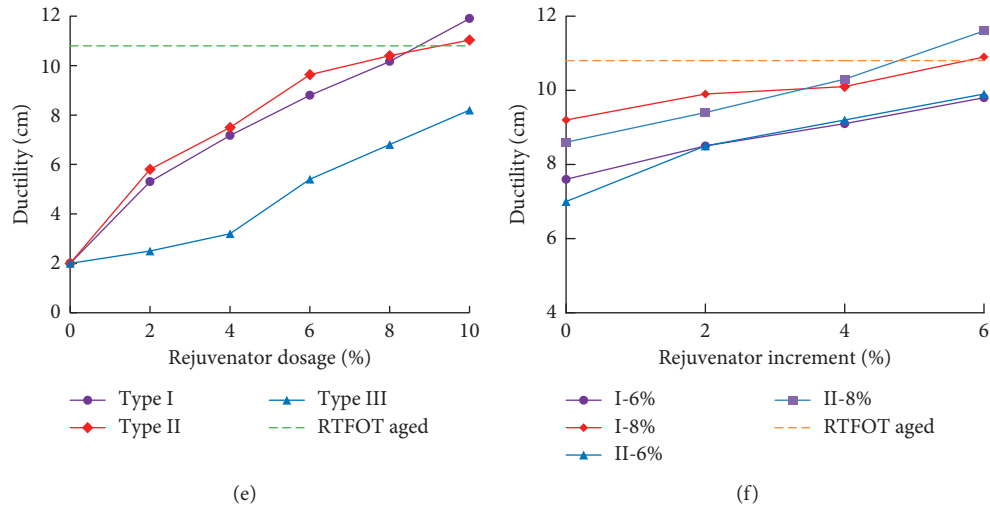


FIGURE 3: Physical properties of the first and second rejuvenated SBSMA. The first rejuvenation (a, c, e); the second rejuvenation (b, d, f).

the effects of the first rejuvenation could be achieved in the second rejuvenation, suggesting the feasibility of multiple rejuvenation of aged SBSMA. Thus, the optimal rejuvenator dosage of the second rejuvenation was 10~12%.

### 3.2. Rheological Properties of Rejuvenated SBSMA

**3.2.1. Dynamic Shear Rheometer Test.** Figure 4 shows the rutting factors ( $G^*/\sin \delta$ ) of the rejuvenated SBSMA with different dosages of three types of rejuvenators. After PAV aging, the rutting factors of SBSMA increased, indicating that the aging strengthened the elastic behavior and the rutting resistance of the virgin SBSMA. The rutting factors decreased with the increases of the rejuvenator dosages and the temperatures, which revealed that the rejuvenators could effectively soften the aged SBSMA and decrease the deformation resistance of the asphalt binders. However, the rutting factors of rejuvenated SBSMA should be higher than those of virgin SBSMA. It is suggested that the dosage of rejuvenators should be controlled within 8%. Under the same rejuvenator dosage (6%), the rejuvenation efficiency of the rejuvenators was Type I  $\approx$  Type III > Type II. The maltene distribution ratio of Types I and III was larger than that of Type II. The rejuvenation efficiency of rejuvenator depended on the ability to restore the original chemical ratio of the asphalt binder components. The rutting factor of the rejuvenated SBSMA with 6% rejuvenator Type I was basically consistent with that of the virgin SBSMA.

**3.2.2. Bending Beam Rheometer Test.** Figures 5(a) and 5(b) illustrate the creep stiffness ( $S(t)$ ) and the rate of relaxation ( $m$ -value) of the different rejuvenated SBSMA. The  $S(t)$  value and  $m$ -value reflect the flexibility of asphalt binders at low-temperature. In general, the asphalt binder with lower  $S(t)$  and higher  $m$ -value have improved low-temperature crack resistance potential. After PAV aging, an increase in  $S(t)$  value and a decrease in the  $m$ -value weaken the resistance to

slow crack growth of SBSMA, increasing the risks of thermal cracking. In general, the low-temperature performance of asphalt binder is related to the proportion of larger molecules. During the aging process, the light components of asphalt binder volatilized, and the polymerization of small molecules increased the proportion of large molecules [22]. The additions of rejuvenators could replenish the small molecules, which were lost in the aging process, and adjust the proportions of asphalt components, thus enhancing the crack resistance of asphalt binder. The additions of rejuvenators decreased the  $S(t)$  value and increased the  $m$ -value of aged SBSMA, indicating that the rejuvenators could recover the low-temperature elasticity and improve the crack resistance of aged SBSMA. Among three rejuvenators, the SBSMA rejuvenated with rejuvenators Type I and Type II had a higher  $S(t)$  value and a lower  $m$ -value, indicating that these asphalt blends had more potential to resist thermal cracking and age-related embrittlement distresses.

Figure 5(c) demonstrates that  $\Delta T_c$  values of rejuvenated asphalt binder are quite different for different types and dosages of rejuvenators. Li et al. [37] have suggested limiting  $\Delta T_c$  at  $-5^\circ\text{C}$  to avoid nonload related cracking due to poor relaxation properties of asphalt binders. The  $\Delta T_c$  values of PAV aged and I-10% binders were  $-8.7^\circ\text{C}$  and  $-5.7^\circ\text{C}$ , respectively, failing to meet minimum  $\Delta T_c$  criteria. All binders were  $m$ -controlled with negative  $\Delta T_c$  values. More  $m$ -controlled binder might tend to thixotropically harden and exhibit brittle behavior when exposed to thermal stresses. Rejuvenated binders tended to have lowly negative  $\Delta T_c$  values. For all rejuvenated binders, a positive increase in the value of  $\Delta T_c$  indicated an enhancement in the stress relaxation ability and less age-related cracking potential of the rejuvenated binders. Excessive dosage of rejuvenator Type I should be avoided to ensure the durability of asphalt binder.

**3.2.3. Superpave Performance Grade.** Superpave PG of the different rejuvenated SBSMA is provided in Figure 6. The high failure temperature of the rejuvenated SBSMA

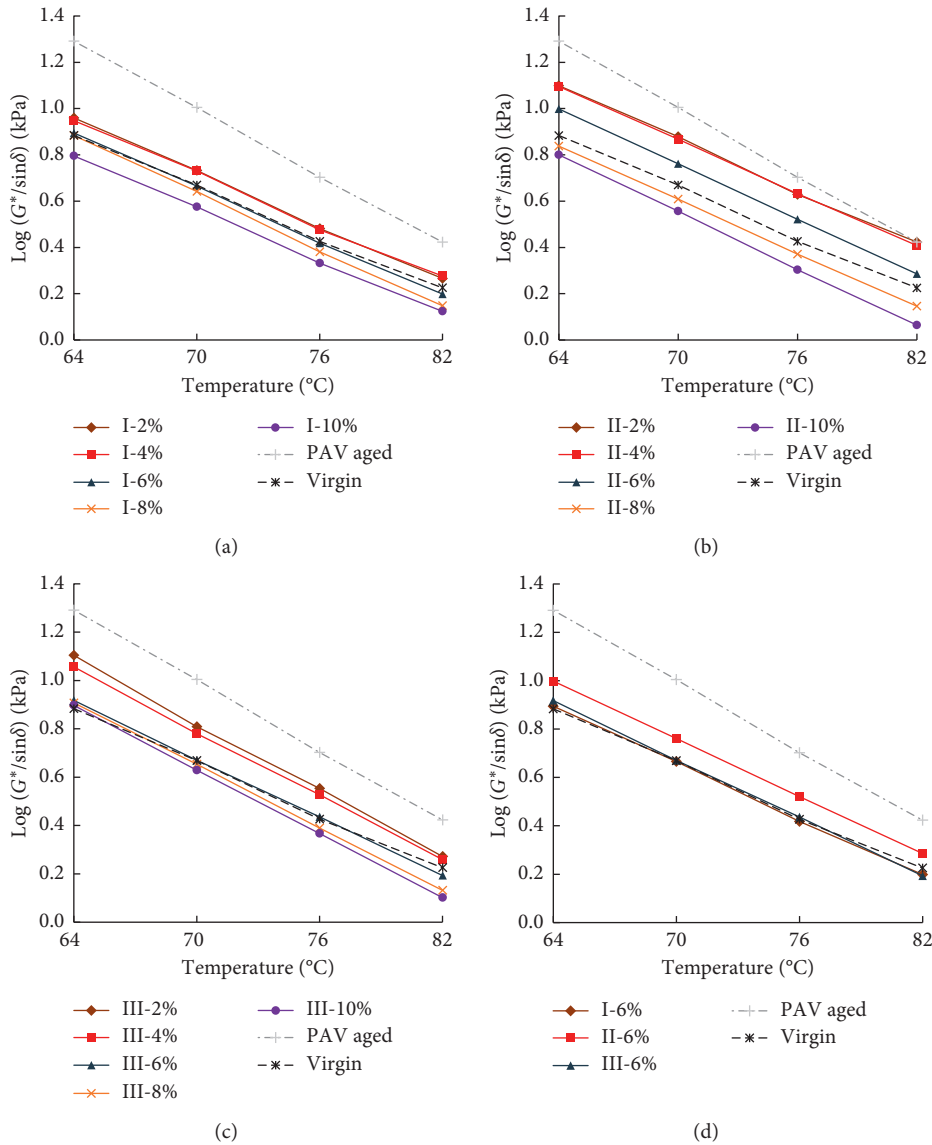


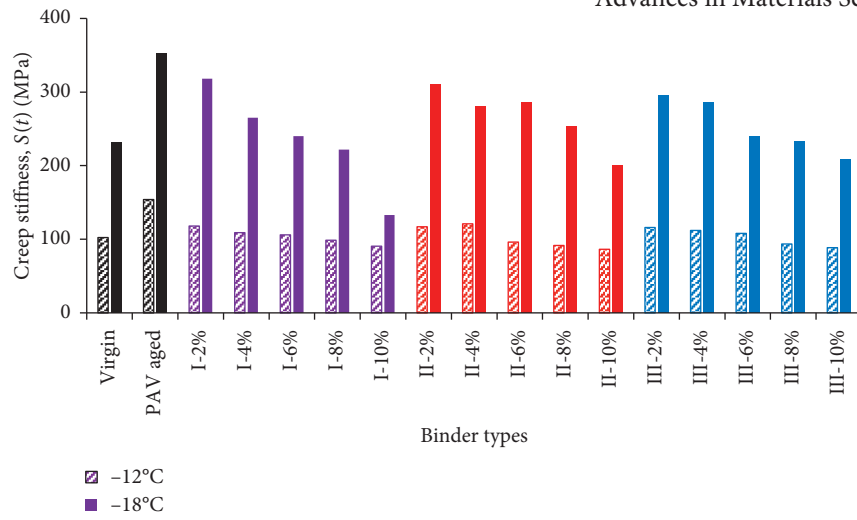
FIGURE 4: Variations of rutting factors with the types and dosages of rejuvenators. (a) Rejuvenator Type I; (b) rejuvenator Type II; (c) rejuvenator Type III; (d) rejuvenator dosage is 6%.

decreased with the increases of the rejuvenator dosages, indicating the softening and regenerating effects of rejuvenators to the aged SBSMA. Similarly, the critical low failure temperature decreased with the additions of rejuvenators exhibited improvement in the flexibility of SBSMA. Rejuvenators that had affinity for various fractions of the asphalt binder would enhance the high- and low-temperature performances of the aged binder through restoration of the original binder asphaltenes-to-maltenes ratio. The addition of 6~8%, by weight of aged SBSMA, of rejuvenator Type I could achieve the target PG of virgin SBSMA, PG 76-22.

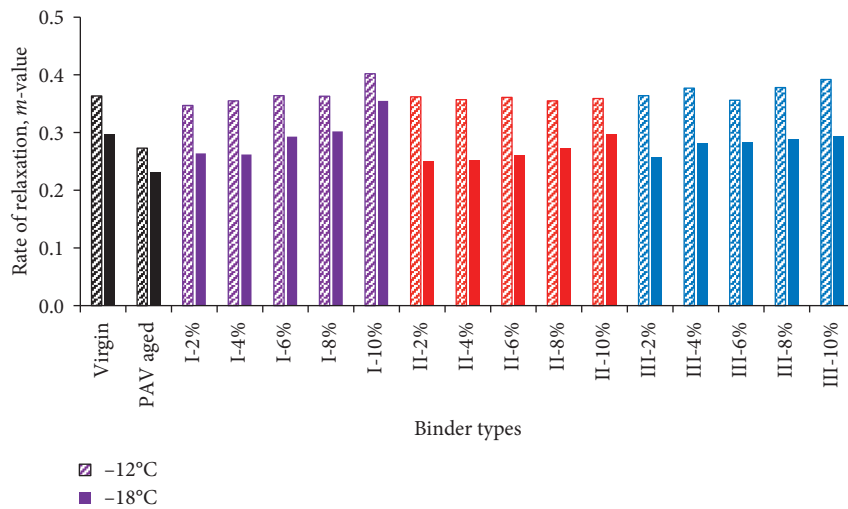
3.2.4. Rutting Performance Based on the MSCR Test. Figures 7(a) and 7(b) show the recovery responses of rejuvenated SBSMA with different types and contents of the

rejuvenators at the stress levels of 0.1 kPa and 3.2 kPa, respectively. A decrease in the recovery response ( $R$ ) and an increase in the nonrecoverable creep compliance ( $J_{nr}$ ) were observed in the rejuvenated asphalt binder suggesting a significant rejuvenation of the asphalt binders. However, as the rejuvenator dosage increased, the  $R$  value decreased while the  $J_{nr}$  value increased indicating a decay in the rutting resistance characteristics. A slight fluctuation of  $R$  value indicated the limited effects of rejuvenators on the recovery performance of the rejuvenated SBSMA. In general, the blends with 4~6% rejuvenators exhibited good stress and strain recovery performance. Additionally, the changes in the  $J_{nr3.2}$  value (with a high stress level) were higher than the  $J_{nr0.1}$  value (with a low stress level), implying severe rutting risks of rejuvenated asphalt binders under heavy traffic loading, particularly in elevated temperature environments [12].

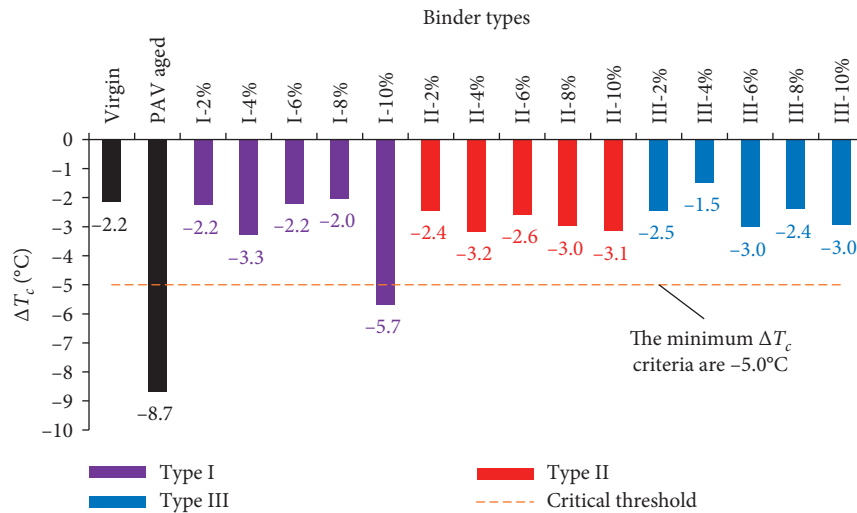




(a)



(b)



(c)

FIGURE 5: Effects of the types and dosages of rejuvenators on (a) creep stiffness ( $S(t)$ ); (b) rate of relaxation ( $m$ -value); (c) difference of BBR creep or  $m$  critical temperature, delta  $T_c$  ( $\Delta T_c$ ).

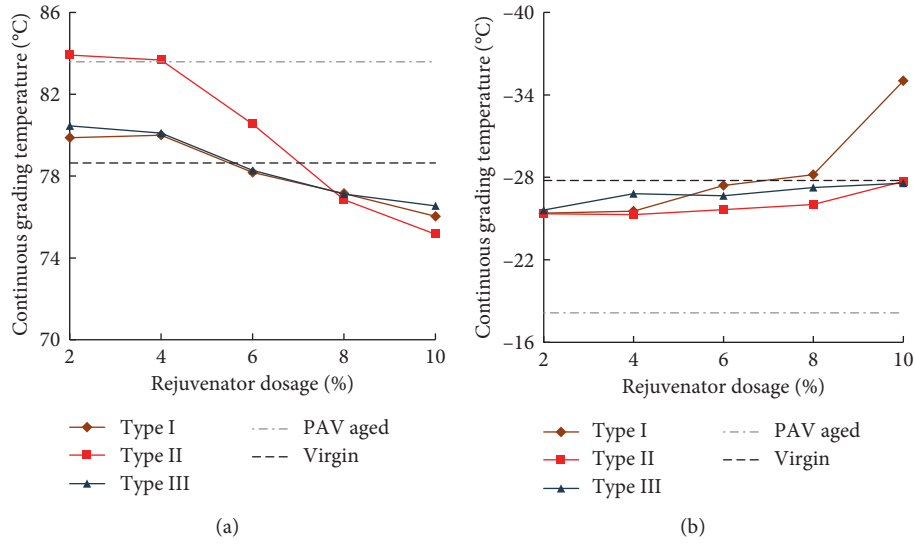


FIGURE 6: Superpave PG of different rejuvenated SBSMA. (a) High-temperature continuous grade; (b) low-temperature continuous grade.

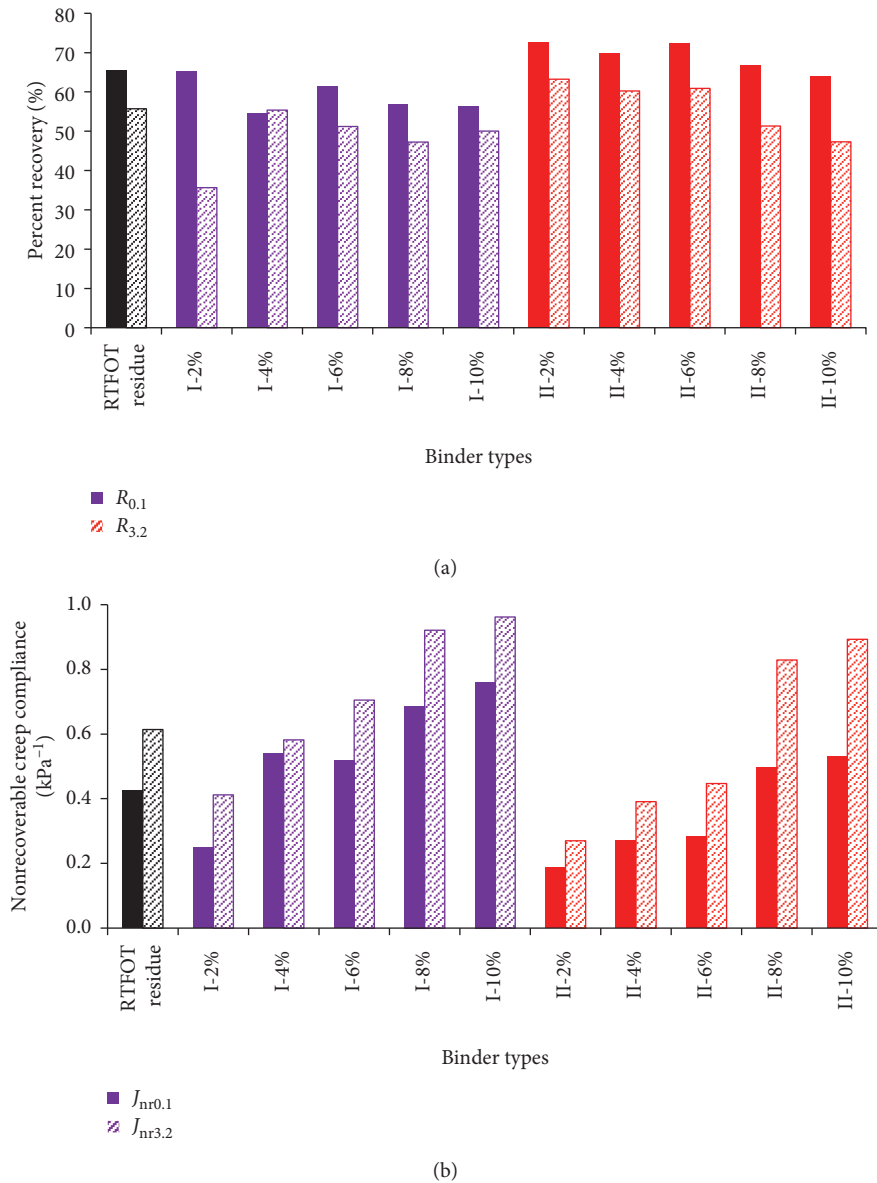


FIGURE 7: Continued.

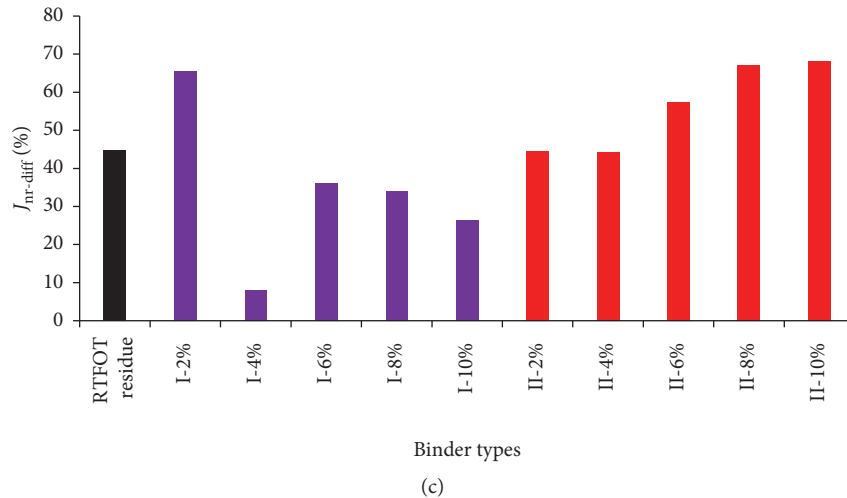


FIGURE 7: Effects of rejuvenators on the rutting parameters of the rejuvenated SBSMA. (a) Percent recovery ( $R$ ); (b) nonrecoverable creep compliance ( $J_{nr}$ ); and (c) stress sensitivity index ( $J_{nr-diff}$ ).

The rheological behavior of asphalt binder was considered in the linear range at a stress level of 0.1 kPa. When the stress level rose to 3.2 kPa, the nonlinear rheological behavior of asphalt binder was closer to field conditions under a heavy traffic loading. The change in the rheological behavior under different stress levels revealed the stress sensitivity of asphalt binders, among others, as a function of temperature and loading.

As can be seen in Figure 7(c), the  $J_{nr-diff}$  values of rejuvenated SBSMA were all less than the limiting value (75%) recommended by AASHTO M332. With the change in the rejuvenator contents, the trends of the  $J_{nr-diff}$  values for the two rejuvenators were different, with Type II exhibiting an almost linearly increasing trend. However, the stress sensitivity (the average of  $J_{nr-diff}$  values) of Type II rejuvenator was about 1.6 times higher than that of Type I rejuvenator. Theoretically, the inference of these test results was that an asphalt pavement comprised of aged SBSMA that had been rejuvenated with Type I rejuvenator had improved durability and serviceability towards heavy traffic loading.

### 3.2.5. Fatigue Performance Based on the LAS Test.

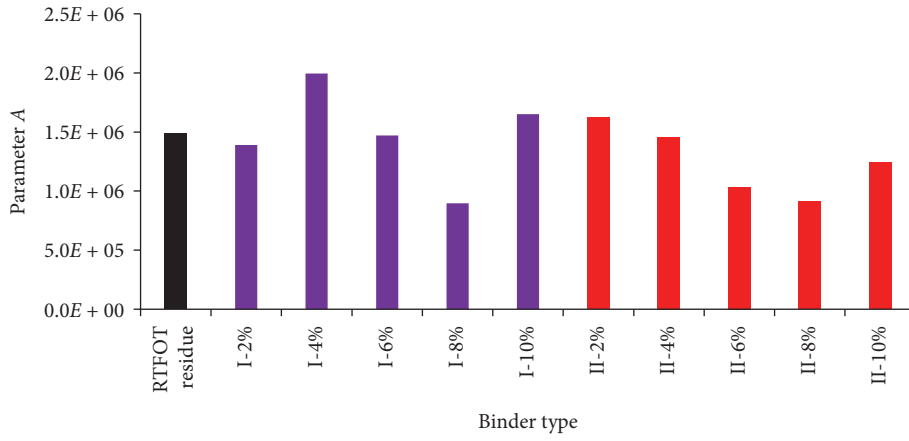
Fatigue  $A$  and  $B$  parameters of the rejuvenated SBSMA were obtained from the LAS test. With an increase in the rejuvenator content, Figure 8 shows an initial decrease in parameter  $A$  to  $8.96 \times 10^5$  (Type I) and  $9.14 \times 10^5$  (Type II), respectively, and thereafter increased to  $1.65 \times 10^6$  (Type I) and  $1.24 \times 10^6$  (Type II). By contrast, the absolute value of parameter  $B$  decreased gradually with an increase in the rejuvenator dosage. In general, parameter  $A$  decreased with the decrease of the storage modulus in the loading process, indicating that the deformation resistance of asphalt binder decreased due to continuous cumulative damage during the loading cycles.

Fatigue parameter  $B$  defines the quantitative measure of the stress and strain sensitivity of the asphalt binder. The higher the absolute value of parameter  $B$  is, the greater the

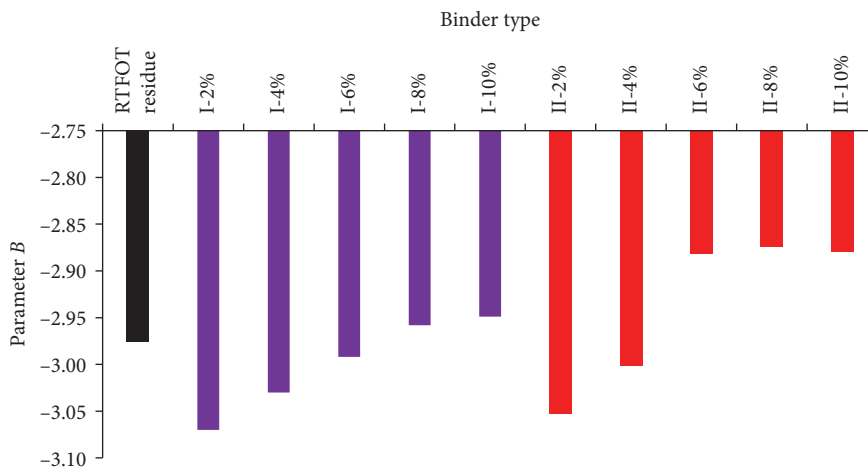
rate of fatigue life reduction of the asphalt binder is with an increase in the strain amplitude. Theoretically, asphalt binders with a higher value for parameter  $A$  and lower absolute value for parameter  $B$  infer to a longer fatigue life for the resultant asphalt mixture and pavement [38]. With increasing rejuvenator dosage, the rejuvenated SBSMA generally exhibited an increasing trend in fatigue performance as observed from the LAS. However, the rejuvenator dosage should be controlled up to an optimum level so as to avoid a counteractive effect that could potentially reduce the fatigue resistance of rejuvenated SBSMA.

The fatigue damage characteristic curves of the asphalt binders are shown in Figure 9. With an increase in the strain level above 15%, the stress was exhibiting a decreasing trend under the critical repeated loading cycles, which indicated the potential occurrence of damage. The peak value of the shear stress was called the yield stress, and the corresponding peak shear strain was called the yield strain. From Figure 9, the further additions (2% to 10%) of the rejuvenators decreased the yield stress (0.349 MPa to 0.280 MPa for Type I; 0.453 MPa to 0.335 MPa for Type II) and increased the yield strain (14.4% to 15.8% for Type I; 13.5% to 16.4% for Type II), respectively, which indicated that the fatigue cracking resistance of the blends had improved as theoretically expected.

The medium-temperature rheological behavior of rejuvenated SBSMA depended significantly on the strain levels, the types, and contents of rejuvenators. In general, asphalt binders have a shorter fatigue life ( $N_f$ ) at higher strain levels and vice versa [39]. For instance, Figure 10 indicates that if the strain level is halved, the fatigue life will, on average, increase by almost 8 times. With an increase in the rejuvenator dosage, there were two peak  $N_f$  values for each blend (124,166 and 110,681 cycles for Type I and 99,039 and 93,102 cycles for Type II at 2.5% strain level, resp.); see Figure 10. Figure 10 further shows that the rejuvenated blends with rejuvenators I-4%, I-10%, II-2%, and II-4% have relatively longer fatigue lives. On average, the fatigue life of the



(a)



(b)

FIGURE 8: LAS test results. (a) Fatigue parameter A; (b) fatigue parameter B.

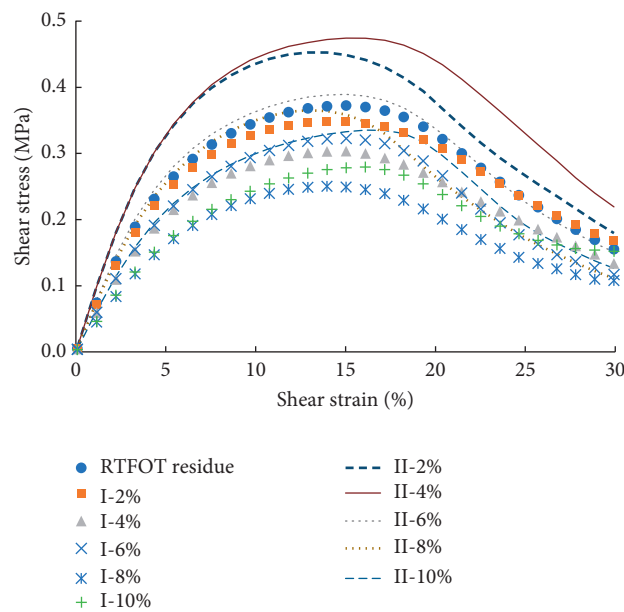


FIGURE 9: Stress-strain curves for the rejuvenated SBS-modified asphalt binders.

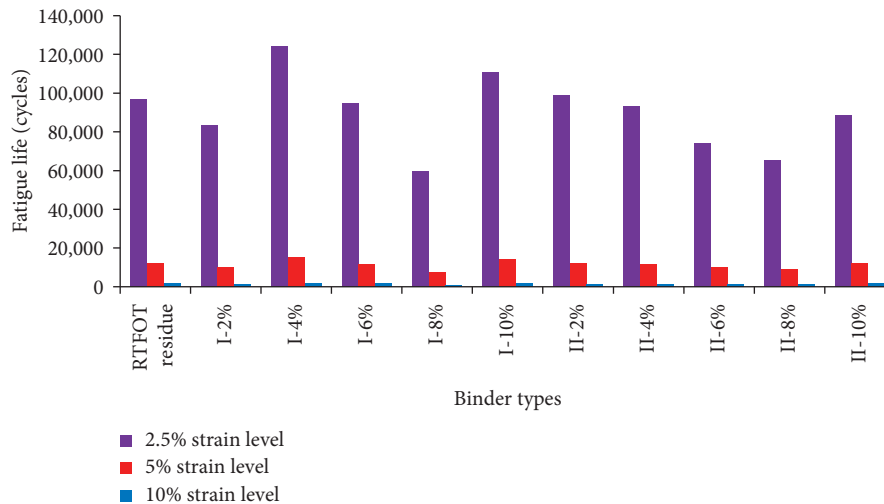


FIGURE 10: Effects of the rejuvenators and strain levels on fatigue life.

rejuvenated SBSMA with 4~10% rejuvenator Type I was about 1.21 times longer than that of the rejuvenator Type II. Overall, the rejuvenator Type I exhibited improved performance in terms of rejuvenating the fatigue damage resistance of the SBSMA.

#### 4. Conclusions and Recommendations

This study investigated the effects of three types of rejuvenators, designated as Type I, Type II, and Type III, with varying dosages (2%, 4%, 6%, 8%, and 10%) and dosages increments (0%, 2%, 4%, and 6%) on the physical/rheological properties and performance characteristics (rutting, thermal, and fatigue cracking resistance) of the first and second rejuvenated SBSMA. From the study findings, the following conclusions and recommendations were drawn:

- (1) Compared to the residues after RTFOT and PAV aging, the physical properties of the first and second rejuvenated SBSMA were improved and presented as the increases of the penetration and ductility and the decreases of the softening point of the asphalt blends. Among the three rejuvenators, the rejuvenation effect of Type I was the most excellent. The optimal rejuvenator dosage was 6~8% for the first rejuvenation, and the optimal rejuvenator dosage for the second rejuvenation was 10~12% (the increment of optimal rejuvenator dosage was 4%).
- (2) The rutting and cracking characteristics of the rejuvenated SBSMA were evaluated using DSR and BBR. The addition of rejuvenator to aged SBSMA was found to decrease the high-temperature rutting resistances ( $G^*/\sin \delta$ ) of the rejuvenated SBSMA. The rejuvenated SBSMA exhibited lower creep stiffness ( $S(t)$ ) and a higher rate of relaxation ( $m$ -value) values compared to aged asphalt binder. It is expected that such improvement in relaxation properties of rejuvenated binders may enhance the low-temperature cracking resistances of rejuvenated pavements. The rejuvenator promoted asphalt

binder durability by making delta  $T_c$  ( $\Delta T_c$ ) parameter less negative. Three types of rejuvenators could all enhance the physical and rheological properties of the aged SBSMA. The target Superpave PG of the rejuvenated SBSMA, PG 76-22, could be achieved with the additions of optimal dosages (6~8%) of rejuvenator Type I.

- (3) The additions of rejuvenators to the asphalt binder blends resulted in a reduction of the percent recovery ( $R$  value) and an increase in the nonrecoverable creep compliance ( $J_{nr}$  value), indicating the positive effects of the rejuvenators on the high-temperature rutting resistance of rejuvenated SBSMA. The stress sensitivity ( $J_{nr-diff}$ ) of the asphalt binder blends with Type I rejuvenator was only 60% of that of Type II rejuvenator. Thus, asphalt mixtures and pavements using Type I rejuvenator were theoretically expected to exhibit more rutting resistance potentials under severe stress conditions.
- (4) The fatigue life of rejuvenated SBSMA was found to significantly depend on the strain levels, rejuvenator type, and dosage, respectively. The addition of rejuvenators improved the elastic properties and correspondingly decreased the yield stresses of the rejuvenated SBS asphalt binders. The fatigue life of the asphalt binder blend with Type I rejuvenator was about 130% to that of Type II rejuvenator.
- (5) The rutting and fatigue characteristics of the rejuvenated SBSMA were successfully evaluated using the MSCR and LAS tests, respectively. Based on these tests, rejuvenator Type I yielded the best rejuvenation/regeneration effects in terms of both the rheological properties and performance characteristics.

Overall, this study has shown that the use of rejuvenators has the potential to enhance the physicorheological properties and performance characteristics of aged SBSMA. For the materials evaluated and tests conducted in this study, rejuvenator Type I, with an optimum dosage of 6~8%, was

found to be the most excellent rejuvenator in terms of enhancing the physicorheological properties and performance characteristics (rutting, thermal, and fatigue cracking resistance) of aged SBSMA. Although limited to the specific materials evaluated in this paper, the study findings, evidently, provide a viable platform for further research into the rejuvenation of aged SBSMA including more laboratory testing, field validation, and practical applications.

### Data Availability

The data used to support the findings of this study are included within the paper.

### Conflicts of Interest

The authors declare that there are no conflicts of interest regarding the publication of this paper.

### Acknowledgments

This work was supported by the Fundamental Research Funds for the Central Universities (Grant no. 3221009602), Kunshan Transportation Development Holding Group Co., Ltd. (Grant no. 8521002599), and the National Natural Science Foundation of China (Grant no. 51778140). The authors also greatly appreciate and gratefully acknowledge the sponsors' funding support. Special thanks and due gratitude also go to all those who helped during the course of this study.

### References

- [1] W. L. Ye, W. Jiang, J. H. Shan et al., "Research on molecular weight distribution and rheological properties of bitumen during short-term aging," *Journal of Materials in Civil Engineering*, vol. 32, no. 3, Article ID 04019377, 2020.
- [2] Z. Leng, Z. F. Tan, H. Y. Yu, and J. Guo, "Improvement of storage stability of SBS-modified asphalt with nanoclay using a new mixing method," *Road Materials and Pavement Design*, vol. 20, no. 7, pp. 1601–1614, 2019.
- [3] C. Z. Zhu, H. L. Zhang, D. M. Zhang, and Z. H. Chen, "Influence of base asphalt and SBS modifier on the weathering aging behaviors of SBS modified asphalt," *Journal of Materials in Civil Engineering*, vol. 30, no. 3, Article ID 04017306, 2018.
- [4] S. P. Wu, Z. J. Zhao, Y. Xiao, M. W. Yi, Z. W. Chen, and M. L. Li, "Evaluation of mechanical properties and aging index of 10-year field aged asphalt materials," *Construction and Building Materials*, vol. 155, pp. 1158–1167, 2017.
- [5] A. Behnood, "Application of rejuvenators to improve the rheological and mechanical properties of asphalt binders and mixtures: a review," *Journal of Cleaner Production*, vol. 231, pp. 171–182, 2019.
- [6] A. Behnood and M. Modiri Gharehveran, "Morphology, rheology, and physical properties of polymer-modified asphalt binders," *European Polymer Journal*, vol. 112, pp. 766–791, 2019.
- [7] C. Q. Yan, W. D. Huang, J. M. Ma et al., "Characterizing the SBS polymer degradation within high content polymer modified asphalt using ATR-FTIR," *Construction and Building Materials*, vol. 233, Article ID 117708, 2020.
- [8] M. S. Cortizo, D. O. Larsen, H. Bianchetto, and J. L. Alessandrini, "Effect of the thermal degradation of SBS copolymers during the ageing of modified asphalts," *Polymer Degradation and Stability*, vol. 86, no. 2, pp. 275–282, 2004.
- [9] C. Q. Yan, F. P. Xiao, W. D. Huang, and Q. Lv, "Critical matters in using attenuated total reflectance fourier transform infrared to characterize the polymer degradation in styrene-butadiene-styrene-modified asphalt binders," *Polymer Testing*, vol. 70, pp. 289–296, 2018.
- [10] C. W. Wei, H. H. Duan, H. L. Zhang, and Z. H. Chen, "Influence of SBS modifier on aging behaviors of SBS-modified asphalt," *Journal of Materials in Civil Engineering*, vol. 31, no. 9, Article ID 04019184, 2019.
- [11] L. F. Walubita, G. S. Simate, and J. H. Oh, "Characterising the ductility and fatigue crack resistance potential of asphalt mixes based on the laboratory direct tensile strength test," *Journal of the South African Institution of Civil Engineering*, vol. 52, no. 2, pp. 31–40, 2010.
- [12] L. F. Walubita, S. I. Lee, A. N. M. Faruk et al., "Texas flexible pavements and overlays: year 5 report-complete data documentation," Report No. FHWA/TX-15/0-6658-3, Texas A&M Transportation Institute (TTI), College Station, TX, USA, 2017.
- [13] D. Q. Sun, G. Q. Sun, X. Y. Zhu et al., "A comprehensive review on self-healing of asphalt materials: mechanism, model, characterization and enhancement," *Advances in Colloid and Interface Science*, vol. 256, pp. 65–93, 2018.
- [14] J. T. Lin, J. H. Hong, C. Huang, J. P. Liu, and S. P. Wu, "Effectiveness of rejuvenator seal materials on performance of asphalt pavement," *Construction and Building Materials*, vol. 55, pp. 63–68, 2014.
- [15] H. Liu, "Research on preventive maintenance technology of asphalt pavement based on penetrating regeneration," Master's Thesis, Southeast University, Nanjing, China, 2019. in chinese
- [16] M. Guo, Y. Q. Tan, D. S. Luo et al., "Effect of recycling agents on rheological and micromechanical properties of SBS-modified asphalt binders," *Advances in Materials Science and Engineering*, vol. 2018, Article ID 5482368, 12 pages, 2018.
- [17] I. Boz and M. Solaimanian, "Investigating the effect of rejuvenators on low-temperature properties of recycled asphalt using impact resonance test," *International Journal of Pavement Engineering*, vol. 19, no. 11, pp. 1007–1016, 2018.
- [18] Z. Zhou, X. Y. Gu, Q. Dong, F. J. Ni, and Y. X. Jiang, "Rutting and fatigue cracking performance of SBS-RAP blended binders with a rejuvenator," *Construction and Building Materials*, vol. 203, pp. 294–303, 2019.
- [19] A. F. Espinoza-Luque, I. L. Al-Qadi, and H. Ozer, "Optimizing rejuvenator content in asphalt concrete to enhance its durability," *Construction and Building Materials*, vol. 179, pp. 642–648, 2018.
- [20] T. Koudelka, P. Coufalik, J. Fiedler, I. Coufalikova, M. Varaus, and F. Yin, "Rheological evaluation of asphalt blends at multiple rejuvenation and aging cycles," *Road Materials and Pavement Design*, vol. 20, no. sup1, pp. S3–S18, 2019.
- [21] M. Elkashef, R. C. Williams, and E. Cochran, "Effect of asphalt binder grade and source on the extent of rheological changes in rejuvenated binders," *Journal of Materials in Civil Engineering*, vol. 30, no. 12, Article ID 04018319, 2018.
- [22] J. A. Shen, S. N. Amirkhanian, and S.-J. Lee, "HP-GPC characterization of rejuvenated aged CRM binders," *Journal of Materials in Civil Engineering*, vol. 19, no. 6, pp. 515–522, 2007.

- [23] M. Zaumanis, R. B. Mallick, L. Poulikakos, and R. Frank, "Influence of six rejuvenators on the performance properties of reclaimed asphalt pavement (RAP) binder and 100% recycled asphalt mixtures," *Construction and Building Materials*, vol. 71, pp. 538–550, 2014.
- [24] B. Y. Cui, X. Y. Gu, D. L. Hu, and Q. Dong, "A multiphysics evaluation of the rejuvenator effects on aged asphalt using molecular dynamics simulations," *Journal of Cleaner Production*, vol. 259, Article ID 120629, 2020.
- [25] E. Fini, A. I. Rajib, D. Oldham, A. Samieadel, and S. Hosseinneshad, "Role of chemical composition of recycling agents in their interactions with oxidized asphaltene molecules," *Journal of Materials in Civil Engineering*, vol. 32, no. 9, Article ID 04020268, 2020.
- [26] G. J. Xu, H. Wang, and W. Sun, "Molecular dynamics study of rejuvenator effect on RAP binder: diffusion behavior and molecular structure," *Construction and Building Materials*, vol. 158, pp. 1046–1054, 2018.
- [27] V. Radhakrishnan, M. Ramya Sri, and K. Sudhakar Reddy, "Evaluation of asphalt binder rutting parameters," *Construction and Building Materials*, vol. 173, pp. 298–307, 2018.
- [28] H. U. Bahia, D. I. Hanson, M. Zeng et al., "Characterization of modified asphalt binders in superpave mix design," NCHRP Report 459, Transportation Research Board, Washington, DC, USA, 2001.
- [29] J. D'Angelo, R. Kluttz, R. N. Dongre, K. Stephens, and L. Zanzotto, "Revision of the superpave high temperature binder specification: the multiple stress creep recovery test (with discussion)," *Journal of the Association of Asphalt Paving Technologists*, vol. 76, pp. 123–162, 2007.
- [30] Q. L. Yang, Q. Liu, J. Zhong, B. Hong, D. W. Wang, and M. Oeser, "Rheological and micro-structural characterization of bitumen modified with carbon nanomaterials," *Construction and Building Materials*, vol. 201, pp. 580–589, 2019.
- [31] A. Behnood, A. Shah, R. S. McDaniel, M. Beeson, and J. Olek, "High-temperature properties of asphalt binders: comparison of multiple stress creep recovery and performance grading systems," *Transportation Research Record: Journal of the Transportation Research Board*, vol. 2574, no. 1, pp. 131–143, 2016.
- [32] C. M. Johnson, H. U. Bahia, and H. Wen, "Evaluation of strain-controlled asphalt binder fatigue testing in the dynamic shear rheometer," in *Proceedings of the 4th International SIVV Congress*, Palermo, Italy, 2007.
- [33] J. M. Yu, Y. F. Guo, L. Peng, F. Guo, and H. Y. Yu, "Rejuvenating effect of soft bitumen, liquid surfactant, and bio-rejuvenator on artificial aged asphalt," *Construction and Building Materials*, vol. 254, Article ID 119336, 2020.
- [34] R. Micaelo, A. Pereira, L. Quaresma, and M. T. Cidade, "Fatigue resistance of asphalt binders: assessment of the analysis methods in strain-controlled tests," *Construction and Building Materials*, vol. 98, pp. 703–712, 2015.
- [35] R. M. Anderson, G. N. King, D. I. Hanson, and P. B. Blankenship, "Evaluation of the relationship between asphalt binder properties and non-load related cracking," *Journal of the Association of Asphalt Paving Technologists*, vol. 80, pp. 615–664, 2011.
- [36] A. I. Rajib, F. Pahlavan, and E. H. Fini, "Investigating molecular-level factors that affect the durability of restored aged asphalt binder," *Journal of Cleaner Production*, vol. 270, Article ID 122501, 2020.
- [37] X. J. Li, N. Gibson, A. Andriescu, and T. S. Arnold, "Performance evaluation of REOB-modified asphalt binders and mixtures," *Road Materials and Pavement Design*, vol. 18, no. sup1, pp. 128–153, 2017.
- [38] P. K. Ashish, D. Singh, and S. Bohm, "Investigation on influence of nanoclay addition on rheological performance of asphalt binder," *Road Materials and Pavement Design*, vol. 18, no. 5, pp. 1007–1026, 2017.
- [39] L. F. Walubita, "Comparison of fatigue analysis approaches for predicting fatigue lives of hot-mix asphalt concrete (HMAC) mixtures," Texas A&M University, College Station, TX, USA, Ph.D. Diss, 2006.

## Research Article

# Electrolytic Manganese Residue-Modified Asphalt Performance Test and Micromechanism Analysis

Tao Fu <sup>1</sup>, Bin Pang,<sup>2</sup> Haoxu Li <sup>1</sup>, Junlin Liang <sup>1</sup> and Huiming Bao <sup>3</sup>

<sup>1</sup>College of Civil Engineering and Architecture, Guangxi University, Nanning 530004, China

<sup>2</sup>The Road and Bridge Engineering Department of Guangxi Vocational and Technical College of Communications, Nanning 530004, China

<sup>3</sup>College of Civil Engineering and Architecture, Guilin University of Technology, Guilin 541004, China

Correspondence should be addressed to Junlin Liang; [ljl\\_1217@126.com](mailto:ljl_1217@126.com) and Huiming Bao; [bhming@163.com](mailto:bhming@163.com)

Received 18 May 2020; Revised 18 July 2020; Accepted 10 August 2020; Published 20 August 2020

Guest Editor: Meng Guo

Copyright © 2020 Tao Fu et al. This is an open access article distributed under the Creative Commons Attribution License, which permits unrestricted use, distribution, and reproduction in any medium, provided the original work is properly cited.

The aim of this paper is to study the feasibility of using an electrolytic manganese residue (EMR) as modified asphalt. In this paper, after grinding the electrolytic manganese residue (EMR) into asphalt, the electrolytic manganese residue- (EMR-) modified asphalt was prepared with different mix ratios. The three major indicators of the modified asphalt were studied, and its modification mechanism was studied by differential scanning calorimetry, infrared spectroscopy, and atomic force microscopy. The adhesion force, surface energy, and dissipation energy of the asphalt before and after modification were analyzed by a force curve. The results show that the surface energy of the electrolytic manganese residue (EMR) is increased after grinding, the high temperature performance of the asphalt is improved, and the temperature sensitivity of the asphalt is decreased; however, the low-temperature performance is not improved obviously. When the powder oil ratio is 9%, the comprehensive performance of the asphalt is the best. The results of the infrared spectrum analysis show that the mixture of the electrolytic manganese residue (EMR) and asphalt does not produce new functional groups, and thus, the preparation method is a physical modification method. The differential scanning calorimetry (DSC) results show that the electrolytic manganese residue (EMR) can enhance the high-temperature stability of asphalt. It is found that the stability and antideformation ability of the modified asphalt improved.

## 1. Introduction

Manganese is widely used in steel, nonferrous alloys, battery materials, the chemical industry, and agriculture [1–4]. China is the world's leading producer of manganese. Manganese products mainly include electrolytic metal manganese, electrolytic manganese dioxide, manganese ferroalloy, and manganese ore. In 2018, China's production capacity of electrolytic manganese residue (EMR) was 2.26 million tons, and the actual output was 1.4 million tons, accounting for 97% of the total output of the production capacity of electrolytic manganese in the world. Electrolytic manganese residue (EMR) is acid leaching slag produced in the process of electrolyte preparation, and it is the key pollutant generated by the electrolytic manganese industry. The grade of manganese ore in China is relatively low, and

8–10 tons of electrolytic manganese residues (EMRs) will be produced for every 1 ton of manganese produced. At present, the amount of electrolytic manganese residue (EMR) in China has exceeded 100 million tons, with an annual increase of more than 10 million tons. Electrolytic manganese residue (EMR) also has the characteristics of a high moisture content (22%~28%), fine particles (up to 70% of particles have sizes <30 μm), a high sulfate content (20%~30%, as calculated by SO<sub>3</sub>), and good thermal stability. The apparent density is 2039 kg/m<sup>3</sup>, and the packing density of wet slag and dry slag is 1785 kg/m<sup>3</sup> and 1982 kg/m<sup>3</sup>, respectively. By improving the technology level of a harmless treatment and utilizing electrolytic manganese residue (EMR), reducing the storage and risk of electrolytic manganese residue (EMR) by scientific and reasonable means is being widely studied [5–8]. Therefore, the effective



utilization of electrolytic manganese residue (EMR) resources can not only produce good environmental and social benefits but also bring good economic benefits to electrolytic manganese residue (EMR) plants [9–11].

At present, many studies have been carried out on the utilization of electrolytic manganese residue (EMR). Wang et al. [10] aimed to prepare nonsintered permeable bricks with a large amount of electrolytic manganese residue (EMR), which is discharged from the electrolytic manganese industry as raw materials. The mechanical properties and environmental properties are studied so that EMR can be successfully applied to pavement materials. Tang's articles [9] also presented relevant research. Zhang et al. [12] studied the chemical composition, mechanical properties, hydration behavior, pore structure, and environmentally friendly properties of materials prepared with different calcium silicon ratios by using EMR and red mud as road base materials. The research results provide a direction for the large-scale and effective utilization of electrolytic manganese residue (EMR). Hou et al. [13] prepared Q-SACs by adding different amounts of electrolytic manganese residue (EMR) (10–45%) to study the chemical composition, basicity, setting time, and compressive strength of the mineral. The results show that the Q-SACs with electrolytic manganese residue (EMR) have a good strength, a low firing temperature, and good mechanical properties. Qin et al. [14] discussed the influence of electrolytic manganese slag on the road performance of an asphalt mixture. The results show that the high-temperature stability performance and corrosion resistance began to significantly increase by adding electrolytic manganese residue (EMR).

The objective of this study was to investigate electrolytic manganese residue- (EMR-) modified asphalt. Additionally, penetration tests, ductility tests, and softening point tests are important tests for future research and practical applications. Otherwise, XRD, IR, DSC, and AFM testing methods are applied to discuss the properties of the EMR-modified asphalt.

## 2. Experimental Design

### 2.1. Materials

**2.1.1. EMR.** In the test, the EMR is the water-quenched slag obtained from the ferromanganese blast furnace of the Bayi ferroalloy plant in Laibin, Guangxi. The EMR contains gray-green loose particles with an average particle size of  $\leq 3$  mm and has a density of approximately  $2.89 \text{ g/cm}^3$  and a loose bulk density of approximately  $723 \text{ kg/m}^3$ . The chemical composition of the EMR is shown in Table 1.

The original EMR particles are grounded by a high-energy ball mill. After grinding for 25 min and 50 min, the diffraction analysis is carried out on the ground EMR by a Panak X'Pert Pro diffractometer in the Netherlands. The results are shown in Figure 1. In Figure 1(a), the peak intensity of the  $\text{SiO}_2$  diffraction peak obtained for the powder after grinding for 25 min is 630 a.u.; in Figure 1(b), the peak intensity of the  $\text{SiO}_2$  diffraction peak obtained for the powder after grinding for 50 min is 496 a.u. With the

TABLE 1: The main components of EMR (%).

$\text{SiO}_2$	$\text{Al}_2\text{O}_3$	CaO	MgO	$\text{Fe}_2\text{O}_3$	$\text{SO}_3$	MnO	Loss
23.86	16.32	37.81	6.52	1.23	0.48	9.60	0.72

increase in the mechanical grinding time, the intensity of the  $\text{SiO}_2$  diffraction peak obtained for the powder decreases, the crystallinity of the crystal decreases, and amorphous substances are produced at the same time. The activity of the EMR increases with the increase in the grinding time.

According to molecular dynamics and the dispersion theory [15], the smaller the particle size is, the larger the specific surface area of the EMR is and the larger the contact area with asphalt is; the longer the grinding time of the EMR is, the smaller the particle size is and the smaller the crystallinity is, thus enhancing the activity. The smaller the particle size is, the more uniform the distribution is and the more stable the blending performance with asphalt is. Therefore, the particle size is approximately  $35 \mu\text{m}$  after ball milling for 50 min, and the EMR is mixed with an asphalt matrix.

**2.1.2. Asphalt Matrix.** The matrix asphalt used in this experiment is the "Donghai brand" 70# road petroleum asphalt produced by Maoming Branch of Sinopec. The corresponding technical indicators of the matrix asphalt are in strict accordance with the technical requirements of the road petroleum asphalt (JTG F40-2004) standard. The penetration, softening point, and ductility indicators of the asphalt matrix are shown in Table 2.

### 2.2. Test Method

**2.2.1. Physical Property Test.** The major physical properties of asphalt, including penetration (temperature susceptibility, ASTM D5), softening point (high-temperature properties, ASTM D36), and ductility (low-temperature properties, ASTM D2801-95), were tested.

**2.2.2. Differential Scanning Calorimetry.** A DSC spectrometer (Zetseh DSC204), which was produced in Germany, was used to determine the functional characteristics of asphalt in the experiment, in which the asphalt was heated at a rate of  $10^\circ\text{C}/\text{min}$ , and the nitrogen flow rate was  $30 \text{ ml}/\text{min}$ . The starting temperature was  $-10^\circ\text{C}$ , and the ending temperature was  $200^\circ\text{C}$ .

**2.2.3. Atomic Force Microscopy.** AFM (Bruke Dimension ICON) was used to test the MA, RMMA, and RMMAFC. In the AFM experiment, a tiny and spiky tip (length:  $125 \mu\text{m}$ ; natural frequency:  $70 \text{ kHz}$ ; spring constant:  $3 \text{ N/m}$ ) was attached at the unsupported end of the cantilever and remained close to the asphalt film. Due to the close contact between the tips and the surface of the film, a repulsive or attractive force between the atoms of the top layer of asphalt and the AFM tip is created, which deflects the cantilever. The extent of the deflection absolutely depends on the force developed between the molecules of the tips and the film.

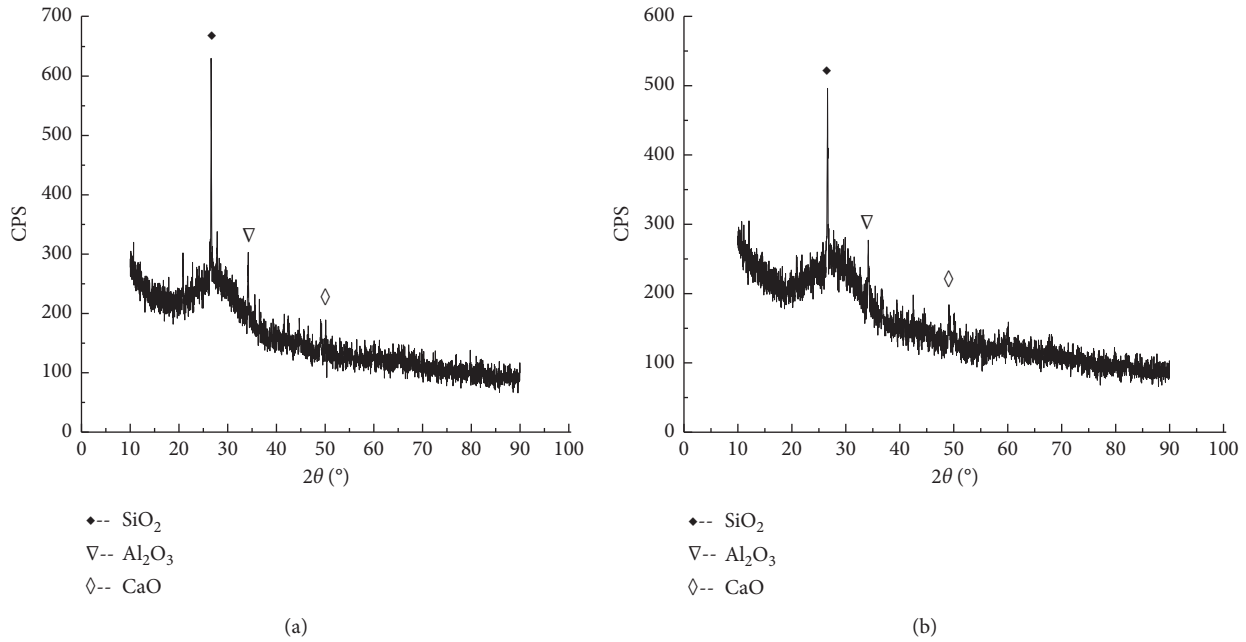


FIGURE 1: XRD patterns of the EMR after different grinding times. (a) 25 min. (b) 50 min.

TABLE 2: Basic properties of the matrix asphalt.

Test project	Test results		Industry standard
	Value	Unit	
Penetration (25°C)	64.2	0.1 mm	60–80
Ductility (15°C)	105.2	cm	$\geq 100$
Softening point	48.1	°C	$\geq 46$
Solubility	99.73	%	$\geq 99.5$
Flash point	298	°C	$\geq 260$

2.2.4. *Fourier Transform Infrared Spectroscopy.* The instrument used in the FTIR experiment is a Nicote 7T40FTIR Fourier transform infrared spectrometer (made in the United States), which was used to determine the functional characteristics of asphalt, and data was collected for the wavenumber range of  $400\text{--}4000\text{ cm}^{-1}$ .

2.3. *Preparation of EMR Asphalt.* The EMR milled for 50 min was dried to a constant mass at  $105^\circ\text{C}$ . An appropriate amount of asphalt was obtained and melted to the flowing state in an oven at  $135^\circ\text{C}$ . The modified asphalt was prepared by a high-speed shear dispersion emulsifier and heated at  $160\text{--}170^\circ\text{C}$  for 30 min, and the asphalt was prepared with a powder:oil ratio of 0%, 3%, 6%, 9%, 12%, and 15%.

### 3. Results and Discussion

#### 3.1. Performance Test of the EMR Asphalt Mortar

3.1.1. *Penetration Test.* The penetration test was carried out at a series of temperatures ( $10^\circ\text{C}$ ,  $15^\circ\text{C}$ ,  $20^\circ\text{C}$ ,  $25^\circ\text{C}$ , and  $30^\circ\text{C}$ ). The needle penetration value is shown in Table 3. With the increase in the powder oil ratio, the needle penetration value at high temperatures decreases continuously, but the change

is not obvious at low temperatures. When the powder:oil ratio reaches 9%, the decrease in the amplitude of the high temperature value is larger than that obtained for the other powder:oil ratios, and then, the effect of increasing the powder:oil ratio on the needle penetration value is not obvious. The penetration index PI, the equivalent softening point  $T_{800}$ , the equivalent brittle point  $T_{1,2}$ , and the plastic temperature range  $\Delta T$  are calculated by linear regression of the one-dimensional first-order equation, which was combined with the penetration values for a series of temperatures. The penetration index PI reflects the degree of penetration changing with temperature. The higher the PI, the lower the temperature sensitivity of asphalt. As shown in the table, when the PI value of the asphalt matrix is  $-0.9$  and when the powder:oil ratio of the EMR micropowder asphalt reaches 9%, the PI first shows a peak value of  $-0.769$ ; then, when the powder:oil ratio reaches 15%, the PI value again shows a peak value of  $-0.741$  and continues to increase the powder:oil ratio, but the PI value decreases. It can be seen that when the powder:oil ratio is 15%, the temperature sensitivity of the asphalt is lower than that of the asphalt prepared with the other powder:oil ratios. The equivalent softening point  $T_{800}$  reflects the high-temperature performance of asphalt. When the powder:oil ratio is 9%, the  $T_{800}$  reaches the peak value of  $51.1^\circ\text{C}$ , which is approximately  $2^\circ\text{C}$  higher than that of the asphalt matrix at  $49.4^\circ\text{C}$ , and then slightly decreases. When the powder:oil ratio is 15%, the peak value of  $51.3^\circ\text{C}$  appears again. The equivalent brittle point  $T_{1,2}$  reflects the low-temperature crack resistance of asphalt.  $T_{1,2}$  first increased with the increase in the powder:oil ratio and then decreased to  $-11.8^\circ\text{C}$  when the powder:oil ratio was 9%. The plastic temperature range  $\Delta T$  represents the difference between  $T_{800}$  and  $T_{1,2}$ . The larger the temperature range is, the wider the temperature range is.  $\Delta T$  first

TABLE 3: Summary table of the test results of three indicators.

R	Penetration test						Ductility				SP		
	Penetration of different temperatures (0.1 mm)					PI	$T_{800}$	$T_{1.2}$	$\Delta T$	1 cm/m in 5°C		5 cm/m in 15°C	°C
	10°C	15°C	20°C	25°C	30°C					cm		cm	
0	12.3	21.1	32.6	61.2	102.5	-0.92	49.40	-11.80	61.25	100.0	150.0	49.2	
3	11.8	21.0	32.5	61.0	101.0	-0.99	49.29	-11.36	60.65	98.0	150.0	52.3	
6	11.5	19.8	32.2	57.8	98.8	-1.00	49.54	-11.97	60.51	97.0	150.0	56.2	
9	11.6	18.8	31.3	52.8	92.3	-0.77	51.08	-11.67	62.75	90.0	141.6	57.9	
12	11.4	19.7	29.9	53.7	91.6	-0.81	50.85	-11.50	62.35	86.0	139.1	57.5	
15	11.3	19.7	30.6	53.7	90.2	-0.74	51.23	-11.79	63.03	84.0	97.3	54.5	
18	11.2	17.3	31.9	53.6	90.2	-0.90	50.55	-10.89	61.44	74.0	78.2	52.3	
21	11.4	18.7	32.2	52.3	89.9	-0.74	51.27	-11.75	63.02	59.0	65.6	50.1	

decreased and then increased with the addition of EMR, reaching the peak value when the powder:oil ratio was 9%, and then,  $\Delta T$  reached the peak value again when the powder:oil ratio was 15%. The comprehensive analysis shows that the addition of EMR can improve the penetration resistance to a certain extent and can improve the high-temperature mechanical properties of asphalt; the best content is a 9% powder:oil ratio, but this ratio has no obvious effect on the low-temperature crack resistance of asphalt

**3.1.2. Ductility Test.** The ductility reflects the extension length of asphalt at a specific temperature and tensile rate and reflects the pavement performance and low-temperature crack resistance. When the powder:oil ratio is less than or equal to 6%, the ductility of the modified asphalt and asphalt matrix is 150 cm. With the increase in the powder:oil ratio, the ductility of asphalt decreased; when the powder:oil ratio reached 15%, the ductility decreased to 87.3 cm. The results show that, with the addition of the inorganic EMR to the organic colloidal material asphalt, a whole blended structure is formed; however with the increase in the ratio of powder to oil, too much EMR lacks enough asphalt colloid to generate adhesion, so the ductility value under the external tensile action is lower than that of the original asphalt matrix.

**3.1.3. Softening Point Test.** The softening point reflects the high-temperature deformation resistance of asphalt. With the addition of EMR, the softening point of asphalt increased. When the powder:oil ratio is 9%, the softening point reaches the peak value of 57.9°C, which is 5.6°C higher than that of 52.3°C when the powder oil ratio is 3%; then, when the powder:oil ratio is increased, the temperature of the softening point decreases close to the performance of the matrix asphalt. The results show that the addition of EMR can reduce the temperature sensitivity of asphalt and improve its high temperature stability, which shows that the softening point temperature of asphalt increases.

**3.2. Infrared Spectrum Analysis.** A Thermo Nexus 470 FT-IR spectrometer was used to test the EMR and asphalt. The test range was 400–4000  $\text{cm}^{-1}$ , and the test was repeated 5 times.

As shown in Figure 2, the peak at 1029  $\text{cm}^{-1}$  in the spectrum of the EMR is the vibration absorption peak of Si-O in the EMR, and the peak at 468  $\text{cm}^{-1}$  is the absorption band position of the alumina-like oxide in the corundum structure; the peaks are 2923  $\text{cm}^{-1}$  and 2852  $\text{cm}^{-1}$  in the spectrum of the matrix asphalt are the C-H ( $\text{CH}_3$ -,  $-\text{CH}_2$ -) stretching vibration bands of asphalt, the peaks at 1460  $\text{cm}^{-1}$  and 1376  $\text{cm}^{-1}$  are the C-H bending vibration bands of asphalt, and the peak at 1602  $\text{cm}^{-1}$  is the stretching vibration band of the carbonyl (C=O) group in asphalt; the spectrum of the asphalt with a 6% powder:oil ratio is basically the same as that of the matrix asphalt, and only the stretching vibration band of the carbonyl (C=O) group shifts to 1608  $\text{cm}^{-1}$ ; in the spectrum of the asphalt with a 9% powder:oil ratio, the stretching vibration band of C-H shifts to 2921  $\text{cm}^{-1}$  and 2851  $\text{cm}^{-1}$ , that is to say, it moves toward the low-frequency direction, and the bending vibration band shifts to 1455  $\text{cm}^{-1}$  and 1382  $\text{cm}^{-1}$ , moving toward the high-frequency region. According to the change in the functional group position in Figure 2 and the factors affecting the band position, it is found that the atoms of N, P, and S in the EMR form hydrogen bonds with the atoms of asphalt that do not shared electron pairs, but the polarity of the hydrogen bond that formed is also weak due to the weak polarity of the atoms of N, P, and S; the stretching vibration frequency of the weak hydrogen bond of the original bond will move toward the low-frequency direction, and the displacement is small. Meanwhile, the bending vibration of asphalt will move toward the high-frequency region, and the band is narrow, which will increase the activity of asphalt. The penetration and softening point performance indexes of asphalt are related to the relative proportion of high and low molecular weight hydrocarbons in the asphalt. After the EMR is added to the asphalt during modification, the  $\text{Al}_2\text{O}_3$  absorption band does not appear in the spectra obtained for the asphalt with 6% and 9% powder:oil ratios. According to the catalytic oxidation mechanism of petroleum asphalt,  $\text{Al}_2\text{O}_3$  adsorbs the small and medium molecular weight components of the aliphatic hydrocarbons and aromatic hydrocarbons under high temperature conditions for oxidation. In the cross-linking and condensation reaction, when the high molecular weight increases, the unreacted part of  $\text{Al}_2\text{O}_3$  will be

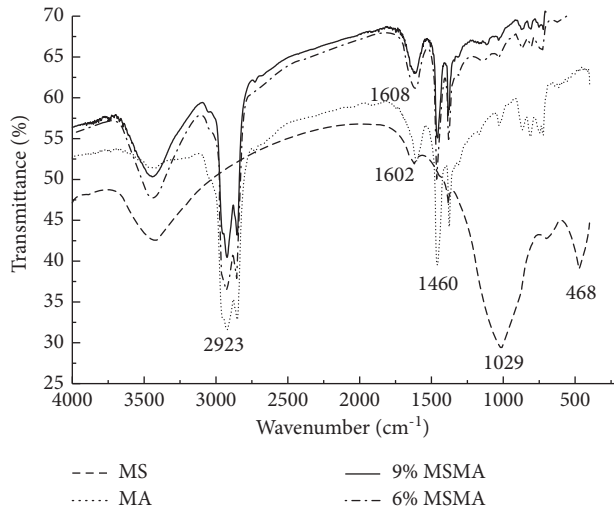


FIGURE 2: Infrared spectra of the EMR and asphalt.

replaced by a low molecular weight component and will continue to play the role of the catalytic oxidant so that the content of the high molecular weight hydrocarbon in the asphalt will increase. In addition, the distribution of the penetration value and penetration index PI will appear as a hump with the increase in the powder:oil ratio, which is consistent with the other results. In addition, as shown in the spectra of the asphalt with a 9% powder:oil ratio, the carbonyl group of the asphalt will be replaced. The shift in the (C=O) stretching vibration band to  $1621\text{ cm}^{-1}$  in the high-frequency direction also indicates that the oxidation of asphalt occurs after the addition of EMR; meanwhile, the intermolecular forces increase, and the polarity increases.

The uniformity of the distribution of the modifier has a great influence on the performance and stability of the asphalt. Because of the complexity of the chemical composition of EMR, a series of physical and chemical reactions may take place after the asphalt is mixed. For the dispersion of the inorganic modifier mixed with asphalt, according to the intensity of the infrared absorption peak at the wavenumber of a specific functional group in the infrared spectra, the literature characterizes the relative amount of the inorganic modifier and asphalt and describes the uniform and stable state of the inorganic modifier mixed with asphalt by comparing whether the relative amount of the two changes linearly as the amount of the modifier changes. In this paper, the infrared absorption strength at the wavenumber  $1602\text{ cm}^{-1}$  (denoted as  $H_{1602}\text{ cm}^{-1}$ ) is used to characterize the relative amount of EMR, and the infrared absorption strength at the wavenumber  $1455\text{ cm}^{-1}$  (denoted as  $H_{1455}\text{ cm}^{-1}$ ) is used to characterize the relative amount of asphalt. The ratio of the two is used to characterize the relative content of EMR and asphalt in the modified asphalt. The results are shown in Table 4 below. At wavenumber  $1602\text{ cm}^{-1}$ , the infrared absorption strength of the EMR is 0.078; at 6%, the infrared absorption strength of the asphalt is 0.068, which is less than that of the EMR; at 9%, the infrared absorption strength of the asphalt is 0.083, which is greater than that of the EMR; these results are different from

those of other modifiers because of the catalytic oxidation of the  $\text{Al}_2\text{O}_3$  component in EMR. When the content of  $\text{Al}_2\text{O}_3$  is small, the crosslinking and condensation reaction occurring between  $\text{Al}_2\text{O}_3$  and asphalt takes place first to generate high molecular weight hydrocarbon. As the content of  $\text{Al}_2\text{O}_3$  continues to increase, the reaction continues to generate high molecular weight material, and the infrared absorption strength increases accordingly. In addition, the unreacted surplus  $\text{Al}_2\text{O}_3$  is also replaced by low molecular weight components. Therefore, although the infrared absorption strength increases, it is close to the infrared absorption strength of EMR. In addition, the linear change in the absorption strength of the two shows that the EMR can be mixed evenly in asphalt, which proves that the addition of EMR can improve the performance of asphalt.

**3.3. Differential Scanning Calorimetry.** The asphalt matrix, asphalt with a 9% powder:oil ratio, and asphalt with a 12% powder:oil ratio were tested by a German DSC 204 differential scanning calorimeter, as shown in the DSC curve obtained for the asphalt samples with different powder:oil ratios in Figure 3.

The base peak area of the DSC curve corresponds to the thermal effect. The DSC curve of the asphalt is shown in Table 5. The energy value of the endothermic peak is characterized by the peak area of the DSC curve. Under the same test conditions, the endothermic peak area of the EMR micropowder series asphalt is lower than that of the asphalt matrix, which indicates that the matrix asphalt changes more than the EMR-modified asphalt in the range of test temperatures. According to the peak temperature of the endothermic peak, the thermal stability of the asphalt with the 9% powder:oil ratio is the best, which is approximately 49% higher than that of the matrix asphalt; the stability of the asphalt with a 12% powder:oil ratio is the second best and is still higher than that of the matrix asphalt. The peak temperature of the endothermic peak of the asphalt matrix increases by approximately 28%, which is consistent with the three major indexes of the EMR micropowder asphalt, the penetration index PI, equivalent softening point  $T_{800}$ , equivalent brittle point  $T_{1,2}$ , and plastic temperature range  $\Delta T$ . The performance of the asphalt with the 9% powder:oil ratio is better than that of the asphalt with the 12% powder:oil ratio. The results show that the heat absorption of the asphalt decreases, the high-temperature stability of the asphalt is obviously improved, and the temperature sensitivity of the asphalt is significantly improved after the addition of the EMR micropowder during the DSC test used to study the performance degradation.

### 3.4. AFM Analysis

**3.4.1. AFM Image Analysis.** Two groups of experiments were carried out on the matrix asphalt (MA) and the 9% EMR-modified asphalt (MRMA). The two-dimensional and three-dimensional microscopic phase diagram of the asphalt under AFM is shown in Figures 4 and 5. Prabir named three parts with different morphologies as the continuous phase,

TABLE 4: Infrared absorption intensity at the wavenumbers  $1602\text{ cm}^{-1}$  and  $1455\text{ cm}^{-1}$ .

Type	MA	6% MRMA	9% MRMA	MS
$H1602\text{ cm}^{-1}$	—	0.068	0.083	0.078
$H1455\text{ cm}^{-1}$	0.105	0.118	0.143	—
$(H1602\text{ cm}^{-1})/(H1455\text{ cm}^{-1})$	—	0.576	0.580	—

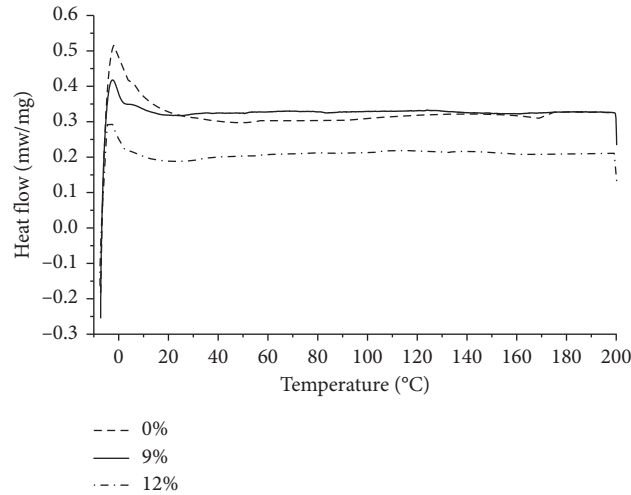


FIGURE 3: DSC curve of asphalt with different powder:oil ratios.

TABLE 5: DSC endothermic peak data of asphalt.

Type	Endothermic peak energy ( $\text{J}\cdot\text{g}^{-1}$ )	Peak temperature ( $^{\circ}\text{C}$ )	Peak width ( $^{\circ}\text{C}$ )
MA	666.47	-1.776	-7.241~200.706
9% MRMA	651.83	3.463	-0.537~199.463
12% MRMA	416.96	2.458	-0.542~199.458

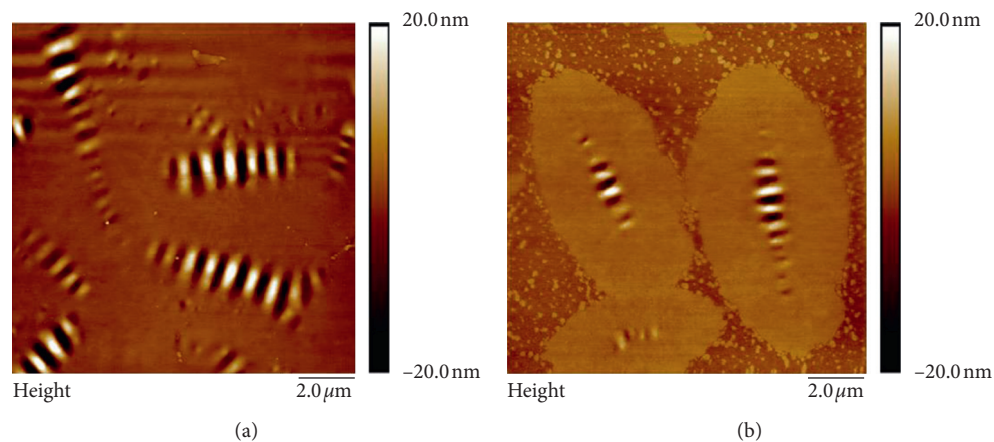


FIGURE 4: 2D AFM image of the (a) MRMA and (b) MA.

periphase, and bee phase. Image Pro Plus is used to process the image to highlight the contour of the bee structure; the bee structure was marked, and the area was counted, as

shown in Figure 6. The statistical results of the area are shown in Table 6. The results and causes are as follows:

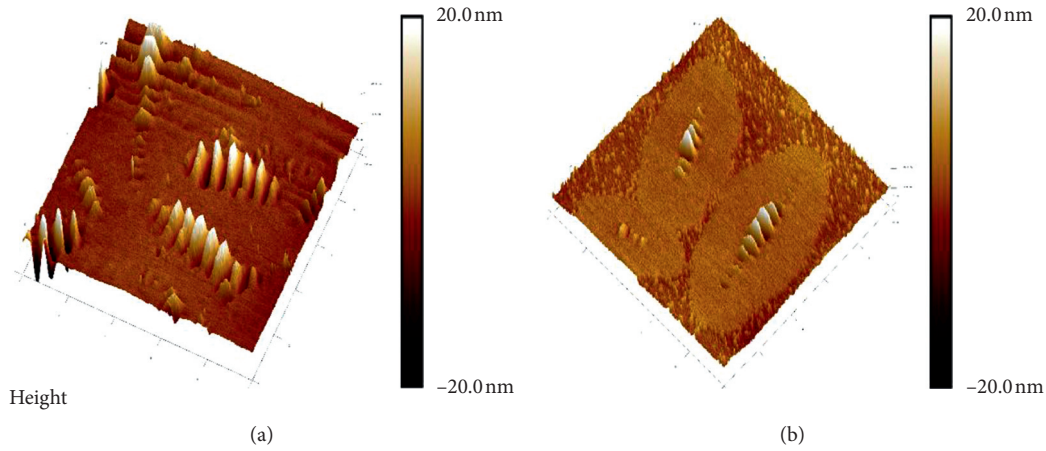


FIGURE 5: 3D AFM image of the (a) MRMA and (b) MA.

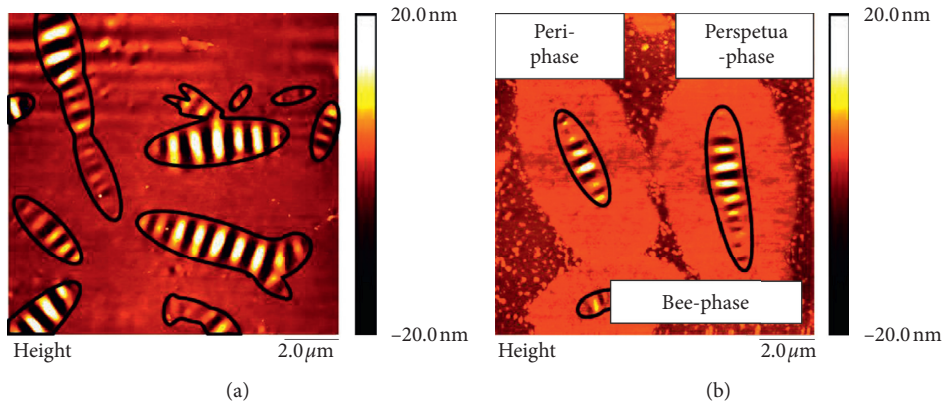


FIGURE 6: Bee structure. (a) MRMA and (b) MA.

TABLE 6: Matrix statistical table of the area of the bee-like structures.

Species of asphalt	Scanning range ( $\mu\text{m}^2$ )	Area			Maximal bee structure ( $\mu\text{m}^2$ )	Proportion of bee structure area (%)
		Continuous phase ( $\mu\text{m}^2$ )	Periphase ( $\mu\text{m}^2$ )	Bee-like structure ( $\mu\text{m}^2$ )		
MRMA	95.61	70.1	0	25.5	6.4	26.6
MA	95.61	37.5	50.2	7.9	4.6	8.3

(1) Before and after EMR modification, the microsurface of the asphalt has a bee structure. Under the influence of the EMR, the inclusion phase disappears, and the continuous phase is relatively flatter on the surface of the MRMA that it is on the surface of the MA; the number of bee structures increases significantly, the size of the bee structures increases, the difference between the sizes of the bee structures increases greatly, and some bee structure distortion and asphalt surface height differences are significant; there is a cross phenomenon between some of the bee structures, and the bee structures are still independent of each other. The bee structure accounts

for more than 24% of the total surface area, which is approximately 3 times the contribution of the MA bee structure. The honeycomb structure on the surface of the MA is rare, isolated, and regular in shape. With a three-phase morphology, obvious inclusions can be observed. The inclusions occupy 52.5% of the surface area of the MA, and the continuous phase is relatively rough, with many needle-like crystals densely distributed.

(2) The change in the bee-like structure of the MRMA showed that EMR could promote the formation and development of the bee-like structure. The asphaltene gum is wrapped by asphaltene to form micelles,

which are suspended in the oil; the chemical stability of the gum is poor, and it easily oxidizes and condenses into asphaltene. When the slurry is cooled, the wax components gather in the gum and asphaltene and grow up gradually by using the wax center as the core; when the content of asphaltene and gum in the slurry increases, the size of the wax nodule center increases at the same time, resulting in only small wax crystals. The surface acicular crystal of the MA is a wax crystal. The extremely polar colloid can wrap around the wax crystal and prevent the growth of the wax crystal. The reduction state of the EMR makes the resin oxidize and condense into asphaltene with a high molecular weight (1 000–100 000), and the wax with a low molecular weight (below 1000) decreases its saturation concentration during cooling. After the wax crystal is unbound, the amount of wax precipitates increases under the effect of cooling crystallization and temperature stress. As a result, the number of MRMA wasps increased. Some studies have shown that the texture of the inclusion phase is hard and that of the continuous phase is soft. Therefore, it is speculated that after the disappearance of the inclusion phase in the EMR; due to the lack of binding of the inclusion phase, the bee-shaped structure develops along the long and short axes, so the size of the bee-shaped structure becomes larger.

- (3) The scale of the EMR particles is in the order of micrometers, and no obvious EMR particles are observed in the scale of nanometers, which indicates that the high-speed shear of the emulsifier makes the EMR evenly spread in the asphalt mortar at high temperatures. In addition, the EMR can react with the asphalt components to form a polymer with stable properties; the inclusion phase of the MRMA disappears, and the asphaltene and long-chain alkane in the mortar disappeared. The surface of the wax crystal adsorbs the polar groups in the asphaltene and the slurry, and the polar groups continue to form a double electric layer with the nearby asphaltene and the slurry. The directional dipole molecules of the double electric layer make the solvation layer wrap around the wax crystal. The inclusion phase consists of eutectic, polar micelle, and solvate layers. When the solvate layers are close to each other, there will be repulsive forces, so the inclusions do not cross each other. The EMR increases the concentration of the ionic compounds in asphalt mortar, and the ionic bond destroys the eutectic effect of the long-chain alkanes and wax crystal, causing the inclusion phase to disappear.

**3.4.2. Force Displacement Curve.** The microcosmic adhesion force ( $F_{ad}$ ) is composed of van der Waals force ( $F_{vdw}$ ), capillary force ( $F_c$ ), electrostatic force ( $F_E$ ), and chemical bond ( $F_B$ ) and is characterized by the lowest point of the withdrawal curve. According to the AFM test process, the

asphalt sample and tip are all exposed to normal temperature air for quite a long time, so  $F_E$  is zero; the silicon nitride probe does not react with asphalt, so  $F_B$  is zero; the capillary force plays a role in promoting contact during the contact process and hindering separation during the withdrawal process, and the main source of microadhesion between the objects in the air is the capillary force, which is composed of hair fine action and liquid bridges. The force displacement curves of the MRMA and MA are shown in Figure 7.

- (1) Adhesion contact hysteresis: the ideal contact withdrawal path of rigid contact should be coincident, but Figure 7 shows that the force displacement path of the probe approaching and withdrawing from the asphalt sample surface is not the same; the approach path is A-B-C-D-E, and the withdrawal path is E-F-G-H-I, which is the phenomenon of adhesion contact lag, which generally exists in the microinterface. The phenomenon of adhesion contact hysteresis leads to the work required to separate the contact interface being greater than the work required to combine them, which leads to the withdrawal curve enveloping the approach curve.
- (2) Contact process: the microcosmic adhesion force ( $F_{ad}$ ) between asphalt and the tip changes as the probe moves down and up, and the mechanical response of the microcantilever changes accordingly. When the probe goes down to the BD section, the resultant force at the cantilever end of the BD section includes van der Waals forces and capillary forces. van der Waals forces show attraction, and the capillary force and attraction are superposed in the same direction. At this time, the resultant force at the free end of the probe microcantilever is downward, the upper end of the cantilever is under tension, the lower end is under pressure, and the tension (pressure) force increases first and then decreases. When the probe goes down to the DE section,  $F_{ad}$  is the superposition of the van der Waals force and capillary force, and the overall performance is the repulsion force. At this time, the upper end of the microcantilever beam is under pressure, and the lower end is under tension; when the probe tip of point E contacts the asphalt surface, the probe stops going down after receiving the peak force.
- (3) Withdrawal process: when the probe is withdrawn to the EF section, the repulsion, attraction, and capillary forces are superposed in different directions, and the repulsion force decreases sharply as a whole; when the probe rises to the elevation corresponding to point F, the elevation corresponding to point F is zero, and the elevation corresponding to point F is lower than that of point D because the capillary force prevents the two interfaces from separating. When the probe is withdrawn to the FH section, the capillary force that prevents separation increases the force required to separate the tip and the asphalt surface. During the lifting process, one end of the microcantilever is subject to the force of lifting and

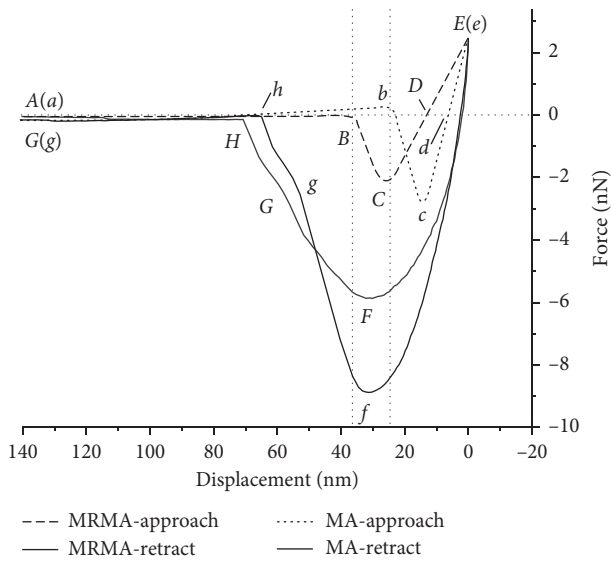


FIGURE 7: Force-displacement curve.

the other end is subject to the adhesion of  $F_{ad}$ , which causes the microcantilever to warp upward; at the G point,  $F_{ad}$  reaches the maximum value, and the separation distance between the interfaces is too large, which causes the capillary force to start to decrease; when the probe is lifted up to an elevation higher than that of the B point, the interface distance between the tip and asphalt is too large, and the van der Waals force is reduced to zero. At a certain point of BH, the liquid bridge forming between the tip of the needle and the asphalt breaks, and the capillary force disappears. This concludes a contact withdrawal cycle.

- (4) The function of a liquid bridge: both the probe exposed to air and the surface of asphalt form a liquid film. When the probe moves down to a certain position, a slit is formed between the tip of the needle and the asphalt surface, which has a very high adsorption potential; as the tip of the needle continues to move down, the slit gradually decreases, the adsorption potential gradually increases, and the free water molecules near the slit area are attracted to the slit area by the influence of the high adsorption potential of the slit area, resulting in condensation; finally, the tip of the needle punctures the water film on the asphalt surface and contacts the asphalt surface. The water molecular group extrudes into the slit area, and the capillary action makes the liquid film near the slit flow to the slit area. The high adsorption potential and extrusion and capillary co-accreration make the contact interface between the probe tip and asphalt form a liquid bridge. When the tip of the probe is separated from the asphalt, the width of the slit will reduce the adsorption potential, the gas-liquid interface of the liquid bridge will evaporate, the water molecule will escape, and the liquid bridge will dissipate; as the probe moves up,

the liquid bridge will be stretched and necked, the liquid bridge will gradually become thinner and longer until it finally breaks, leaving liquid masses on the tip of the probe and the asphalt surface. The fracture of the liquid bridge indicates that the probe tip is completely separated from the asphalt surface, which marks the end of a contact withdrawal cycle.

- (5) Difference between contact curves: the distance between the tip of the needle and the asphalt surface needed to produce attraction is called the attractive distance, which is expressed by  $D_a$ ; the height of the tip when the tip is completely separated from the asphalt surface is called the detached height, which is expressed by  $H_d$ . It can be seen from Figure 7 that, during the process of approaching,  $D_a$  (MRMA)  $>$   $D_a$  (MA), but the peak attraction of the asphalt to the tip of the needle is  $F$  (MRMA)  $>$   $F$  (MA). The CE segment is more moderate than the CE segment. The van der Waals force can only be induced by a pitch molecular group and probe tip molecular group within a certain distance. The elevation of the convex part of the bee-shaped MRMA structure is high, and the distribution is dense; thus, the probe tip can sense the van der Waals force at a higher height relative to that of the MA, and  $D_a$  (MRMA)  $>$   $D_a$  (MA) as the probe continues to move down. The attractive part and repulsive part of the van der Waals force change as the distance changes, and the liquid film collides on the asphalt surface at C (c). The viscosity of a liquid film with a micro- or nanoscale thickness is 4~8 orders of magnitude higher than that of bulk water (at 25°C, the viscosity of water is approximately 1 MPa s and the viscosity of asphalt is approximately  $2.3 \times 10^{11}$  MPa s), and the smaller the thickness is, the greater the viscosity is. When the probe is hit by the viscous resistance of the highly viscous liquid film and the repulsive force on the asphalt surface, the forward resistance of the probe increases gradually, and the force displacement curve turns at C (c); meanwhile, the CE (CE) segment does not obviously turn or jump. Therefore, it is considered that the thickness of the liquid film is the abscissa corresponding to the point C (c). The thickness of the liquid film of the MRMA is  $X_C = 26.5$  nm and that of the MA is  $X_C = 14.1$  nm.  $X_C >$   $X_C$ , indicating that the viscosity of the MRMA film is lower than that of the MA, which is the reason why the CE segment is more moderate than the CE segment. Due to the influence of the EMR, the number of honeycombs on the surface of the MRMA increases, the rough porous honeycombs have a higher adsorption potential than the smooth honeycombs, which is more conducive to the aggregation of water molecules, and the thickness of the liquid film on the surface of the MRMA increases. Therefore, the peak value of attraction during the process of exposure is  $F_{MRMA} >$   $F_{MA}$ . As the probe penetrates into the liquid film, the viscous resistance becomes larger, and the van der Waals



force changes from an attractive force to a repulsive force. The viscous resistance and van der Waals repulsive force are superposed, so the repulsive force sensed by the tip of the probe increases until it reaches the peak force.

- (6) Differences in the withdrawal curves: during the process of withdrawal, the peak value of the adsorption force of the asphalt on the tip of the needle is  $F_{MRMA} < F_{MA}$ , that is to say that  $F_{ad}(MRMA) < F_{ad}(MA)$ ,  $H_d(MRMA) > H_d(MA)$ , the GH segment is nearly parallel to the GH segment, the abscissa is  $x_F < x_B$ , and  $x_f > x_b$ . The abscissa of point  $F$  is between  $B$  and  $C$ , indicating that when the MRMA produces the maximum adhesion force,  $F_{ad}(MRMA)$  includes the van der Waals force and the capillary force; the abscissa of point  $F$  is behind point  $B$ , indicating that when the maximum adhesion force is generated, there is no van der Waals force between the tip of the needle and the asphalt, and the adhesion force at this time is mainly composed of the capillary force. The thin liquid film of the MA has a high viscosity and a greater adhesion to the tip than that of the MRMA, and there is a long chain of oil molecules adhering to the tip, resulting in  $F_{ad}(MRMA) < F_{ad}(MA)$ . The GH segment is nearly parallel to the GH segment, indicating that during the later stage of the contact withdrawal cycle, the stress of the probe is the same as that of the MRMA and MA, the liquid bridge neck shrinks to the fracture, and the tip of the probe disengages from the adhesion interface; as the probe continues to lift up, the liquid bridge is stretched to the necking state, and finally, the liquid bridge breaks at  $h$  and  $H$  points.

**3.4.3. Surface Energy and Dissipation Energy.** The surface energy and dissipation energy of the MRMA and MA were calculated by the adhesion contact theory combined with the force displacement curve produced by AFM to explore the micromodification mechanism of the EMR from the point of view of work and energy [16, 17].

After the force displacement curve is obtained, we need to analyze the data, so we need to choose an appropriate theoretical model. There are many commonly used theories, but the JKR theory is suitable for high adhesion systems; in addition, the rigid requirement of the object is low. Johnson, Kendall, and Roberts use the surface energy theory to modify the Hertz theory and obtain the JKR contact mechanics model [18]. Based on this model, the relationship between adhesion and the adhesion work is as follows:

$$F = \frac{3}{2}\pi RW, \quad (1)$$

where  $R$  is the equivalent radius of the curvature of the probe tip and  $W$  is the adhesion work.

The JKR model realizes the transformation from adhesion to adhesion work, and then, according to the principle of work energy transformation [19, 20], the transformation from adhesion work to surface energy is based on the

Fowkes model. The transformation relationship is shown in formulae (2) and (3):

$$\gamma_{ab} = \gamma_a + \gamma_b - 2\sqrt{\gamma_a^d \gamma_b^d}, \quad (2)$$

$$W_{ab} = 2\sqrt{\gamma_a^d \gamma_b^d}, \quad (3)$$

where  $\gamma_{ab}$  is interface energy;  $\gamma^d$  is dispersion component of the surface energy; and  $W_{ab}$  is adhesion work between interfaces.

For materials composed of nonpolar hydrocarbons, the dispersion component plays an absolutely dominant role in the surface energy component, so  $\gamma_a \approx \gamma_a^d$ . The expression of adhesion work can be approximately treated as follows:

$$W_{ab} = 2\sqrt{\gamma_a \gamma_b}. \quad (4)$$

It can be seen from formula (4) that, in the case of obtaining the probe surface energy  $\gamma_b$ , combined with the adhesion work between the probe and asphalt surface, the surface energy  $\gamma_a$  of asphalt can be calculated. According to the parameters provided by the manufacturer, the equivalent radius of the curvature of the probe is 20 nm, and the surface energy parameter is 1389.99 mJ/m<sup>2</sup>. The calculation results of the asphalt adhesion work and surface energy are shown in Table 7.

According to the data in Table 7, the following analysis can be performed:

- (1) The surface microadhesion of the MRMA is only 62% that of the MA. At the same time and at the same temperature, the wax is more stable than the oil, and the wax crystal causes the free radicals of the molecular chain to cross each other and form clusters; meanwhile, the long chain molecules of the oil can produce displacement and adhesion under the external load; at the same time and at the position where maximum adhesion occurs, the viscous resistance of the membrane prevents the tip from leaving the asphalt surface. Therefore, the MA is more sensitive than the MRMA to the contact of the needle tip, has stronger attraction forces, and shows greater surface adhesion. It is proved that the bee structure is the structure formed by the development of a wax nodule center, and its component is a wax component. Waxy crystallization can increase the brittleness of asphalt and lead to the decrease in adhesion. The waxy crystallization of the MRMA to the surface of asphalt results in a slight decrease in the surface low-temperature crack resistance and an increase in the internal adhesion.
- (2) The surface energy of the MRMA is 45% that of the MA. The increase in the asphaltene content will lead to the decrease in the surface energy; in addition, the oxidation condensation of the EMR will lead to the increase in the asphaltene content in the MRMA system, so the surface energy of the MRMA will decrease but will decrease to a lower energy than that of the MA. The decrease in the surface energy of the

TABLE 7: The calculation results of the asphalt adhesion work and surface energy.

Species of asphalt	Adhesion (nN)	Interfacial energy ( $\text{mJ} \cdot \text{m}^{-2}$ )	Adhesive work ( $\text{mJ} \cdot \text{m}^{-2}$ )
MRMA	5.70	0.66	60.48
MA	9.18	1.47	97.40

MRMA shows that compared with the MA, the MRMA and other substances consume less energy to form surfaces, and it is easier to form a new surface; the decrease in the surface energy of the MRMA also shows that the MRMA is easier than the MA to disperse, which is conducive to the emulsification of asphalt. The theory of solid physics points out that the surface of an object with a high surface energy is in a high energy state, and the surface of the system is unstable; thus, the surface energy is reduced through the adsorption of other substances and surface polymerization to ensure the thermodynamic stability of the system. A high surface energy is one of the reasons why the adhesion force of the MA is greater than that of the MRMA. To reduce the surface energy of the MA system, the adsorption of the probe tip is more obvious, which shows that the MA system is more unstable than the MRMA system. Therefore, the stability of the MRMA is better than that of the MA.

- (3) The results show that the adhesive work of the MRMA is 62% that of the MA. The MA has a higher surface energy than the MRMA, and a surface with a high surface energy tends to reduce its surface energy. High energy surfaces will absorb more dissipative energy to reduce the surface energy, causing more surface damage and plastic deformation. The MRMA has a higher surface stiffness than the MA, which will convert more external force into elastic potential energy and will release it during the withdrawal stage so that the part of external force that is converted into dissipation energy will be reduced; meanwhile, it is more difficult for a wax surface than an oil surface to produce interfacial damage and plastic deformation, so the MRMA has a lower sensitivity than the MA to external force energy. Therefore, the dissipation energy of the MRMA is lower than that of the MA. During a contact withdrawal cycle, the MA receives more dissipated energy than the MRMA. Under cyclic loading, more damage is accumulated quickly in the microstructure of the MA than in that of the MRMA; in addition, damage develops more rapidly toward the direction of structural failure, so it is easier to produce fatigue damage in the MA than in the MRMA.

#### 4. Conclusion

Powder:oil ratios of 0%, 3%, 6%, 9%, 12%, and 15% of the EMR with a particle size of approximately  $35 \mu\text{m}$  were mixed into the matrix asphalt. To compare the modification effect of the different powder:oil ratios, the penetration test, softening point test, and ductility test were carried out. At

the same time, by also performing an X-ray diffraction test, an infrared spectrum analysis, an atomic force microscope analysis, and a differential scanning calorimetry analysis, the modification effect and mechanism of the EMR micro-powder asphalt were explored:

- (1) After grinding, the crystallinity of the EMR particles decreased, and at the same time, amorphous substances were produced, the specific surface area of the powder increased, and the activity of the powder increased.
- (2) The high-temperature performance of the asphalt improved, and the temperature sensitivity of the asphalt reduced after the EMR was added. However, the low-temperature performance of the asphalt was not significantly improved. The comprehensive performance of the asphalt was the best when the powder:oil ratio was 9%.
- (3) The N, P, S, and other atoms in the EMR formed weak hydrogen bond with the atoms in the asphalt, which did not share the electron pair, so the activity of the asphalt was enhanced. At the same time, the  $\text{Al}_2\text{O}_3$  in the EMR adsorbed the small and medium molecular components of aliphatic hydrocarbons and aromatic hydrocarbons for oxidation, cross-linking, and condensation reactions at high temperatures. When the high molecular weight increased, the unreacted part of  $\text{Al}_2\text{O}_3$  was replaced by the low molecular weight part and continued to play the role of the catalytic oxidant and increased the content of the high molecular weight hydrocarbon in the asphalt component to improve the performance of the matrix asphalt.
- (4) The compatibility between the EMR and asphalt is good, so it is more suitable to describe the micro-adhesion contact of asphalt materials with the JKR theory; a high surface energy will make asphalt absorb more dissipation energy, so the surface energy will decrease, resulting in the instability of the system; EMR can reduce the surface energy of the MRMA by increasing the asphaltene component, so the stability of the MRMA is better than that of the MA.

#### Data Availability

The datasets used and analyzed during the current study are available from the corresponding author on reasonable request.

#### Conflicts of Interest

The authors declare no conflicts of interest.

## Acknowledgments

The research was supported by National Natural Science Foundation of China. (Grant no. 51768016) and Innovation Project of Guangxi Graduate Education, China (Grant no. YCSW2020043).

## References

- [1] A. J. Brown, P. S. Francis, J. L. Adcock, K. F. Lim, and N. W. Barnett, "Manganese (III) and manganese (IV) as chemiluminescence reagents: a review," *Analytica Chimica Acta*, vol. 624, no. 2, pp. 175–183, 2008.
- [2] F. Han and L. Wu, *Industrial Solid Waste Recycling in Western China*, pp. 127–164, Springer, Singapore, 2019.
- [3] L. J. Y. Zhao and L. Zhou, "Improvement of bending fatigue test for asphalt surfacing on orthotropic steel bridge deck," *Advances in Civil Engineering Materials*, vol. 5, no. 1, pp. 325–336, 2016.
- [4] G. S. Kumar and S. N. Suresh, "Evaluation of workability and mechanical properties of nonfoaming warm mix asphalt mixtures," *Advances in Civil Engineering Materials*, vol. 7, no. 1, pp. 132–157, 2018.
- [5] B. Liu, Y. Zhang, M. Lu, Z. Su, G. Li, and T. Jiang, "Extraction and separation of manganese and iron from ferruginous manganese ores: a review," *Minerals Engineering*, vol. 131, pp. 286–303, 2019.
- [6] M. K. Sinha and W. Purcell, "Reducing agents in the leaching of manganese ores: a comprehensive review," *Hydrometallurgy*, vol. 187, pp. 168–186, 2019.
- [7] J. Lu, D. Dreisinger, and T. Glück, "Manganese electrodeposition—a literature review," *Hydrometallurgy*, vol. 141, pp. 105–116, 2014.
- [8] A. P. Das, L. B. Sukla, N. Pradhan, and S. Nayak, "Manganese biomining: a review," *Bioresource Technology*, vol. 102, no. 16, pp. 7381–7387, 2011.
- [9] B. Tang, S. Gao, Y. Wang, X. Liu, and N. Zhang, "Pore structure analysis of electrolytic manganese residue based permeable brick by using industrial CT," *Construction and Building Material*, vol. 208, pp. 697–709, 2019.
- [10] Y. Wang, S. Gao, X. Liu, B. Tang, E. Mukiza, and N. Zhang, "Preparation of non-sintered permeable bricks using electrolytic manganese residue: environmental and NH<sub>3</sub>-N recovery benefits," *Journal of Hazardous Materials*, vol. 378, p. 120768, 2019.
- [11] C. Fang, R. Yu, S. Liu, and Y. Li, "Nanomaterials applied in asphalt modification: a review," *Journal of Materials Science & Technology*, vol. 29, no. 7, pp. 589–594, 2013.
- [12] Y. Zhang, X. Liu, Y. Xu, B. Tang, Y. Wang, and E. Mukiza, "Preparation and characterization of cement treated road base material utilizing electrolytic manganese residue," *Journal of Cleaner Production*, vol. 232, pp. 980–992, 2019.
- [13] P.-K. Hou, J.-S. Qian, Z. Wang, and C. Deng, "Production of quasi-sulfoaluminate cementitious materials with electrolytic manganese residue," *Cement and Concrete Composites*, vol. 34, no. 2, pp. 248–254, 2012.
- [14] F. Qin, Z. B. He, Q. N. Huang, and L. Q. Su, "Experiment study on the performance of manganese slag powder asphalt mixture," *Applied Mechanics and Materials*, vol. 71–78, pp. 3933–3937, 2011.
- [15] T. Zhou, L. Cao, E. H. Fini, L. Li, Z. Liu, and Z. Dong, "Behaviors of asphalt under certain aging levels and effects of rejuvenation," *Construction and Building Materials*, vol. 249, p. 118748, 2020.
- [16] I. Menapace, L. Garcia Cucalon, F. Kaseer et al., "Effect of recycling agents in recycled asphalt binders observed with microstructural and rheological tests," *Construction and Building Materials*, vol. 158, pp. 61–74, 2018.
- [17] D. Oldham, A. Hung, M. M. Parast, and E. H. Fini, "Investigating bitumen rejuvenation mechanisms using a coupled rheometry-morphology characterization approach," *Construction and Building Materials*, vol. 159, pp. 37–45, 2018.
- [18] K. L. Johnson and J. A. Greenwood, "An adhesion map for the contact of elastic spheres," *Journal of Colloid and Interface Science*, vol. 192, no. 2, pp. 326–333, 1997.
- [19] L. D. Poulidakos, S. D. Santos, M. Bueno, S. Kuentzel, M. Hugener, and M. N. Partl, "Influence of short and long term aging on chemical, microstructural and macro-mechanical properties of recycled asphalt mixtures," *Construction and Building Materials*, vol. 51, pp. 414–423, 2014.
- [20] M. Wang and L. Liu, "Investigation of microscale aging behavior of asphalt binders using atomic force microscopy," *Construction and Building Materials*, vol. 135, pp. 411–419, 2017.

## Research Article

# Investigating the Fatigue Characteristics of Large Stone Asphalt Mixtures Based on the Disturbed State Concept

Jianhui Wei <sup>1</sup>, Tao Fu,<sup>2</sup> Yongjun Meng <sup>2</sup>, and Chengming Xiao<sup>3</sup>

<sup>1</sup>College of Architecture and Civil Engineering, Shangqiu Normal University, Shangqiu 476000, China

<sup>2</sup>College of Civil Engineering and Architecture, Guangxi University, Nanning 530004, China

<sup>3</sup>Road and Bridge Engineering, Guangxi Transport Vocational and Technical College, Nanning 530023, China

Correspondence should be addressed to Yongjun Meng; hitmengyj@163.com

Received 18 March 2020; Revised 5 June 2020; Accepted 10 July 2020; Published 19 August 2020

Guest Editor: Meng Guo

Copyright © 2020 Jianhui Wei et al. This is an open access article distributed under the Creative Commons Attribution License, which permits unrestricted use, distribution, and reproduction in any medium, provided the original work is properly cited.

The mechanical response characteristics of large stone asphalt mixtures (LSAMs) are key factors in studying its fatigue characteristics during cyclic loading tests. Based on disturbed state concept (DSC) and viscoelastic continuum damage model (VECD), a series of tests using an overlay test (OT) were carried out to investigate the fatigue characteristics of LSAM. The results showed that disturbance and damage increased with decreasing frequency and increasing loading displacement and aging degree, while the asphalt content had no obvious adverse effect on the increase in damage. In addition, the disturbance and damage grew rapidly in the early stage of loading and reduced in the later stage of loading. On the contrary, based on DSC, the constitutive model modified with disturbance function ( $D$ ) defined by external work could describe the mechanical properties, and the evolution process of disturbance function ( $D$ ) could reflect the damage change in cyclic loading tests. The research conclusion can enrich the theoretical research on the fatigue failure response and mechanism of LSAM under cyclic loading and expand the application scope of DSC in the field of pavement.

## 1. Introduction

Semirigid materials are prone to fatigue cracking under repeated traffic loads and thermal gradients, which will destroy the pavement structure [1–4]. The inhomogeneity of the internal microstructure of asphalt mixtures will lead to differences in the damage location and mode [5, 6]. External environmental factors, such as test temperatures, aging, and loading, increase the complexity of describing fatigue characteristics of asphalt mixtures [2, 7]. To improve the fatigue resistance of asphalt mixtures, a variety of innovative products and technologies have been proposed in recent years. It is noteworthy that, with its nominal diameter of the largest dimension greater than 26.5 mm, LSAM has a good retarding effect on crack propagation because coarse aggregates can form a stable skeleton structure [8–11]. A great deal of attention has focus on fatigue behavior of conventional asphalt mixture. However, there are relatively few research studies on LSAM fatigue performance, especially on its constitutive model.

The applications of the viscoelastic continuum damage (VECD) model for predicting the fatigue performance of asphalt mixtures have been widely used in the past two decades [12–14]. Wang and Kim proposed a failure criterion by using the VECD model and considered that the attenuation of the pseudostiffness is a material constant that is independent of the loading mode, temperature, and stress/strain amplitude [15]. Babadopulos et al. studied the fatigue performance of aged asphalt mixtures using the VECD model [16]. Haddadi et al. used the VECD model to study the fatigue behavior of asphalt mixtures. The material constant  $a$  was inversely proportional to the slope of the central part of the relaxation modulus curve obtained by the bending dynamic test with a four-point bending beam device [17]. Sabouri and Kim proposed a new failure criterion using the VECD model and pointed out that the characteristic relationship between the average release rate of the pseudostrain energy and the final fatigue life during fatigue testing of recycled asphalt mixtures and nonrecycled asphalt

mixtures was independent of the loading mode, strain amplitude, and temperature [18].

Furthermore, numerous studies have proposed quantitative methods for investigating damage and establishment of constitutive models [5, 7, 19–22], but these methods still have some shortcomings in reflecting the damage evolution and establishment of constitutive models of materials. From a macroscopic perspective, the influence of the change in the material structure on the mechanical properties has received increasing attention. The disturbed state concept (DSC) provides a unified modeling method for engineering materials [23–26], which can consider various responses such as elasticity, plasticity, creep, microcracking and fracture, softening, and healing within a unified coupling framework. However, due to the lack of test data for calibration and field measurement for validation, DSC has not been widely used in the field of pavement.

Although the literature shows wide application prospect of VECD in fatigue performance of conventional asphalt mixtures, few studies have applied VECD approach into the results of the OT fatigue test on LSAM. In this study, the OT test is employed to investigate the fatigue performance of LSAM, including assessment the effects on fatigue performance of frequency, loading displacement, asphalt-aggregate ratio, and aging degree. In addition, this paper establishes a constitutive model of LSAM under repeated loading-based DSC model. Disturbance  $D$  was used to determine evolution of damage in materials. Meanwhile, the effects of frequency, loading displacement, asphalt-aggregate ratio, and aging degree on fatigue performance and change in disturbance were detected as well. The research conclusion not only enriches the theoretical research on the fatigue performance of LSAM under cyclic loading but also expands the application scope of DSC in the field of pavement.

## 2. Materials and Methods

**2.1. Materials and Specimen Preparation.** In the test, the binder is AH-70 heavy traffic paving asphalt, the aggregates are limestone aggregates, and the filler is limestone ore powder. The aggregate gradation design for LSAM-30 is shown in Table 1. The LSAM-30 test results and the technical specifications obtained from the Marshall test are shown in Table 2. Therefore, the optimum asphalt-aggregate ratio is 3.38%. Referring to the method of T0703-2011, which is stipulated in JTG E20-2011 [27], test specimens are trimmed into prismatic specimens with dimensions of 150 mm × 100 mm × 60 mm originating from a rutting plate with dimensions of 300 mm × 300 mm × 100 mm. In the short-term aging test, the rutting plates were made after the loose asphalt mixture was heated in an oven at 135°C ± 0.5°C for 4 hours ± 5 min. Then, the specimens were placed in an oven at 85°C ± 0.5°C for 3 days for the long-term aging test. Unlike the traditional aging test in which the aging time is set to 5 days, the aging time is set to 3 days in this paper. This is because the traditional aging test is equivalent to asphalt pavement, which has been in service

for 5–7 years. However, asphalt pavement will crack within 2-3 years.

**2.2. Test Methodology.** Because the overlay tester (OT) test can directly simulate crack initiation and propagation, to improve the reliability and practicability of OT testing, many research studies have been done on the OT test [28–31]. In the conventional OT test, the triangle waveform cannot reflect the actual pavement stress effectively and the thickness of 38 mm is not appropriate for the requirements of coarse aggregate. So a haversine loading and thickness of 60 mm were adopted in subsequent tests. In the previous research results [32], the specimen with a thickness of 60 mm was simulated by the finite element method. The results show that the LSAM with the thickness of 60 mm meets the test objectives. The OT test can not only effectively evaluate the reflective cracking of asphalt mixtures but also has good application prospects in studying fatigue cracking and low-temperature cracking.

In the study, test temperature was set at 25°C, and specific test conditions are shown in Table 3. The loading displacement waveform is shown in Figure 1. The output data from the OT test are shown in Figure 2. Peak load, number of cycles, and temperature are automatically recorded. An example of measured load and number of cycles is shown in Figure 2(a), and the peak load against number of cycles is shown in Figure 2(b). As shown in Figure 2, with the increase in the number of cycles, the peak load gradually decreases until fracture. During the test, three parallel tests were carried out for each group of specimens, and the average value of the test results was obtained. The specimen gluing process was performed as follows: (1) ensure that the bonding surface of the specimen and base plate was clean; (2) apply Vaseline on the spacer bar and inserted the spacer bar between the base plates; (3) place a piece of tape to cover the gap; (4) glue the specimens to the base plates with epoxy; and (5) add a 2.5 kg weight on top of the specimen for no less than 24 hours at room temperature. In each group, three specimens were placed in the environment box for no less than 4 hours, and the temperature was set at the test temperature ±0.5°C. Displacement control was applied during the test.

## 3. VECD Model and DSC Model

**3.1. VECD Model.** The mathematical expression of the pseudostrain is shown in (1a), where  $\varepsilon = D/d$ , in which  $D$  and  $d$  are the tension displacement and steel plate spacing, respectively (shown in Figure 1), and  $E(t - \tau)$  is relaxation modulus which can be obtained by a Prony series in the first load stage from OT, as shown in (1b):

$$\varepsilon^R(t) = \frac{1}{E^R} \int_0^t E(t - \tau) \frac{\partial \varepsilon}{\partial \tau} d\tau, \quad (1a)$$

$$E(t) = E_\infty + \sum_{i=1}^N E_i e^{-(t/\rho_i)}, \quad (1b)$$

TABLE 1: Aggregate gradation for LSAM-30.

Diameter (mm)	37.5	31.5	26.5	19	16	13.2	9.5	4.75	2.36	1.18	0.6	0.3	0.15	0.075
Passing rate (%)	100	97.6	86.6	70.0	63.4	57.1	49.0	34.3	24.0	16.8	11.9	8.2	5.7	4.0

TABLE 2: Marshall test results at an optimal asphalt content.

Asphalt-aggregate ratios (%)	Volume of air voids, VV (%)	Voids filled with asphalt, VFA (%)	Voids in the mineral aggregates, VMA (%)	Marshall stability (kN)	Flow value (0.1 mm)
3.38%	3.4	59.1	11.9	30	65
Specification requirement	3–6	60–75	>11	>15	40–70

TABLE 3: The specific test conditions.

	Frequency (Hz)	Asphalt-aggregate ratios (%)	Loading displacement amplitude (mm)	Aging
Group 1	1	3.38	0.3	Nonaging
	5			
	10			
Group 2	5	3.38	0.1	Nonaging
			0.2	
			0.3	
Group 3	10	3.38	0.3	Nonaging
		3.6		
		3.9		
Group 4	10	3.38	0.3	Nonaging
				Short aging
				Long aging

where  $E(t)$  is the relaxation modulus,  $E_{\infty}$  is the long-term equilibrium modulus,  $E_i$  is the components of relaxation modulus,  $\rho_i$  is the relaxation time, and  $N$  is the number of elements in Prony series.

Based on the concept of the pseudostrain and continuous damage theory, the pseudostiffness  $C$  is the ratio of the peak stress to the corresponding pseudostrain [17]:

$$C = \frac{\sigma}{I \times \varepsilon^R}, \quad (2)$$

where  $I = \sigma_1/\varepsilon_1^R$  is the variable used to normalize pseudostiffness  $C$  and  $\sigma_1$  and  $\varepsilon_1^R$  are the stress and pseudodisplacement at the end of the first cycle, respectively.

The  $C$ - $S$  curve under the uniaxial tension test is different from that under the uniaxial compression test. Likewise, the  $C$ - $S$  curve under the tension-compression test is different from that under the uniaxial tension test. Researchers believe that damage only accumulates in the tensile portion of each cycle [33, 34]. Park et al. [35] calculated the damage parameter  $S$  in asphalt mixtures by using the following equation:

$$\frac{dS}{dt} = \left( -\frac{\partial W^R}{\partial S} \right)^{\alpha}, \quad (3)$$

where  $W^R$  is the pseudostrain energy density function,  $\alpha$  is a constant related to the rate of damage growth, and  $t$  is the time.  $\alpha = 1 + (1/m)$  for strain-controlled tests, while  $\alpha = 1/m$  for stress-controlled tests, where  $m$  represents the maximum slope of the relaxation modulus vs. the time graph in log-log scale. For asphalt mixtures, the functions of the

stress and pseudostrain energy density under uniaxial loading are expressed as follows:

$$\sigma = \frac{\partial W^R}{\partial \varepsilon^R} = IC(S)\varepsilon^R, \quad (4)$$

$$W^R = \frac{I}{2}C(S)\varepsilon^{R^2}. \quad (5)$$

Damage parameters  $S$  are obtained from formulas (3) and (5):

$$\frac{dS}{dt} = \left[ -I \frac{\varepsilon^{R^2}}{2} \frac{dC}{dt} \right]^{(\alpha/1+\alpha)}. \quad (6)$$

In repeated load tests, the following relationships are established:

$$N = ft \longrightarrow \frac{dN}{dt} = f \longrightarrow dt = \frac{dN}{f}, \quad (7)$$

where  $N$  is the number of cycles and  $t$  is the time. In consideration of  $(dC/dt) = ((dC/dN)(dN/dt))$  and  $(dS/dt) = ((dS/dN)(dN/dt))$ , the following equation is derived from (6):

$$\frac{dS}{dN} f = \left[ -I \frac{\varepsilon^{R^2}}{2} \frac{dC}{dN} f \right]^{(\alpha/1+\alpha)}, \quad (8)$$

$$S_M = \sum_{i=1}^M \left[ \left( \frac{I}{2} (\varepsilon_i^R)^2 (C_{i-1} - C_i) \right)^{(\alpha/1+\alpha)} \left( \frac{N_i - N_{i-1}}{f} \right)^{(1/1+\alpha)} \right], \quad (9)$$

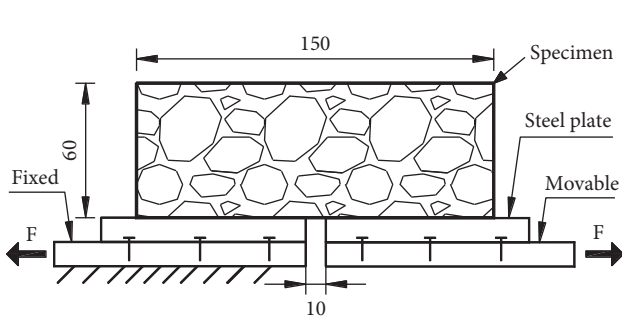


FIGURE 1: Test schematic diagram (unit: mm) and test loading model diagram in OT.

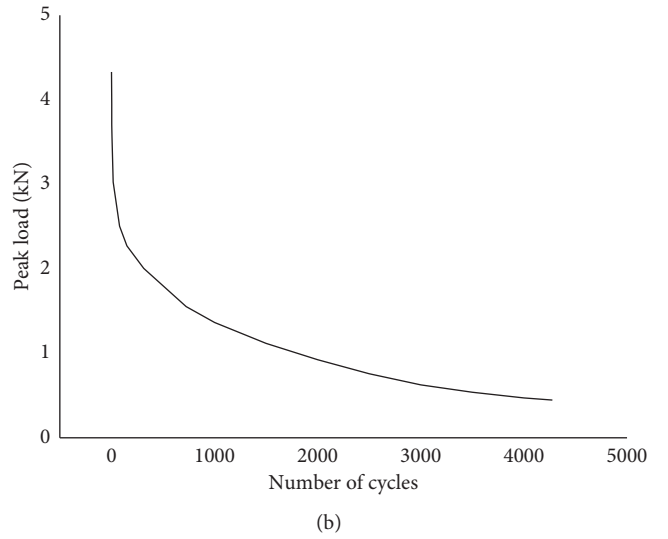
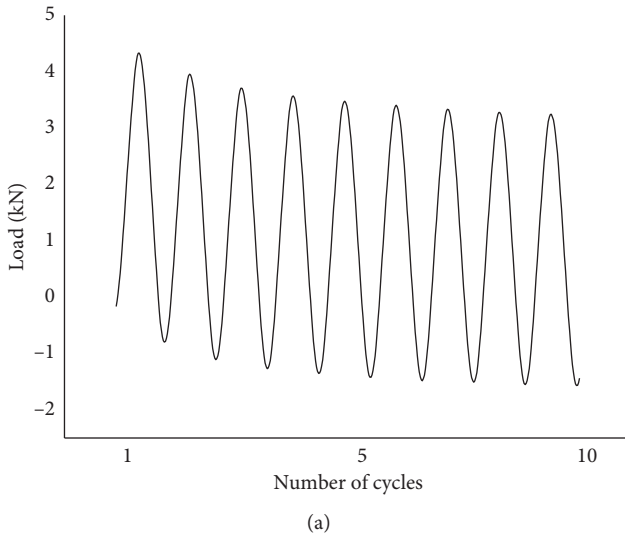


FIGURE 2: OT results data: (a) example of load cycles; (b) peak load reduction curve.

where  $S_M = S(N_M)$ ,  $C_i = C(N_i)$ , and  $\varepsilon_i^R = \varepsilon^R(N_i)$ .

**3.2. Constitutive Model Based on the DSC.** In the DSC model, the forces (mechanical force and thermal and environmental forces) cause a disturbance of the material microstructure, resulting in material changes in the internal microstructure from a relatively intact state (RI) after an automatic adjustment process to a fully adjusted state (FA). This self-adjusting process may involve the relative movement of particles that produce microcracks and damage. It can cause obvious disturbance. This disturbance is defined by a disturbance function  $D$ , which represents the relationship between the observation response and initial response and describes the evolution of the disturbance with the macroscopic mechanical response to simulate the constitutive relationship of the materials:

$$d\sigma_{ij}^a = (1 - D)d\sigma_{ij}^i + Dd\sigma_{ij}^c + dD(\sigma_{ij}^c - \sigma_{ij}^i), \quad (10a)$$

$$d\sigma_{ij}^a = (1 - D)C_{ijkl}^i d\varepsilon_{kl}^i + DC_{ijkl}^i d\varepsilon_{kl}^i + dD(\sigma_{ij}^c - \sigma_{ij}^i), \quad (10b)$$

where  $\sigma_{ij}$  and  $\varepsilon_{ij}$  are the stress and strain, respectively;  $C_{ijkl}$  is the elastic coefficient; and  $a$ ,  $i$ , and  $c$  represent the observation state, RI, and FA, respectively.

The relative intact (RI) state is defined by an ideal elastic-plastic model, and for the uniaxial stress state, the elastic coefficient tensor  $C^e = E$  ( $E$  is the elasticity modulus). The fully adjusted (FA) state under uniaxial tension is defined based on the approximation of the ultimate asymptotic response of the material, and the ultimate tensile stress  $\sigma^c$  is defined by the stress during material failure.

Figure 3 shows a schematic diagram of the mechanical response of a material in a DSC model and the first cycle hysteretic loop curve in the low cycle fatigue test. For the loading section of the first period, as shown in Figure 3, the linear relationship between the load and displacement is obvious. It shows that the material maintains an elastic deformation in the first period of loading, and it is considered that there is no damage in the material at this stage. Therefore, the first loading period is considered as the RI; thus, the work of the external force during the first loading process is  $W_0$ . During the loading process, the work done by the external force per cycle is  $W_i$ , and the work done by the external force in the last cyclic loading cycle is  $W_c$ . Thus, the disturbance  $D$  is defined as

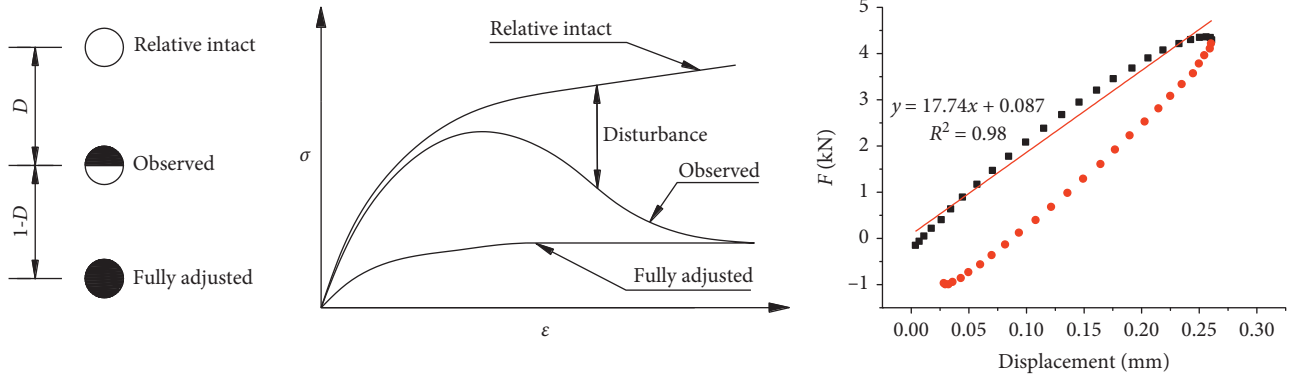


FIGURE 3: Schematic of the stress-strain behavior in the DSC and definition of the initial state.

$$D = \frac{W_0 - W_i}{W_0 - W_c} \quad (11)$$

According to the fatigue test on the asphalt mixture, the cumulative disturbance is nonlinear. The evolution equation of the disturbance can be expressed as follows:

$$D = 1 - \left[ 1 - \left( \frac{N}{N_f} \right)^r \right]^a, \quad (12)$$

where  $r$  and  $a$  are fitting parameters and  $N$  and  $N_f$  are the number of loading cycles and fatigue life, respectively. Based on the RI and FA states and once disturbance is defined, the DSC equations under repeated loading can be derived as

$$\sigma_{ij}^a = (1 - D)\sigma_{ij}^i + D\sigma_{ij}^c. \quad (13)$$

After normalizing the peak load of each cycle, (13) can be expressed as follows:

$$\frac{\sigma_{ij}^a}{\sigma_{(1)}^a} = (1 - D) + D \frac{\sigma_{ij}^c}{\sigma_{(1)}^c}, \quad (14)$$

where  $\sigma_{ij}^a$  is the observed stress in the fatigue test,  $\sigma_{ij}^i$  is the stress in the RA,  $\sigma_{ij}^c$  is the stress in the FA,  $\sigma_{(1)}^a$  is the maximum stress in the first loading cycle, and  $D = D_n$  is the disturbance corresponding to each loading cycle.

#### 4. Results and Discussion

In the  $C$ - $S$  curve (in Figure 4),  $S$  represents the damage in the specimens during the test, and  $C$  represents the normalized pseudostiffness. The slower the  $C$ - $S$  curve descends, the longer the curve is, the better the performance of the asphalt mixture will be. It can be seen from Figure 4 that the pseudostiffness decreases with increasing damage, and the rate of decrease in the pseudostiffness in the early stage is faster than that in the later stage. The  $C$ - $S$  curves of 5 Hz and 10 Hz are higher than that obtained for 1 Hz, which indicates that increasing the frequency can slow down the damage development rate and prolong the service life. The decline rate of the  $C$ - $S$  curve of 0.1 mm is slower than that of 0.2 mm and 0.3 mm, but the curve of 0.3 mm decreases faster. This indicates that increasing the loading displacement will accelerate the damage and failure of the specimens. The  $C$ - $S$

curve of the asphalt-aggregate ratio of 3.6% is shorter and lower than that of the other two asphalt-aggregate ratios. The two curves of 3.38% and 3.9% indicate that increasing the asphalt content does not substantially improve the tensile strength, but increasing the asphalt content can prolong the fatigue life of the specimens. The  $C$ - $S$  curve becomes shorter after aging, and the rate of decrease gradually increases with the aging degree, which indicates that aging has an effect on the fatigue life. The brittleness of the aged asphalt mixtures increases, the damage increases rapidly with increasing aging degree, and the fatigue life of the aged asphalt mixtures decreases.

It can be seen from Figure 5 that the disturbance increases rapidly in the early stage of loading displacement; when the fatigue life ratio is approximately 0.2, the disturbance increases slowly. This indicates that the integrity of the materials decreases substantially, and the damage increases rapidly during early loading. However, the damage increases slowly, and the rate of cumulative damage slows down during later loading. The disturbance decreases with the increase in the frequency until the fatigue life ratio is approximately 0.8, which indicates that increasing the loading frequency can prolong the fatigue life. The disturbance increases with the increase in the loading displacement, which indicates that the damage caused by a loading displacement of 0.1 mm is smaller than that with a larger loading displacement. The disturbance curves of the loading displacements of the 0.2 mm and 0.3 mm almost overlap, which indicates that the damage in the specimens under these two conditions does not change substantially. The disturbance curve of the asphalt-aggregate ratio of 3.6% is higher than that of the other two asphalt-aggregate ratios, which indicates that the damage develops faster when the asphalt-aggregate ratio is 3.6%. Aging will increase the modulus of the asphalt mixture and weaken its tensile strain, so aging will accelerate the development of damage in the specimens. That is, the disturbance increases with the increase in the aging degree.

Figure 6 shows evolution of pseudostiffness with the increasing number of cycles, and it suggests that an exponential function can capture the trend of pseudostiffness with the increasing number of cycles. Equation (15) is an example of fitted exponential function:



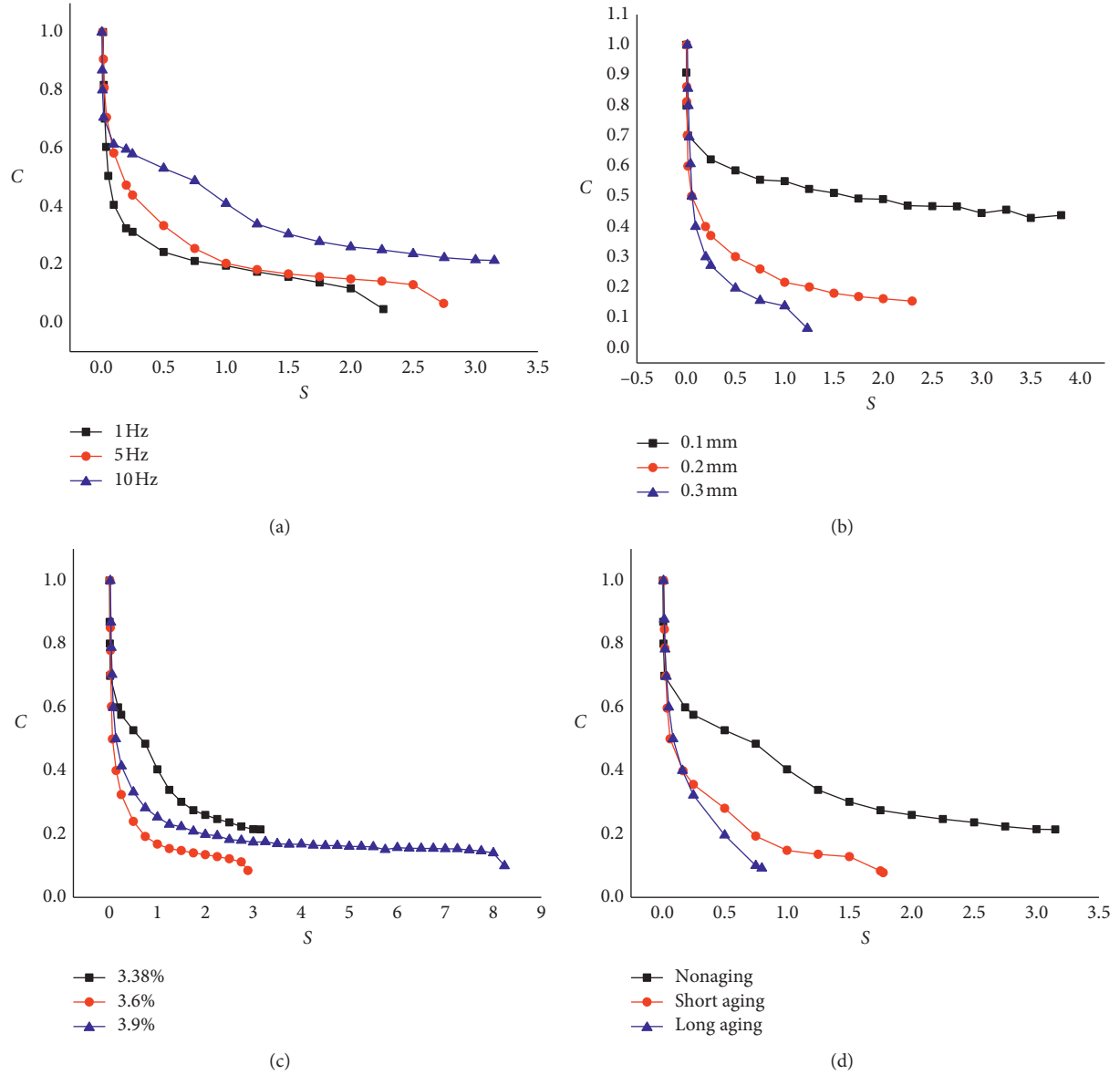


FIGURE 4: Damage characteristic curves corresponding to (a) frequency, (b) displacement, (c) asphalt-aggregate ratio, and (d) aging degree.

$$C = 1 - \exp\left[-A\left(\frac{N}{N_f}\right)^Z\right], \quad (15)$$

where  $A$  and  $Z$  are fitting coefficients. It can be seen from Figure 6 that the curve can be fitted well by an exponential function, and the pseudostiffness develops rapidly in the early stage but slows down in the later stage, which is consistent with the variation trend of the disturbance curve. This indicates that the DSC model proposed in this paper can effectively reflect the evolution of damage.

The calculation results of the parameters in (12) and (15) are shown in Table 4. It can be seen from Table 4 that parameters  $r$  and  $a$  increase with increasing frequency. An increasing loading displacement will increase parameter  $a$ , while parameter  $r$  shows a trend of decreasing first and then

increasing. The increase in the asphalt content and aging will decrease parameter  $a$ . Both parameters  $A$  and  $Z$  decrease with increasing displacement.  $Z$  decreases with increasing frequency. Increasing the asphalt content will increase parameter  $Z$ , while aging will decrease parameter  $Z$ .

Figure 7 shows the test results and theoretical calculation results of the peak load varying with the loading cycle. The relationship between the peak load obtained from the test and the number of cycles is in good agreement with the calculated results, which indicates that the proposed constitutive model under repeated loading can reflect the variation in its mechanical properties. The increase in the frequency and loading displacement can substantially increase the peak load. The influence of aging and increasing the asphalt content on the peak load is not obvious, but increasing the asphalt content can delay the load attenuation

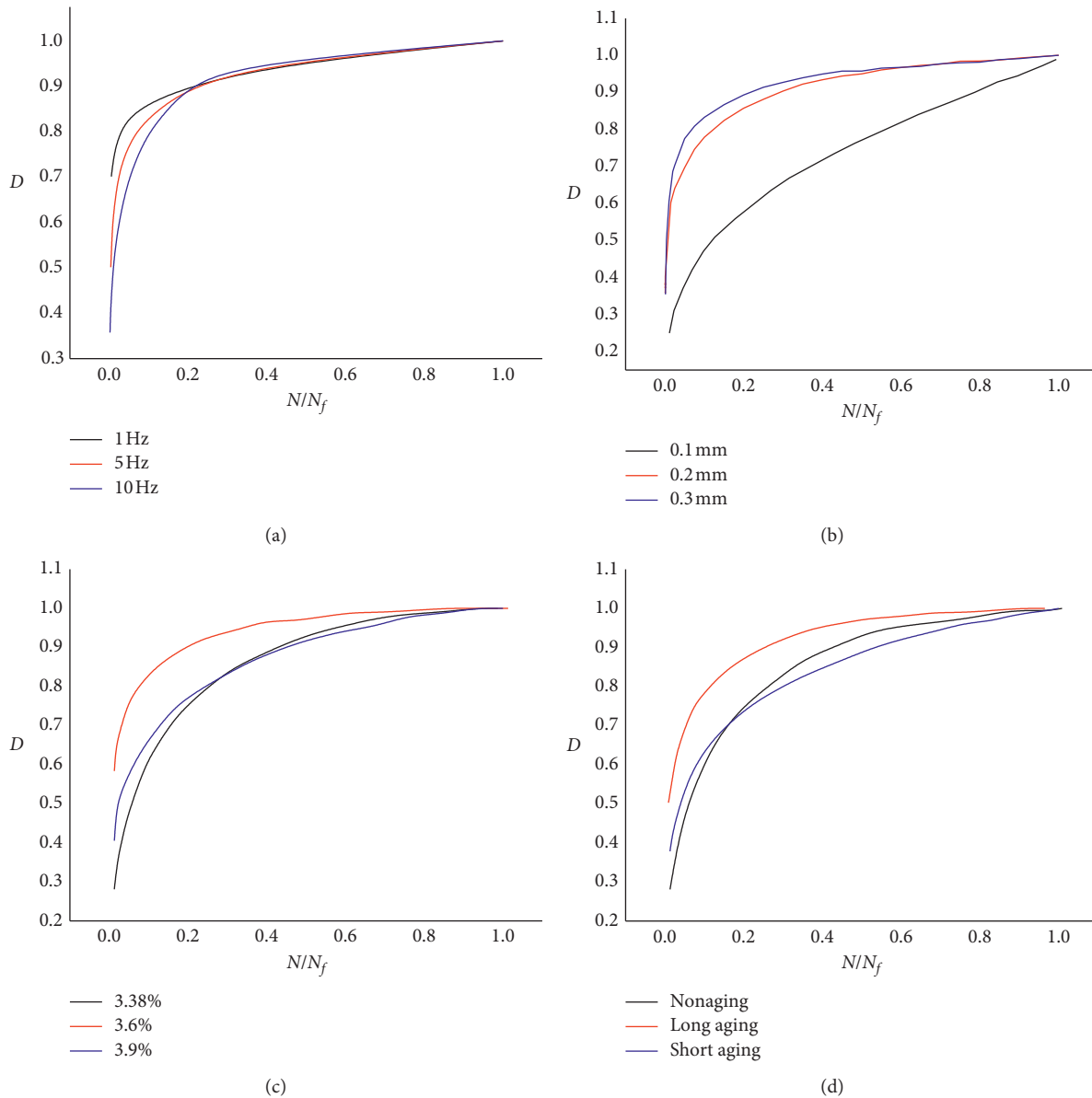


FIGURE 5: Disturbance  $D$  characteristic curves corresponding to the (a) frequency, (b) loading displacement, (c) asphalt-aggregate ratio, and (d) aging degree.

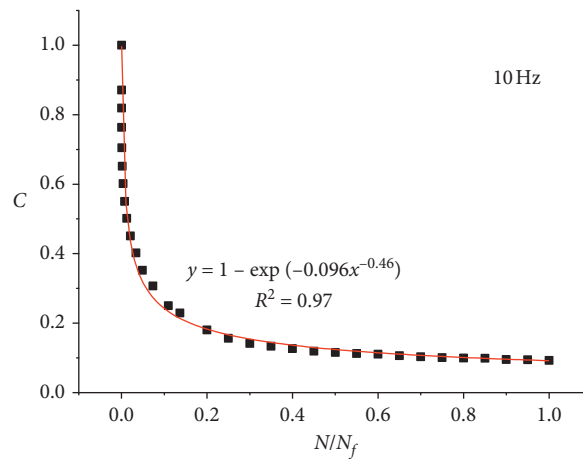


FIGURE 6:  $C - N/N_f$  curve (10 Hz).

TABLE 4: The calculation parameters.

Test conditions		$r$	$a$	$A$	$Z$
Standard		0.4	1.93	0.159	-0.422
Group 1	1 Hz	0.053	0.82	0.154	-0.285
	5 Hz	0.25	1.8	0.125	-0.379
Group 2	0.1 mm	0.28	0.85	0.598	-0.173
	0.2 mm	0.17	1.17	0.204	-0.318
Group 3	3.6%	0.22	1.93	0.131	-0.321
	3.9%	0.25	1.34	0.194	-0.253
Group 4	Short aging	0.26	1.96	0.113	-0.375
	Long aging	0.24	1.18	0.151	-0.435

Note. The standards in Table 4 are as follows: the asphalt-aggregate ratio is 3.38%, the temperature is 25°C, the loading frequency is 10 Hz, the displacement amplitude is 0.3 mm, and nonaging.

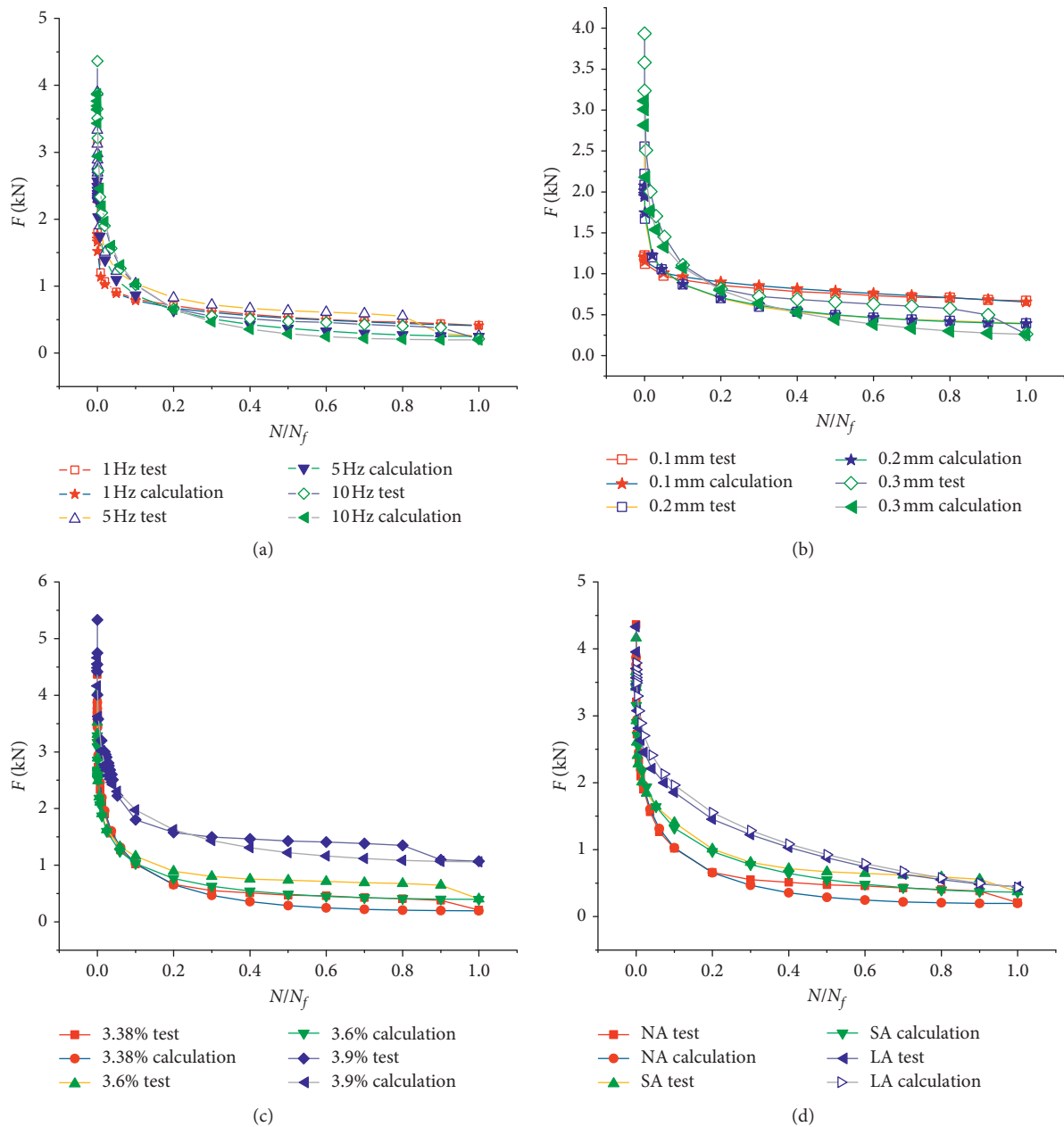


FIGURE 7: Test and theoretical curves corresponding to the (a) frequency, (b) loading displacement, (c) asphalt-aggregate ratio, and (d) aging degree.

speed, which is conducive to delaying the development of cracks, while aging can accelerate the load attenuation speed and crack expansion.

## 5. Conclusions

In this paper, a constitutive model of the LSAM under repeated loading is proposed based on the DSC theory. Through the analysis of the fatigue characteristics of the LSAM under different conditions, it is shown that the model proposed in this paper can reflect its mechanical properties, and the disturbance can reflect the damage evolution during the fatigue process. The conclusions are summarized as follows:

- (1) Damage develops rapidly in the early stage of loading and slows down in the later stage of loading. Damage increases with the decrease in the frequency, the increase in the loading displacement, and the increase in aging degree. The asphalt content has no obvious adverse effect on the increase in damage.
- (2) The magnitude of the disturbance reflects the damage degree. The results show that the disturbance increases with decreasing frequency and increasing loading displacement and aging degree. The pseudostiffness evolution model in this study can reflect the relationship between the pseudostiffness and the number of loading cycles.
- (3) The VECD model can effectively reflect the fatigue characteristics of the LSAM. Increasing the loading displacement, decreasing the frequency, and increasing the aging degree will increase the decline rate of the C-S curve. That is, the fatigue life will be shortened.

## Data Availability

The data used to support the findings of this study are available from the corresponding author upon request.

## Conflicts of Interest

The authors declare that there are no conflicts of interest regarding the publication of this paper.

## Acknowledgments

This paper was based on work supported by the National Science Foundation of China (grant no. 51968006).

## References

- [1] T. Hu, J. Zi, J. Li, L. Mao, S. Jin, and W. Zhou, "Laboratory and field investigation of interlayer bonding between asphalt concrete layer and semi-rigid base constructed by using continuous construction method," *Construction and Building Materials*, vol. 150, pp. 418–425, 2017.
- [2] J. S. Qian, X. R. Chen, C. Jin, and W. Fu, "Influence of combined load on the performance of geosynthetics as antireflective cracking system in semirigid base asphalt pavements," *Journal of Materials in Civil Engineering*, vol. 30, no. 9, p. 7, 2018.
- [3] X. Wang, K. Li, Y. Zhong, Q. Xu, and C. Li, "XFEM simulation of reflective crack in asphalt pavement structure under cyclic temperature," *Construction and Building Materials*, vol. 189, pp. 1035–1044, 2018.
- [4] X. Wang and Y. Zhong, "Reflective crack in semi-rigid base asphalt pavement under temperature-traffic coupled dynamics using XFEM," *Construction and Building Materials*, vol. 214, pp. 280–289, 2019.
- [5] E. Masad, V. T. F. Castelo Branco, D. N. Little, and R. Lytton, "A unified method for the analysis of controlled-strain and controlled-stress fatigue testing," *International Journal of Pavement Engineering*, vol. 9, no. 4, pp. 233–246, 2008.
- [6] F. Xiao, P. E. Wenbin Zhao, and S. N. Amirkhanian, "Fatigue behavior of rubberized asphalt concrete mixtures containing warm asphalt additives," *Construction and Building Materials*, vol. 23, no. 10, pp. 3144–3151, 2009.
- [7] S. Lv, C. Liu, J. Zheng, Z. You, and L. You, "Viscoelastic fatigue damage properties of asphalt mixture with different aging degrees," *KSCE Journal of Civil Engineering*, vol. 22, no. 6, pp. 2073–2081, 2018.
- [8] H. B. Guo and S. F. Chen, "Numerical simulation of the reflective crack propagation path for open-graded large stone asphalt mixes," *Advanced Materials Research*, vol. 152–153, no. 7, pp. 180–183, 2010.
- [9] Q. Lu, J. Zi, H. Wang, Q. Huang, and W. Wan, "Coupled numerical analysis of anti-crack mechanism of large stone asphalt mixture," *Journal of Highway and Transportation Research and Development (English Edition)*, vol. 4, no. 2, pp. 22–26, 2010.
- [10] X.-l. Wang, X.-m. Huang, and G.-j. Bian, "Mechanism analysis of the use of LSPM for reflection crack prevention of semi-rigid base asphalt mixture," *Journal of Highway and Transportation Research and Development (English Edition)*, vol. 11, no. 3, pp. 8–15, 2017.
- [11] Y. Zhao and X. Huang, "Design method and performance for large stone porous asphalt mixtures," *Journal of Wuhan University of Technology-Mater. Sci. Ed.*, vol. 25, no. 5, pp. 871–876, 2010.
- [12] W. Cao, A. Norouzi, and Y. R. Kim, "Application of viscoelastic continuum damage approach to predict fatigue performance of Binzhou perpetual pavements," *Journal of Traffic and Transportation Engineering (English Edition)*, vol. 3, no. 2, pp. 104–115, 2016.
- [13] A. Norouzi and Y. R. Kim, "Mechanistic evaluation of fatigue cracking in asphalt pavements," *International Journal of Pavement Engineering*, vol. 18, no. 6, pp. 530–546, 2017.
- [14] H. Sadek, E. Masad, H. Al-Khalid, and O. Sirin, "Probabilistic analysis of fatigue life for asphalt mixtures using the viscoelastic continuum damage approach," *Construction and Building Materials*, vol. 126, pp. 227–244, 2016.
- [15] Y. Wang and Y. R. Kim, "Development of a pseudo strain energy-based fatigue failure criterion for asphalt mixtures," *International Journal of Pavement Engineering*, vol. 20, no. 10, pp. 1–11, 2019.
- [16] L. Babadopulos, J. L. S. Ferreira, J. B. Soares, L. A. H. do Nascimento, and V. Branco, "Aging-effect incorporation into the fatigue-damage modeling of asphalt mixtures using the S-VECD model," *Journal of Materials in Civil Engineering*, vol. 28, no. 12, p. 11, 2016.
- [17] F. Haddadi, M. Ameri, M. H. Mirabimoghadam, and H. R. A. Hosseini, "Validation of a simplified method in viscoelastic continuum damage (VECD) model developed for

- flexural mode of loading,” *Construction and Building Materials*, vol. 95, pp. 892–897, 2015.
- [18] M. Sabouri and Y. R. Kim, “Development of a failure criterion for asphalt mixtures under different modes of fatigue loading,” *Transportation Research Record: Journal of the Transportation Research Board*, vol. 2447, no. 1, pp. 117–125, 2014.
- [19] X. Luo, R. Luo, and R. L. Lytton, “Characterization of asphalt mixtures using controlled-strain repeated direct tension test,” *Journal of Materials in Civil Engineering*, vol. 25, no. 2, pp. 194–207, 2013.
- [20] H. K. Salama and K. Chatti, “Evaluation of fatigue and rut damage prediction methods for asphalt concrete pavements subjected to multiple axle loads,” *International Journal of Pavement Engineering*, vol. 12, no. 1, pp. 25–36, 2011.
- [21] Y. Sun, C. Fang, J. Wang, X. Yuan, and D. Fan, “Method of fatigue-life prediction for an asphalt mixture based on the plateau value of permanent deformation ratio,” *Materials*, vol. 11, no. 5, p. 722, 2018.
- [22] J. Zhang, Y. D. Wang, and Y. Su, “Fatigue damage evolution model of asphalt mixture considering influence of loading frequency,” *Construction and Building Materials*, vol. 218, pp. 712–720, 2019.
- [23] C. S. Desai, “Constitutive modeling of materials and contacts using the disturbed state concept: Part 1—Background and analysis,” *Computers & Structures*, vol. 146, pp. 214–233, 2015.
- [24] C. S. Desai, “Constitutive modeling of materials and contacts using the disturbed state concept: Part 2—Validations at specimen and boundary value problem levels,” *Computers & Structures*, vol. 146, pp. 234–251, 2015.
- [25] C. S. Desai, “Disturbed state concept as unified constitutive modeling approach,” *Journal of Rock Mechanics and Geotechnical Engineering*, vol. 8, no. 3, pp. 277–293, 2016.
- [26] S. Zhi, W. W. Gun, L. X. Hui, and T. Bo, “Evaluation of fatigue crack behavior in asphalt concrete pavements with different polymer modifiers,” *Construction and Building Materials*, vol. 27, no. 1, pp. 117–125, 2012.
- [27] Research Institute of Highway Ministry of Transport, “Transport RIoHMo: standard test methods of bitumen and bituminous mixtures for highway engineering,” China Communications Press, Beijing, China, JTG E20-2011, 2011.
- [28] V. Garcia, J. Garibay, I. Abdallah, and S. Nazarian, “Performance of the overlay tester in monotonic and cyclic loading modes,” in *Proceedings of the International Conference on Transportation and Development*, American Society of Civil Engineers, Houston, Texas, June 2016.
- [29] V. M. Garcia, J. Garibay, I. Abdallah, and S. Nazarian, “Overlay tester results from dense-graded asphalt concrete mixes: accuracy in characterizing crack susceptibility,” *Transportation Research Record: Journal of the Transportation Research Board*, vol. 2631, no. 1, pp. 30–38, 2017.
- [30] J. S. Li, J. Oh, B. Naik, G. S. Simate, and L. F. Walubita, “Laboratory characterization of cracking-resistance potential of asphalt mixes using overlay tester,” *Construction and Building Materials*, vol. 70, pp. 130–140, 2014.
- [31] L. F. Walubita, A. M. Faruk, J. Zhang, and X. D. Hu, “Characterizing the cracking and fracture properties of geosynthetic interlayer reinforced HMA samples using the overlay tester (OT),” *Construction and Building Materials*, vol. 93, pp. 695–702, 2015.
- [32] J. H. Wei, J. J. Shi, and J. L. Liang, “Overlay test to investigate the crack propagation of a large-size asphalt mixture,” *Journal of Materials in Civil Engineering*, vol. 32, no. 5, Article ID 04020097, 2020.
- [33] J. S. Daniel and Y. R. Kim, “Development of a simplified fatigue test and analysis procedure using a viscoelastic, continuum damage model,” in *Proceedings of the Association Asphalt Paving Technologists*, Colorado Springs, CO, USA, March 2002.
- [34] B. S. Underwood, Y. R. Kim, and M. N. Guddati, “Improved calculation method of damage parameter in viscoelastic continuum damage model,” *International Journal of Pavement Engineering*, vol. 11, no. 6, pp. 459–476, 2010.
- [35] S. W. Park, Y. Richard Kim, and R. A. Schapery, “A viscoelastic continuum damage model and its application to uniaxial behavior of asphalt concrete,” *Mechanics of Materials*, vol. 24, no. 4, pp. 241–255, 1996.

## Research Article

# Modeling of Surface Drainage during the Service Life of Asphalt Pavements Showing Long-Term Rutting: A Modular Hydromechanical Approach

Stefan Alber <sup>1</sup>, Barbara Schuck,<sup>1</sup> Wolfram Ressel,<sup>1</sup> Ronny Behnke <sup>2</sup>,  
Gustavo Canon Falla,<sup>3</sup> Michael Kaliske <sup>2</sup>, Sabine Leischner,<sup>3</sup> and Frohmut Wellner<sup>3</sup>

<sup>1</sup>Institute for Road and Transport Science, Universität Stuttgart, Faculty of Civil and Environmental Engineering, 70569 Stuttgart, Germany

<sup>2</sup>Institute of Structural Analysis, Technische Universität Dresden, Faculty of Civil Engineering, 01062 Dresden, Germany

<sup>3</sup>Institute of Urban and Pavement Engineering, Technische Universität Dresden, Faculty of Civil Engineering, 01062 Dresden, Germany

Correspondence should be addressed to Stefan Alber; [stefan.alber@isv.uni-stuttgart.de](mailto:stefan.alber@isv.uni-stuttgart.de)

Received 7 April 2020; Revised 8 July 2020; Accepted 13 July 2020; Published 12 August 2020

Guest Editor: Meng Guo

Copyright © 2020 Stefan Alber et al. This is an open access article distributed under the Creative Commons Attribution License, which permits unrestricted use, distribution, and reproduction in any medium, provided the original work is properly cited.

This paper presents a modular hydromechanical approach to assess the short- and long-term surface drainage behavior of arbitrarily deformable asphalt pavements. The modular approach consists of three steps. In the first step, the experimental characterization of the thermomechanical asphalt material behavior is performed. In the second step, information about the long-term material behavior of the asphalt mixtures is integrated on the structural scale via a finite element (FE) tire-pavement model for steady-state rolling conditions and time homogenization in order to achieve a computationally efficient long-term prediction of inelastic deformations of the pavement surface (rut formation). In the third step, information regarding the current pavement geometry (deformed pavement surface) is used to carry out a surface drainage analysis to predict, e.g., the thickness of the water film or the water depth in the pavement ruts as a function of several influencing quantities. For chosen numerical examples, the influence of road geometry (cross and longitudinal slope), road surface (mean texture depth and state of rut deformation), and rainfall properties (rain intensity and duration) on the pavement surface drainage capacity is assessed. These parameters are strongly interrelated, and general statements are not easy to find. Certain trends, however, have been identified and are discussed.

## 1. Introduction

The ultimate goal of pavement design is to provide an optimal structure that meets the required service life while ensuring safety and minimizing costs and environmental impacts.

One major problem is the rapid increase in the volume of traffic with growing axle loads, which leads to amplified fatigue mechanisms and the premature failure of pavement structures. A further effect is intensified rut formation [1]. Increased temperatures, due to global warming, exacerbate this effect [2]. Rutting is related to the long-term behavior of the pavement structure and describes the accumulation of permanent vertical deformations due to repeated traffic

loading. Rutting is undesirable due to several reasons: (1) increased risk of water infiltration (through cracks) into the pavement structure with several deterioration effects, (2) higher fuel consumption as a result of a higher level of friction on the outside edge of the tire profile, and (3) accumulation of water (or even ice) constituting a potential traffic safety risk due to aquaplaning.

In this context, an increasing demand on design asphalt mixtures with a high resistance to permanent deformation at high temperatures is observable. To optimize the design of these materials, detailed analyses of the inelastic deformation are required. Hence, the results of laboratory tests can be used to determine the constitutive material relations

between dynamic variables (i.e., stresses and forces) and kinematic quantities (i.e., strains and displacements). The most commonly used laboratory tests are the static creep-recovery test and the cyclic uniaxial compression (CUCT) test. Creep-relaxation tests are popular because of their simplicity. However, some authors have reported that the results do not correlate well with actual in-service pavement rutting [3]. The CUCT is, on the other hand, more compatible with in-field conditions, and the results are more consistent with in-service rutting measurements [4]. Since rutting is, in general, a long-term phenomenon, accelerated test procedures are important for the reduction of testing times [5].

By using the results of appropriate laboratory tests, numerical modeling techniques provide additional means for predicting the rutting behavior of asphalt pavements on the structural scale. These simulations employ material parameters which are obtained via the results of laboratory tests on the material scale. Material tests are also essential for the calibration and validation of any kind of numerical model in order to obtain realistic and reliable simulation results. Compared to the outcome of rutting tests on a laboratory scale, an advantage of modeling ruts (in combination with real tire models) is also that a more realistic geometrical form of the rut can be determined. Numerical models for rutting with different methodological approaches can be found in the literature (e.g., [1, 5–12]).

The combination of laboratory tests and numerical modeling is a promising way to make predictions regarding pavement rutting. The rut depth itself can be one of the results. However, further conclusions for the pavement performance can be drawn by coupling the results of the laboratory tests and the structural simulation with a model which deals with the surface drainage of the pavement.

Various methods to calculate or model pavement surface drainage exist in the literature. The still widely used Gallaway et al.'s equation was developed from empirical relationships and experimental data [13]. Based on calculations, road criteria are suggested to reduce the risk of hydroplaning. The equation can also be used to estimate the hydroplaning speed (the speed in which hydroplaning occurs) as a function of road and car tire characteristics. Anderson et al. [14] and Cristina and Sansalone [15] developed a 1D kinematic wave model of the surface runoff, while Hermann [16] calculated slope lines that predict the 1D flow lines of runoff caused by road geometry. These models cannot be used to calculate water film depth distributions, but runoff coefficients, drainage inlet designs, or an estimation of the drainage capacity of a roadway can be obtained. A more sophisticated model has been developed by Charbeneau et al. [17]. A diffusion wave model is used to numerically simulate 2D water depth distributions over the pavement surface. A study to evaluate the influence of longitudinal slope on the maximum water depth and its location is also included. While some of these models are applicable to complex road geometries and alignments, in-depth parameter studies are still needed to evaluate the complex mechanism of pavement surface runoff.

Furthermore, German guidelines use the simple value of rut depth (considering the specific cross slope situation as well) to describe the risk of aquaplaning. With a better knowledge of the surface drainage mechanism, this assessment could be improved. A 2D surface drainage model can provide additional information about the risk of critical water depths in the ruts leading to aquaplaning. Other important parameters, such as longitudinal slope and the geometrical form of the ruts—in interaction with the cross slope—can be integrated into the surface drainage model and improve information on the risk of aquaplaning in a specific case. Furthermore, it is possible to consider the effects of the surface texture in and next to the ruts or even their development over time. In this way, much more information about (future) surface drainage behavior can be determined than by merely using the value of rut depth to describe the risk of aquaplaning.

In this contribution, it is exemplarily shown that the experimental and numerical analysis of geometrical changes (deformations in the form of ruts) of arbitrary asphalt pavements can be combined and coupled with an analysis of functional properties addressing road users' needs regarding safety and comfort. Therefore, a modular hydromechanical approach consisting of three steps (experimental material testing, long-term structural deformation finite element (FE) modeling, and surface drainage modeling) is proposed. This approach is also one of the first steps towards a more comprehensive, future vision of long-term pavement performance and its prediction with the help of in situ monitoring, data collection, data management, and modeling techniques—often called a “digital twin” in the context of industrial products or processes.

## 2. Modular Hydromechanical Approach

The present approach consists of several unidirectionally coupled modules (material, structure, and drainage) to describe the long-term behavior of arbitrary asphalt pavements from the material scale to the structural scale and to derive the surface drainage features over the long term. A graphical overview of the methodologies is provided in Figure 1.

The flowchart of the modular analysis is depicted in Figure 2. A modular hydromechanical analysis starts with the selection and experimental testing of different materials used for the specific pavement design. From material databases or additional experimental characterization tests, model parameters are derived, which are used in the subsequent numerical analysis to describe the thermo-mechanical material behavior of the pavement materials on the structural scale via adequate models. To realistically capture the phenomena of tire-pavement interaction within the structural model, a representative rolling tire in steady-state motion and parts of the pavement construction are discretized and included in the numerical model. Via a long-term simulation of the selected tire-pavement configuration, geometrical information regarding the permanent deformation of the pavement surface is obtained. The geometrical data is used as input for the numerical surface drainage

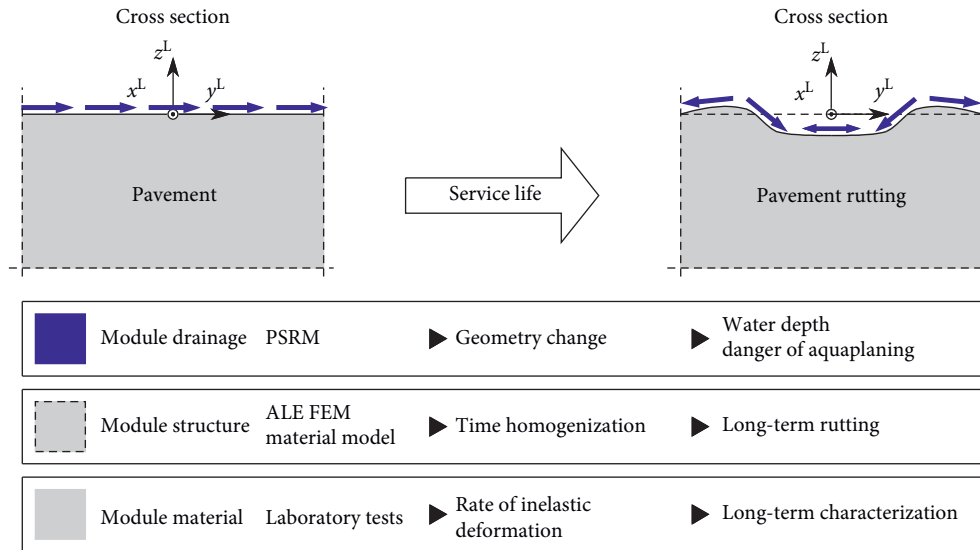


FIGURE 1: Overview of the modular unidirectional hydromechanical investigation for deformable asphalt pavements subjected to rut formation during their service life: pavement surface runoff model (PSRM) and arbitrary Lagrangian–Eulerian finite element method (ALE FEM).

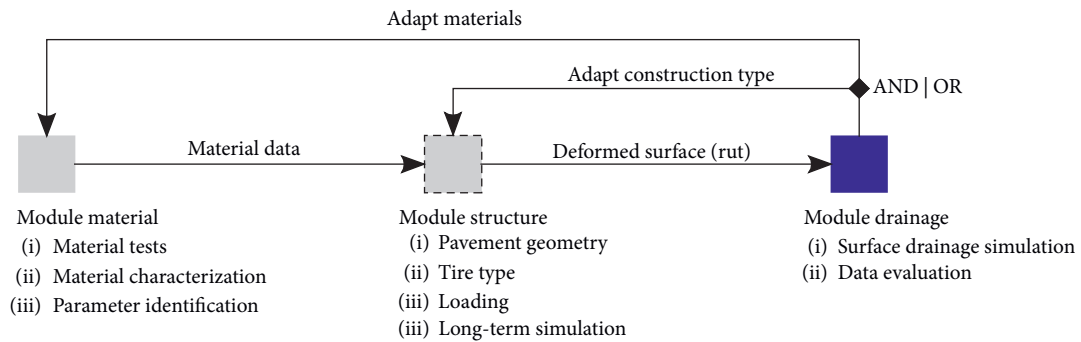


FIGURE 2: Flowchart of the modular analysis.

analysis. As a result of the unidirectionally coupled holistic analysis, pavement materials or the construction type of the pavement can be varied to optimize the short- and long-term drainage features (loop).

In the following subsections, more information on each module is provided, with a focus on the geometry-dependent model for surface drainage in this contribution.

**2.1. Material Characterization.** The objective of the experimental material characterization is to reveal the material’s short- and long-term response to cyclic loading. Particularly for the prediction of plastic deformations, the quantification of accumulated inelastic deformations is important. The existence of different testing facilities and the general need of a test methodology for accurate inelastic strain measurements during the experimental testing of asphalt materials have already been briefly discussed in the introduction. To assess the thermomechanical material behavior of asphalt mixtures, i.e., to also take into account the influence of temperature, the short- and long-term tests are performed at different testing temperatures. The outcome of these force-

controlled tests (strain-time plots) is then used to identify sets of material model parameters for each testing temperature. Besides the temperature-dependent mechanical response of the material, other thermal characteristic values such as heat capacity, thermal conductivity, and mass density also have to be identified from experiments. These additional quantities are used as the input parameters of the thermomechanical tire-pavement model (see [2, 18]).

**2.2. Tire-Pavement Model for the Long-Term Prediction of Permanent Surface Deformation.** The experimentally assessed asphalt behavior is numerically represented via a continuum mechanical model for asphalt [19] with several sets of model parameters to capture the asphalt’s temperature dependency. While the material response to short-term loading (e.g., tire overrun) only shows deformations in the small strain range, long-term deformations (accumulation of inelastic deformation sections) show large deviations from the pavement’s initial geometry. Hence, a material model considering large strains was employed. Furthermore, a continuum mechanical material model



formulation—see, e.g., [20–22] for an overview—is chosen to enable a numerically efficient representation of the short- and long-term behavior of asphalt materials on the macroscale within numerical simulations in the framework of the finite element method (FEM). Within the material model, the evolution of inelastic deformations is described via an endochronic plasticity approach [23]. A detailed derivation and explanation of the approach is available in [24].

The temperature dependency of the asphalt is captured via parametrization via sets of model parameters identified for discrete testing temperatures (see Section 2.1). Furthermore, the thermal properties of the asphalt mixture are described with the thermal conductivity and the volumetric heat capacity, which are assumed as constant (temperature- and deformation-independent) in the material model.

To integrate and evaluate the short- and long-term material response on the structural scale (pavement structure), different numerical methods are available. Often, the FEM is used to carry out numerical simulations of pavement structures (see, e.g., [19, 25]). As a further development with respect to numerical efficiency, the semianalytical finite element method (SAFEM) has recently been proposed in [26].

In this contribution, an FE discretized configuration of tire and pavement is considered (see Figure 3). A detailed description of the tire-pavement model for the long-term prediction of pavement rutting is available in [27]. In the following, a brief overview of the underlying theory and assumptions is provided.

For a numerically efficient but still detailed analysis of the tire-pavement interaction, a stationary state of the tire in motion is numerically represented with the help of an ALE steady-state transport simulation. The idea of the steady-state analysis is based on the special description and decomposition of the motion of the tire and the pavement with respect to several configurations (initial configuration with Lagrangian frame  $x^L$ , moving reference configuration fixed to the tire axle with coordinate systems  $x'$  and  $x^{ALE}$ , and current configuration).

Due to the steady-state motion of tire and pavement, time derivatives (of quantities belonging to the current configuration) with respect to the moving reference configuration are redundant and the computational cost can be significantly decreased. In this context, the rotation of the tire is represented by the flow of the tire material through the fixed FE mesh of the tire, and no fine FE resolution of the whole circumferential direction of the tire is required (see Figure 3). The translation is represented in the same manner by a flow of the pavement material through the FE mesh of the pavement. Inelastic material behavior (e.g., viscoelastic or elastoplastic material features) is included in the FE analysis for both tire and pavement via a special ALE formulation for inelastic material (evaluation of the history of the material along streamlines formed by consecutive integration points of the regular FE mesh) (see [2, 18]). In the tire-pavement model, longitudinal and cross slopes of the pavement are omitted since their influence on the rut formation is

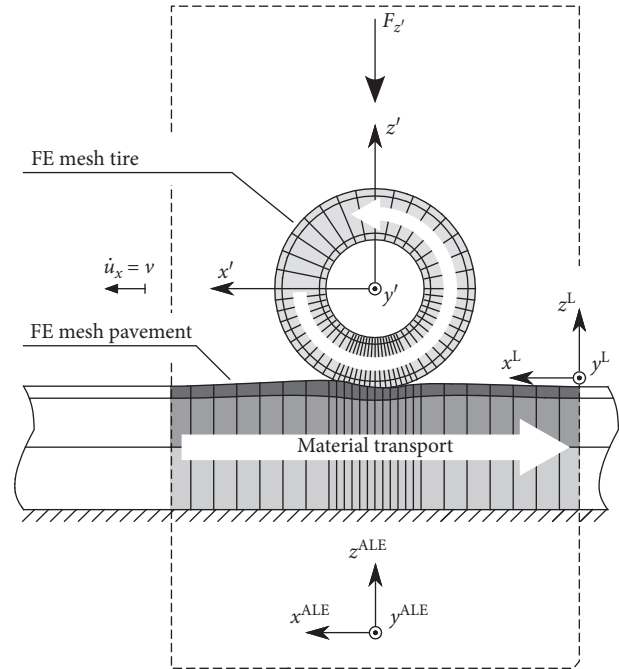


FIGURE 3: FE tire-pavement model for the structural analysis of the tire-pavement interaction using an ALE framework for both tire and pavement.

judged as negligible for standard sections of the road network.

The long-term prediction of the pavement's rutting performance requires the use of a numerically efficient strategy. In this context, time homogenization—see, e.g., [28–33]—on several time scales has been used for the multifield problem (displacement and temperature as solution fields) as proposed in [27]. From the mechanical loading (tire overrun [34]) and boundary conditions (temperature variations), distinct time scales have been identified for which a time-homogenized response of the pavement structure is computed and evaluated with respect to a reference cross section of the pavement.

Information regarding the geometry of the deformed pavement surface (cross-sectional direction) as a function of the number of load cycles (tire overruns) are then transferred to the surface drainage analysis.

**2.3. Geometry-Dependent Model for Surface Drainage.** In the past, models for the surface drainage of pavements have often been developed solely from experimental data and were not based on physical modeling. Descriptive parameters or equations were derived from experimental results to gain a reduced model of pavement drainage, as in [35–37]. In some of these cases, the experiments have been explained by simplified analytical approaches [38–40], e.g., based on the Gauckler–Manning–Strickler equation, which is commonly used in hydromechanics for the calculation of flow conditions in open channels. Another often-used simplification is the assumption of 1D flow [16, 40, 41].

In this contribution, a 2D numerical model called the Pavement Surface Runoff Model (PSRM), developed at the

University of Stuttgart [42], is used to calculate the water depth, depending on the evolving surface geometry described in Section 2.2. While experimental data is used to calibrate some coefficients, the equations are based on a physical model of surface flow.

The PSRM was designed to model pavement surface runoff and can, therefore, only simulate infiltration processes into porous pavements in a simplified way. A number of models dealing with flow and drainage in porous pavements have previously been proposed (e.g., [43, 44]). Porous pavement drainage is also addressed in the authors' DFG Research Group FOR 2089 [45] (see, e.g., [46, 47]).

The numerical calculations of the PSRM, which are based on fundamental hydromechanical modeling, use the DuMu<sup>X</sup> software toolbox [48, 49]. This toolbox was developed to solve different flow problems by using the DUNE framework [50, 51]. DUNE itself is a C++ toolbox for solution approaches for differential equations, also beyond hydromechanical flow modeling.

In the PSRM, standard geometries (e.g., superelevated transition sections with different cross slopes and longitudinal slopes or different pavement widths) can be generated for ideal even surfaces. More realistic and complex (uneven) topographies and geometries of pavement surfaces can be imported using 3D surface data. This data can either be measured or—as done in the present modular hydromechanical investigation—calculated based on a structural tire-pavement model (Section 2.2) so that even complex geometries (e.g., intersections or ruts) can be taken into account. Furthermore, the roughness of the pavement surface can be considered in the PSRM as mean texture depth (MTD), which has a major influence on water reservoirs in the texture and on the flow resistance in many cases. Five different surface textures with discrete MTD values between 0.4 and 1.8 mm can be used as input parameters for the PSRM simulations.

In the PSRM, rainfall is simplified to a spatially uniform event, which is constant in time, as it is also implemented in a simplified way in other (pavement) drainage models. Furthermore, the rainfall intensity  $i$  (mm/min) constitutes another input parameter.

**2.3.1. Mathematical Description of the Pavement Runoff Model.** The Navier–Stokes equations are a set of fundamental equations concerning fluid mechanics and characterize the conservation of mass, momentum, and energy in hydrosystems with a set of nonlinear partial differential equations.

If water is treated as an incompressible fluid and its motion as a temperature-independent flow, the conservation of energy can be neglected. For laminar flow conditions in combination with an ideal frictionless fluid and vertically acting gravity, the so-called incompressible Euler equations can be derived from the Navier–Stokes equations.

It is assumed that laminar flow is the only drawback of the PSRM compared to surface drainage situations in reality. In measurements, water flow has been observed in the full range between laminar and fully turbulent conditions (see [17, 41]). However, in [41], it was concluded that fully turbulent flow will only occur in unusually strong rainfall events. Based on this outcome, it seems reasonable to assume laminar flow and, hence, to further simplify the mathematical formulation.

In pavement surface runoff, the horizontal spread of the water film is much larger than the water depth. For cases like these, the depth-averaged shallow water equations are ideal [42]. They state that, in shallow free-surface problems, the vertical flow velocity and its derivatives are very small (hydrostatic pressure distribution) and can, therefore, be neglected.

Integrating the incompressible Euler equations over the flow depth, the depth-averaged shallow water equations in their general form are obtained for a simplified model of the pavement surface (see Figure 4):

$$\frac{\partial}{\partial t} \begin{pmatrix} h \\ uh \\ vh \end{pmatrix} + \frac{\partial}{\partial x} \begin{pmatrix} uh \\ u^2h + \frac{1}{2}gh^2 \\ uvh \end{pmatrix} + \frac{\partial}{\partial y} \begin{pmatrix} vh \\ uvh \\ v^2h + \frac{1}{2}gh^2 \end{pmatrix} = \begin{pmatrix} 0 \\ ghS_{0,x} \\ ghS_{0,y} \end{pmatrix}. \quad (1)$$

So far, (1) is only applicable to a smooth surface. The right-hand side of the equation represents the source and sink terms of the flow problem. The surface slope  $S_0$  in the  $x$ - and  $y$ -direction acts as a source, since the gravity  $g$  acts on the momentum of the fluid.

The equation has to be further adapted for the modeling of pavement surface runoff. In surface drainage, the discharge  $q$  can be a source or a sink term in the system since water can be added (e.g., rain) or it can be removed from the system (e.g., discharge at pavement gutters and inlets, evaporation, and infiltration). Hence, the discharge has to be included as a source term in the shallow water equations.

Furthermore, assuming a smooth pavement surface is not practical. Flow resistance has a large effect on flow velocities. In free flow cases, the roughness of the surface acts as shear stress against the gravitational force and decelerates the flow [42]. Therefore, higher surface roughness does not necessarily lead to an improvement of the drainage function of the road. Formulating the influence of flow resistance is particularly difficult. Even if slope friction is only considered in terms of bottom resistance with resistance of shape, wave, flow fluctuations, wind and rain neglected, the flow resistance would still have to be calculated via direct numerical simulation (DNS) (see [42]). For this reason, an empirical equation for the flow resistance was used. After a theoretical comparison, the Darcy–Weisbach equation was chosen for the PSRM (rather than the equations by Chézy or

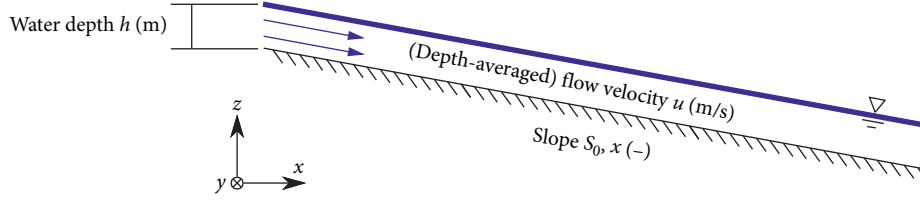


FIGURE 4: Model of water flow with velocity  $u$  over a pavement surface in the  $x$ -direction. The flow velocity  $v$  in the  $y$ -direction can be modeled analogously.

Manning) [42]. Darcy–Weisbach uses the dimensionless coefficient  $f$  as an empirical value, derived from a theoretical background. This formulation has the advantage that it can be applied to all flow regimes (laminar, transient, and turbulent).

Assuming a steady state, an expression for the slope friction  $S_f$  (caused by the base friction of the rough pavement surface) can be derived from the Darcy–Weisbach theories in the  $x$ - and  $y$ -direction:

$$\begin{aligned} S_{f,x} &= f \frac{u\sqrt{u^2 + v^2}}{8gh}, \\ S_{f,y} &= f \frac{v\sqrt{u^2 + v^2}}{8gh}. \end{aligned} \quad (2)$$

For this case, the Darcy–Weisbach coefficient  $f(Fr_k, \lambda, S_0)$  depends on the texture-related Froude number  $Fr_k$ , the inundation ratio  $\lambda$ , and the bottom slope  $S_0$  [42]. The texture-related Froude number  $Fr_k$ , in turn, is defined in the derivation of these equations as the Froude number with mean texture depth MTD as the characteristic length:

$$Fr_k = \frac{u}{\sqrt{g\text{MTD}}}. \quad (3)$$

Equation (3) provides  $Fr_k$  in the  $x$ -direction with the corresponding flow velocity  $u$ . For the  $y$ -direction, the texture-related Froude number can be computed via the flow velocity  $v$ .

The inundation ratio  $\lambda$ , as a describing parameter of the Darcy–Weisbach coefficient  $f$ , is defined as the relationship of the water depth to the characteristic length of the rough surface, i.e. the water depth compared to the height of the pavement texture. The influencing parameters are investigated and compared to experimental data from [16]. It seems that the texture-related Froude number has a larger influence on  $f$  than the inundation ratio [42]. Furthermore, the data indicates that inserting the inundation ratio into the definition of the Darcy–Weisbach coefficient does not increase the accuracy [42]. For this reason,  $\lambda$  as a variable of the coefficient  $f$  is dropped. The influence of the bottom slope  $S_0$  on the Darcy–Weisbach coefficient is investigated via a curve fitting process [42] and is found to have a significant influence on  $f$  and, therefore, is kept as a secondary parameter.

The coefficient  $f$  itself is then derived empirically. Experimental findings [16, 41] are used to obtain the parameters of the following relation:

$$f = a_1 S_0^{a_2} Fr_k^{a_3}. \quad (4)$$

The free parameters are identified via the least squares method [42]:

$$f = 3.50 S_0^{0.47} Fr_k^{-1.50}. \quad (5)$$

The experiments [16, 41] employed to calibrate the PSRM for pavement roughness/texture are carried out on five different realistic pavement surfaces. As described in [41], the test equipment consists of  $2.5 \text{ m} \times 1.0 \text{ m}$  samples ( $2.5 \text{ m}^2$ ) of three different asphalt types (SMA 11, SMA 8, and a mastic asphalt) and two concrete surfaces obtained by different texturing methods. The variation of MTD is between  $0.4 \text{ mm}$  and  $1.8 \text{ mm}$ . The flow conditions in the experiments can be assumed as 1D (no cross slope), with a flow path length of  $2.5 \text{ m}$ . An inflow construction at the top of the pavement sample ensures steady-state flow conditions. In the experiments, a variation of longitudinal slopes and runoff rates (simulating different rain intensities at certain flow path lengths) are tested. Water film thicknesses are measured using an ultrasonic device, which measures distances on the dry surfaces and on the surfaces with water flow, respectively. The measured difference between the distances, repeated at 27 fixed points on the surface, results in an average water depth. The experiments are described in more detail in [16, 41, 47].

More experimental data might improve the accuracy and applicability of the model. Although the model is only valid and applicable for five discrete values of MTD, these are, in fact, within a sufficiently wide range compared to realistic pavements.

Including the discharge  $q$  as a source, as described above, and the slope friction  $S_f$  in the  $x$ - and  $y$ -direction in (1), the depth-averaged shallow water equations applicable to pavement surface runoff are obtained via [42]:

$$\frac{\partial}{\partial t} \begin{pmatrix} h \\ uh \\ vh \end{pmatrix} + \frac{\partial}{\partial x} \begin{pmatrix} uh \\ u^2h + \frac{1}{2}gh^2 \\ uvh \end{pmatrix} + \frac{\partial}{\partial y} \begin{pmatrix} vh \\ uvh \\ v^2h + \frac{1}{2}gh^2 \end{pmatrix} = \begin{pmatrix} q \\ ghS_{0,x} - ghS_{f,x} \\ ghS_{0,y} - ghS_{f,y} \end{pmatrix}. \quad (6)$$

### 2.3.2. Numerical Approach of the Pavement Runoff Model.

The PSRM uses the finite volume method (FVM) on a Cartesian grid to gain numerical solutions to the previously derived shallow water equations. A 2D grid is used and the conserved variables are stored as cell-averaged values at the center of each cell. The pavement is implemented as an impervious boundary, and no-flow conditions are imposed on the right and left sides of the model domain.

The numerical approach was implemented in DuMuX (as explained in Section 2.3); see [47] for a more detailed description and [42] for the complete derivation of the mathematical equations and the numerical approach.

### 3. Numerical Examples of the Hydromechanical Approach

Most drainage models for porous (e.g., [43, 44, 52]) or nonporous (e.g., [14–16]) asphalt materials mainly focus on the determination of critical water depths and the choice of design parameters for adequate and safe drainage conditions (e.g., required cross slope, adequate longitudinal slope, thickness of porous friction course, and spacing of sub-drains). In addition, many modeling approaches and predictions of water depths for certain pavement geometries often consider simplified ideally even surfaces, which, in terms of pavements, do not exist in reality.

In the following, the surface drainage model (Section 2.3) is coupled to the material description (Section 2.1) and the structural tire-pavement model (Section 2.2) to show the influence of deformation (e.g., rutting) on the pavement's drainage performance. The objective of the considered examples is to show how changing pavement surface geometries effects drainage and, therefore, if the drainage functions of the pavement are also fulfilled in the long term (during the service life of the pavement). If these life-cycle approaches for pavement drainage properties are based on basic material and structural modeling, substantial improvements of such analyses can be expected.

To demonstrate the fundamental features of the hydromechanical approach, the simple but illustrative example of a tire running on an artificial test section (thin asphalt layer on deformable subbase material), as sketched in Figure 5, is considered. Systematic analyses, e.g., for varying parameters of the material, pavement construction types, traffic, wheel loads, pavement slopes, and several further parameters, are beyond the scope of this contribution. The geometry, thermomechanical boundary conditions, and material features of the benchmark example are provided in detail in [27]. The geometry and material data of the tire are available in [34]. The tire is subjected to a vertical load of  $F_z = 3300$  N and a steady-state translational velocity of 80 km/h in the  $x$ -direction. Regarding the input parameters and assumptions used for this example, it should be noted that this is not representative of highly loaded real pavements. The main objective of this study is to show the method itself and its possibilities and not (yet) to analyze more realistic pavement structures and tire loads.

As a result of the structural analysis, the permanent surface deformation (given in Figure 6) of the test section is used as a starting point for the surface drainage analysis.

Information regarding the permanent surface deformation (2D) of a representative part of the cross section subjected to rut formation is used to generate a 3D geometrical model of the road surface, including the longitudinal and cross slopes via inter- and extrapolation of the geometrical data. Figure 7 shows a virtual pavement surface.

To achieve this result, the following steps are carried out. As can be seen in Figure 6, the rut-related deformations force the road material to the sides of the rut beyond the normal level. It is assumed that this bulge on the outer side of each rut decreases linearly to the normal level in 0.3 m (see Figure 7(b)). This rut geometry is then doubled at a distance of 1.5 m (equal to one track width) and thus forms the cross-sectional geometry of a lane with a width of 3.5 m. The cross sections are then extrapolated for different longitudinal and cross slopes over a length of 10 m. A local minimum of the pavement surface exists in the middle of the track (see Figure 7(b)). This is due to the raised edges of the ruts and has an influence on the surface drainage. The pavement surface runoff model (PSRM) used for the surface drainage analysis could be utilized for even larger road sections (e.g., several lanes) or a more complex alignment of the road (e.g., curves or transition zones). The grid for the numerical modeling is calculated in PSRM based on these 3D geometrical models of the road surface. This allows a 2D calculation of the water depths in all surface directions. The grid size and, therefore, the resolution for the numerical calculations are 0.05 m in the following examples.

For the numerical examples of surface drainage, a variation of rain intensities  $i$ , rainfall durations, and texture depths (MTD) have been simulated. The longitudinal slopes  $s$ , cross slopes  $c$ , and the simulated time span of rut formation  $n$  from the tire-pavement simulation (Section 2.2) are also part of the investigated examples.

The chosen rain intensities represent (short) heavy rainfall events (e.g., “showers” during a thunderstorm) as they usually appear in Germany. The intensities of heavy rainfall events vary widely within Germany. Therefore, the determination of an “average” value for a certain duration of heavy rainfall events has a great uncertainty; the rain intensities which are chosen in the following examples have been varied accordingly. Statistical analyses of rain intensities in Germany [53] have been considered in order to choose adequate rain intensities. For further applications of the model, any other rain intensities and durations can be simulated as well.

Table 1 provides the selected input values for the following drainage examples. One influencing quantity of pavement surface drainage (depicted in the table in bold characters) is the focus of each example. While the influence of cross and longitudinal slope is examined in Example 1, the influence of different assumed rainfall intensities with a duration of 15 minutes is presented in Example 2. In Example 3, the water depth accumulation during one rainfall event is analyzed, and the drainage conditions over the time span of rut formation (30 years) are examined in Example 4. Finally, the influence of texture depth on the drainage capacity is illustrated in Example 5. Since this parameter is strongly coupled with the cross and longitudinal slopes of the pavement, the influence of these parameters is also studied.

The simulation results show a 2D distribution of water film depths (WFD) in different colors plotted over the pavement surface. The overall water depth is related to the texture depth (MTD), so the resulting water depth given in

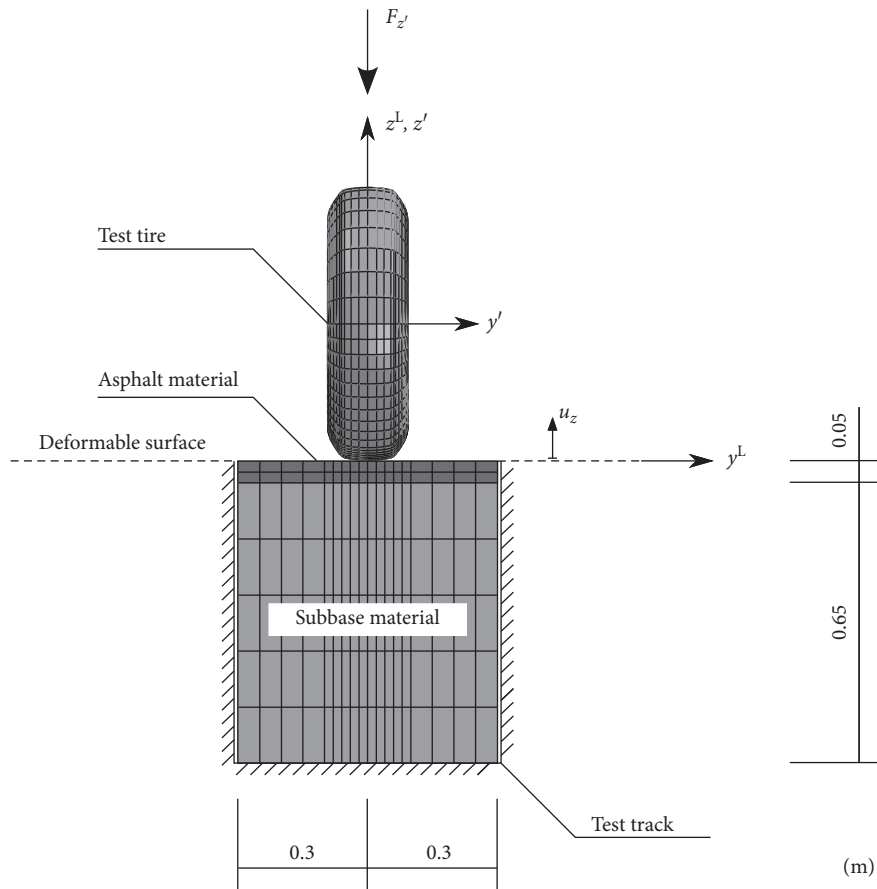


FIGURE 5: Geometry and FE discretization of the benchmark example (cross section of the near field: thin asphalt layer on subbase material of the test track, both with elastoplastic material behavior) and FE model of the test tire [27].

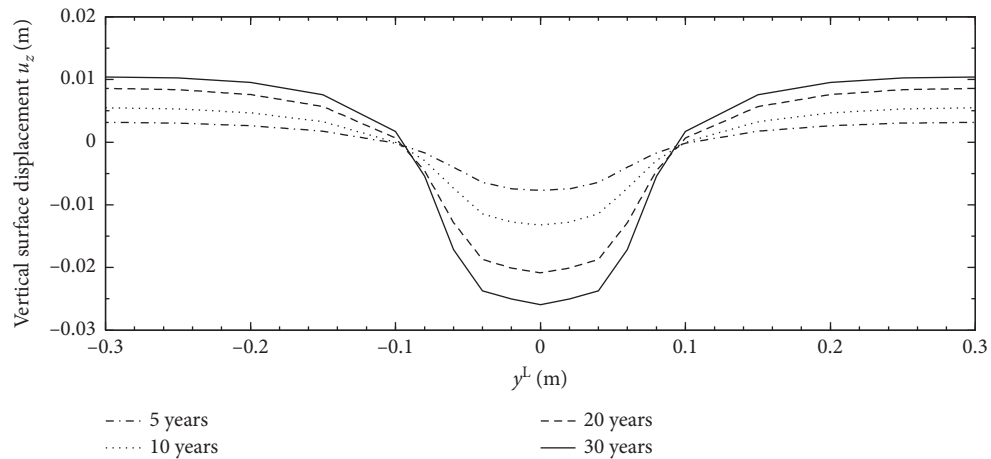


FIGURE 6: Deformed surface of the test track (cross-sectional direction) plotted for a global time of 5 years, 10 years, 20 years, and 30 years (number of load cycles = about  $7 \cdot 10^7$  per year) [27].

the figures represents the water height above the texture peaks, which is assumed to be relevant to aquaplaning aspects.

*Example 1.* Effects of cross slope and longitudinal slope in combination with rut depth

Rain intensity of 0.75 mm/min with a duration of 15 min and an MTD value of 0.4 mm were chosen for the simulation. The cross slope  $c$  was chosen as 2.5% and 5.0%, whereas the longitudinal slope  $s$  was chosen as 1.0% and 4.0%. The geometry of the ruts is taken from the outcome of

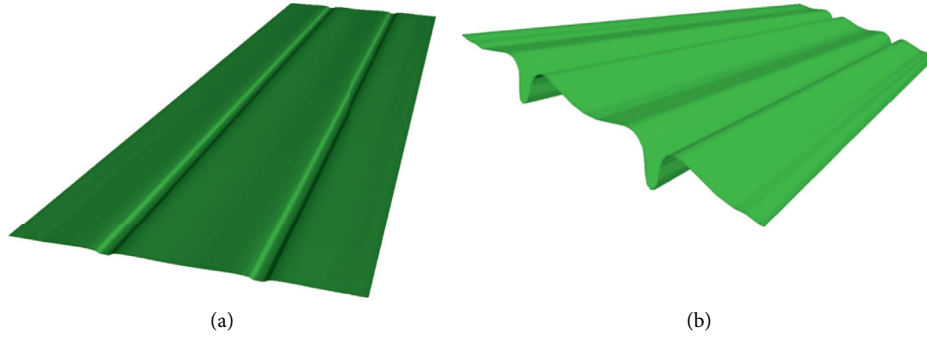


FIGURE 7: Generated deformed pavement surface. (a) Unscaled. (b) 10x vertically scaled.

TABLE 1: Simulation parameters for numerical examples of surface drainage (influencing quantities highlighted in bold).

Example	$i$ (mm/min)	Duration (s)	MTD (mm)	$c$ (%)	$s$ (%)	$n$ (years)
1	0.75	900	0.4	<b>2.5, 5.0</b>	<b>1.0, 4.0</b>	30
2	<b>0.75, 2.0</b>	900	0.4	2.5	1.0	30
3	0.75	<b>10-900</b>	0.4	2.5	2.0	30
4	0.75	900	0.4	2.5	2.0	<b>1-30</b>
5	0.75	900	<b>0.4, 0.9</b>	<b>2.5, 5.0</b>	<b>1.0-4.0</b>	30

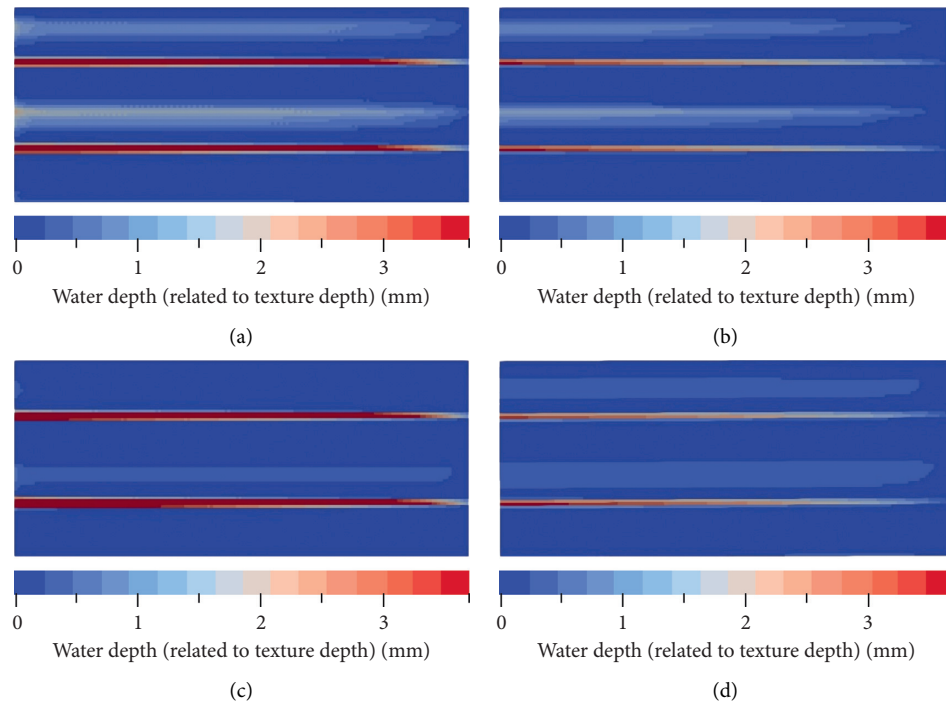


FIGURE 8: Example 1: effects of cross slope  $c$  and longitudinal slope  $s$  on the drainage of a pavement surface with ruts (rut depth and geometry after 30 years). (a)  $c = 2.5\%$ ,  $s = 1.0\%$ . (b)  $c = 2.5\%$ ,  $s = 4.0\%$ . (c)  $c = 5.0\%$ ,  $s = 1.0\%$ . (d)  $c = 5.0\%$ ,  $s = 4.0\%$ .

the tire-pavement simulation of a 30-year case. The corresponding rut depth and geometry are depicted in Figure 6.

The results in Figure 8 show, as expected, higher water depths in the ruts than in the surrounding area. The runoff along the ruts is better for longitudinal slopes  $s$  with a higher gradient (here: 4.0%), leading to lower water depths

compared to longitudinal slopes with a lower gradient (here: 1.0%).

The bulges at the edge of the ruts result in a backwater effect, which occurs next to the (higher edges of the) ruts in all cases. This effect is more significant with cross slopes with a lower gradient, and thus higher water depths appear here.

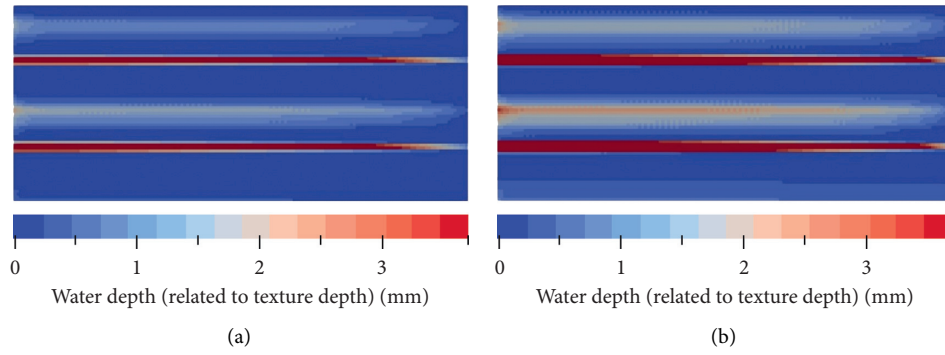


FIGURE 9: Example 2: effects of different rain intensities  $i$  on the drainage of a pavement surface with ruts (rut depth and geometry after 30 years). (a)  $i = 0.75$  mm/min, duration 15 min. (b)  $i = 2.0$  mm/min, duration 15 min.

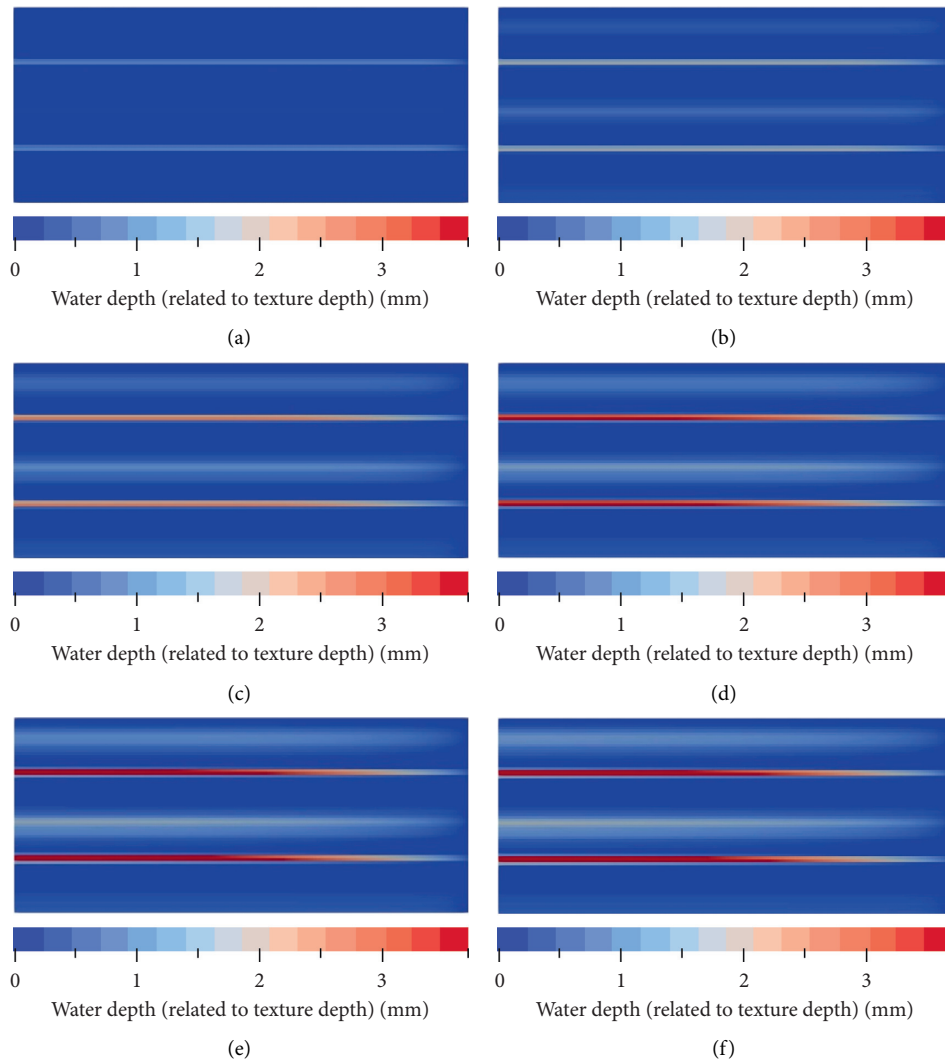


FIGURE 10: Example 3: evolution of water depths in (and outside of) the ruts after the beginning of a heavy rainfall (rut depth and geometry after 30 years). (a)  $t = 10$  s. (b)  $t = 30$  s. (c)  $t = 45$  s. (d)  $t = 60$  s. (e)  $t = 80$  s. (f)  $t = 900$  s (15 min).

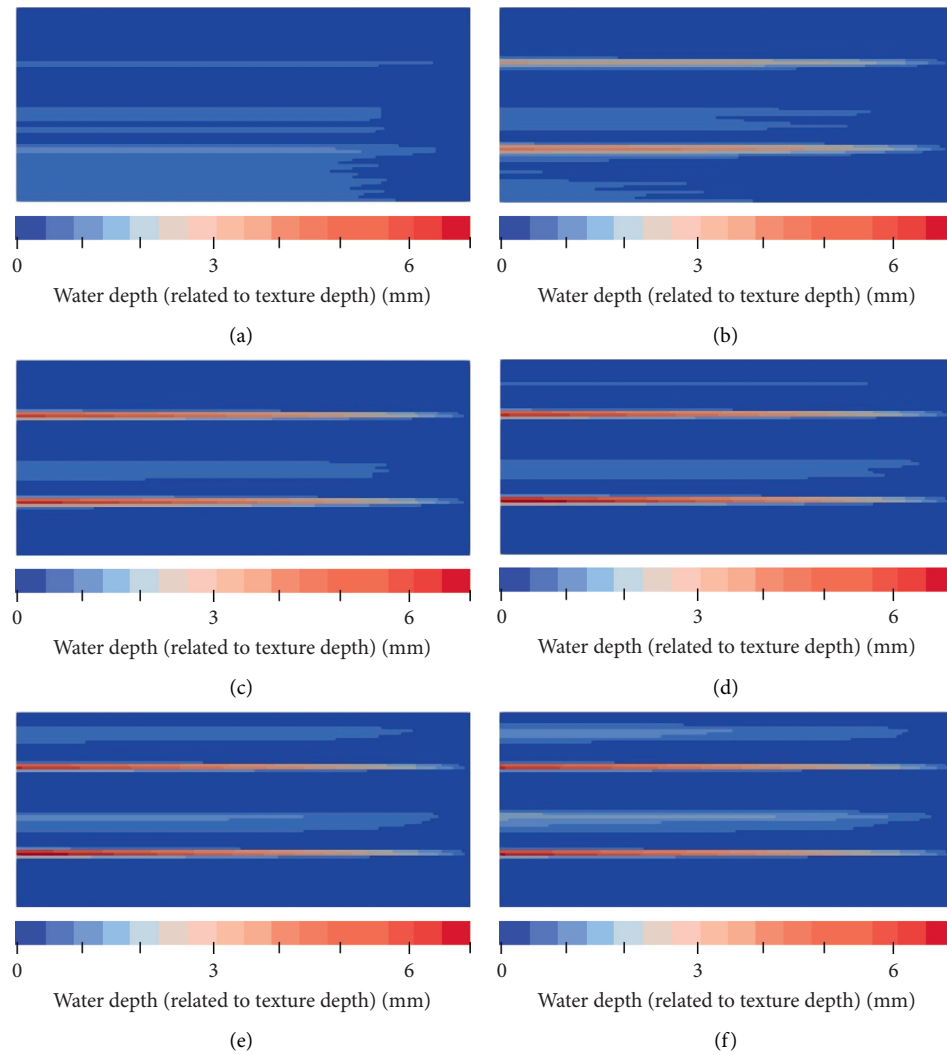


FIGURE 11: Example 4: effects of increasing rutting on the drainage of a pavement surface. (a)  $t = 1$  year. (b)  $t = 5$  years. (c)  $t = 10$  years. (d)  $t = 15$  years. (e)  $t = 20$  years. (f)  $t = 30$  years.

The effect of the longitudinal slopes on the backwater effect is ambiguous. The area of increased water depths is smaller with a cross slope of  $c = 2.5\%$ . For the cross slope of  $c = 5.0\%$ , the area of increased water depths increases with steeper longitudinal slopes, which might be an effect of longer flow paths while the values of water depths themselves are smaller compared to  $c = 2.5\%$ .

*Example 2. Comparison of different rain intensities*

For this example, rain intensity is set to 0.75 mm/min and 2.0 mm/min, respectively, with a duration of 15 min in each case. An MTD value of 0.4 mm was chosen. The cross slope  $c$  is 2.5 % and the longitudinal slope  $s$  is 1.0 %. The geometry of the ruts is taken from the outcome of the tire-pavement simulation of a 30-year case (see Figure 6).

In Figure 9, it can be seen that higher rain intensities lead to an increase of water depths in the ruts as well as in the area next to the bulges at the edges of the ruts (backwater effects). This seems to be an obvious result, but the effects can be

quantified in relation to several other input parameters using the method described in this paper.

*Example 3. Water depths during heavy rainfall*

The time required to reach a critical depth of water in the ruts in the case of a heavy rainfall is investigated in this example. As in Example 2, only the influence of the rainfall properties is the focus. However, in this example, not the rain intensity, but the rain duration is analyzed.

The simulations are based on a rain intensity of 0.75 mm/min with a duration of 15 min, an MTD value of 0.4 mm, a cross slope of  $c = 2.5\%$ , a longitudinal slope of 2.0%, and the calculated rut geometry over 30 years.

Critical states regarding aquaplaning tend to be reached earlier within the ruts than outside of the ruts. With the help of calculations, as shown in Figure 10, the discrete time at which a critical value occurs can be estimated. Figure 10 also shows that high values of water depth are reached in the ruts after a relatively short time. After approximately 80 s of rainfall, a



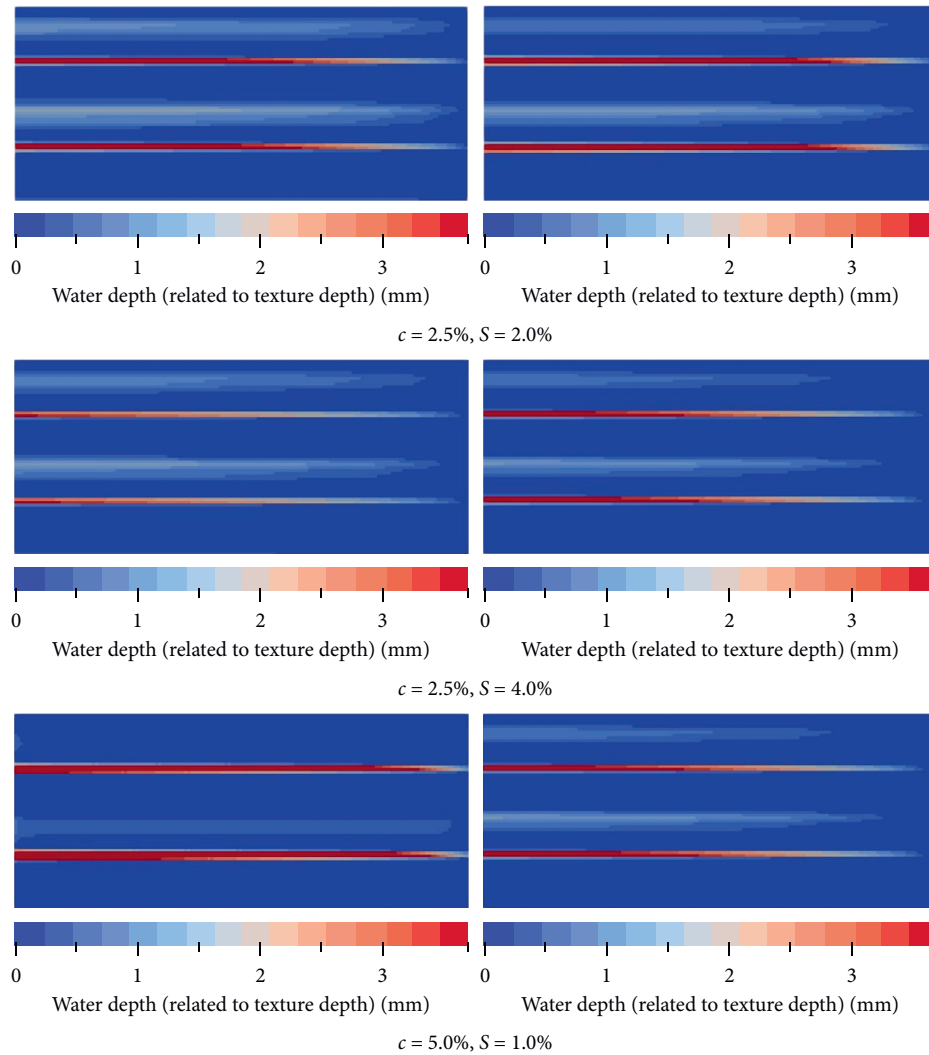


FIGURE 12: Example 5: effect of texture roughness (MTD) on the drainage of a pavement surface with ruts (rut depth and geometry after 30 years). Left: MTD = 0.4 mm; right: MTD = 0.9 mm.

nearly steady-state condition is reached, i.e., the water depth values in the ruts do not change over time. Therefore, the duration of a rain event does not seem to be such an influencing factor as the rain intensity (see Example 2).

It can also be seen that critical values of water depth seem to appear in the ruts earlier than outside the ruts.

*Example 4.* Development of drainage with increasing rutting during the pavement's service life

In this example, simulations have been carried out for a rain intensity of 0.75 mm/min with a duration of 15 min, an MTD value of 0.4 mm,  $c = 2.5\%$ , and  $s = 2.0\%$ .

In Figure 11, the development of ruts and the drainage effects are shown for different periods of time. The increase of rutting and the decreasing drainage properties can be observed exemplarily. The related rut geometries and rut depth values are given in Figure 6. Within the ruts, the water depths increase significantly in comparison to the surrounding area.

*Example 5.* Effects of texture on the drainage of a pavement surface with ruts

In this example, the calculations are carried out with a rain intensity of 0.75 mm/min with a duration of 15 min. Two MTD values with different cross slopes  $c$  in combination with different longitudinal slopes  $s$  are investigated. The calculated rut geometry after 30 years is considered.

Different roughness properties of pavement surfaces—numerically expressed via the MTD—have a significant effect on surface drainage. In general, higher MTD values offer a certain water drainage capability in texture cavities, but also increase the flow resistance. Both effects coexist, but one of them can be predominant in different geometric situations (e.g., depending on the slope or flow path length) and, in consequence, can have a major influence on water depth. This contradictory influence of surface roughness on pavement drainage has not yet been sufficiently discussed either qualitatively or quantitatively.

These different (contradictory) effects can be seen in the results depicted in Figure 12. Water depth values are influenced by different texture roughness values in the ruts as well as in the area next to the ruts (backwater area next to

the bulges) in an ambiguous way. An interesting question in this context could be how the deformation and the macrotexture change in the ruts and how drainage and the resulting water depths are influenced.

#### 4. Conclusions

This paper presents a modular hydromechanical approach to assess the short- and long-term surface drainage behavior of arbitrary, deformable asphalt pavements.

Firstly, the results of the laboratory tests of the materials used in the pavement provide information about the material's mechanical short- and long-term characteristics at different temperatures.

Secondly, an FE model dealing with tire-pavement interaction is used to predict the long-term permanent deformation performance of arbitrary asphalt pavements on the structural scale. The model assumes steady-state rolling conditions in order to carry out computationally efficient analyses. In addition, the efficiency is increased by computing the long-term structural response using a time homogenization technique. Based on material parameters from experimental material characterization tests, the structural model provides rut depths and the rut geometry for arbitrary tire-pavement configurations as a function of the number of load cycles.

Thirdly, the results of the long-term pavement modeling (rut depths and rut geometry as a function of the load cycles) are used in a unidirectional coupling to predict the surface drainage behavior of the rutted pavement surface, especially the water depth within the ruts. The basic hydromechanical modeling is based on depth-averaged shallow water equations. This modeling technique can consider ruts (and uneven areas in general) in a pavement because of its 2D runoff simulation. Modeling water runoff instead of using the rut depth as a benchmark for the risk of aquaplaning offers an additional benefit. Important pavement design and surface parameters can be included in the surface drainage model, e.g., cross slope, longitudinal slope, or even transition areas, which have a major influence on the surface drainage behavior. It can be shown that the surface texture (represented by MTD values) also affects the runoff behavior and the resulting water depths. Varying these parameters enables the pavement's drainage performance and related aquaplaning risks to be assessed. Thus, a prediction of the functional property of surface drainage as well as its implications on road safety could be improved by the present modular coupling, which delivers more precise results by including information about material and simulated surface geometries as a function of the pavement's service life.

Regarding this interdisciplinary hydromechanical modular approach, it is obvious that the combination and coupling of experimental and numerical methods (material, structure, and drainage) can fundamentally improve prediction methods for the long-term, multiphysical behavior of asphalt pavements and their performance. Future research work will concentrate on systematic parameter analyses using the hydromechanical modular approach for application-oriented studies regarding varying material

characteristics, existing pavement construction types as well as varying traffic, wheel loads, pavement slopes, etc.

#### Data Availability

Parts of the raw data supporting the modular analysis are from previously reported studies and datasets, which have been cited in the text. The processed drainage data are available from the corresponding author upon request.

#### Conflicts of Interest

The authors declare that there are no conflicts of interest regarding the publication of this paper.

#### Acknowledgments

The authors gratefully acknowledge the financial support by the Deutsche Forschungsgemeinschaft (DFG) under Grants KA 1163/30, RE 1620/4, WE 1642/11, and LE 3649/2 within the DFG Research Group FOR 2089.

#### References


- [1] G. Wang, R. Roque, and D. Morian, "Effects of surface rutting on near-surface pavement responses based on a two-dimensional axle-tire-pavement interaction finite-element model," *Journal of Materials in Civil Engineering*, vol. 24, no. 11, pp. 1388–1395, 2012.
- [2] I. Wollny, F. Hartung, and M. Kaliske, "Numerical modeling of inelastic structures at loading of steady state rolling—thermo-mechanical asphalt pavement computation," *Computational Mechanics*, vol. 57, no. 5, pp. 867–886, 2016.
- [3] E. R. Brown, P. S. Kandhal, and J. Zhang, "Performance testing for hot mix asphalt," NCAT Report No. 01-05, National Center for Asphalt Technology, Auburn, AL, USA, 2001.
- [4] A. Zeißler, F. Wellner, I. Wollny, C. Zopf, and M. Kaliske, "Experimental testing and investigation of the stress-dependent material behaviours of asphalt via the triaxial test," in *Proceedings of the PIARC XXIVth World Road Congress Conference*, Mexico City, Mexico, September 2011.
- [5] Y.-C. Suh and N.-H. Cho, "Development of a rutting performance model for asphalt concrete pavement based on test road and accelerated pavement test data," *KSCE Journal of Civil Engineering*, vol. 18, no. 1, pp. 165–171, 2014.
- [6] S. Erlingsson, "Modelling of rutting development in pavement structures," *Procedia—Social and Behavioral Sciences*, vol. 48, pp. 321–330, 2012.
- [7] P. Tian, A. Shukla, L. Nie, G. Zhan, and S. Liu, "Characteristics' relation model of asphalt pavement performance based on factor analysis," *International Journal of Pavement Research and Technology*, vol. 11, no. 1, pp. 1–12, 2018.
- [8] M. Shojaeifard, M. Baghani, and H. Shahsavari, "Rutting investigation of asphalt pavement subjected to moving cyclic loads: an implicit viscoelastic-viscoplastic-viscodamage FE framework," *International Journal of Pavement Engineering*, pp. 1–15, 2018.
- [9] B. Ali, M. Sadek, and I. Shahrou, "Finite-element model for urban pavement rutting: analysis of pavement rehabilitation methods," *Journal of Transportation Engineering*, vol. 135, no. 4, pp. 235–239, 2009.

- [10] O. O. R. Famiyesin, T. G. Davies, and A. H. C. Chan, "Numerical modelling of cyclic loading on reinforced unbound pavements," *Computers & Structures*, vol. 68, no. 1–3, pp. 231–249, 1998.
- [11] B. Feyissa, "Analysis and modeling of rutting for long life asphaltconcrete pavement," Ph.D. thesis, Technische Universität Darmstadt, Darmstadt, Germany, 2009.
- [12] P. Kettl, B. Lenhof, K. Runesson, and N.-E. Wiberg, "Simulation of inelastic deformation in road structures due to cyclic mechanical and thermal loads," *Computers & Structures*, vol. 85, no. 1-2, pp. 59–70, 2007.
- [13] B. M. Gallaway, D. L. Ivey, G. Hayes et al., *Pavement and geometric design criteria for minimizing hydroplaning*, Texas Transportation Institute, Texas A&M University, College Station, TX, USA, 1979.
- [14] D. A. Anderson, R. S. Huebner, J. R. Reed, J. C. Warner, and J. J. Henry, "Improved surface drainage of pavements—Final report," Pennsylvania Transportation Institute, Wingate, PA, USA, 1998.
- [15] C. M. Cristina and J. J. Sansalone, "Kinematic wave model of urban pavement rainfall-runoff subject to traffic loadings," *Journal of Environmental Engineering*, vol. 129, no. 7, pp. 629–636, 2003.
- [16] S. Hermann, "Simulationsmodell zum Wasserabfluss- und Aquaplaning-Verhalten auf Fahrbohnoberflchen," Ph.D. thesis, Universität Stuttgart, Stuttgart, Germany, 2008.
- [17] R. J. Charbeneau, J. Jeong, and M. E. Barrett, "Highway drainage at superelevation transitions," Center for Transportation Research, University of Texas at Austin, Austin, TX, USA, 2008.
- [18] I. Wollny and M. Kaliske, "Numerical simulation of pavement structures with inelastic material behaviour under rolling tyres based on an arbitrary Lagrangian Eulerian (ALE) formulation," *Road Materials and Pavement Design*, vol. 14, no. 1, pp. 71–89, 2013.
- [19] M. Oeser, "Nichtlineare numerische Simulationsmodelle für Verkehrswegebefestigungen unter Berücksichtigung von mechanischen, thermischen und hydraulischen Einwirkungen," Technische Universität Dresden, Dresden, Germany, Habilitationsschrift, 2010.
- [20] M. Oeser and T. Pellinien, "Computational framework for common visco-elastic models in engineering based on the theory of rheology," *Computers and Geotechnics*, vol. 42, pp. 145–156, 2012.
- [21] A. Zbiciak, "Mathematical description of rheological properties of asphalt-aggregate mixes," *Bulletin of the Polish Academy of Sciences: Technical Sciences*, vol. 61, no. 1, pp. 65–72, 2013.
- [22] T. Blume, "Mikromechanisch begründete Modellbildung des thermomechanischen Werkstoffverhaltens von Asphalt," Ph.D. thesis, Technische Universität Braunschweig, Braunschweig, Germany, 2018.
- [23] C. Netzker, H. Dal, and M. Kaliske, "An endochronic plasticity formulation for filled rubber," *International Journal of Solids and Structures*, vol. 47, no. 18-19, pp. 2371–2379, 2010.
- [24] C. Zopf, M. A. Garcia, and M. Kaliske, "A continuum mechanical approach to model asphalt," *International Journal of Pavement Engineering*, vol. 16, no. 2, pp. 105–124, 2015.
- [25] M. Oeser, *Numerische Simulation des nichtlinearen Verhaltens flexibler mehrschichtiger Verkehrswegebefestigungen*, Ph.D. thesis, Technische Universität Dresden, Dresden, Germany, 2004.
- [26] P. Liu, D. Wang, F. Otto, J. Hu, and M. Oeser, "Application of semi-analytical finite element method to evaluate asphalt pavement bearing capacity," *International Journal of Pavement Engineering*, vol. 19, no. 6, pp. 479–488, 2018.
- [27] R. Behnke, I. Wollny, F. Hartung, and M. Kaliske, "Thermo-mechanical finite element prediction of the structural long-term response of asphalt pavements subjected to periodic traffic load: tire-pavement interaction and rutting," *Computers & Structures*, vol. 218, pp. 9–31, 2019.
- [28] M. Bhattacharyya, A. Fau, U. Nackenhorst, D. Néron, and P. Ladevèze, "A multi-temporal scale model reduction approach for the computation of fatigue damage," *Computer Methods in Applied Mechanics and Engineering*, vol. 340, pp. 630–656, 2018.
- [29] T. Guennouni, "Sur une méthode de calcul de structures soumises à des chargements cycliques: l'homogénéisation en temps," *ESAIM: Mathematical Modelling and Numerical Analysis*, vol. 22, no. 3, pp. 417–455, 1988.
- [30] S. Haouala, "Time and space (4D) homogenization for visco-elastic-viscoplastic solids under large numbers of cycles," Ph.D. thesis, Catholic University of Leuven, Leuven, Belgium, 2016.
- [31] C. Oskay and J. Fish, "Fatigue life prediction using 2-scale temporal asymptotic homogenization," *International Journal for Numerical Methods in Engineering*, vol. 61, no. 3, pp. 329–354, 2004.
- [32] Q. Yu and J. Fish, "Temporal homogenization of viscoelastic and viscoplastic solids subjected to locally periodic loading," *Computational Mechanics*, vol. 29, no. 3, pp. 199–211, 2002.
- [33] D. Cojocar and A. Karlsson, "A simple numerical method of cycle jumps for cyclically loaded structures," *International Journal of Fatigue*, vol. 28, no. 12, pp. 1677–1689, 2006.
- [34] R. Behnke and M. Kaliske, "Finite element based analysis of reinforcing cords in rolling tires: influence of mechanical and thermal cord properties on tire response," *Tire Science and Technology*, vol. 46, no. 4, pp. 294–327, 2018.
- [35] C. F. Izzard, "The surface-profile of overland-flow," *Transactions, American Geophysical Union*, vol. 25, no. 6, pp. 959–968, 1944.
- [36] D. C. Woo and E. F. Brater, "Spatially varied flow from controlled rainfall," *Journal of the Hydraulics Division: HY Proceedings of the American Society of Civil Engineers*, vol. 88, pp. 31–56, 1962.
- [37] N. F. Ross and K. Russam, "The depth of rain water on road surfaces," Road Research Laboratory, RRL Report LR 236, Ministry of Transport, Crowthorne, England, UK, 1968.
- [38] H. J. Höcker, "Die Oberflächenentwässerung von Fahrbohn und ihre Bedeutung für den Straßenentwurf," in *Forschung Straßenbau und Straßenverkehrstechnik*, Vol. 118, Wirtschaftsverlag NW, Bonn, Germany, 1971.
- [39] B. M. Gallaway, J. G. Rose, and R. E. Schiller Jr., "The relative effects of several factors affecting rainwater depths on pavement surfaces," *Highway Research Record*, vol. 396, pp. 59–71, 1972.
- [40] R. S. Huebner, D. A. Anderson, J. C. Warner, and J. R. Reed, "PAVDRN: computer model for predicting water film thickness and potential for hydroplaning on new and reconditioned pavements," *Transportation Research Record: Journal of the Transportation Research Board*, vol. 1599, no. 1, pp. 128–131, 1997.
- [41] W. Ressel and S. Hermann, "Aquaplaning und Verkehrssicherheit in Verwindungsbereichen dreistreifiger Richtungsfahrbohn-Berechnung der Wasserfilmdicke," in *Forschung Straßenbau und Straßenverkehrstechnik*, Vol. 997, Wirtschaftsverlag NW, Bonn, Germany, 2008.
- [42] A. Wolff, "Simulation of pavement surface runoff using the depth-averaged shallow water equations," Ph.D. thesis, Universität Stuttgart, Stuttgart, Germany, 2013.

- [43] V. Ranieri, "Runoff control in porous pavements," *Transportation Research Record: Journal of the Transportation Research Board*, vol. 1789, no. 1, pp. 46–55, 2002.
- [44] B. J. Eck, M. E. Barrett, and R. J. Charbeneau, "Coupled surface-subsurface model for simulating drainage from permeable friction course highways," *Journal of Hydraulic Engineering*, vol. 138, no. 1, pp. 13–22, 2012.
- [45] M. Kaliske, I. Wollny, R. Behnke, and C. Zopf, "Holistic analysis of the coupled vehicle-tire-pavement system for the design of durable pavements," *Tire Science and Technology*, vol. 43, pp. 86–116, 2015.
- [46] W. Ressel and I. Rucker, "A numerical drainage model to simulate infiltration into porous pavements for higher road safety," *Internationales Stuttgarter Symposium Automobil- und Motorentechnik*, pp. 455–465, Springer Vieweg, Wiesbaden, Germany, 2017.
- [47] W. Ressel, A. Wolff, S. Alber, and I. Rucker, "Modelling and simulation of pavement drainage," *International Journal of Pavement Engineering*, vol. 20, no. 7, pp. 801–810, 2019.
- [48] B. Flemisch, J. Fritz, R. Helmig, J. Niessner, and B. Wohlmuth, "DuMu<sup>X</sup>: A multi-scale multi-physics toolbox for flow and transport processes in porous media," in *Proceedings of the ECCOMAS Conference 2007*, pp. 82–87, Paris, France, September 2007.
- [49] B. Flemisch, M. Darcis, K. Erbertseder et al., "DuMux: DUNE for multi-{phase, component, scale, physics, ...} flow and transport in porous media," *Advances in Water Resources*, vol. 34, no. 9, pp. 1102–1112, 2011.
- [50] P. Bastian, M. Blatt, A. Dedner et al., "A generic grid interface for parallel and adaptive scientific computing. Part I: abstract framework," *Computing*, vol. 82, no. 2-3, pp. 103–119, 2008.
- [51] P. Bastian, M. Blatt, A. Dedner et al., "A generic grid interface for parallel and adaptive scientific computing. Part II: implementation and tests in DUNE," *Computing*, vol. 82, no. 2-3, pp. 121–138, 2008.
- [52] S. A. Tan, T. F. Fwa, and K. C. Chai, "Drainage considerations for porous asphalt surface course design," *Transportation Research Record: Journal of the Transportation Research Board*, vol. 1868, no. 1, pp. 142–149, 2004.
- [53] G. Malitz and H. Ertel, "KOSTRA-DWD-2010 Starkniederschlagshöhen für Deutschland (Bezugszeitraum 1951 bis 2010)," Deutscher Wetterdienst, Offenbach, Germany, Abschlussbericht, 2015.

## Research Article

# Research on Rheological Properties of High-Percentage Artificial RAP Binder with WMA Additives

Weiying Wang <sup>1</sup>, Songchang Huang,<sup>1</sup> Yongchun Qin,<sup>1</sup> Yiren Sun,<sup>2</sup> Rui Dong,<sup>3</sup> and Jingyun Chen <sup>2</sup>

<sup>1</sup>Key Laboratory of Transport Industry of Road Structure and Material, Research Institute of Highway Ministry of Transport, Beijing 100088, China

<sup>2</sup>School of Transportation and Logistics, Dalian University of Technology, Dalian 116024, China

<sup>3</sup>Qilu Transportation Development Group Co., Ltd., Ji'nan 250000, China

Correspondence should be addressed to Jingyun Chen; [chenjy@dlut.edu.cn](mailto:chenjy@dlut.edu.cn)

Received 30 March 2020; Revised 10 June 2020; Accepted 25 June 2020; Published 6 August 2020

Guest Editor: Meng Guo

Copyright © 2020 Weiying Wang et al. This is an open access article distributed under the Creative Commons Attribution License, which permits unrestricted use, distribution, and reproduction in any medium, provided the original work is properly cited.

With the development of pavement recycling technology, the requirement of reclaimed asphalt pavement (RAP) is substantially increasing. Warm-mix recycled asphalt (WMRA) technology has made great progress, which can effectively decrease the working temperature and improve the RAP content. In this study, the rheological properties of recycled binders with incorporation of high-percentage artificial RAP binder (30–70%) were evaluated using two types of warm-mix asphalt (WMA) additives, i.e., polyethylene wax (R) and surfactant (M). The dynamic shear rheometer (DSR) and beam bending rheometer (BBR) tests were conducted on the recycled binders. The results showed that the temperature and frequency played an important role in determining the complex shear modulus of the high-percentage WMRA binders. The dependency of phase angle on frequency increased after the long-term aging. The WMA additive R had a relatively huge impact on the rheological properties of asphalt, which mainly occurred before the PAV aging of recycled asphalt binder; the WMA additive M had no significant impact on the rheological properties of recycled asphalt binder. The WMA additive R enhanced the low-temperature rheology of recycled asphalt binder, while the WMA additive M enhanced the high-temperature rheology of recycled asphalt binder. Both of these types of WMA additives improved the antifatigue performance of recycled asphalt binder. The increased content of RAP binder improved the high-temperature performance and reduced the low-temperature performance of the recycled asphalt binder. However, it had no obvious impact on the fatigue performance. In addition, there was a good linear relation between the RAP binder content and the two indexes of the multiple stress creep recovery (MSCR) test.

## 1. Introduction

The pavement recycling technology has attracted increasing attention due to its environmental sustainability and economic benefits. Some guidelines and specifications were introduced at home and abroad, making the pavement recycling technology more and more mature in engineering application [1–5]. Currently, the main asphalt pavement recycling technologies include hot central plant recycling, hot in-place recycling, cold central plant recycling, and cold in-place recycling [6]. Among them, hot central plant recycling is most widely applied. However, the mixing temperature for hot recycling in asphalt plant is generally

about 170°C. The excessive mixing temperature can cause secondary aging of the reclaimed asphalt and produce a large amount of asphalt fume and toxic gas, which will pollute the environment and cause damage to the health of construction staff. In addition, the utilization rate of RAP in the hot central plant recycling is generally between only 20% and 30%.

With the development of recycling technology, the demand for higher-percentage RAP has been increasing. The National Cooperative Highway Research Program (NCHRP) report recommended to increase the content of RAP in recycled asphalt mixture and proposed that the recycled asphalt mixture can have the same uniformity and

pavement performance as normal asphalt mixture when the content of RAP is increased through improving the design of mixture and standardizing the management and disposal of RAP [1]. Studies have shown that the content of RAP has a significant impact on the performance of recycled asphalt pavement. In particular, when the content of RAP is increased, the impact is more significant [7, 8]. Because the increased content of RAP may cause a series of problems, such as worse low-temperature crack resistance, antifatigue performance, water damage resistance, secondary aging caused by high-temperature construction, and partial mixing in the mixing process, namely, the ineffective utilization of waste asphalt in RAP [4, 9, 10]. These potential issues during the realization of recycling at large proportion pose a great challenge to pavement performance.

It is urgently needed to increase the content of RAP without reducing the pavement performance. Researchers have performed a range of related studies. Due to the existence of RAP lumps, the actual surface area of RAP is less than that of normal aggregate. Therefore, sufficient preheating can loosen RAP and increase the flow of the aged asphalt in RAP. With the increase of preheating time, the performance of reclaimed asphalt mixture is improved [11], and the content of RAP is also increased accordingly. In terms of partial mixing in the mixing process of recycled asphalt mixture and high-percentage recycled hot-mixture asphalt, Shirodkar et al. plotted a mixing curve at different degrees of mixing and observed the influence of partial mixing on the selection of new asphalt grade [12, 13]. The utilization of recycling agent is an effective means to improve the content of RAP [14, 15]. The recycling agent is a type of low-viscosity oil, which is characterized by low viscosity, low solubility, and high aromatic content. It is easy to spread evenly in asphalt and has good compatibility with RAP binder, which can reduce the viscosity of asphalt and supplement the missing ingredients in the aging process to soften RAP binder and restore its physical properties. Moreover, selecting appropriate recycling agent and accurately determining its content are able to improve the pavement performance of recycled asphalt mixture [16, 17].

Although those approaches mentioned above improved the content of RAP in the recycled mixture and also provided guidance for the design and construction of asphalt mixture with high percentage of RAP, higher construction temperature will inevitably generate numerous emissions in the process of mixing and construction, which will still damage the environment and consume a large amount of energy. Moreover, the secondary aging of asphalt in the mixture is inevitable due to high-temperature construction, which is less susceptible to the durability of recycled asphalt pavement. Based on the above considerations, numbers of researchers turned their attention to the WMA technology and attempted to add WMA additives into recycled asphalt mixture to reduce the construction temperature while

increasing the RAP content. Thus, warm-mix recycled asphalt (WMRA) has been rapidly applied and promoted [18, 19].

WMRA has the following advantages: (1) it can effectively reduce the heating temperature of RAP by about 20°C so as to reduce the bonding of RAP in the heating barrel and improve the proportion of RAP to over 40% [20]; (2) the warm mix technology can reduce the construction temperature of recycled asphalt mixture by 20°C to 40°C, prevent secondary aging of asphalt in RAP, save energy, reduce the emission of asphalt fume and toxic gases, and truly realize green transportation and resource recycling; and (3) the construction workability is improved. As the cooling rate of WMRA mixture is generally 50% of that of hot-mix recycled asphalt mixture, the compaction time of WMRA mixture can be prolonged, so that the compaction time is more sufficient and compaction is more effective [21–24]. Therefore, as an emerging technology of green transportation, WMRA has attracted increasing attention and recognition from the industry. Asphalt binder plays a key role in recycled asphalt mixture, especially for high percentage of recycling [25]. Therefore, there is an urgent need to investigate the rheological properties of high-percentage WMRA binder.

Overall, the literature review shows that the application of the WMRA techniques has a potential to enhance requirement of RAP. However, limited studies have been reported so far to characterize the aging, antideformation, and fatigue performance of WMRA binders in terms of the rheological properties. The present study was undertaken to investigate the effects of RAP binder and WMA additives on recycled binders on complex modulus and phase angle from frequency sweep, antideformation at high temperature, and fatigue behavior of WMRA binders. It is expected that the present research study would be useful in improving the understanding of the performance of WMRA binders with higher RAP contents.

The objective of this paper is to evaluate the rheological properties of recycled asphalt binders containing high percentage of artificial RAP binder (30% to 70%) with incorporation of two types of WMA additives. The main purposes of this paper are as follows: (1) to analyze the changing tendency of the rheological properties of recycled asphalt binder with different contents of RAP binder and (2) to analyze the influence of different types of WMA additives on the rheological properties of high percentage of WMRA binder. A series of laboratory tests were conducted, including dynamic shear rheometer (DSR) tests and beam bending rheometer (BBR) tests.

## 2. Materials and Methods

*2.1. Materials.* A virgin asphalt binder 90#, commonly used in the north area of China, was selected as the base asphalt in this study to obtain the recycled asphalt binders. Considering that the RAP from milling pavement has complex sources and its own characteristics [7, 26], the

TABLE 1: Properties of 90# asphalt and RAP binders.

Binder type	Unaged			RTFO		PAV		
	Penetration (25°C) (0.1 mm)	Softening point (°C)	Viscosity (135°C) (Pa·s)	( $G^*/\sin(\delta)$ ) (58°C) (kPa)	( $G^*/\sin(\delta)$ ) (58°C) (kPa)	$G^* \sin(\delta)$ (25°C) (kPa)	Stiffness (-12°C) (MPa)	$m$ -value (-12°C)
90#	84.3	46.0	0.246	1.9	3.5	1989	196	0.4
RAP binder	37.4	54.1	0.496	9.0	—	2830	—	—

artificial RAP binder was chosen in this paper in light of its more stable and controllable properties. The artificial RAP binder was obtained by subjecting the virgin binder to the rolling thin-film oven (RTFO) and long-term pressurized aging vessel (PAV) according to the AASHTO T240 and R28 for the following performance tests [27, 28]. The properties of the virgin and artificial RAP binders are shown in Table 1. It should be noted that the  $G^* \sin(\delta)$  (2825 kPa) was obtained when the RAP binder was subjected to further RTFO and PAV aging.

In this study, the recycled binders without WMA additives as control binders were produced by blending the virgin asphalt with various percentages (30%, 50%, and 70%) of artificial RAP binder by total weight. The virgin asphalt and RAP binder were mixed slowly according to their blending proportion using a glass bar for 10 minutes, so that the virgin and RAP binders could be mixed preliminarily. Then the mechanical stirring was utilized at 140°C for 15 minutes to make the two binders blend adequately. It should be noted that the blending time was not for too long so as to avoid the binders aging. For brevity, they were denoted as 30%-C, 50%-C, and 70%-C, respectively.

Two types of WMA additives, named R and M, were utilized to investigate the effect on the rheological property of the recycled binders. WMA additive R is a polyethylene wax which is a kind of white powder and M is a kind of surfactant, which are recommended to be added into the recycled binders at a rate of 3% and 0.5% by total weight of asphalt binders, respectively. According to the determined percentage of the two types of WMA additives, respectively, each of the WMA additive and recycled binder were blended using a glass bar slowly until there was no WMA additive on the surface of the mixed binder. Similar to the blending process of the RAP and virgin binders, the mechanical stirring was utilized at 140°C for 15 minutes to make binders blend adequately. The blending time should not be for too long so as to avoid the binders aging. Two types of original WMA binders containing WMA additives R and M were named R-WMA and M-WMA. According to the WMA additive used, the recycled binders containing artificial RAP binder were named RAP-R and RAP-M. Additionally, various percentages (30%, 50%, and 70%) of RAP-R and RAP-M were denoted as 30%-RAP-R, 30%-RAP-M, etc.

**2.2. Frequency Sweep Test.** The frequency sweep test is a primary test method to study the rheological property of asphalt binder. In this part, the complex shear modulus ( $G^*$ ) and phase angle ( $\delta$ ) were measured at different temperatures (4°C, 16°C, 28°C, 40°C, 52°C, and 64°C) in the frequency range of 0.1~50 Hz at each temperature. Using the time-temperature superposition principle, the results were shifted to a reference temperature of 28°C to conduct master curves of complex modulus and phase angle. This paper utilized the 2S2P1D model to fit the master curves describing the rheological properties of asphalt binders [29–31]. As shown in Figure 1, the 2S2P1D model consists of two springs, two parabolic creep elements, and one dashpot with 7 parameters, which can be determined using the following formulation:

$$G^*(i\omega) = G_e + \frac{G_g - G_e}{1 + \alpha(i\omega\tau_0)^{-k} + (i\omega\tau_0)^{-h} + (i\omega\beta\tau_0)^{-1}}, \quad (1)$$

where  $G_e$  is the static modulus. When the material is rheological solid,  $G_e > 0$ , and when the material is rheological fluid,  $G_e = 0$ . In this paper,  $G_e$  is 0.  $G_g$  is the glassy modulus ( $G_g = 10^9$  Pa).  $\alpha$ ,  $k$ ,  $h$ ,  $\beta$ , and  $\tau_0$  are parameters of this model and  $0 < k < h < 1$ . Meanwhile,  $\beta$  is constant and defined by

$$\eta = (G_g - G_e)\beta\tau_0, \quad (2)$$

where  $\eta$  is the Newtonian viscosity.

Complex shear modulus  $G^*$  consists of two parts, which are the energy storage shear modulus  $G'$  and loss shear modulus  $G''$ . Besides,  $G^*$  can be separated as follows [32]:

$$G^* = G' + iG'' \quad (3)$$

Therefore, on the basis of the (3), the 2S2P1D model can be separated and rewritten as follows:

$$\begin{aligned} G^*(\omega) &= \frac{G_g}{1 + A(\omega) + iB(\omega)} \\ &= \frac{G_g \times (1 + A(\omega) - iB(\omega))}{(1 + A(\omega))^2 + B^2(\omega)} \\ &= \left[ \frac{G_g \times (1 + A(\omega))}{(1 + A(\omega))^2 + B^2(\omega)} \right] + i \left[ \frac{G_g \times (-B(\omega))}{(1 + A(\omega))^2 + B^2(\omega)} \right], \end{aligned} \quad (4)$$

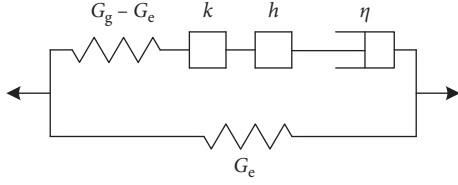


FIGURE 1: 2S2P1D model.

where

$$A(\omega) = \alpha(\omega\tau)^{-k} \times \cos\left(\frac{k\pi}{2}\right) + (\omega\tau)^{-h} \times \cos\left(\frac{h\pi}{2}\right),$$

$$B(\omega) = -(\omega\beta\tau)^{-1} - \alpha(\omega\tau)^{-k} \times \sin\left(\frac{k\pi}{2}\right) - (\omega\tau)^{-h} \times \sin\left(\frac{h\pi}{2}\right). \quad (5)$$

Then, the master curves of complex modulus and phase angle can be obtained according to (3) and (4). Besides, the objective error function is defined as

$$f_2 = \frac{1}{M} \sqrt{\sum_{j=1}^M \left(1 - \frac{G'_{c,j}}{G'_{m,j}}\right)^2} + \frac{1}{M} \sqrt{\sum_{j=1}^M \left(1 - \frac{G''_{c,j}}{G''_{m,j}}\right)^2}, \quad (6)$$

where  $G'_{c,j}$  and  $G''_{c,j}$  are the predicted energy storage shear modulus and loss shear modulus, respectively, and  $G'_{m,j}$  and  $G''_{m,j}$  are the actual values, correspondingly.

**2.3. BBR Low-Temperature Rheological Property.** The rheological property of asphalt binder is the most significant factor for the low-temperature cracking of asphalt pavement [33]. Thus, this paper utilized the CAM model to fit the master curves and Burgers' model to analyze the viscoelasticity of recycled binders. The reference temperature was  $-12^\circ\text{C}$ .

The CAM model is defined as

$$S(t) = S_{\text{glass}} \left[ 1 + \left(\frac{t}{\lambda}\right)^\beta \right]^{(-\kappa/\beta)}, \quad (7)$$

where  $S_{\text{glass}} = 3 \times 10^3$  MPa is constant and  $\lambda$ ,  $\beta$ , and  $\kappa$  are the parameters of this model.

The objective error function is defined as

$$f_1 = \frac{1}{M} \sqrt{\sum_{j=1}^M \left(1 - \frac{D_{c,j}}{D_{m,j}}\right)^2}, \quad (8)$$

where  $D_{c,j}$  is the model predictive value of creep compliance;  $D_{m,j}$  is the actual value of creep compliance; and  $M$  is the number of data points.

The asphalt binder is subjected to the flexural deflection as the BBR test time goes on; the bending tendency is depicted in Figure 2.

As per the deflection of the binder, the Burgers model was employed to evaluate the viscoelastic property through

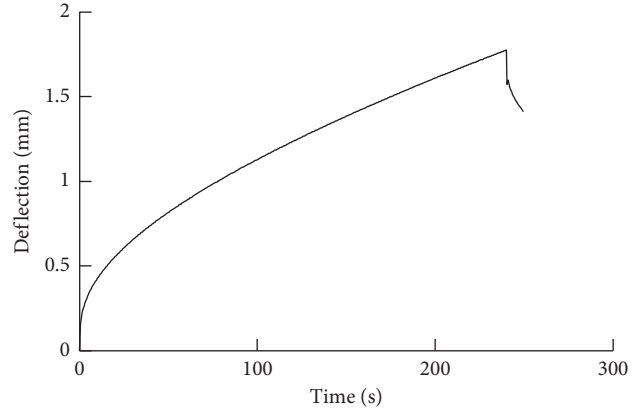


FIGURE 2: Loading time-deflection figure of BBR asphalt beam.

the analysis of its parameters. The Burgers model is composed of one Maxwell's model and one Kelvin's model including four components in series [34, 35], as shown in Figure 3.

The creep compliance is determined by the following equation:

$$D(t) = \frac{1}{E_1} \left(1 - e^{-(E_1/\eta_1)t}\right) + \frac{1}{E_2} + \frac{t}{\eta_2}, \quad (9)$$

where  $E_1$  and  $\eta_1$  are the delayed elastic modulus and viscous parameter of the Kelvin model and  $E_2$  and  $\eta_2$  are the instantaneous elastic modulus and viscosity coefficient of the Maxwell model.

In this study, the BBR tests were conducted at 4 temperatures ( $-6$ ,  $-12$ ,  $-15$ , and  $-18^\circ\text{C}$ ) in accordance with AASHTO T313 [36] using the recycled asphalt binders subjected to long-term aging.

**2.4. Multiple Stress Creep Recovery (MSCR) Tests.** The MSCR test according to AASHTO TP70 [37] is conducted on the binders to evaluate the high-temperature performance of rutting resistance on the basis of the creep characteristic of binders [21, 38, 39]. All the binders were short-term aged using RTFO test. Two creep stress levels, 0.1 kPa and 3.2 kPa, were adopted in this test involving 10 consecutive cycles, and each cycle consists of a creep loading period (1 s) and a recovered period (9 s). The nonrecoverable creep compliance ( $J_{nr}$ ) and percent recovery ( $R$ ) can be determined using the following formulations:

$$J_{nr} = \frac{\gamma_{nr}}{\tau}, \quad (10)$$

$$R = \frac{\gamma_p - \gamma_{nr}}{\gamma_p - \gamma_0}, \quad (11)$$

where  $\gamma_p$ ,  $\gamma_{nr}$ , and  $\gamma_0$  are the peak strain, the residual strain, and the initial strain in each cycle, respectively, and  $\tau$  is the shear stress. So,  $\gamma_p$  is the strain recorded at the end of 1s,  $\gamma_{nr}$  is the strain recorded at the end of the 10 s creep phase, which is the unrecoverable strain, and  $\gamma_0$  is the strain at the beginning of 1 s. Thus, equation (10) is the expression of the nonrecoverable creep compliance ( $J_{nr}$ ). ( $\gamma_p - \gamma_0$ )



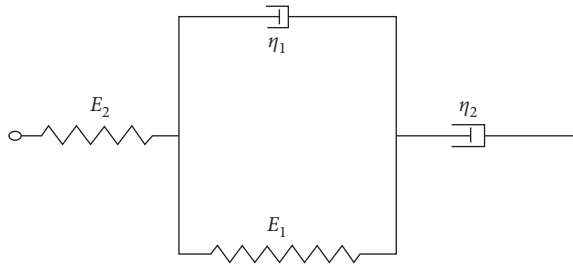


FIGURE 3: Burgers' model.

represents the total strain recorded during the loading period, while  $(\gamma_p - \gamma_m)$  represents the recoverable strain during the recovered period. Thus, equation (11) is the expression of percent recovery (R).

In this study, the MSCR test was performed at four temperatures, 46°C, 52°C, 58°C, and 64°C.

**2.5. Linear Amplitude Sweep (LAS).** Linear amplitude sweep (LAS) test, that is, asphalt accelerated fatigue test, is the main test method used to evaluate the fatigue performance of asphalt in the specifications of AASHTO [40]. In this test, the strain-controlled loading method was adopted. The amplitude of loaded sine wave increased linearly from 0.1% to 30%, and the sweep time was 300 s.

In the LAS test, elastic deformation and plastic deformation will occur to asphalt in turn under repeated loading. When the load is applied to a certain phase, the strain of the material continues to increase and the stress decreases, indicating yield of the material. When the material yields, the normal stress is the yield stress of the material. At this time, the corresponding strain is the yield strain. The larger the yield stress, the stronger the resistance to deformation under a certain load. The larger the yield strain, the greater the deformation under maximum load, and the better the elasticity of the asphalt material. And studies show that there is also a peak of phase angle in the LAS test. If the peak of shear stress is taken as the yield stress of the material, the final failure of the material can be used to analyze by the peak of phase angle, because the peak of phase angle always lags behind the yield stress [41]. In this paper, the peak of shear stress is taken as the yield stress, and the corresponding strain is the yield strain.

The LAS test is an accelerated procedure to assess the fatigue resistance of asphalt binders according to AASHTO TP 101-14 [42]. As we all know, the traditional strain-controlled fatigue equation is defined as

$$N_f = A(\gamma_{\max})^{-B}, \quad (12)$$

where  $\gamma_{\max}$  is the amplitude of the applied shear strain;  $A$  is the fatigue law coefficient obtained from the following equation:  $A = (f \times (D_f)^{[1+(1-C_2)\alpha]}/\{[1+(1-C_2)\alpha] \times (\pi C_1 C_2)^\alpha\})$ ;  $B = 2\alpha$ . The two coefficients can be determined from the LAS test.

The LAS test contains two main steps. In the first step, a frequency sweep, whose frequency is varied from 0.2 to 30 Hz at a constant shear strain amplitude of 0.1% within the LVE range, is performed to determine the damage analysis “ $\alpha$ ” parameter. “ $\alpha$ ” is obtained by the following equations:

$$\log G'(\omega) = m(\log \omega) + b, \quad (13)$$

$$G'(\omega) = G^*(\omega) \times \cos \delta(\omega), \quad (14)$$

$$\alpha = \frac{1}{m}. \quad (15)$$

In the second step, an amplitude sweep is carried out to identify the damage accumulation of the binders over a range of amplitude levels linearly from 0 to 30% at a constant frequency level of 10 Hz in 5 min. The viscoelastic continuum damage (VECD) model is introduced to determine the fatigue life of the binders [43–46]. By means of the VECD theory, the fatigue behavior under varying strain levels of binders can be predicted [47].

The damage accumulation  $D$  with testing time can be obtained as follows:

$$D(t) \cong \sum_{i=1}^N [\pi \gamma_0^2 (C_{i-1} - C_i)]^{(\alpha/(1+\alpha))} (t_i - t_{i-1})^{(1/(1+\alpha))}, \quad (16)$$

where  $C(t) = (G^*(t)/G^*(Initial))$  is the material integrity parameter. The power law model has been introduced for analytically relating the material integrity  $C$  to the damage intensity  $S$  as follows [43, 48]:

$$C(t) = C_0 - C_1 \times D^{C_2}, \quad (17)$$

where  $C_0 = 1$  is the initial value of  $C$ , and  $C_1$  and  $C_2$  are curve fitting parameters.

According to Singh's research [47], the maximum peak shear stress is introduced to define the failure point as follows:

$$D_f = \left( \frac{C_0 - C_{\text{Peakstress}}}{C_1} \right)^{(1/C_2)}. \quad (18)$$

The calculation formula for fatigue life is

$$N_f = A(\gamma_{\max})^{-B}, \quad (19)$$

where  $\gamma_{\max}$  is the expected maximum strain level (%);  $A$  and  $B$  are the fatigue correlation coefficients;  $A = (f \times (D_f)^{[1+(1-C_2)\alpha]}/\{[1+(1-C_2)\alpha] \times (\pi C_1 C_2)^\alpha\})$ ;  $B = 2\alpha$ ; and  $f$  is the loading frequency.

In this study, the LAS test was conducted at 20°C using the long-term asphalt binders.

### 3. Results and Discussion

**3.1. Frequency Sweep Analysis.** To assess the availability of 2S2P1D model fitting the master curves, Figure 4 illustrates the master curves of complex shear modulus and phase angles of the three types of virgin asphalt binders, in which the reference temperature is 28°C.

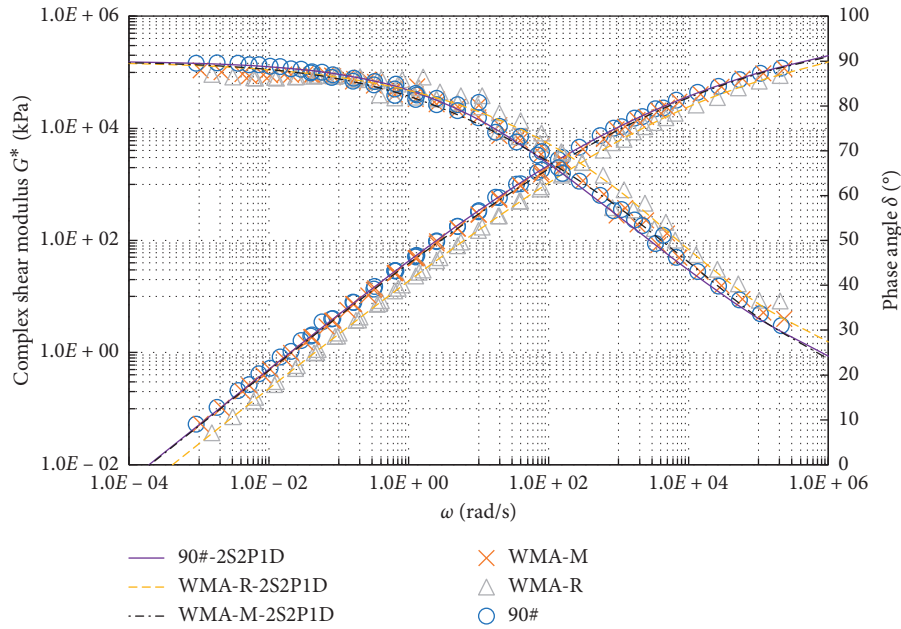


FIGURE 4: Complex shear modulus and phase angle master curves of three types of virgin asphalt binders.

It can be observed that the 2S2P1D model is available for the WMA binders in this paper. With respect to the effect of WMA additives on the rheological property of binders, Figure 4 displays that the incorporation of WMA additive R causes lower complex shear modulus and higher phase angle.

It can be seen from Figure 4, there is no noticeable difference between the WMA-M binder and 90# base asphalt in terms of complex shear modulus and phase angle, and the master curves fitted by the 2S2P1D model for the two binders almost coincide with each other. It indicates that the addition of WMA additive M has no remarkable impact on the viscoelasticity of asphalt. The complex shear modulus of WMA-R binder is less than that of the other two binders; nevertheless, there is no big difference in the phase angle in the low frequency region. As the frequency increases, the phase angle of WMA-R binder is slightly larger than that of WMA-M binder and 90# base asphalt.

The result reveals that the addition of WMA additive R decreases the complex shear modulus of asphalt, increases the phase angle, and slightly reduces antideformation property. However, the addition of WMA additive M with the recommended dosage had little impact on the rheological properties of asphalt. It may be because the WMA additive M is a type of surfactant, which is mainly used as a bridge to build a better connection between the asphalt and aggregate, so that the asphalt and aggregate can be coated completely at a lower temperature. Thus, the WMA additive M mainly has an effect on the asphalt mixture, while the viscosity of asphalt binder has no remarkable reduction, while the WMA additive R is a type of organic agent, which can reduce the viscosity of asphalt binders significantly, so that the rheological properties of recycled asphalt binders change a lot comparing to those of control and RAP-M binders. Besides, due to the mechanism of the two WMA additives, it is possible to utilize more RAP in recycled

asphalt mixture at a lower temperature with a well coating condition.

In this paper, three types of recycled asphalt binders with 30%, 50%, and 70% of RAP binder were selected to analyze the master curves of complex shear modulus and phase angle of the asphalt binders before and after PAV aging.

The master curves of the complex shear modulus and phase angle of the control binder before and after PAV aging are shown in Figures 5–7. It can be seen that the master curves of the complex shear modulus before and after aging fit well with 2S2P1D model. As the content of RAP binder increases, master curves of complex shear modulus exhibit significant change. After PAV aging, the complex shear modulus improved significantly in the low frequency region compared to that prior to aging. However, it does not change significantly in the high frequency region. It indicates that PAV aging has a relatively greater impact when the load frequency is relatively lower. It can be seen by the comparison that the fitting precision of the phase angle master curve after PAV aging is obviously worse than that before aging, indicating that the viscoelasticity of recycled binder becomes more complex under the load frequency after aging. There is no big difference in the phase angle in high- and low-frequency regions; an obvious difference is shown in the intermediate frequency region. It indicates that the control binder exhibits stronger elasticity at  $0.01\text{--}10^4$  rad/s after aging.

The master curves of complex shear modulus and phase angle of RAP-M binder before and after PAV aging are shown in Figures 8–10 above. It can be seen that the trend is approximately similar to that of the master curve of the control binder. It indicates that the addition of M has little impact on the rheological properties of recycled binder.

The master curves of the complex shear modulus and phase angle of RAP-R binder before and after PAV aging

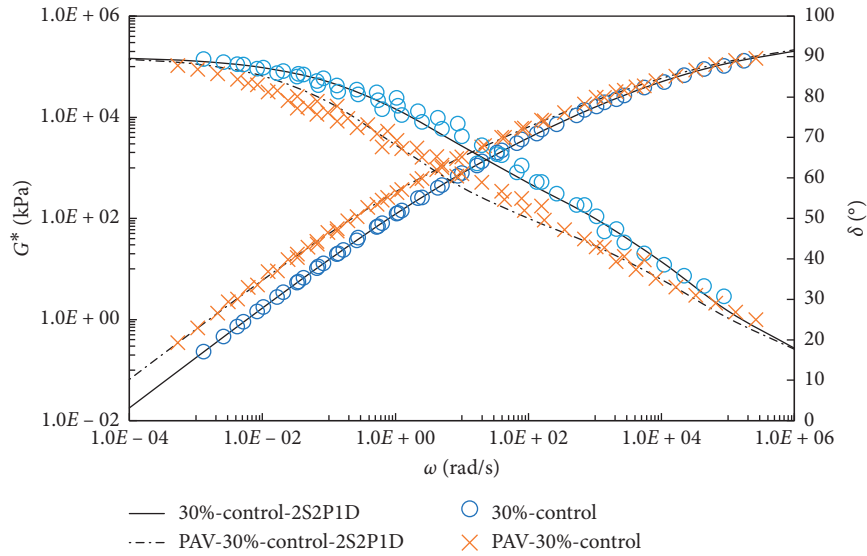


FIGURE 5: Complex shear modulus and phase angles master curves for control binder containing 30% RAP binder before and after PAV aging.

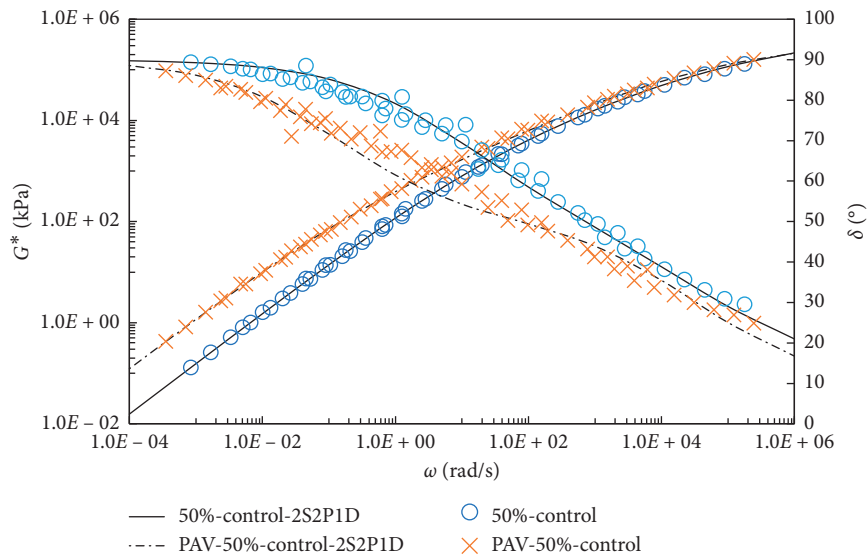


FIGURE 6: Complex shear modulus and phase angles master curves for control binder containing 50% RAP binder before and after PAV aging.

are shown in Figures 11–13. The complex shear modulus shows a trend similar to that of the control binders. Due to the addition of *R*, the phase angle changes greatly. In particular, when the RAP binder content is 50% and 70%, the phase angle of RAP-R binder tends to decrease at low frequency prior to PAV aging, which is even less than that after aging. There is a relatively distinct deviation error in the fitting curve of the 2S2P1D model. This may be explained by the fact that comparing the control and RAP-

M binders, the viscosity of RAP-R binder was reduced significantly with the addition of WMA additive *R*. As the temperature went up, that is, corresponding to the medium and low frequency, the reduced viscosity caused the change of rheological property of RAP-R binder. Furthermore, the phase angle represents the viscosity and elasticity of asphalt. When the RAP binder content increases, the viscoelasticity of RAP-R binder may present a nonlinear change. Thus, the master curves of phase angle are not ideal

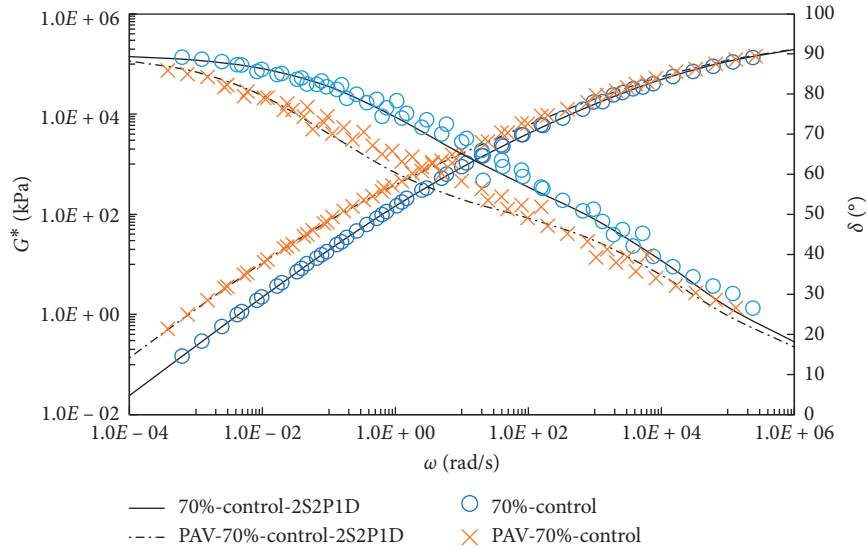


FIGURE 7: Complex shear modulus and phase angles master curves for control binder containing 70% RAP binder before and after PAV aging.

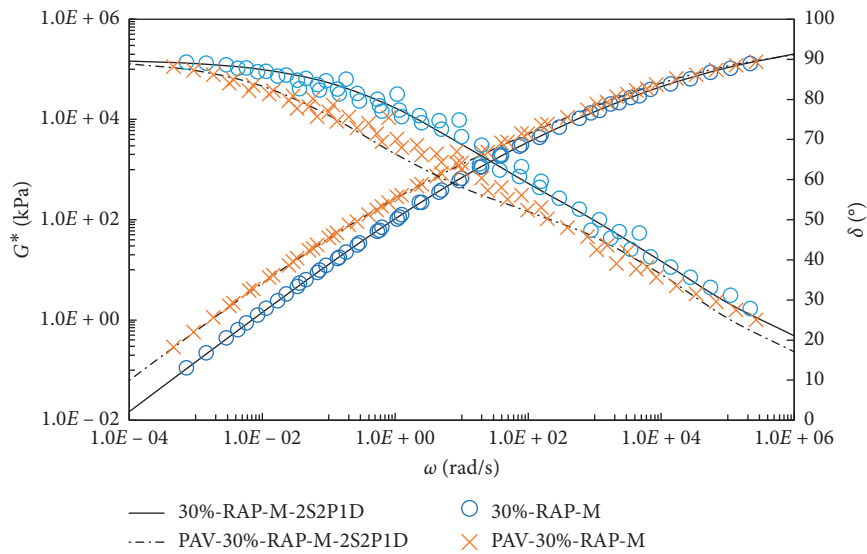


FIGURE 8: Complex shear modulus and phase angles master curves for RAP-M binder containing 30% RAP binder before and after PAV aging.

in the low and medium frequency regions using the 2S2P1D model.

But after PAV aging, the viscoelasticity of RAP-R binder tends to be normal. Therefore, the influence of  $R$  on the viscoelasticity of the recycled asphalt occurs before PAV aging.

3.2. Analysis of Low-Temperature Rheology in the BBR Test.

The three types of recycled binders with 30%, 50%, and 70% of RAP binder after PAV aging are chosen to analyze the low-temperature rheological properties of recycled asphalt binder. The master curves are plotted as shown in Figures 14(a)–14(c).

It can be seen from Figure 14 that the master curves of creep compliance of the three types of recycled asphalt binder are below the 90# base asphalt curve. It indicates that, due to the addition of RAP binder, the recycled asphalt binder is harder than the 90# base asphalt at low temperature, and the creep performance is reduced. Therefore, the ability to resist crack at low temperature is poor. However, with the increase of the content of RAP binder, the creep compliance curves have no remarkable change; thus, the RAP binder contents have little effect on the rheological properties at low temperature in this research.

It can be seen by the comparison that the addition of  $R$  obviously improved the low-temperature creep performance

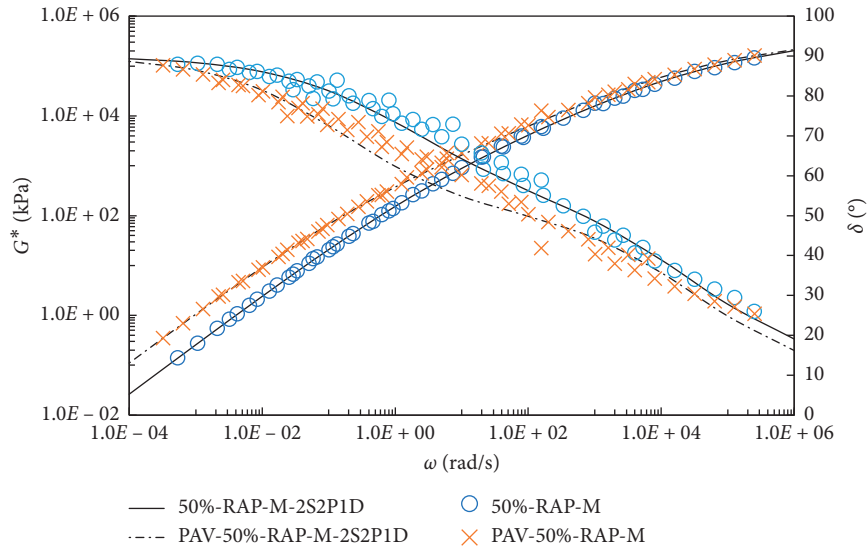


FIGURE 9: Complex shear modulus and phase angles master curves for RAP-M binder containing 50% RAP binder before and after PAV aging.

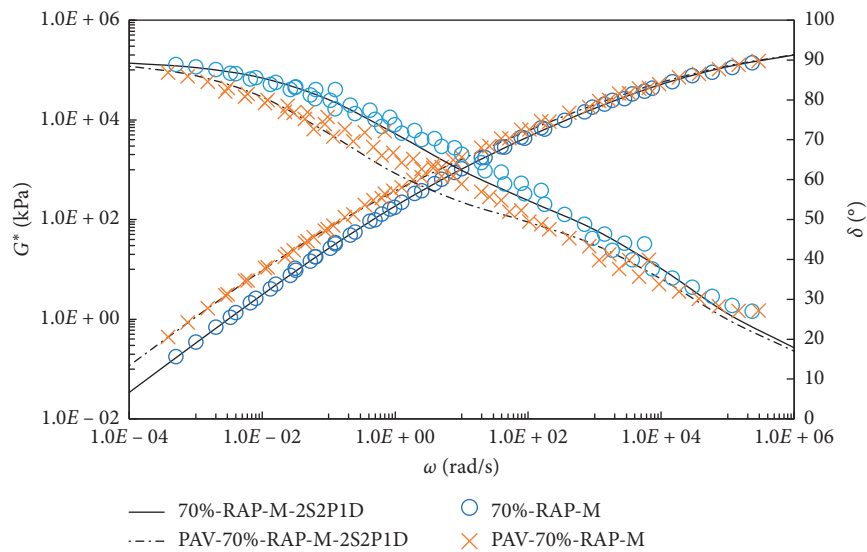


FIGURE 10: Complex shear modulus and phase angles master curves for RAP-M binder containing 70% RAP binder before and after PAV aging.

of the recycled binder. When the RAP binder content is 30%, it reaches the same level as 90# base asphalt, while the difference between 50%-R binder or 70%-R binder and 90# base asphalt is also obviously less than the other two types of recycled asphalt. In general, the low-temperature creep performance of the three binders is ranked as follows: RAP-R binder > RAP-M binder > control binder.

Creep compliance at different temperatures was fitted to obtain the four viscoelastic parameters of the Burgers model. At the same time, the corresponding delay time  $\tau = (\tau_1/E_1)$  and relaxation time  $\lambda = (\lambda_2/E_2)$  can be calculated. The

results at different temperatures are shown in Figures 15(a)–15(d).

It can be observed from Figure 15 that the Burgers model parameters of the three types of recycled binders increase as the temperature decreases. The lower the temperature, the greater the variation. In Figure 15(a), at the same temperature, the elastic modulus of RAP-R is the smallest, while that of the control binder is the largest. It indicates that the control binder is the hardest and RAP-R is the softest.  $E_2$  represents the instantaneous elastic modulus. At the same temperature, RAP-R binder has the smallest  $E_2$ , while  $E_2$  of

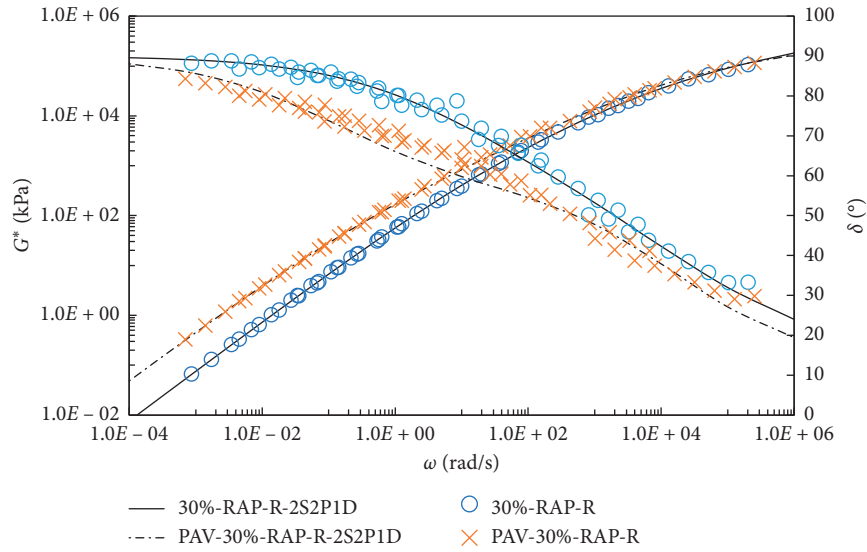


FIGURE 11: Complex shear modulus and phase angles master curves for RAP-R binder containing 30% RAP binder before and after PAV aging.

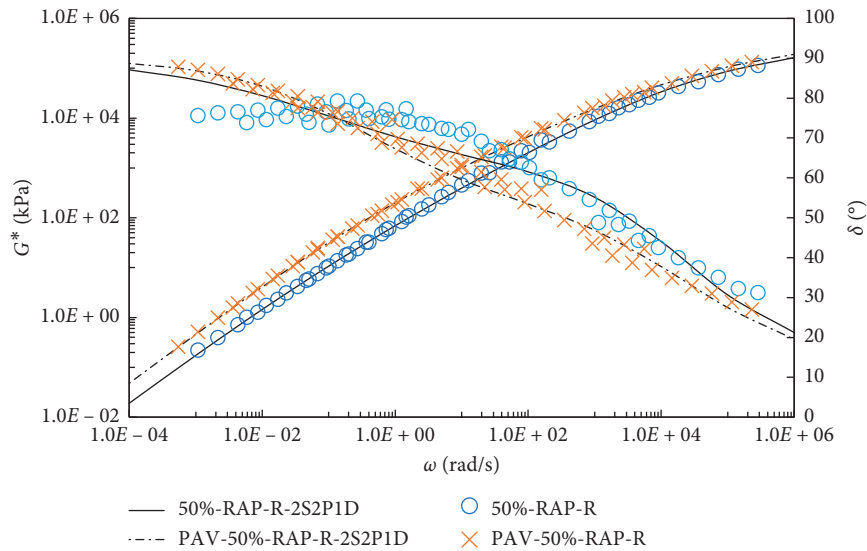


FIGURE 12: Complex shear modulus and phase angles master curves for RAP-R binder containing 50% RAP binder before and after PAV aging.

RAP-M binder and control binder is almost the same.  $\eta_2$  represents the viscosity coefficient of unrecoverable deformation. When the temperature decreases,  $\eta_2$  increases, indicating the reduction of the viscous component of asphalt; at the same temperature, RAP-R binder has the smallest  $\eta_2$ , which indicates that it has the highest viscosity and the low-temperature crack resistance is better than that of the other two recycled binders. Besides, with the increase of the RAP binder content,  $\eta_2$  increases gradually, which shows that the RAP binder content will reduce the low-temperature performance of the recycled binder.

The calculation results of the relaxation time  $\lambda$  are shown in Figure 16. The relaxation time  $\lambda$  represents that the stress dissipates over time. The longer the relaxation time, the lower the relaxation rate and the slower the dissipation of stress. Figure 16 depicts that with the decrease of temperature, the relaxation time is prolonged. There is a good linear relation between  $\lambda$  and temperature, and the linear regression equations and correlation coefficients are shown in Table 2. The addition of *R* significantly reduces the relaxation time of recycled asphalt binder. The relaxation time of RAP-M binder is also less than that of the control binder.

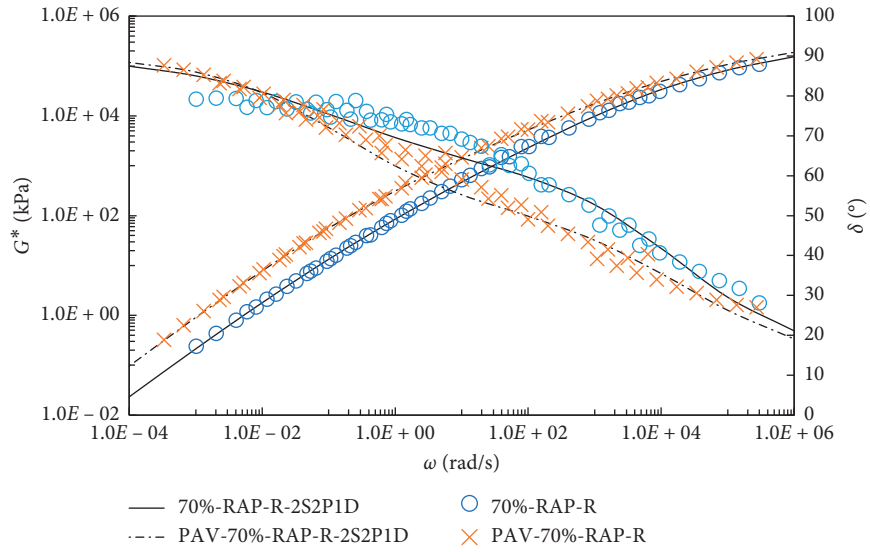
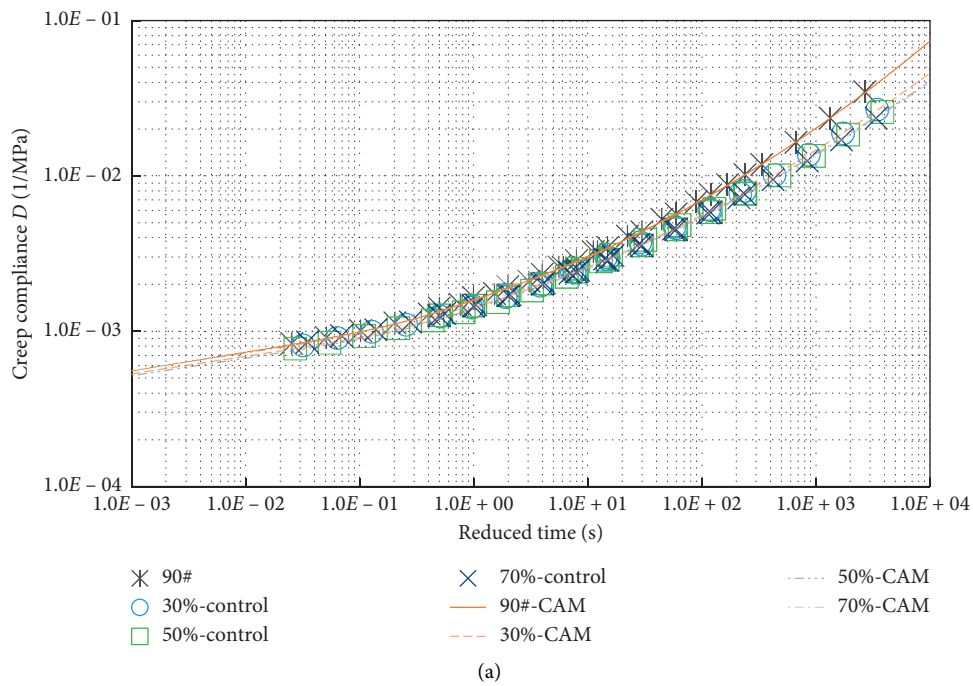


FIGURE 13: Complex shear modulus and phase angles master curves for RAP-R binder containing 70% RAP binder before and after PAV aging.



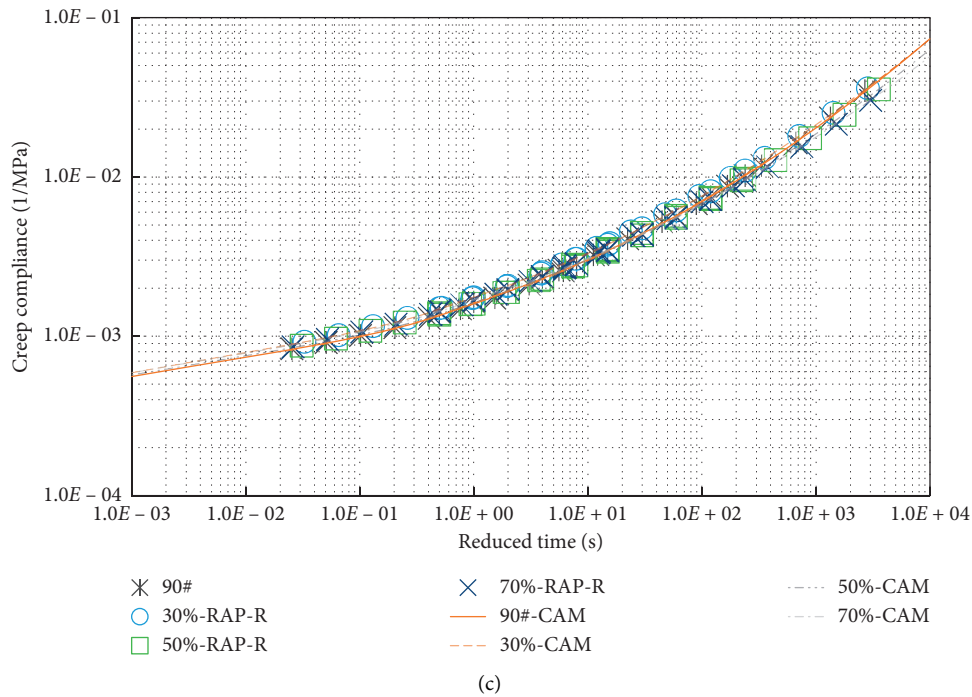
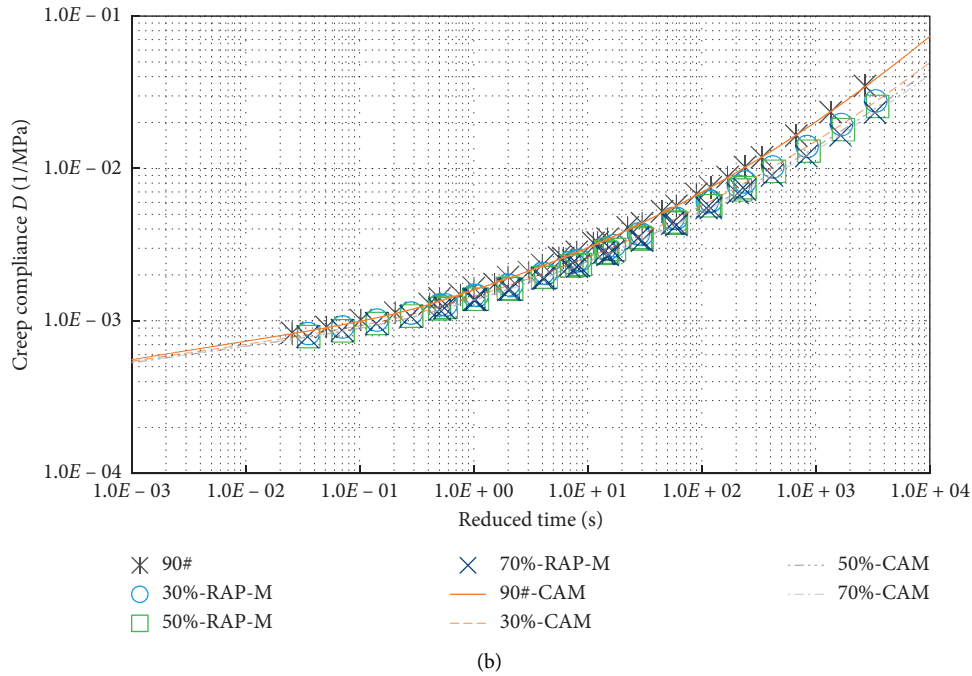


FIGURE 14: Master curves from the CAM model for BBR data of three types of recycled binders. (a) Control binder, (b) RAP-M binder, and (c) RAP-R binder.

Therefore, the performances at low temperature of RAP-R and RAP-M binders are both improved. In addition, the increased content of RAP binder decreases the viscous property of asphalt, prolongs the relaxation time of stress, and reduces the low-temperature crack resistance.

3.3. Analysis of MSCR Test Results. A comparative analysis is first made based on the test results of the recycled binder with 50% of RAP binder at 3.2 kPa, as shown in Figures 17(a) and 17(b).

Figure 17(a) shows the strain–time curve of the control binder with 50% of RAP binder at different test temperatures. As the temperature increases, the strain increases significantly at a growing rate. When the temperature is up to 64°C, the strain is the largest, and there is no distinct recovery under each cycle of loading and unloading. It indicates that the elastic component of the control binder has nearly disappeared at 64°C.

Figure 17(b) gives the strain–time curve of the three types of recycled binder at 46°C. During the MSCR test, two



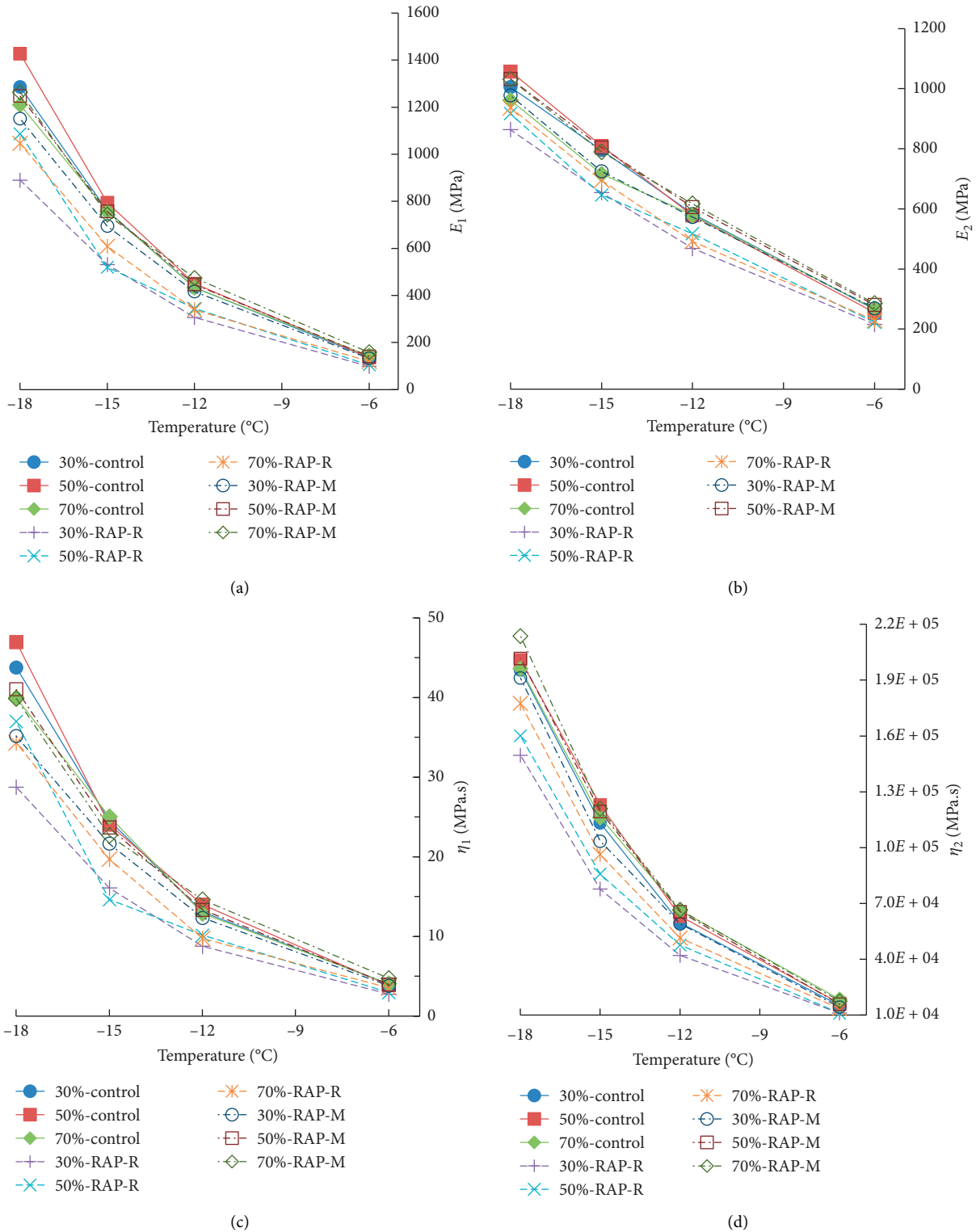


FIGURE 15: Parameters of Burgers' model for WMRA binders at various temperatures. (a) Delayed elastic parameter  $E_1$ . (b) Instant elastic parameter  $E_2$ . (c) Delayed viscous parameter  $\eta_1$ . (d) Viscous flow parameter  $\eta_2$ .

loads at different stress levels were applied to simulate different loads on the real pavement due to diverse traffic volumes. As a result, the difference in deformation can exhibit the antideformation property. The strains of the three types of recycled binders are ranked as follows: RAP-

R > control > RAP-M, which indicates that the addition of M enhances the antideformation property of the recycled binder, while the addition of R has an opposite effect. At high temperatures, the addition of R makes the recycled binder more like a viscous fluid.

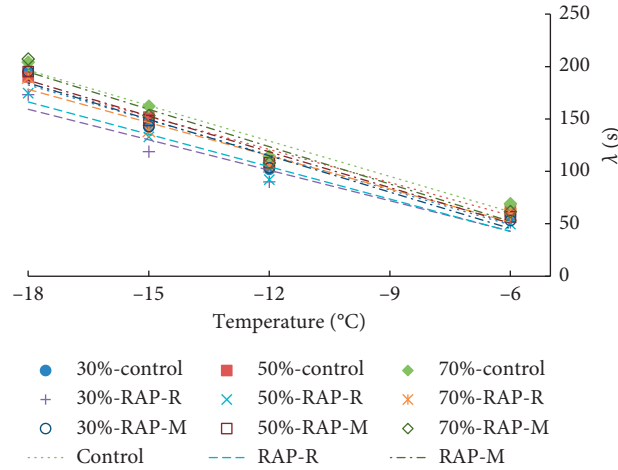
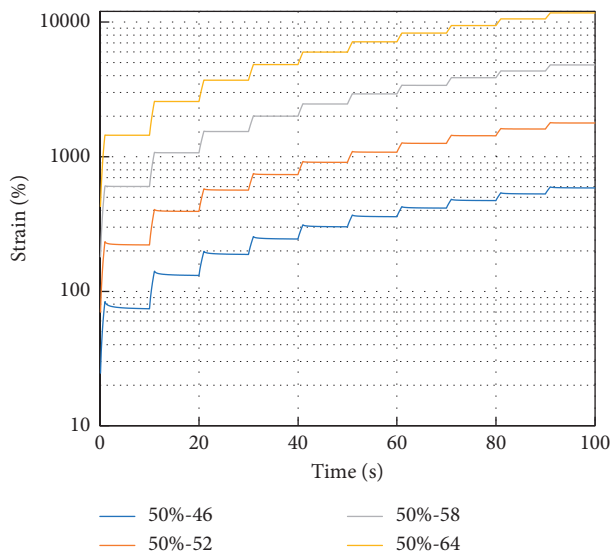


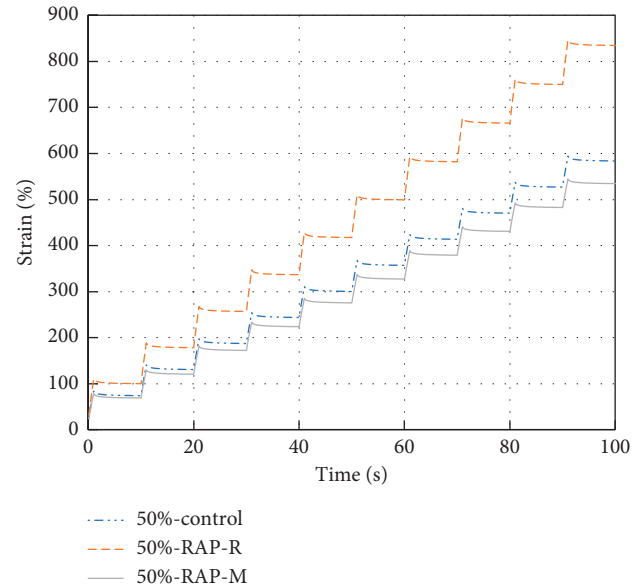
FIGURE 16: Relationship of relaxation time  $\lambda$  and temperature.

TABLE 2: Linear regression function and correlation coefficients between relationship of relaxation time  $\lambda$  and temperature.

Control (%)	Functions and $R^2$	RAP-R (%)	Functions and $R^2$	RAP-M (%)	Functions and $R^2$
30	$y = -11.135x - 17.901$ ; $R^2 = 0.9560$	30	$y = -9.6889x - 15.205$ ; $R^2 = 0.9342$	30	$y = -11.569x - 23.828$ ; $R^2 = 0.9663$
50	$y = -10.486x - 4.8829$ ; $R^2 = 0.9765$	50	$y = -10.3x - 19.091$ ; $R^2 = 0.9680$	50	$y = -11.377x - 17.876$ ; $R^2 = 0.9778$
70	$y = -11.245x - 5.972$ ; $R^2 = 0.9679$	70	$y = -10.551x - 11.693$ ; $R^2 = 0.9619$	70	$y = -11.882x - 19.037$ ; $R^2 = 0.9557$



(a)



(b)

FIGURE 17: Strains curve of MSCR: (a) various temperatures and (b) various recycled binders.

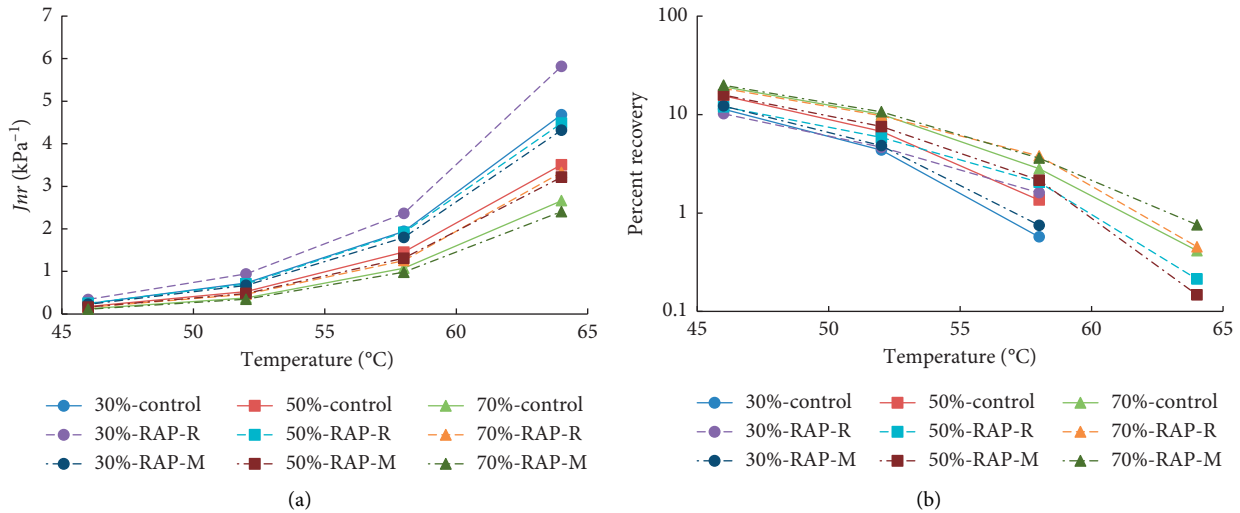


FIGURE 18: MSCR parameters of three types of recycled binders: (a)  $J_{nr}$  (kPa) and (b) R (%).

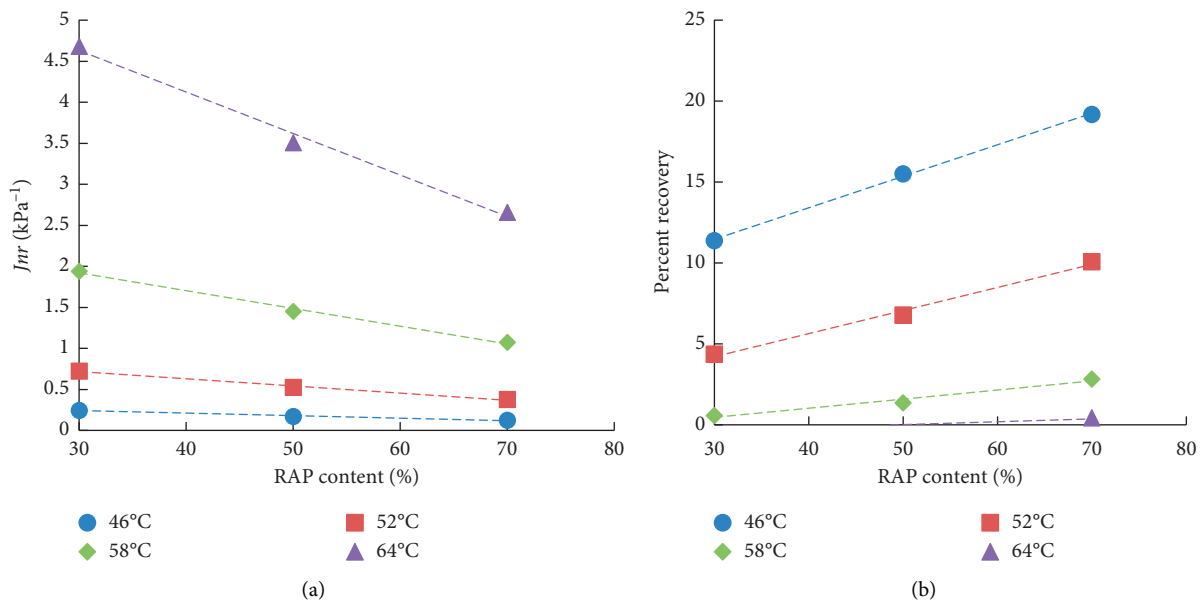


FIGURE 19: Relationship of aging asphalt content and MSCR parameters for control binders: (a) unrecoverable creep compliance and (b) creep percent recovery.

The unrecoverable creep compliance  $J_{nr}$  and percent recovery R of recycled asphalt binders at 3.2 kPa at the four temperatures are shown in Figures 18(a)–18(b).

The creep percent recovery represents the elastic deformation capacity of asphalt binders. The creep percent recovery of the recycled binders with different RAP binder contents at different temperatures are shown in Figure 18(b). The results of recycled binders containing 30% RAP binder are not shown in Figure 18(b), as their percent recovery is close to 0. By comparison, it can be found that the creep percent recovery of the RAP-M binder is higher than that of control and RAP-R binders under the same condition;

therefore, RAP-M binder is more suitable for high-temperature regions. Although the addition of R leads to a minimum percent recovery, the combined use of RAP binder can offset its disadvantage in the high-temperature performance. Moreover, RAP-R binder has the best low-temperature performance; thus, it can be introduced in colder regions. Despite the fact that the creep percent recovery represents the viscoelastic deformation capacity of asphalt binders, the accumulation of final permanent deformation depends primarily on the unrecoverable compliance ( $J_{nr}$ ). Through the comparison from Figure 18(a), the antipermanent deformation capacity of the three types of

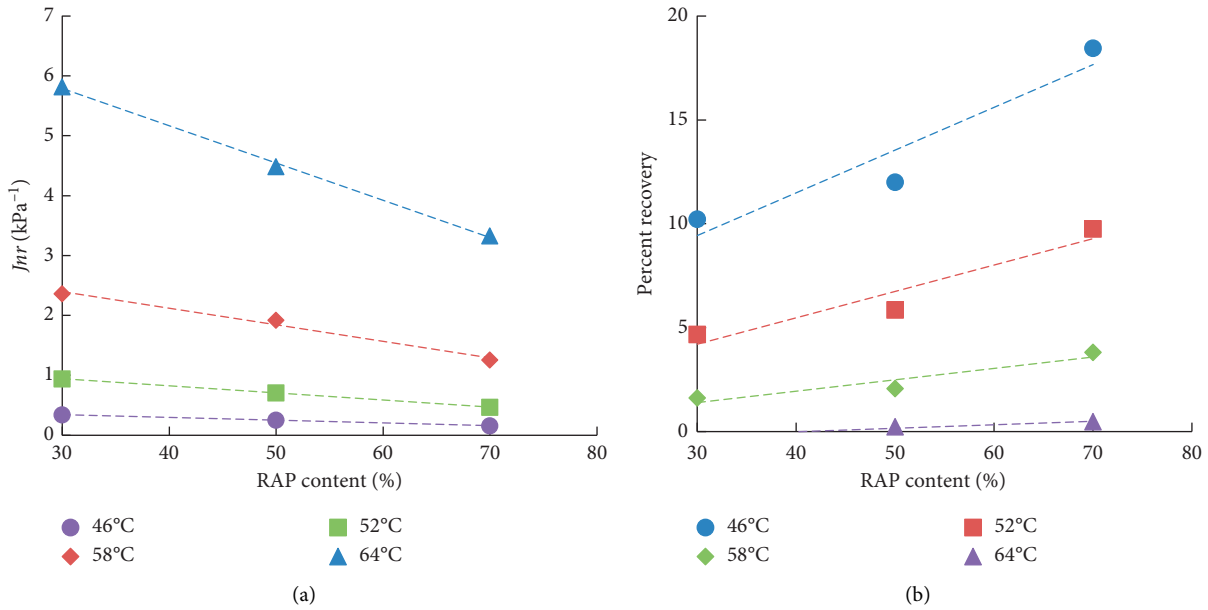


FIGURE 20: Relationship of aging asphalt content and MSCR parameters for RAP-R binders: (a) unrecoverable creep compliance and (b) creep percent recovery.

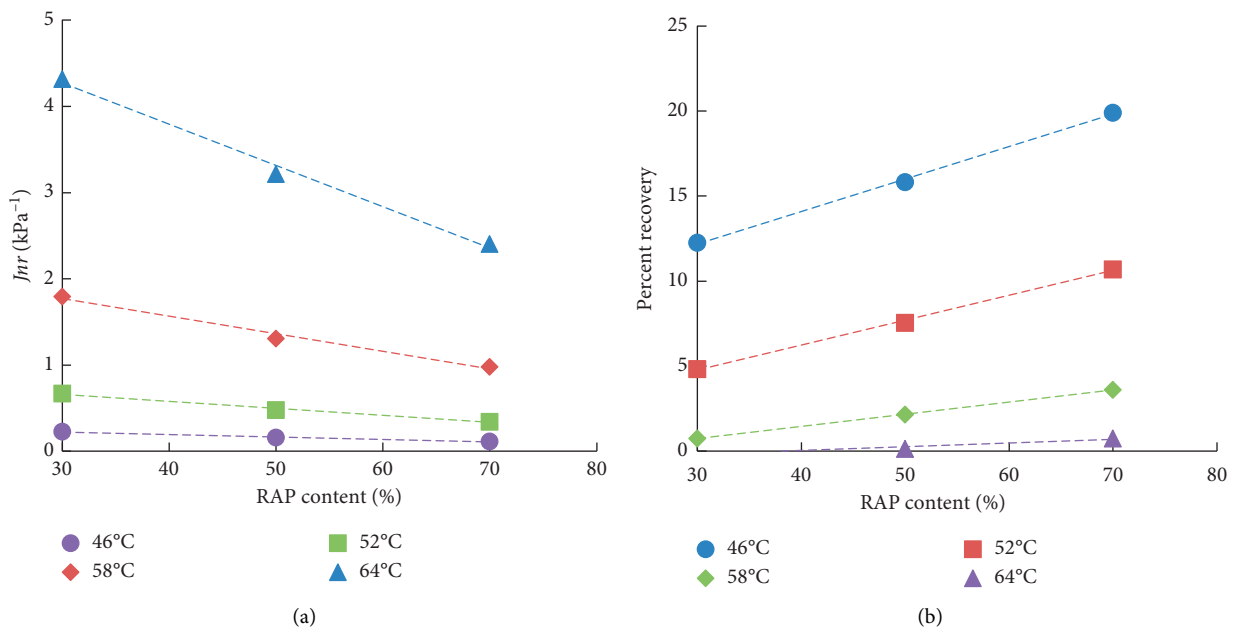


FIGURE 21: Relationship of aging asphalt content and MSCR parameters for RAP-M binders: (a) unrecoverable creep compliance and (b) creep percent recovery.

recycled binder under the same condition is  $\text{RAP-M} > \text{control} > \text{RAP-R}$ .

The increment of RAP binder content of recycled binder can reduce the unrecoverable creep compliance ( $J_{nr}$ ) and improve the creep percent recovery R. The relationships between  $J_{nr}$  and R and RAP binder content are shown in Figures 19–21. It can be observed that there is a good linear relation displayed between the RAP binder content and either  $J_{nr}$  or R. As the temperature increases, the impact of RAP binder content on  $J_{nr}$  and R decreases at

a growing rate. Therefore,  $J_{nr}$  and R can be predicted based on the figures of the recycled binders containing different contents of RAP binder, which is able to assess the actual high-temperature pavement performance of high-percentage WMRA. Meanwhile, on the premise of satisfying low-temperature and fatigue performance, increasing the RAP binder content can improve not only the recycling efficiency and high-temperature performance but also the requirements of traffic volume level for the WMRA pavement.

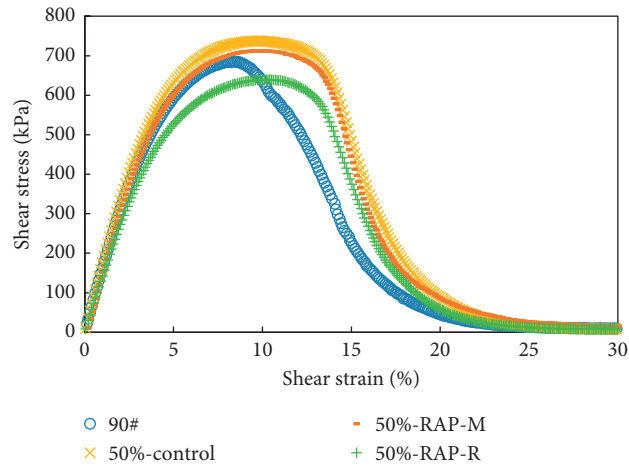


FIGURE 22: Shear stress and phase angle of LAS test.

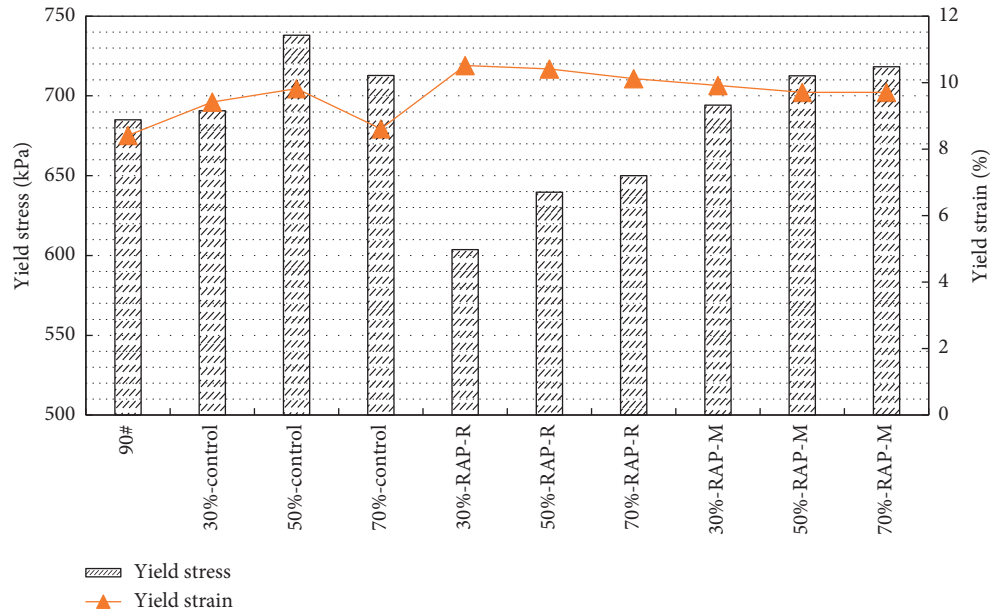


FIGURE 23: Comparison between yield stress and yield strain of various recycled binders.

3.4. Analysis of LAS Fatigue Characteristics. Similar trends are observed for different artificial RAP contents; thus, only the recycled binders containing 50% artificial RAP binder are typically presented in Figure 22. The dependency of asphalt materials on the applied strain and the damage induced under loading can be exhibited from the shear stress and strain curve in Figure 22 [49, 50]. According to the peak shape of the shear stress and strain curve, the two types of WMRA binders have relatively wider peaks, indicating that the combined use of the RAP binder and WMA additives lowers the dependency of asphalt binder on the strain; thus, the antifatigue performance of WMRA binder is improved. In contrast, the 90# base asphalt has a relatively narrower peak, so the antifatigue performance is slightly reduced compared with the two types of WMRA binders.

The yield stresses and yield strains of the asphalt binders are obtained from the shear stress and strain curves in Figure 22, and the results are shown in Figure 23.

The yield stresses of the 10 asphalt samples at 20°C are ranked as follows: 50%-control > 70%-RAP-M > 50%-RAP-M ≈ 70%-control > 30%-RAP-M > 30%-control > 90# > 70%-RAP-R > 50%-RAP-R > 30%-RAP-R. Meanwhile, the yield strains are 30%-RAP-R > 50%-RAP-R > 70%-RAP-R > 30%-RAP-M > 50%-control > 50%-RAP-M ≈ 70%-RAP-M > 30%-control > 70%-control > 90#. Compared with 90# base asphalt, the yield stress and yield strain of the control binder are improved due to the addition of RAP binder, which exhibits an obvious peak value with the increase of the RAP binder content. Incorporating the two types of WMA additives, the yield stress and yield strain of WMRA binders show a regular change as the RAP binder content increases. The RAP binder

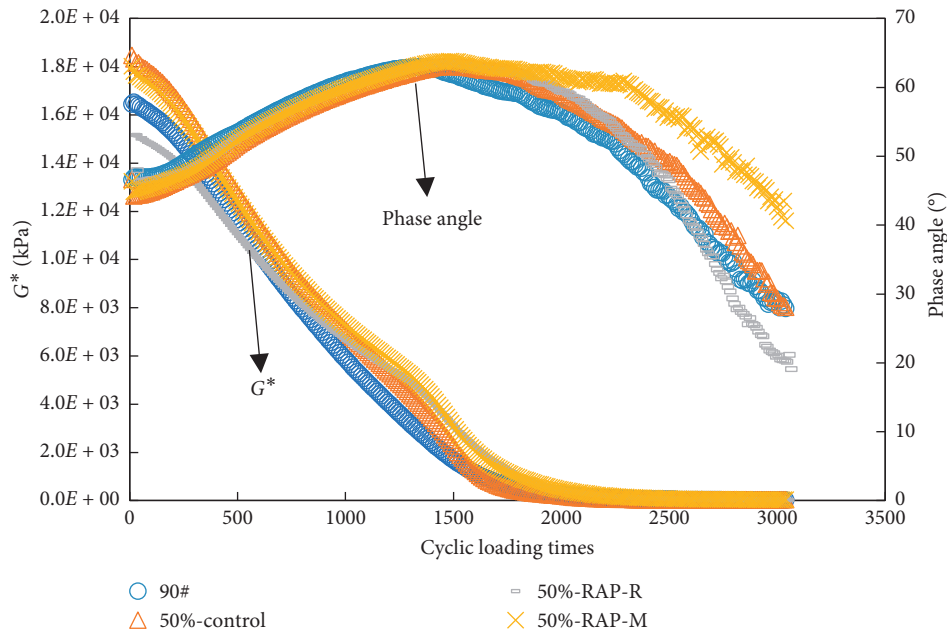


FIGURE 24: Relationship between complex shear modulus or phase angles and cyclic loading times.

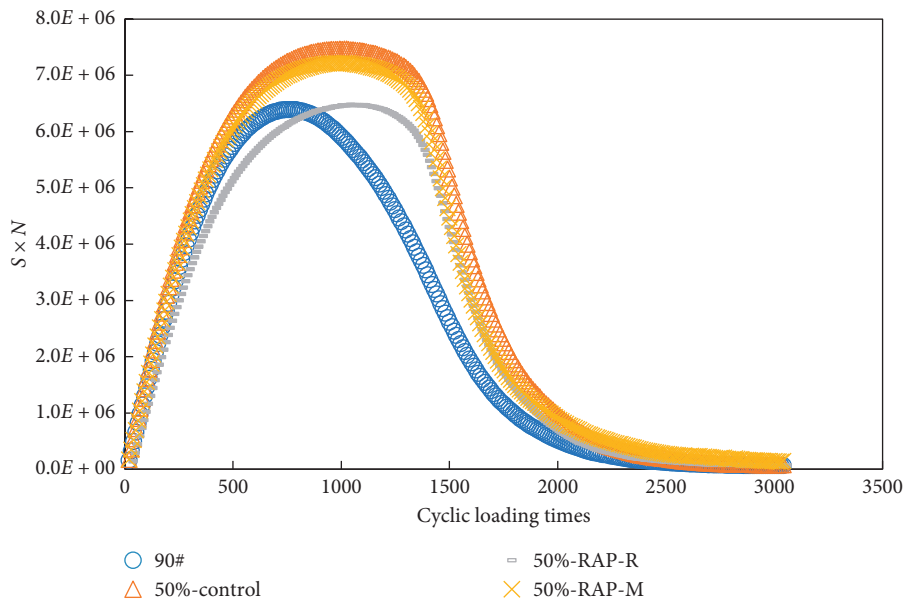


FIGURE 25: Relationship between  $S \times N$  values and cyclic loading times.

content is positively correlated to the yield stress and negatively correlated to the yield strain. The yield stress is reduced and the yield strain is increased with the incorporation of R comparing with other asphalt binders, which suggests that the antideformation property of RAP-R binder is weakened, while the addition of M can improve the antideformation property and deformation extent of the recycled binder.

However, the increment of the RAP binder content has no significant impact on the recycled binder on the whole with the action of M.

In this paper, three methods were adopted to evaluate the fatigue failure of high-percentage WMRA binders: (1) the modulus decreasing to 50% of the initial value; (2) the peak of phase angle; and (3) the peak of  $S \times N$  index, where S is the

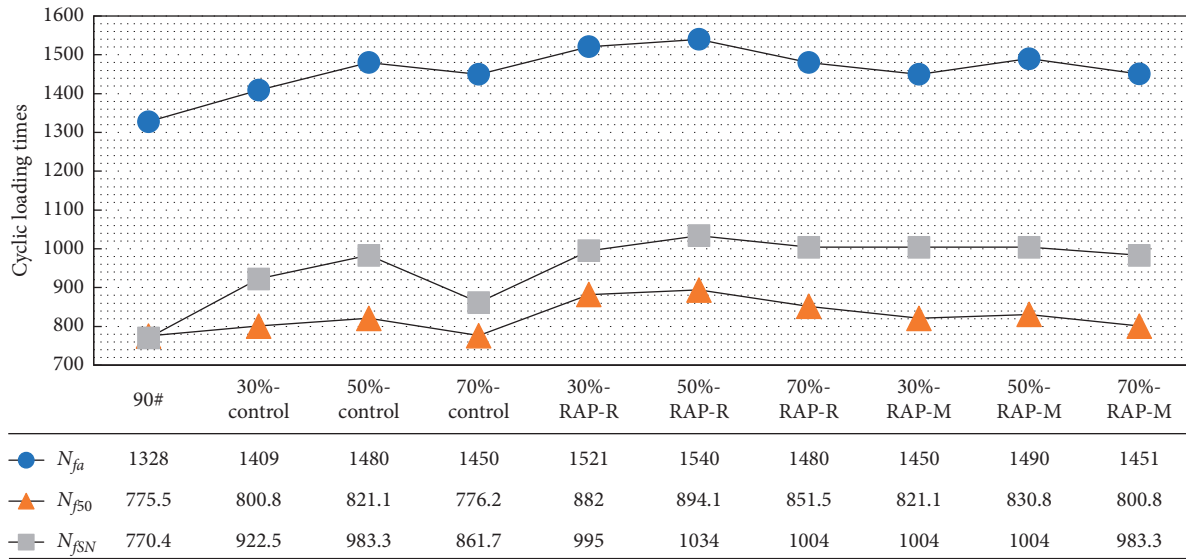


FIGURE 26: Fatigue life results of the three methods.

ratio of the instantaneous modulus to the initial modulus and  $N$  is the loading times [51]. The relation curve between each of the three methods and the cyclic loading times is plotted, respectively, as shown in Figures 24 and 25.

The fatigue lives, calculated using the three methods, are denoted as  $N_{f50}$ ,  $N_{fa}$ , and  $N_{fSN}$ , respectively, and are shown in Figure 26.

In Figure 26, the fatigue lives of asphalt binders of the three methods are ranked as  $N_{fa} > N_{fSN} > N_{f50}$ . The difference between the fatigue lives can be ascribed to the fact that the fatigue failure obtained through the three methods corresponding to the process of fatigue failure is varied. However, the changing tendencies of fatigue lives of the 10 asphalt binders obtained by the three methods are almost the same, indicating that the influence of the RAP binder content and WMA additives on the antifatigue performance of recycled binders is almost the same in the process of fatigue failure. In general, the additions of R and M both improve the fatigue life of recycled asphalt binders, while the effect of R is more noticeable. The RAP binder contents have different effects on different recycled asphalt binders, which indicates that the evaluation of fatigue failure of recycled asphalt binders, especially high-percentage WMRA binder, is comparatively complex considering the combined use of RAP binder and WMA additive.

Then, the VECD model is employed to analyze the LAS test results, and the parameters are shown in Table 3.

The integrity parameter  $C$  represents the damage degree of the asphalt material. When  $C$  is equal to 1, the material is intact. When  $C$  is equal to 0, the material has been completely damaged [44]. According to (15), the damage characteristic curve of three types of recycled binder with different contents of RAP binder can be obtained, as shown in Figures 27(a)–27(c), to evaluate the antifatigue

performance of the recycled binder. In Figure 27(a), the curve of 70%-control binder is close to that of 90# base asphalt. The curves of 30%-control binder and 50%-control binder are above that of 90# base asphalt when the damage intensity is larger than 60, indicating that the damage of 30%-control and 50%-control binder is slower than that of 90# base asphalt. The damage curves of RAP-R and RAP-M binders are shown in Figures 27(b) and 27(c). With the combined use of RAP binder and WMA additive, the curves of RAP-R and RAP-M binders are above that of 90# base asphalt, indicating that the addition of RAP binder will not reduce the antifatigue performance of the asphalt binder; instead, the performance can be further enhanced by adding the WMA additive, R in particular.

The parameter  $\alpha$  represents the slope of the fatigue life and the strain in the log-coordinate. The larger the  $\alpha$ , the more sensitive the fatigue life to strain. Table 3 illustrates that  $\alpha$  of 90# base asphalt is the smallest and that of the three types of recycled binder increases as the RAP binder content increases, indicating that the recycled asphalt binder is more sensitive to the applied strain with the incorporation of RAP binder.  $\alpha$  is ranked as follows: RAP-R < RAP-M < control, containing the same RAP binder content, indicating that the addition of WMA additive makes the asphalt binder less sensitive to the strain.

According to (18) and (19), the fatigue lives with different strains (1%, 3%, and 5%) can be obtained, as shown in Figures 28–30.

The three figures show that as the strain level increases, the fatigue life of the asphalt binders gradually decreases. The fatigue life of the three types of recycled asphalt binder with 50% of RAP binder presents a peak value, indicating that the current fatigue life is the highest in this regard, especially at high strain level. This is consistent with the previous study in Figure 28. Therefore, emphasis must be placed on the fact

TABLE 3: Resulting parameters of the VECD model.

Type of asphalt	$\alpha$	$C_0$	$C_1$	$C_2$	$A$	$B$
90#	1.49276	1	0.10296	0.4175	$1.52E + 05$	2.98552
30%-control	1.573317	1	0.10953	0.39992	$3.68E + 05$	3.146633
50%- control	1.614987	1	0.10154	0.40942	$5.64E + 05$	3.229974
70%- control	1.666944	1	0.10809	0.4076	$3.85E + 05$	3.333889
30%-RAP-R	1.510802	1	0.0991	0.41276	$3.75E + 05$	3.021604
50%-RAP-R	1.577785	1	0.08369	0.44346	$5.38E + 05$	3.15557
70%-RAP-R	1.60901	1	0.10124	0.40828	$4.85E + 05$	3.218021
30%-RAP-M	1.547988	1	0.10309	0.41102	$3.77E + 05$	3.095975
50%-RAP-M	1.608493	1	0.11199	0.39416	$5.40E + 05$	3.216986
70%-RAP-M	2.656452	1	0.11497	0.38876	$6.08E + 05$	3.312904

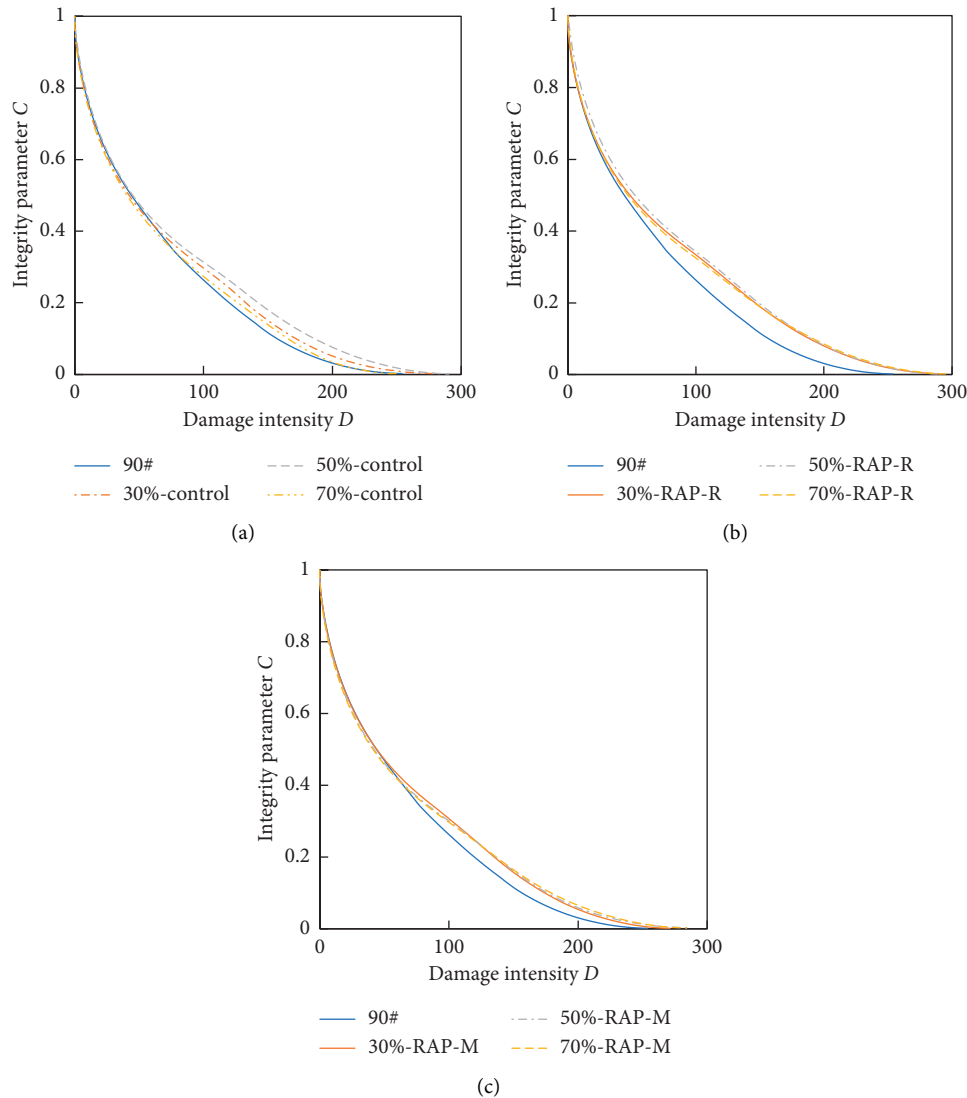


FIGURE 27: Typical damage plots for various recycled binders. (a) Control binder; (b) RAP-R binder; and (c) RAP-M binder.

that when the RAP content is more than 50%, the fatigue performance will be reduced. However, even though the percentage of RAP binder is high, the fatigue life is still longer than that of 90# base asphalt. Moreover, comparing

with the control binder, the fatigue life is improved due to the addition of two types of WMA additives. As a result, the antifatigue performance of high-percentage WMRA binders can satisfy the requirements of pavement.



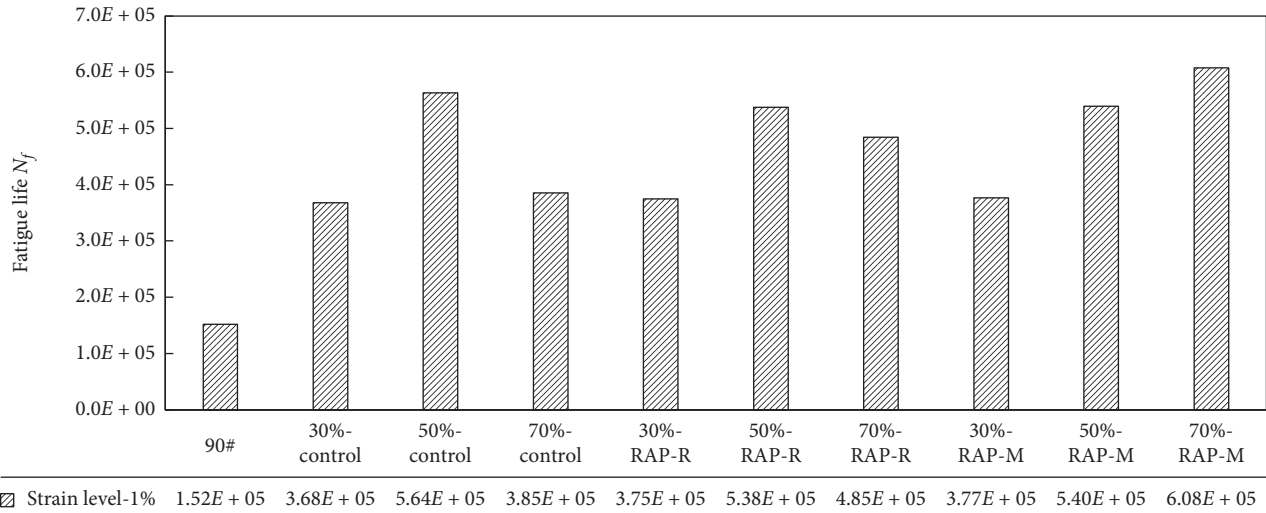


FIGURE 28:  $N_f$  at applied strain level of 1% for various asphalt binders.

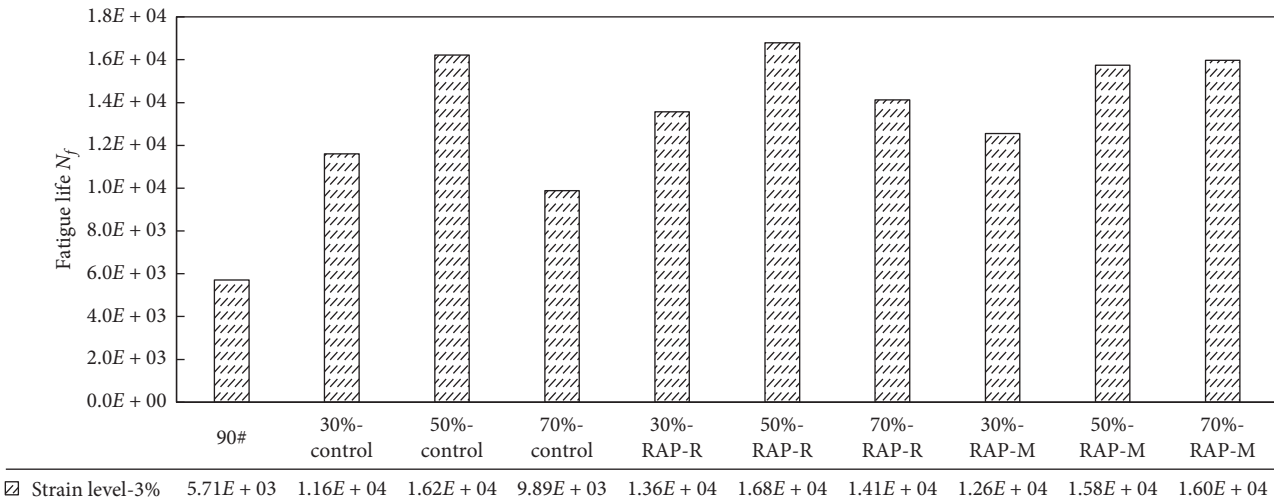


FIGURE 29:  $N_f$  at applied strain level of 3% for various asphalt binders.

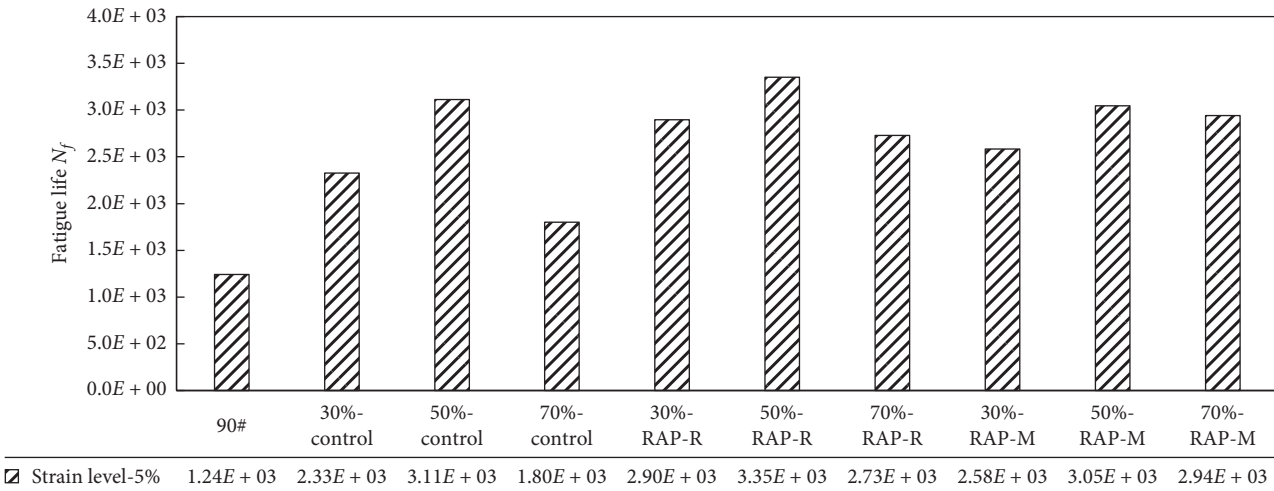


FIGURE 30:  $N_f$  at applied strain level of 5% for various asphalt binders.

#### 4. Conclusions

Based on the observations and analyses from this study, the main conclusions can be drawn as follows:

- (1) The addition of WMA additive R reduced the anti-deformation property of asphalt binders, and the viscoelasticity of RAP-R binder changed remarkably before aging, while the addition of WMA additive M had little impact on the rheological property of asphalt
- (2) Regardless of whether subjected to long-term aging or not, the RAP binder content had no significant effect on the rheology property of WMRA binders. It presents a bad fitting of phase angle using 2S2P1D model, especially for the RAP-R binder with 50% and 70% RAP binder contents
- (3) The performance of low-temperature crack resistance of recycled binders was reduced comparing with the 90# base asphalt, due to the addition of RAP binder. The low-temperature performance of the three types of recycled binders was ranked as RAP-R binder > RAP-M binder > control binder
- (4) It should be noted that in terms of master curves of creep compliance, with the increase of the RAP binder content, the creep compliance changed slightly, whereas considering the parameters analysis of Burgers' model, the performance of low-temperature crack resistance was reduced with the increase of the RAP binder content
- (5) The antideformation property of recycled binders was enhanced with the addition of RAP binder. In terms of  $J_{nr}$  and R at 3.2 kPa from the MSCR test, the antideformation property and elasticity of RAP-M binder were better than control and RAP-R binders, while the addition of WMA additive R remarkably lowered the rutting resistance
- (6) There were both good linear relationships between the RAP binder content of the three types of recycled binder and  $J_{nr}$  or R. Furthermore, the increment of RAP binder content of recycled binder can reduce the unrecoverable creep compliance ( $J_{nr}$ ) and improve the creep percent recovery R
- (7) The addition of RAP binder could not reduce the antifatigue performance of recycled asphalt binders, but there were different effects on the three types of recycled asphalt binders depending on the change of RAP binder content. The fatigue life of recycled asphalt binders was improved with the incorporation of WMA additives R and M, and the effect of WMA additive R was more significant
- (8) The Nf predicted-based VECD method presents a peak value when the RAP binder content is 50% for all the three types of WMRA binders. Therefore, emphasis must be placed on the fact that when the RAP content is more than 50%.

It should be mentioned that further research needs to be carried out to explain some results obtained from this paper, such as selecting another model to fit the phase angle of WMRA binders more accurate and exploring the components of WMA additive R to explain the WMA mechanism. Besides, the RAP binder extracted from the milling asphalt pavement should be recycled comparing with the conclusions of this research.

#### Data Availability

The data used to support the findings of this study are available from the corresponding author upon request.

#### Conflicts of Interest

The authors confirm that there are no conflicts of interest regarding the publication of this paper.

#### Authors' Contributions

Weiyang Wang wrote, reviewed, and edited the original draft. Songchang Huang was responsible for conceptualization of the study. Yongchun Qin was responsible for resources management. Yiren Sun was responsible for research methodology. Rui Dong was responsible for investigation. Jingyun Chen was involved in supervision and project administration.

#### Acknowledgments

This study was sponsored by the National Key R&D Program of China (2018YFB1600100), China Postdoctoral Science Foundation (2019M650614). Fundamental Research Funds for the Central Research Institutes (2018-9007) and Science and Technology Project of Department of Transportation of Shanxi Province (2018-1-1). The supports are gratefully acknowledged.

#### References

- [1] National Cooperative Highway Research Program, *NCHRP 9-46: Improved Mix Design, Evaluation, and Materials Management Practices for HMA with High RAP Content*, TRB and National Research Council, Washington, DC, USA, 2008.
- [2] P. S. Kandhal and K. Y. Foo, "Designing recycled hot mix asphalt mixtures using superpave technology," NCAT Report No. 96-5, National Center for Asphalt Technology, Auburn, AL, USA, 1997.
- [3] P. S. Kandhal, S. S. Rao, D. E. Watson, and B. Young, "Performance of recycled hot mix asphalt mixtures," NCAT Report No. 95-1, National Center for Asphalt Technology, Auburn, AL, USA, 1995.
- [4] R. McDaniel and R. M. Anderson, *Recommended Use of Reclaimed Asphalt Pavement in the Superpave Mix Design Method: Technician's Manual*, NCHRP Report 452, Transportation Research Board of the National Academies, Washington, DC, USA, 2001.

- [5] R. S. McDaniel, H. Soleymani, R. M. Anderson, P. Turner, and R. Peterson, *Recommended Use of Reclaimed Asphalt Pavement in the SuperPave™ Mixture Design Method*, NCHRP Final Report (9–12), TRB, National Research Council, Washington, DC, USA, 2000.
- [6] Research Institute of Highway Ministry of Transport, *Technical Specifications for Highway Asphalt Pavement Recycling, JTG F41-2008*, China communication press, Beijing, China, 2008.
- [7] S.-J. Lee, S. N. Amirkhani, N.-W. Park, and K. W. Kim, “Characterization of warm mix asphalt binders containing artificially long-term aged binders,” *Construction and Building Materials*, vol. 23, no. 6, pp. 2371–2379, 2009.
- [8] A. Stimilli, G. Ferrotti, C. Conti, G. Tosi, and F. Canestrari, “Chemical and rheological analysis of modified bitumens blended with “artificial reclaimed bitumen”” *Construction and Building Materials*, vol. 63, pp. 1–10, 2014.
- [9] B. Huang, X. Shu, and D. Vukosavljevic, “Laboratory investigation of cracking resistance of hot-mix asphalt field mixtures containing screened reclaimed asphalt pavement,” *Journal of Materials in Civil Engineering*, vol. 23, no. 11, pp. 1535–1543, 2011.
- [10] A. Cannone Falchetto, A. Montepara, G. Tebaldi, and M. O. Marasteanu, “Microstructural and rheological investigation of asphalt mixtures containing recycled asphalt materials,” *Construction and Building Materials*, vol. 35, pp. 321–329, 2012.
- [11] T. Ma, X. Huang, Y. Zhao, Y. Zhang, and H. Wang, “Influences of preheating temperature of RAP on properties of hot-mix recycled asphalt mixture,” *Journal of Testing and Evaluation*, vol. 44, no. 2, 2016.
- [12] P. Shirodkar, Y. Mehta, A. Nolan et al., “A study to determine the degree of partial blending of reclaimed asphalt pavement (RAP) binder for high RAP hot mix asphalt,” *Construction and Building Materials*, vol. 25, no. 1, pp. 150–155, 2011.
- [13] P. Shirodkar, Y. Mehta, A. Nolan, E. Dubois, D. Reger, and L. McCarthy, “Development of blending chart for different degrees of blending of RAP binder and virgin binder,” *Resources, Conservation and Recycling*, vol. 73, pp. 156–161, 2013.
- [14] T. Ma, X. Huang, Y. Zhao, and U. B. Hussain, “Compound rejuvenation of polymer modified asphalt binder,” *Journal of Wuhan University of Technology-Material Science Education*, vol. 25, no. 6, pp. 1070–1076, 2010.
- [15] S. Junan, S. Amirkhani, and J. A. Miller, “Effects of rejuvenating agents on superpave mixtures containing reclaimed asphalt pavement,” *Journal of Materials in Civil Engineering*, vol. 19, no. 5, pp. 376–384, 2007.
- [16] X. Yu, M. Zaumanis, S. dos Santos, and L. D. Poulikakos, “Rheological, microscopic, and chemical characterization of the rejuvenating effect on asphalt binders,” *Fuel*, vol. 135, pp. 162–171, 2014.
- [17] M. Zaumanis, R. B. Mallick, and R. Frank, “Evaluation of different recycling agents for restoring aged asphalt binder and performance of 100 % recycled asphalt,” *Materials and Structures*, vol. 48, no. 8, pp. 2475–2488, 2014.
- [18] J. Jie, S. Zhi, X. Ying, and X. Shifa, “Experimental research on performance of warm-recycled mixture asphalt with SMA,” *China Journal of Highway and Transport*, vol. 26, no. 5, pp. 28–33, 2013.
- [19] F. Xiao, X. Hou, S. Amirkhani, and K. W. Kim, “Superpave evaluation of higher RAP contents using WMA technologies,” *Construction and Building Materials*, vol. 112, pp. 1080–1087, 2016.
- [20] R. B. Mallick, P. S. Kandhal, and R. L. Bradbury, “Using warm-mix asphalt technology to incorporate high percentage of reclaimed asphalt pavement material in asphalt mixtures, transportation research record,” *Journal of the Transportation Research Board*, vol. 2051, no. 1, pp. 71–79, 2008.
- [21] L. Gungat, N. I. M. Yusoff, and M. O. Hamzah, “Effects of RH-WMA additive on rheological properties of high amount reclaimed asphalt binders,” *Construction and Building Materials*, vol. 114, pp. 665–672, 2016.
- [22] A. Buss, R. C. Williams, and S. Schram, “The influence of warm mix asphalt on binders in mixes that contain recycled asphalt materials,” *Construction and Building Materials*, vol. 77, pp. 50–58, 2015.
- [23] M. Tao and R. B. Mallick, “Effects of warm-mix asphalt additives on workability and mechanical properties of reclaimed asphalt pavement material,” 2009.
- [24] R. West, A. Kvasnak, N. Tran, B. Powell, and P. Turner, “Testing of moderate and high reclaimed asphalt pavement content mixes,” *Transportation Research Record Journal of the Transportation Research Board*, vol. 2126, no. 1, pp. 100–108, 2009.
- [25] A. J. d. Barco Carrión, D. Lo Presti, and G. D. Airey, “Binder design of high RAP content hot and warm asphalt mixture wearing courses,” *Road Materials and Pavement Design*, vol. 16, no. sup1, pp. 460–474, 2015.
- [26] B. F. Bowers, B. Huang, and X. Shu, “Refining laboratory procedure for artificial RAP: a comparative study,” *Construction and Building Materials*, vol. 52, no. 2, pp. 385–390, 2014.
- [27] American Association of State Highway and Transportation Officials, AASHTO R 28, *Standard Practice for Accelerate Aging of Asphalt Binder Using a Pressurized Aging Vessel, PAV*, Washington, DC, USA, 2012.
- [28] American Association of State Highway and Transportation Officials, AASHTO T 240–13, *Standard Method of Test for Effect of Heat and Air on a Moving Film of Asphalt (Rolling Thin-Film Oven Test)*, American Association of State Highway and Transportation Officials, Washington, DC, USA, 2013.
- [29] N. I. Md. Yusoff, D. Mounier, G. Marc-Stéphane, M. Rosli Hainin, G. D. Airey, and H. Di Benedetto, “Modelling the rheological properties of bituminous binders using the 2S2P1D Model,” *Construction and Building Materials*, vol. 38, pp. 395–406, 2013.
- [30] F. Olard and H. Di Benedetto, “General “2S2P1D” model and relation between the linear viscoelastic behaviours of bituminous binders and mixes,” *Road Materials and Pavement Design*, vol. 4, no. 2, pp. 185–224, 2003.
- [31] Y. Sun, B. Huang, J. Chen, X. Jia, and Y. Ding, “Characterizing rheological behavior of asphalt binder over a complete range of pavement service loading frequency and temperature,” *Construction and Building Materials*, vol. 123, pp. 661–672, 2016.
- [32] American Association of State Highway and Transportation Officials, AASHTO T 315-08, *Standard Method of Test for Determining the Rheological Properties of Asphalt Binder Using a Dynamic Shear Rheometer (DSR)*, American Association of State Highway and Transportation Officials, Washington, DC, USA, 2012.
- [33] L. Wang, J. Wei, and Y. Zhang, “Evaluation on low temperature performance of paving asphalt using bending beam rheometer,” *Journal of China University of Petroleum*, vol. 33, pp. 150–153, 2009.
- [34] S. Aflaki and P. Hajikarimi, “Implementing viscoelastic rheological methods to evaluate low temperature

- performance of modified asphalt binders,” *Construction and Building Materials*, vol. 36, pp. 110–118, 2012.
- [35] S. Aflaki, P. Hajikarimi, E. H. Fini, and B. Zada, “Comparing effects of biobinder with other asphalt modifiers on low-temperature characteristics of asphalt,” *Journal of Materials in Civil Engineering*, vol. 26, no. 3, pp. 429–439, 2014.
- [36] American Association of State Highway and Transportation Officials, *AASHTO T 313-08, Standard Method of Test for Determining the Flexural Creep Stiffness of Asphalt Binder Using the Bending Beam Rheometer (BBR)*, American Association of State Highway and Transportation Officials, Washington, DC, USA, 2008.
- [37] American Association of State Highway and Transportation Officials, *AASHTO TP 70-11, Standard Method of Test for Multiple Stress Creep Recovery (MSCR) Test of Asphalt Binder Using a Dynamic Shear Rheometer (DSR)*, American Association of State Highway and Transportation Officials, Washington, DC, USA, 2011.
- [38] Y. Sun, J. Chen, B. Huang, J. Liu, W. Wang, and B. Xu, “Novel procedure for accurately characterizing nonlinear viscoelastic and irrecoverable behaviors of asphalt binders,” *ASCE’s International Journal of Geomechanics*, vol. 20, no. 3, Article ID 04019198, 2020.
- [39] A. Golalipour, H. U. Bahia, and H. A. Tabatabaee, “Critical considerations toward better implementation of the multiple stress creep and recovery test,” *Journal of Materials in Civil Engineering*, vol. 29, no. 5, 2017.
- [40] C. Hintz and H. Bahia, “Simplification of linear amplitude sweep test and specification parameter,” *Transportation Research Record: Journal of the Transportation Research Board*, vol. 2370, no. 1, pp. 10–16, 2013.
- [41] M. Huang, X. Wang, and W. Huang, “Analysis of influencing factors for self-healing of fatigue performance of asphalt rubber mixture,” *China Journal of Highway and Transport*, vol. 26, no. 4, pp. 16–22, 2013.
- [42] American Association of State Highway and Transportation Officials, *AASHTO TP 101-14, Standard Method of Test for Estimating Damage Tolerance of Asphalt Binders Using the Linear Amplitude Sweep*, American Association of State Highway and Transportation Officials, Washington, DC, USA, 2014.
- [43] C. Hintz, R. Velasquez, C. Johnson, and H. Bahia, “Modification and validation of linear amplitude sweep test for binder fatigue specification,” *Transportation Research Record: Journal of the Transportation Research Board*, vol. 2207, no. 1, pp. 99–106, 2011.
- [44] Y. Sun, W. Wang, and J. Chen, “Investigating impacts of warm-mix asphalt technologies and high reclaimed asphalt pavement binder content on rutting and fatigue performance of asphalt binder through MSCR and LAS tests,” *Journal of Cleaner Production*, vol. 219, pp. 879–893, 2019.
- [45] M. Sadeq, E. Masad, H. Al-Khalid, O. Sirin, and L. Mehrez, “Linear and nonlinear viscoelastic and viscoplastic analysis of asphalt binders with warm mix asphalt additives,” *International Journal of Pavement Engineering*, vol. 19, no. 10, pp. 857–864, 2016.
- [46] C. M. Johnson, H. Wen, and H. U. Bahia, “Practical application of viscoelastic continuum damage theory to asphalt binder fatigue characterization,” in *Proceedings of the Asphalt Paving Technology: Association of Asphalt Paving Technologists-Proceedings of the Technical Sessions*, pp. 597–631, Bangkok, Thailand, December 2009.
- [47] D. Singh, P. K. Ashish, A. Kataware, and A. Habal, “Evaluating performance of PPA-and-elvaloy-modified binder containing WMA additives and lime using MSCR and LAS tests,” *Journal of Materials in Civil Engineering*, vol. 29, no. 8, 2017.
- [48] J. Xiaoyang, H. Baoshan, B. F. Bowers, and Z. Sheng, “Infrared spectra and rheological properties of asphalt cement containing waste engine oil residues,” *Construction and Building Materials*, vol. 50, pp. 683–691, 2014.
- [49] P. K. Ashish, D. Singh, and S. Bohm, “Investigation on influence of nanoclay addition on rheological performance of asphalt binder,” *Road Materials and Pavement Design*, vol. 18, no. 5, pp. 1007–1026, 2016.
- [50] R. Micaelo, A. Pereira, L. Quaresma, and M. T. Cidade, “Fatigue resistance of asphalt binders: assessment of the analysis methods in strain-controlled tests,” *Construction and Building Materials*, vol. 98, pp. 703–712, 2015.
- [51] American Society of Testing Materials, *ASTM D7460-10, Standard Test Method for Determining Fatigue Failure of Compacted Asphalt Concrete Subjected to Repeated Flexural Bending*, ASTM International, West Conshohocken PA, USA, 2010.

## Research Article

# Effect of Used Motor Oil and Bitumen as Additive on the Permeability and Mechanical Properties of Low Plastic Soil

Kamran Iqbal <sup>1</sup>, Chengshun Xu,<sup>1</sup> Hassan Nasir <sup>2</sup>, Muhammad Alam <sup>3</sup>,  
Asim Farooq <sup>2</sup> and Edward J. Williams<sup>4</sup>

<sup>1</sup>Department of Civil Engineering, Beijing University of Technology, Beijing, China

<sup>2</sup>Department of Civil Engineering, CECOS University of IT and Emerging Sciences, Peshawar, Pakistan

<sup>3</sup>Department of Civil Engineering, Abasyn University, Peshawar, Pakistan

<sup>4</sup>Department of Civil Engineering, University of Michigan-Dearborn, Dearborn, Michigan, USA

Correspondence should be addressed to Kamran Iqbal; [kamran@emails.bjut.edu.cn](mailto:kamran@emails.bjut.edu.cn)

Received 16 April 2020; Accepted 8 July 2020; Published 30 July 2020

Guest Editor: Zhen Leng

Copyright © 2020 Kamran Iqbal et al. This is an open access article distributed under the Creative Commons Attribution License, which permits unrestricted use, distribution, and reproduction in any medium, provided the original work is properly cited.

Stability of permeable soils near large-scale water reservoirs for paved and unpaved road pavements is all too frequently compromised due to excessive seepage and the climatic conditions of that area. In this research, a multilevel research approach was adopted by conducting a comparative study of the microspectroscopy through Fourier transform infrared (FTIR) spectra to investigate the maximum absorbance correlation along with mechanical investigations (such as the compressive strength, modified proctor test, California bearing ratio test, and swell percentage test). The native low plastic soil sample (CL) was blended with varying percentages of petroleum additives (bitumen and used motor oil) independently at 0%, 4%, 8%, 12%, 16%, and 20%. A comparison of results in the case of bitumen and used motor oil revealed that a decrease in Atterberg's limits occurred accompanied by an increase of bitumen blending percentage, while used motor oil (UMO) increased the plastic limit. Maximum dry density (MDD) increases while optimum moisture content (OMC) decreases with the increase in bitumen. Used motor oil (UMO) initially (up to 4%) increased the MDD and subsequently decreased it. Investigative reports show that bitumen causes a decrease in swell percentage and increases California bearing ratio (CBR), whereas UMO causes a continuous increase in percentage swell and decrease in CBR. The addition of bitumen in soil resulted in a decrease in the coefficient of permeability ( $k$ ), while UMO has a significant result of up to 4%. Regarding the control sample, spectrum analysis through FTIR effectively supports the laboratory results as the intensity of peaks increases with the oil, and bitumen concentration reveals that oil and bitumen impart cementitious property to the soil. Moreover, this research work by experiment supported and strengthened the idea of soil pavement stabilization through bitumen, which gives antiwater stability, and facilitates low-cost construction by obtaining raw material on the spot. UMO adversely affects soil properties beyond 4% addition by weight.

## 1. Introduction

Considering the material quality, plus transport, economic, and political issues, engineers sometimes must use low-quality soil during road construction. These low-quality soil materials are prone to show unattractive engineering behavior, such as low bearing capacity, susceptibility to differential settlement, high percentage swell, high moisture susceptibility, and poor permeability or seepage behavior. This type of unwanted soil behavior is generally attributed to the nature of the soil and the fine-grained components

present in the soil material. Thus, fine-grained soils such as silts and clays proved to be the most problematic materials [1]. Stabilizing such type of local material has millions of years of history [2]. This research attempted to improve certain desired geotechnical properties such as shear strength parameters ( $c-\phi$ ), permeability, CBR, and the compaction behavior of locally available soil of Peshawar, Pakistan, through used motor oil (UMO) and bitumen.

UMO, also known as waste crankcase oil or waste engine oil, is a lubricating oil used in the crankcase of an internal combustion engine [3]. This UMO is a mixture of 90%

hydrocarbons and some other metals such as sulphur, chlorine, and magnesium for about 10%. It cannot be easily differentiated in chemical components other than to say that the major part is either aliphatic or aromatic hydrocarbons [4, 5]. After use, it loses its original desired properties due to the breakdown of the additives during the combustion process. It is considered as the main source of environmental pollution if contaminated or burnt in the air because it contains a high level of heavy metals [6]. Pakistan produces 11246 tons of UMO annually. If most of the quantity does not recycle, it will pollute the environment because the waste recycling concept and circular economy is a positive approach to analyse economic, social, and environmental impacts [7]. In this present research, impacts of waste UMO have been studied to reuse in the stabilization of low plastic soil. Many methods of soil stabilization with oil have been proposed by different researchers. Researchers such as Evgin et al., Khomehchiyan et al., and Ukpong et al. studied the changing behavior of soil by considering the effects of crude oil [8–10]. Rasheed et al. demonstrate that the PL and LL increase, while MDD and OMC decrease with the increase in oil percentage as an additive in soil [11]. The behavior of motor oil on cohesion and CBR was studied by Nazir who stated that cohesion decreases while the angle of internal friction  $\phi$  increases with an increase in the tendency of motor oil in soil [12].

Bitumen, a by-product of crude petroleum, had also been used for soil stabilization for a very long time in the form of cutback, emulsified, and foamed bitumen [13]. Bitumen, when mixed with soil, helps in binding of the soil particles thereby increasing the cohesive strength of the soil [14]. Nicholson stated that bitumen and its products are mostly used in the soil as an additive, to provide water repulsion and/or adding cohesive strength to the soil [15]. Grouting with hot bitumen for the remedial measure was first introduced in the end of the 19<sup>th</sup> century [16]. Dr. Erich Schonian is one of those scientists who wrote first about the behavior of hot bitumen's penetration in cracks and voids [17]. Bituminous substances are used to stabilize the soil, particularly for stabilizing subgrade, subbase, or even base course of road carrying higher traffic load [18]. This research paper expostulated upon hot bitumen in soil stabilization for the stability of road embankment.

Bitumen is a viscous elastic material mostly produced by the crude oil distillation process. It is frequently used in the asphalt pavement with some other civil works such as waterproofing, insulating material, tank material, and flooring material. Bitumen, if mixed in soil, will affect its geotechnical properties [19]. Nasr, in his research, investigates the behavior of strip footing on bitumen-contaminated sand (0–5%) by weight [20]. Michael studied contaminants in the soil stabilization process in soil stabilization using emulsified bitumen following bench-scale evaluation [21]. Vishal Kumar uses emulsified bitumen with a small amount of cement, for gravel road soil stabilization by considering CBR as a key factor in his experimental work [22].

Research on low plastic soil shows that the Phi " $\phi$ " angle of internal friction increases while cohesion " $C$ " decreases when the oil content increases [14]. Initially, soils had been

stabilized by cement and lime, but this trend was changed by the innovation known as foamed bitumen stabilization [23]. Paul and Gnanendran suggest that soil stabilization as an aggregate and bitumen mixture could make a waterproof layer in sublayers of a road embankment [24]. Jones et al. follow indirect tensile stabilization for experimental work on cement-bitumen showing that soil achieves early strength, thereby allowing traffic in the curing stage [25].

Dr. Arora explained that bitumen are hydrocarbons, readily soluble in carbon disulphide ( $CS_2$ ) and are obtained from refined petroleum products. It can be used as a cutback, emulsified, and even directly. Any inorganic soil can be stabilized through bitumen. It makes soil waterproof by plugging its voids and helps cohesive soil in lower moisture content and higher bearing capacity [26].

This research has the potential to minimize the failures of local road and highways in Pakistan by imparting strength and stability to the poor material used in the road construction and reduce the water seepage effect, both of which cause serious damage to the roads. This research will help to investigate the geotechnical properties and internal chemical spectroscopy (Atterberg's limits, compaction test, shear strength parameters, CBR, permeability, and FTIR) of low plastic soil with the hope of stabilization with UMO and bitumen. Stabilization of the native soil has been seriously felt acutely because of the premature failure of the local roads due to population growth, environmental factors, and minimum resources that collectively lead to huge economic and environmental losses to the country.

## 2. Materials and Methods

Figure 1 shows work scheme followed in this research work from soil collection, stabilization with bitumen, and UMO to independent investigation for the expected change in geotechnical properties. Continuous and gentle mixing was applied for both the liquid additives to ensure proper mixing. At room temperature, the mixing of bitumen with soil is quite difficult, so bitumen was heated to a temperature of 140°C with constant stirring. Then the dry soil was weighed, and the required % of bitumen was added and mixed at 110–115°C by weight at 4% increment rate.

*2.1. Collection of Materials.* In this research, a soil sample was collected from the Warsak road area situated in the northeast of Peshawar, Pakistan. To ensure satisfactory results, the sample was collected at 1 meter depth below the ground surface in airtight bags to minimize the natural moisture loss. This soil sample then was placed in an oven for drying to measure the natural moistures contents at 105°C for a 24-hour time interval. After the sieve analysis test, sieve # 40 down material was stored for testing. Eighty (80) kilograms of two samples were separated for testing the stabilization by UMO and bitumen independently. UMO was collected from a local auto workshop. Bitumen (60 grade) was taken from the National Highway Authority (NHA) construction material laboratory. In this paper, authors restrict their research to 0%, 4%, 8%, 12%, 16%, and 20% for

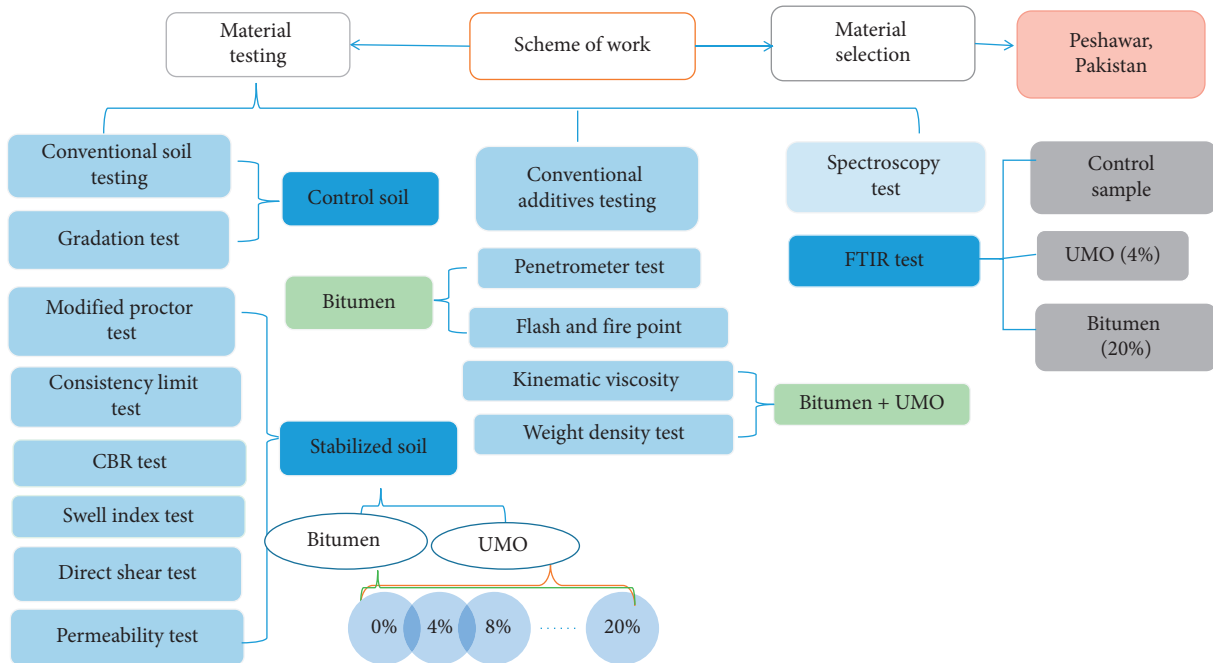


FIGURE 1: Work scheme flow chart.

both UMO and bitumen as soil stabilization independently. The unified soil classification system' (USCS)' soil classification Chart Method D-2487 found that testing soil is inorganic clay of low plasticity or lean clay (CL) in nature.

**2.2. Preparation of Samples.** Oven-dried samples were used for each investigation, at a 4% increment of UMO and bitumen independently. Bitumen was added after heating it up to 140°C so that it can be poured and mixed easily without any hard lumps or air contents. Mixing was carefully done using spades until uniformity of color was perceived at 110–115°C. Mixing in the case of UMO was easy as oil is less viscous as compared to bitumen even if heated. The sticking property of bitumen with soil particles makes flocculants in the soil sample.

**2.3. Laboratory Tests.** This research study was supported by various laboratory tests.

The physical properties of both UMO and bitumen were investigated and listed in Table 1. For this purpose, unit mass density, viscosity, flash, and fire points were calculated. The bitumen penetrometer test (ASTM D-5), the flash and fire point test (ASTM D-92), the weight density test (ASTM D-4052), and kinematic viscosity tests for oil (ASTM D-445) and for bitumen (ASTM D-2170) were performed. Table 2 summarizes the corresponding physical and chemical properties of the local soil sample.

Table 3 describes the overall performed testing summary on the soil sample stabilized with UMO and bitumen at a 4% increment rate. Tests such as the specific gravity test (ASTM D854-00), the particle size distribution test (ASTM D-422), Atterberg's limit test (ASTM D-4318), the modified proctor test (ASTM D-1557), the CBR test (ASTM D-1883-99), the

direct shear test (ASTM D-3080), and the falling head permeability test (ASTM D-5084) were performed. Along with these basic geotechnical investigation tests, some microscopic analysis was also performed to visualize the basic internal changes due to the two types of additives.

### 3. Results and Discussion

**3.1. Particle Size Distribution Test.** Oven-dried weighed sample is poured on the sieve column with largest opening at the top (2" sieve) to lower sieves with smaller openings (#200 sieve) having a pan at the base. It was mechanically shaken for 12 minutes using mechanical shakers. After shaking, material received by each sieve was weighed with the digital balance having up to 0.1 gram sensitivity. Weight retained on every sieve is divided by total sample weight to get the percentage value of each sieve. To get a specific size range, each passing percentage value was analyzed and drawn as shown in Figure 2.

**3.2. Compaction Test.** The oven-dried soil sample was investigated to check the effects of UMO and bitumen on MDD and OMC, as presented in Figures 3 and 4. After each soil sample was divided into different suitable quantities, water was added in the probable OMC range. After three or four trials, we obtained the required OMC value. While calculating MDD and OMC, Figures 3 and 4 show that MDD increases by increasing bitumen up to 20%. In the case of UMO, MDD increases up to 4% by 1.94%, and thereafter inversely decreases. Normally, dry density decreases when increasing the rate of used motor oil [10, 27]. UMO shows this trend up to 4%. On further addition of used oil above 4%, the clusters of soil particles lose their cohesion due to a higher oil absorption rate causing reduction of soil unit

TABLE 1: Properties of petroleum’s additives.

Material	Color	Penetration at 25°C (0.01 mm)	Flash and fire point (°C)	Softening point (°C)	Kinematic viscosity (cst at 100°C)	Weight density (kN/m <sup>3</sup> )	Ductility (cm)
UMO	Bluish black	—	161, 167	—	8.19	8.7	—
Bitumen	Shining black	64	243, 259	44	341	9.31	87

TABLE 2: Physical and chemical characteristics of local soil sample.

Soil type	Color	Density (g/cm <sup>3</sup> )	Unit weight (kN/m <sup>3</sup> )	Chemical analysis (%)						Composition (%)		
				Ca	O	C	Si	Al	Others	Sand	Silt	Clay
CL	Yellowish brown	2.06	20.20	1.234	22	3.67	34	18	20.39	22	30	48

TABLE 3: Laboratory investigation of UMO and bitumen-stabilized soil.

	%	MDD gm/cm <sup>3</sup>	OMC %	CBR %	“C” kPa	Φ° degree	LL %	PL %	PI %	“k”
Used motor oil	0	2.06	12.5	10.8	38	17	47.4	27.6	19.8	5.282 × 10 <sup>-6</sup>
	4	2.1	12.1	10	33	18	45.9	29.1	16.8	5.202 × 10 <sup>-6</sup>
	8	2.01	12	6.9	32.1	18.8	43.2	29.3	13.9	5.009 × 10 <sup>-6</sup>
	12	1.93	10.3	0	30	20	42.7	30.4	12.3	5.017 × 10 <sup>-6</sup>
	16	1.87	8.8	0	26	21	40.6	31.3	9.3	5.152 × 10 <sup>-6</sup>
	20	1.84	7.6	0	22	23	38.2	32.1	6.1	5.209 × 10 <sup>-6</sup>
Bitumen	0	2.06	12.5	10.8	38	17	47.4	27.9	19.7	5.282 × 10 <sup>-6</sup>
	4	2.13	13.7	12.7	38.7	16	42.3	23.89	18.5	5.162 × 10 <sup>-6</sup>
	8	2.23	13.4	14.4	39.4	14.7	39.7	21.6	18.1	4.990 × 10 <sup>-6</sup>
	12	2.29	13.21	15	41	13.8	35.5	18.5	17	4.292 × 10 <sup>-6</sup>
	16	2.37	12.6	18	45	13	33.6	18	15.6	3.702 × 10 <sup>-6</sup>
	20	2.42	9.9	21	51	6	31.2	16.6	14.6	3.382 × 10 <sup>-6</sup>

MDD, maximum dry density, C, cohesion, OMC, optimum moisture content, “φ,” angle of internal friction, PL, plastic limit, CBR, California bearing ratio, “k,” coefficient of permeability, LL, liquid limit, and PI, plasticity index.

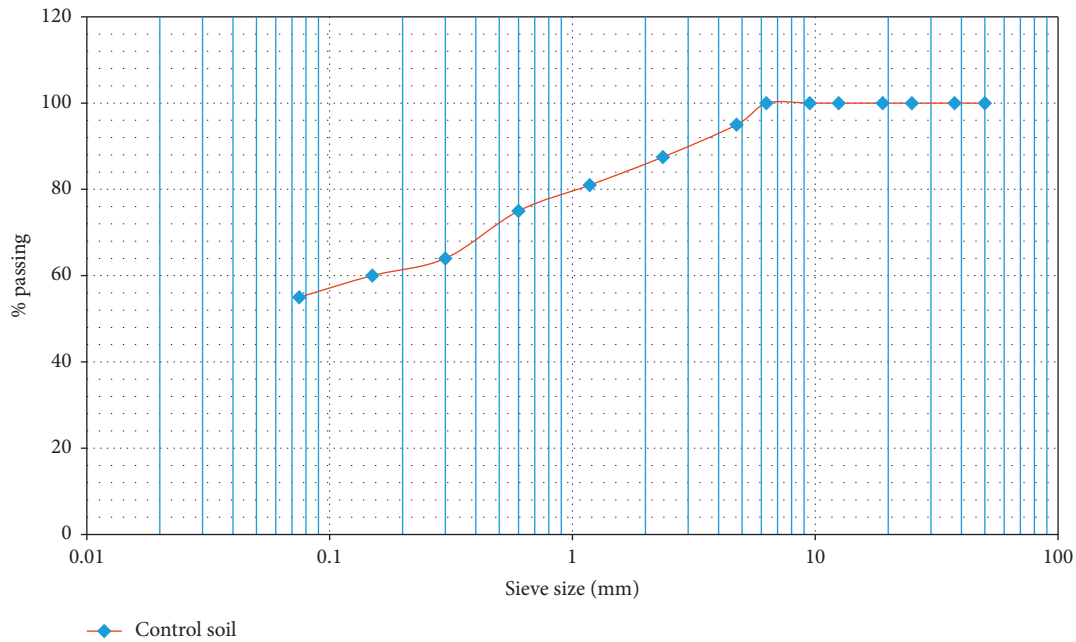


FIGURE 2: Particle size distribution.



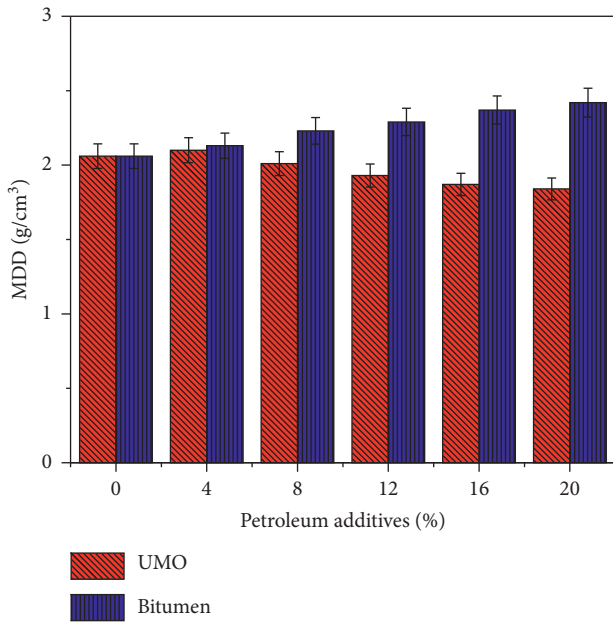


FIGURE 3: Variation of maximum dry density (MDD) with bitumen and UMO content.

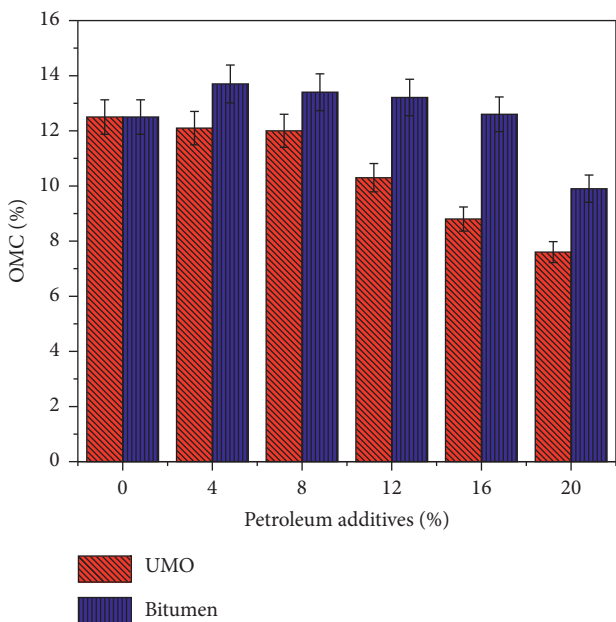


FIGURE 4: Variation of optimum moisture content (OMC) with bitumen and UMO content.

density. On the other hand, bitumen as a stabilizer in soil shows an ascending approach and increases the MDD as high as 17.47%. Because bitumen holds the soil particles in clusters which increases the compressibility of soil, bitumen increases the soil density. Further, bitumen itself is cohesive in nature at low temperature; hence, it causes the particles of the soil to cohere, leading to an increase in the effective cohesion and maximum density.

Figure 4 shows the OMC value, and it reveals that that OMC in bitumen-stabilized soil initially increases up to 4%

and thereafter decreases. Bitumen increased OMC in the first 4% increment because of bunches formation in the soil, which increase the absorbing characteristic of soil. On further addition of UMO in soil, OMC continuously decreases for 39%. According to Al-Homoud et al., cutback bitumen decreases MDD and increases OMC up to 7% [28]. The declination in OMC is due to the repelling property of oil and bitumen. While UMO plays a part in decreasing the moisture content, UMO has itself low viscosity, which acts like water, so extra water than OMC will make the water film thicker, in consequence of which binding of particles does not take place that cause reduction in MDD [29]. Ojuri et al. studied the effect of UMO in soil stabilization and found that MDD and OMC decrease when increasing UMO contents [30].

3.3. *CBR Test.* Figure 5 shows the effect of UMO and the bitumen effect on soaked CBR. It is clear from the figure that the soaked CBR increased by increasing bitumen rate and decreased with increasing UMO. Zumrawi et al. worked on expansive soil stabilization with bitumen and fly ash. Their results are quite in line with our experimental results [30, 31]. Andavan et al. illustrated that bitumen emulsion brings considerable improvement in the CBR value if properly mixed [32]. The similar result was found by carrying a number of tests on bitumen-stabilized expansive soil by Krishnaiah et al. [33]. On the other hand, as the swell percentage increases with used motor oil, it shows no resistance to standard piston penetration that gives zero CBR above 8% oil addition [27].

3.4. *Swell Percentage Index Test.* Prior to the soaking CBR test, percentage swell was measured for various UMO and bitumen contents from 0% to 20% at a 4% increment interval rate. Figure 6 shows that heated bitumen causes a reduction in swell percentage rate, while UMO increases in the swell index. Singh et al. reported a significant increase in swell percentage in CL soil with UMO that ultimately increases differential settlement [27].

Bitumen imparts cohesive property to the soil and does not allow water to enter; hence, the swell index decreases [32]. Al-Homoud et al. found a significant reduction in the swell index by treating soil with bitumen [28]. On the other hand, the UMO makes a thin film around the soil individual particle or sum of particles and makes it even coarser. Thus, when soil is stabilized with UMO, moisture and oil contents stored in the void spaces developed internal stresses that cause free void spaces and leads to decrease in the cohesion and increase in the swell percentage.

3.5. *Direct Shear Test.* The reduction in the shear strength of soil sample due to water can be minimized by introducing a waterproofing material such as bitumen in the soil sample. The best way to do this is by providing a layer coating of a waterproofing agent [34].

Figures 7 and 8 show the direct shear parameters that are cohesive (attractive force between soil particles) and the

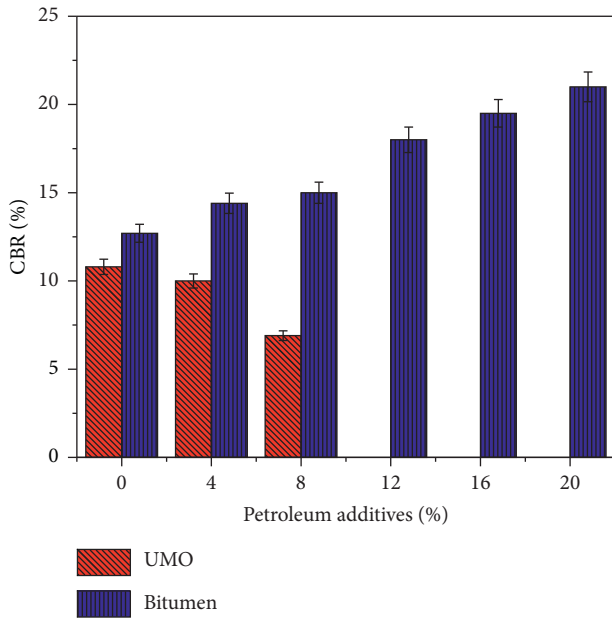


FIGURE 5: Variation of California bearing ratio (CBR) with bitumen and UMO contents.

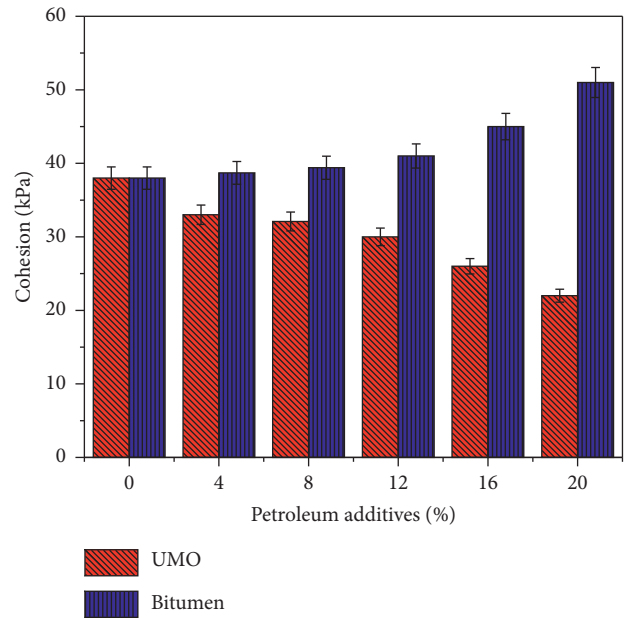


FIGURE 7: Variation of cohesion "C" with bitumen and UMO contents.

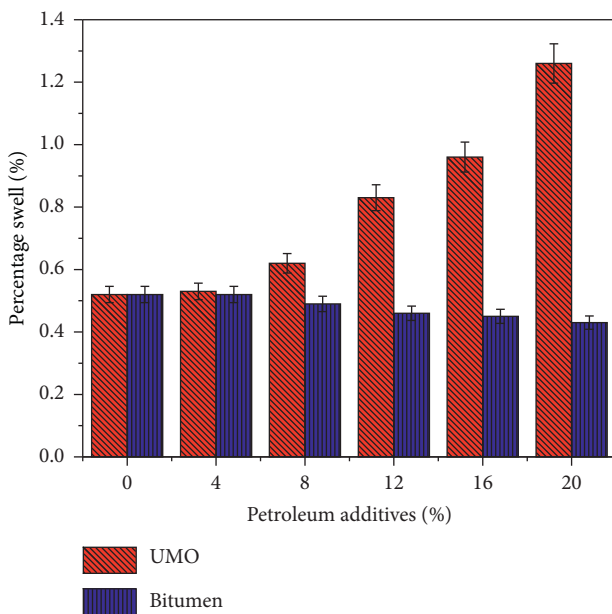


FIGURE 6: Variation of percentage swell with bitumen and UMO contents.

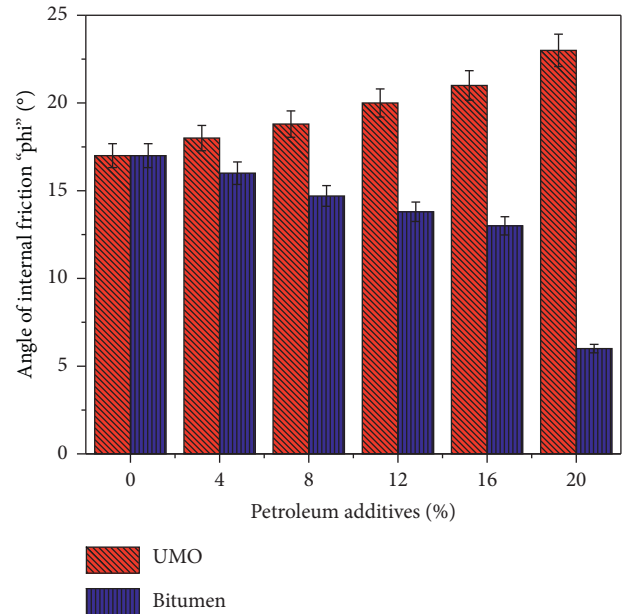


FIGURE 8: Variation of the angle of internal friction ( $\phi$ ) with bitumen and UMO contents.

angle of internal friction  $\phi$  (resistance to shearing movement) based on Coulomb's shear strength theory. Results show that cohesion increases by increasing the rate of bitumen. The angle of internal friction increases to a peak value for UMO concentration of 20%. While it gives the lowest value at 20% bitumen concentration as shown in Figure 8.

Conversely, cohesion decreases with increased rate of bitumen, which is obviously a sign of losing shear strength. There is less cohesion between the soil particles and the particles of oil; hence, UMO, the shear strength, decreases.

Figure 8 shows the angle of internal friction "phi" that decreases in the case of bitumen, while it increases in the UMO case.

3.6. *Atterberg's Limit Test.* A higher variation in the case of consistency limits is observed in both bitumen and used motor oil used as a soil stabilizer. Figure 9 shows that both bitumen and used motor oil decrease the rate of liquid limit. The decrease in the liquid limit (both oil and bitumen case) and plastic limit (bitumen case only) is because of the

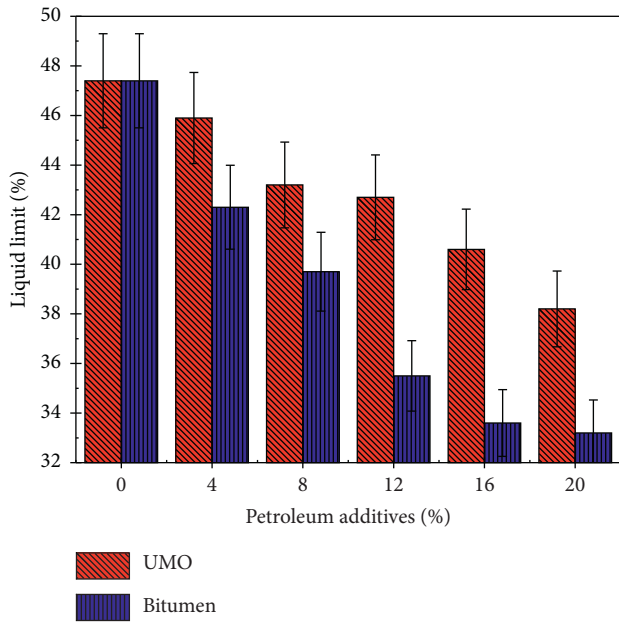


FIGURE 9: Variation of liquid limit with bitumen and UMO stabilization.

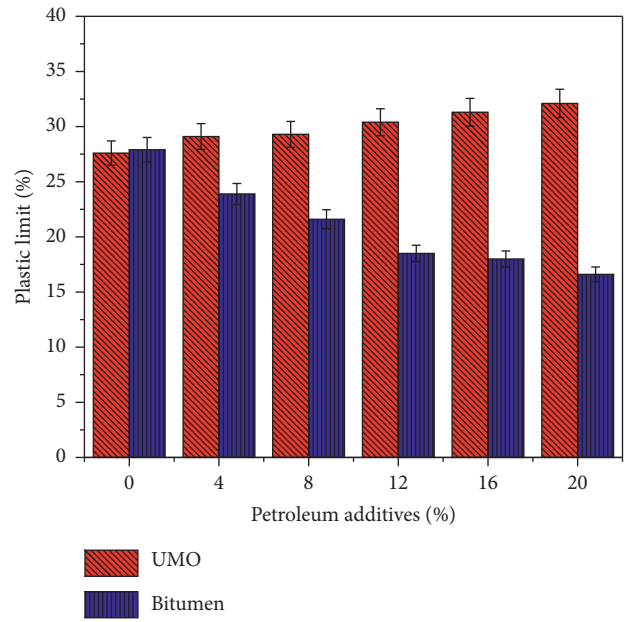


FIGURE 10: Variation of plastic limit with bitumen and UMO stabilization.

flocculation and agglomeration of the minerals present in the soil due to isomorphous substitution of cations at the surface of soil particles that resembles previous findings [35–37]. However, increases in the plastic limit with UMO might be due to the particle thickness due to the cation effect between soil particles and used oil (Figure 10). Salih et al. found that UMO not only increases the PL but also LL and PI [38]. Rasheed et al. reported that Atterberg’s value of overconsolidated clay decreases by increasing UMO contents [11]. LL and PL decrease by increasing UMO contents [19, 27]. Figure 11 shows that the plasticity index of the soil decreases while increasing both Bitumen and UMO.

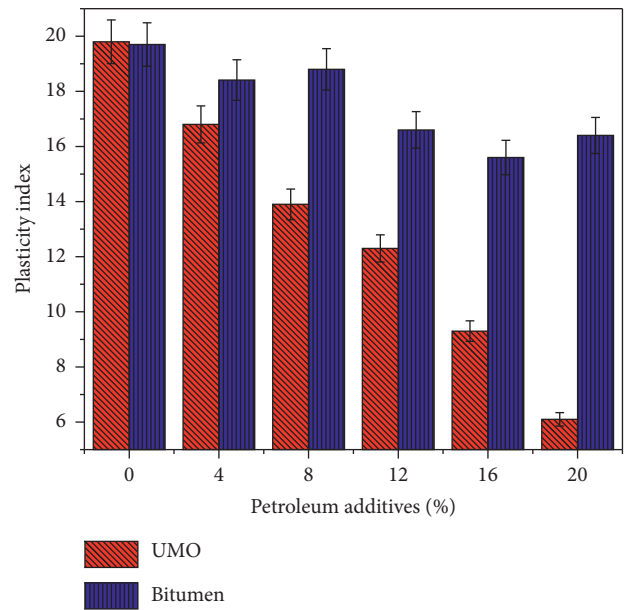


FIGURE 11: Variation of plasticity index with bitumen and UMO stabilization.

**3.7. Permeability Test.** For safe operation of traffic and long life period, remote water and hinterland water which intercept the road embankment is an important element [39]. Figure 12 describes the coefficient of the permeability “k” test, conducted on the used motor oil and bituminous stabilized soil. It is observed that up to 8% UMO addition causes a decrease in the permeability effect of the local soil and beyond great increases because of the coarser effect of the soil. It is observed that the coefficient of permeability “k” fell by 5.83%, but on further addition of UMO, the permeability increases up to 4.5% as the soil sample coarsens with the addition of UMO as a soil stabilizer.

The increasing rate of bitumen from 0% to 20% reduces the coefficient of permeability to go as low as 40% and thus minimizes the deleterious impact of percolated water. The reason is that the strong adhesive force of bitumen prevented the water from percolating through the voids by blocking the pathways. Venkatesh demonstrated that bitumen causes reduction in the permeability of soil [40]. Resistance to water or impermeability is mostly estimated by the value of water

absorption or penetration. According to Fang, if bitumen in liquid form is mixed with soil up to 5-6%, irrespective of the type of soil, the absorption will be less than 2% [41].

**3.8. FTIR Test.** Functional groups and molecular structures have different absorptions rate of infrared radiation. Therefore, chemical compositions of control and modified soil samples were identified through the analysis of infrared absorption spectrum. Spectrometry was performed having a wavenumber 500–4000  $\text{cm}^{-1}$  with 0.1 accuracy wavelength.

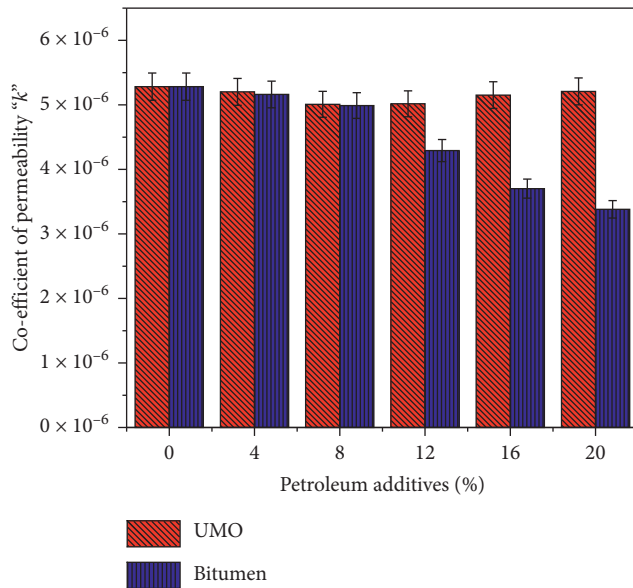


FIGURE 12: Relationship between coefficient of permeability “ $k$ ” with bitumen and UMO contents.

FTIR tests were performed for the soil sample at which maximum dry density (strength) was obtained in the stabilization process. As seen in Figure 3, UMO gives maximum dry density at 4%, while bitumen does so at 20%. Through FTIR tests, we compared the changing spectrum of 4% UMO stabilized soil sample and 20% bitumen-stabilized soil sample to that of control soil sample.

FTIR results for control soil and stabilized soil with UMO and bitumen were observed with tremendous changes in the peaks values. The difference in transmission or absorbance usually arises due to difference in concentration, as described by Lambert’s law [42], which states that absorption depends on path length, concentration, and strength of absorbance band. In Figure 13, different peaks can be seen: a very broad peak at  $3600\text{ cm}^{-1}$  shows that the OH group is present, a very small peak at  $3000\text{ cm}^{-1}$  shows that the CH group is present at lowest intensity, the peak at  $2500\text{ cm}^{-1}$  shows the SH group, the peak at  $1500\text{ cm}^{-1}$  shows the N-O group, and a very sharp and intense peak at  $1000\text{ cm}^{-1}$  represents C-O. So, it is clear from Figure 13 that natural soil contained compounds having C-O, NO, SH, and CH functional groups, but the concentration of S-H and N-O containing compounds are low. In Figure 13, the position of the peak is identical but the intensity of peaks varies, peaks at  $3600\text{ cm}^{-1}$  become broad and increase in length, which shows that more absorbance occurs in this case due to increase in the concentration of compounds, while the intensity of peaks at  $3000\text{ cm}^{-1}$  and  $1500\text{ cm}^{-1}$  increases, which is an indication of the concentration of CH and NO containing compounds increment after addition of used oil into the soil. Similarly, in Figure 13, the intensity of peaks increase, and peaks at  $3600\text{ cm}^{-1}$ ,  $3000\text{ cm}^{-1}$ , and  $1500\text{ cm}^{-1}$  become more intense, which show the concentration of CH, and NO containing compounds increased after the addition of bitumen to the soil. The peaks at  $2500\text{ cm}^{-1}$  and  $1000\text{ cm}^{-1}$  did not show more increase in intensity, which confirm that

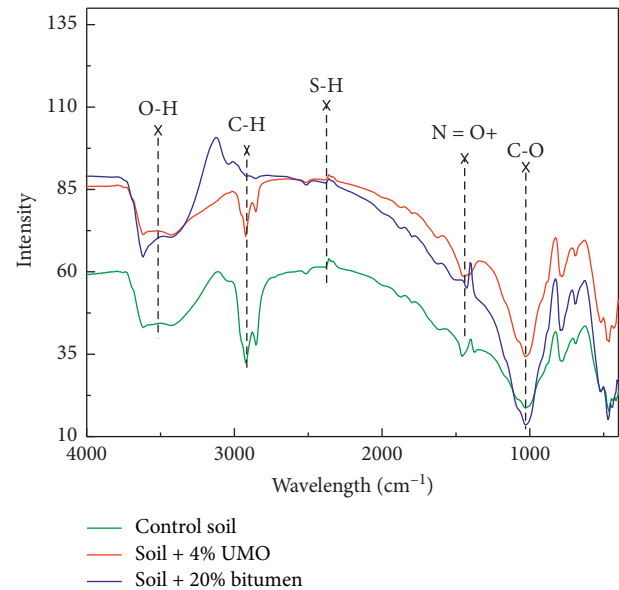


FIGURE 13: FTIR wavelength intensity spectra.

when bitumen is added to soil, the amount of SH and C-O containing compounds are not increased. Figure 12 shows that oil and bitumen are organic compounds, and they increase the intensity of soil by leaving the hydrocarbons and sulphur content in the soil mix, which impart cementitious properties to the soil mix. UMO contains a lesser amount of hydrocarbons but more carbonyl groups from ketones or acids, while bitumen contains a greater number of hydrocarbons. A large number of hydrocarbons makes the soil hard and gives antiwater characteristic to the soil, decreases the ability to absorb water, and makes it waterproof. So far, from the FTIR result, it is confirmed that bituminous is more effective instead of waste oil in soil stabilization.

## 4. Conclusions

In this research work, the stabilizing effect of UMO and bitumen was studied by mixing it with a local soil sample to evaluate its geotechnical properties and specifying the application of that soil in embankment layers. Mechanical and chemical laboratory tests were performed, and graphical tools were used to reach the following conclusions:

- (1) The local roads and district highways condition can be improved by using the waste motor oil up to 4% effectively. This research work illustrates that 4% of UMO is the effective percentage for soil stabilization. Above 4%, it has an inverse effect on soil stabilization.
- (2) Bitumen as a stabilizer agent was proved to be more effective than UMO. Native soil can be stabilized up to 20% bitumen and used in the embankment layers.
- (3) CBR results show that bitumen is a better stabilizer to give strength to the soil as compared to UMO.
- (4) Swell percentage in the case of UMO shows a tremendous rise that reduces the soaked CBR to 0%.

- (5) Bitumen reduces the permeability of the soil more effectively as compared to motor oil.
- (6) The liquid limit tends to decrease with the addition of bitumen and UMO. Similarly, plasticity decreases with bitumen increasing. It initially increases and then decreases with UMO increasing.
- (7) The variation in graph peaks from the FTIR test indicates that bitumen impart more cementing characteristic than UMO because of more hydrocarbons, which give higher concentration.

## Data Availability

The data used to support this study are available from the corresponding author upon request.

## Conflicts of Interest

The authors declare that they have no conflicts of interest.

## Authors' Contributions

Kamran Iqbal designed and executed the laboratory test plan, developed the methodology and empirical data, contributed to conceptualization of the research, and drafted the manuscript. Prof. Dr. Xu Chengshun provided guidance and suggestions to improve this study. Prof. Dr. Hassan Nazir analyzed the test results and checked the validity of the data. Prof. Dr. Muhammad Alam contributed to the review process, enhanced the methodology, and helped in technical writing. Asst. Prof. Dr. Asim Farooq contributed to conceptualization and presented the discussion along with illustrative examples in the manuscript. Prof. Dr. Edward J. Williams, being a native speaker and experienced writer, improved and tightened the English writing of the manuscript.

## Acknowledgments

This research was undertaken with the support of Prof. Dr. Xu Cheng-shun, Beijing University of Technology, Beijing, China. The authors would like to thank Dr. Asim Farooq and Prof. Edward J. Williams for their valuable guidance and motivation during the entire research work.


## References

- [1] J. Mitchell and J. Younger, "Abnormalities in hydraulic flow through fine-grained soils," in *Permeability and Capillarity of Soils*, ASTM International, West Conshohocken, PA, USA, 1967.
- [2] T. E. Kowalaski and D. W. Starry, "Characterization and improvement of soils and materials session," in *Proceedings of the Annual Conference of the Transportation Association of Canada*, Saskatoon, Canada, October 2007.
- [3] A. Rashid, X. Chen, K. Harijan, Z. A. Dhakan, and M. Ammar, "A comparative study of recycling of used engine oil using extraction by composite solvent, single solvent and acid treatment methods," *ISRN Chemical Engineering*, vol. 2013, Article ID 952589, 5 pages, 2013.
- [4] F. A. Carey and R. M. Giuliano, *Organic Chemistry*, McGraw-Hill Education, New York, NY, USA, 2017.
- [5] K. Ramadass, M. Megharaj, K. Venkateswarlu, and R. Naidu, "Ecological implications of motor oil pollution: earthworm survival and soil health," *Soil Biology and Biochemistry*, vol. 85, pp. 72–81, 2015.
- [6] M. Gyasi, *Levels of Contaminants in Used Motor Oil and Their Potential Effect on the Environment (Doctoral Dissertation)*, KNUSTSpace, Kumasi, Ghana, 2016.
- [7] P. Falcone and E. Imbert, "Social life cycle approach as a tool for promoting the market uptake of bio-based products from a consumer perspective," *Sustainability*, vol. 10, no. 4, p. 1031, 2018.
- [8] E. Evgin and B. M. Das, "Mechanical behavior of an oil contaminated sand," in *Proceedings of the Mediterranean Conference on Environmental Geotechnology*, pp. 101–108, Cesme, Turkey, May 1992.
- [9] M. Khamehchiyan, A. H. Charkhabi, and M. Tajik, "Effects of crude oil contamination on geotechnical properties of clayey and sandy soils," *Engineering Geology*, vol. 89, no. 3–4, pp. 220–229, 2007.
- [10] E. C. Ukpong and I. C. Umoh, "Effect of crude oil spillage on geotechnical properties of lateritic soil in Okoroete, Eastern Obololo," *International Journal of Engineering and Applied Sciences*, vol. 7, no. 1, pp. 12–24, 2015.
- [11] Z. N. Rasheed, F. R. Ahmed, and H. M. Jassim, "Effect of crude oil products on the geotechnical properties of soil," *WIT Transaction on Ecology and The Environment*, vol. 186, pp. 353–362, 2014.
- [12] A. K. Nazir, "Effect of motor oil contamination on geotechnical properties of over consolidated clay," *Alexandria Engineering Journal*, vol. 50, no. 4, pp. 331–335, 2011.
- [13] J. M. Bhatnagar, N. L. Goswami, and S. M. Singh, "Stabilized soil in brickmaking," *Batiment International, Building Research and Practice*, vol. 16, no. 3, pp. 177–181, 1988.
- [14] D. R. Vazquez, "Environmental impact of used motor oil," *The Science of the Total Environment*, vol. 79, no. 1, pp. 1–23, 1989.
- [15] P. G. Nicholson, "Admixture soil improvement," *Soil Improvement and Ground Modification Methods*, pp. 231–288, Elsevier, Amsterdam, Netherlands, 2015.
- [16] A. Naudts and S. Hooye, "Hot bitumen grouting: the antidote for catastrophic inflows," in *Grouting and Ground Treatment*, pp. 1293–1304, ASCE Library, New Orleans, LA, USA, 2003.
- [17] E. Schönian, *The Shell Bitumen Hydraulic Engineering Handbook*, Shell Bitumen, The Hague, Netherlands, 1999.
- [18] K. Onyelowe, D. Bui Van, C. Igboayaka, F. Orji, and H. Ugwuanyi, "Rheology of mechanical properties of soft soil and stabilization protocols in the developing countries-Nigeria," *Materials Science for Energy Technologies*, vol. 2, no. 1, pp. 8–14, 2019.
- [19] H. J. Pincos, N. J. Meegoda, and P. Ratnaweera, "Treatment of oil-contaminated soils for identification and classification," *Geotechnical Testing Journal*, vol. 18, no. 1, pp. 41–49, 1995.
- [20] A. M. Nasr, "Behavior of strip footing on fiber-reinforced cemented sand adjacent to sheet pile wall," *Geotextiles and Geomembranes*, vol. 42, no. 6, pp. 599–610, 2014.
- [21] M. F. Conway, "Bench-scale evaluation of asphalt emulsion stabilization of contaminated soils," *Journal of Soil Contamination*, vol. 2, no. 2, pp. 157–165, 1993.
- [22] V. K. Pala, "An experimental investigation on use of bitumen emulsion in the construction of gravel road," *American Journal of Educational Research and Reviews*, vol. 4, 2019.
- [23] Y. Huan, K. Siripun, P. Jitsangiam, and H. Nikraz, "A preliminary study on foamed bitumen stabilisation for Western

- Australian pavements,” *Scientific Research and Essays*, vol. 5, no. 23, pp. 3687–3700, 2010.
- [24] D. K. Paul and C. T. Gnanendran, “Characterization of lightly stabilized granular base materials using monotonic and cyclic load flexural testing,” *Journal of Materials in Civil Engineering*, vol. 28, no. 1, Article ID 04015074, 2015.
- [25] D. Jones, A. Rahim, S. Saadeh, and J. T. Harvey, *Guidelines for the Stabilization of Subgrade Soils in California*, University of California, Oakland, CA, USA, 2012.
- [26] K. R. Arora, *Soil Mechanics and The Foundation Engineering Books*, Standard Publishers, Delhi, India, 1987.
- [27] S. K. Singh, R. K. Srivastava, and S. John, “Studies on soil contamination due to used motor oil and its remediation,” *Canadian Geotechnical Journal*, vol. 46, no. 9, pp. 1077–1083, 2009.
- [28] A. S. Al-Homoud, T. Khedaywi, and A. M. Al-Ajlouni, “Studies on the control of swell and collapse potential of selected Jordanian soils using asphalt stabilization,” *Soils and Foundations*, vol. 35, no. 2, pp. 15–23, 1995.
- [29] A. Patel, *Geotechnical Investigations and Improvement of Ground Conditions*, Woodhead Publishing, Sawston, UK, 2019.
- [30] O. O. Ojuri and O. O. Ogundipe, “Modeling used engine oil impact on the compaction and strength characteristics of a lateritic soil,” *Electronic Journal of Geotechnical Engineering*, vol. 17, p. 3491, 2012.
- [31] M. Zumrawi and M. Awad, “Effect of bitumen and fly ash on expansive soil properties,” *Journal of Scientific and Engineering Research*, vol. 2017, no. 49, pp. 228–237, 2017.
- [32] S. Andavan and B. M. Kumar, “Case study on soil stabilization by using bitumen emulsions—a review,” *Materials Today: Proceedings*, vol. 22, pp. 1200–1202, 2020.
- [33] D. R. V. Krishnaiah, P. Dayakar, K. Venkatraman, and B. BIST, “Effect of bituminous admixtures on CBR strength of expensive soil,” *International Journal of Pure and Applied Mathematics*, vol. 119, no. 12, 2018.
- [34] H. F. Winterkorn, “Granulometric and volumetric factors in bituminous soil stabilization,” in *Proceedings of Highway Research Board*, vol. 36, pp. 773–782, Washington, DC, USA, 1957.
- [35] S. I. Adedokun, “Valorization of spent engine oil contaminated lateritic soil with high calcium waste wood ash,” *Journal of Engineering Research*, vol. 7, no. 1, 2019.
- [36] A. B. Salahudeen and J. Ochepo, “Effect of bagasse ash on some engineering properties of lateritic soil,” *Jordan Journal of Civil Engineering*, vol. 9, no. 4, pp. 468–476, 2015.
- [37] T. Ramzi, A. Amer, A. Ali, and A. Hilia, “Use of cement kiln dust in soil stabilization,” *Engineering Journal of the University of Qatar*, vol. 14, pp. 61–76, 2001.
- [38] N. B. Salih, T. A. Abdalla, and S. A. Ali, “Effect of waste engine oil contamination on the geotechnical properties of cohesive soils in sulaimani city, Iraq,” *Association of Arab Universities Journal of Engineering Sciences*, vol. 27, no. 1, pp. 11–18, 2020.
- [39] A. R. Dawson, “Water in road structures,” in *Geotechnical, Geological and Earthquake Engineering*, Springer, Berlin, Germany, 2009.
- [40] S. Venkatesh, “Silty soil stabilization using bituminous emulsion,” *International Journal and Magazine of Engineering, Technology, Management and Research*, vol. 4, no. 10, 2017.
- [41] H.-Y. Fang, *Foundation Engineering Handbook*, p. 923, Kluwer Academic Publishers, Boston, MA, USA, 1991.
- [42] D. F. Swinehart, “The beer-lambert law,” *Journal of Chemical Education*, vol. 39, no. 7, p. 333, 1962.

## Research Article

# Research of Deicing and Melting Snow on Airport Asphalt Pavement by Carbon Fiber Heating Wire

Xin Su,<sup>1,2</sup> Yong Lai ,<sup>1</sup> Yan Liu,<sup>2</sup> Daoxun Ma,<sup>2</sup> and Peng Wang<sup>2</sup>

<sup>1</sup>China Airport Construction Group Co.,Ltd., Beijing 100101, China

<sup>2</sup>Beijing Super-Creative Technology Co.,Ltd., Beijing 100621, China

Correspondence should be addressed to Yong Lai; [cacclaiyong@126.com](mailto:cacclaiyong@126.com)

Received 30 April 2020; Accepted 10 July 2020; Published 27 July 2020

Guest Editor: Meng Guo

Copyright © 2020 Xin Su et al. This is an open access article distributed under the Creative Commons Attribution License, which permits unrestricted use, distribution, and reproduction in any medium, provided the original work is properly cited.

In the paper, the method of deicing and melting snow by the carbon fiber heating wire (CFHW) embedded in the airport asphalt pavement is proposed to improve the security of airport operation. The field experiment of deicing and melting snow on the airport asphalt pavement is conducted. Deicing and melting snow, asphalt pavement temperature, ice-free area ratio, and snow-free area ratio are analyzed. Electrical power with  $350 \text{ W/m}^2$  is input to the airport asphalt pavement for deicing and melting snow by the CFHW. In the experiment, 3 mm ice can be melted, and the average infrared ray temperature (IRT) of the airport asphalt pavement surface can achieve an increment of  $13.0^\circ\text{C}$  in 2.5 hours when the air temperature is from  $-7.5^\circ\text{C}$  to  $-2.2^\circ\text{C}$ . Snow with 3.2 mm precipitation can be melted in 2 hours when the air temperature is from  $-4.8^\circ\text{C}$  to  $-3.5^\circ\text{C}$ , and the asphalt pavement temperature can achieve an increment of  $5.9^\circ\text{C}$  at the depth of 0.5 cm. The results show that the method of deicing and melting snow on the airport asphalt pavement by the CFHW is practicable in the cold zone.

## 1. Introduction

Ice and snow on the airport asphalt pavement affect aircraft takeoff, landing, and taxiing in winter because ice and snow increase the braking distance of the aircraft. The conventional methods of removing ice and snow by using airport pavement deicing fluid and deicing equipment induce flight delay and need a lot of manpower, deicing fluid, and machinery. It is necessary to conduct timely and high-efficient removal of ice and snow to avoid the adverse effect of deicing fluid and machinery on the airport asphalt pavement [1]. Some scholars study how to improve the performance of bitumen and asphalt mixture to avoid negative effect [2–4]. At the same time, some methods of deicing and melting snow on the pavement have been researched, such as asphalt mixture containing the snow-melting agent [5], hydraulic heating system [6–10], electrically conductive concrete [11–13], carbon fiber grille [14], and CFHW [15–19]. The recent research of deicing and melting snow on the pavement mainly focuses on the CFHW [1]. Zhao

et al. studied deicing on the bridge deck and concrete pavement by the CFHW [15, 16]. In frozen and snowy weather, the results of laboratory and field experiments verified the validity of the electrothermal method of deicing and melting snow on the pavement and bridge deck under an appropriate input power. The authors studied the effects of heat flux, wire spacing, wind speed on the concrete pavement temperature, and deicing on the cement concrete pavement by the CFHW [1, 17, 18]. The authors also studied the snow-melting effect, temperature, and energy distribution along the depth of the airport cement concrete pavement [19]. Due to different materials of airport cement concrete and asphalt pavement, the physical properties, construction methods, and dimensions of two kinds of pavement are also different. These determine the difference of deicing and melting snow between airport cement concrete and asphalt pavement. Therefore, the method of deicing and melting snow by the CFHW requires a study on the application of the airport asphalt pavement. In order to prevent ice and snow accumulation, the temperature of the airport

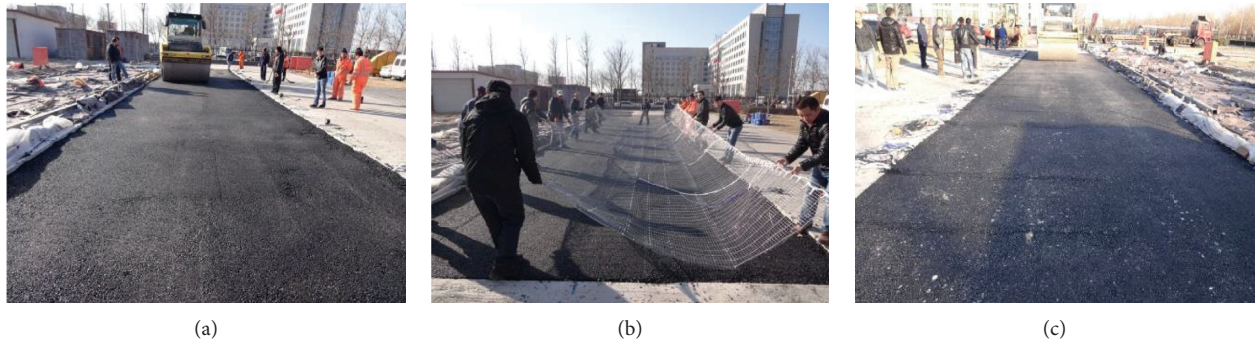


FIGURE 1: Airport asphalt pavement construction. (a) Lower layer. (b) Heating system layout. (c) Upper layer.

asphalt pavement surface must maintain above  $0^{\circ}\text{C}$ . Finally, the full-scale experiments of deicing and melting snow are performed in the real environment of ice and snow.

## 2. Materials and Methods

**2.1. Raw Materials.** The airport asphalt pavement includes the lower layer and the upper layer, and their thickness is 8 cm and 7 cm, respectively. The asphalt mixture of the lower layer is AC-25. The asphalt mixture of the upper layer is SMA-13.

**2.2. Airport Asphalt Pavement.** According to specifications for asphalt pavement design of civil airports, the design and construction of the airport asphalt pavement were implemented. Airport asphalt pavement construction is shown in Figure 1. The airport asphalt pavement is made of 1# and 2# asphalt pavement. The sizes of 1# and 2# asphalt pavement are  $5\text{ m} \times 10\text{ m}$ . The thickness of the lower layer and the upper layer is 8 cm and 7 cm, respectively. The CFHW was tied to steel wire gauze, which was buried in the middle of the lower layer and the upper layer. The depth of the CFHW is 7 cm. The spacing of the CFHW is 10 cm. At the depth of 0.5 cm and 15 cm, six sensors for testing temperature were evenly and vertically buried in the asphalt pavement. The vertical distance between the sensor and the CFHW is 5 cm.

**2.3. Experimental Instrument.** The experimental instrument contains a power distribution control box, infrared thermal image instrument, temperature sensor, temperature data receiver, and adapter. The power distribution control box provides electric energy for the asphalt pavement. The infrared thermal image instrument can measure the temperature of the asphalt pavement surface. The temperature sensor can measure  $-50 \sim 150^{\circ}\text{C}$ , and its accuracy is  $0.1^{\circ}\text{C}$ . The temperature data receiver is used to receive temperature information. The temperature data receiver and data adapter are connected. The asphalt pavement temperature is measured by using six temperature sensors at 0.5 cm and 15 cm depth, respectively. The airport asphalt pavement temperature is the average temperature of the asphalt pavement at the same depth.

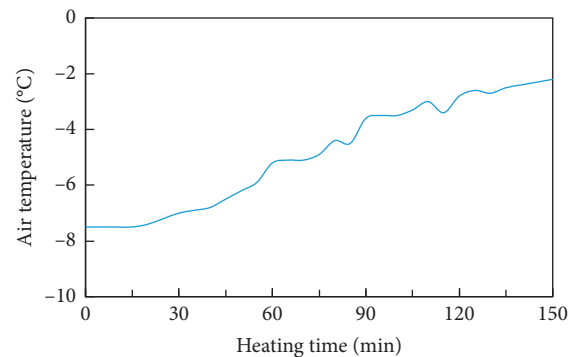


FIGURE 2: Air temperature variation.

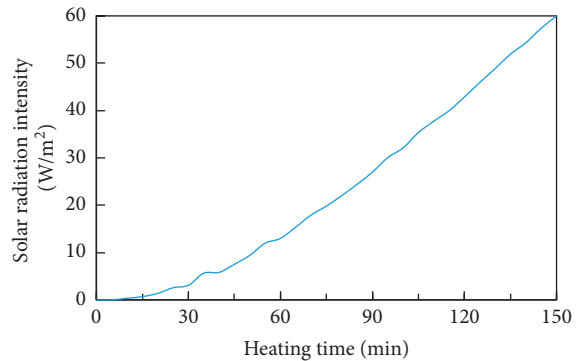


FIGURE 3: Solar radiation intensity variation.

## 3. Results and Discussion

In the test, each circuit voltage is 220V, and the electrical power is  $350\text{ W}/\text{m}^2$ . The airport asphalt pavement is exposed in the outdoor environment, which is near Beijing Capital International Airport.

**3.1. Deicing and Asphalt Pavement Temperature.** On January 22, 2014,  $0^{\circ}\text{C}$  water was evenly sprayed on the 1# airport asphalt pavement in the experiment, the amount of which was  $3\text{ mm}/\text{m}^2$ . When the time was from 0:00 to 7:30, water was frozen into ice because the air temperature was always below  $0^{\circ}\text{C}$ , and then the asphalt pavement began to be energized and heated. No ice was on the 2# airport asphalt



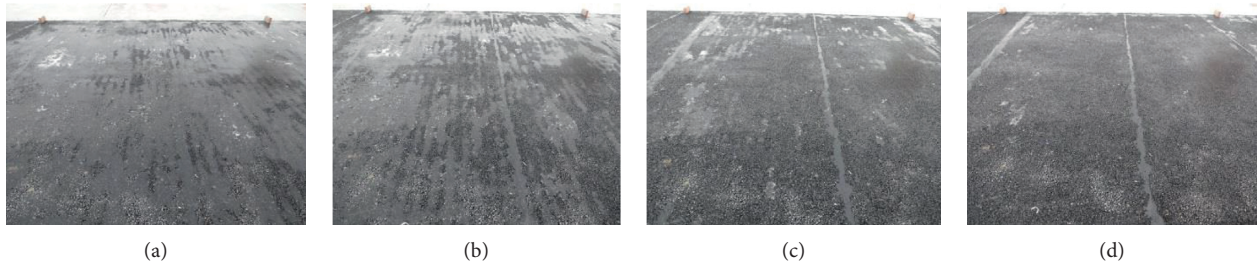


FIGURE 4: Melting ice on the 1# airport asphalt pavement. (a) 90 minutes. (b) 110 minutes. (c) 130 minutes. (d) 150 minutes.

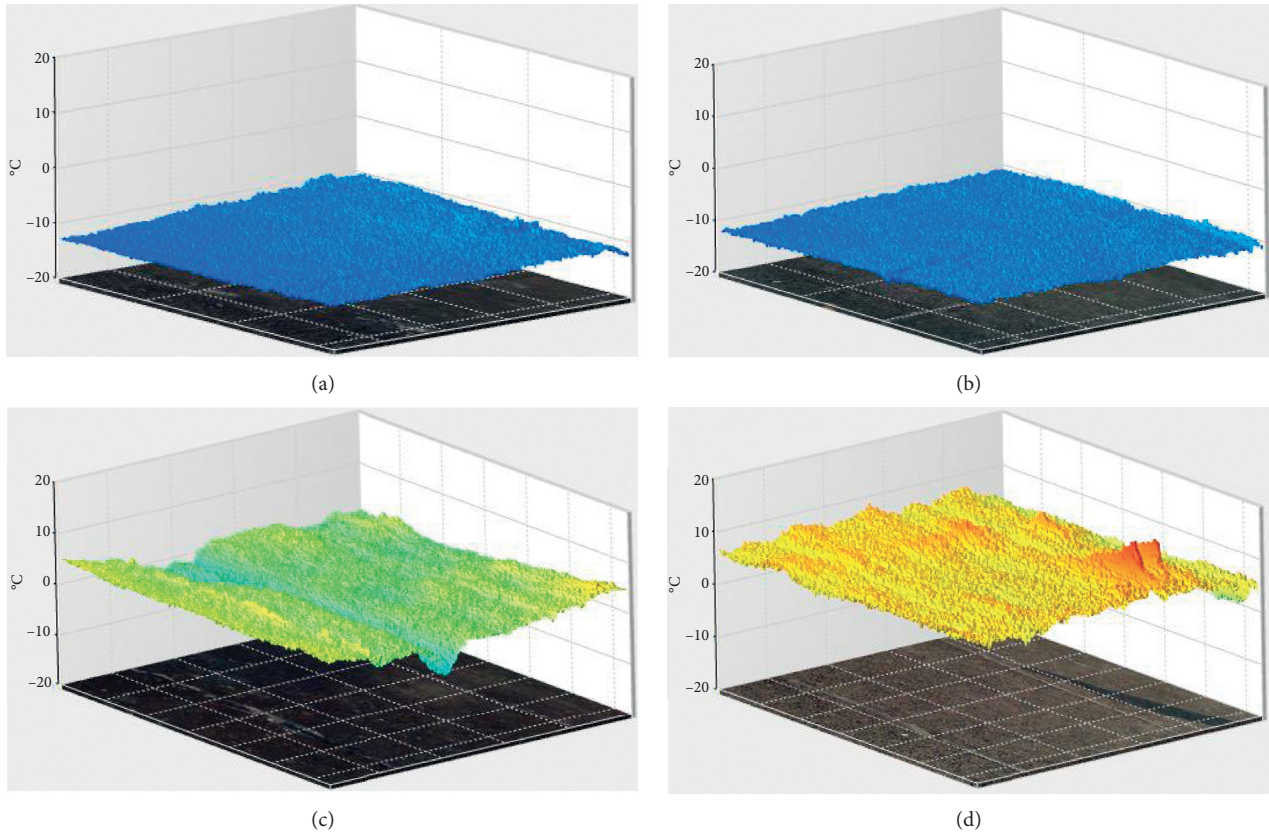


FIGURE 5: The IRT of the asphalt pavement surface. (a) Initial time (1# asphalt pavement). (b) Initial time (2# asphalt pavement). (c) 150 minutes (1# asphalt pavement). (d) 150 minutes (2# asphalt pavement).

pavement. The wind speed and relative humidity were 1.0–2.4 m/s and 30%–45%, respectively. Figure 2 shows that the air temperature raises from  $-7.5^{\circ}\text{C}$  to  $-2.2^{\circ}\text{C}$  in 150 minutes. The solar radiation intensity is  $0\text{--}60\text{ W/m}^2$  in Figure 3.

Figure 4 shows the process of deicing on the 1# airport asphalt pavement. Ice begins to melt at 90 minutes. In the paper, the evaluation criterion for the performance of deicing is ice-free area ratio, which is the ratio of the ice-free area to the total area. At 90 minutes, 110 minutes, 130 minutes, and 150 minutes, the ice-free area ratio is 0, 0.25, 0.78, and 1, respectively. Ice on the 1# airport asphalt pavement is completely melted in 150 minutes. It can be seen that the ice melts faster in the later stage.

The asphalt pavement surface temperature is accurately measured by using the infrared thermal image instrument. Figure 5 shows the IRT of the airport asphalt pavement surface at the beginning and end of heating. At the beginning of heating, the IRT of the 1# asphalt pavement surface is from  $-12.7^{\circ}\text{C}$  to  $-10.1^{\circ}\text{C}$ , and the average IRT is  $-11.5^{\circ}\text{C}$ . The IRT of the 2# asphalt pavement surface is from  $-12.4^{\circ}\text{C}$  to  $-9.9^{\circ}\text{C}$ , and the average IRT is  $-11.1^{\circ}\text{C}$ . At the end of heating, the asphalt pavement is heated for 2.5 hours. The IRT of the 1# asphalt pavement surface is from  $0.1^{\circ}\text{C}$  to  $2.8^{\circ}\text{C}$ , and the average IRT is  $1.5^{\circ}\text{C}$ . The IRT of the 2# asphalt pavement surface is from  $4.1^{\circ}\text{C}$  to  $8.4^{\circ}\text{C}$ , and the average IRT is  $6.3^{\circ}\text{C}$ .

Figure 6 shows the asphalt pavement temperature variation with heating time at different depths of the pavement.

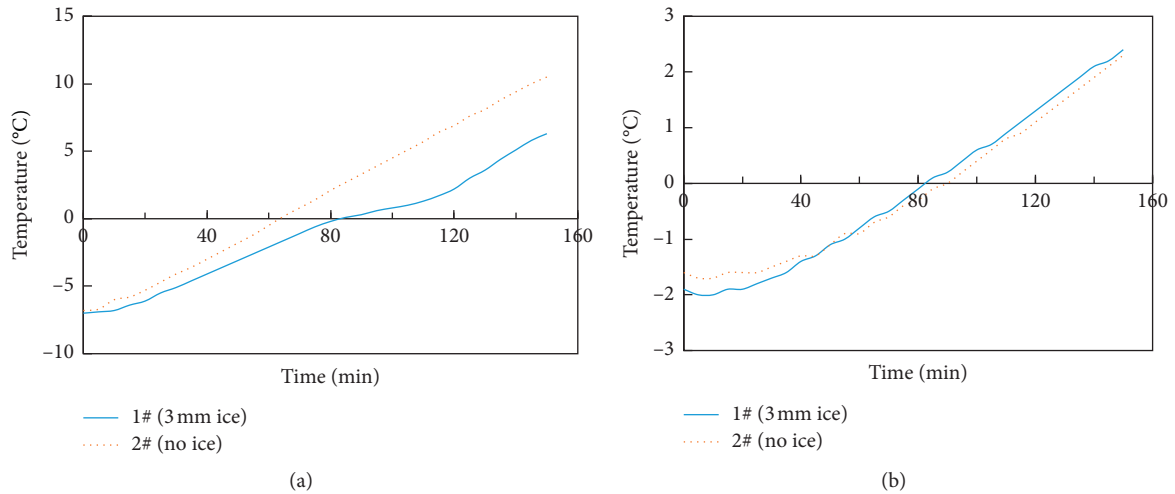


FIGURE 6: The asphalt pavement temperature variation with heating time. (a) 0.5 cm depth. (b) 15 cm depth.

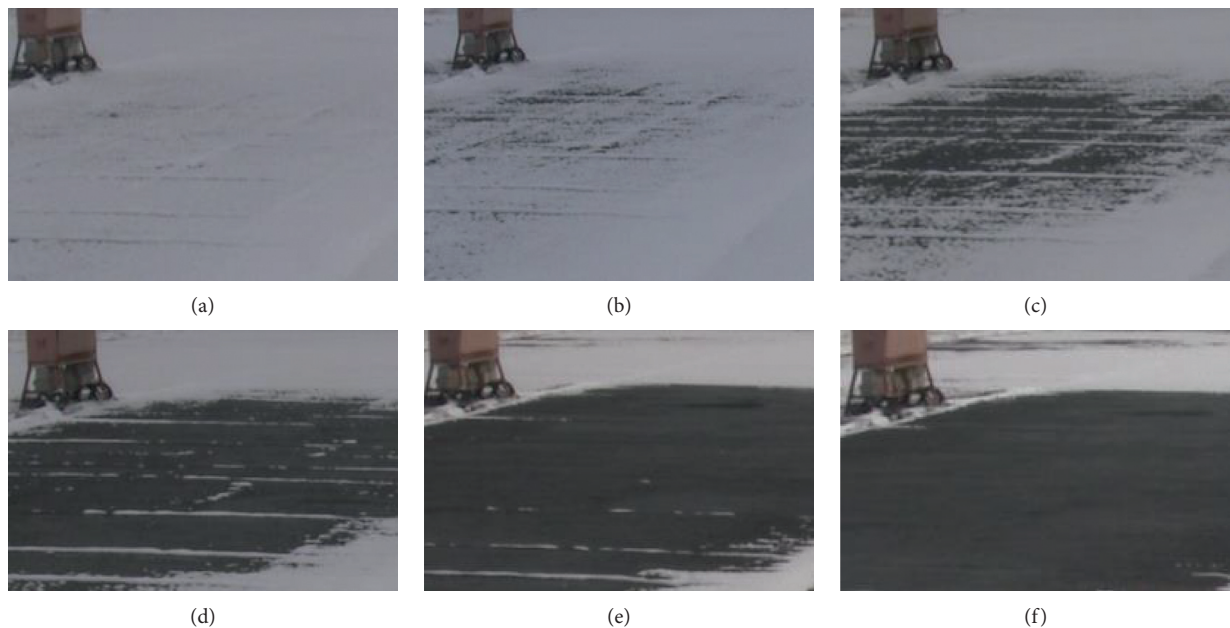


FIGURE 7: Melting snow on 1# asphalt pavement. (a) 60 minutes. (b) 80 minutes. (c) 90 minutes. (d) 100 minutes. (e) 110 minutes. (f) 120 minutes.

As shown in Figure 6(a), the temperature of the 1# asphalt pavement is always lower than that of the 2# asphalt pavement at the depth of 0.5 cm because of the ice on the 1# asphalt pavement. Their temperature difference increases from 0.2°C to 4.7°C in 150 minutes. At the depth of 0.5 cm, the heating process of the 1# asphalt pavement includes three stages: rising stage, stable stage, and rapid rising stage. The asphalt pavement temperature of the rising stage is less than 0°C. The asphalt pavement temperature of the stable stage is from 0.5°C to 2°C. The asphalt pavement temperature of the rapid rising stage is more than 2°C. In the process of 150 minutes of heating, it can be seen in Figure 6(b) that 1# and 2# asphalt pavement temperature difference at the depth of 15 cm is less than 0.3°C at the same time. At the end of

heating, 1# and 2# asphalt pavement temperature increases by 4.3°C and 3.9°C, respectively.

**3.2. Melting Snow and Asphalt Pavement Temperature.** Snowfall stopped when the time was 9:00 on January 21, 2016. The accumulated snow thickness is 3 cm. The total precipitation is 3.2 mm. The heating time was from 9:00 to 11:00. The experiment was tested from 9:00 to 11:00. The wind speed and relative humidity were 0.3–1.8 m/s and 80%–88%, respectively. The air temperature rose from -4.8°C to -3.5°C in 2 hours. The solar radiation intensity was 37–79 W/m<sup>2</sup>.

Figure 7 shows the process of melting snow on the 1# asphalt pavement. The initial time of melting snow is 60

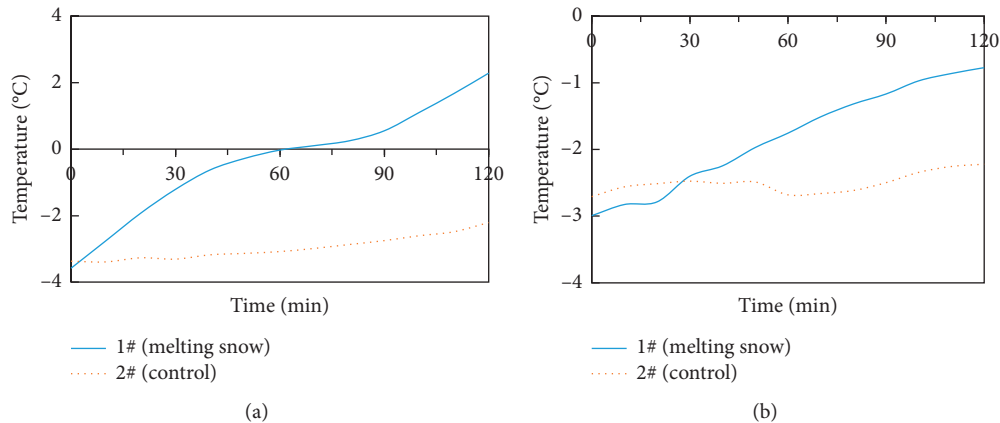


FIGURE 8: The asphalt pavement temperature variation with time. (a) 0.5 cm depth. (b) 15 cm depth.

minutes. The snow-free area ratio is 0, 0.02, 0.21, 0.72, 0.94, and 1 at 60 minutes, 80 minutes, 90 minutes, 100 minutes, 110 minutes, and 120 minutes, respectively. Most of the snow is melted from 60 minutes to 100 minutes. Snow on the 1# asphalt pavement is completely melted in 120 minutes. The control group is the 2# asphalt pavement that is not heated. At the depth of 0.5 cm, it can be seen in Figure 8(a) that 1# asphalt pavement temperature increases from  $-3.6^{\circ}\text{C}$  to  $2.3^{\circ}\text{C}$  in 120 minutes because of heating; 2# asphalt pavement temperature increases from  $-3.4^{\circ}\text{C}$  to  $-2.2^{\circ}\text{C}$  in 120 minutes because of weather condition. 1# asphalt pavement temperature curves of melting snow and ice are similar. 1# asphalt pavement temperature for melting snow includes three stages that are the rising stage, stable stage, and rapid rising stage. At the depth of 15 cm, it can be seen in Figure 8(b) that 1# asphalt pavement temperature increases from  $-3.0^{\circ}\text{C}$  to  $-0.8^{\circ}\text{C}$  in 120 minutes, and 2# asphalt pavement temperature is between  $-2.7^{\circ}\text{C}$  and  $-2.2^{\circ}\text{C}$  in 120 minutes.

#### 4. Conclusions

Deicing and melting snow by the CFHW buried in the airport asphalt pavement is studied in the paper. It is practicable for deicing and melting snow that the depth of the CFHW is 7 cm, and the CFHW spacing is 10 cm in the airport asphalt pavement. According to frozen and snowy weather in Beijing, the electrical power with  $350\text{ W/m}^2$  is input to the airport asphalt pavement for deicing and melting snow in these experiments. The results of the full-scale field experiment show that it is effective for deicing and melting snow on the airport asphalt pavement by the CFHW. When the air temperature is from  $-7.5^{\circ}\text{C}$  to  $-2.2^{\circ}\text{C}$ , 3 mm ice can be melted in 2.5 hours; the average IRT of the asphalt pavement surface increases by  $13.0^{\circ}\text{C}$ . When the air temperature is from  $-4.8^{\circ}\text{C}$  to  $-3.5^{\circ}\text{C}$ , snow with 3.2 mm precipitation can be melted in 2 hours; and the asphalt pavement temperature can achieve an increment of  $5.9^{\circ}\text{C}$  at the depth of 0.5 cm. It is an hour when the ice-free area ratio is from 0 to 1 for deicing. It is also an hour when the snow-free area ratio is from 0 to 1 for melting snow. The findings indicate that the technique of deicing and melting snow on

the airport asphalt pavement by the CFHW is practicable in actual engineering of the cold zone.

#### Data Availability

The data used to support the conclusions of the study are included within the article.

#### Conflicts of Interest

The authors declare no conflicts of interest.

#### Authors' Contributions

Xin Su and Yong Lai conceived and designed the experiments; Yong Lai and Yan Liu performed the experiments; Yong Lai, Daoxun Ma, and Peng Wang analyzed the data; and Xin Su and Yong Lai wrote the paper.

#### Acknowledgments

This work was financially supported by Science and Technology Project of CAAC (MHRD20140107) and Security Capacity Building Project of CAAC (20180275).

#### References

- [1] Y. Lai, Y. Liu, X. Su, D. X. Ma, and P. Wang, "The influence of heat flux on melting ice on concrete pavement with carbon fibre heating wire," *IOP Conference Series: Materials Science and Engineering*, vol. 392, pp. 2–6, 2018.
- [2] Q. Yang, X. Li, L. Zhang et al., "Performance evaluation of bitumen with a homogeneous dispersion of carbon nanotubes," *Carbon*, vol. 158, pp. 465–471, 2020.
- [3] M. Guo and Y. Tan, "Interaction between asphalt and mineral fillers and its correlation to mastics' viscoelasticity," *International Journal of Pavement Engineering*, vol. 10, pp. 1–10, 2019.
- [4] M. Guo, H. Liu, Y. Jiao et al., "Effect of WMA-RAP technology on pavement performance of asphalt mixture: a state-of-the-art review," *Journal of Cleaner Production*, vol. 266, p. 121704, 2020.
- [5] Z. Min, Y. Xia, X. Li, and Z. Tao, "Performances evaluation of epoxy asphalt mixture containing snow-melting agent,"

- Construction and Building Materials*, vol. 155, pp. 762–769, 2017.
- [6] X. B. Liu and J. D. Spitler, “A simulation tool for the design of the hydronic bridge snow melting system,” in *Proceedings of the 12th International Road Weather Conference*, Bingen, Germany, June 2004.
- [7] X. B. Liu, S. J. Rees, and J. D. Spitler, “Modeling snow melting on heated pavement surfaces part I: model development,” *Applied Thermal Engineering*, vol. 27, pp. 1115–1124, 2006.
- [8] X. Liu, S. J. Rees, and J. D. Spitler, “Modeling snow melting on heated pavement surfaces. Part II: experimental validation,” *Applied Thermal Engineering*, vol. 27, no. 5-6, pp. 1125–1131, 2007.
- [9] M. Chen, S. Wu, H. Wang, and J. Zhang, “Study of ice and snow melting process on conductive asphalt solar collector,” *Solar Energy Materials and Solar Cells*, vol. 95, no. 12, pp. 3241–3250, 2011.
- [10] H. Xu and Y. Tan, “Modeling and operation strategy of pavement snow melting systems utilizing low-temperature heating fluids,” *Energy*, vol. 80, pp. 666–676, 2015.
- [11] C. Y. Tuan and S. Yehia, “Evaluation of electrically conductive concrete containing carbon products for deicing,” *ACI Materials Journal*, vol. 101, pp. 287–293, 2004.
- [12] Z. F. Hou, Z. Q. Li, and K. J. Guang, “The joule heating analysis of electrically conductive concrete for roadway deicing system,” in *Proceedings of the Seventh International Symposium on Structural Engineering for Young Exports*, pp. 977–1001, Tianjin, China, 2002.
- [13] P. Xie and J. J. Beaudoin, “Electrically conductive concrete and its application in deicing,” in *Proceedings of the Second CANMET/ACI International Symposium*, pp. 399–417, Las Vegas, NV, USA, 1995.
- [14] Y. Lai, Y. Liu, and D. Ma, “Automatically melting snow on airport cement concrete pavement with carbon fiber grille,” *Cold Regions Science and Technology*, vol. 103, pp. 57–62, 2014.
- [15] H.-M. Zhao, S.-G. Wang, Z.-M. Wu, and G.-J. Che, “Concrete slab installed with carbon fiber heating wire for bridge deck deicing,” *Journal of Transportation Engineering*, vol. 136, no. 6, pp. 500–509, 2010.
- [16] H. M. Zhao, Z. M. Wu, S. G. Wang, J. J. Zheng, and G. J. Che, “Concrete pavement deicing with carbon fiber heating wires,” *Cold Regions Science and Technology*, vol. 65, pp. 413–420, 2011.
- [17] Y. Lai, Y. Liu, and D. X. Ma, “The Influence of carbon fiber heating wire spacing on concrete pavement temperature,” *Materials Research Innovations*, vol. 85, pp. 804–808, 2016.
- [18] Y. Lai, Y. Liu, D. X. Ma, P. Wang, and X. Su, “The Influence of wind speed on melting ice on concrete pavement with carbon fiber heating wire,” in *Proceedings of the International Workshop on Materials, Chemistry and Engineering*, pp. 313–318, Xiamen, China, March 2018.
- [19] Y. Liu, Y. Lai, and D. X. Ma, “Melting snow on airport cement concrete pavement with carbon fibre heating wires,” *Materials Research Innovations*, vol. 19, pp. 95–99, 2015.

## Research Article

# Crude Oil Source Identification of Asphalt via ATR-FTIR Approach Combined with Multivariate Statistical Analysis

Ruibo Ren,<sup>1</sup> Wenmiao Fan,<sup>1</sup> Pinhui Zhao ,<sup>1</sup> Hao Zhou,<sup>1</sup> Weikun Meng,<sup>1</sup> and Ping Ji<sup>2</sup>

<sup>1</sup>Shandong Provincial Key Laboratory of Road and Traffic Engineering in Colleges and Universities, School of Transportation Engineering, Shandong Jianzhu University, Jinan 250101, China

<sup>2</sup>Shandong Hi-Speed Engineering Testing Co., Ltd., Jinan 250101, China

Correspondence should be addressed to Pinhui Zhao; zhaopinhui08@163.com

Received 14 February 2020; Revised 15 May 2020; Accepted 3 June 2020; Published 6 July 2020

Guest Editor: Meng Guo

Copyright © 2020 Ruibo Ren et al. This is an open access article distributed under the Creative Commons Attribution License, which permits unrestricted use, distribution, and reproduction in any medium, provided the original work is properly cited.

The types of crude oil for producing asphalt have a decisive influence on various performance measures (including aging resistance and durability) of asphalt. To discriminate and predict the crude oil source of different asphalt samples, a discrimination model was established using 12 greatly different infrared (IR) characteristic absorption peaks (CAPs) as predictive variables. The model was established based on diverse fingerprint recognition technologies (such as principal component analysis (PCA) and multivariate logistic regression analysis) by using attenuated total reflectance-Fourier transform infrared spectroscopy (ATR-FTIR). In this way, the crude oil source of different asphalt samples can be effectively discriminated. At first, by using PCA, the 12 CAPs in the IR spectra of asphalt samples were subjected to dimension reduction processing to control the variables of key factors. Moreover, the scores of various principal components in asphalt samples were calculated. Afterwards, the scores of principal components were analysed through modelling based on multivariate logistic regression analysis to discriminate and predict the crude oil source of different asphalt samples. The result showed that the logistic regression model shows a favourable goodness of fit, with the prediction accuracy reaching 93.9% for the crude oil source of asphalt samples. The method exhibits some outstanding advantages (including ease of operation and high accuracy), which is important when controlling the source and quality and improving the performance of asphalt.

## 1. Introduction

Asphalt pavements are widely used: as a black binding material produced from oil, asphalt is widely used as the binder in asphaltic mixtures [1–3]. Due to the differences in origins and production modes of crude oil for producing asphalt, the properties of crude oil exert important influences on the performance of asphalt mixtures, which also lead to significant differences in the performance of the various asphalt produced therewith [4–8].

The conventional performance of the same grade of asphalt is very similar; however, different asphalt exhibit large differences in various aspects, including high- and low-temperature performance, durability, and fatigue properties, which are considered as external expressions of chemical composition, molecular structure, and transformation of

asphalt [9–11]. Furthermore, the study shows that the differences in the composition and structure of asphalt mainly depend on the source of crude oil and refining process of asphalt production. Due to the differences in the geological structure, oil generation conditions, and age, the nature and composition of crude oil in different regions are very different. However, crude oil with similar properties and composition in the same region has similar processing, storage, and transportation options. At the same time, most of the petroleum asphalt is produced by distillation currently, and the molecules in the asphalt retain their original state in the crude oil. Therefore, most of the composition and structure of asphalt are inherited from crude oil; that is to say, the structural performance of asphalt mainly depends on the source of crude oil. Because the asphalt is produced by different types of crude oil, the physical and chemical

composition information about asphalt is unique. Just like the human fingerprint information, these components which can express the unique structure of asphalt can be called the “oil fingerprint” of asphalt. It is because of the uniqueness of “oil fingerprint” information of asphalt that it is feasible to discriminate the oil fingerprints of asphalt from different crude oil sources [12–16].

At present, as the composition and structure of asphalt are extremely complex, the characterization of its structure requires more high-resolution and high-throughput analysis means and equipment, so there are few reports on the identification and analysis of asphalt oil fingerprints [17]. However, the identification and analysis of marine oil spill fingerprints has always been an issue of widespread concern. Similar to the method and purpose of identifying “oil fingerprints” of oil spills at sea, the purpose of recognising oil fingerprints of asphalt is to attain oil fingerprint information of asphalt through different methods such as physical, chemical, and biological methods [18]. Moreover, by applying multivariate statistical methods (including principal component analysis (PCA) and regression analysis), the chemical composition variables of oil fingerprints are summarised, classified, and discriminated [19, 20]. On this basis, qualitative and quantitative relationships between data are obtained to distinguish the crude oil source of asphalt, thus effectively controlling their qualities. Meanwhile, some testing methods used in the “oil fingerprint” identification of marine oil spills have been successfully used to analyse the composition and structure of asphalt [21–23]. For example, a gas chromatograph-mass spectrometer (GC-MS) was used to explore the chemical compositions of smoke released by asphalt materials during heating [24, 25]. Gel permeation chromatography (GPC) and thin-layer chromatography (TLC) were used to measure the molecular weights and the composition distributions of asphalt [26–28]. Nuclear magnetic resonance (NMR) and Fourier transform infrared spectroscopy (FTIR) were used to investigate the compositions, structures, and functional groups of asphalt [29, 30]. In all analytical techniques, compared with other methods (including GC-MS and NMR), which generally show some disadvantages (including high cost, damage to samples, and being laborious and time consuming during analysis), infrared (IR) spectroscopy is the most widely used technique in investigating asphalt materials. The reason is that IR spectroscopy shows many outstanding advantages, including being label-free, rapid, nondestructive, and low-cost, with simple sample preparation [31–33]; however, in the above analysis, the chemical structures of asphalt are qualitatively analysed, mainly aiming at those of a certain or multiple specific asphalt samples while lacking quantitative research into the types of asphalt. The research into discrimination of the types of asphalt, tracing of the production area, and quality control of asphalt has not yet been reported.

Therefore, by utilising attenuated total reflectance-Fourier transform infrared spectroscopy (ATR-FTIR), the characteristic functional groups of asphalt from different crude oil source were discriminated and quantitatively analysed. Based on multivariate statistics, PCA and logistic regression analysis were conducted on IR spectral data to

establish a discriminant function. An accurate, nondestructive, stable method of discriminating the crude oil source of asphalt samples was explored, which provides a scientific basis for realising reasonable selection, supervision quality, and guaranteed origins of asphalt.

## 2. Experimental Raw Materials and Methods

**2.1. Experimental Materials.** During the experiment, 33 asphalt samples were purchased from factories in China for producing asphalt. Before being applied, the asphalt samples were sealed in original oxygen-free containers at 5°C to prevent the samples from being oxidised. Additionally, all asphalt samples were unprocessed before use. As mentioned in Section 1, the differences in the “oil fingerprint” of asphalt are determined by the crude oil from which it is produced. Due to the same geological structure, oil generation conditions, and age in the same region, the composition and chemical structure of crude oil are also very similar. Therefore, the “oil fingerprints” of asphalt produced by crude oil from the same region are very similar, such as crude oil from the Middle East Gulf region, including Saudi Arabia, Iran, Kuwait, Iraq, and United Arab Emirates, crude oil from South America, including Marry, Poscan, Maya, and Castilla, and crude oil from the Bohai Rim region of China, such as Bohai Bay, Huanxiling, and Caoheidian. The crude oil of 33 asphalt samples came from the above three regions. According to the names of the three regions, the crude oil source of asphalt is divided into three categories: Middle East, South America, and the Bohai Rim region of China. The basic performance measures (penetration ratio (ASTM D5), ductility ratio (ASTM D113), and softening point (ASTM D36)) of asphalt and the crude oil source of asphalt are listed in Table 1. It is worth noting that the last digit of the asphalt number listed in Table 1 represents different sampling batches of the same asphalt.

**2.2. FTIR Analysis.** Through ATR-FTIR (using a Cary 630 FTIR microscope), the IR spectra of asphalt samples were explored. Within the range of 400–4,000  $\text{cm}^{-1}$ , 64 scans were conducted, each at a resolution of 1  $\text{cm}^{-1}$ . The samples were placed on the horizontal ATR crystal made of zinc selenide, being subjected to multiple reflections. After each operation, the ATR crystal was cleaned using acetone.

The original spectrum data were first subjected to baseline correction by applying the OMNIC software to eliminate baseline effects. Afterwards, based on the standardised variation diagram of preprocessed spectrum data, the difference in masses of different samples was eliminated.

**2.3. Multivariate Statistical Analysis.** Through the combination of principal component analysis (PCA) and multiple logistic regression analysis, the infrared spectrum data are analysed to establish the discrimination model of the crude oil source of asphalt. Logistic regression analysis is a multivariate analysis method to analyse and predict attribute-dependent variables based on single or multiple continuous or attribute-independent variables. Furthermore, each

TABLE 1: Basic properties and crude oil source of asphalt.

Asphalt number	Asphalt name <sup>1</sup>	Penetration (0.1 mm)	Ductility (cm, 10°C)	Softening point (°C)	Source	Category
1	MM-1	79.6	65.7	47.3	Middle East (Saudi Arabia)	1
2	Q-1	75.4	>100	46.5	South America (Marry & Poscan)	2
3	SK (BY)-1	69.7	52.2	46.9	Middle East (Saudi Arabia)	1
4	Q-2	61.5	39.0	48.5	South America (Marry & Poscan)	2
5	SL-1	63.4	47.5	47.0	Middle East (Saudi Arabia)	1
6	CMR-1	67.5	>100	47.2	South America (Marry)	2
7	LH-1	76.6	>100	45.6	South America (Marry & Poscan)	2
8	QPK-1	61.8	>100	46.8	Middle East (Iran)	1
9	MM-2	61.1	16.0	49.6	Middle East (Saudi Arabia)	1
10	QP-1	68.9	33.2	48.7	Middle East (Kuwait)	1
11	JB-1	67.3	74.0	47.5	South America (Marry & Poscan)	2
12	SK (XY)-1	71.5	47.9	47.2	Middle east (Saudi Arabia)	1
13	ZH-1	67.4	13.5	48.1	South America (Maya & Castilla)	2
14	JL-1	64.2	35.6	48.2	Middle East (Kuwait)	1
15	HR-1	63.2	85.2	48.6	South America (Marry & Poscan)	2
16	AS-1	62.1	84.3	47.4	Middle East (Saudi Arabia)	1
17	XT-1	62.7	23.9	48.8	Middle East (Saudi Arabia)	1
18	ZH-2	64.0	>100	50.1	South America (Maya& Castilla)	2
19	LH-2	69.0	>100	47.0	South America (Marry & Poscan)	2
20	QL-1	64.0	21.3	50.0	Middle east (Kuwait)	1
21	KL-1	79.8	>100	47.2	Bohai Rim region of China (Bohai Bay)	3
22	KL-2	61.0	57.8	49.5	Bohai Rim region of China (Bohai Bay)	3
23	SL-2	65.0	30.0	49.2	Middle East (Saudi Arabia)	1
24	SK (NB)-1	71.0	47.9	48.4	Middle East (Saudi Arabia)	1
25	Q-3	75.0	>100	47.3	South America (Marry & Poscan)	2
26	DSZ-1	69.0	>100	50.0	Bohai Rim region of China (Huanxiling)	3
27	CMR-2	68.2	>100	47.9	South America (Marry)	2
28	JB-2	64.6	74.0	46.3	South America (Marry & Poscan)	2
29	ZH-3	63.5	>100	51.2	South America (Maya & Castilla)	2
30	LH-3	68.7	>100	47.9	South America (Marry & Poscan)	2
31	DSZ-2	78.4	>100	48.6	Bohai Rim region of China (Huanxiling)	3
32	SZ-1	61.9	57.8	49.3	Bohai Rim region of China (Bohai Bay)	3
33	SZ-2	68.0	>100	50.9	Bohai Rim region of China (Bohai Bay)	3

<sup>1</sup>In this column, 1, 2, and 3 indicate the different sampling batches of the same asphalt.

variable is required to be independent of each other in variable screening and parameter estimation. In many studies, there is a certain degree of linear dependence between their variables, which is called multicollinearity. This multiple collinear relationship may increase the mean square error and standard error of the estimated parameters, which leads to the instability of the analysis results of the logistic regression model. The main reason for the problem of multicollinearity is the overlap of information. However, PCA can reduce the repeatability of information and achieve the purpose of eliminating multicollinearity by extracting independent principal components from explanatory variables.

For this reason, this study used a multinomial logistic regression model based on PCA to improve the discrimination accuracy of the model. First of all, the PCA was used to reduce the dimension of the CAPs variables of the infrared

spectrum, so that the variables with strong correlation were integrated into the same principal components. The principal components were independent of each other; thus, the multiple collinear relationship between variables was eliminated. Then, by using these principal components as independent variables, the discriminant model of crude oil source of asphalt was obtained by logistic regression analysis.

*2.3.1. PCA Analysis.* PCA refers to a simplification of multidimensional data to several relevant variables (principal components) through a dimension reduction approach. Each principal component reflects most of the information of original variables, and the contained information is not repeated. PCA can compress countless information and simplify complex problems [34]. The modelling process of PCA is as follows:

(1) Calculation of the correlation coefficient matrix:

$$R = \begin{bmatrix} r_{11} & r_{12} & \cdots & r_{1p} \\ r_{21} & r_{22} & \cdots & r_{2p} \\ \vdots & \vdots & & \vdots \\ r_{p1} & r_{p2} & \cdots & r_{pp} \end{bmatrix}, \quad (1)$$

where  $r_{ij}$  ( $i, j = 1, 2, \dots, p$ ) refers to the correlation coefficient of original variables  $X_i$  and  $X_j$ ,  $r_{ij} = r_{ji}$ , which can be calculated by using the following formula:

$$r_{ij} = \frac{\sum_{k=1}^n (X_{ki} - \bar{X}_i)(X_{kj} - \bar{X}_j)}{\sqrt{\sum_{k=1}^n (X_{ki} - \bar{X}_i)^2 \sum_{k=1}^n (X_{kj} - \bar{X}_j)^2}} \quad (2)$$

(2) Calculating eigenvalues and eigenvectors:

The characteristic equation  $|\lambda I - R| = 0$  was solved. Generally, the eigenvalues were calculated by using the Jacobi method and, in descending order are  $\lambda_1 \geq \lambda_2 \geq \dots \geq \lambda_p \geq 0$ . The eigenvectors  $e_i$  ( $i = 1, 2, \dots, p$ ) corresponding to eigenvalue  $\lambda_1$  were separately calculated, satisfying  $\|e_i\| = 1$ , that is,  $\sum_{j=1}^p e_{ij}^2 = 1$ , where  $e_{ij}$  denotes the  $j^{\text{th}}$  component of vector  $e_i$ .

(3) Calculating contribution and cumulative contribution of principal components:

$$\text{contribution} : \frac{\lambda_i}{\sum_{k=1}^p \lambda_k}, \quad (i = 1, 2, \dots, p), \quad (3)$$

$$\text{cumulative contribution} : \frac{\sum_{k=1}^i \lambda_k}{\sum_{k=1}^p \lambda_k}, \quad (i = 1, 2, \dots, p). \quad (4)$$

In general, the eigenvalues with the cumulative contribution not lower than 70% are taken.  $\lambda_1, \lambda_2, \dots, \lambda_m$  are the corresponding first, second,  $\dots$ ,  $m^{\text{th}}$  ( $m \leq p$ ) principal components.

(4) Calculating the loads of principal components:

$$l_{ij} = p(Z_i, X_j) = \sqrt{\lambda_i} e_{ij}. \quad (i = 1, 2, \dots, p). \quad (5)$$

(5) Scores of various principal components:

$$Z = \begin{bmatrix} z_{11} & z_{12} & \cdots & z_{1m} \\ z_{21} & z_{22} & \cdots & z_{2m} \\ \vdots & \vdots & & \vdots \\ z_{n1} & z_{n2} & \cdots & z_{nm} \end{bmatrix}. \quad (6)$$

**2.3.2. Logistic Regression Analysis.** Logistic regression is a multivariate analysis method for investigating the relationship between binomial or multinomial observation results (dependent variable) and influencing factors (independent variable), belonging to probabilistic nonlinear regression methods. The logistic regression when the

dependent variable only shows two or more states belongs to binomial logistic regression and multinomial logistic regression, respectively [35, 36]. For discriminating and classifying the crude oil of asphalt, multinomial logistic regression is applied to conduct data analysis, owing to the crude oil of asphalt being sourced from the Bohai Rim region of China, South America, and the Middle East.

(1) Model fitting:

For multinomial logistic regression, a certain level of dependent variables is defined as the reference level herein. Compared with the other levels,  $i-1$  ( $i$  refers to the number of dependent variables) generalised logistic regression models were fitted. By taking three-level dependent variables as an example, it is supposed that the values of dependent variables are 1, 2, and 3; the probabilities corresponding to the values are  $\pi_1$ ,  $\pi_2$ , and  $\pi_3$ , respectively. Based on  $m$ -independent variables, two models are fitted as follows:

$$\text{logit} \frac{\pi_1}{\pi_3} = \alpha_1 + \beta_{11}X_1 + \beta_{12}X_2 + \dots + \beta_{1m}X_m, \quad (7)$$

$$\text{logit} \frac{\pi_2}{\pi_3} = \alpha_2 + \beta_{21}X_1 + \beta_{22}X_2 + \dots + \beta_{2m}X_m. \quad (8)$$

(2) Meaning of regression parameters:

For multinomial logistic regression, each independent variable contains  $(m-1)$  parameters. The parameter  $\beta_{1m}$  represents an independent variable  $x_m$  that changes one unit on the premise that other independent variables remain unchanged, and it reflects the variation of the log-odds ratio (OR) of class  $i$ . The OR is subjected to logarithmic transformation to obtain the linear mode ( $\ln(p_i/1-p_i) = \beta_0 + \beta_1X_1 + \beta_2X_2 + \dots + \beta_nX_n$ ) of the logistic regression model.

### 3. Results and Discussion

**3.1. Establishment of Discrimination Indices for Crude Oil Source of Asphalt.** FTIR is an important means of identifying organic compounds. When irradiating organics using the IR light, the molecules absorb the IR light leading to vibrational energy level transition, and different chemical bonds or functional groups show diverse absorption frequencies. The contents of various materials are reflected in their IR absorption spectra, which can be quantitatively analysed according to peak location and absorption intensity. The structural composition of asphalt is complex, and asphalt shows significant differences in behaviour. For these reasons, it fails to effectively characterize the difference of behaviours of asphalt from different crude oil only by quantitatively comparing the peak areas of IR spectrograms. Therefore, by observing the shapes and locations of IR spectrograms, 12 significant characteristic absorption peaks (CAPs) were selected to analyse the transmittances of absorption peaks.



The IR absorption spectra of 33 asphalt samples are similar. By using the mean value method, the mutual mode of the IR spectrogram of all asphalt samples was constructed (Figure 1): the assignments of 12 characteristics peaks are as follows: the strong absorption peaks around  $2850\text{ cm}^{-1}$  and  $2920\text{ cm}^{-1}$  are triggered by the stretching vibration of  $\text{CH}_2$ , and a very weak absorption peak around  $1700\text{ cm}^{-1}$  is induced by the stretching vibration of  $\text{C}=\text{O}$ . Moreover, the vibration of the benzene ring leads to the absorption peak in the vicinity of  $1600\text{ cm}^{-1}$ , and the absorption peaks at  $1380\text{ cm}^{-1}$  and  $1460\text{ cm}^{-1}$  are caused by the bending vibration of  $\text{CH}_3$ . The fingerprint region appears below  $1300\text{ cm}^{-1}$ , in which the absorption peaks at  $1166\text{ cm}^{-1}$  and  $1032\text{ cm}^{-1}$  are triggered by the stretching vibrations of  $\text{C}=\text{S}$  and  $\text{S}=\text{O}$ , respectively. The stretching vibration of  $\text{CH}$  results in a weak absorption peak around  $969\text{ cm}^{-1}$ , while the absorption peaks at  $872\text{ cm}^{-1}$  and  $812\text{ cm}^{-1}$  are induced by vibrations of an isolated hydrogen and two adjacent hydrogen atoms on the benzene ring, respectively. Additionally, the absorption peak at  $723\text{ cm}^{-1}$  is also caused by the stretching vibration of  $\text{CH}_2$ .

**3.2. Analysis of Predictive Variables Based on Descriptive Statistics.** The IR spectra of all asphalt samples are similar, and it is difficult to distinguish the differences among asphalt samples by comparing spectrograms alone. Hence, 12 significantly different CAPs were selected from the spectrograms to describe the transmittances of absorption peaks based on descriptive statistics. From two aspects of centralised location (including indices such as average and median) and degree of dispersion (including indices such as extreme value), the samples are described so as to reflect spectrographic data (Table 2).

In Table 2, according to the analysis result of descriptive statistics on the transmittances of 12 CAPs, it can be seen that the asphalt produced by crude oil from the Bohai Rim region of China showed a larger transmittance. By contrast, the transmittances of asphalt produced by crude oil from the Middle East and South America were consistently low. However, it is impossible to distinguish the oil source of asphalt based on the descriptive statistics of infrared spectral transmittance of asphalt. Therefore, it is necessary to introduce multivariate statistical analysis methods, such as multinomial logistic regression analysis based on PCA described in Section 2.3.

**3.3. Correlation Analysis of Predictive Variables.** Correlation analysis aims to explore the correlation among multiple variables, which is also an important parameter for evaluating the fingerprint variables of asphalt [37]. In order to further evaluate whether the selected 12 variables were of sufficient significance to the prediction model, a correlation analysis of the 12 CAP variables was required. Generally, correlation analysis is conducted by applying Pearson and Spearman correlation coefficients. The Pearson correlation

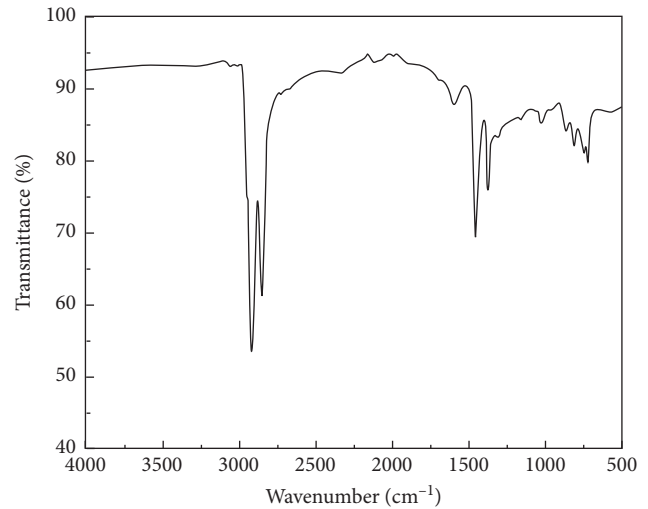


FIGURE 1: The common mode of infrared fingerprints of the asphalt.

coefficient is generally applicable to data satisfying a normal distribution, and the Spearman correlation coefficient is employed for data that do not satisfy a normal distribution. Therefore, before the correlation test, it is necessary to test the normal distribution of 12 variables to determine the appropriate correlation test method.

By using the skewness-kurtosis test method, whether the transmittances of the 12 CAPs of 33 asphalt samples conform to a normal distribution was assessed, and through the K-S test as an auxiliary analysis method, the accuracy of the test results was ensured [38, 39]. The 12 variables were processed by importing them into SPSS19 (Tables 3 and 4).

It can be seen from Table 3 that the values of skewness and kurtosis of transmittances of the 12 CAPs of all asphalt samples produced by three origins of oil fluctuate within a certain small positive and negative range around zero. It can be further seen from Table 4 that the asymptotic significances of the 12 variables all exceed 0.05. Moreover, based on the result of the skewness-kurtosis test, it can be considered that the 12 variables of 33 asphalt samples all conform to a normal distribution, which provides a basis for determining the method for testing correlation among variables. Therefore, the Pearson correlation coefficient is used to analyse the correlation between variables (Table 5).

As shown in Table 5, the IR CAP at  $2850\text{ cm}^{-1}$  showed a significant correlation with those at  $2920$ ,  $1460$ , and  $723\text{ cm}^{-1}$ , respectively. Additionally, there are significant correlations between each IR CAP at  $1700$ ,  $1600$ ,  $1460$ ,  $1380$ ,  $1166$ ,  $1032$ ,  $969$ ,  $872$ ,  $812$ , and  $723\text{ cm}^{-1}$ . Moreover, multiple CAPs exhibited a high correlation. The aforementioned CAPs with high correlation covered all 12 CAPs. This showed that the 12 selected CAPs contained most of the fingerprint information about the asphalt, thus providing a basis for selecting variables capable of discriminating the different crude oil sources of asphalt.

TABLE 2: Descriptive statistics analysis of the 12 CAPs.

Statistical indicators	Oil source	Average value	Median value	Maximum value	Minimum value
2920 <sup>-1</sup>	Middle East	52.10	51.62	55.46	49.83
	South America	55.85	54.20	61.02	53.29
	Bohai Rim region of China	54.39	53.29	56.64	53.23
2850 <sup>-1</sup>	Middle East	59.82	59.51	63.60	58.43
	South America	63.26	62.39	67.38	60.74
	Bohai Rim region of China	62.97	62.36	64.88	61.69
1700 <sup>-1</sup>	Middle East	91.07	91.14	91.96	89.28
	South America	91.46	91.50	92.29	90.83
	Bohai Rim region of China	92.92	92.41	94.06	92.29
1600 <sup>-1</sup>	Middle East	87.31	87.37	88.25	85.10
	South America	87.67	87.49	88.74	87.20
	Bohai Rim region of China	90.66	90.26	91.63	90.08
1460 <sup>-1</sup>	Middle East	68.71	68.64	70.10	67.64
	South America	69.81	69.81	71.68	68.27
	Bohai Rim region of China	72.03	72.18	72.24	71.67
1380 <sup>-1</sup>	Middle East	75.51	75.48	76.95	74.08
	South America	76.11	76.12	77.26	74.77
	Bohai Rim region of China	78.51	78.50	78.96	78.07
1166 <sup>-1</sup>	Middle East	85.26	85.41	86.33	83.43
	South America	85.88	85.91	86.84	84.65
	Bohai Rim region of China	89.48	89.10	90.25	89.08
1032 <sup>-1</sup>	Middle East	84.37	84.49	86.35	82.29
	South America	85.78	86.30	86.80	82.57
	Bohai Rim region of China	90.10	89.81	90.68	89.81
969 <sup>-1</sup>	Middle East	86.53	86.72	87.73	84.97
	South America	87.28	87.22	88.10	85.98
	Bohai Rim region of China	90.33	90.15	90.69	90.14
872 <sup>-1</sup>	Middle East	83.74	83.93	84.64	81.00
	South America	84.86	84.67	86.09	83.79
	Bohai Rim region of China	88.97	88.53	89.86	88.50
812 <sup>-1</sup>	Middle East	80.73	81.12	81.85	77.23
	South America	82.70	82.79	83.88	80.40
	Bohai Rim region of China	88.63	88.24	89.43	88.21
723 <sup>-1</sup>	Middle East	78.18	78.14	80.74	76.17
	South America	81.32	81.38	82.70	78.25
	Bohai Rim region of China	85.61	84.90	87.15	84.78

TABLE 3: The skewness-kurtosis test of the 12 CAPs.

Statistical indicators (cm <sup>-1</sup> )	Skewness	Kurtosis
2920	1.123	1.279
2850	0.797	0.130
1700	0.713	1.241
1600	1.120	1.379
1460	0.509	-1.149
1380	0.509	-0.728
1166	1.129	0.600
1032	0.737	-0.213
969	0.926	0.074
872	1.052	0.735
812	0.975	0.245
723	0.651	0.459

### 3.4. Establishment of Logistic Regression and Discriminant Model Based on PCA

3.4.1. *PCA on All Variables.* According to the correlation analysis of variables, it can be seen that the information contained in the 12 CAPs shows a certain repeatability. PCA not only can remove repeated information but can retain key information, thus realising dimension reduction. Furthermore, it makes the modelling for logistic regression and discrimination more reliable due to reducing the disturbance caused by accidental factors.

The transmittances of the 12 CAPs of 33 asphalt samples are input into the SPSS19 software for PCA. The results are displayed in Table 6 and Figure 2. As shown in Table 6, there

TABLE 4: The Kolmogorov-Smirnov test of a single sample.

Statistical indicators	2920 $\text{cm}^{-1}$	2850 $\text{cm}^{-1}$	1700 $\text{cm}^{-1}$	1600 $\text{cm}^{-1}$	1460 $\text{cm}^{-1}$	1380 $\text{cm}^{-1}$	1166 $\text{cm}^{-1}$	1032 $\text{cm}^{-1}$	969 $\text{cm}^{-1}$	872 $\text{cm}^{-1}$	812 $\text{cm}^{-1}$	723 $\text{cm}^{-1}$
Number of samples	33	33	33	33	33	33	33	33	33	33	33	33
Kolmogorov-Smirnov	1.14	0.77	0.68	1.33	0.99	0.75	1.30	0.98	1.08	1.35	1.14	0.86
Asymptotically significant (bilateral)	0.15	0.59	0.73	0.06	0.27	0.63	0.07	0.28	0.19	0.05	0.14	0.43

TABLE 5: Pearson correlation coefficients of transmittances of the 12 CAPs.

Correlation coefficient (cm <sup>-1</sup> )	2920 cm <sup>-1</sup>	2850 cm <sup>-1</sup>	1700 cm <sup>-1</sup>	1600 cm <sup>-1</sup>	1460 cm <sup>-1</sup>	1380 cm <sup>-1</sup>	1166 cm <sup>-1</sup>	1032 cm <sup>-1</sup>	969 cm <sup>-1</sup>	872 cm <sup>-1</sup>	812 cm <sup>-1</sup>	723 cm <sup>-1</sup>
2920	1.00											
2850	0.94	1.00										
1700	0.15	0.35	1.00									
1600	0.22	0.41	0.91	1.00								
1460	0.49	0.61	0.71	0.84	1.00							
1380	0.30	0.40	0.72	0.85	0.96	1.00						
1166	0.13	0.32	0.89	0.96	0.84	0.88	1.00					
1032	0.07	0.28	0.85	0.88	0.75	0.79	0.97	1.00				
969	0.12	0.30	0.86	0.92	0.83	0.88	0.99	0.98	1.00			
872	0.25	0.46	0.89	0.97	0.86	0.87	0.98	0.94	0.96	1.00		
812	0.23	0.43	0.84	0.93	0.86	0.87	0.98	0.96	0.98	0.99	1.00	
723	0.42	0.63	0.79	0.86	0.83	0.77	0.90	0.91	0.90	0.94	0.95	1.00

TABLE 6: Result of principal component analysis.

Number of principal components	Eigenvalue	Variance contribution (%)	Cumulative variance contribution (%)
1	9.319	77.658	77.658
2	1.860	15.498	93.156
3	1.017	3.508	96.664
4	0.255	2.123	98.787
5	0.081	0.677	99.464
6	0.031	0.256	99.720
7	0.019	0.159	99.879
8	0.006	0.051	99.931
9	0.004	0.033	99.964
10	0.003	0.021	99.985
11	0.002	0.013	99.998
12	0.000	0.002	100.000

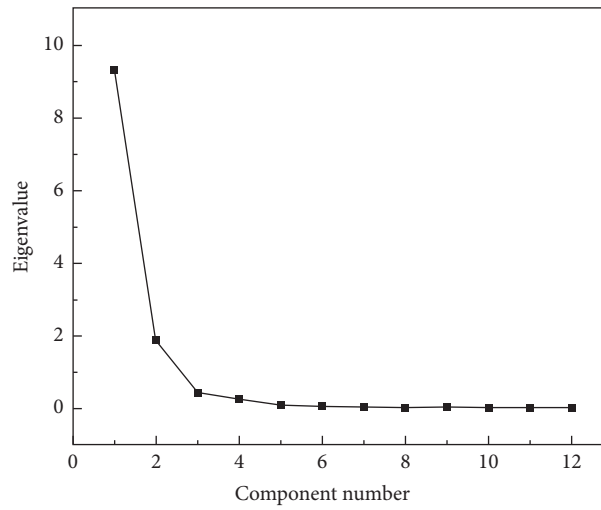


FIGURE 2: Analysis of the scree plot of principal components.

are three principal components whose eigenvalues exceed one. The first, second, and third principal components explain 77.658%, 15.498%, and 3.508% of the nature of the original variables, respectively. The cumulative variance contribution of the three principal components is 96.664% (research shows that there is a high explanation rate when the cumulative contribution is higher than 70%). It can be seen from the scree

plot (Figure 2) that the broken lines of the first three principal components are steep while later tending to become shallower. This further indicates that it is appropriate to extract the three principal components (PCA1, PCA2, and PCA3). According to the correlation coefficients between the principal component and the original variables, the principal components  $Y_1$ ,  $Y_2$ , and  $Y_3$  are separately expressed as follows:

$$Y_1 = 0.035x_1 + 0.055x_2 + 0.095x_3 + 0.103x_4 + 0.098x_5 + 0.097x_6 + 0.104x_7 + 0.100x_8 + 0.104x_9 + 0.106x_{10} + 0.106x_{11} + 0.102x_{12}, \quad (9)$$

$$Y_2 = 0.503x_1 + 0.449x_2 - 0.088x_3 - 0.056x_4 + 0.128x_5 - 0.001x_6 - 0.115x_7 - 0.138x_8 - 0.120x_9 - 0.042x_{10} - 0.049x_{11} + 0.069x_{12}, \quad (10)$$

$$Y_3 = -0.025x_1 + 0.393x_2 + 0.527x_3 + 0.049x_4 - 0.781x_5 - 0.997x_6 + 0.004x_7 + 0.305x_8 - 0.025x_9 + 0.129x_{10} + 0.069x_{11} + 0.471x_{12}, \quad (11)$$

where  $x_1, x_2, \dots, x_{12}$  represent the transmittances of CAPs at 2920, 2850, 1700, 1600, 1460, 1380, 1166, 1032, 969, 872, 812, and 723  $\text{cm}^{-1}$ , respectively.

**3.4.2. The Process and Result of Multinomial Logistic Analysis.** By substituting the transmittances of the 12 CAPs of 33 asphalt samples into formulae (9–11), the scores of the

TABLE 7: The scores of each principal component.

Asphalt number	Asphalt name <sup>2</sup>	PCA1	PCA2	PCA3
1	MM-1	-0.446	-0.840	-0.024
2	Q-1	-0.537	0.876	1.484
3	SK (BY)-1	-0.870	-0.225	-0.392
4	Q-2	-0.383	0.118	-1.233
5	SL-1	-0.986	0.240	-0.471
6	CMR-1	-1.796	0.963	-0.386
7	LH-1	-0.865	-1.151	0.438
8	QPK-1	-0.123	-0.995	-0.555
9	MM-2	-1.042	-0.455	-0.089
10	QP-1	-0.593	-1.212	-0.046
11	JB-1	-0.742	-1.037	-0.711
12	SK (XY)-1	-1.152	-0.335	0.338
13	ZH-1	-0.470	-0.919	-0.641
14	JL-1	-0.113	-0.717	-1.306
15	HR-1	-0.523	-0.757	0.423
16	AS-1	-0.316	-0.098	1.739
17	XT-1	-0.268	0.156	2.187
18	ZH-2	0.418	2.666	-0.827
19	LH-2	-0.434	2.149	-1.062
20	QL-1	-0.451	0.336	0.688
21	KL-1	0.175	-0.225	-0.545
22	KL-2	-0.153	0.221	0.312
23	SL-2	0.627	1.081	0.147
24	SK (NB)-1	-0.268	0.156	2.187
25	Q-3	0.418	2.666	-0.827
26	DSZ-1	0.175	-0.225	-0.545
27	CMR-2	-0.153	0.221	0.312
28	JB-2	1.536	-0.789	-0.679
29	ZH-3	1.626	-0.611	-1.122
30	LH-3	2.273	0.072	1.503
31	DSZ-2	1.536	-0.789	-0.679
32	SZ-1	1.626	-0.611	-1.122
33	SZ-2	2.273	0.072	1.503

<sup>2</sup>In this column, 1, 2, and 3 indicate the different sampling batches of the same asphalt.

three principal components can be calculated (Table 7). Moreover, the scores of the principal components are taken as factors, and three kinds of origins of asphalt are considered as dependent variables. Among them, the crude oil from the Bohai Rim region of China is regarded as a reference group to establish a multinomial logistic regression

model based on principal components. On this basis, the parameters of the three principal components used for the logistic regression model are obtained.

Based on the parameter from regression, the logistic regression model can be obtained as follows:

$$\begin{aligned}
 \text{logit}p_1 &= 17.130 - 40.988Y_1 + 5.758Y_2 - 1.788Y_3, \\
 \text{logit}p_2 &= 22.543 - 21.163Y_1 + 9.509Y_2 + 0.024Y_3, \\
 \text{logit}p_3 &= 0 \text{ (reference group)},
 \end{aligned}
 \tag{12}$$

where  $p_1$ ,  $p_2$ , and  $p_3$  refer to the probabilities of crude oil sources (the Middle East, South America, and Bohai Rim region of China) of asphalt and  $Y_1$ ,  $Y_2$ , and  $Y_3$  denote the first, second, and third principal components, respectively.

By substituting expressions (9), (10), and (11) into expression (12), the expression (formula (13)) for

characterising the relationship between the logistic regression model and the 12 variables can be acquired. During discrimination and prediction, the probabilities of crude oil sources of asphalt can be separately acquired by substituting the transmittances of the 12 CAPs of the asphalt. The maximum probability corresponds to the predicted origin:

TABLE 8: The test of the logistic regression model.

Test of goodness of fit	Coefficient	Chi-square	Significance level
	Pearson		5.502
	Deviance	6.078	1
Test of pseudo <i>R</i> -squared	Cox and Snell	Nagelkerke	McFadden
	0.849	0.971	0.971
Test of likelihood ratio	Parameter	Chi-square	Significance level
	B	13.521	0.001
	F1	47.335	0.000
	F2	8.554	0.014
	F3	3.389	0.042

TABLE 9: The discrimination result of multinomial logistic regression.

Observed value	Predicted value			Discrimination accuracy (%)
	Middle East	South America	Bohai Rim region of China	
Middle East	14	1	0	93.3
South America	1	11	0	91.7
Bohai Rim region of China	0	0	6	100.0
Percentage (%)	45.5	36.4	18.2	93.9

$$\begin{aligned}
\text{logit } p_1 &= 17.130 + 1.506x_1 - 0.372x_2 - 5.343x_3 - 4.632x_4 - 1.883x_5 - 2.199x_6 \\
&\quad - 4.932x_7 - 5.439x_8 - 4.909x_9 - 4.817x_{10} - 4.750x_{11} - 4.626x_{12}, \\
\text{logit } p_2 &= 22.543 + 4.042x_1 + 3.115x_2 - 2.835x_3 - 2.711x_4 - 0.876x_5 - 2.086x_6 \\
&\quad - 3.294x_7 - 3.421 - 3.343x_9 - 2.640x_{10} - 2.708x_{11} - 1.491x_{12}, \\
\text{logit } p_3 &= 0 \text{ (reference group)}.
\end{aligned} \tag{13}$$

Additionally, to validate whether the model shows adequate practical meaning, it is necessary to test the goodness of fit, pseudo *R*-squared, and likelihood ratio of the model. The tests (including the Pearson chi-square test and the deviance chi-square test) of goodness of fit can test whether the model fits the original data, or not. If the significance level exceeds 0.05, the fitting effect is favourable. The pseudo *R*-squared value can verify the degree of explanation offered by the model for information contained in its original variables, which is shown in Cox, Nagelkerke and McFadden pseudo *R*-squared values. The closer the result is to 1, the better the explanation. The likelihood ratio test measures the contribution of original variables to the model. If the significance level is lower than 0.05, the contribution of original variables is high.

According to the test result (Table 8) obtained through use of the logistic regression model, the goodness of fit, pseudo *R*-squared, and likelihood ratio of the model all satisfy test requirements. This indicates that the extracted principal components PCA1, PCA2, and PCA3 also retain key information about the data while effectively realising dimension reduction, which makes a significant contribution to the construction of the logistic regression model. The final result obtained through model regression is also meaningful.

**3.4.3. Validation of Discriminatory Effect of the Model.** By taking IR CAPs of 33 original asphalt samples as verification samples, the discrimination effect obtained through

the multinomial logistic regression model in multivariate statistical analysis was evaluated by applying formula (13). The discrimination result of multinomial logistic regression in multivariate statistical analysis is shown in Table 9.

As shown in Table 9, discrimination accuracies of 15, 12, and six asphalt samples separately produced by crude oil sourced from the Middle East, South America, and Bohai Rim region of China are 93.3%, 91.7%, and 100%, respectively. The comprehensive discrimination accuracy is 93.9%. The above result showed that multivariate logistic regression analysis based on PCA can rapidly discriminate the origins of asphalt.

## 4. Conclusions

Based on ATR-FTIR technology, the infrared spectra of 33 kinds of asphalt produced by crude oil from the Middle East, South America, and Bohai Rim region of China were collected. Furthermore, the 12 selected CAPs of infrared spectra were analysed by multivariate statistics. The comprehensive accuracy of the logistic regression model based on PCA in discriminating asphalt, which were produced by crude oil from three different regions reached 93.9%. The results indicated that the combination of ATR-IR spectral analysis and multivariate statistics can accurately and nondestructively discriminate between different crude oil source of asphalt. Moreover, the method shows some remarkable advantages, including ease of operation, rapidity, and high

accuracy, which is important when controlling the origins and quality of asphalt and improving the performance thereof.

The method provided in this paper is suitable for the oil source identification of base asphalt produced by crude oil from different regions and can also provide reference for other kinds of asphalt, such as polymer-modified asphalt. However, the accuracy and applicability of this method need to be further improved. In particular, whether the asphalt produced by crude oil mixing from different regions can be effectively identified needs further research.

## Data Availability

The data used to support the findings of this study are available from the corresponding author upon request.

## Conflicts of Interest

The authors declare that they have no conflicts of interest.

## Acknowledgments

This work was financially supported by the National Natural Science Foundation of China (no. 51608511), Key R&D Project of Shandong Province (2018GGX105013), and Project of Science and Technology Support for Youth Entrepreneurship in Colleges and Universities of Shandong Province (2019KJG004). The authors would like to acknowledge many coworkers, students, and laboratory assistants for providing technical help on instrument analysis.

## References

- [1] S. Zhao and J. Liu, "Using recycled asphalt pavement in construction of transportation infrastructure: Alaska experience," *Journal of Cleaner Production*, vol. 177, pp. 155–168, 2018.
- [2] Y. Tan and M. Guo, "Using surface free energy method to study the cohesion and adhesion of asphalt mastic," *Construction and Building Materials*, vol. 47, pp. 254–260, 2013.
- [3] P. Li, J. Liu, and S. Zhao, "Implementation of stress-dependent resilient modulus of asphalt-treated base for flexible pavement design," *International Journal of Pavement Engineering*, vol. 19, no. 5, pp. 439–446, 2018.
- [4] F. C. G. Martinho and J. P. S. Farinha, "An overview of the use of nanoclay modified bitumen in asphalt mixtures for enhanced flexible pavement performances," *Road Materials and Pavement Design*, vol. 20, no. 3, pp. 671–701, 2019.
- [5] F. Xiao, D. Ma, J. Wang, D. Cai, L. Lou, and J. Yuan, "Impacts of high modulus agent and anti-rutting agent on performances of airfield asphalt pavement," *Construction and Building Materials*, vol. 204, pp. 1–9, 2019.
- [6] Y. Sun, W. Wang, and J. Chen, "Investigating impacts of warm-mix asphalt technologies and high reclaimed asphalt pavement binder content on rutting and fatigue performance of asphalt binder through MSCR and LAS tests," *Journal of Cleaner Production*, vol. 219, pp. 879–893, 2019.
- [7] M. Guo, Y. Tan, D. Luo et al., "Effect of recycling agents on rheological and micromechanical properties of SBS-modified asphalt binders," *Advances in Materials Science and Engineering*, vol. 2018, Article ID 5482368, 12 pages, 2018.
- [8] W. Y. Fan, X. Xin, M. Liang et al., "Study on rheology and storage stability of modified asphalt," *Journal of China University of Petroleum*, vol. 39, pp. 165–170, 2015.
- [9] M. Lagos-Varas, D. Movilla-Quesada, J. P. Arenas et al., "Study of the mechanical behavior of asphalt mixtures using fractional rheology to model their viscoelasticity," *Construction and Building Materials*, vol. 200, pp. 124–134, 2019.
- [10] P. Wang, Z. J. Dong, Y. Q. Tan et al., "Effect of multi-walled carbon nanotubes on the performance of styrene-butadiene-styrene copolymer modified asphalt," *Materials and Structures*, vol. 50, no. 1, p. 17, 2017.
- [11] M. Guo, Y. Tan, L. Wang, and Y. Hou, "Diffusion of asphaltene, resin, aromatic and saturate components of asphalt on mineral aggregates surface: molecular dynamics simulation," *Road Materials and Pavement Design*, vol. 18, no. 3, pp. 149–158, 2017.
- [12] Y. Xue, Z. Ge, F. Li, S. Su, and B. Li, "Modified asphalt properties by blending petroleum asphalt and coal tar pitch," *Fuel*, vol. 207, pp. 64–70, 2017.
- [13] V. Y. Pivsaev, P. E. Krasnikov, A. A. Pimenov, and D. E. Bykov, "Enhancement of adhesive properties of road asphalts, waste oil processing products," *Petroleum Chemistry*, vol. 55, no. 1, pp. 80–83, 2015.
- [14] M. N. Siddiqui, "NMR fingerprinting of chemical changes in asphalt fractions on oxidation," *Petroleum Science and Technology*, vol. 28, no. 4, pp. 401–411, 2010.
- [15] M. N. Siddiqui, "NMR finger printing of chemical changes in asphalt fractions on oxidation," *Petroleum Science and Technology*, vol. 27, no. 17, pp. 2033–2045, 2009.
- [16] R. Ren, K. Han, P. Zhao et al., "Identification of asphalt fingerprints based on ATR-FTIR spectroscopy and principal component-linear discriminant analysis," *Construction and Building Materials*, vol. 198, pp. 662–668, 2019.
- [17] C. M. Xu, Y. Liu, S. Q. Zhao et al., "Analysis of heteroatomic compounds in petroleum asphaltene by high resolution mass spectrometry," *Journal of China University of Petroleum*, vol. 37, pp. 190–195, 2013.
- [18] Q. F. Wu and Z. C. Tang, "Study on the determinants of economic compensation for ecological damage caused by oil spill at sea," *Journal of China University of Petroleum*, vol. 34, pp. 1–8, 2018.
- [19] Y. Zhong, H. Wang, G. Lu, Z. Zhang, Q. Jiao, and Y. Liu, "Detecting functional connectivity in fMRI using PCA and regression analysis," *Brain Topography*, vol. 22, no. 2, pp. 134–144, 2009.
- [20] M. Kharbach, R. Kamal, M. A. Mansouri et al., "Selected-ion flow-tube mass-spectrometry (SIFT-MS) fingerprinting versus chemical profiling for geographic traceability of Moroccan argan oils," *Food Chemistry*, vol. 263, pp. 8–17, 2018.
- [21] P. Y. Zhou, C. S. Chen, J. J. Ye et al., "Combining molecular fingerprints with multidimensional scaling analyses to identify the source of spilled oil from highly similar suspected oils," *Marine Pollution Bulletin*, vol. 93, no. 1-2, pp. 121–129, 2015.
- [22] A. Ismail, M. E. Toriman, H. Juahir et al., "Chemometric techniques in oil classification from oil spill fingerprinting," *Marine Pollution Bulletin*, vol. 111, no. 1-2, pp. 339–346, 2016.
- [23] J. M. Bayona, C. Domínguez, and J. Albaigés, "Analytical developments for oil spill fingerprinting," *Trends in Environmental Analytical Chemistry*, vol. 5, pp. 26–34, 2015.
- [24] E. C. Y. Chan, P. K. Koh, M. Mal et al., "Metabolic profiling of human colorectal cancer using high-resolution magic angle spinning nuclear magnetic resonance (HR-MAS NMR) spectroscopy and gas chromatography mass spectrometry



- (GC/MS),” *Journal of Proteome Research*, vol. 8, no. 1, pp. 352–361, 2009.
- [25] Y. Li, S. Wu, and S. Amirkhanian, “Investigation of the graphene oxide and asphalt interaction and its effect on asphalt pavement performance,” *Construction and Building Materials*, vol. 165, pp. 572–584, 2018.
- [26] G. Xu and H. Wang, “Molecular dynamics study of oxidative aging effect on asphalt binder properties,” *Fuel*, vol. 188, pp. 1–10, 2017.
- [27] N. Nciri and N. Cho, “A thorough study on the molecular weight distribution in natural asphalts by gel permeation chromatography (GPC): the case of Trinidad lake asphalt and asphalt ridge bitumen,” *Materials Today: Proceedings*, vol. 5, no. 11, pp. 23656–23663, 2018.
- [28] D. O. Larsen, J. L. Alessandrini, A. Bosch, and M. S. Cortizo, “Micro-structural and rheological characteristics of SBS-asphalt blends during their manufacturing,” *Construction and Building Materials*, vol. 23, no. 8, pp. 2769–2774, 2009.
- [29] H. Yao, Q. Dai, and Z. You, “Fourier transform infrared spectroscopy characterization of aging-related properties of original and nano-modified asphalt binders,” *Construction and Building Materials*, vol. 101, pp. 1078–1087, 2015.
- [30] F. Zhang, J. Yu, and J. Han, “Effects of thermal oxidative ageing on dynamic viscosity, TG/DTG, DTA and FTIR of SBS-and SBS/sulfur-modified asphalts,” *Construction and Building Materials*, vol. 25, no. 1, pp. 129–137, 2011.
- [31] A. Dazzi, C. B. Prater, Q. Hu, D. B. Chase, J. F. Rabolt, and C. Marcott, “AFM-IR: combining atomic force microscopy and infrared spectroscopy for nanoscale chemical characterization,” *Applied Spectroscopy*, vol. 66, no. 12, pp. 1365–1384, 2012.
- [32] M. Lopes, V. Mouillet, L. Bernucci, and T. Gabet, “The potential of attenuated total reflection imaging in the mid-infrared for the study of recycled asphalt mixtures,” *Construction and Building Materials*, vol. 124, pp. 1120–1131, 2016.
- [33] Y. Xiong, G. Chen, S. Guo, and G. Li, “Lifetime prediction of NBR composite sheet in aviation kerosene by using nonlinear curve fitting of ATR-FTIR spectra,” *Journal of Industrial and Engineering Chemistry*, vol. 19, no. 5, pp. 1611–1616, 2013.
- [34] G. Y. Chen and S. E. Qian, “Denoising of hyperspectral imagery using principal component analysis and wavelet shrinkage,” *IEEE Transactions on Geoscience and Remote Sensing*, vol. 49, no. 3, pp. 973–980, 2010.
- [35] S. Tonidandel and J. M. LeBreton, “Determining the relative importance of predictors in logistic regression: an extension of relative weight Analysis,” *Organizational Research Methods*, vol. 13, no. 4, pp. 767–781, 2010.
- [36] R. Azen and N. Traxel, “Using dominance analysis to determine predictor importance in logistic regression,” *Journal of Educational and Behavioral Statistics*, vol. 34, no. 3, pp. 319–347, 2009.
- [37] J. Adler and I. Parmryd, “Quantifying colocalization by correlation: the Pearson correlation coefficient is superior to the Mander’s overlap coefficient,” *Cytometry Part A*, vol. 77A, no. 8, pp. 733–742, 2010.
- [38] A. Soberón and W. Stute, “Assessing skewness, kurtosis and normality in linear mixed models,” *Journal of Multivariate Analysis*, vol. 161, pp. 123–140, 2017.
- [39] A. D. Ho and C. C. Yu, “Descriptive statistics for modern test score distributions,” *Educational and Psychological Measurement*, vol. 75, no. 3, pp. 365–388, 2015.

## Research Article

# Micromechanical Prediction Model of Viscoelastic Properties for Asphalt Mastic Based on Morphologically Representative Pattern Approach

Zhichen Wang,<sup>1</sup> Naisheng Guo ,<sup>1</sup> Xu Yang ,<sup>2</sup> and Shuang Wang<sup>3</sup>

<sup>1</sup>School of Transportation Engineering, Dalian Maritime University, Dalian 116026, Liaoning, China

<sup>2</sup>Department of Civil and Environmental Engineering, Michigan Technological University, Houghton, MI 49931-1295, USA

<sup>3</sup>School of Computer Science, Lyceum of the Philippines University, Manila, Batangas 4200, Philippines

Correspondence should be addressed to Naisheng Guo; [naishengguo@dlnu.edu.cn](mailto:naishengguo@dlnu.edu.cn)

Received 16 April 2020; Accepted 3 June 2020; Published 28 June 2020

Guest Editor: Meng Guo

Copyright © 2020 Zhichen Wang et al. This is an open access article distributed under the Creative Commons Attribution License, which permits unrestricted use, distribution, and reproduction in any medium, provided the original work is properly cited.

This paper is devoted to the introduction of physicochemical, filler size, and distribution effect in micromechanical predictions of the overall viscoelastic properties of asphalt mastic. In order to account for the three effects, the morphologically representative pattern (MRP) approach was employed. The MRP model was improved due to the arduous practical use of equivalent modulus formula solution. Then, a homogeneous morphologically representative model (H-MRP) with the explicit solution was established based on the homogenization theory. Asphalt mastic is regarded as a composite material consisting of filler particles coated structural asphalt and free asphalt considering the physicochemical effect. An additional interphase surrounding particles was introduced in the H-MRP model. Thus, a modified H-MRP model was established. Using the proposed model, a viscoelastic equation was derived to predict the complex modulus and subsequently the dynamic modulus of asphalt mastic based on the elastic-viscoelastic correspondence principle. The dynamic shear rheological tests were conducted to verify the prediction model. The results show that the predicted modulus presents an acceptable precision for asphalt mastic mixed with 10% and 20% fillers volume fraction, as compared to the measured ones. The predicted modulus agrees reasonably well with the measured ones at high frequencies for asphalt mastic mixed with 30% and 40% fillers volume fraction. However, it exhibits underestimated modulus at low frequencies. The reasons for the discrepancy between predicted and measured dynamic shear modulus and the factors affecting the dynamic shear modulus were also explored in the paper.

## 1. Introduction

Asphaltic material is a typical rheological material. Asphalt mastic is regarded as a composite material consisting of asphalt and fillers, which plays an essential role in the binding between aggregates in asphalt mixture. Dynamic shear modulus is the leading indicator to evaluate the viscoelastic properties of asphalt mastic. A large number of dynamic shear rheological tests have been conducted to explore the influence of different asphalt and fillers on the dynamic shear modulus of asphalt mastic [1–3]. However, plenty of factors are influencing the viscoelastic properties of asphalt mastic, and it is unrealistic and uneconomic to analyze these factors through a large amount of tests. Thus, it

is necessary to propose the prediction methods that can be used to obtain the dynamic shear modulus of asphalt mastic.

The empirical prediction models were proposed under the support of NCHRP, including the Witczak 1–37A model, improved Witczak model, and NCHRP 1–40D model [4–6]. In order to provide the parameters of asphalt binder for the prediction model of asphalt mixtures, an empirical prediction model for the dynamic shear modulus of asphalt binder was established by Bari and Witczak [7]. However, the model was adopted under specific conditions in the United States, and it may not be applicable in other regions. Therefore, it is necessary to get rid of the empirical method and predict the macroscopic properties from the volume and mechanical properties of the components. The

micromechanics method of composite materials provides a reliable method for this work.

The classical micromechanical methods of composite materials, including composite sphere model [8], self-consistent model [9], generalized self-consistent model (Christensen Lo model) [10], and Mori Tanaka method [11], have been widely used in the equivalent properties prediction of the particle and fiber-reinforced composite materials. Some scholars applied these classical micromechanical methods to establish the micromechanical model of asphalt mixtures. Pang et al. utilized a composite sphere model to predict the elastic modulus of the asphalt mixture [12]. Luo et al. adopted the self-consistent model and generalized self-consistent model to predict the dynamic modulus of the asphalt mixture [13, 14]. Zhu et al. presented a micromechanical model considering the effect of the interface between asphalt and aggregate [15, 16].

Asphalt mastic was considered as a known matrix in the above prediction models. The modulus test of asphalt mastic should be conducted repeatedly to provide the input parameters for the models due to the variety of the fillers concentration. Therefore, it is also necessary to establish the micromechanical model of asphalt mastic. Asphalt mastic is regarded as a composite material composed of spherical filler particles embedded in asphalt binder. A lot of different methods have been presented to establish the micromechanical model of asphalt mastic. Yin et al. applied four micromechanics methods, that is, dilution model, self-consistent model, generalized self-consistent model, and Mori Tanaka method, to predict the dynamic shear modulus of asphalt mastic [17]. Underwood and Kim presented 12 existing micromechanical methods to predict the dynamic shear modulus of asphalt mastic [18]. However, the results show that the micromechanical model considerably underestimates the viscoelastic properties of asphalt mastic.

The percolation effect of fillers and asphalt is considered by Shashidhar and Shenoy [19]. There is an increasing probability of the particles touching one another and the filler becoming percolated; then a modified method was proposed for the prediction model by percolation theory. They use the calculation to suggest that percolation phenomenon onset occurs at 2%–10%. However, the mechanical data compiled by multiple scholars suggest that a filler concentration of approximately 42% is more appropriate for asphalt mastics [20–22]. Li et al. utilized Ju-Chen model to predict the dynamic shear modulus of asphalt mastic considering the interparticle interaction [23]. However, the interaction between fillers is difficult to measure, and it is not easy to judge whether it actually occurred. Therefore, it is necessary to ascertain the interior structural components and interaction mechanism of asphalt mastic and to establish a targeted micromechanical model.

An experiment was conducted by Davis and Castorena using atomic force microscopy [24]. The microscopic variation of asphalt near the filler particle surface was founded, which indicated that the physicochemical effect has occurred between the fillers and asphalt. The physicochemical process of selective adsorption of the asphalt binder compounds by

the aggregate particles occurring in asphaltic composites is also widely reported [25–27]. A structural asphalt layer will be formed on the surface of the fillers under the physicochemical effect; thus, a four-phase micromechanical model of asphalt mastic was proposed by Underwood and Kim [18]. The model is based on the classical n-layer sphere model derived from point-approaches, according to which the Representative Volume Element (RVE) is defined through some statistical information on points belonging to such or such phase. It is meaningless to endow them with any individual geometrical or physical specific property of these phase elements, such as their size, their mutual distances, or their superficial area. Thus, the influence of the particle size and distribution of fillers were not taken into consideration in the four-phase micromechanical model.

In order to consider the distribution and size effects in micromechanical predictions model, a morphologically representative pattern (MRP) approach has been proposed for composite materials [28, 29], which could be applied for asphalt mastic. The objective of this paper strives to establish a new micromechanical model considering the physicochemical, filler size, and distribution effect based on the MRP approach. The new proposed model is used to predict the dynamic shear modulus of asphalt mastic, and the prediction results were compared with the experiment results of the asphalt mastic with different filler volume fractions to validate its applicability. In additions, the influence of model parameters on the prediction results is also analyzed.

## 2. Micromechanical H-MRP Model

Marcadon et al. proposed a morphology representative pattern (MRP) model considering distribution and size effects in micromechanical predictions of the overall elastic moduli of particulate composite materials [28]. The composition of MRP model comes from the composite sphere model [8]. However, the spherical particles with different particle sizes are replaced by a series of spherical particles with the same particle size. The MRP model consists of matrix-coated spheres (two-phase pattern) and the remaining matrix (pure matrix pattern); see Figure 1.

The far-field uniform strain of two patterns is equal to the total strain,  $\langle \epsilon \rangle = \mathbf{E}$ . Marcadon et al. obtained the equivalent modulus solution formula of the MRP model characterized by nonlinear equations [28]. Although mathematical software such as Mathematica can be used for auxiliary calculation, some negative solutions appear frequently, which make it difficult to be applied. The homogenization method is employed to improve the MRP model. The two-phase pattern in the MRP model is homogenized into an equivalent medium by using the generalized self-consistent method. Subsequently, the medium is put into the remaining matrix. The self-consistent method is applied for homogenization into the equivalent composite material. Thus, an improved model is established, called homogenized MRP model (H-MRP), as shown in Figure 2.

According to the MRP approach, each pattern consists of one particle surrounded by a concentric shell of the matrix of variable thickness depending on the packing density, with an

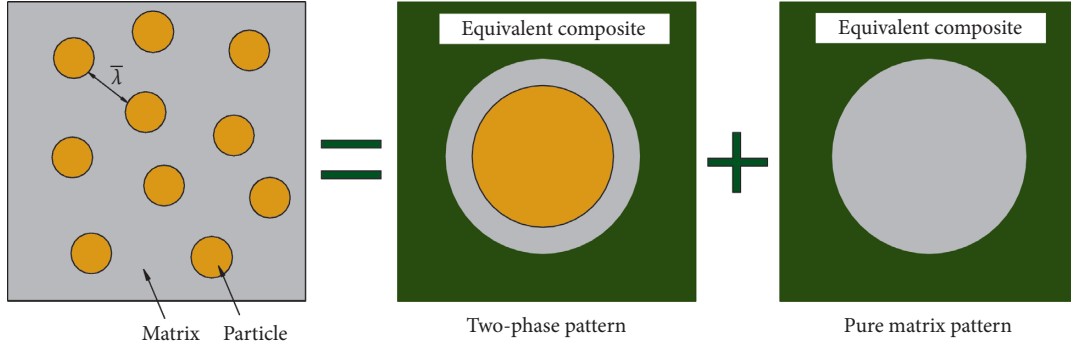


FIGURE 1: MRP model.

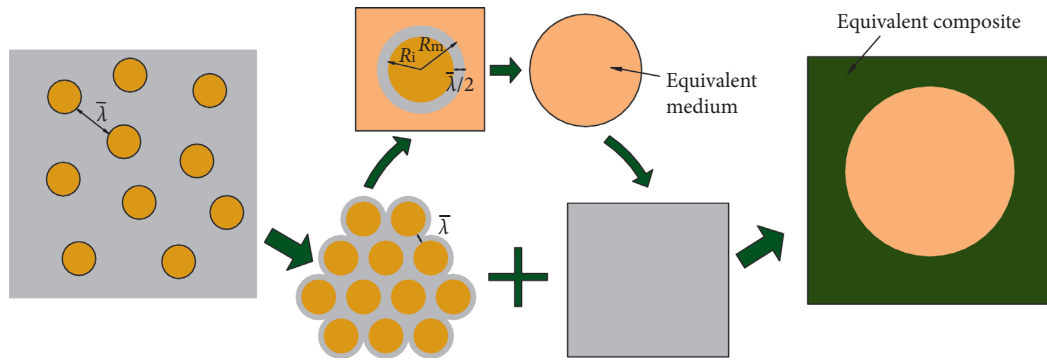


FIGURE 2: Homogenized MRP model (H-MRP model).

additional pattern of the residual pure matrix. The shell thickness may then be correlated with the mean distance between nearest-neighbor particles, say  $\bar{\lambda}$ . The first two patterns are made of two concentric spheres, with a particle at the core and a shell, with the thickness  $R_m - R_i = (\bar{\lambda}/2)$ , constituted with the pure matrix. Therefore, the volume fraction of particles in the two-pattern approach  $c_i$  is calculated as

$$c_i = \frac{f_i}{c_H} = \frac{R_i^3}{R_m^3} = \frac{R_i^3}{(R_i + (\bar{\lambda}/2))^3} = \frac{1}{(1 + (\bar{\lambda}/(2R_i))^3)} \quad (1)$$

where  $f_i$  is the volume fraction of inclusions;  $c_H$  is the volume fraction of two-phase pattern;  $R_i$  and  $R_m$  are the particle and matrix radius, respectively. From equation (1), it is apparent already that the effective properties simultaneously depend on the particle size  $R_i$  and on the mean distance  $\bar{\lambda}$  through the ratios  $(\bar{\lambda}/(2R_i))$ , so that  $(\bar{\lambda}/(2R_i))$  is defined as the particle distribution coefficient. It is an important parameter reflecting particle distribution characteristics.

According to the composite sphere (CS) model [8], the bulk modulus of the equivalent medium  $K_H$  can be obtained by

$$K_H = K_m + \frac{c_i(K_i - K_m)(3K_m + 4G_m)}{3K_m + 4G_m + 3(1 - c_i)(K_i - K_m)} \quad (2)$$

where  $K_i$  and  $K_m$  are the bulk moduli of inclusions and matrix, respectively;  $G_m$  is the shear modulus of the matrix.

According to the generalized self-consistent (GSC) model [10], the shear modulus of the equivalent medium  $G_H$  is given by

$$A\left(\frac{G_H}{G_m}\right)^2 + 2B\left(\frac{G_H}{G_m}\right) + C = 0, \quad (3)$$

where  $A$ ,  $B$ , and  $C$  are functions related to the modulus and volume fraction of particles and matrix, expressed as

$$\begin{aligned} A &= 8\left(\frac{G_i}{G_m} - 1\right)(4 - 5\nu_m)\eta_1 c_i^{10/3} \\ &\quad - 2\left[63\left(\frac{G_i}{G_m} - 1\right)\eta_2 + 2\eta_1\eta_3\right]c_i^{7/3} + 252\left(\frac{G_i}{G_m} - 1\right)\eta_2 c_i^{5/3} \\ &\quad - 50\left(\frac{G_i}{G_m} - 1\right)(7 - 12\nu_m + 8\nu_m^2)\eta_2 c_i + 4(7 - 10\nu_m)\eta_2\eta_3, \end{aligned} \quad (4)$$

$$\begin{aligned} B &= -2\left(\frac{G_i}{G_m} - 1\right)(1 - 5\nu_m)\eta_1 c_i^{10/3} \\ &\quad + 2\left[63\left(\frac{G_i}{G_m} - 1\right)\eta_2 + 2\eta_1\eta_3\right]c_i^{7/3} - 252\left(\frac{G_i}{G_m} - 1\right)\eta_2 c_i^{5/3} \\ &\quad + 75\left(\frac{G_i}{G_m} - 1\right)(3 - \nu_m)\eta_2 \nu_m c_i + \frac{3}{2}(15\nu_m - 7)\eta_2\eta_3, \end{aligned} \quad (5)$$

$$C = 4 \left( \frac{G_i}{G_m} - 1 \right) (5\nu_m - 7) \eta_1 c_i^{10/3} - 2 \left[ 63 \left( \frac{G_i}{G_m} - 1 \right) \eta_2 + 2\eta_1 \eta_3 \right] c_i^{7/3} + 252 \left( \frac{G_i}{G_m} - 1 \right) \eta_2 c_i^{5/3} + 25 \left( \frac{G_i}{G_m} - 1 \right) (\nu_m^2 - 7) \eta_2 c_i - (7 + 5\nu_m) \eta_2 \eta_3, \quad (6)$$

$$\eta_1 = (49 - 50\nu_i \nu_m) \left( \frac{G_i}{G_m} - 1 \right) + 35 \left[ \frac{G_i}{G_m} (\nu_i - 2\nu_m) + (2\nu_i - \nu_m) \right], \quad (7)$$

$$\eta_2 = 5\nu_i \left( \frac{G_i}{G_m} - 8 \right) + 7 \left( \frac{G_i}{G_m} + 4 \right), \quad (8)$$

$$\eta_3 = \frac{G_i}{G_m} (8 - 10\nu_m) + (7 - 5\nu_m), \quad (9)$$

where  $\nu_m$  is Poisson's ratio of the matrix.

The equivalent shear modulus can be written in an explicit expression as

$$G_H = \frac{\sqrt{B^2 - AC} - B}{A} G_m. \quad (10)$$

The equivalent medium is embedded in the remaining matrix. From equation (1), the volume fraction of equivalent medium  $c_H$  is given by

$$c_H = \frac{f_i}{c_i} = f_i \left( 1 + \frac{\bar{\lambda}}{2R_i} \right)^3. \quad (11)$$

According to the self-consistent (SC) model [9], the bulk modulus  $K_c$  and shear modulus  $G_c$  of the composite can be obtained as follows:

$$K_c = K_m + \frac{c_H (K_H - K_m) (3K_c + 4G_c)}{3K_H + 4G_c}, \quad (12)$$

$$G_c = G_m + \frac{5c_H G_c (G_H - G_m) (3K_c + 4G_c)}{3K_c (3G_c + 2G_H) + 4G_c (2G_c + 3G_H)}. \quad (13)$$

It can be found that the explicit expressions of the GSC model and SC model are used to obtain the equivalent modulus of the composite, which is convenient for engineering application.

The spherical particles and the matrix in the composite are regarded as elastic materials. Let Young's modulus ratio

$(E_i/E_m) = 10$  and Poisson's ratio  $\nu_i = \nu_m = 0.3$ ; the MRP model was employed to predict the equivalent modulus of composite with different particle distribution coefficient by Majewski et al. [29]. The predicted results of H-MRP model are obtained by using the same model parameters as the MRP model. The comparison results are shown in Figures 3(a) and 3(b).

It can be seen from Figure 3 that the prediction results of H-MRP model proposed in this study are consistent with the MRP model. The predicted modulus of the H-MRP model is between the GSC model and SC model. Since the predicted results of the H-MRP model are related to the mean minimum distance between nearest-neighbor particles  $\bar{\lambda}$ , there are two limit cases: (1) When  $\bar{\lambda} = 0$ , the thickness of the particle-coated matrix layer in the composite sphere is 0. The equivalent material is still spherical particles after homogenization, which is equivalent to the self-consistent model. Therefore, the upper limit of the H-MRP model is the SC model. (2) When the particles in the composite sphere coated the overall matrix, there is no remaining matrix, expressed as

$$\frac{\bar{\lambda}}{(2R_i)} = f_i^{-(1/3)} - 1. \quad (14)$$

It is equivalent to the GSC model, so the lower limit of the H-MRP model is the GSC model.

### 3. Micromechanical Model of Asphalt Mastic considering the Physicochemical Effect

A structural asphalt layer on the surface of fillers should be produced by physicochemical interaction between asphalt and fillers, and the outside of it is a free asphalt layer without physicochemical effect. Therefore, it is proposed to transform the two-phase pattern of spherical filler particles coated asphalt in H-MRP model into a three-phase pattern of fillers coated structural and free asphalt. The modified H-MRP model is shown in Figure 4.

When studying distribution effects in Section 2, we already noticed (see Figure 2) that a GSC model and SC model are chosen. A similar conclusion can be drawn with the 4-phase model [30] when coated particles are dealt with (see Figure 4). Let  $R_1$ ,  $R_2$ , and  $R_3$  be, respectively, the radii of the three different spheres in the composite sphere in Figure 4, by beginning the numbering from the center of the composite sphere.

The effective moduli  $K_{\text{eff}}$  and  $G_{\text{eff}}$  of the equivalent medium are then determined from equations (46) and (51) of Herve and Zaoui [30].

$$K_{\text{eff}} = K_3 + \frac{(3K_3 + 4G_3)R_2^3 [(K_1 - K_2)R_1^3 (3K_3 + 4G_2) + (K_2 - K_3)R_2^3 (3K_1 + 4G_2)]}{3(K_2 - K_1)R_1^3 [R_2^3 (3K_3 + 4G_2) + 4R_3^3 (G_3 - G_2)] + (3K_1 + 4G_2)R_2^3 [3R_2^3 (K_3 - K_2) + R_3^3 (3K_3 + 4G_3)]}, \quad (15)$$

$$G_{\text{eff}} = \frac{\sqrt{B'^2 - A'C' - B'}}{A'} G_3, \quad (16)$$

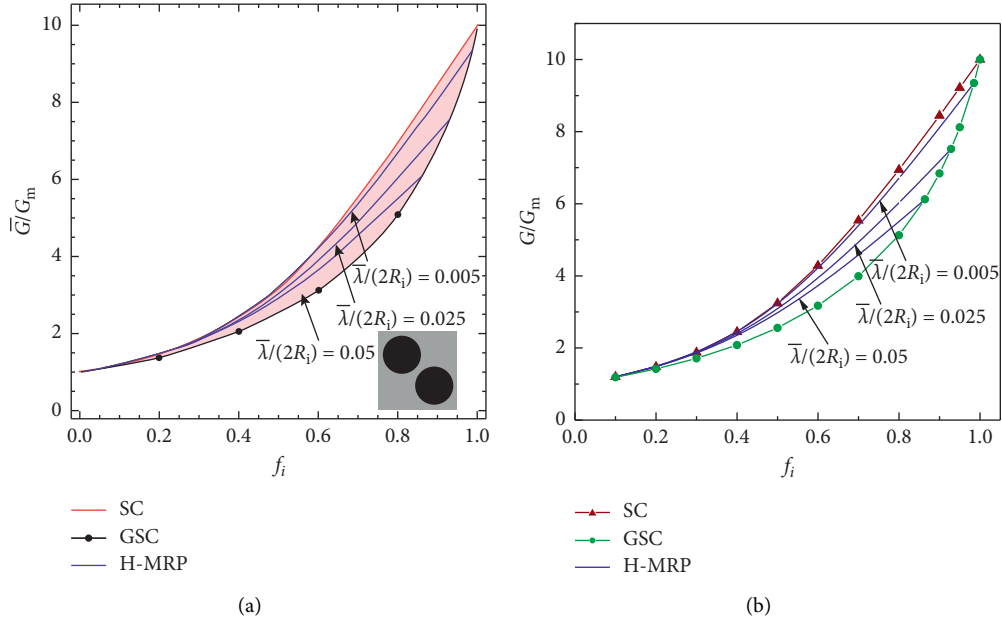


FIGURE 3: Predicted results of the micromechanical model under different particle distribution coefficients. (a) MRP model [29]. (b) H-MRP model

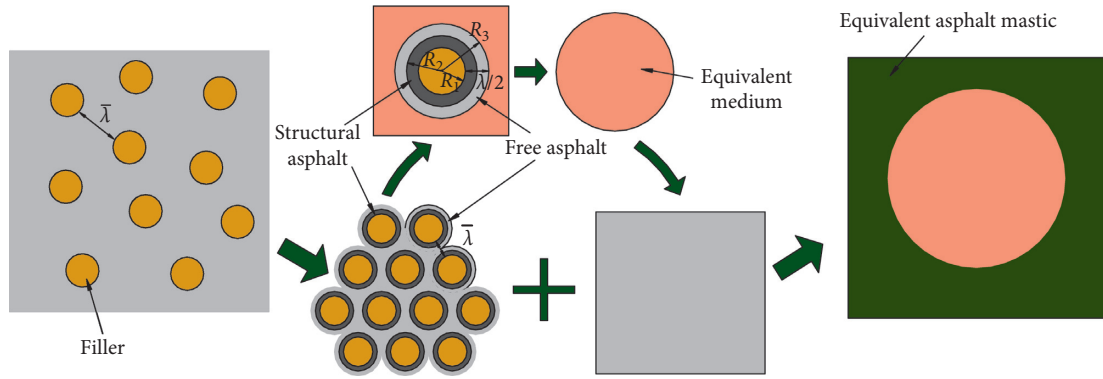


FIGURE 4: Modified H-MRP model.

where  $R_1$ ,  $R_2$ , and  $R_3$  are the radii of fillers, structural asphalt, and free asphalt, respectively.  $A'$ ,  $B'$ , and  $C'$  are given by

$$\begin{aligned}
 A' &= 4R_3^{10}(1-2\nu_3)(7-10\nu_3)Z_{12} + 20R_3^7(7-12\nu_3+8\nu_3^2)Z_{42} \\
 &+ 12R_3^5(1-2\nu_3)(Z_{14}-7Z_{23}) \\
 &+ 20R_3^3(1-2\nu_3)^2Z_{13} + 16(4-5\nu_3)(1-2\nu_3)Z_{43},
 \end{aligned} \quad (17)$$

$$\begin{aligned}
 B' &= 3R_3^{10}(1-2\nu_3)(15\nu_3-7)Z_{12} + 60R_3^7(\nu_3-3)\nu_3Z_{42} \\
 &- 24R_3^5(1-2\nu_3)(Z_{14}-7Z_{23}) \\
 &- 40R_3^3(1-2\nu_3)^2Z_{13} - 8(1-5\nu_3)(1-2\nu_3)Z_{43},
 \end{aligned} \quad (18)$$

$$\begin{aligned}
 C' &= -R_3^{10}(1-2\nu_3)(7+5\nu_3)Z_{12} + 10R_3^7(7-\nu_3^2)\nu_3Z_{42} \\
 &+ 12R_3^5(1-2\nu_3)(Z_{14}-7Z_{23}) \\
 &+ 20R_3^3(1-2\nu_3)^2Z_{13} - 8(7-5\nu_3)(1-2\nu_3)Z_{43},
 \end{aligned} \quad (19)$$

$$Z_{\alpha\beta} = \bar{P}_{\alpha 1}^{(2)}\bar{P}_{\beta 2}^{(2)} - \bar{P}_{\beta 1}^{(2)}\bar{P}_{\alpha 2}^{(2)}, \quad (20)$$

$$\mathbf{P}^{(n)} = \prod_{k=1}^n \mathbf{M}^{(k)}, \quad (21)$$

$$\mathbf{M}^{(k)} = \mathbf{L}_{k+1}^{-1}(R_k)\mathbf{L}_k(R_k), \quad (22)$$

with

$$\mathbf{L}_k(r) = \begin{bmatrix} r & \frac{6\nu_k}{1-2\nu_k}r^3 & \frac{3}{r^4} & \frac{5-4\nu_k}{1-2\nu_k}\frac{1}{r^2} \\ r & \frac{7-4\nu_k}{1-2\nu_k}r^3 & \frac{2}{r^4} & \frac{2}{r^2} \\ G_k & \frac{3\nu_k}{1-2\nu_k}G_k r^2 & \frac{12}{r^5}G_k & \frac{2(\nu_i-5)}{1-2\nu_k}\frac{G_k}{r^3} \\ G_k & \frac{7+2\nu_k}{1-2\nu_k}G_k r^2 & \frac{8}{r^5}G_k & \frac{2(1+\nu_k)}{1-2\nu_k}\frac{G_k}{r^3} \end{bmatrix}. \quad (23)$$

The viscoelastic properties of the equivalent medium can be directly converted from the elastic solutions from the micromechanical models using the elastic-viscoelastic correspondence principle. The correspondence principle states that the effective complex material properties for a viscoelastic material can be obtained by replacing the elastic material properties by the Laplace transformed material properties [31, 32]. It is reasonable to assume that structural asphalt and free asphalt are viscoelastic, while fillers are elastic. Based on the elastic-viscoelastic correspondence principle, equations (15) and (16) can be expressed in the frequency domain as follows:

$$K_{\text{eff}}^* = K_3^* + \frac{(3K_3^* + 4G_3^*)R_2^3[(K_1 - K_2^*)R_1^3(3K_3^* + 4G_2^*) + (K_2^* - K_3^*)R_2^3(3K_1 + 4G_2^*)]}{3(K_2^* - K_1)R_1^3[R_2^3(3K_3^* + 4G_2^*) + 4R_3^3(G_3^* - G_2^*)] + (3K_1 + 4G_2^*)R_2^3[3R_2^3(K_3^* - K_2^*) + R_3^3(3K_3^* + 4G_3^*)]}, \quad (24)$$

$$G_{\text{eff}}^* = \frac{\sqrt{B''^2 - A''C''} - B''}{A''}G_3^*, \quad (25)$$

where  $K_{\text{eff}}^*$  and  $G_{\text{eff}}^*$  are the complex moduli of the equivalent medium.  $K_2^*$ ,  $G_2^*$ ,  $K_3^*$ , and  $G_3^*$  are the complex moduli of the structural asphalt and free asphalt, respectively.  $A''$ ,  $B''$ , and  $C''$  are derived from equations (17) to (23) by replacing  $G_k$  by  $G_k^*$  and  $\nu_k$  by  $\nu_k^*$ .

From equations (12) and (13), the complex bulk modulus  $K_{\text{ms}}^*$  and complex shear modulus  $G_{\text{ms}}^*$  of asphalt mastic are given by

$$K_{\text{ms}}^* = K_3^* + \frac{c_{\text{eff}}(K_{\text{eff}}^* - K_3^*)(3K_{\text{ms}}^* + 4G_{\text{ms}}^*)}{3K_{\text{eff}}^* + 4G_{\text{ms}}^*}, \quad (26)$$

$$G_{\text{ms}}^* = G_3^* + \frac{5c_{\text{eff}}G_{\text{ms}}^*(G_{\text{eff}}^* - G_3^*)(3K_{\text{ms}}^* + 4G_{\text{ms}}^*)}{3K_{\text{ms}}^*(3G_{\text{ms}}^* + 2G_{\text{eff}}^*) + 4G_{\text{ms}}^*(2G_{\text{ms}}^* + 3G_{\text{eff}}^*)}, \quad (27)$$

where  $c_{\text{eff}}$  is the volume fraction of equivalent medium, calculated as

$$c_{\text{eff}} = \frac{f_1}{c_1} = f_1 \left[ 1 + \left( \frac{\bar{\lambda}}{(2R_1)^3} \right) \right], \quad (28)$$

where  $f_1$  is the volume fraction of fillers in asphalt mastic;  $c_1$  is the volume fraction of fillers in three-phase pattern.

The storage modulus  $G'$  and loss modulus  $G''$  of asphalt mastic are calculated from equations (26) and (27) by using the complex modulus relation  $G^* = G' + iG''$ . The dynamic shear modulus of asphalt mastic  $|G^*|$  is calculated as

$$|G^*| = \sqrt{(G')^2 + (G'')^2}. \quad (29)$$

#### 4. Viscoelastic Properties Prediction and Validation for Asphalt Mastic

The dynamic shear modulus of asphalt mastic with different filler volume fractions was collected from the literature reported by Underwood and Kim [18]. The volume fractions

of fillers are, respectively, 10% (MS10), 20% (MS20), 30% (MS30), and 40% (MS40). Based on the time-temperature equivalence principle, the master curves of the dynamic shear modulus of asphalt mastic  $|G_{\text{ms}}^*|$  are shown in Figure 5.

The fillers in asphalt mastic are stone materials, and the elastic modulus and Poisson's ratio of the filler could be valued as  $E_1 = 56$  GPa and  $\nu_1 = 0.25$  [32]. Di Benedetto obtained that Poisson's ratio of the asphalt varies with frequency from 0.48 to 0.5, and the phase angle is from  $-0.18$  to  $-1.29^\circ$  [33]. Approximate values of 0.49 and  $0^\circ$  are used as Poisson's ratio and phase angle of asphalt for computing convenience.

Assuming that the fillers are uniformly distributed as body-centered cubic, the fillers distribution coefficient is shown as [29]

$$\frac{\bar{\lambda}}{(2R_1)} = \left[ \frac{\sqrt{3}\pi}{(8f_1)} \right]^{1/3} - 1. \quad (30)$$

The fillers are regarded as spherical; the cumulative passing percentage of particle size  $d_i$  of the fillers is expressed as  $P_i$ , ( $i = 1, \dots, m$ ). The average particle size of sieve  $i$  is represented by  $(d_i + d_{i-1})/4$ . The number of filler particles of sieve  $i$  in unit mass  $N_i$  is expressed as

$$N_i = \frac{(P_i - P_{i-1})}{\rho_f (4/3)\pi ((d_i + d_{i-1})/4)^3}, \quad (31)$$

where  $\rho_f$  is the density of fillers.

From equation (31), the specific surface area of filler particles  $S_f$  is given by

$$S_f = \sum_{i=1}^m 4\pi \left( \frac{d_i + d_{i-1}}{4} \right)^2 N_i. \quad (32)$$

The number of filler particles in asphalt mastic is  $N$ ; the relationship between the average radius  $\bar{R}$  of all spherical particles and the specific surface area  $S$  is calculated as

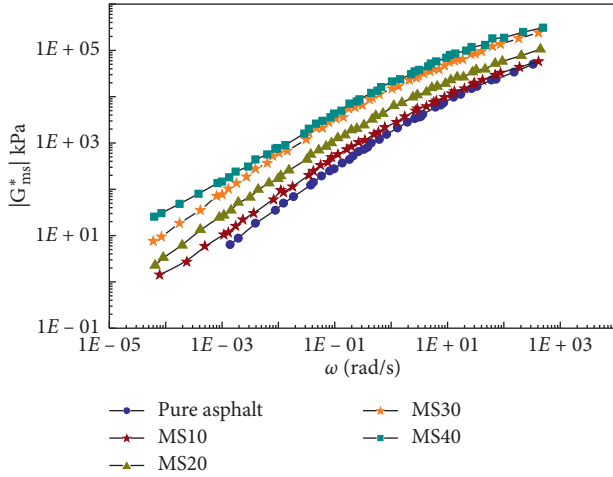


FIGURE 5: Master curves of the dynamic shear modulus of asphalt mastic.

$$S = \frac{4\pi\bar{R}^2 N}{(4/3)\pi\bar{R}^3 \rho_f N} = \frac{3}{\bar{R}\rho_f} \quad (33)$$

From equation (33), the average radius of filler particles is given by

$$\bar{R} = \frac{3}{S\rho_f} \quad (34)$$

The dynamic shear moduli of structural asphalt in equations (24) and (25) are assumed to satisfy the logarithmic mean value relationship between filler and asphalt. The complex shear modulus of structural asphalt can be expressed as

$$G_2^* = 10^{((\lg G_1 + \lg G_{ba}^*)/2)}, \quad (35)$$

where  $G_1$  and  $G_{ba}^*$  are the complex shear moduli of fillers and asphalt, respectively.

The mixed model proposed by Underwood and Kim [18] is employed to characterize the interaction between structural asphalt and free asphalt; the complex shear modulus of free asphalt can be obtained:

$$|G_3^*| = \frac{|G_{ba}^*| \times |G_2^*| \times c_3}{|G_2^*| - |G_{ba}^*| \times c_2}, \quad (36)$$

where  $c_2$  and  $c_3$  are the volume fractions of structural asphalt and free asphalt in the total asphalt.

Figure 6 shows the dynamic shear moduli of structural asphalt and free asphalt calculated from equations (35) and (36). It can be seen that the structural asphalt absorbs the polar component of the matrix asphalt until it is saturated, which leads to a significant increase in the complex modulus. A small number of polar components are lost in the free asphalt, resulting in a slight decrease in the complex modulus.

The thickness of the structural asphalt layer is related to the physicochemical reaction between asphalt and fillers. Underwood et al. have obtained that the thickness of structural asphalt layer is 0.2–0.63  $\mu\text{m}$  when the volume

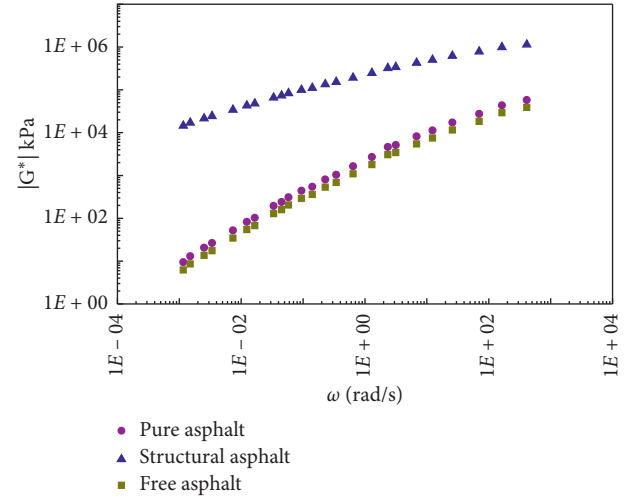


FIGURE 6: Dynamic shear modulus of structural asphalt and free asphalt.

fraction of fillers in asphalt mastic is 10%–60% by microscopic analysis. Therefore, the volume fraction of structural asphalt was determined as  $c_{sa} = 30\%$ , and the structural asphalt thickness  $d_s$  and volume fraction of each component are calculated as shown in Table 1.

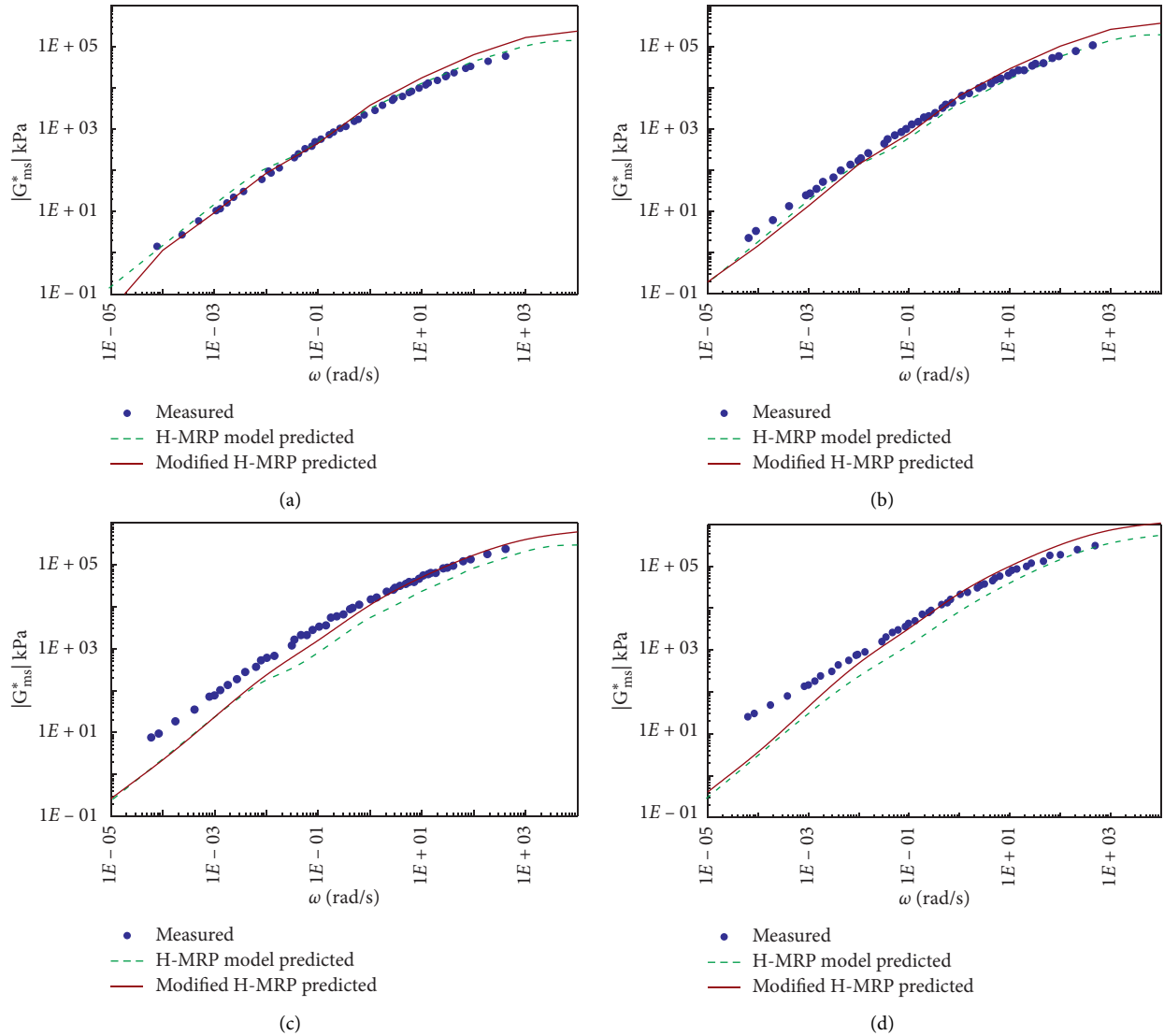
The H-MRP and modified H-MRP models are applied to predict the dynamic shear modulus of asphalt mastic  $|G_{ms}^*|$  with different filler volume fractions. Figure 7 presents the predicted and measured  $|G_{ms}^*|$  values for asphalt mastic. It can be seen that when the volume fraction of fillers is 10% and 20%, the predicted results of the two models are close to the measured ones. However, the predicted modulus of the modified H-MRP model is higher than the measured modulus at high frequency. It shows that when the content of fillers is low, the physicochemical effect between asphalt and fillers may be weak. Therefore, the volume fraction of structural asphalt assumed as  $c_{sa} = 30\%$  overestimates the physicochemical effects. The volume fraction of structural asphalt should be lower than 30%; however, when the volume fraction of structural asphalt is 0%, the modified H-MRP model is equivalent to the H-MRP model. It can be seen from Figures 7(a) and 7(b) that the modulus predicted by the H-MRP model is closer to the measured modulus than the modified H-MRP model. Therefore, it is suggested to apply H-MRP model to predict the viscoelasticity of asphalt mastic, while the volume fraction is less than 20%.

When the volume fractions of fillers are 30% and 40%, the predicted value of the modified H-MRP model is closer to the measured ones compared with the H-MRP model, which could be attributed to the fact that the physicochemical effect is strengthened when the volume fractions of fillers are high, so it is reasonable to assume  $c_{sa} = 30\%$ . The predicted dynamic modulus is much closer to the measured ones at high frequencies than at low frequencies. It indicated that the proposed models underestimated the viscoelastic effect of asphalt at low frequencies, asphalt mastic can be considered as asphalt with the addition of fillers in it, and fillers are basically elastic. With the elastic fillers added to asphalt, the proportions of the elastic and viscous



TABLE 1: Thickness of structural asphalt layer and volume fraction of each component.

Mastic types	$d_s$ ( $\mu\text{m}$ )	Asphalt mastic		Asphalt		
		Fillers (%)	Structural asphalt (%)	Free asphalt (%)	Structural asphalt (%)	Free asphalt (%)
MS10	2.22	10	27.1	62.9	30.1	69.9
MS20	1.22	20	24.1	55.9	30.1	69.9
MS30	0.79	30	21.2	48.8	30.2	69.8
MS40	0.54	40	18.2	41.8	30.3	69.7

FIGURE 7: Comparison of predicted and measured  $|G_{ms}^*|$  values. (a) MS10. (b) MS20. (c) MS30. (d) MS40.

components in asphalt mastic are different from those in pure asphalt, which will definitely cause the change in the elastic and viscous components of the complex modulus. Therefore, asphalt mastic should exhibit higher modulus than that of pure asphalt due to the addition of elastic fillers. The dynamic modulus is not a linear elasticity but a viscoelasticity. The equivalent modulus of elasticity is directly transferred to viscoelasticity by using the elastic-viscoelastic correspondence principle, which weakens the effect of

viscosity. Asphalt mastic behaves more like a viscous material at low frequencies. Therefore, the difference between predicted and measured moduli was larger. With the increase in the loading frequency, asphalt mastic shows more elastically and the predicted modulus was much closer to the measured value.

In order to analyze the effect of the structural asphalt volume fraction on the prediction modulus, the structural asphalt volume fraction  $c_{sa}$  was taken from 10% to 60% for

comparative analysis. Due to space limitation, the effect of  $c_{sa}$  on the dynamic modulus of MS30 is shown here only; see Figure 8. The modulus of structural asphalt is higher than that of free asphalt, so the predicted modulus increases as the volume fraction of structural asphalt increases. It can be seen that the increase in the volume fraction of structural asphalt is an effective method to increase the dynamic modulus of asphalt mastic through the improvement of the physico-chemical effect between fillers and asphalt. From the analysis of Figure 7, the underprediction at low frequencies is caused by the elastic-viscoelastic conversion, which is not related to the structural asphalt volume fraction. When the structural asphalt volume fraction is 40%–50%, the prediction modulus is still lower than the measured value at low frequency. It can be found from Figure 8 that the measured modulus of asphalt mastic is among the predicted values when the volume fraction of structural asphalt is 20%–50%; the volume fraction of structural asphalt of different types of fillers and asphalt will be measured by nano-micro experiments in future research.

## 5. Parameters Influencing the Dynamic Shear Modulus of Asphalt Mastic

**5.1. Effect of Fillers Distribution.** The prediction results in Figure 7 were obtained under the assumption that the distribution of fillers is uniform, but the fillers are non-uniformly distributed in the asphalt mastic actually. In order to analyze the influence of fillers distribution on the prediction results of the model, the distribution coefficients are 0.025, 0.05, and 0.25 for comparative analysis. Due to space limitation, the influence of the filler distribution coefficient on the prediction results of MS30 is given here only; see Figure 9.

The decrease in the distribution coefficient means that the particles are dense. From the predicted results in Figure 3, it can be observed that the distribution coefficient decreases and the predicted modulus increases. However, Figure 9 shows an opposite prediction trend. It can be found that the distribution coefficient decreases, and the prediction  $|G_{ms}^*|$  decreases. This is due to the use of different prediction models. The prediction results in Figure 3 are obtained by MRP model, and the structural asphalt layer by physico-chemical effect is not considered in the model. The distribution coefficient decreases, which results in the decrease of the thickness of the asphalt in the adsorption structure of the fillers considering physicochemical effect. When  $\bar{\lambda}/(2R_1) = 0.25$ , there is a small amount of accumulation of fillers, and the predicted value slightly decreases. When  $\bar{\lambda}/(2R_1) = 0.05$  and 0.025, a large number of agglomerations occur in fillers, and the predicted value decreases obviously. Therefore, in order to improve the viscoelasticity of asphalt mastic, the agglomeration of fillers should be avoided in the actual production process of asphalt mastic.

**5.2. Effect of Fillers Gradation.** In order to analyze the influence of the fillers grade on the predicted results of the dynamic shear modulus of asphalt mastic, three different

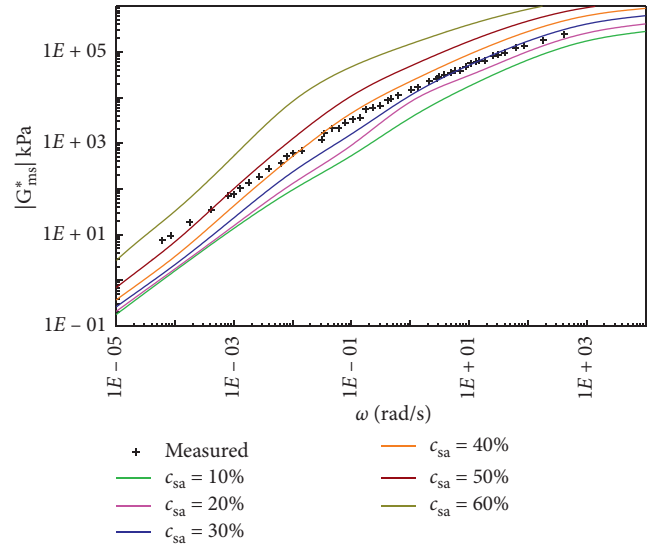


FIGURE 8: Effect of structural asphalt volume fraction on the prediction modulus of MS30.

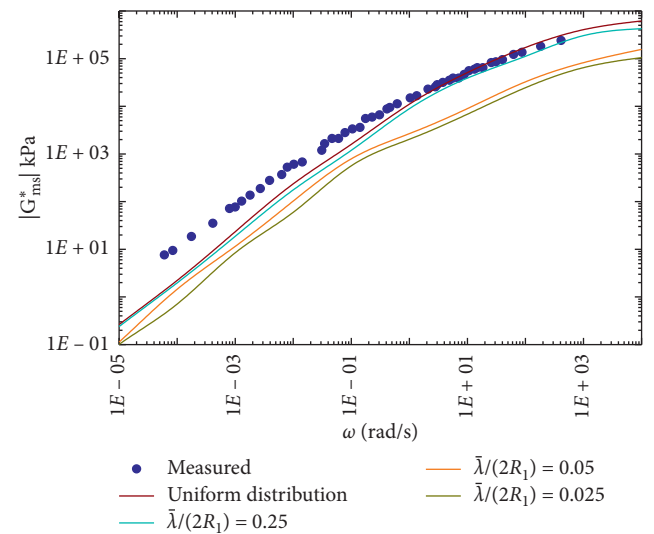


FIGURE 9: Effect of fillers distribution on the predicted  $|G_{ms}^*|$ .

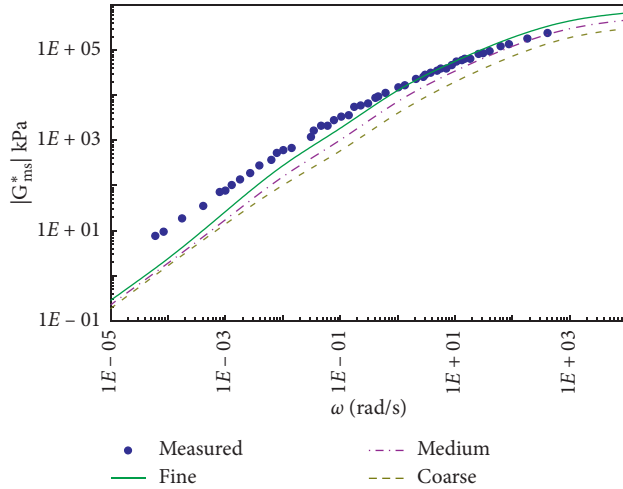
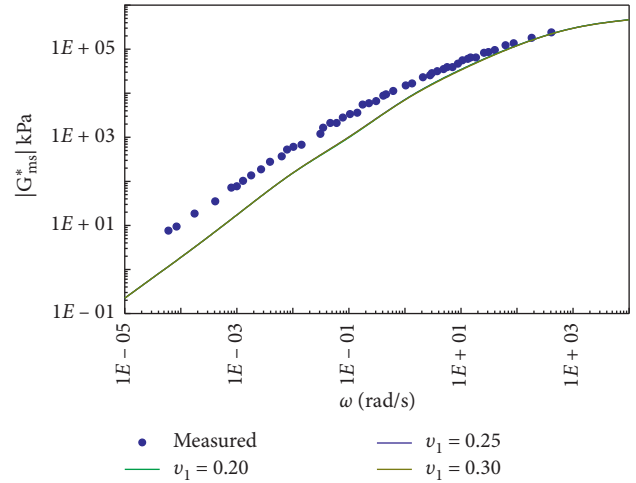
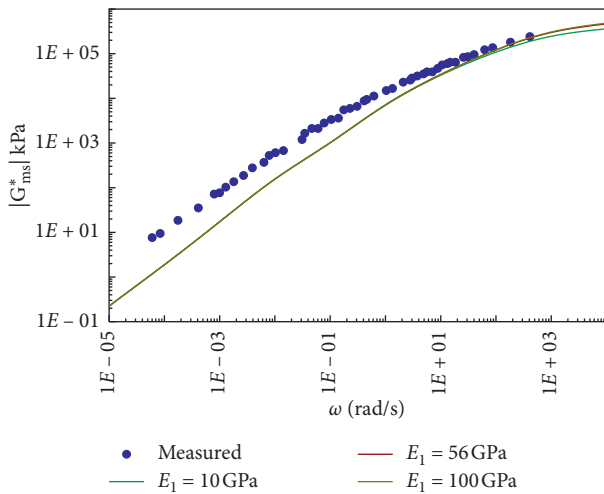
grades of fine, medium, and coarse are used for comparative analysis; see Table 2. Here, only the predicted dynamic shear modulus of the MS30 is shown; see Figure 10.

It can be seen from Figure 10 that the fillers gradation has a considerable influence on the predicted  $|G_{ms}^*|$  of MS30, which indicated that the H-MRP model proposed in this study could be well considered for the effect of fillers particle size. Asphalt mastic mixed with fine-grade fillers has the highest predicted modulus; it is due to the fact that the increase of the specific surface area of fillers will enhance the cementation of structural asphalt so that the modulus value increased.

**5.3. Effect of Young's Modulus and Poisson's Ratio of Fillers.** The influences of Young's modulus  $E_1$  and Poisson's ratio  $\nu_1$  of fillers on the predicted  $|G_{ms}^*|$  of MS30 are shown in Figures 11

TABLE 2: Different types of fillers gradation.

Mastic types	Sieve opening, mm (%)							
	0.075	0.030	0.023	0.017	0.0077	0.0038	0.0029	0.0013
Coarse	100	50	43	29	14	8	3	0
Medium	100	57	50	36	21	15	10	7
Fine	100	64	57	43	28	22	17	10

FIGURE 10: Effect of fillers gradation on predicted  $|G_{ms}^*|$ .FIGURE 12: Effect of Poisson's ratio of fillers on predicted  $|G_{ms}^*|$ .FIGURE 11: Effect of modulus of fillers on predicted  $|G_{ms}^*|$ .

and 12. It can be seen that the dynamic modulus of the asphalt mastic increases as the modulus and Poisson's ratio of fillers increase within a certain range; the magnitude of the increase in  $|G_{ms}^*|$  is comparably small, which means that the contribution of aggregate to the dynamic modulus improvement of the mixture is limited, given the fixed portion of fillers.

## 6. Conclusion

- (1) A micromechanical prediction model of asphalt mastic was established based on the morphologically

representative pattern (MRP) approach. The influences of physicochemical effect between fillers and asphalt, distribution of fillers, and the filler particle size were considered in the model. An explicit solution was derived to predict the dynamic modulus of asphalt mastic.

- (2) The DSR test was conducted to verify the prediction effect of the model. When the fillers volume fractions were 10% and 20%, the predicted value was relatively close to the experimental value. When the volume fractions of fillers were 30% and 40%, the predicted value was lower than the measured ones at low frequencies; the reasons for the underprediction were investigated.
- (3) The micromechanical model developed in this paper was able to reflect the effect of factors during a parameter influencing analysis. Based on the sensitivity analysis, the use of uniformly distributed fillers and fine fillers was an effective way to increase the dynamic modulus of asphalt mastic.
- (4) In the proposed model, the volume fraction of the structural asphalt and the distribution coefficient of the fillers were assumed; the nano-micro test would be conducted to obtain these parameters in the future research to improve the model proposed in this paper.

## Data Availability

The data used to support the findings of this study are included within the article.

## Conflicts of Interest

The authors declare that there are no conflicts of interest regarding the publication of this paper.

## Acknowledgments

This study was funded by the Liaoning Highway Administration Bureau under Grant no. 201701 and National Natural Science Foundation of China under Grant no. 51308084.

## References

- [1] M. C. Liao, G. Airey, and J. S. Chen, "Mechanical properties of filler-asphalt mastics," *International Journal of Pavement Research & Technology*, vol. 6, no. 5, pp. 576–581, 2013.
- [2] J. P. Zhang, J. Z. Pei, and B. G. Wang, "Micromechanical-rheology model for predicting the complex shear modulus of asphalt mastic," *Advanced Materials Research*, vol. 168–170, pp. 523–527, 2010.
- [3] G. G. Al-Khateeb, T. S. Khedaywi, and M. F. Irfaeya, "Mechanical behavior of asphalt mastics produced using waste stone sawdust," *Advances in Materials Science and Engineering*, vol. 2018, Article ID 5362397, 10 pages, 2018.
- [4] M. W. Witzczak and O. A. Fonseca, "Revised predictive model for dynamic (complex) modulus of asphalt mixtures," *Transportation Research Record: Journal of the Transportation Research Board*, vol. 1540, no. 1, pp. 15–23, 1996.
- [5] J. Bari and M. W. Witzczak, "Development of a new revised version of the Witzczak  $E^*$  predictive model for hot mix asphalt mixtures," *Journal of the Association of Asphalt Paving Technologists*, vol. 75, pp. 381–423, 2006.
- [6] M. Witzczak, M. El-Basyouny, and S. El-Badawy, "Incorporation of the new (2005)  $E^*$  predictive model in the MEPDG, NCHRP1-40D," Final report, Arizona State University, Tempe, AZ, USA, 2007.
- [7] J. Bari and M. Witzczak, "New predictive models for viscosity and complex shear modulus of asphalt binders: for use with mechanistic-empirical pavement design guide," *Transportation Research Record Journal of the Transportation Research Board*, vol. 2001, pp. 9–19, 2007.
- [8] Z. Hashin, "The elastic moduli of heterogeneous materials," *Journal of Applied Mechanics*, vol. 29, no. 1, pp. 143–150, 1962.
- [9] R. Hill, "A self-consistent mechanics of composite materials," *Journal of the Mechanics and Physics of Solids*, vol. 13, no. 4, pp. 213–222, 1965.
- [10] R. M. Christensen and K. H. Lo, "Solutions for effective shear properties in three phase sphere and cylinder models," *Journal of the Mechanics and Physics of Solids*, vol. 27, no. 4, pp. 315–330, 1979.
- [11] T. Mori and K. Tanaka, "Average stress in matrix and average elastic energy of materials with misfitting inclusions," *Acta Metallurgica*, vol. 21, no. 5, pp. 571–574, 1973.
- [12] S.-S. Pang, Y. Li, and J. B. Metcalf, "Elastic modulus prediction of asphalt concrete," *Journal of Materials in Civil Engineering*, vol. 11, no. 3, pp. 236–241, 1999.
- [13] R. Luo and R. L. Lytton, "Self-consistent micromechanics models of an asphalt mixture," *Journal of Materials in Civil Engineering*, vol. 23, no. 1, pp. 49–55, 2011.
- [14] E. Aigner, R. Lackner, and C. Pichler, "Multiscale prediction of viscoelastic properties of asphalt concrete," *Journal of Materials in Civil Engineering*, vol. 21, no. 12, pp. 771–780, 2009.
- [15] X.-y. Zhu, X. Wang, and Y. Yu, "Micromechanical creep models for asphalt-based multi-phase particle-reinforced composites with viscoelastic imperfect interface," *International Journal of Engineering Science*, vol. 76, pp. 34–46, 2014.
- [16] X.-Q. Fang and J.-Y. Tian, "Elastic-adhesive interface effect on effective elastic moduli of particulate-reinforced asphalt concrete with large deformation," *International Journal of Engineering Science*, vol. 130, pp. 1–11, 2018.
- [17] H. M. Yin, W. G. Buttlar, G. H. Paulino, and H. D. Benedetto, "Assessment of existing micro-mechanical models for asphalt mastics considering viscoelastic effects," *Road Materials and Pavement Design*, vol. 9, no. 1, pp. 31–57, 2008.
- [18] B. S. Underwood and Y. R. Kim, "A four phase micro-mechanical model for asphalt mastic modulus," *Mechanics of Materials*, vol. 75, pp. 13–33, 2014.
- [19] N. Shashidhar and A. Shenoy, "On using micromechanical models to describe dynamic mechanical behavior of asphalt mastics," *Mechanics of Materials*, vol. 34, no. 10, pp. 657–669, 2002.
- [20] W. G. Buttlar and R. Roque, "Evaluation of empirical and theoretical models to determine asphalt mixture stiffnesses at low temperatures," *Asphalt Paving Technology Association of Asphalt Paving Technologists Proceedings of the Technical Sessions*, vol. 65, pp. 99–141, 1996.
- [21] B. S. Underwood and Y. R. Kim, "Experimental investigation into the multiscale behaviour of asphalt concrete," *International Journal of Pavement Engineering*, vol. 12, no. 4, pp. 357–370, 2011.
- [22] B. Delaporte, H. D. Benedetto, P. Chaverot et al., "Linear viscoelastic properties of bituminous materials: from binders to mastics," *Asphalt Paving Technology Association of Asphalt Paving Technologists Proceedings of the Technical Sessions*, vol. 76, pp. 455–494, 2007.
- [23] R. Li, Z. Fan, and P. Wang, "Micromechanics prediction of effective modulus for asphalt mastic considering inter-particle interaction," *Construction and Building Materials*, vol. 101, pp. 209–216, 2015.
- [24] C. Davis and C. Castorena, "Implications of physico-chemical interactions in asphalt mastics on asphalt microstructure," *Construction and Building Materials*, vol. 94, pp. 83–89, 2015.
- [25] C. Clopotel, R. Velasquez, and H. Bahia, "Measuring physico-chemical interaction in mastics using glass transition," *Road Materials and Pavement Design*, vol. 13, no. 1, pp. 304–320, 2012.
- [26] Y. Veytskin, C. Bobko, and C. Castorena, "Nanoindentation and atomic force microscopy investigations of asphalt binder and mastic," *Journal of Materials in Civil Engineering*, vol. 28, no. 6, Article ID 04016019, 2016.
- [27] M. Guo, Y. Tan, J. Yu, Y. Hue, and L. Wang, "A direct characterization of interfacial interaction between asphalt binder and mineral fillers by atomic force microscopy," *Materials & Structures*, vol. 50, no. 2, pp. 141.1–141.11, 2017.
- [28] V. Marcadon, E. Herve, and A. Zaoui, "Micromechanical modeling of packing and size effects in particulate composites," *International Journal of Solids and Structures*, vol. 44, no. 25–26, pp. 8213–8228, 2007.
- [29] M. Majewski, M. Kurska, P. Holobut, and K. Kowalczyk-Gajewska, "Micromechanical and numerical analysis of packing and size effects in elastic particulate composites," *Composites Part B: Engineering*, vol. 124, pp. 158–174, 2017.
- [30] E. Herve and A. Zaoui, "inclusion-based micromechanical modelling," *International Journal of Engineering Science*, vol. 31, no. 1, pp. 1–10, 1993.

- [31] S. W. Park and R. A. Schapery, "Methods of interconversion between linear viscoelastic material functions. Part I-a numerical method based on Prony series," *International Journal of Solids and Structures*, vol. 36, no. 11, pp. 1653–1675, 1999.
- [32] X. Shu and B. Huang, "Dynamic modulus prediction of hma mixtures based on the viscoelastic micromechanical model," *Journal of Materials in Civil Engineering*, vol. 20, no. 8, pp. 530–538, 2008.
- [33] H. Di Benedetto, F. Olard, C. Sauzéat, and B. Delaporte, "Linear viscoelastic behaviour of bituminous materials: from binders to mixes," *Road Materials and Pavement Design*, vol. 5, no. 1, pp. 163–202, 2004.

## Research Article

# Influence of Antistripping Additives and Rejuvenators on Healing Performance of Moisture-Damaged HMA

Dae-Wook Park <sup>1</sup>, Tam Minh Phan <sup>1</sup> and Yeong-Min Kim <sup>2</sup>

<sup>1</sup>Department of Civil Engineering, Kunsan National University, Gunsan 54150, Republic of Korea

<sup>2</sup>Department of Civil Engineering, Kyung Hee University, Yongin, Gyeonggi, 17104, Republic of Korea

Correspondence should be addressed to Yeong-Min Kim; choozang@kict.re.kr

Received 18 February 2020; Revised 5 April 2020; Accepted 28 April 2020; Published 29 May 2020

Guest Editor: Zhen Leng

Copyright © 2020 Dae-Wook Park et al. This is an open access article distributed under the Creative Commons Attribution License, which permits unrestricted use, distribution, and reproduction in any medium, provided the original work is properly cited.

This study aims to evaluate the effect of different rejuvenators and antistripping agents on the healing performance of hot mix asphalt (HMA). Two damage HMA series (e.g., moisture damage and aged damage) were subjected to either induction or microwave heating. A PG64-22 virgin and aged binder were used and modified with several additives. Three long-term aged binders (e.g., PAV5, PAV15, and PAV20) were conducted by pressure aging vessel (PAV) test. The moisture damage series fabricating with a new binder was further categorized into four different freeze-thaw (FT) cycles (e.g., 0FT, 1FT, 3FT, and 5FT). Also, the aged series was fabricated with three different aged binders. A total of eight damage-healing cycles were applied to all asphalt mixtures, examined by the three-point bending test. The moisture resistance of modified asphalt mixture was examined by indirect tensile strength test. Overall, asphalt mixtures modified with either antistripping additives or rejuvenators not only obtained higher moisture resistance but also gained better healing performance under moisture damage. In addition, the study showed a probable correlation between moisture damage and long-term aging in terms of healing performance, such as PAV15 and 3FT cycles and PAV20 and 5FT cycles.

## 1. Introduction

Moisture damage is one of the main factors affecting the durability of asphalt mixtures [1]. The application of freezing and thawing cycles is adopted to replicate in-service moisture damage on pavements. Moisture damage greatly affects internal structure and consequently results in pavement degradation. This occurs when moisture from either rainwater or snowmelt makes its way into existing microcracks during high temperature, after which, as the temperature drops below freezing point, the moisture within the microcracks begins to freeze and expand. The repetition of this occurrence leads to accelerate aging of asphalt binders [2]. The strength of interaction is reduced, which creates a weak asphalt-aggregate system [3]. However, moisture damage can be prevented either by improving the adhesion strength of asphalt aggregate or by preventing water

intrusion on asphalt concrete [4]. Nowadays, antistripping agent is used to enhancing moisture resistance of asphalt mixture. This additive agent can improve internal structure of asphalt mixture, which enhances the adhesive of aggregate and binder [5]. In addition to reducing water intrusion, microcracks healing is also a promising solution [6]. Electromagnetic induction, microwave, and infrared have been used to heat asphalt concrete for healing purposes. It has been proved that the healing level of asphalt concrete can be improved by induction and microwave heating. During the heating process, mixture containing conductive additives is exposed to high frequency alternating magnetic fields. Based on the Joule law, the eddy current heats conductive particle. Then, the heat energy diffuses into the asphalt mixture to increase sample temperature [7]. A sufficient temperature leads to low viscosity of asphalt binder, and the binder can fill microcracks. This phenomenon is explained by the fact

that asphalt binder is a temperature-dependent material. The first applied induction heating on the road has been taken on the A58 near Vlissingen in Netherland. After three years of paving time, the healing result was promising; this road could be heated in the expected time [8].

Aging is another factor influencing the performance of asphalt mixture, which occurs during production and construction and continues throughout the services life of asphalt pavements. Long-term aging caused asphalt binder to stiffen and embrittle, which leads to a high potential of cracking [9]. Repetition of the healing process may lead to similar aging attributes, which are easily recognized at late damage-healing cycles. According to SHRP, 20 hours aging in the PAV simulates the asphalt binder aging that occurs during 5–10 years of in-service HMA pavements [10]. Previous researches have been proved that rejuvenators could be used to restore some of the mechanical properties of an aged asphalt binder [11, 12]. Wang et al. confirmed that sufficient rejuvenator could improve physical properties and crack resistance [13]. However, it was found that there was a lack of research focused on the performance of healed HMA under both moisture damage and aging effects. In reality, asphalt mixtures are subjected to aging and moisture damage simultaneously [14–16]. Hence, further investigation is also needed on the correlation between the long-term aging process and moisture damage.

This research aims to study the effect of different additive agents (e.g., antistripping agent and rejuvenator) on the healing performance of moisture damage asphalt mixture. Induction heating and microwave heating are used to heat asphalt mixture. Long-term aging is considered to find the correlation between moisture damage and aging in terms of healing performance. Two sample series are fabricated to archive the research objectives. First, the unaged asphalt binder is modified with four types of additive agents. These samples are going on to four different freeze-thaw (FT) cycles. Second series was fabricated with three levels of PAV asphalt binder (e.g., PAV5, PAV15, and PAV20). The healing performance of mixture is assumed by the three-point bending (TPB) test, while the moisture resistance is conducted to indirect tensile strength (ITS) test. Steel wool fiber (SWF) is utilized to obtain a prime healing performance. All test samples are applied to eight damage-healing (DH) cycles. During healing process, the infrared camera (FlukeTiS20 model) is used to record the surface temperature of sample. The ANOVA and Tukey HSD post hoc are employed to find the correlation between moisture damage and aging in terms of healing performance.

## 2. Materials and Methods

**2.1. Materials.** Laboratory-fabricated HMA mixtures were used to conduct a series of experiments. Table 1 shows the gradation of experiment aggregate. The bitumen PG 64-22 had a penetration at 25°C of 70 mm/10s and a density of 1.02 g/cm<sup>3</sup>. The SWF has a diameter ranging from 70 to 130 μm, a density of 7.18 g/cm<sup>3</sup>, a length of 4–4.5 mm, and thermal conductivity of 80 W/mK. The antistripping additives consist of silane additive,

TABLE 1: Aggregate gradation.

Sieve size (mm)	Aggregate		
	Coarse (33%)	Fine (60.5%)	Filler (6.5%)
19	100	100	100
12.5	83	100	100
9.5	35.5	100	100
4.75	1.7	79.3	100
2.36		41.3	100
0.6		16.5	100
0.3		10.5	100
0.15		6.2	56
0.075		4	47

amine type surfactant, and stabilizer. Two kinds of antistripping additives named A and B have different proportions of silane additive to amine type surfactant. Rejuvenator types 1 and 2 had a viscosity of 79–90 and 60 cSt at 60°C and a density of 0.93 and 0.8 g/cm<sup>3</sup> at 20°C, respectively. Further, three levels of long-term aged asphalt binder (e.g., 5 hours, 15 hours, and 20 hours) were used to fabricate aged mixtures.

**2.2. Sample Preparation.** The asphalt mixtures were prepared according to the Superpave Mix Design Method [17]. Two sample series were designed in this experiment (as shown in Figure 1). Table 2 shows the mix proportion of the moisture damage series. Four additives were used in this series, while only two additives were used in the aged series (Table 3). This is because of the weight limitation of binder from the PAV process. The SWF was utilized in both series to gain an optimum healing performance [18–20]. All test specimens were prepared according to the Superpave Mix Design Method [17], with an optimum asphalt binder content of 5.4% and target air void of 4 ± 0.5%.

Asphalt binder-additive mixing process involved preheating the asphalt binder for an hour at 160°C. Once preheated, two percent of additive was then introduced and stirred thoroughly unto the binder. The mixture was allowed to sit in the oven for an additional hour (at 160°C), stirring the mixture at 30 minutes interval. Based on ITS test requirements, a cylindrical test specimen had a dimension of 63.5 mm in height and 100 mm in diameter (Figure 2(a)). The TPB specimen which has a dimension of 100 mm in both height and diameter was followed. After curing for one day at room temperature (25°C), the TPB molded specimen was cut into six equal semicircular samples with an overall size of 30 mm thick, 50 mm height, and 100 mm in width (Figure 2(b)). To ensure cracking of the sample at midpoint during the three-point bending test, a 10 mm depth and 2 mm thick notch were made at the base of the sample. This preexisting cut will ensure crack propagation at midsection. The notch dimension was based on the finding of García [21]. After cutting, these samples were let to dry at room temperature for 48 hours (to remove liquid due to cutting). Each mixture condition was prepared with three replicates to compute the average results.

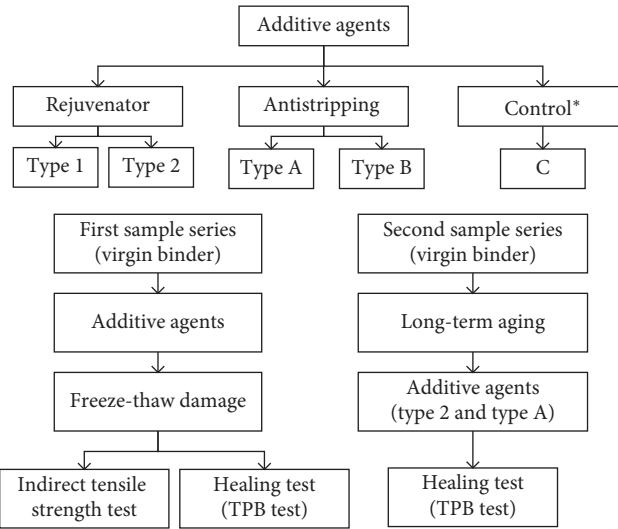


FIGURE 1: Research flowchart. \*Mixture without additive agent.

TABLE 2: Mix proportion of moisture damage series.

	New binder (by wt. of total mix)	Additive agent (by wt. of binder)					SWF (by wt. of binder)
		C	Type 1	Type 2	Type A	Type B	
Induction heating	5.4%			2%			6%
Microwave heating	5.4%			2%			2%

TABLE 3: Mix proportion of aged series.

	Aged binder (by wt. of total mix)			Additive agent (by wt. of binder)			SWF (by wt. of binder)
	PAV5	PAV15	PAV20	C	Type 2	Type A	
Induction heating		5.4%			2%		6%
Microwave heating		5.4%			2%		2%

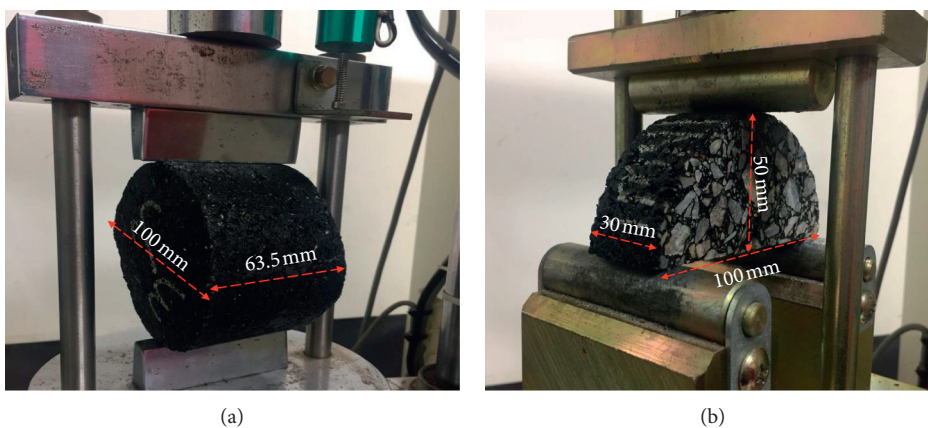


FIGURE 2: Test setup for (a) ITS test and (b) TPB test.

2.3. Test Methods

2.3.1. Aged Binder Process. The asphalt binder underwent short-term and long-term aging. Short-term aging was simulated first, using RTFO (Rolling Thin-Film Oven) in

accordance with D2872-12 [22], typically subduing binder for 85 min at 163°C. The binder from the short-term aging process was further used for long-term aging simulation with the pressure aging vessel (PAV), which mimics the aging of road pavements during its life span. The PAV test



was conducted with a pressure of 2070 kPa on three different time periods: 5 hours, 15 hours, and 20 hours. Finally, specimens were fabricated using the long-term aged binder to investigate the effect of aging on healing performance.

**2.3.2. Freeze-Thaw Process.** The moisture damage series included 4 groups of freeze-thaw cycle: unconditioned/control (0FT), one cycle (1FT), three cycles (3FT), and five cycles (5FT). According to AASHTO T 283 [23], one freeze-thaw cycle includes saturating samples on a sealed vacuum container. Samples were supported by steel grills inside the container to acquire a minimum of 25 mm water above its surface. A relative vacuum of 13–67 kPa was applied on the sealed container for 5–10 min. Once finished, the vacuum pressure was removed, and the samples were left submerged approximately 5–10 min more. Then, the saturated specimens were transferred unto sealed plastic bags filled with 10 ml water and kept inside a freezer at  $-18^{\circ}\text{C}$  for 16 hours, after which, the specimens were placed unto a hot water bath at  $60^{\circ}\text{C}$ ; once the ice has melted, the sealed plastic was removed, and samples were left at this temperature for 24 hours. Finally, the specimens were then again transferred in a water bath at  $25^{\circ}\text{C}$  for 2 hours.

To investigate the effect of additive agents on moisture susceptibility, the indirect tensile strength test was conducted. The indirect tensile strength was recorded by applying a loading rate of 50 mm/min. The indirect tensile strength  $S_t$  is calculated using

$$S_t = \frac{2P}{\pi Dt}, \quad (1)$$

where  $P$  is the maximum load (kN),  $t$  is thickness of specimen (mm), and  $D$  is the diameter of specimen (mm).

**2.3.3. Damage-Healing Process.** To obtain brittle condition before TPB test, samples were placed in a refrigerator at aged binder process  $-18^{\circ}\text{C}$  for 2 hours. TPB test contained a loading roller at midpoint on the semicircular arch sample, supported by two fix rollers spaced at 80 mm apart (Figure 2(b)). A testing machine with a capacity of 100 kN was used in this experiment. The test was performed under the loading rate of 0.9 mm/min until failure, and the load was reduced 25% of the peak load. The test was carried out at room temperature (approximately  $25^{\circ}\text{C}$ ). After the TPB test, the damaged specimens were kept in ambient condition for 24 hours covered with paper a towel to ensure that the condensate moisture from freezing has totally dried.

Two healing treatments were used unto damaged samples: the induction heating generator and microwave heating machine. The induction heater used in this study has a capacity of 50 kW and a maximum frequency of 35 kHz. The damaged sample was placed under the induction heating coil and heated until  $90^{\circ}\text{C}$  (as shown in Figure 3). In addition, microwave heating treatment was conducted using a microwave oven with a maximum frequency of 2.45 MHz and a power capacity of 700 W. Damaged sample was subjected to electromagnetic waves for 50 seconds [20]. The surface temperature was recorded by an infrared camera (Figure 4).

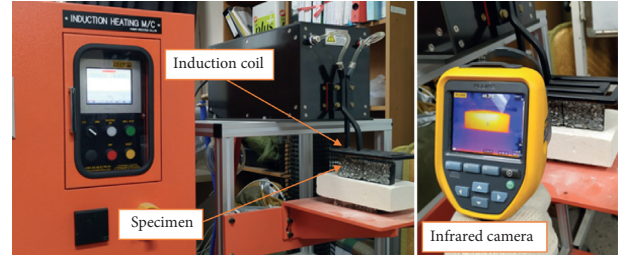


FIGURE 3: Induction heating test setup.



FIGURE 4: Microwave heating test setup.

After healing treatment, healed samples were allowed to rest approximately three hours to achieve stable room temperature. Rested and healed samples were again conditioned in a refrigerator for two hours and tested for the TPB test. This equates to one DH cycle. Based on preliminary research recommendations and the author's team experiment, the healing performance of the test samples was conducted until eight damage-healing cycles. The healing level of the asphalt mixture sample  $S_h$  (%) was calculated by

$$S_h = \frac{F_n}{F_0} \times 100, \quad (2)$$

where  $F_0$  is the force of the initially tested sample (0 DH cycle) (kN).  $F_n$  is the force of sample after the damage-healing process ( $n^{\text{th}}$  DH cycle) (kN).

### 3. Results and Discussion

**3.1. Results of Surface Temperature after Healing Process.** Figure 5 shows the relationship between surface temperature and several freeze-thaw cycles of unaged asphalt mixture composed of different types of additive agents. Overall, the temperature gradually decreased at every FT cycle. The results indicated that samples treated by microwave heating obtained a higher temperature than that of induction heating. This occurrence can be explained by the fact that any material exposed to electromagnetic radiation heats up, while magnetic induction only affects conductive objects (i.e., SWF) [24]. Among four types of additive agents and control samples, type 2 achieved the highest surface temperature in both microwave and induction heating. In addition, the trends of temperature variation between antistripping additives and rejuvenators were most similar.

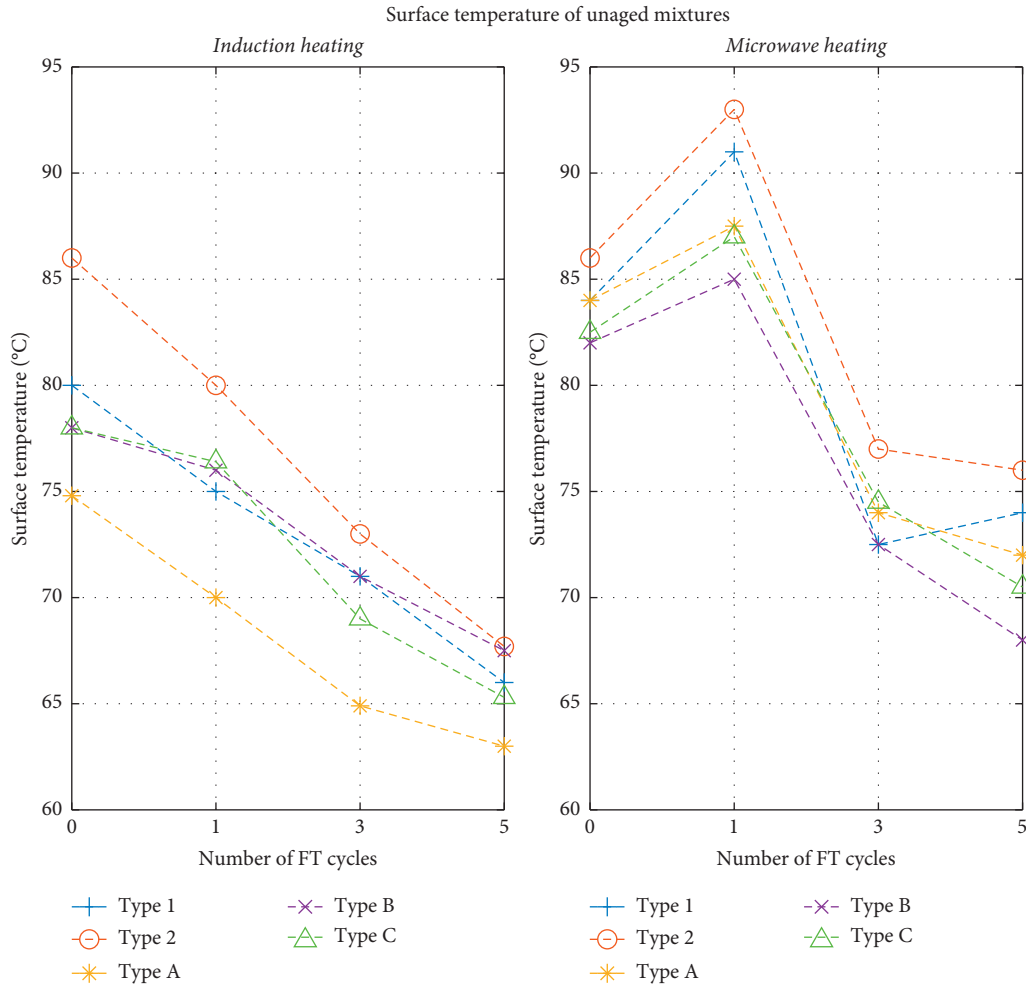


FIGURE 5: Surface temperature after heating.

By using microwave heating, the average surface temperature was increased after one FT cycle and decreased subsequently (see Figure 5). The type 2 mixture had the highest surface temperature of 93.5°C, and type A presented the lowest temperature with 68.8°C (after five FT cycles). The increase in temperature at the early stages of FT cycle can be explained by the change of air void content. After one FT cycle, air void content within samples might have been sufficient to hold a substantial amount of water, which led to an increase in temperature. However, with successive FT cycles, the repetition of freezing and thawing may have caused much air void volume expansion [25], with bigger air gaps that led to the flow of moisture rather than retention [26]. Therefore, this may have caused a decrease in temperature due to the decrease in moisture content.

Under induction heating, the average surface temperature of samples gradually decreased with increasing FT cycles. The highest temperature was recorded in type 2 additive samples with 85°C (at 0 FT cycles), and the lowest was type A with 63°C (after 5 FT cycles). As mentioned before, when the number of FT cycles was increased, there would be higher air void content, thereby breaking the interconnecting bonds of the mixture (especially SWF). This phenomenon which led to heat transfer was interrupted. In

addition, the water retained on the samples played a role as a thermal absorbing material, which lowers the temperature. Therefore, the temperature of test samples gradually reduced with an increasing FT cycle when using induction heating method. Temperature attainment after the healing process plays an important role during real-scale heating scenarios. With the results presented, it is conclusive that although it reached the margin of 80–90°C, it is within boundaries of a regular asphalt pavement working temperature.

3.2. Results of Moisture Resistance. To better understand and express the indirect tensile strength of samples in this experiment, the tensile strength ratio (TSR) was computed. TSR is defined as the ratio of the tensile strength of both wet-conditioned (i.e., 1, 3, and 5 FT cycles) and dry-conditioned samples (i.e., 0 FT cycles). The tensile strength ratio can be calculated by following equation:

$$TSR_k^i = \frac{K_i}{K_0} \times 100, \tag{3}$$

where  $TSR_k^i$  is tensile strength ratio of mixture with type “K” additive agent at cycle “i,”  $K_i$  is the wet-conditioned tensile strength of mixture with “K” additive agent at cycle “i,” and

$K_0$  is the dry-conditioned tensile strength of mixture with “K” additive agent.

The results from Figure 6 show that additive could enhance moisture resistance of modified asphalt mixture. Particularly, mixtures containing antistripping archived the highest indirect tensile strength. With the dry condition, type A mixture showed the highest value of 1.89 MPa; however, the control mixture presented the lowest indirect tensile strength, which was 1.45 MPa. Overall, TSR of all asphalt mixtures decreased at every freeze-thaw cycle. The control mixture showed the lowest TSR values of 53% and 19% after one and five FT cycles, respectively. The decrease in TSR could be caused by the presence of more air void content after succeeding in FT cycles. The antistripping additive samples had better results compared to samples modified with rejuvenators. This can be explained by the fact that antistripping additive increases adhesion between binder and aggregates, giving stronger tensile strength. Although lower in TSR percentage, the rejuvenator improved the moisture damage resistance of test samples by at most 85% over control. According to KS F 2398, the damage due to moisture is controlled by specific limits of the TSR. Under one cycle of freeze thaw, all of the antistripping samples meet the minimum criteria of TSR value of 80% [27].

Moreover, (4) was developed to analyze the effect of introducing additive agents unto the mixture at different freeze-thaw cycles:

$$E_k^i = \frac{K_i - C_i}{C_i} \times 100, \quad (4)$$

where  $E_k^i$  is the tensile strength percentage improvement of mixture with type “K” additive agent at cycle “i,”  $K_i$  is the tensile strength of mixture with “K” additive agent at cycle “i,” and  $C_i$  is the tensile strength of control sample (without additive agent) at cycle “i.”

Figure 7 illustrates the effect of adding additive agents. The bar graph shows that all mixtures with additive can improve tensile strength. The antistripping additive samples had significant improvement in tensile strength compared to rejuvenator additive samples. The improvement of the antistripping additive is visible in unconditioned state (0 FT cycles). Type B additive increased tensile strength by 32% over the control sample. On the other hand, rejuvenator additive samples imposed a slight increase of only 8% (at 0 FT cycles). The increase in tensile strength is caused by the characteristic of each additive. The antistripping additives can improve the adhesive between asphalt binders and aggregates, while rejuvenator can restore the mechanical properties of an aged binder [12].

### 3.3. Results of Healing Performance

3.3.1. *Without Moisture Damage (0 FT Cycles)*. Table 4 shows the initial force of the moisture-damage series. Without moisture damage (i.e., 0 FT cycles), the mixtures containing additive agents were slightly improved initial force of asphalt mixture. The type B mixture was 7%

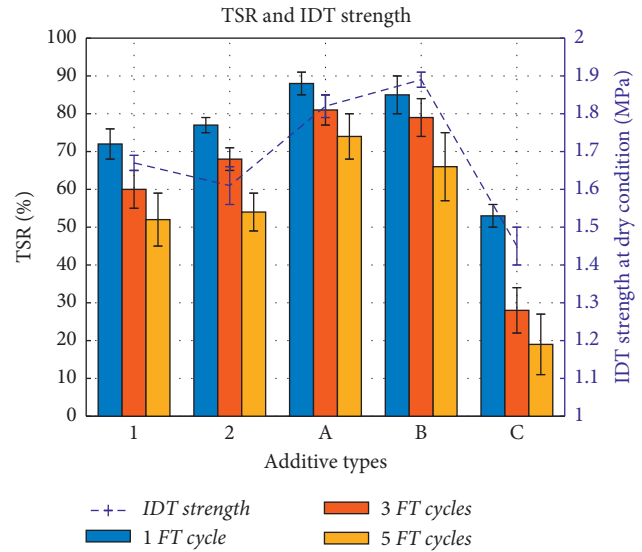


FIGURE 6: TSR and IDT strength of moisture-damaged mixtures.

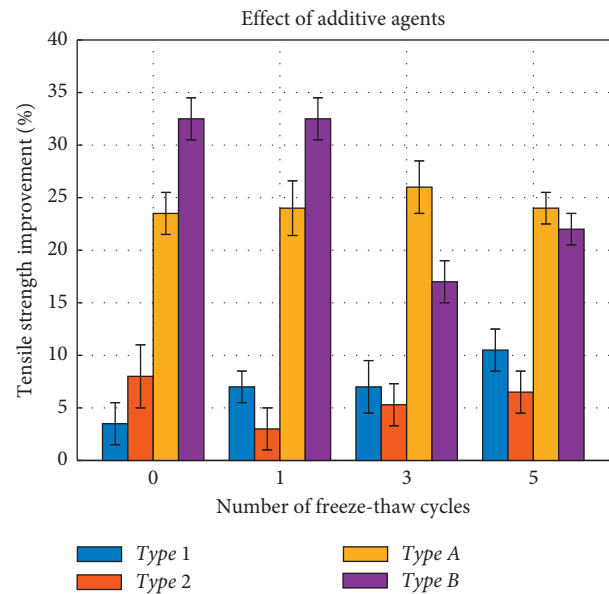


FIGURE 7: Tensile strength improvement.

higher than the control mixture. In addition, the healing performance of samples without moisture damage is shown in Figure 8. In general, the healing levels of all mixes decreased at every damage-healing cycle. The microwave heating method indicated a higher healing level than induction heating method. This outcome agrees well with the results previously discussed from attained surface temperature after the healing process. The higher surface temperature helps sufficient crack healing [18].

Under the microwave heating treatment, the effect of antistripping additives was less than that of rejuvenators. This can be seen at the fourth DH cycle, with rejuvenator type 2 mixture having a healing level of 76% compared to

TABLE 4: The initial force of moisture damage asphalt mixtures (kN).

Freeze-thaw cycle	Mixture types				
	Type C	Type A	Type B	Type 1	Type 2
0	2.45 ± 0.10	2.56 ± 0.13	2.62 ± 0.11	2.53 ± 0.11	2.55 ± 0.13
1	2.31 ± 0.12	2.52 ± 0.14	2.54 ± 0.15	2.43 ± 0.13	2.47 ± 0.13
3	2.11 ± 0.09	2.45 ± 0.09	2.47 ± 0.12	2.39 ± 0.12	2.38 ± 0.12
5	1.95 ± 0.11	2.21 ± 0.12	2.32 ± 0.17	2.33 ± 0.16	2.21 ± 0.14

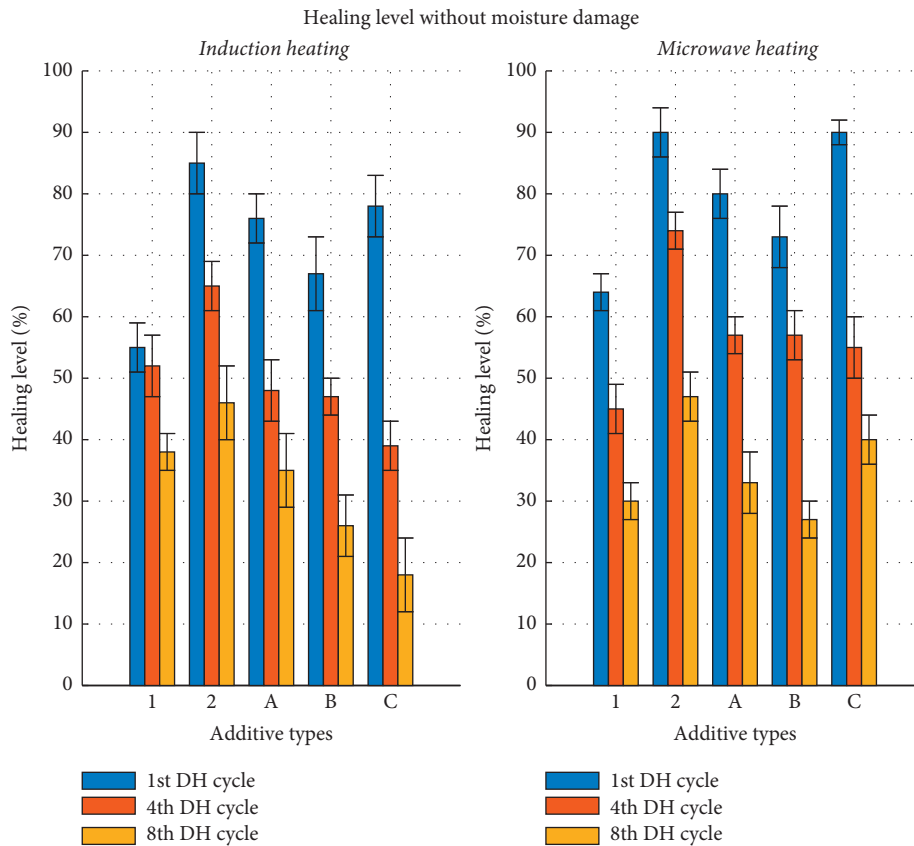


FIGURE 8: Healing level of unaged mixtures without moisture damage.

55% for antistripping additive type B mixture. Type 2 mixture showed a promising healing performance with a level of 76% and 47% under 4 and 8 DH cycles, respectively. Additionally, the type 1 mixture had the lowest healing level of 43% and 29% corresponding to 4 and 8 DH cycles. It can be explained due to the high viscosity of rejuvenator additive 1, which causes slow and inefficient diffusion into the asphalt. In the early stages of DH cycles, the difference in the healing level of the control sample and additive agent sample was insignificant. Control samples also have healing capabilities effective until four DH cycles. Furthermore, from the fifth DH cycles, the effect of an additive agent, specifically rejuvenators, can have a significant impact on continuing the healing level above 50%. Adding an appropriate rejuvenator (type 2 with lower viscosity) helps asphalt binder reduce its viscosity, which can explain a higher level of healing [28].

The healing result under induction heating is shown in Figure 8. In early cycles of DH, the mixtures without additive agents (control) and type 2 had a better healing level compared to other mixtures, obtaining 79% and 83%, respectively. However, after 4 cycles, the healing performance of the control sample dropped significantly by 39%. The results might be due to the repetition of damage-healing cycles, which lead to aging and oxidization of asphalt binder. As a result, it caused high viscosity that prevented the capillary flow of asphalt binders to repair cracks.

3.3.2. *With Moisture Damage (1, 3, and 5 FT Cycles).* The effect of additive agents was proved after one FT cycle (Table 4). The initial force of additive mixtures was approximately 10% higher than the control mixture. The healing performance of asphalt mixtures suffering from

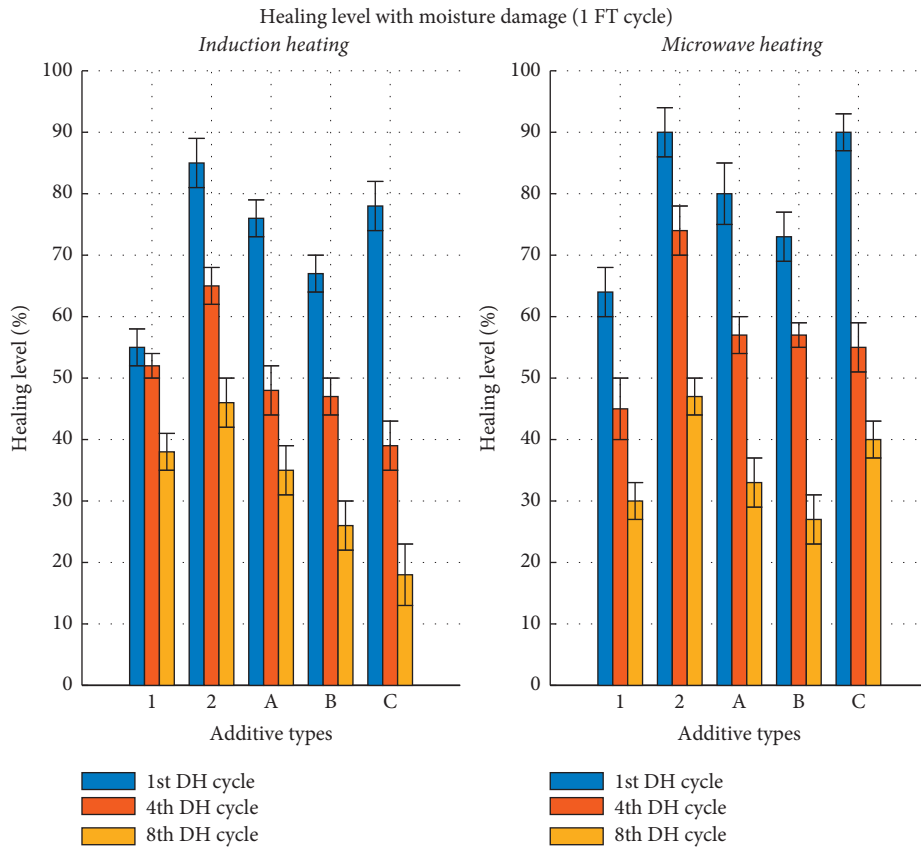


FIGURE 9: Healing level of unaged mixtures with moisture damage (1 FT cycle).

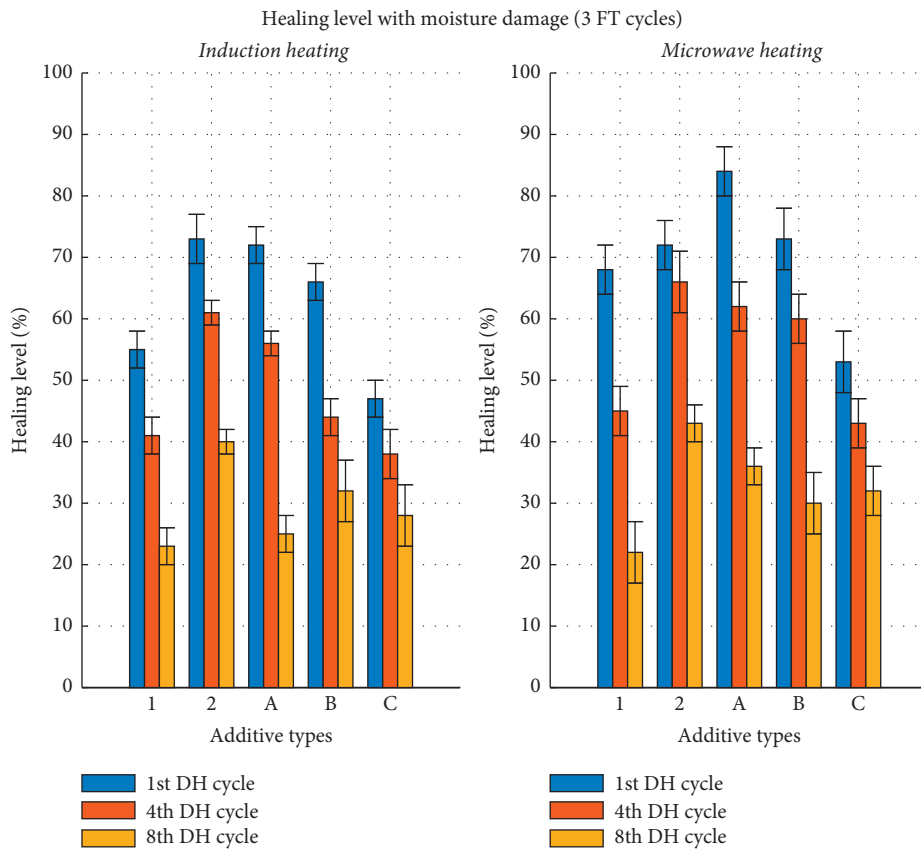


FIGURE 10: Healing level of unaged mixtures with moisture damage (3 FT cycles).

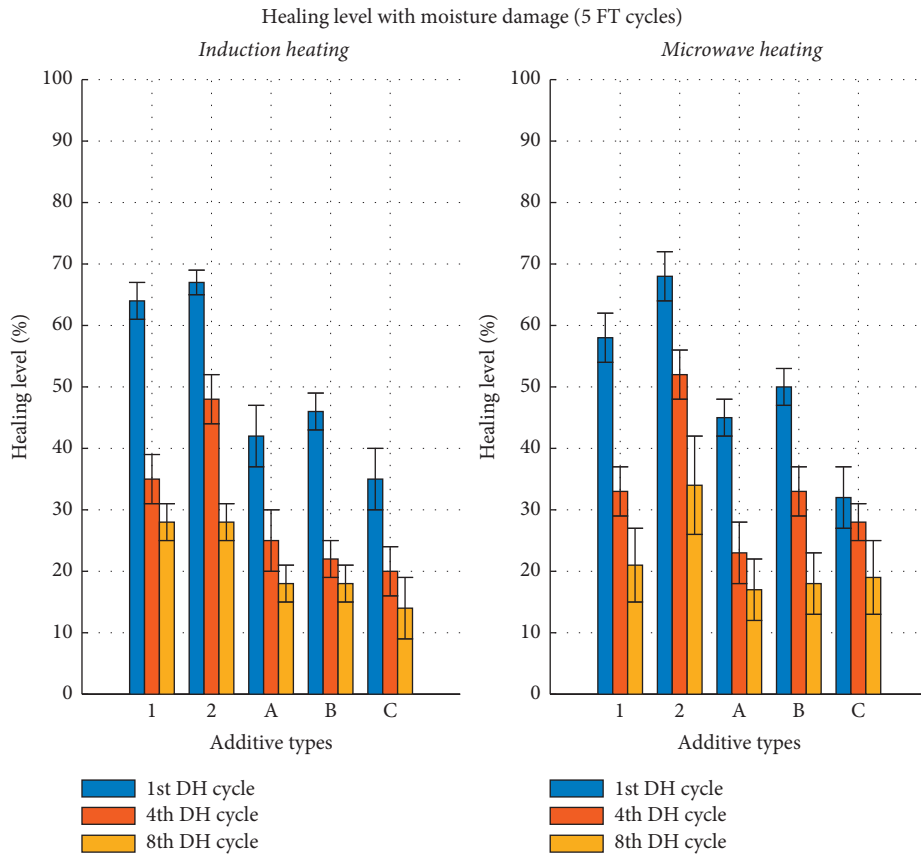


FIGURE 11: Healing level of unaged mixtures with moisture damage (5 FT cycles).

moisture damage is shown in Figures 9–11. Overall, the healing level decreased with increasing damage-healing cycle. Similarly, with the increasing FT cycles, the healing level decreased. This occurrence was observed for both microwave and induction heating method. Moreover, microwave heating showed a slight advantage in the healing level over induction heating for all FT cycles. Observing the figures, all mixtures with additive agents showed improvement in the healing level over control samples. However, during the late DH cycles, the gap on the healing level becomes less significant. This might be attributed to the limitation of the healing characteristics of a mixture with an additive agent during excessive DH cycles.

Figure 9 shows the corresponding healing level on every type of additive agent that underwent one FT cycle. It can be observed that type A antistripping additive obtained the highest healing level at 83% during one DH cycle. It is important to note that mixtures with type 2 rejuvenator additive had a better healing performance overall. At 8 DH cycles, type 2 additive mixture showed an 8% higher healing level compared to type A mixture. By further observing Figures 10 and 11, type 2 additive samples show consistency in its healing level, obtaining 69% at 5 FT cycles on 1 DH cycle. Furthermore, it seems that antistripping additive can heal significantly only at the early cycles of FT. With Figure 11, the significant difference in using a rejuvenator additive over antistripping additive can be seen. This further proves the

TABLE 5: The initial force of aged damage asphalt mixtures (kN).

PAV damage	Mixture types		
	Type C	Type A	Type 2
5 h	2.36 ± 0.13	2.52 ± 0.12	2.57 ± 0.14
15 h	2.26 ± 0.15	2.41 ± 0.16	2.43 ± 0.13
20 h	2.01 ± 0.15	2.28 ± 0.17	2.25 ± 0.16

advantageous effect of using rejuvenator for optimum self-healing characteristics.

Similar trend results with microwave heating can be observed, with type 2 additive showing best healing performance and consistency on all mixtures. With moisture damage at 5 FT cycles, type 2 rejuvenator additive samples showed 20% and 32% higher healing level compared to type B antistripping additive samples and control samples, respectively. It is obvious that the healing performance of the mix with rejuvenators was better than that of the mixture with antistripping additives. The antistripping additives can protect the asphalt mixture from water intrusion and increase the adhesion of the aggregate to the asphalt binder. However, in terms of healing performance, rejuvenators with low viscosity can increase the flowability of an asphalt binder; hence, the binder can easily flow to repair microcracks. This observation also explains the high healing level of rejuvenator type 2 additive, which had the lowest viscosity value. The results highlight the important

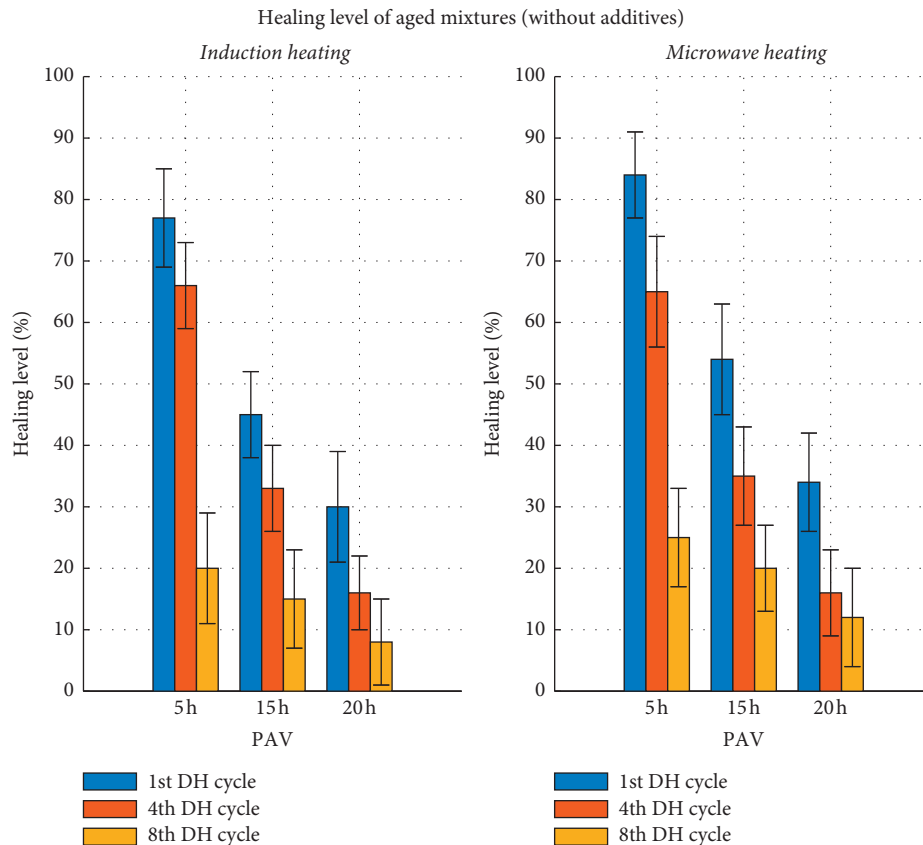


FIGURE 12: Healing level of aged mixtures without additive agents.

role of the viscosity of an additive agent in providing a self-healing ability.

**3.3.3. With Long-Term Aging.** The containing of additive agents could enhance the initial force of aged asphalt mixtures (Table 5). Mixtures with additive agents gain a 10% higher compared to the control mixture. The healing level results of aged asphalt mixture without an additive agent are shown in Figure 12. Observing the general trend portrayed by the figure, aging shows a great influence on the healing performance of asphalt mixture. The longer aging exposure caused a smaller healing level. From both healing treatments, 5 hours aged mixture showed the highest healing result among other levels of aging. At the first DH cycle of PAV-5 hrs samples, the healing performance of induction and microwave was 78% and 83%, respectively. During subsequent DH cycles until the fourth cycle, the healing level remained over 65%. Meanwhile, the healing level of 15 hours and 20 hours significantly decreased by 50% in the first cycle of damage healing. It can be explained that longer aging exposure makes asphalt binder stiffer. The research result from Lin confirmed that penetration and ductility decrease with the increase of aging time. Particularly, penetration decreases significantly after PAV for 20 hours.

Figure 13 illustrates the healing performance of aged mixture modified with 2 additive agents (i.e., type 2 and type A) that undergone two different healing treatments. Overall, the healing level of aged mixtures is improved by using additive agents. Particularly, using rejuvenator additive type 2 showed good performance. At the initial stage of damage healing, all samples with rejuvenator additive kept their healing level over 70%. The healing level of type 2 and type A showed a slight improvement compared to the control mixture; however, the improvement was significant only during late DH cycles on longer aging exposure. Different from rejuvenator additive, antistripping additive causes an increment of cohesion free energy [29], which is evident at the first stage of damage-healing.

The analysis of variance (ANOVA) with Tukey's HSD post hoc was used to evaluate the statistical significance of the change in healing performance with moisture-damaged and aging time (shown in Table 6). The result from ANOVA indicates that the healing performances of asphalt mixtures are significantly affected by moisture damage and long-term aging. However, there is no significant difference at  $\alpha = 0.05$  level between 3 FT cycles and 15 hours and also 5 FT cycles and 20 hours. In other words, a statistical correlation may be found between moisture damage and long-term aging within the scope and procedure of this experiment.

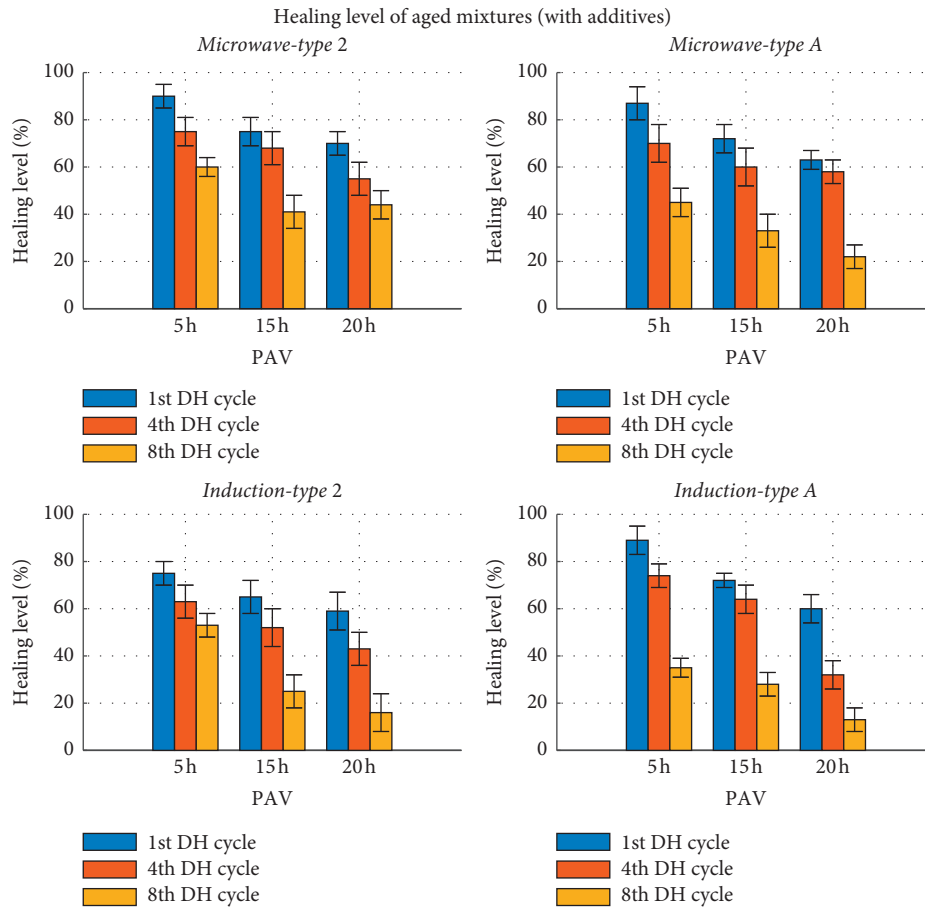


FIGURE 13: Healing level of aged mixtures modified with two additive agents.

TABLE 6: Tukey’s HSD post hoc summary result.

Types of damaged	PAV 5 hours	PAV 15 hours	PAV 20 hours
1 FT cycle	S	N	N
3 FT cycles	S	N	N
5 FT cycles	S	S	N

N: nonsignificant; S: significant.

#### 4. Conclusions

In this study, the indirect tensile strength test and the three-point bending test were conducted to investigate the effect of additive agents on the healing performance of hot mix asphalt under moisture and long-term aging damage. A series of test results showed that adding additive agents can improve the healing performance of asphalt mixture after being subjected to damage. The main research conclusions are presented as follows:

- (i) Microwave heating method shows a better healing option than that of induction heating. The entire asphalt mixture heats up with electromagnetic radiation, while for magnetic induction, thermal energy disseminates only through conductive materials, that is, steel wool fibers.
- (ii) Mixing asphalt binder with antistripping additive can obtain significant moisture resistance.

However, if healing performance is the primary goal of the mixture, a low viscosity rejuvenator additive is best.

- (iii) Three to four damage-healing cycles on asphalt mixture, with or without moisture damage, are able to achieve prime healing performance.
- (iv) The application of rejuvenators leads to the softening of the asphalt binder. This concept may enhance the healing performance of asphalt to some extent. Asphalt binders with rejuvenator may be softened faster under heating treatment, and the use of rejuvenator is expected to accelerate the crack healing process.

Following the statistic results of healing performance, there may have been a correlation between freeze-thaw cycles and long-term aging time in terms of healing performance, such as 3 freeze-thaw cycles with 15 hours of aging time and 5 freeze-thaw cycles with 20 hours of aging time. The mechanism correlation needs to be clarified in further studies.

#### Data Availability

The experimental data used to support the findings of this study will be made available from the corresponding author upon request.



## Conflicts of Interest

The authors declare that there are no conflicts of interest regarding the publication of this paper.

## Acknowledgments

This research was supported by Basic Science Research Program through the National Research Foundation of Korea (NRF) funded by the Ministry of Education (no. NRF-2017R1D1A1B03032594).

## References

- [1] G. D. Airey, "State of the art report on ageing test methods for bituminous pavement materials," *International Journal of Pavement Engineering*, vol. 4, no. 3, pp. 165–176, 2003.
- [2] T. Ma, X.-m. Huang, E. Mahmoud, and E. Garibaldy, "Effect of moisture on the aging behavior of asphalt binder," *International Journal of Minerals, Metallurgy, and Materials*, vol. 18, no. 4, pp. 460–466, 2011.
- [3] C. Miller, D. N. Little, A. Bhasin, N. Gardner, and B. Herbert, "Surface energy characteristics and impact of natural minerals on aggregate-bitumen bond strengths and asphalt mixture durability," *Transportation Research Record: Journal of the Transportation Research Board*, vol. 2267, no. 1, pp. 45–55, 2012.
- [4] T. A. Rafiqul and A. Mohiuddin, "Evaluating the relationship between permeability and moisture damage of asphalt concrete pavements," *Journal of Materials in Civil Engineering*, vol. 27, no. 5, Article ID 4014172, 2015.
- [5] D.-W. Park, W.-J. Seo, J. Kim, and H. V. Vo, "Evaluation of moisture susceptibility of asphalt mixture using liquid anti-stripping agents," *Construction and Building Materials*, vol. 144, pp. 399–405, 2017.
- [6] J. Norambuena-Contreras and A. Garcia, "Self-healing of asphalt mixture by microwave and induction heating," *Materials & Design*, vol. 106, pp. 404–414, 2016.
- [7] H. Li, J. Yu, S. Wu et al., "Study on the gradient heating and healing behaviors of asphalt concrete induced by induction heating," *Construction and Building Materials*, vol. 208, pp. 638–645, 2019.
- [8] v. B. Gerbert, "Self healing asphalt-extending the service life by induction heating of asphalt," in *Proceedings of the 6th Eurasphalt and Eurobitume Congress*, Prague, Czech Republic, June 2016.
- [9] M. D. Elwardany, F. Yousefi Rad, C. Castorena, and Y. R. Kim, "Evaluation of asphalt mixture laboratory long-term ageing methods for performance testing and prediction," *Road Materials and Pavement Design*, vol. 18, no. 1, pp. 28–61, 2017.
- [10] H. Bahia and D. Anderson, "The pressure aging vessel (PAV): a test to simulate rheological changes due to field aging," in *Physical Properties of Asphalt Cement Binders*, J. Hardin, Ed., pp. 67–88, West Conshohocken, PA, USA, 1994.
- [11] D. Kuang, W. Liu, Y. Xiao, M. Wan, L. Yang, and H. Chen, "Study on the rejuvenating mechanism in aged asphalt binder with mono-component modified rejuvenators," *Construction and Building Materials*, vol. 223, pp. 986–993, 2019.
- [12] A. F. Espinoza-Luque, I. L. Al-Qadi, and H. Ozer, "Optimizing rejuvenator content in asphalt concrete to enhance its durability," *Construction and Building Materials*, vol. 179, pp. 642–648, 2018.
- [13] F. Wang, L. Zhang, B. Yan et al., "Diffusion mechanism of rejuvenator and its effects on the physical and rheological performance of aged asphalt binder," *Materials*, vol. 12, no. 24, 2019.
- [14] S. Y. Teh and M. O. Hamzah, "Asphalt mixture workability and effects of long-term conditioning methods on moisture damage susceptibility and performance of warm mix asphalt," *Construction and Building Materials*, vol. 207, pp. 316–328, 2019.
- [15] P. K. Das, R. Balieu, N. Kringos, and B. Birgisson, "On the oxidative ageing mechanism and its effect on asphalt mixtures morphology," *Materials and Structures*, vol. 48, no. 10, pp. 3113–3127, 2015.
- [16] P. K. Das, H. Baaj, N. Kringos, and S. Tighe, "Coupling of oxidative ageing and moisture damage in asphalt mixtures," *Road Materials and Pavement Design*, vol. 16, no. 1, pp. 265–279, 2015.
- [17] M. R. B. McGennis, R. M. Anderson, T. W. Kennedy, and M. Solaimanian, *Background of Superpave Asphalt Mixture Design and Analysis*, National Asphalt Training Center Demonstration Project 101, Lexington, KY, USA, 1995.
- [18] B. H. Dinh, D.-W. Park, and T. H. M. Le, "Effect of rejuvenators on the crack healing performance of recycled asphalt pavement by induction heating," *Construction and Building Materials*, vol. 164, pp. 246–254, 2018.
- [19] H. Li, J. Yu, Q. Liu et al., "Induction heating and healing behaviors of asphalt concretes doped with different conductive additives," *Advances in Materials Science and Engineering*, vol. 2019, Article ID 2190627, 10 pages, 2019.
- [20] T. M. Phan, D.-W. Park, and T. H. M. Le, "Crack healing performance of hot mix asphalt containing steel slag by microwaves heating," *Construction and Building Materials*, vol. 180, pp. 503–511, 2018.
- [21] Á. García, "Self-healing of open cracks in asphalt mastic," *Fuel*, vol. 93, pp. 264–272, 2012.
- [22] ASTM D2872-12, *Standard Test Method for Effect of Heat and Air on a Moving Film of Asphalt (Rolling Thin-Film Oven Test)*, American Society for Testing Materials, West Conshohocken, PA, USA, 2012.
- [23] AASHTO T 283, *Standard Method of Test for Resistance of Compacted Asphalt Mixtures to Moisture-Induced Damage*, American Association of State Highway and Transportation Officials, Washington, DC, USA, 2014.
- [24] J. Norambuena-Contreras, R. Serpell, G. Valdés Vidal, A. González, and E. Schlangen, "Effect of fibres addition on the physical and mechanical properties of asphalt mixtures with crack-healing purposes by microwave radiation," *Construction and Building Materials*, vol. 127, pp. 369–382, 2016.
- [25] P. Pan, S. Wu, X. Hu, P. Wang, and Q. Liu, "Effect of freezing-thawing and ageing on thermal characteristics and mechanical properties of conductive asphalt concrete," *Construction and Building Materials*, vol. 140, pp. 239–247, 2017.
- [26] X. Chen and B. Huang, "Evaluation of moisture damage in hot mix asphalt using simple performance and superpave indirect tensile tests," *Construction and Building Materials*, vol. 22, no. 9, pp. 1950–1962, 2008.
- [27] AASHTO T 283, *Testing Method for Resistance of Compacted Asphalt Mixtures to Moisture Induced Damage*, American Association of State Highway and Transportation Officials, Washington, DC, USA, 2012.
- [28] T. Ma, X. Huang, Y. Zhao, and Y. Zhang, "Evaluation of the diffusion and distribution of the rejuvenator for hot asphalt recycling," *Construction and Building Materials*, vol. 98, pp. 530–536, 2015.
- [29] G. H. Hamed and S. A. Tahami, "The effect of using anti-stripping additives on moisture damage of hot mix asphalt," *International Journal of Adhesion and Adhesives*, vol. 81, pp. 90–97, 2018.

## Research Article

# Effects of Surfactant Warm-Mix Additives on the Rheological Properties of High-Viscosity Asphalt

Jingtao Shi <sup>1,2</sup>, Weiyu Fan <sup>1</sup>, Yi Lin <sup>1</sup>, Pinhui Zhao <sup>1</sup> and Jian Ouyang <sup>3</sup>

<sup>1</sup>State Key Laboratory of Heavy Oil Processing, College of Chemical Engineering, China University of Petroleum (East China), Qingdao 266580, China

<sup>2</sup>Petrochina Fuel Oil Company Limited Research Institute, Beijing 100195, China

<sup>3</sup>School of Transportation and Logistics, Dalian University of Technology, Dalian 116024, China

Correspondence should be addressed to Weiyu Fan; 15853256892@139.com, Pinhui Zhao; zhaopinhui08@163.com, and Jian Ouyang; ouyangjian@dlut.edu.cn

Received 20 January 2020; Accepted 6 March 2020; Published 25 April 2020

Guest Editor: Meng Guo

Copyright © 2020 Jingtao Shi et al. This is an open access article distributed under the Creative Commons Attribution License, which permits unrestricted use, distribution, and reproduction in any medium, provided the original work is properly cited.

In order to evaluate the possibility of the application of warm mixing technology in high-viscosity asphalt mixture, in this paper, the effects of surfactant warm-mix additives (WMAs) on physical and rheological properties of high-viscosity asphalt (HVA) which was prepared with self-developed SBS/C<sub>9</sub> petroleum resin blends (SPR) modifier were measured. The results indicate that the addition of WMA can decrease the viscosity and softening point but improve the penetration and ductility of warm-mix HVA. With the increase of the content of WMA, the modulus, failure temperature, viscosity, and recovery rate of warm-mix HVA all increased at first and then decreased, and the maximum value appeared when the modifier content was 1.0%–1.5%. Moreover, when the amount of WMA is 1.5%, the low-temperature performance of warm-mix HVA reaches the best value. Thus, the amount of WMA is of great importance for the warm-mix HVA, and in order to achieve ideal rheological properties, the recommended amount of WMA is 1.0%–1.5%. Considering economic improvement and environmental protection, WMA could be an alternative for increasing the workability of HVA.

## 1. Introduction

Porous asphalt pavement has various advantages such as a high void ratio, large frictional resistance attributed to the rough surface, skid and rutting resistance, and sound absorption and noise reduction [1, 2]. Therefore, it can reduce the thickness of water film on the pavement, water spray, and noise in wet weather, thus improving the skid resistance and enhancing driver safety [3–5]. Thus, porous asphalt pavements have been widely used in many countries [6]. Due to functional requirement of drainage, it is necessary to realise a void ratio greater than 18% through the formation of an interlocked skeleton structure by increasing the amount of coarse aggregates and reducing the amount of fine aggregates when designing porous asphalt mixtures; However, the structure has high internal frictional resistance and a low cohesion, and the bonding property of the binder can be

crucial if it is expected to acquire a large strength and resistance to external failure [7, 8]. Ordinary modified asphalts fail to satisfy the requirements for practical application and therefore the application of HVA is inevitable [9, 10]. Based on many years of practical experience in Japan, the concept of HVA was proposed to improve the long-term performance and durability of porous asphalt mixtures. For HVA, the dynamic viscosity at 60°C is a key parameter [11–13]. The higher its value, the better the high-temperature performance, deformation resistance, and cohesiveness of asphalt binders [9]. However, with the increase of dynamic viscosity at 60°C, the viscosity of HVA at 135°C is also higher than that of the ordinary modified asphalt binder [14]. There is no doubt that this problem will increase the difficulty of construction, thus making asphalt mixtures harder to be produced and compacted for construction [15]. However, as HVA can satisfy machinability requirements, it is necessary

to heat the HVA to a higher temperature, which is likely to accelerate the aging of asphalts and increases energy consumption and harmful gas emission during construction. This hinders the development and application of HVA to some extent [16].

Warm-mix asphalt technology is considered to be an effective solution to improve the workability of asphalt mixture and control the construction temperature at a low level by decreasing the viscosity of asphalts. Compared with hot-mix asphalt technology, warm-mix asphalt technology can lower the mixing and compaction temperatures, thus saving energy consumption and reducing the emission of harmful gas. Therefore, warm-mix asphalt technology can probably be classified as green technology for road construction [17, 18]. The application of warm-mix asphalt technology to the porous asphalt pavement can not only improve functional pavements but also can be beneficial to the environment. However, whether or not the application of different kinds of warm-mix asphalt technology exerts unfavourable effects on the performance of finished HVA is waiting to be further explored. Rodríguez-Alloza et al. [19] evaluated the influence of four types of warm-mix additives (Sasobit, Asphaltan A, Asphaltan B, and Licomont BS 100) on the performance of the crumb rubber modified asphalt (CRMA). The results showed that the WMAs can successfully reduce the viscosity of CRMA, improve the softening point, and lower the penetration. Additionally, the four types of WMAs do not exert great influence on the elastic recovery and ductility of asphalts at 25°C. Sanchez-Alonso et al. investigated the influences of three kinds of warm-mix asphalt technology (including chemical WMAs, organic WMAs, and foamed asphalt) on the performance of asphalt mixtures. The results revealed that the addition of WMA reduces the construction temperature. At the temperature adopted in the experiment, compared with hot-mix asphalt mixture, the water sensitivity of warm-mix asphalt mixture is improved [20]. Podolsky et al. explored the influences of biological base WMA on the compactness and low-temperature cracking of matrix asphalt and polymer-modified asphalt mixture. They suggested that, compared with a hot-mix asphalt mixture, the addition of WMA reduces the construction temperature and still generates similar compaction performance. Furthermore, WMA polymer-modified asphalt mixture is similar to hot-mix asphalt mixture in low-temperature cracking terms [21]. Zheng et al. investigated the influences of three types of WMAs (RH, EC-120, and Sasobit) on dynamic viscosity at 60°C, Brookfield viscosity at 135°C, high-temperature rheological properties, and low-temperature creep properties of styrene-butadiene-styrene (SBS) HVA. The results suggested that these WMAs significantly reduce the high-temperature viscosity (135°C) of SBS HVA asphalts while EC-120 and Sasobit decrease the absolute viscosity (60°C). Moreover, EC-120 can increase the high-temperature rheological properties and improve the low-temperature creep properties of asphalt mixtures [6]. Frigio et al. explored the moduli and fatigue performance of warm-mix porous asphalt mixture before and after aging process. They found that warm-mix asphalt technology lowers the construction temperature and reduces the elastic

modulus of the mixture, with no influence on the fatigue performance of mixture after long-term aging [22]. However, at present, there are few studies on the rheological properties of the high-viscosity asphalt with a surfactant warm mixing agent.

In this study, the influences of the dosage of surfactant WMA on physical properties and rheological properties of HVA which was modified by a self-developed SPR modifier were characterized.

## 2. Materials and Measurement

**2.1. Materials.** The AH-70 asphalts purchased from Petro-China Company Limited (Qinhuangdao, Hebei Province, China) were taken as the base asphalts. The physical properties and four-component compositions of the base asphalts are summarised in Table 1. The self-developed SBS/C<sub>9</sub> petroleum resin blends (SPR) were chosen as the modifier. The SPR modifier was prepared via a simple one-pot polymer alloying process by taking SBS and C<sub>9</sub> petroleum resin as main raw materials (see preparation process in Supplementary Section). In addition, the molecular weight of SPR is 211114 and its melting point is 111.40°C. The Evotherm M1 developed by MeadWestvaco Investment Co., Ltd. (China) was used as the surfactant WMA. The density of Evotherm M1 is 0.95 g/cm<sup>3</sup> at 20°C, and the kinematic viscosity is 960 mPa s at 25°C. Furthermore, based on our previous researches, when the content of Evotherm M1 is 1.0 wt%, the mixing temperature of high-viscosity asphalt mixture decreases by about 30°C if it is to meet the volume requirement.

**2.2. Preparation of Samples.** Based on the results of our previous researches on the high-viscosity asphalt and warm-mix asphalt, by using a stirrer with a temperature-control electric jacket, the warm-mix HVA (WHVA) was prepared, and the preparation process of warm-mix HVA is shown in Figure 1. To minimise the influence of other factors, the preparation technology is optimised according to previous research, and the temperature variation was no greater than 1°C during its preparation. The molten asphalt was poured into a cylindrical vessel after being weighed, and then the vessel was heated in the electric jacket. In this case, the asphalts were heated to 175°C while stirring at 300 rpm, to which the SPR modifier was slowly added. After the stirring rate was adjusted to 800 rpm, the asphalts were stirred for 2.5 h. Thereafter, WMA was slowly added to the asphalts and stirred the mixture for 0.5 h to obtain warm-mix HVA. For comparison, the prepared warm-mix HVA in which the dosage of WMA accounts for 0 wt% (no added WMA), 0.5 wt%, 1.0 wt%, 1.5 wt%, and 2.0 wt% of HVA were separately numbered: WHVA0, WHVA0.5, WHVA1.0, WHVA1.5, and WHVA2.0, respectively.

**2.3. Physical Properties Test.** Conventional tests were carried out to evaluate the properties of warm-mix HVA, including penetration (ASTM D5), softening point (ASTM D36), ductility (ASTM D113), kinematic viscosity (ASTM D4402), motive viscosity (60°C) (ASTM D4402), and elastic recovery (ASTM D6084).

TABLE 1: Physical properties and chemical compositions of AH-70 asphalt.

Properties	Specifications	Measured values
Penetration (25°C, 0.1 mm)	ASTM D5	69
Penetration index (PI)	ASTM D5	-1
Softening point (R&B, °C)	ASTM D36	48.5
Ductility (15°C, cm)	ASTM D113	168
Kinematic viscosity (135°C, Pa·s)	ASTM D4402	0.475
Density (15°C, g·cm <sup>-3</sup> )	ASTM D70	1.014
Saturates (wt%)		16.29
Aromatics (/wt%)		39.68
Resins (wt%)	ASTM D4124	30.68
Asphaltenes (wt%)		13.35

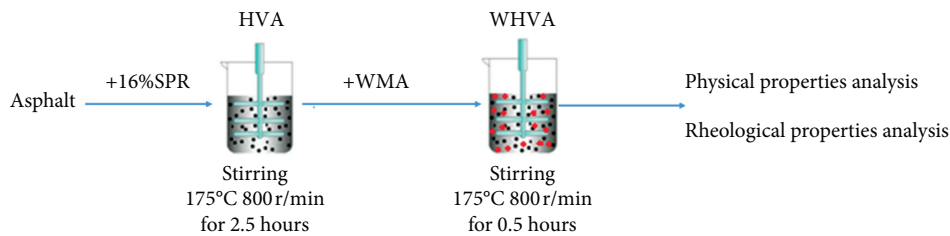


FIGURE 1: Preparation process of warm-mix HVA.

**2.4. Rheological Test.** By applying a MCR302 DSR rheometer (Anton Paar), the rheological behaviours of the warm-mix high-viscosity asphalt were explored. Strain and stress sweep tests were previously employed on each sample to obtain the linear viscoelastic range. Within the linear viscoelastic range, the samples were subjected to small-amplitude oscillatory shear testing to acquire the isothermal sweep results at frequencies of 0.1 to 50 rads at 5°C, 25°C, 40°C, 55°C, and 75°C. In the temperature sweep test, the strain control mode was adopted, the frequency was at 10 rad/s, and the temperature was incrementally increased (by 10°C steps) from 30°C to 120°C. It is worth noting that a 25 mm diameter plate-plate geometry with a 1 mm gap was used for measurements at room temperature (20°C) or above, while an 8 mm diameter plate-plate geometry with a 2 mm gap was applied for tests below the room temperature. In the multistress creep recovery (MSCR) test, 10 cycles were applied, each of which consisted of 1 s of creep and 9 s of recovery. The two processes were separately conducted at 0.1, 1.6, and 3.2 kPa. Moreover, a steady-state viscous flow test was conducted on the samples under the steady-state shear mode of the rheometer, with a 25 mm diameter plate-plate geometry with a 1 mm gap. The viscous flow properties of the samples were measured within a large range ( $10^{-3}$  to  $10^1$  s<sup>-1</sup>) of shear rates at 60°C. The creep behaviours of the high-viscosity asphalt at a low temperature were characterized by applying a bending beam rheometer (BBR) to attain two indices, creep stiffness  $S$  and the rate of change  $m$  of the stiffness with time [23].

By using the time-temperature equivalence principle, the viscoelasticity within wide frequency and temperature ranges was acquired. However, the viscoelasticity spanning several orders of magnitude was rarely measured directly.

The time-temperature equivalence principle indicates that the influence of prolonging the test duration (or decreasing the frequency) on mechanical properties of materials is equivalent to that of increasing the temperature. According to the time-temperature equivalence principle, various viscoelastic parameters measured through experiment can be superimposed through shift factors to draw a master curve.

### 3. Results and Discussion

**3.1. Physical Properties.** The effects of WMA on physical properties of warm-mix HVA are shown in Figure 2. The penetration, softening point, ductility, elastic recovery, and viscosity indices reflecting physical properties separately can reflect high- and low-temperature performance, mechanical properties, and workability of asphalts. As shown in Figure 2, with increasing dosage of WMA, the physical properties of warm-mix HVA generally show the following changes: rising penetration, decreasing softening point, growing ductility, reducing Brookfield viscosity at 135°C and dynamic viscosity at 60°C, and an insignificantly changing elastic recovery. This indicated that the addition of WMA can lower the viscosity of warm-mix HVA and therefore improve its workability.

The warm-mix asphalt technology based on WMA is expected to reduce the viscosity (high-temperature viscosity) of asphalts during construction through addition of WMA while showing an insignificant influence on the low-temperature viscosity and rutting resistance. Therefore, it is important to determine an appropriate dosage of WMA for warm-mix HVA. Through measuring different effects of the

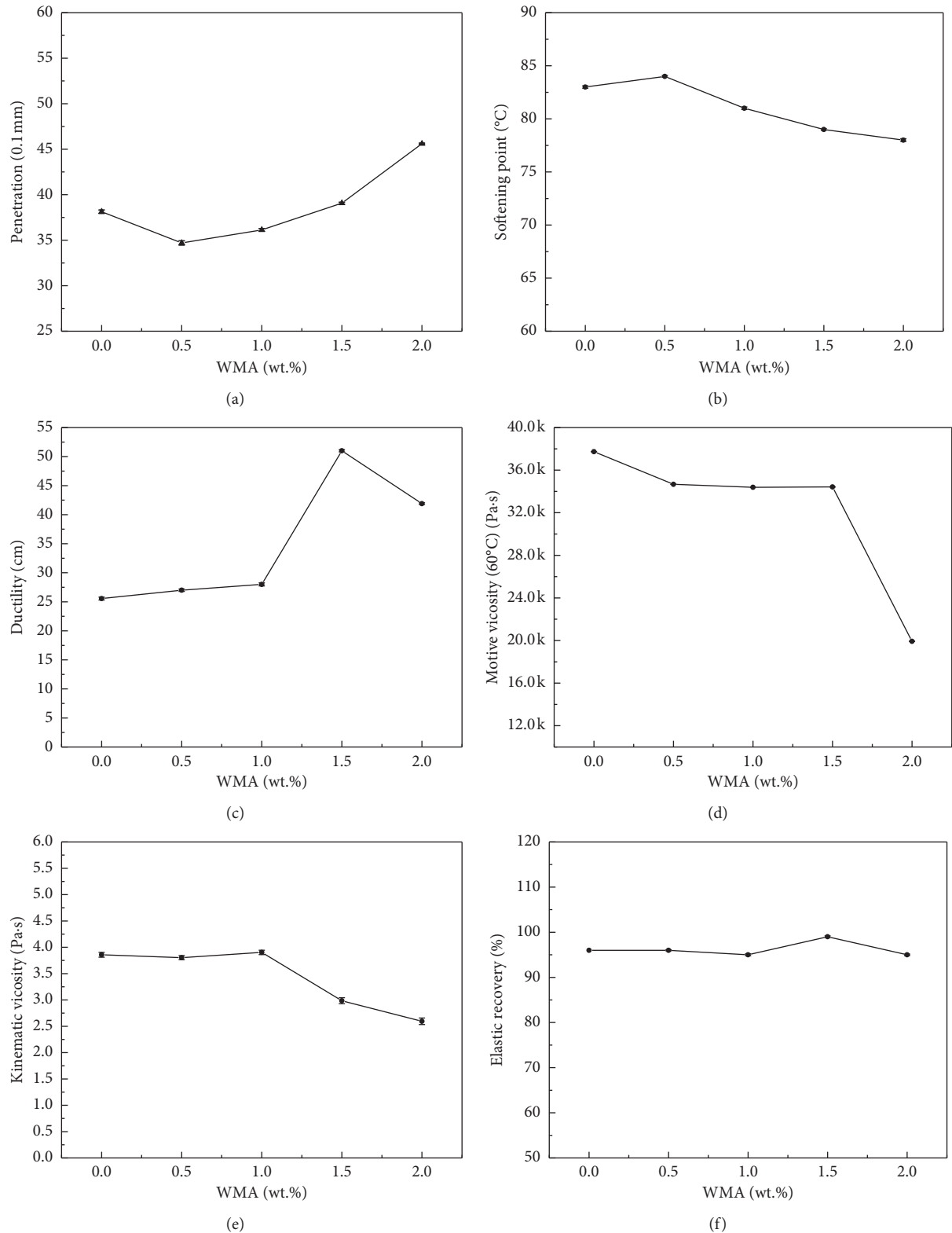


FIGURE 2: Physical properties of warm-mix HVA: (a) penetration; (b) softening point; (c) ductility; (d) motive viscosity (60°C); (e) kinematic viscosity (135°C); (f) elastic recovery.

dosage of WMA on physical properties of the warm-mix HVA, it can be seen that the appropriate dosage of WMA was between 0.5 and 1.5 wt%.

**3.2. Rheological Properties.** The utilisation of the porous asphalt pavement depends on the mechanical and viscoelastic properties of HVA. The linear viscoelasticity of warm-

mix HVA is sensitive to changes in composition and structure of the polymers and dosage of WMA. Due to the complexity of the systems, it is difficult to deduce the characteristics of the internal structures of warm-mix HVA. The rheological parameters within the linear viscoelastic range were independent of changing stress and strain while were only related to the material properties. Therefore, the linear viscoelasticity of asphalts was sensitive to changes in the internal structures of modified asphalts. Testing the linear viscoelasticity is a powerful way of investigating the effects of different structures of polymers and the dosages of WMA on performances of warm-mix HVA. In this section, through a frequency sweep, temperature sweep, steady-state shear testing, MSCR testing, and low-temperature creep testing, the rheological properties of warm-mix HVA were measured.

**3.2.1. Frequency Sweep at Intermediate and High Temperatures.** The master curves of warm-mix HVA at 25°C at different dosages of WMA are shown in Figure 3. The master curves are obtained through the shift in frequency-sweep curves at 5°C, 25°C, 40°C, 55°C, and 70°C. As shown in Figure 3, the dosage of WMA exerted complex effects on the complex modulus  $G^*$  of warm-mix HVA. Over the whole frequency range, there was a significant difference in the master curves of warm-mix HVA with different dosages of WMA. In a low  $\omega$  range, the addition of WMA caused the value of  $G^*$  warm-mix HVA to increase and then decrease. It reached a maximum at a dosage of WMA of 1.0 wt%. Adding less than 1.0 wt% WMA can improve the high-temperature performance of warm-mix HVA while excessive amount of WMA will destroy the high-temperature performance and rutting resistance of warm-mix HVA.

As shown in the master curves in Figure 3(a), the time-temperature equivalence principle can be applied to a warm-mix HVA. The change of shift factors with temperature is shown in Figure 3(b). It can be seen that the warm-mix HVA with different dosages of WMA exhibited different shift factors at different temperatures. The temperature dependence of the shift factor can characterise the temperature susceptibility of samples. The dependence of shift factors on temperature can be described by utilising an Arrhenius-like equation or Williams-Landel-Ferry (WLF) equation [24]. Here, we applied the Arrhenius-like equation to describe the change of shift factors with temperature.

It can be seen from Figure 4(a), although warm-mix HVA with different dosages of WMA showed approximate shift factors, the difference in shift factors can be quantitatively distinguished according to the slope of the Arrhenius-like equation. That is, the activation energy  $E_a$  was used to characterise the systems, as shown in Figure 4(b).

Figure 4(b) shows that the addition of WMA reduced the activation energy of the warm-mix HVA, indicating that the sensitivity of the warm-mix HVA to temperature decreased. Moreover, with the increase of WMA, the activation energy of the warm-mix HVA first decreased and then stabilised. This is because the change of activation energy is mainly determined by SPR modifier molecules. The hydrophilic

segment of Evotherm M1 is composed of long-chain aliphatic alkanes. Furthermore, the aliphatic alkanes can be adsorbed by SPR modifier molecules to promote their swelling and dispersion in asphalt and then play a better role in modification. However, when the amount of WMA reaches a certain value, the adsorption reaches equilibrium and the activation energy tends to equilibrium as well.

**3.2.2. Temperature Sweeps.** Apart from the master curve, the samples were subjected to temperature sweep within a large temperature range to explore the linear viscoelasticity of warm-mix HVM asphalts. The changes in storage modulus  $G'$ , loss modulus  $G''$ , and rutting factor  $G^*/\sin\delta$  with temperature are shown in Figure 5. With increasing temperature, the values of  $G'$  and  $G''$  of the warm-mix HVA decreased and presented complex changes with temperature as well. Within the medium- and high-temperature range (30°C to 70°C), the values of  $G'$  and  $G''$  of various samples were similar and showed a consistent rate of change with temperature. Above 80°C, especially in the ultrahigh-temperature range (above 100°C),  $G'$  and  $G''$  differed significantly. The relative values of  $G'$  and  $G''$  of various samples, in descending order, were WHVA1.0, WHVA0.5, WHVA1.5, WHVA0, and WHVA2.0. Considering the rate of change, WHVA2.0 showed the largest rate of reduction with increasing temperature, followed by WHVA0. It is worth noting that WHVA1.0, WHVA0.5, and WHVA1.5 exhibited similar rates of change: within the temperature range of 90°C to 100°C,  $G' \sim T$  and  $G'' \sim T$  curves of the samples both showed a zone of low gradient. In that case, the slope of the curves was at a minimum. When the temperature was higher than 100°C,  $G'$  and  $G''$  decreased significantly.

AASHTO code M320 defines the rutting factor  $G^*/\sin\delta$  to characterise the rutting resistance of asphalts and requires that  $G^*/\sin\delta$  of new asphalts be no lower than 1.0 kPa. The changes in rutting factor  $G^*/\sin\delta$  with temperature are shown in Figure 5(c):  $G^*/\sin\delta$  decreased with increasing temperature, and these were consistent with the change of  $G'$  and  $G''$ . The changes in failure temperature when various samples showed rutting with WMA are shown in Figure 5(d), the failure temperature of warm-mix HVA increased at first and then decreased with increasing dosage of WMA, and it reached a maximum when the dosage of WMA was 1.5 wt%.

As described above, at low content, WMA can promote the dispersion of modifiers in asphalt and play a better role in modification. However, due to the low viscosity of WMA, when the content of WMA exceeds a certain value, the viscosity and rutting resistance of warm-mix HVA will decrease.

**3.2.3. Flow Behaviour.** The linear viscoelasticity was obtained under a small-amplitude deformation. Nonlinear viscoelasticity measured under a large-amplitude deformation can reveal useful information, especially that distinguishing differences in modified asphalts caused by changes to polymer structures and that establishing relationships between structure and performance.

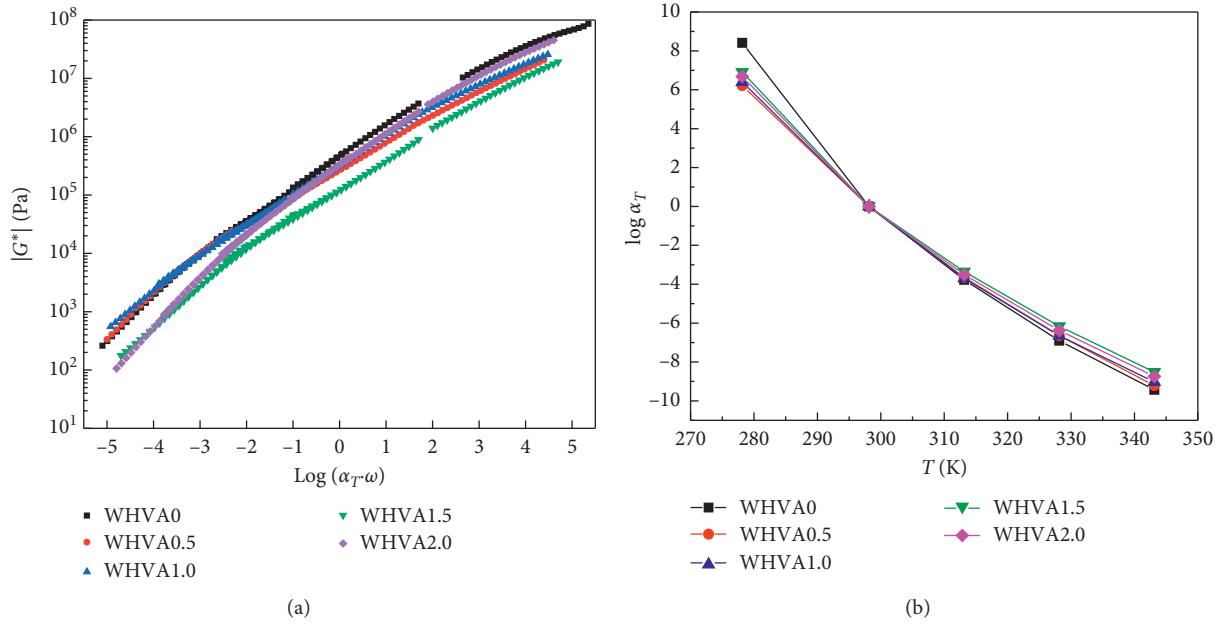


FIGURE 3: (a) Master curves and (b) shift factors at different temperatures for warm-mix HVA.

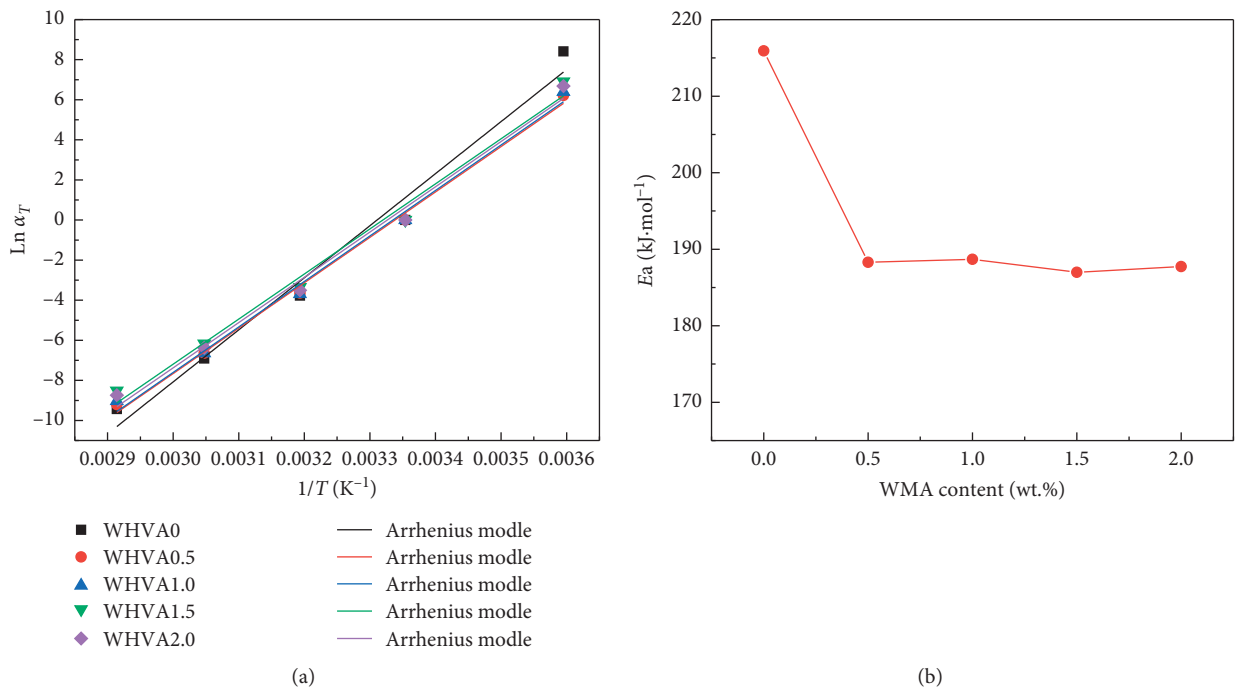


FIGURE 4: (a) Evolutions of shift factors versus temperature and (b) variations of activation energy as a function of WMA contents for warm-mix asphalt.

The change in steady-state viscosity of warm-mix HVA at 60°C with shear rate (that is, the viscous flow curve) is shown in Figure 6. Within the whole range of shear rates tested, the viscosity of the warm-mix HVA decreased slightly with increasing shear rate, showing shear thinning behaviour. The viscous flow curve can be fitted by applying the Cross model [24], and the fitting parameters of warm-mix HVA obtained by using the Cross model are listed in Table 2.

As shown in Table 2,  $\eta_0$ ,  $\eta_\infty$ ,  $\lambda$ , and  $d$  denote the zero-shear viscosity (ZSV), the viscosity corresponding to an infinite shear rate, the characteristic time, and flow index, respectively. The value of  $\eta_0$  of warm-mix HVA increased at first and then decreased with increasing dosage of WMA. When the dosage of WMA was 1.0 wt%,  $\eta_0$  of warm-mix HVA was maximised. For warm-mix HVA, within the dosage range of WMA tested in the study, the addition of

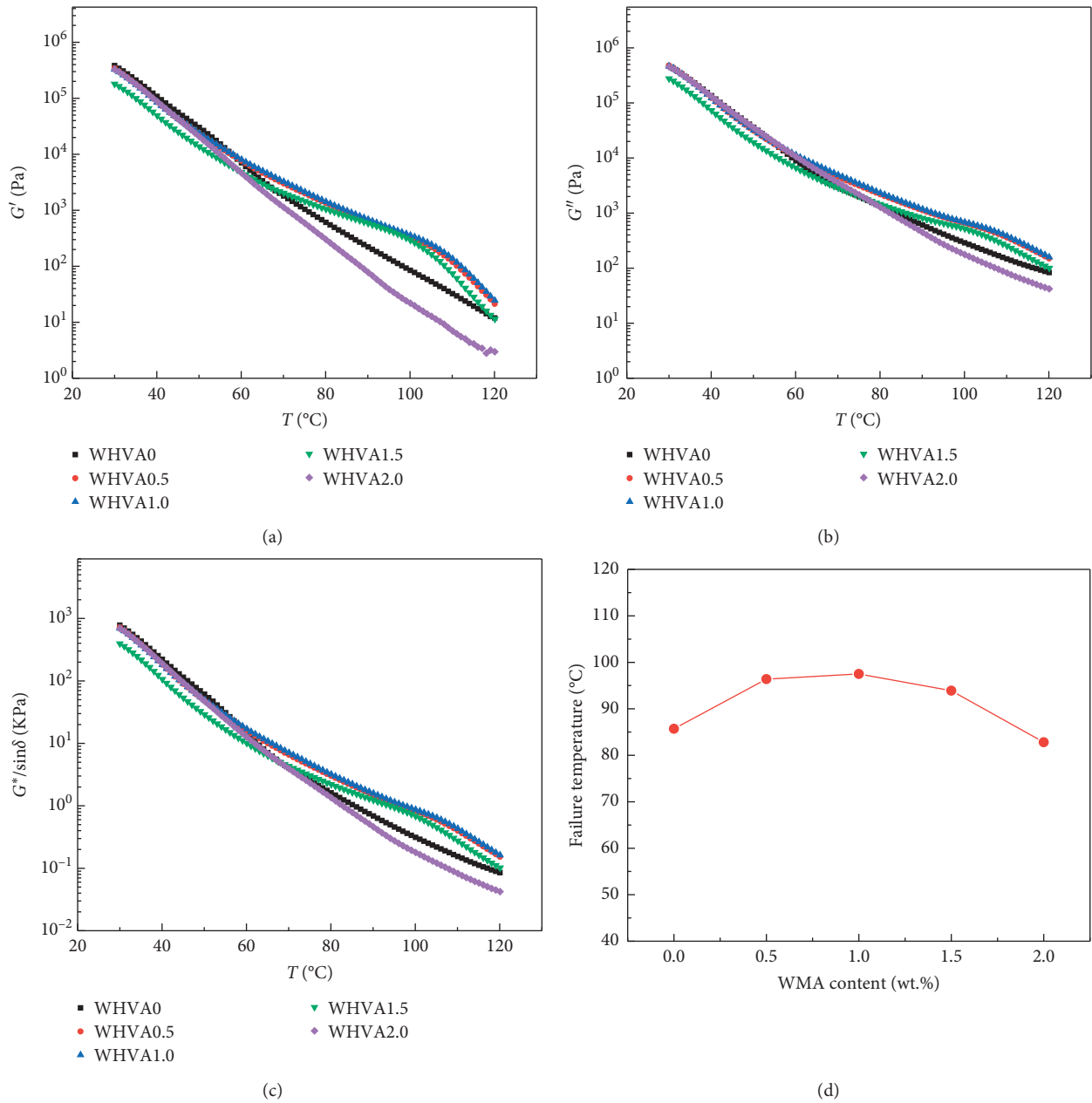


FIGURE 5: Evolution of (a)  $G'$ , (b)  $G''$ , and (c)  $G^*/\sin\delta$  versus temperature and (d) temperature calculated at the point of  $G^*/\sin\delta = 1.0$  kPa for warm-mix HVA.

WMA increased the ZSV ( $\eta_0$ ) of HVA. The reason for this result is consistent with that in Section 3.2.4.

**3.2.4. MSCR.** MSCR is an index developed in recent years to evaluate high-temperature performance of modified asphalts. In this study, MSCR was conducted at 60°C under three stress levels (100, 1600, and 3200 Pa). Through MSCR, two parameters (involving recovery rate  $R$  and non-recoverable compliance  $J_{nr}$ ) can be acquired.  $R$  and  $J_{nr}$  were separately calculated based on recoverable and non-recoverable strains. The strain responses of warm-mix HVA within ten cycles at 60°C under 100 Pa are shown in Figure 7.

When the dosage of WMA was between 0 and 1.0 wt%, the higher the strain on warm-mix HVA when the creep stage ended, the higher the strain when the recovery stage was completed in a creep-recovery cycle. The strain decreased with increasing dosage of WMA; however, the strains on WHVA1.5 and WHVA2.0 samples were much greater than those on the other samples.

To characterise the effects of WMA on high-temperature performances of warm-mix HVM asphalts, Figure 8 shows the changes of recovery rate of warm-mix HVA with dosage of WMA at 40°C and 60°C under three stresses. It can be seen from Figure 8(a) that, at 40°C, with increasing dosage of WMA, the recovery rate of warm-mix HVA increased at



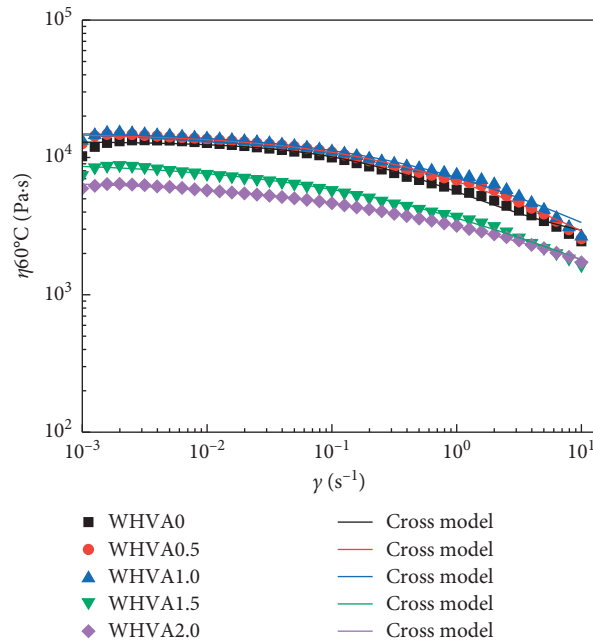


FIGURE 6: Flow curves of warm-mix HVA at 60°C as a function of WMA content.

TABLE 2: The resulting Cross model parameters as a function of WMA content for warm-mix HVA.

		Various WMA contents (wt.%)				
		0	0.5	1.0	1.5	2.0
HVA	$\eta_0$ (Pa·s)	13034	15021	15434	9332	55
	$\eta_\infty$ (Pa·s)	2118	1.252	$3.3561E-82$	$3.784E-30$	300.242
	$\lambda$ (s)	2.679	1.536	1.362	2.960	1.896
	$D$	0.759	0.520	0.490	0.423	0.409

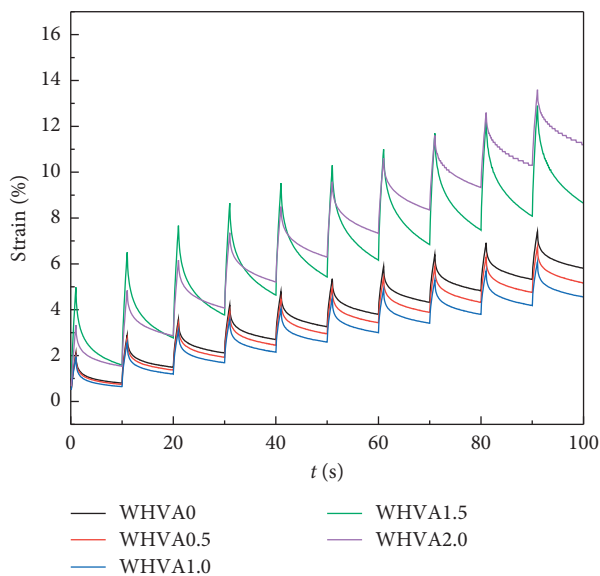


FIGURE 7: Strain response in the MSCR test (ten cycles) for warm-mix HVA at 60°C and 100 Pa.

first, then decreased, and finally slightly increased, and it reached its maximum and minimum at dosages of WMA of 0.5 wt% and 1.5 wt%, respectively. At 60°C, with increasing

dosage of WMA, the recovery rate of warm-mix HVA increased at first, then decreased, and finally increased slightly, and its maximum appeared at 1.5 wt% dosage of WMA, indicating that the recoverability of the asphalt pavement was the strongest. Additionally, increasing temperature and stress also resulted in the significant reduction of  $R$  of warm-mix HVA samples.

The change in nonrecoverable compliance  $J_{nr}$  with dosage of WMA is shown in Figure 8(b):  $J_{nr}$  increased with increasing temperature. The difference between  $J_{nr,100}$  and  $J_{nr,3200}$  increased with increasing dosage of WMA. At 40°C, the  $J_{nr}$  of warm-mix HVA increased and then decreased with increasing dosage of WMA, and its maximum was found when the dosage of WMA was 1.5 wt%. At 60°C,  $J_{nr}$  first decreased, then increased with increasing dosage of WMA, and was minimised when the dosage of WMA was 1.0 wt%.

**3.2.5. Low-Temperature Creep Behaviour.** To characterise the influence of the dosage of WMA on low-temperature creep behaviour in warm-mix HVA, the creep behaviours of warm-mix HVA under different loading durations at  $-18^\circ\text{C}$  and  $-24^\circ\text{C}$  were tested in the BBR. The changes in creep stiffness  $S$  and  $m$  with loading time are shown in Figure 9. Ductility of the system decreased. When the dosage of WMA was 1.5 wt%, minimum  $s$  and maximum  $m$  were found

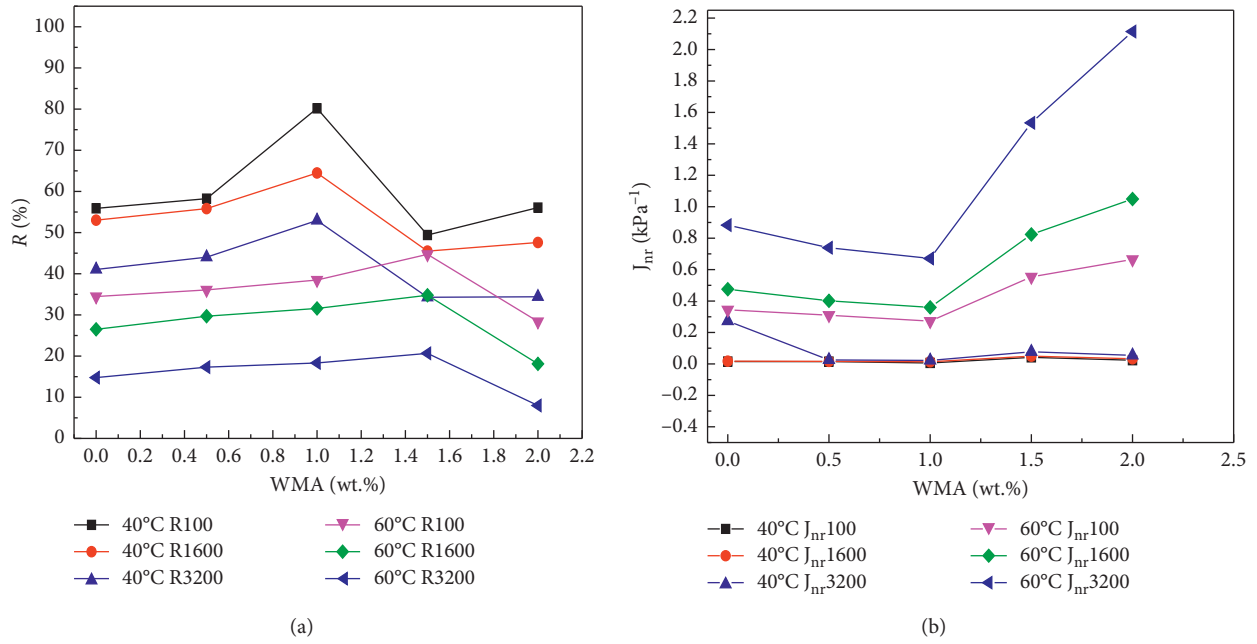


FIGURE 8: (a) The percent recovery and (b) nonrecoverable creep compliance calculated from the MSCR test at 40°C and 60°C and three stress levels for warm-mix HVA.

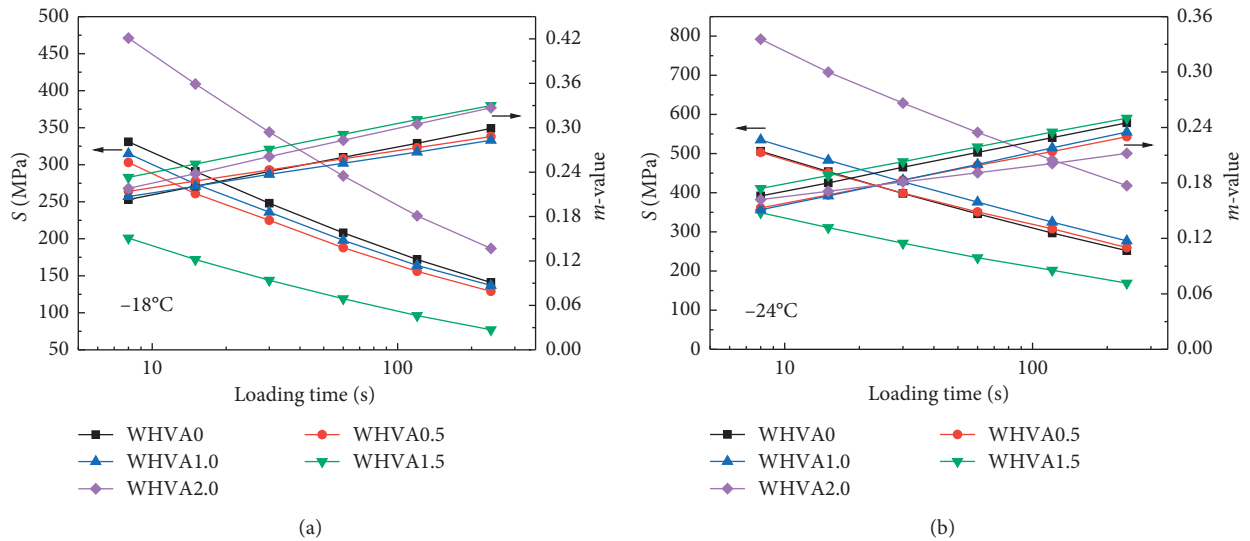


FIGURE 9: Continued.

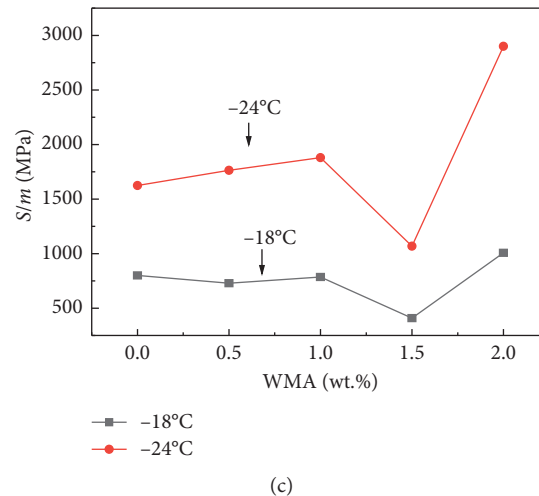


FIGURE 9: Evolution of  $S$  and  $m$  values versus loading time for warm-mix HVA at (a)  $-18^{\circ}\text{C}$  and (b)  $-24^{\circ}\text{C}$ , and (c) the ratio of creep stiffness  $S$  and  $m$  as a function of WMA content at  $-18$  and  $-24^{\circ}\text{C}$ .

similar to that at  $-18^{\circ}\text{C}$ . As for a warm-mix HVA, at  $-18^{\circ}\text{C}$ , the  $S$  of WHVA1.5 was minimised; however, the  $S$  of WHVA2.0 was maximised. WHVA1.5 exhibited the largest  $m$ . At  $-24^{\circ}\text{C}$ ,  $S$  and  $m$  of warm-mix HVA showed a similar trend to those at  $-8^{\circ}\text{C}$ . This implied an optimal low-temperature performance of the warm-mix HVA system at a dosage of WMA of 1.5 wt%.

At low temperature, a low  $S$  and a high  $m$  represent a strong cracking resistance of the asphalts. The coefficient  $I$  was defined to characterise the low-temperature cracking resistance of asphalts, that is, the ratio of  $S$  to  $m$  at 60 s. The lower the value of  $I$ , the better the low-temperature performance. At  $-18^{\circ}\text{C}$  and  $-24^{\circ}\text{C}$ , the changes in  $S/m$  values of warm-mix HVA with changing dosage of WMA are shown in Figure 9(c): the  $S/m$  values of the warm-mix HVA decreased at first and then rose with increasing dosage of WMA.  $I$  was minimised when the dosage of WMA was 1.5 wt%. With increasing dosage of WMA, the value of  $I$  increased; therefore, for warm-mix HVA, the most suitable dosage of WMA was 1.5 wt% from the perspective of low-temperature performance.

#### 4. Conclusion

The effects of surfactant WMA on physical and rheological properties of HVA prepared with the self-developed SPR modifier were measured. The addition of WMA can decrease the viscosity and improve the workability of HVA. With the increase of WMA content, penetration and ductility increased; softening point, kinematic viscosity at  $135^{\circ}\text{C}$ , and motive viscosity at  $60^{\circ}\text{C}$  decreased; and elasticity recover was unchanged.

Meanwhile, with the increase of WMA content, the modulus, failure temperature, viscosity, and recovery rate of warm-mix HVA increased at first and then decreased, and the maximum value appeared at 1.0%–1.5%. Moreover, when the amount of WMA is 1.5%, the low-temperature

performance of warm-mix HVA shows the best value. Thus, for HVA, in order to achieve ideal rheological properties, the recommended amount of WMA is 1.0%–1.5%.

As a conclusion, WMA could be an alternative for increasing workability of HVA. However, the amount of a warm mixing agent must be reasonably determined because it has a great influence on high-low temperature performance of warm-mix HVA. Moreover, in the future research, we will pay more attention to the effect of WMA on the performance of high-viscosity asphalt mixture, especially the durability.

#### Data Availability

The data used to support the findings of this study are available from the corresponding author upon request.

#### Conflicts of Interest

The authors declare no conflicts of interest.

#### Acknowledgments

We would like to acknowledge many coworkers, students, and laboratory assistants for providing technical support on instrument analysis. Thanks are due to Dr. Edward C. Mignot, Shandong University, for linguistic advice. This work was financially supported by the National Natural Science Foundation of China (No. 51608511), Key R & D Project of Shandong Province (2018GGX105013), and Project of Science and Technology Support for Youth Entrepreneurship in Colleges and Universities of Shandong Province (2019KJG004).

#### Supplementary Materials

It includes preparation method of the high-viscosity modifier SJH. (*Supplementary Materials*)

## References

- [1] Y. Sun, Z. Gu, J. Wang, C. Fang, and X. Yuan, "Study on relaxation damage properties of high viscosity asphalt sand under uniaxial compression," *Advances in Civil Engineering*, vol. 2018, Article ID 1498480, 12 pages, 2018.
- [2] L. Li, H. Geng, and Y. Sun, "Simplified viscosity evaluating method of high viscosity asphalt binders," *Materials and Structures*, vol. 48, no. 7, pp. 2147–2156, 2015.
- [3] L.-T. Geng, Q. Xu, R.-B. Ren, L.-Z. Wang, X.-L. Yang, and X.-Y. Wang, "Performance research of high-viscosity asphalt mixture as deck-paving materials for steel bridges," *Road Materials and Pavement Design*, vol. 18, no. 1, pp. 208–220, 2017.
- [4] A. Moriyoshi, T. Jin, T. Nakai, H. Ishikawa, K. Tokumitsu, and A. Kasahara, "Construction and pavement properties after seven years in porous asphalt with long life," *Construction and Building Materials*, vol. 50, pp. 401–413, 2014.
- [5] Q. Liu and D. Cao, "Research on material composition and performance of porous asphalt pavement," *Journal of Materials in Civil Engineering*, vol. 21, no. 4, pp. 135–140, 2009.
- [6] X. Y. Zheng, S. M. Easa, T. Ji, Z. L. Jiang, and A. O. Abd El Halim, "Influence of warm-mix additives on physical, rheological, and morphological properties of high-viscosity asphalt," *Journal of Materials in Civil Engineering*, vol. 31, no. 2, 12 pages, 2019.
- [7] B. Xu, M. Li, S. Liu, J. Fang, R. Ding, and D. Cao, "Performance analysis of different type preventive maintenance materials for porous asphalt based on high viscosity modified asphalt," *Construction and Building Materials*, vol. 191, pp. 320–329, 2018.
- [8] F. Zhang and C. Hu, "Preparation and properties of high viscosity modified asphalt," *Polymer Composites*, vol. 38, no. 5, pp. 936–946, 2017.
- [9] F. Zhang, C. Hu, and W. Zhuang, "The research for low-temperature rheological properties and structural characteristics of high-viscosity modified asphalt," *Journal of Thermal Analysis and Calorimetry*, vol. 131, no. 2, pp. 1025–1034, 2018.
- [10] H. Wang, Z. You, J. Mills-Beale, and P. Hao, "Laboratory evaluation on high temperature viscosity and low temperature stiffness of asphalt binder with high percent scrap tire rubber," *Construction and Building Materials*, vol. 26, no. 1, pp. 583–590, 2012.
- [11] X. Qin, S. Zhu, X. He, and Y. Jiang, "High temperature properties of high viscosity asphalt based on rheological methods," *Construction and Building Materials*, vol. 186, pp. 476–483, 2018.
- [12] S. Li, T. Shields, S. Noureldin, and Y. Jiang, "Field evaluation of surface friction performance of chip seals in Indiana," *Transportation Research Record: Journal of the Transportation Research Board*, vol. 2295, no. 1, pp. 11–18, 2012.
- [13] A. Shenoy, "Model-fitting the master curves of the dynamic shear rheometer data to extract a rut-controlling term for asphalt pavements," *Journal of Testing and Evaluation*, vol. 30, no. 2, pp. 95–102, 2002.
- [14] L. Qu, Y. Gao, H. Yao et al., "Preparation and performance analysis of high-viscosity and elastic recovery modified asphalt binder," *Advances in Civil Engineering*, vol. 2019, Article ID 6070685, 16 pages, 2019.
- [15] F. Zhang and C. Hu, "The composition and ageing of high-viscosity and elasticity asphalts," *Polymer Composites*, vol. 38, no. 11, pp. 2509–2517, 2017.
- [16] J. Zhang, G. Liu, L. Xu, and J. Pei, "Effects of WMA additive on the rheological properties of asphalt binder and high temperature performance grade," *Advances in Materials Science and Engineering*, vol. 2015, Article ID 467891, 7 pages, 2015.
- [17] H. Yu, Z. Zhu, Z. Leng et al., "Effect of mixing sequence on asphalt mixtures containing waste tire rubber and warm mix surfactants," *Journal of Cleaner Production*, vol. 246, Article ID 119008, 2020.
- [18] J. Ouyang, J. Zhao, and Y. Tan, "Modeling mechanical properties of cement asphalt emulsion mortar with different asphalt to cement ratios and temperatures," *Journal of Materials in Civil Engineering*, vol. 30, no. 10, Article ID 4018263, 2018.
- [19] A. M. Rodríguez-Alloza, J. Gallego, and I. Pérez, "Study of the effect of four warm mix asphalt additives on bitumen modified with 15% crumb rubber," *Construction and Building Materials*, vol. 43, pp. 300–308, 2013.
- [20] E. Sanchez-Alonso, A. Vega-Zamanillo, D. Castro-Fresno, and M. DelRio-Prat, "Evaluation of compactability and mechanical properties of bituminous mixes with warm additives," *Construction and Building Materials*, vol. 25, no. 5, pp. 2304–2311, 2011.
- [21] J. H. Podolsky, A. Buss, R. C. Williams, and E. W. Cochran, "The rutting and stripping resistance of warm and hot mix asphalt using bio-additives," *Construction and Building Materials*, vol. 112, pp. 128–139, 2016.
- [22] F. Frigio, S. Raschia, D. Steiner, B. Hofko, and F. Canestrari, "Aging effects on recycled WMA porous asphalt mixtures," *Construction and Building Materials*, vol. 123, pp. 712–718, 2016.
- [23] Y. Ye, G. Xu, L. Lou, X. Chen, D. Cai, and Y. Shi, "Evolution of rheological behaviors of styrene-butadiene-styrene/crumb rubber composite modified bitumen after different long-term aging processes," *Materials*, vol. 12, no. 15, 2345 pages, 2019.
- [24] M. Liang, P. Liang, W. Fan et al., "Thermo-rheological behavior and compatibility of modified asphalt with various styrene-butadiene structures in SBS copolymers," *Materials & Design*, vol. 88, pp. 177–185, 2015.

## Research Article

# Mechanism and Rheological Properties of High-Modulus Asphalt

Xinquan Xu <sup>1,2</sup>, Guilin Lu,<sup>1</sup> Jun Yang <sup>1</sup>, and Xinhai Liu<sup>2</sup>

<sup>1</sup>School of Transportation, Southeast University, No. 2 Sipailou, Nanjing 210096, China

<sup>2</sup>Guangdong Hualu Transport Technology Co., Ltd, No. 1180 Guangcong Eighth Road, Guangzhou 510435, China

Correspondence should be addressed to Jun Yang; yangjun@seu.edu.cn

Received 18 February 2020; Revised 23 March 2020; Accepted 30 March 2020; Published 22 April 2020

Guest Editor: Meng Guo

Copyright © 2020 Xinquan Xu et al. This is an open access article distributed under the Creative Commons Attribution License, which permits unrestricted use, distribution, and reproduction in any medium, provided the original work is properly cited.

High-modulus asphalt concrete (HMAC) is considered as an effective paving material for addressing the increasing heavy traffic and rutting problems. Therefore, one high-modulus agent was used in this study to prepare high-modulus asphalt binder with different dosages. The objective of this study is to investigate the performance and modification mechanism of high-modulus asphalt. The effects of high-modulus agent on the viscoelastic properties of asphalt with different dosages were quantified via rheological tests as compared to base binder and styrene-butadiene-styrene- (SBS-) modified asphalt. Moreover, the modification mechanism of the high-modulus agent was examined using fluorescence microscopy and infrared spectrum test. Based on rutting and dynamic modulus tests, the differences of road performances between high-modulus modified asphalt mixture and SBS-modified asphalt mixture were compared. The results demonstrate that the high-modulus agent improves the high-temperature performance and viscoelastic properties of the matrix asphalt. When the dosage increases to 6.67%, the modification effect is better than that of the SBS-modified asphalt. Furthermore, the results of the rutting test show that the high-modulus modified asphalt mixture has better resistance to deformation than the SBS-modified asphalt mixture. The dynamic modulus test further demonstrates that the high-modulus modified asphalt mixture exhibits superior performance in high-temperature range. Fluorescence microscopy shows that the high-modulus agent particles can swell in the asphalt to form polymer links that improve the viscoelastic properties of the asphalt. Based on the results of the infrared spectrum test, it can be concluded that a high-modulus agent changes the asphalt matrix via physical blending modification.

## 1. Introduction

To improve the strength of asphalt pavement and reduce its thickness, France was the first country to adopt high-modulus asphalt concrete (HMAC) [1]. When the complex modulus was larger than 14000 MPa at 15°C and 10 Hz, the asphalt concrete can be called HMAC. Practically, researchers determined that HMAC has excellent high-temperature rutting resistance, fatigue resistance, and water stability. Due to these benefits, HMAC is gradually used in the joint and surface layers [2, 3]. The selection of high-modulus asphalt is extremely important to the production of HMAC. Generally, there are three methods to obtain high-modulus binders that increases the stiffness of asphalt concrete: (1) using hard-grade asphalt binders that have low penetration and high softening points [1]; (2) using a polymer modifier, such as styrene-butadiene-styrene (SBS)

and lake asphalt [4, 5]; and (3) using a high-modulus agent [6, 7].

In recent years, in South China, rutting has become one of the most common distresses of asphalt pavement in high temperature and heavy traffic areas. Because HMAC has excellent high-temperature rutting resistance, the investigation on the performance of HMAC has become popular with researchers. Xiao et al. [8] added two types of high-modulus agents to 70# asphalt and SBS-modified asphalt and studied the performance of modified asphalt and asphalt mixture. They reported that the high-temperature performances of asphalt and asphalt mixture improved after adding a high-modulus agent, but their low-temperature performances slightly decreased. Cao et al. [9] used SBS-modified asphalt and an antirutting agent for compound modification of asphalt concrete and similar conclusions were obtained. Considering that high-modulus admixture

may reduce the performance of asphalt concrete, Cheng [10] examined the effects of different types of admixtures on the cracking resistance of HMAC and concluded that a mineral fiber admixture could effectively improve the cracking resistance of asphalt concrete. Wang [11] studied the fatigue performance of a high-modulus asphalt mixture and determined that the inorganic modifier calcium sulfate crystal improved the fatigue resistance of HMAC. By investigating and analyzing 80 normal asphalt pavements with HMAC base or conventional asphalt concrete base in Poland, Rys et al. [12] concluded that pavements with high-modulus asphalt bases had a 2.45 times higher probability of being cracked compared to pavements with conventional asphalt concrete bases. Some researchers have investigated the mechanical characteristics of HMAC in the pavement structure and suggested that when HMAC is applied to the middle surface layer, it can bear the maximum shear stress generated by vehicle load better and thus reduce rutting and achieve the best combination of pavement performance and cost. Wang et al. [13] tested the uniaxial penetration and compressive resilient modulus of HMAC, SBS-modified asphalt concrete, and 70# asphalt concrete at 15°C, 20°C, 40°C, and 60°C. They reported that HMAC has relatively high shear strength and compressive resilient modulus at the different temperatures. Si et al. [14, 15] established the structural models of high-modulus asphalt pavement and conventional asphalt pavement. Using the finite element method and the discrete element method, they investigated the mechanical properties of high-modulus asphalt pavement and reported that HMAC pavement can improve the deformation resistance of asphalt pavement and reduce the deformation of asphalt material in each layer and the rutting potential. Wang et al. [16] and Yang [17] explored the modification mechanism of the high-modulus modifier using scanning electron microscopy, differential scanning calorimetry (DSC), and Fourier transform infrared spectroscopy (FTIR). They explained the mechanism for improving the dynamic modulus of asphalt mixture from the perspective of the interaction between functional groups, additives, and aggregates. To summarize, most of previous research on high-modulus asphalt and HMAC focused on their macroscopic performances and engineering applications. However, there have been very few studies on the mechanism of the high-modulus agent and the rheological properties of high-modulus asphalt. Therefore, the scarcity of relevant research makes it more difficult to determine the function of the high-modulus agent in the asphalt mixture accurately, leading to unstable quality of the high-modulus asphalt mixture.

The study evaluates the effect of the high-modulus agent on the rheological properties of asphalt, along with its mechanism and performance in the application process. The main objectives of this study are (1) to introduce a high-modulus agent as a modifier to improve the performance of asphalt and asphalt mixture, (2) to investigate the influence of high-modulus agent on the rheological properties of asphalt binder, (3) to determine the rutting resistance and dynamic modulus of HMAC, and (4) to study the mechanism of high-modulus agent and its role in improving the performance of asphalt in the process. To achieve these

objectives, 70# asphalt was selected as base asphalt and was modified with a high-modulus agent to obtain high-modulus asphalt. In comparison, the rheological properties of high-modulus asphalt and SBS-modified asphalt at high and low temperatures were studied via rheological testing. The mechanism of high-modulus agent modification in the asphalt was analyzed via fluorescence microscopy and FTIR. Furthermore, the rutting test and dynamic modulus test of the asphalt mixtures were conducted to investigate the road performance. Figure 1 shows the flowchart of the steps and tasks followed in this research project.

## 2. Materials and Methods

### 2.1. Materials

*2.1.1. Asphalt Binders and Modifiers.* In the comparative study, the 70# asphalt and SBS-modified asphalt used in the test were provided by Shell and came from the same production batch, and the content of SBS was 4.5%. High-modulus modified asphalt was prepared using 70# asphalt that was selected as base binder. The main technical indexes of 70# asphalt and SBS-modified asphalt were tested by the standard test method of asphalt and asphalt mixture [18].

Table 1 shows the basic properties of the two types of bitumen. It can be seen from Table 1 that the main technical indexes of base asphalt and SBS-modified asphalt meet the requirements of Chinese specification [19].

Crumb rubber has been successfully applied into asphalt pavement as a performance enhancer for many decades, and many studies have proved that asphalt rubber (AR) can provide better rutting and fatigue resistance [20–22]. It was also found that the rubberized asphalt mixture provided higher modulus than the mixture with hard-grade binder and SBS-modified asphalt mixture [23]. In this study, crumb rubber was selected as a high-modulus agent from Dongguan Yinxi Technology Co., Ltd., China. Figure 2 shows the selected high-modulus agent, which is mainly composed of rubber plastic alloy material, and its basic properties are shown in Table 2.

High-modulus modified asphalt was prepared via the high-speed shear method. Table 3 shows the dosage of the high-modulus modifier and the asphalt serial number. The different dosages used in this study were based on the field experience. In Guangdong Province, China, the dosage of high-modulus agent is generally 0.2%–0.4% of the total mass of asphalt mixture. According to the optimal asphalt content (around 4.5% for AC-20), the ratio of high-modulus agent to asphalt binder is 4.45%, 6.67%, and 8.89%, respectively, when the percentage of high-modulus agent by mass of asphalt mixture was 0.2%, 0.3%, and 0.4%, respectively. To prepare JG1, JG2, and JG3, 70# asphalt was heated to 140°C, and the corresponding dosage of the high-modulus agent was slowly added to the asphalt. Then, the mixture was sheared at 3500 rpm for 15 min and then at 6000 rpm for 45 min. Both JG0 and FG0 were not mixed with high-modulus agent but high-speed sheared for 60 min and heated at 140°C for 3 h to simulate the aging process of the blending asphalt binders.

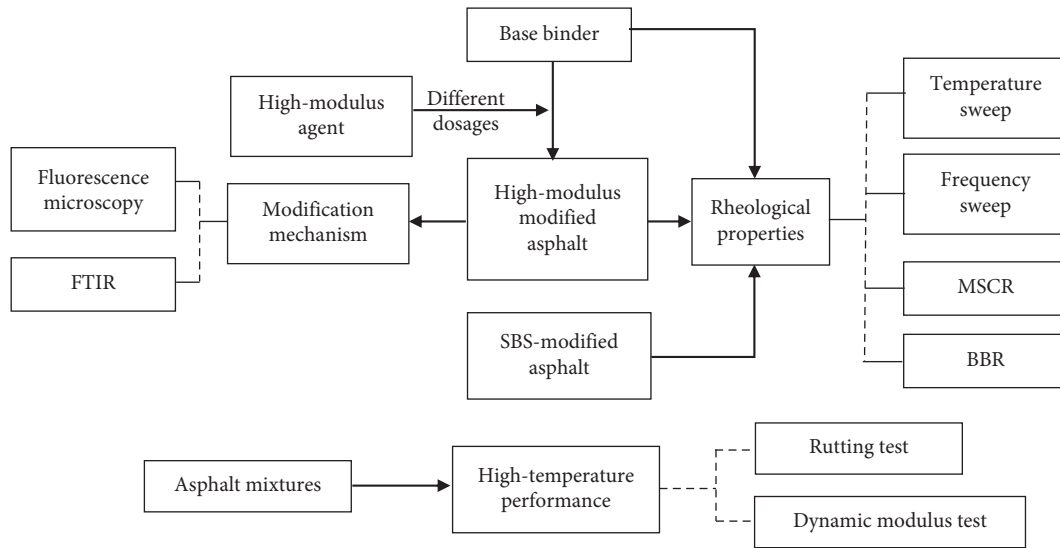


FIGURE 1: Flowchart of the test program.

TABLE 1: Technical indexes of 70# asphalt and SBS-modified asphalt.

Test properties	70# asphalt		SBS-modified asphalt		
	Test results	Technical index	Test results	Technical index	
P25°C, 100 g, 5 s (0.1 mm)	61	60–80	55	40–60	
$T_{R\&B}$ (°C)	48.5	≥46	81	≥60	
Ductility (cm)	5°C	—	34.4	≥20	
	10°C	18.3	—	—	
RTFOT (163°C, 85 min)	Mass loss (%)	0.092	±0.8	±1.0	
	Penetration ratio	72	≥61	80	≥65
	Ductility (cm)	5°C	—	22	≥15
	10°C	6.2	≥6	—	



FIGURE 2: High-modulus agent used in this study.

TABLE 2: Technical indexes of the high-modulus agent.

Particle size (mm)	Density (g/cm <sup>3</sup> )	Particle morphology	Color
1–6	0.92–0.98	Granular solid	Black

2.1.2. *Mixtures.* To prevent rutting, the high-temperature stability of the middle surface of the asphalt pavement is crucial [14]. To evaluate the practical effect of the high-modulus modifier in road performance, the AC-20 mixture,

TABLE 3: High-modulus agent dosage and asphalt serial number.

Asphalt type	70# asphalt	SBS-modified asphalt			
High-modulus agent dosage (%)	0	4.45	6.67	8.89	0
Serial number	JG0	JG1	JG2	JG3	FG0

Note. The high-modulus agent content is the ratio of the high-modulus agent to the asphalt quality.

which is commonly used in the middle surface of asphalt pavement, was selected to explore the effect of the high-modulus modifier on the high-temperature performance of asphalt mixture. Table 4 shows the gradation used in the test. The asphalt consumption is 4.14%, and the designed void ratio is 4.1%.

## 2.2. Test Methods

2.2.1. *Dynamic Shear Rheological Test.* The dynamic shear rheological test is considered as an important method to investigate the influence of the loading conditions and temperature on the properties of the asphalt as well as to analyze the viscoelastic properties of asphalt [24, 25]. The Malvern Kinexus dynamic shear rheometer (DSR) was used

TABLE 4: Gradation of the AC-20 asphalt mixture.

Sieve size (mm)	26.5	19	16	13.2	9.5	4.75	2.36	1.18	0.6	0.3	0.15	0.075
Passing rate (%)	100	96.4	85.2	73.2	57.1	33.2	25.2	18.8	14	10.4	8.2	6

in the temperature-sweep test and the frequency-sweep test. In the temperature-sweep test, the diameter of the plates was 25 mm and the gap between two plates was 1 mm, the control strain was set at 0.1%, the control frequency was 1.592 Hz (10 rad/s), and the temperature range was from 58°C to 112°C with an interval of 6°C. For the frequency-sweep test, the diameter of the plates was 25 mm with a gap of 2 mm. The control strain was set at 0.1%. The selected temperatures were 5, 20, and 35°C, and the frequency range was 0.1–100 rad/s. Each order of magnitude had 10 frequency points, thus yielding 30 frequency points. Based on DSR frequency-sweep test results, the sigmoidal function [26, 27] was used to fit the master curves of the complex shear modulus of the asphalt, as shown in equation (1). Considering 20°C as the reference temperature, based on the time-temperature superposition principle, the Williams–Landel–Ferry (WLF) equation was used to calculate the shift factor of the complex shear modulus at different temperatures. The WLF equation is shown in equation (2).

$$Lg|G^*| = \delta + \frac{\alpha}{1 + e^{\beta + \gamma Lg f_r}}, \quad (1)$$

where  $|G^*|$  is the complex shear modulus (GPa);  $f_r$  is the reduced frequency at the reference temperature (Hz); and  $\delta$ ,  $\alpha$ ,  $\beta$ , and  $\gamma$  are constants.

$$Lg\alpha_T = -\frac{C_1(T - T_0)}{C_2 + (T - T_0)}, \quad (2)$$

where  $T$  is the test temperature (°C);  $\alpha_T$  is the shift factor at temperature  $T$ ;  $T_0$  is the reference temperature (°C); and  $C_1$  and  $C_2$  are constants. Two replicates were prepared and tested for each type of binder.

**2.2.2. Multistress Creep Recovery Test.** Many studies have shown that  $G^*/\sin\delta$  cannot be used to evaluate accurately the high-temperature properties of the polymer-modified asphalt [28, 29]. NCHRP 9–10 proposed a method of evaluating the performance of modified asphalt based on multistress creep recovery (MSCR) tests [30]. The creep recovery rate ( $R$ ) was used to characterize the elastic deformation capacity of the asphalt binder, the unrecoverable creep compliance ( $J_{nr}$ ) was used to characterize the resistance potential of asphalt binder to permanent deformation accumulation, and the unrecoverable creep compliance difference ( $J_{nr-diff}$ ) was used to characterize the sensitivity of asphalt binder to loading stress. Note that the higher  $R$  value implies the improvement of elastic deformation capacity of the asphalt binder, lower  $J_{nr}$  indicates the increase of permanent deformation resistance, and  $J_{nr-diff}$  decreases with the decrease of stress sensitivity. The loading mode of the MSCR test is close to the actual situation of the pavement load, which can demonstrate the viscoelastic characteristics of asphalt well. In this study, the temperature of 60°C was

selected, and MSCR test was conducted to evaluate the viscoelastic characteristics of high-modulus modified asphalt according to AASHTO TP-70. Two replicates were prepared and tested for each binder.

**2.2.3. Bending Beam Rheological Test.** The bending beam rheometer (BBR) test is a grading test method of evaluating the low-temperature performance of asphalt recommended by the Strategic Highway Research Program (SHRP) [18, 25]. In the test, the deflection values were used to calculate the stiffness of asphalt binder; the equation is shown as follows:

$$S(t) = \frac{PL^3}{4bh^3\delta(t)}, \quad (3)$$

where  $P$  is the applied constant load (100 g or 0.98 N);  $L$  represents the distance between beam supports (102 mm);  $b$  represents beam width (12.7 mm);  $h$  is beam thickness (6.25 mm);  $S(t)$  represents asphalt binder stiffness at a specific time (MPa); and  $\delta(t)$  is the deflection at a specific time (mm).

Stiffness value was calculated at 60 s, and the slope of stiffness versus time is called  $m$ -value. The creep stiffness from the BBR test is a measure of the development of thermal stresses in the asphalt binder. The two parameters are used as indicators of asphalt binder to characterize the thermal cracking potential at the low temperature. With a higher  $S$ , the asphalt becomes more brittle at low temperature, and it is more likely to crack at low temperature. With a higher  $m$  value, the stress relaxation performance the asphalt is better, and the possibility of low-temperature cracking decreases. The grading standard is that the stiffness modulus ( $S$ ) should not exceed 300 MPa, and the creep rate ( $m$ ) should not be less than 0.3. In this study, CANNON BBR was used and the test temperature was  $-10^\circ\text{C}$ . Two replicates were prepared and tested for each binder.

**2.2.4. Fluorescence Microscopy.** Fluorescence microscopy was used to observe the distribution of the modifier in the asphalt. By using excitation light of different colors, the fluorescent dye samples, which are difficult to be observed using an ordinary microscope, were clearly observed and identified. In Figure 3, the magnification of the objective lens was 10–100 times and that of the eyepiece was 10 times. Three replicates were tested for each prepared binder.

**2.2.5. Infrared Spectrum Test.** In this experiment, the attenuated total reflection method was used in the Agilent Cary 630 FTIR (Figure 4) to conduct infrared spectrum detection on the high-modulus modifier, 70# asphalt, and high-modulus modified asphalt samples, so as to determine the basic chemical composition and modification



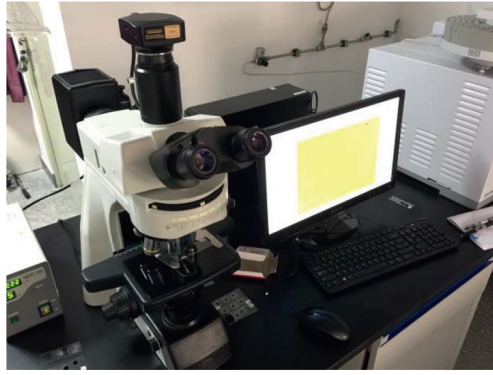


FIGURE 3: Fluorescence microscope.



FIGURE 4: Infrared spectrum test of asphalt: (a) infrared spectrometer; (b) asphalt samples.

mechanism of the high-modulus modifier. Three replicates were tested for each prepared binder.

**2.2.6. Rutting Test.** The rutting test was used to test the high-temperature antirutting capacity of the asphalt mixture by simulating the actual wheel movement on the asphalt pavement by the reciprocating movement of the wheel on the plate-shaped test piece. HMAC is widely used in South China to address the serious rutting problem. Considering these two factors including high temperature and precipitation in this area, two sets of rutting tests were conducted at 60°C and 70°C to evaluate the high-temperature rutting resistance of the asphalt mixture. Furthermore, a drying group and a soaking group were set to analyze the water stability. Additionally, considering the overload phenomenon, the test loading was increased from 0.7 to 0.9 MPa for three comparative analyses. Following the rutting test method of asphalt mixture (T0719-2011) [18], the size of the rutting test samples was 300 × 300 × 50 mm, and dynamic stability (DS) was calculated as follows:

$$DS = \frac{42 \times (60 - 45)}{d_{60} - d_{45}}, \quad (4)$$

where DS is the dynamic stability in cycle/mm;  $d_{60}$  is the rutting depth at 60 min in mm; and  $d_{45}$  is the rutting depth at 45 min in mm. Two replicates were tested for each prepared sample.

**2.2.7. Dynamic Modulus Test.** Due to the fact that the modulus of HMAC is different from that of conventional asphalt concrete mixture [14, 26], the dynamic modulus test was used. The multifunctional material testing machine (UTM-100) was used for this test, and the test samples were 100 mm in diameter and 150 mm in height. The dynamic modulus test was performed with the loading frequencies of 0.1, 0.5, 1, 5, 10, and 25 Hz at 4°C, 15°C, 25°C, 35°C, 45°C, and 60°C. The test was conducted from low temperature to high temperature with the decrease of loading frequencies so as to enhance the testing accuracy. The dynamic modulus test was conducted with constant strain, making sure that the stress-strain relationship within the loading range remained linear. In the control mode, sinusoidal load was applied to the samples, and the strain was controlled between 85 and 115  $\mu\epsilon$ . The room temperature was selected as the reference temperature. According to the time-temperature superposition principle, the master curve of the dynamic modulus of the asphalt mixture was fitted using the sigmoidal function. Two replicates were prepared and tested for each type of sample.

### 3. Results and Discussion

#### 3.1. Rheological Properties of Asphalt

**3.1.1. Analysis of Temperature-Sweep Test Results.** Figure 5 shows the temperature-sweep test results. In Figure 5(a), it can be seen that the complex modulus ( $G^*$ ) of

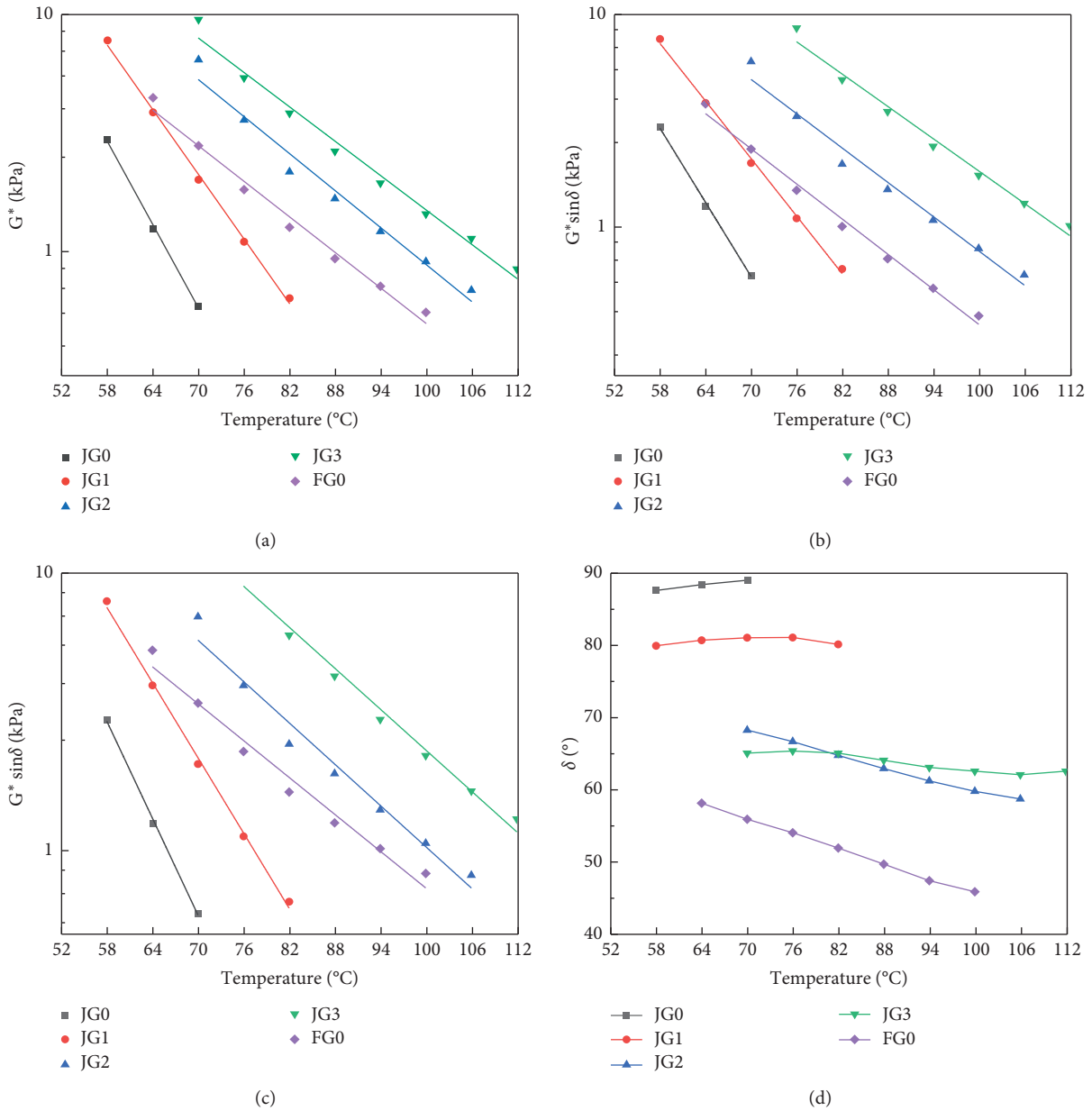


FIGURE 5: Relationship between the viscoelastic properties of asphalt and temperature: (a) complex modulus versus temperature; (b) fatigue factor versus temperature; (c) rutting factor versus temperature; (d) phase angle versus temperature.

the asphalt decreases with the increase of temperature, indicating the poor deformation resistance of asphalt at high temperature. Compared with JG0, the complex modulus of JG1, JG2, and JG3 with the high-modulus modifier considerably improved. And with the content of the high-modulus agent increasing, the complex modulus increases. Taking the temperature of 70°C as an example, the complex modulus of JG1, JG2, and JG3 increases by 2.4, 9.9, and 15.1 times, respectively, compared with the figure for JG0. If the content of the high-modulus agent is equal to that of SBS (4.5%), SBS-modified asphalt has a higher complex modulus as the temperature surpasses 64°C. With the content of the high-modulus agent increasing to 6.67%, the complex modulus of the high-modulus modified asphalt is higher than that of the

SBS-modified asphalt. This indicates that the high-modulus modified asphalt has better high-temperature stability when a certain content of the high-modulus agent is used. With high-modulus agent content increasing, the slopes of the complex modulus curves rapidly decrease and then remain stable, which indicates that the addition of the high-modulus agent may lead to the decline of the temperature sensitivity of the asphalt. When the content increases to 6.67% or more, no significant difference in the slopes of curves can be found among the high-modulus modified asphalt and the SBS-modified asphalt. This means that the two types of asphalt show similar temperature sensitivity.

Figures 5(b) and 5(c) show the fatigue factors and the rutting factors of the samples versus temperature. The

change trends of both are consistent with the complex modulus, which demonstrates that the high-modulus modified asphalt containing 6.67% high-modulus agent or more has better high-temperature performance and fatigue performance than the SBS-modified asphalt. The result of better rutting resistance of high-modulus modified asphalt is consistent with previous finding in the literature [23]. In Figure 5(d), it can be observed that the phase angle of asphalt significantly decreases with the increase of high-modulus agent content, from  $89.0^\circ$  of JG0 to  $68.2^\circ$  of JG2 at  $70^\circ\text{C}$ ; it means that the addition of the high-modulus modifier can contribute to the improvement of the elastic performance of asphalt at high temperature. However, when the content was higher than 6.67%, the decrease of the phase angle is not obvious. It may be attributed to the formation and enhancement of a polymer link network with relatively small content, which improves the elastic properties of the asphalt. But the additional increase has no significant effect on the link network, indicating that the improvement of the elastic properties of the asphalt with the addition of the high-modulus agent is limited. It also can be found that the SBS-modified asphalt shows the lowest phase angle, which indicates that SBS-modified asphalt has better elastic recovery performance than 70# asphalt. And the addition of the high-modulus modifier can narrow the gap between the two types of asphalt to some extent.

**3.1.2. Analysis of Frequency-Sweep Test Results.** Selecting  $20^\circ\text{C}$  as the reference temperature, the master curves of the complex shear modulus and the main curve of the phase angle are shown in Figure 6.

As shown in Figure 6(a), compared with the SBS-modified asphalt, 70# asphalt has a higher modulus at higher frequencies ( $10^0$ – $10^4$  rad/s) and a lower modulus at low frequencies ( $10^{-3}$ – $10^0$  rad/s). According to the time-temperature superposition principle, low frequency is equivalent to a temperature increase. Similar to the results obtained before, the SBS-modified asphalt shows lower temperature sensitivity and better high-temperature performance. After the addition of the high-modulus modifier, the master curve of the complex shear modulus of the asphalt reflects a positive correlation. In the high-frequency band ( $10^2$ – $10^4$  rad/s), the complex shear modulus of the asphalt somewhat changes with the content. In the low-frequency band ( $10^{-3}$ – $10^2$  rad/s), if the content of the high-modulus agent is not more than 6.67%, the complex shear modulus of the asphalt significantly increases with the increase of the content under the same loading frequency, indicating that the high-temperature performance of the high-modulus modified asphalt considerably improves. When the dosage is further increased, the complex modulus does not continue to increase, which confirms that the improvement of the high-temperature performance of the asphalt is limited despite the addition of the high-modulus agent. Similar to Figure 6(a), the master curves of the phase angle in Figure 6(b) show that the addition of the high-modulus agent can effectively improve the viscoelasticity of the asphalt, reduce the phase angle of the asphalt, and enhance the

elastic recovery ability of the asphalt. In the low-frequency band ( $10^{-3}$ – $10^{-1}$  rad/s), the phase angles of JG0 and JG1 are significantly higher than those of the SBS-modified asphalt, which indicates that JG0 and JG1 are more similar to viscoelastic fluids at high temperature and more likely to flow compared to the SBS-modified asphalt. With further increase in the high-modulus agent content, the viscoelasticity of the asphalt significantly improves. When the content is 6.67%, the modified asphalt has the best elastic performance and viscoelasticity. The increase in the content of the asphalt makes the phase angle of the asphalt increase, which may be attributed to the heterogeneous dispersion of the high-modulus modifier and the weakening of the link with the asphalt, leading to the increase of the phase angle of the asphalt.

**3.1.3. Analysis of the MSCR Results.** The MSCR results are shown in Figure 7. In both stress conditions (0.1 kPa or 3.2 kPa), with the increase of high-modulus agent, the shear strain of the asphalt gradually decreases, and when the high-modulus agent content increases to 6.67%, the strain response of the asphalt remains stable, which demonstrates that the addition of the high-modulus agent improves the deformation resistance of the asphalt. It is also found that JG2 showed lower strain response compared with the SBS-modified asphalt, indicating the high-temperature deformation resistance of JG2 is better than that of the SBS-modified asphalt. Moreover, comparing the shear-strain curves of the 70# asphalt, the high-modulus modified asphalt, and the SBS-modified asphalt, it can be seen that the shear strain of the 70# asphalt increases gradually during the loading time but does not significantly recover during the unloading time. However, the shear strain of SBS-modified asphalt during the loading time is significantly less than that of 70# asphalt, and the residual shear strain of creep stress after unloading is smaller, which shows that SBS-modified asphalt has better elastic recovery performance than 70# asphalt at high temperature.

Table 5 shows the calculation results of the rheological parameters of the 70# asphalt, the high-modulus modified asphalt, and the SBS-modified asphalt based on the MSCR test. With the increase of high-modulus agent content,  $R$  value increases considerably and then tends to remain stable, and  $J_{nr}$  decreases first and then tends to remain stable. This demonstrates that the addition of the high-modulus additive can lead to the enhancement of the high-temperature elastic deformation recovery capacity and the improvement of the antirutting ability. At 0.1 kPa, the  $R$  values of JG2 and JG3 are higher than those of SBS-modified asphalt, whereas  $J_{nr}$  values of JG2 and JG3 are lower than those of the SBS-modified asphalt. At 3.2 kPa, the  $J_{nr}$  values of JG2 and JG3 are  $0.184\text{ kPa}^{-1}$  and  $0.154\text{ kPa}^{-1}$ , respectively, which are lower than those of the SBS-modified asphalt. Moreover, the  $R$  value of JG3 is 48.2%, which is slightly lower than that of the SBS-modified asphalt. With the increase of high-modulus agent content, the  $J_{nr-diff}$  value of the high-modulus modified asphalt increases gradually, which is greater than those of the 70# matrix asphalt and the SBS-modified

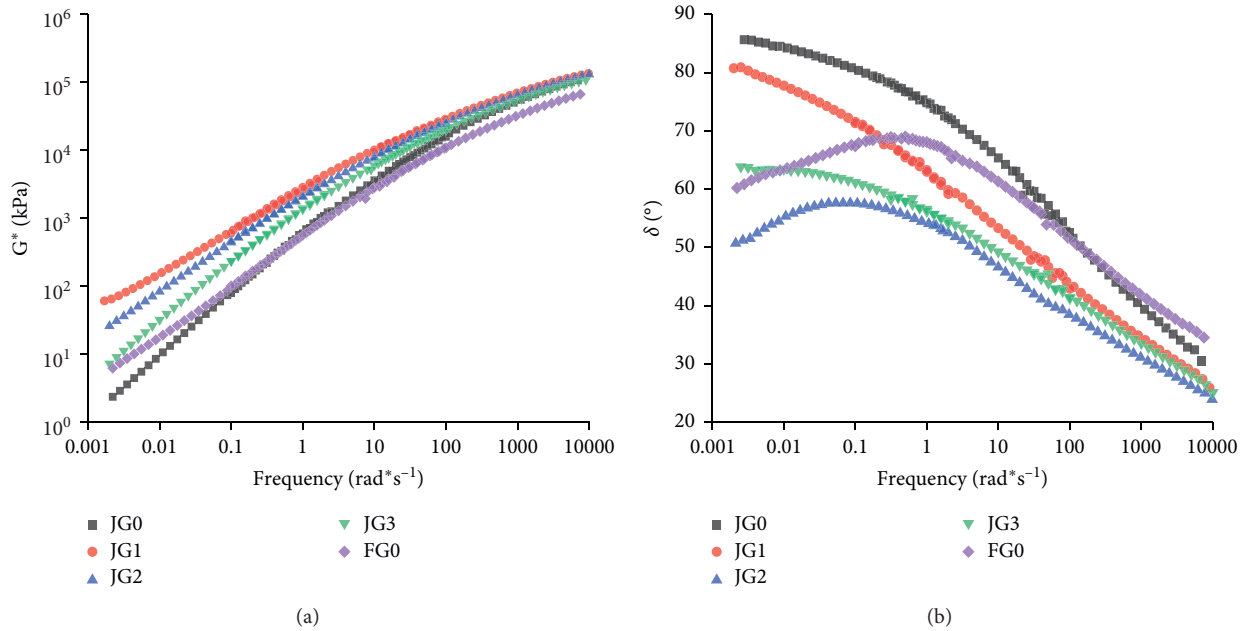


FIGURE 6: Frequency-sweep test results: (a) master curve of complex shear modulus; (b) master curve of phase angle.

asphalt, indicating that the high-modulus additive increases the sensitivity of asphalt to load.

**3.1.4. Low-Temperature Performance of Asphalt.** Figure 8 shows the BBR test results for the high-modulus modified asphalt. With the increase of high-modulus additive content, the creep stiffness of the asphalt increases, whereas the  $m$ -value gradually decreases. This indicates that the addition of the high-modulus agent increases the stiffness of the asphalt but reduces its flexibility, which makes it stiffer and more brittle and thus causes damage to its low-temperature performance. Therefore, the determination of the content of the high-modulus agent needs more caution. According to the test results for the high- and low-temperature performance of the high-modulus modified asphalt with different high-modulus agent contents, adding 6.67% high-modulus agent to 70# asphalt is recommended for preparing HMAC in engineering applications.

### 3.2. High-Temperature Performance of Asphalt Mixtures

**3.2.1. Analysis of Rutting Test Results.** The rutting test was conducted on three types of asphalt mixtures using 70# asphalt, SBS-modified asphalt, and JG2 as binder, and the test results are shown in Table 6. Obviously, the addition of the high-modulus agent can significantly improve the DS of the 70# asphalt mixture. Moreover, the improvement effect of high modulus-modified asphalt is better compared with SBS-modified asphalt under all test conditions. Under the standard test conditions (0.7 MPa, 60°C), the DS of the high-modulus modified asphalt mixture is 6.8 times more than that of the base asphalt mixture, whereas there is 5.2 times increase in the SBS-modified asphalt mixture. Under high-temperature and heavy-load conditions (0.9 MPa, 70°C), the

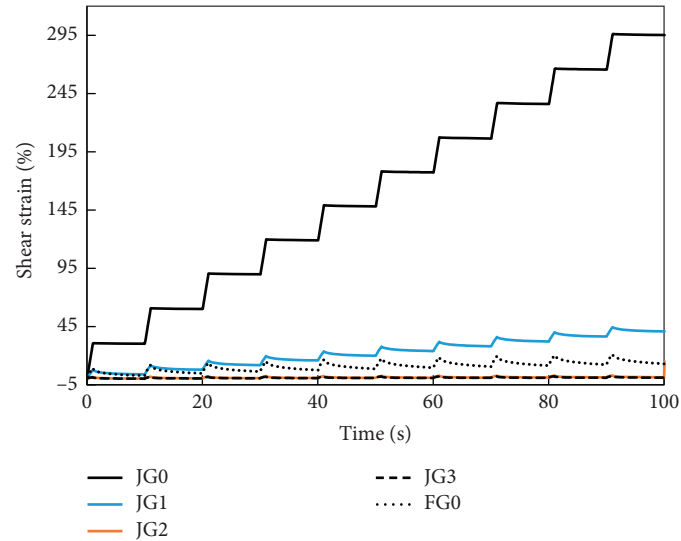
high-modulus agent has a particularly prominent effect on the high-temperature performance of the mixture. After adding the high-modulus agent, the DS of the asphalt mixture increases significantly. Compared with the base asphalt mixture, there is 12.4 times increase in the high-modulus asphalt mixture. And the DS of JG2 mixture is about 40 percent higher than that of the SBS-modified asphalt mixture, which demonstrates that the HMAC has better rutting resistance under special conditions such as high temperature and heavy load. When the humidity increased during the test, the DS of the three asphalt mixtures decreased. However, the decrease in the DS of the high-modulus modified asphalt mixture was only 11.1%, which was considerably lower than those of the 70# asphalt mixture (22.2%) and the SBS-modified asphalt mixture (19.9%), confirming that the asphalt mixture modified by the high-modulus agent has good water stability.

### 3.2.2. Analysis of Dynamic Modulus Test Results.

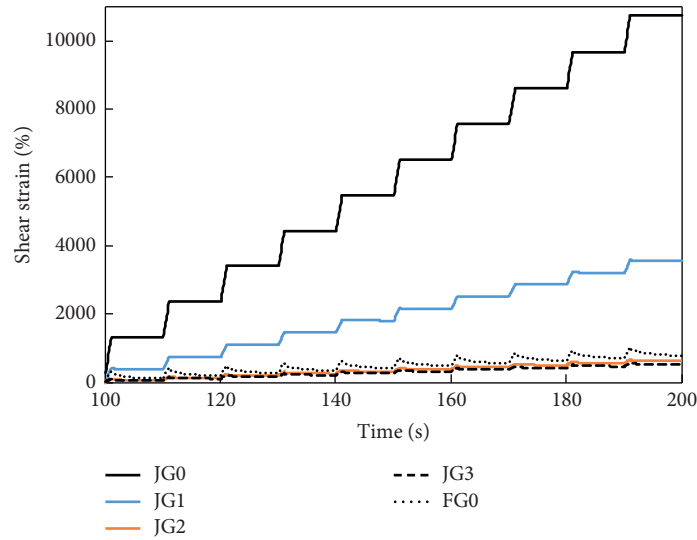
Figure 9 shows the dynamic modulus master curves of HMAC and the SBS-modified asphalt mixture; it can be seen that HMAC has higher modulus under both high- and low-temperature conditions. This conclusion is consistent with the results of the asphalt frequency-sweep test, which further confirms that high-modulus modified asphalt has good applicability in high-temperature range.

### 3.3. Modification Mechanism

**3.3.1. Fluorescence Microscopic Observations.** The mechanical properties of polymers come from the entanglement between chains. Only when the entanglement between different molecules is formed in the interface area, can the interface have a certain mechanical strength. Based on the



(a)



(b)

FIGURE 7: MSCR test curves at 60°C: (a) 0.1 kPa; (b) 3.2 kPa.

TABLE 5: MSCR test results.

Rheological parameters	Stress	JG0	JG1	JG2	JG3	FG0
$R$ (%)	0.1 kPa	2.3	48.4	95.4	98.1	89.2
	3.2 kPa	-0.3	3.4	41.3	48.2	77.8
$J_{nr}$ (kPa <sup>-1</sup> )	0.1 kPa	2.907	0.400	0.007	0.002	0.095
	3.2 kPa	3.222	1.096	0.184	0.154	0.211
$J_{nr-diff}$ (%)	—	10.8	174.2	2409.5	6354.9	122.9

minimum energy principle, the addition of modifiers causes redistribution in the system, and the system tends to a new equilibrium by reducing the surface energy [28]. Moreover, some polymer segments of the modifier particles diffuse into the asphalt phase to form an interface layer, which slows down the movement of the molecules. Furthermore, some polymers have high stability and strong network structure with the asphalt molecular chain, which helps improve the mechanical properties of the asphalt mixture. In addition,

the polar graft copolymer component present in the high-modulus agent can lead to the formation of a stronger polymer link between aggregate surface and asphalt compared to the structural asphalt and can improve the modulus and the high-temperature performance of the asphalt mixture. According to previous studies [31, 32], one high-modulus modifier (a polyolefin modifier) tends to form a network in the binder system possibly because of the swelling through fluorescence microscope observation.

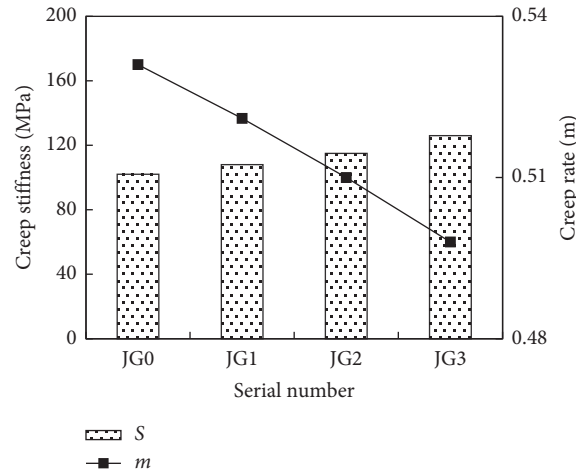


FIGURE 8: The relationship between  $S$ ,  $m$ , and the high-modulus modified asphalt content.

TABLE 6: Dynamic stability results (cycle/mm).

Test conditions	Asphalt binder type		
	70# asphalt	SBS-modified asphalt (FG0)	High-modulus asphalt (JG2)
0.7 MPa, 60°C, dry	1866	9856	12670
0.7 MPa, 60°C, wet	1452	7892	11253
0.7 MPa, 70°C, dry	868	6524	7624
0.9 MPa, 70°C, dry	233	2112	2886

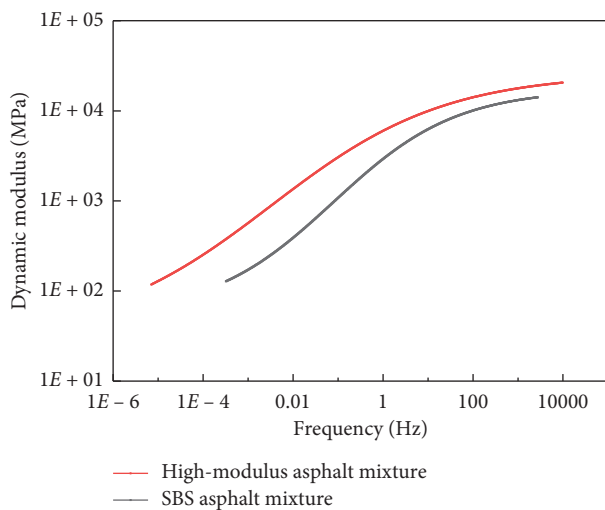


FIGURE 9: Dynamic modulus master curve of the asphalt mixtures.

Based on this, the modification mechanism of the high-modulus modifier used in this study was investigated using fluorescence microscopic test. Figure 10 shows a fluorescent micrograph of JG3 at different development times. There is a clear interface between the high-modulus agent and the asphalt before high-temperature development. With the increase of the development time, the difference between the yellow pattern (representing the high-modulus agent) and the orange background (representing the asphalt) becomes smaller, and the boundary between them becomes fuzzy gradually. This shows that the sheared high-modulus agent particles can swell and develop in the high-temperature

environment, absorb the light components of the asphalt, form polymer links, distribute more homogeneously in the origin asphalt, and improve the viscoelastic properties and high-temperature performance of asphalt.

**3.3.2. Infrared Spectrum Analysis.** Apart from the observed results from fluorescence microscope, using infrared spectrum test can also help to investigate the modification mechanism of high-modulus agent in the binder. In the previous study [17], Yang reported that there was neither new chemical reaction nor the formation of new functional groups in the asphalt containing one high-modulus modifier through infrared spectrum test. Figure 11 shows the infrared spectrum of the high-modulus modifier. There are four obvious sharp infrared absorption peaks of the high-modulus modifier at 715, 1468, 2847, and 2914  $\text{cm}^{-1}$ . The 715  $\text{cm}^{-1}$  peak represents the in-plane rolling vibration absorption peak of  $-(\text{CH}_2)_n-$  ( $n \geq 4$ ), the 1468  $\text{cm}^{-1}$  peak represents the bending vibration absorption peak of  $-\text{CH}_2-$ , the 1468  $\text{cm}^{-1}$  peak represents the symmetric stretching vibration absorption peak of  $-\text{CH}_2-$ , and the 2914  $\text{cm}^{-1}$  peak represents the asymmetric stretching vibration absorption peak of  $-\text{CH}_2-$ . Figures 12(a)–12(c) show the infrared spectrum of the high-modulus modifier, the 70# matrix asphalt, and the high-modulus modified asphalt JG2, respectively. The infrared spectrum of the high-modulus modified asphalt is the superposition of the infrared spectrum of the high-modulus modifier and the infrared spectrum of the 70# asphalt. There is no new infrared absorption peak in the infrared spectrum of the high-modulus modified

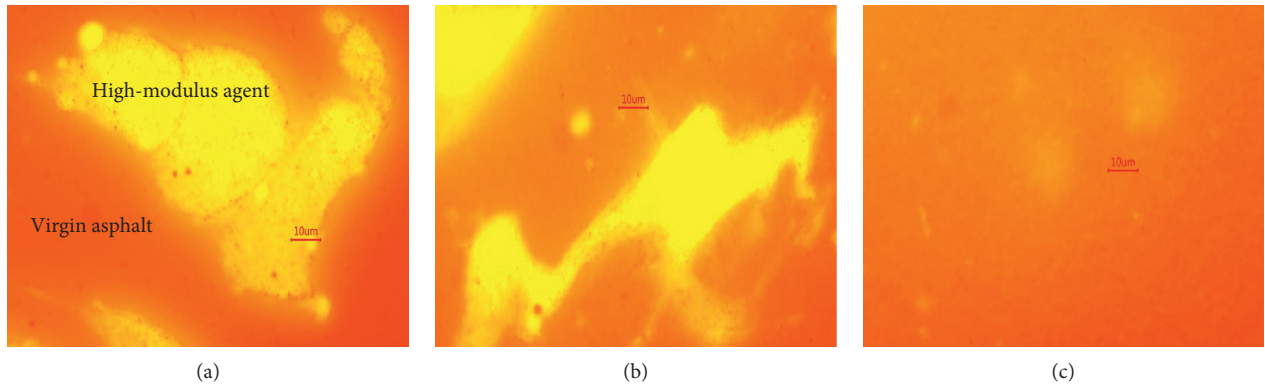


FIGURE 10: Fluorescence micrograph of different developmental times of the JG3 asphalt: (a) 0 h; (b) 1 h; (c) 1.5 h.

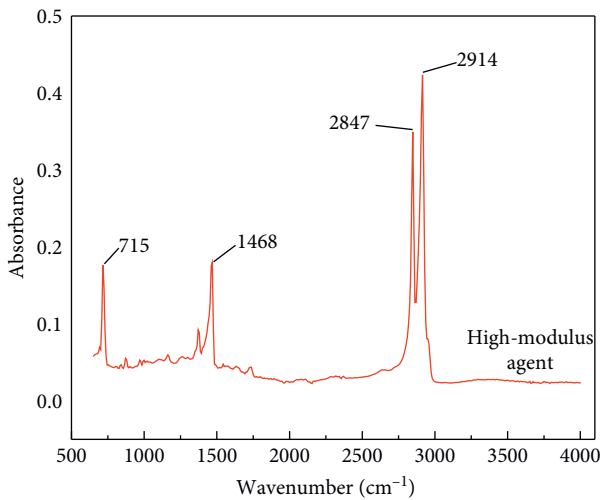


FIGURE 11: Infrared spectrum of the high-modulus agent.

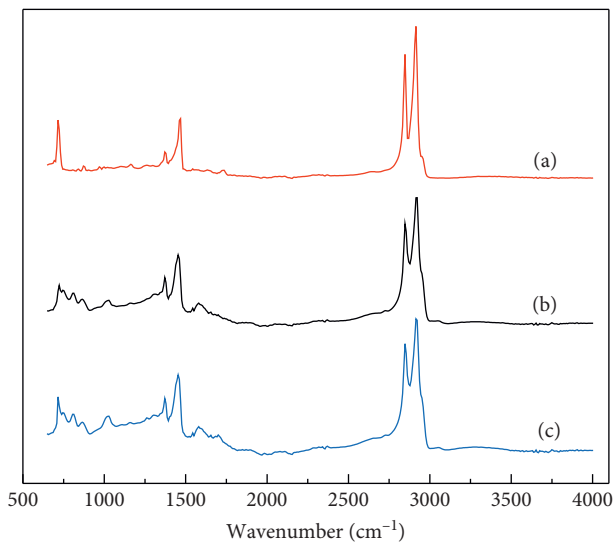


FIGURE 12: Infrared spectrum of (a) the high-modulus modifier, (b) the 70# matrix asphalt, and (c) the high-modulus modified asphalt JG2.

asphalt JG2. Therefore, it can be concluded that the modification of the base asphalt by adding the high-modulus modifier is purely physical blending modification, the modifier and the base asphalt are not chemically bonded, and no new substances are formed. This behavior is consistent with the macroscopic morphology observed by fluorescence microscopy. The high-modulus modifier only exhibits physical changes such as swelling of the matrix asphalt.

#### 4. Conclusions

In this study, the rheological properties of high-modulus asphalt, 70# asphalt, and SBS-modified asphalt, high-temperature performance of asphalt mixtures, and the modification mechanism of the high-modulus agent in the binder were discussed via a series of laboratory tests. The results confirm that HMAC has excellent road performance in high-temperature areas, and the following conclusions could be drawn:

- (1) The addition of a high-modulus agent can significantly improve the high-temperature performance and viscoelastic properties of the asphalt binder and reduce the temperature sensitivity of the matrix asphalt to some extent. When the content of the high-modulus modifier increases to 6.67%, the modified asphalt has better high-temperature performance than SBS-modified asphalt.
- (2) The rutting resistance of HMAC is better than that of SBS-modified asphalt mixture, especially under high-temperature and heavy-load conditions. And the water stability of HMAC is better than that of SBS-modified asphalt mixture. The modulus of HMAC is higher than that of SBS-modified asphalt concrete under high and low temperature, which indicates that HMAC has good applicability in high-temperature range.
- (3) By using the fluorescence microscopy test and infrared spectrum test, it can be found that the high-modulus agent particles develop by swelling in a high-temperature environment, absorbing the light components of asphalt. Some polymer chain

segments of the modifier particles diffuse into the asphalt phase to form an interface layer, which slows down the movement of the molecules; some polymers can exhibit high stability and strong network structure with the asphalt molecular chain, which improves the high-temperature performance and viscoelastic property of the asphalt.

## Data Availability

The experimental data used to support the findings of this study are included within the article.

## Conflicts of Interest

The authors declare that there are no conflicts of interest regarding the publication of this paper.

## Acknowledgments

The authors sincerely acknowledge the funding support from the National Natural Science Foundation of China (grant no. 51778140) and the Guangdong Provincial Department of Transportation (grant no. 2016-02-013).

## References

- [1] F. Ma and Z. Fu, "Application of hard asphalt and high modulus asphalt concrete in France," *Journal of China & Foreign Highway*, vol. 28, no. 6, pp. 221–223, 2008, (in Chinese).
- [2] M. Zheng, P. Li, J. Yang, H. Li, Y. Qiu, and Z. Zhang, "Fatigue character comparison between high modulus asphalt concrete and matrix asphalt concrete," *Construction and Building Materials*, vol. 206, pp. 655–664, 2019.
- [3] F. Zhu and M. Zhang, "Analysis of HiMA popularization and application for african," *Highway Engineering*, vol. 34, no. 6, pp. 94–98, 2009, (in Chinese).
- [4] R. Zhang, H. Wang, J. Gao, Z. You, and X. Yang, "High temperature performance of SBS modified bio-asphalt," *Construction and Building Materials*, vol. 144, pp. 99–105, 2017.
- [5] H. J. Lee, J. H. Lee, and H. M. Park, "Performance evaluation of high modulus asphalt mixtures for long life asphalt pavements," *Construction and Building Materials*, vol. 21, no. 5, pp. 1079–1087, 2007.
- [6] X. Wang, Y.-J. Qiu, S.-Y. Xue, Y. Yang, and Y. Zheng, "Study on durability of high-modulus asphalt mixture based on TLA and fibre composite modification technology," *International Journal of Pavement Engineering*, vol. 19, no. 10, pp. 930–936, 2018.
- [7] T. Ma, H. Wang, X. Huang, Z. Wang, and F. Xiao, "Laboratory performance characteristics of high modulus asphalt mixture with high-content RAP," *Construction and Building Materials*, vol. 101, pp. 975–982, 2015.
- [8] F. Xiao, D. Ma, J. Wang, D. Cai, L. Lou, and J. Yuan, "Impacts of high modulus agent and anti-rutting agent on performances of airfield asphalt pavement," *Construction and Building Materials*, vol. 204, pp. 1–9, 2019.
- [9] W. Cao, S. Liu, and Y. Li, "Rutting-resistance performance of SBS and anti-rutting additive composite-modified asphalt-concrete mixtures," *Journal of Testing and Evaluation*, vol. 44, no. 2, pp. 921–929, 2016.
- [10] M. Cheng, "Study on crack resistance and treatment measure of high modulus asphalt mixture," *Highway Engineering*, vol. 41, no. 5, pp. 46–51, 2016, (in Chinese).
- [11] X. Wang, "Road performance of high modulus asphalt concrete additive calcium sulfate whisker," *Journal of Chongqing Jiaotong University (Natural Sciences)*, vol. 30, no. 6, pp. 1331–1334, 2011, (in Chinese).
- [12] D. Rys, J. Judycki, M. Pszczola, M. Jaczewski, and L. Mejlun, "Comparison of low-temperature cracks intensity on pavements with high modulus asphalt concrete and conventional asphalt concrete bases," *Construction and Building Materials*, vol. 147, pp. 478–487, 2017.
- [13] G. Wang, L. Liu, and L. Sun, "Research on anti-deformation properties of high modulus asphalt concrete," *Journal of Tongji University Natural Science*, vol. 40, no. 2, pp. 0217–0222, 2012, (in Chinese).
- [14] C. Si, H. Cao, E. Chen et al., "Dynamic response analysis of rutting resistance performance of high modulus asphalt concrete pavement," *Applied Sciences*, vol. 8, p. 2701, 2017.
- [15] S. Chundi, Z. Xiaodong, Y. Zhanping et al., "Micro-mechanical analysis of high modulus asphalt concrete pavement," *Construction and Building Material*, vol. 220, pp. 128–141, 2019.
- [16] L. Wang, P. Wang, Q. Xu et al., "Mechanism research on additives of high modulus asphalt mixtures," *Journal of Chang'an University (Natural Science)*, vol. 35, no. 6, pp. 42–48, 2015, (in Chinese).
- [17] P. Yang, *Study on Properties of High Modulus Asphalt and its Mixture*, South China University of Technology, Guangzhou, China, (in Chinese), 2012.
- [18] Ministry of Transport of the People's Republic of China, *Standard Test Methods of Bitumen and Bituminous Mixtures for Highway Engineering (JTG E20-2011) by the Ministry of Transport of the People's Republic of China*, China Communication Press, Beijing, China, (in Chinese), 2011.
- [19] Ministry of Transport of the People's Republic of China, *Technical Specifications for Construction of Highway Asphalt Pavements (JTG F40-2004) by the Ministry of Transport of the People's Republic of China*, China Communication Press, Beijing, China, (in Chinese), 2004.
- [20] H. Yu, Z. Leng, Z. Zhou, K. Shih, F. Xiao, and Z. Gao, "Optimization of preparation procedure of liquid warm mix additive modified asphalt rubber," *Journal of Cleaner Production*, vol. 141, pp. 336–345, 2017.
- [21] D. Wang, D. Li, J. Yan et al., "Rheological and chemical characteristic of warm asphalt rubber binders and their liquid phases," *Construction and Building Materials*, vol. 193, pp. 547–556, 2018.
- [22] H. Wang, X. Liu, M. van de Ven, G. Lu, S. Erkens, and A. Skarpas, "Fatigue performance of long-term aged crumb rubber modified bitumen containing warm-mix additives," *Construction and Building Materials*, vol. 239, p. 117824, 2020.
- [23] J. Yan, Z. Leng, C. Ling, J. Zhu, and L. Zhou, "Characterization and comparison of high-modulus asphalt mixtures produced with different methods," *Construction and Building Materials*, vol. 237, p. 117594, 2020.
- [24] S. Hassanpour-Kasanagh, P. Ahmedzade, A. M. Fainleib, and A. Behnood, "Rheological properties of asphalt binders modified with recycled materials: a comparison with styrene-butadiene-styrene (SBS)," *Construction and Building Materials*, vol. 230, p. 117047, 2020.
- [25] G. W. Loulizi, I. L. Flintsch, Q. Al- et al., "Comparing resilient modulus and dynamic modulus of hot-mix asphalt as material properties for flexible pavement design," *Transportation*



- Research Record Journal of the Transportation Research Board*, vol. 1, pp. 161–170, 2006.
- [26] H. P. Wang, J. Yang, X. Q. Shi et al., “Research on dynamic modulus and master curve of high modulus asphalt mixture,” *Journal of Highway and Transportation Research and Development*, vol. 32, no. 8, pp. 12–18, 2015, (in Chinese).
- [27] Y. Guo, F. Ni, and P. Xiao, “Dynamic rheological properties of modified asphalt based on linear viscoelastic range,” *Journal of Jiangsu University (Natural Science Edition)*, vol. 32, no. 4, pp. 460–463, 2011, (in Chinese).
- [28] Y. Guo, L. Xu, L. Wu et al., “High temperature performance evaluation of modified asphalt based on multiple stress creep recovery test,” *Journal of Building and Material*. vol. 21, no. 1, pp. 154–159, 2018, (in Chinese).
- [29] A. Asif, A. Naveed, A. Muhammad et al., “Performance evaluation of bone glue-modified asphalt,” *Advances in Materials Science and Engineering*, vol. 2019, p. 13, 2019.
- [30] A. E. Alvarez, E. Ovalles, and A. Epps Martin, “Comparison of asphalt rubber-aggregate and polymer modified asphalt-aggregate systems in terms of surface free energy and energy indices,” *Construction and Building Materials*, vol. 35, no. 10, pp. 385–392, 2012.
- [31] X. Zou, A. Sha, W. Jiang, and X. Huang, “Modification mechanism of high modulus asphalt binders and mixtures performance evaluation,” *Construction and Building Materials*, vol. 90, pp. 53–58, 2015.
- [32] H. Yu, Z. Zhu, Z. Zhang, J. Yu, M. Oeser, and D. Wang, “Recycling waste packaging tape into bituminous mixtures towards enhanced mechanical properties and environmental benefits,” *Journal of Cleaner Production*, vol. 229, 2019.